

AD-A266 730

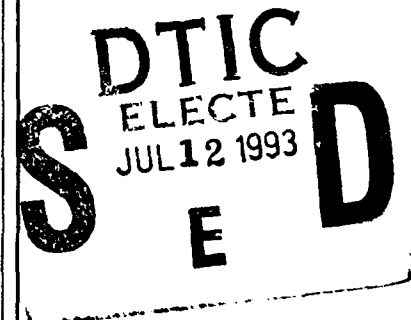


RLE Progress Report

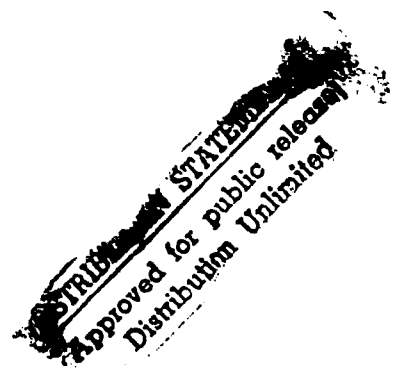
No. 135

January 1 - December 31, 1992

Submitted by

Professor Jonathan Allen
Professor Daniel Kleppner

The RESEARCH LABORATORY of ELECTRONICS
MASSACHUSETTS INSTITUTE of TECHNOLOGY
CAMBRIDGE, MASSACHUSETTS 02139-4307



93-15561



93 7 08 14 3

Accession For	
NTIS	CRA&I <input checked="" type="checkbox"/>
DTIC	TAB <input type="checkbox"/>
Unannounced <input type="checkbox"/>	
Justification	
By	
Distribution /	
Availability Codes	
Dist	Avail and/or Special
A-1	

DTIC QUALITY INSPECTED 8

RLE Progress Report Number 135

Cover and title page:

Graduate student Julie E. Greenberg places the fingers and thumb of her left hand on the mouth and neck of Research Specialist Joyce Manzella to demonstrate use of the Tadoma method of speechreading. This natural method of tactual communication is employed by deaf-blind individuals who have received special training in its use. In Tadoma, the hand of the "receiver" is placed on the face and neck of the "sender" so that the thumb rests lightly on the lips, and the fingers fan out over the face and neck. By monitoring various actions associated with speech production (e.g., lip and jaw movements, airflow at the mouth, and vibrations on the neck), an experienced Tadoma user is able to comprehend conversational speech with a high degree of accuracy. Research on the Tadoma method has provided valuable background information for the development of synthetic tactile devices for the deaf and deaf-blind. See page 293 for a further description of this research which is being carried out in RLE's Sensory Communication Group.

Our special thanks to the following staff members of the RLE Communications Group for their substantial contributions: Mary J. Ziegler for editing and scanning; Mary S. Greene for formatting, proofreading, and preparation of the publications and personnel chapters; Rita C. McKinnon for proofreading, and Markuené A. Sumler for formatting. We also want to thank David W. Foss, Manager of the RLE Computer Facility, for his time and technical assistance.

We thank the faculty, staff, and students of RLE for their generous cooperation.

Editor:	Barbara Passero
Associate Editor:	Mary J. Ziegler
Design and Illustration:	Robert H. Priest
Photography:	John F. Cook
Printer:	DS Graphics, Pepperell, Massachusetts
Typesetting:	This report was produced with IBM's BookMaster Software.

© Massachusetts Institute of Technology. 1993. All rights reserved.
ISSN 0163-9218

REPORT DOCUMENTATION PAGE			Form Approved OMB No. 0704-0188	
<small>Public reporting burden for this collection of information is estimated to average 1 hour per response, including the time for reviewing instructions, searching existing data sources, gathering and maintaining the data needed, and completing and reviewing the collection of information. Send comments regarding this burden estimate or any other aspect of this collection of information, including suggestions for reducing this burden, to Washington Headquarters Services, Directorate for Information Operations and Reports, 1215 Jefferson Davis Highway, Suite 1204, Arlington, VA 22202-4302, and to the Office of Management and Budget, Paperwork Reduction Project (0704-0188), Washington, DC 20503.</small>				
1. AGENCY USE ONLY (Leave blank)		2. REPORT DATE June 1993		3. REPORT TYPE AND DATES COVERED Technical Report
4. TITLE AND SUBTITLE Research Laboratory of Electronics Progress Report No. 135			5. FUNDING NUMBERS DAAL03-92-C-0001	
6. AUTHOR(S) Prof. J. Allen and RLE Principal Investigators				
7. PERFORMING ORGANIZATION NAME(S) AND ADDRESS(ES) Research Laboratory of Electronics Massachusetts Institute of Technology 77 Massachusetts Avenue Cambridge, MA 02139			8. PERFORMING ORGANIZATION REPORT NUMBER	
9. SPONSORING / MONITORING AGENCY NAME(S) AND ADDRESS(ES) U. S. Army Research Office P. O. Box 12211 Research Triangle Park, NC 27709-2211			10. SPONSORING / MONITORING AGENCY REPORT NUMBER ARO 28925.58-EL	
11. SUPPLEMENTARY NOTES The view, opinions and/or findings contained in this report are those of the author(s) and should not be construed as an official Department of the Army position, policy, or decision, unless so designated by other documentation.				
12a. DISTRIBUTION / AVAILABILITY STATEMENT Approved for public release; distribution unlimited.			12b. DISTRIBUTION CODE	
13. ABSTRACT (Maximum 200 words)				
14. SUBJECT TERMS			15. NUMBER OF PAGES	
			16. PRICE CODE	
17. SECURITY CLASSIFICATION OF REPORT UNCLASSIFIED			18. SECURITY CLASSIFICATION OF THIS PAGE UNCLASSIFIED	19. SECURITY CLASSIFICATION OF ABSTRACT UNCLASSIFIED
			20. LIMITATION OF ABSTRACT UL	

Table of Contents

Introduction	1
PART I SOLID STATE PHYSICS, ELECTRONICS AND OPTICS	
Section 1 Materials and Fabrication	
Chapter 1 Heterostructures for High Performance Devices	7
<i>Professor Clifton J. Fonstad, Jr.</i>	
•1.1 Introduction	7
•1.2 MBE-Grown InGaAlAs Laser Diodes for Optical Fiber Communication Applications	7
•1.3 Design and Fabrication of Distributed Feedback (DFB) InGaAlAs Laser Diodes Grown by Molecular Beam Epitaxy	8
•1.4 Feasibility Study of 1.55 μm Intersubband Transition in InGaAs/AlAs Quantum-Well Heterostructures	8
•1.5 Growth and Characterization of High Quality InGaAlAs Multiple Quantum Wells	9
1.6 New Three-Terminal Laser Diodes with Dynamic Control of Gain and Refractive Index	10
1.7 Laser Diode Modeling and Design for Narrow Linewidth Operation	10
1.8 Evaluation of GaAs MESFET VLSI Circuits as Substrates for III-V Heterostructure Epitaxy	11
1.9 Low Temperature Growth of GaAlAs Laser Diodes	12
1.10 Optical Input and Output Circuitry for High Density, High Speed GaAs MESFET-based OEICs	12
1.11 High Density GaAs MESFET-based OEIC Neural Systems	13
1.12 Applications of Resonant Tunneling Diodes in GaAs MESFET VLSI	14
1.13 Investigation of Infrared Intersubband Emission from InGaAs/AlAs/InP Quantum-Well Heterostructures	14
1.14 Infrared Characterization of InGaAs/AlAs/InP Quantum-Well Heterostructures	15
1.15 Analysis of the Symmetry Properties of Quantum Well Subband Energy Levels	15
1.16 Microwave Characterization, Analysis, and Modeling of Emitter-Down Heterojunction Bipolar Transistors	16
1.17 Damage-Free In-Situ UHV Etching and Cleaning of III-V Heterostructures Using Molecular Beams	17
1.18 Publications	17
Chapter 2 High-Frequency InAlAs/InGaAs Metal-Insulator-Doped Semiconductor Field-Effect Transistors (MIDFETs) for Telecommunications	19
<i>Professor Jesús A. del Alamo</i>	
•2.1 Introduction	19
•2.2 Drain-current Injection Technique for the Measurement of Breakdown Voltage	20
•2.3 Physics of Breakdown in InAlAs/n ⁺ -InGaAs HFETs	21
•2.4 Publications	23

Table of Contents

Chapter 3	Chemical Beam Epitaxy of Compound Semiconductors	25
	<i>Professor Leslie A. Kolodziejski</i>	
• 3.1	Introduction	25
• 3.2	Photo-Assisted Metalorganic Molecular Beam Epitaxy of ZnSe Using a Combination of Solid and Gaseous Sources	26
• 3.3	Epitaxial Lattice-Matched III-V Buffer Layers for Wide Bandgap II-VI Visible Sources	29
3.4	Fabrication of Novel Channel Dropping Filters for Wavelength Division Multiplexed Photonic System Applications	30
• 3.5	Publications	30
Chapter 4	Focused Ion Beam Microfabrication	31
	<i>Dr. John Melngailis</i>	
4.1	Introduction	31
4.2	Tunable Gunn Diodes - Optimization for Microwave Applications	31
4.3	Dose Rate Effects in the Implantation of Si in GaAs	32
4.4	Limited Lateral Straggle of Focused-Ion-Beam Implants	32
4.5	Focused Ion Beam Implantation in GaAs for Transistor Optimization	33
4.6	Confined Carrier Distributions in III-V Semiconductors Created by Focused Ion Beams	33
4.7	Focused Ion Beam Lithography for X-ray Mask Making	33
4.8	Focused Ion Beam Induced Deposition of Copper	34
4.9	Focused Ion Beam Induced Deposition and Ion Milling as a Function of Angle of Ion Incidence	34
4.10	Publications	35
Section 2	Quantum-Effect Devices	
Chapter 1	Statistical Mechanics of Quantum Dots	39
	<i>Professor Boris L. Altshuler</i>	
• 1.1	Project Description	39
• 1.2	Publications	40
Chapter 2	Single Electron Transistors	41
	<i>Professor Marc A. Kastner</i>	
• 2.1	Project Description	41
• 2.2	Publications	44
Chapter 3	Differential Resistance Through a Quantum Dot: Signature of Kondo Correlation ..	45
	<i>Professor Patrick A. Lee</i>	
• 3.1	Project Description	45
• 3.2	Publications	46
Chapter 4	Submicron and Nanometer Structures Technology and Research	47
	<i>Professor Henry I. Smith</i>	
4.1	Submicron Structures Laboratory	47
• 4.2	X-Ray Nanolithography	47
4.3	Improved Mask Technology for X-Ray Lithography	48

• 4.4	Improved Scanning Electron Beam Lithography	50
• 4.5	A High-Precision Mask Alignment Scheme	51
• 4.6	Achromatic Holographic Lithography	53
4.7	Fabrication of T-gate Devices using X-ray Lithography	53
• 4.8	Tenth-micron MOSFET Device Technology	54
4.9	Studies of Coulomb Charging Effects in Semiconductor Nanostructures	57
4.10	Study of Quasi-One-Dimensional Wires in GaAs/AlGaAs Modulation Doped Field-Effect Transistors	58
4.11	Planar-Resonant-Tunneling Field-Effect Transistors PRESTFET)	59
4.12	Dual Electron Waveguide Device Fabricated Using X-ray Lithography	61
• 4.13	Far-Infrared Spectroscopy of Arrays of Quantum Dots and Wires	61
4.14	Ridge-Grating Distributed-Feedback Lasers Fabricated by X-Ray Lithography	62
4.15	Channel-Dropping Filters Fabricated by X-Ray Lithography	63
4.16	Novel Superconducting Tunneling Structures	63
• 4.17	Submicrometer-Period Transmission Gratings for X-ray and Atom-Beam Spectroscopy and Interferometry	65
4.18	High-Dispersion, High-Efficiency Transmission Gratings for Astrophysical X-ray Spectroscopy	65
4.19	Submicron-Thickness X-ray Window Technology	65
• 4.20	GaAs Epitaxy on Sawtooth-Patterned Silicon	66
• 4.21	Publications	66

Section 3 Optics and Devices

Chapter 1 Optics and Quantum Electronics 71

*Professor Hermann A. Haus, Professor Erich P. Ippen, Professor James G. Fujimoto,
Professor Peter L. Hagelstein, Dr. Santanu Basu*

• 1.1	Additive Pulse Modelocking	71
• 1.2	Fiber Ring Laser	72
1.3	Long Distance Fiber Communications	72
1.4	Squeezing	73
1.5	Integrated Optics Components: the Channel Dropping Filter	74
1.6	Tunable Semiconductor Lasers	74
• 1.7	Nonlinear Properties of InGaAsP Optical Amplifiers	75
1.8	Ultrafast Index Nonlinearities in Active Waveguides	76
1.9	Femtosecond Pulse Generation and Amplification in F-center Systems	77
• 1.10	Coherent Phonons In Electronic Materials	77
• 1.11	Femtosecond Studies of Fullerenes	78
• 1.12	Ultrashort Pulse Generation in Solid State Lasers	79
• 1.13	Studies of Ultrafast Phenomena in Materials	81
• 1.14	Time Domain Diagnostics of Waveguide Devices	83
1.15	Laser Medicine	85
1.16	Observation of Gain in Ni-like Nb	90
1.17	Pump Pulse Length	92
1.18	End-pumped X-ray Lasers	93
1.19	The Kinetics and Hydrodynamics of Laser-Generated Plasmas	94
1.20	An Analytical Solution of the 2D Exciton-Phonon Matrix Element	96
1.21	Quantum Dot Diode Lasers	97
1.22	Coherent Fusion Theory	98
1.23	Deuterated Metal Experiments	100

Table of Contents

Chapter 2	Optical Propagation and Communication	103
	<i>Professor Jeffrey H. Shapiro, Dr. Robert H. Rediker, Dr. Ngai C. Wong</i>	
2.1	Introduction	103
2.2	Squeezed States of Light	103
2.3	Optical Frequency Division and Synthesis	105
2.4	Fiber-Coupled External-Cavity Semiconductor High Power Laser	106
2.5	Analog Processing of Optical Wavefronts Using Integrated Guided-Wave Optics	107
Chapter 3	High-Frequency (> 100 GHz) Electronic Devices	109
	<i>Professor Qing Hu</i>	
3.1	Facility for Millimeter-wave and THz Frequencies	109
3.2	Millimeter-wave and Infrared Superconducting Focal-plane Receiver Arrays	109
3.3	Photon-assisted Quantum Transport in Quantum Point Contacts	110
3.4	High-Tc Superconducting Josephson Devices	112
3.5	Far-infrared (THz) Lasers Using Multiple Quantum Wells	114
3.6	Publications	116
Section 4	Surfaces and Interfaces	
Chapter 1	Statistical Mechanics of Surface Systems and Quantum-Correlated Systems	119
	<i>Professor A. Nihat Berker</i>	
• 1.1	Introduction	119
• 1.2	Renormalization-Group Approach to Electronic Systems	119
• 1.3	Suzuki-Trotter Approach to Electronic Systems	120
• 1.4	Phase Diagrams of Semiconductor Alloys	120
• 1.5	Renormalization-Group Theory of an Internal Critical Endpoint Structure	121
• 1.6	Phase Diagrams of the Ising Model on the Square Lattice with Crossed Diagonal Bonds	121
• 1.7	Publications	121
Chapter 2	Synchrotron X-Ray Studies of Surface Disordering	123
	<i>Professor Robert J. Birgeneau</i>	
• 2.1	Introduction	123
• 2.2	Metal Surface Studies	123
• 2.3	Semiconductor Surface Studies	124
• 2.4	Model Surface Overlayers	124
Chapter 3	Chemical Reaction Dynamics at Surfaces	127
	<i>Professor Sylvia T. Ceyer</i>	
• 3.1	A New Mechanism for Dissociative Chemisorption on Si: Atom Abstraction	127
3.2	New Mechanisms for Surface Processes	128
3.3	The Chemistry of Bulk Hydrogen	129

Chapter 4	Semiconductor Surface Studies	131
	<i>Professor John D. Joannopoulos</i>	
• 4.1	Introduction	131
• 4.2	Surface Reconstruction	131
• 4.3	Computation at Large Length Scales	133
• 4.4	Publications	135
Chapter 5	Epitaxy and Step Structures on Semiconductor Surfaces	137
	<i>Professor Simon G.J. Mochrie</i>	
• 5.1	Structure and Phase Behavior of the Si(113) Surface	137
• 5.2	Publications	140
PART II	APPLIED PHYSICS	
Section 1	Atomic, Molecular and Optical Physics	
Chapter 1	Quantum Optics and Photonics	145
	<i>Professor Shaoul Ezekiel</i>	
1.1	Optical Data Storage with Raman Excited Spin Echoes	145
1.2	Phase-dependent Velocity Selective Coherent Population Trapping in a Folded Three-level Λ System under Standing Wave Excitation	146
1.3	Continuous Pol-Grad Pre-Cooling for Loading a Subrecoil Temperature Trap	148
1.4	Raman Gain in a Λ Three-level System with Closely Spaced Ground States	149
1.5	Brillouin Laser Fiberoptic Gyroscope	151
Chapter 2	Basic Atomic Physics	155
	<i>Professor Daniel Kleppner, Professor David E. Pritchard</i>	
• 2.1	Millimeter-Wave Frequency Measurement of the Rydberg Constant	155
2.2	The Diamagnetic Rydberg Atom	158
• 2.3	Precision Mass Spectroscopy of Ions	161
• 2.4	Atom Interferometry	163
Chapter 3	Neutrality of Molecules by the Pulsed Gas Flow Method	171
	<i>Professor John G. King</i>	
3.1	Introduction	171
3.2	Project Description	171
Section 2	Plasma Physics	
Chapter 1	Plasma Dynamics	175
	<i>Professor George Bekefi, Professor Abraham Bers, Professor Bruno Coppi, Professor Miklos Porkolab, Professor Jonathan S. Wurtele, Dr. Ronald C. Englade, Dr. Stefano Migliuolo, Dr. Abhay K. Ram, Dr. Barrett Rogers, Dr. Linda E. Sugiyama</i>	
1.1	Relativistic Electron Beams	175
1.2	Plasma Wave Interactions - RF Heating And Current Generation	181
1.3	Physics of Thermonuclear Plasmas	192
1.4	Versator II Tokamak Research Program	198

Table of Contents

Section 3 Electromagnetics

Chapter 1	Electromagnetic Wave Theory and Applications	203
	<i>Professor Jin Au Kong, Professor Terry Orlando, Dr. Robert T. Shin, Dr. Y. Eric Yang</i>	
1.1	Remote Sensing of Earth Terrain	203
• 1.2	Electromagnetic Waves in Multilayer Media	205
1.3	Aircraft Landing Systems: ILS, MLS, GPS, and SVS	207
1.4	Publications	208
1.5	Superconducting Transmission Lines	209

Section 4 Radio Astronomy

Chapter 1	Radio Astronomy	215
	<i>Professor Bernard F. Burke, Professor David H. Staelin, Professor Jacqueline N. Hewitt, Dr. Philip W. Rosenkranz</i>	
1.1	Extragalactic Radio Source Studies	215
1.2	The Study of Exoplanets	216
1.3	Studies of Gravitational Lenses	217
1.4	Radio Interferometry of Nearby dMe Stars	218
1.5	Algorithms for Advanced Microwave Sounding Unit Operational Use	218
1.6	Earth Observing System: Advanced Microwave Sounding Unit	219
1.7	High-Resolution Passive Microwave Imaging of Atmospheric Structure	219
1.8	Rapid Precision Net-Form Manufacturing	219
1.9	Conformal Experiment Design	220
1.10	Recognition of Natural Nearly Repetitive Signals	221

PART III SYSTEMS AND SIGNALS

Section 1 Computer-Aided Design

Chapter 1	Custom Integrated Circuits	227
	<i>Professor Jonathan Allen, Professor John L. Wyatt, Jr., Professor Jacob White, Professor Srinivas Devadas</i>	
1.1	Custom Integrated Circuits	227
1.2	Analog VLSI Systems for Integrated Image Acquisition and Early Vision Processing	229
1.3	Parallel Algorithms for Device Simulation	238
1.4	Numerical Simulation of Short Channel MOS Devices	239
1.5	Circuit Simulation Algorithms	239
1.6	Parallel Circuit Simulation Algorithms	240
1.7	Microelectromechanical CAD (MEMCAD)	240
1.8	Numerical Techniques for Simulating Josephson Junction Arrays	241
1.9	Efficient 3-D Interconnect Analysis	241
1.10	Techniques for Logic Synthesis, Formal Verification and Testing	242
Chapter 2	Computer-Integrated Design and Manufacture of Integrated Circuits	247
	<i>Professor Donald E. Troxel</i>	
2.1	Introduction	247
2.2	Principal Objectives	248
2.3	Principal Accomplishments	248

2.4	Process Flow Representation	250
2.5	Technology CAD Framework	251
2.6	Publications	252

Section 2 Digital Signal Processing

Chapter 1 Digital Signal Processing Research Program 255

Professor Alan V. Oppenheim, Professor Arthur B. Baggeroer, Professor Gregory W. Wornell

1.1	Introduction	255
1.2	Oceanographic Signal Processing	256
1.3	Segmentation of Polarimetric Synthetic Aperture Radar Images Using Markov Random Field Techniques	256
1.4	Signal Synthesis from Marine Mammal Communications	257
1.5	Analysis, Synthesis, and Applications of Synchronized Chaotic Systems	257
1.6	High-Resolution Direction Finding for Multidimensional Scenarios	258
1.7	Signal Processing Applications of Chaotic Dynamical Systems	258
1.8	Wavelet-Based Representation and Algorithms for Generalized Fractal Signals	259
1.9	Acoustic Tomography through Matched Field Processing	259
1.10	Binary Data Transmission and Detection with Chaotic Signals	260
1.11	Real-Time Active Noise Cancellation	260
1.12	State and Parameter Estimation with Chaotic Systems	261
1.13	Nonlinear Models for Signal Processing	261
1.14	Model-Based Analysis of Music	262
1.15	Active Noise Cancellation	262

Chapter 2 Advanced Television and Signal Processing Program 263

Professor Jae S. Lim

2.1	Introduction	263
2.2	Advanced Television Research Program	263
2.3	Speech Signal Processing	267

Chapter 3 Combined Source and Channel Coding for High-Definition Television 269

Professor William F. Schreiber

3.1	Project Description	269
-----	---------------------------	-----

PART IV BIOELECTRONICS

Section 1 Genetic Analysis

Chapter 1 Genosensor Technology Development 275

Dr. Mark Hollis

1.1	Introduction	275
1.2	Development of Genosensor Arrays for DNA Decoding	275
1.3	Microdetection Technology for Automated DNA Sequencing	276

Table of Contents

PART V LANGUAGE, SPEECH AND HEARING

Section 1 Speech Communication

Chapter 1	Speech Communication	281
	<i>Professor Kenneth N. Stevens, Dr. Joseph S. Perkell, Dr. Stefanie Shattuck-Hufnagel</i>	
1.1	Introduction	282
1.2	Speech Production Planning	282
1.3	Studies of Speech Production	283
1.4	Speech Research Related to Special Populations	284
1.5	Models for Lexical Representation and Lexical Access	287
1.6	Studies of the Acoustics, Perception, and Modeling of Speech Sounds	287
1.7	Development of Computer and Data Processing Facilities	288
1.8	Publications	288

Section 2 Sensory Communication

Chapter 1	Sensory Communication	293
	<i>Professor Louis D. Braida, Nathaniel I. Durlach, Dr. William M. Rabinowitz, Dr. Charlotte M. Reed, Dr. Mandayam A. Srinivasan, Dr. Patrick M. Zurek</i>	
1.1	Introduction	293
1.2	Hearing Aid Research	293
1.3	Multimicrophone Hearing Aids	302
1.4	Cochlear Prostheses	303
1.5	Binaural Hearing	304
1.6	Clinical Applications of Binaural Hearing	304
1.7	Tactile Communication of Speech	304
1.8	Super-Auditory Localization for Improved Human-Machine Interfaces	306
1.9	Research on Reduced-Capability Human Hands	307
1.10	Mechanistic Modeling of Primate Fingerpad	309
1.11	Biomechanics of Skin-Object Contact	311
1.12	Human and Robot Hands: Mechanics, Sensorimotor Functions and Cognition	313
1.13	Publications	314

Section 3 Auditory Physiology

Chapter 1	Signal Transmission in the Auditory System	319
	<i>Professor Lawrence S. Frishkopf, Professor Nelson Y.S. Kiang, Professor William T. Peake, Professor William M. Siebert, Professor Thomas F. Weiss, Dr. Bertrand Delgutte, Dr. Donald K. Eddington, Dr. Dennis M. Freeman, Dr. John J. Guinan, Jr., Dr. John J. Rosowski</i>	
1.1	Introduction	319
1.2	Signal Transmission in the External and Middle Ear	319
1.3	Cochlear Mechanisms	321
1.4	Electrical Stimulation of the Auditory Nerve	324
1.5	Interactions of Middle-Ear Muscles and Olivocochlear Efferents	324
1.6	Cochlear Efferent System	325
1.7	Cochlear Implants	326

Section 4 Linguistics

Chapter 1	Linguistics	331
	<i>Professor Noam Chomsky, Professor Morris Halle</i>	
1.1	Introduction	331
1.2	Abstracts of Doctoral Dissertations	331

APPENDICES

Appendix A	RLE Publications and Papers Presented	339
A.1	Meeting Papers	339
A.2	Journal Articles	350
A.3	Books/Chapters in Books	360
A.4	RLE Publications	361
A.5	RLE Theses	362
A.6	Miscellaneous	364
Appendix B	Current RLE Personnel	365
Appendix C	Milestones	371
C.1	New Faculty and Staff	371
C.2	Promotions	371
C.3	Chair Appointments	371
C.4	Awards and Honors	371
Appendix D	RLE Research Support Index	373

Project Staff and Subject Index	377
--	------------

Introduction

The Research Laboratory of Electronics

The Research Laboratory of Electronics (RLE) was established in 1946 as the Institute's first interdepartmental laboratory. Originally organized under the joint sponsorship of the Departments of Physics and Electrical Engineering, RLE has broadened its interests to cover a wide range of research.

The RLE environment provides both the freedom of action essential in an academic institution and the availability of large-scale laboratory facilities and services required by researchers. RLE's interdisciplinary setting offers many opportunities for creative and collaborative research. By fostering this powerful combination of research and education, RLE effectively penetrates beyond the horizon of new ideas and information.

RLE Progress Report

RLE Progress Report Number 135 describes research programs at RLE for the period January 1 through December 31, 1992. Each chapter of the *Progress Report* contains both a statement of research objectives and a summary of research efforts for research projects listed. Faculty, research staff, students and others who participated in these projects are identified at the beginning of each project, along with sources of funding.

There are four appendices at the end of the report: Appendix A is a bibliography of RLE publications and papers presented by RLE staff during 1992; Appendix B is a roster of current RLE staff; Appendix C is a list of RLE faculty and staff milestones and honors received during 1992; and Appendix D is an index of RLE sponsors. In addition, the Project Staff and Subject Index provides access to the information in this report.

RLE Progress Report Number 135 was produced by the RLE Communications Office. Further inquiries may be addressed to:

Research Laboratory of Electronics
Room 36-412
Massachusetts Institute of Technology
Cambridge, Massachusetts 02139-4307
Tel. (617) 253-2566
Fax (617) 258-7864

Part I Solid State Physics, Electronics and Optics

Section 1 Materials and Fabrication

Section 2 Quantum-Effect Devices

Section 3 Optics and Devices

Section 4 Surfaces and Interfaces

Section 1 Materials and Fabrication

Chapter 1 Heterostructures for High Performance Devices

Chapter 2 High-Frequency InAlAs/InGaAs Metal-Insulator-Doped Semiconductor Field-Effect Transistors (MIDFETs) for Telecommunications

Chapter 3 Chemical Beam Epitaxy of Compound Semiconductors

Chapter 4 Focused Ion Beam Microfabrication

Chapter 1. Heterostructures for High Performance Devices

Academic and Research Staff

Professor Clifton G. Fonstad, Jr.

Visiting Scientists and Research Affiliates

Yuzo Hirayama,¹ Jae-Jin Lee,² Tadatsugu Minami,³ Sheila Prasad⁴

Graduate Students

Rajni J. Aggarwal, Woo-Young Choi, Isako Hoshino, Paul S. Martin, Lung-Han Peng, Yakov Royter, Krishna V. Shenoy, Jurgen H. Smet

Technical and Support Staff

Karen Chenausky, Charmaine A. Cudjoe-Flanders, Angela R. Odoardi, Richard R. Perilli

1.1 Introduction

The broad objective of our research effort is to develop III-V quantum heterostructures for high performance electronic, optoelectronic, and photonic devices for applications in high speed optical communications and signal processing. To this end, we are developing: (1) new, higher performance materials systems including InP-based InGaAlAs heterostructures and <111> oriented strained layer superlattices; (2) novel approaches to integrate laser diodes on VLSI-level electronic integrated circuits; (3) a new family of quantum-well-base, tunnel-barrier n-n-n transistors and near- and far-infrared optoelectronic devices; and (4) new damage-free in situ processing techniques for fabricating advanced quantum structure and embedded heterostructures.

The following sections describe our progress during the past year in the above research areas. Our group works closely with Professors Hermann A. Haus, Erich P. Ippen, and James G. Fujimoto to develop the optical device application, characterization, and modeling aspects of this program, with Professor Henry Smith to develop a novel distributed feedback laser structure, and with Professor Sylvia T. Ceyer to develop new in situ processing techniques.

1.2 MBE-Grown InGaAlAs Laser Diodes for Optical Fiber Communication Applications

Sponsors

DARPA/NCIPT
Joint Services Electronics Program
Contract DAAL03-92-C-0001

Project Staff

Woo-Young Choi, Professor Clifton G. Fonstad, Jr.

Semiconductor laser diodes with the lasing wavelength of 1.3 to 1.5 μm are an essential element of long-distance optical fiber communication systems that have revolutionized modern telecommunication networks. The material system of InGaAsP is most often used for laser diodes for such applications. We are investigating the feasibility of alternate material system of InGaAlAs for the same application.

The main advantage of InGaAlAs over InGaAsP is that quantum wells based on InGaAlAs have larger conduction band and smaller valence band offsets. For high speed modulation the hole transport can be a limiting factor; over-confinement of holes in

¹ Toshiba Corporation Ltd., Kawasaki, Japan.

² Electronics and Telecommunications Research Institute (ETRI), Daejeon, Korea.

³ Kanagawa Institute, Ishikawa, Japan.

⁴ Northeastern University, Boston, Massachusetts.

InGaAsP quantum wells is undesirable. The other advantage of this material is that, unlike InGaAsP, InGaAlAs can be successfully grown by solid source MBE without toxic gases. This "environmental" factor will undoubtedly become increasingly important as the price of disposing of environment pollutants grows.

The advantages listed above are not realized without a few challenges. First, the high percentage of aluminum in the device structure can trap impurities that can reduce the optical quality of the resulting materials. To reduce this possibility as much as possible, we have investigated the optical quality of materials obtained under various growth conditions and have determined optimal growth conditions for each device structure desired. Although we plan to do more growth-related studies, so far we have demonstrated device performances of InGaAlAs quantum well laser diodes that are comparable to those produced with InGaAsP.

Second, it is essential that laser devices for long-distance optical fiber communication applications operate with single longitudinal modes. Since InGaAlAs is not suitable for regrowth, techniques that are commonly used to achieve single mode selection cannot be applied to MBE-grown InGaAlAs. We are developing a novel ridge-grating distributed feedback (DFB) process in which gratings are made on the side walls of ridges, removing the need for regrowth (see following section). For this process, we are collaborating with Professor Henry I. Smith's group at MIT since the x-ray lithography technique he and his colleagues have developed are particularly applicable for this process.

In addition to the above issues, we are also investigating the optimal use of strained multiple-quantum wells for the laser diode applications and reliable ridge waveguide processing techniques.

1.3 Design and Fabrication of Distributed Feedback (DFB) InGaAlAs Laser Diodes Grown by Molecular Beam Epitaxy

Sponsors

DARPA/NCIPT
Joint Services Electronics Program
Contract DAAL03-92-C-0001

Project Staff

Woo-Young Choi, Professor Clifton G. Fonstad, Jr.
in collaboration with Professor Henry I. Smith

It is essential that laser diodes for optical fiber communications applications operate with a single oscillation frequency. Typically, schemes of distributed feedback (DFB) or distributed Bragg reflector (DBR) are used in which gratings above or below the active layer (DFB) or outside the active layer (DBR) perform the act of frequency selection. To make such a device structure, either epitaxial growth is initiated on a corrugated substrate or regrowth is performed on the epitaxial material onto which gratings have been formed.

In this project, we are pursuing a DFB device structure in which gratings are formed entirely after complete epitaxial growth. Our motivation for this approach stems from the fact that we are working on laser diodes grown by conventional solid-source molecular beam epitaxy (MBE) technology. Due to its growth kinetics, successful MBE growth on the corrugated surface is very difficult. The present structure is also more suitable for use with the InGaAlAs system (see preceding section).

We have proposed a ridge stripe structure in which gratings are made on the side walls of the ridge as well as on the bottom channels next to the ridge. According to our initial calculation, there is enough coupling between the optical wave and gratings to result in the single mode selection.

To realize such a device structure, we are collaborating with Professor Smith's group and utilizing its x-ray lithography technology. Currently, we are in the process of combining x-ray lithography technology with ridge-strip laser diode fabrication technology.

1.4 Feasibility Study of 1.55 μm Intersubband Transition in InGaAs/AlAs Quantum-Well Heterostructures

Sponsors

Joint Services Electronics Program
Contract DAAL03-92-C-0001
National Science Foundation
Toshiba Corporation Ltd.

Project Staff

Yuzo Hirayama, Jurgen H. Smet, Professor Clifton G. Fonstad, Jr. in collaboration with Professor Erich P. Ippen and Professor Qing Hu

Realization of a 1.55 μm intersubband transition using InGaAs/AlAs quantum wells is an interesting topic for basic physics as well as for its potential applications. Very fast relaxation times and large optical nonlinearities, which are useful for

advanced photonic devices such as a high speed photonic switch, are expected. A wavelength of $1.55\text{ }\mu\text{m}$ is most suitable for optical communication systems. We plan to study carrier dynamics in these quantum well structures using femtosecond pump and probe techniques.

Structures in which the energy separation between the first and fourth subband corresponds to a wavelength of $1.55\text{ }\mu\text{m}$ were designed and fabricated on InP substrates by MBE techniques. Strain compensated structures were also fabricated. To reveal subband structures in these quantum well samples, a conventional optical absorption measurement system and a newly developed photomodulated transmission measurement system were built. The latter system is basically a modulation spectroscopy method, having a high signal-to-noise ratio. Therefore, it is suitable for measurements of very narrow single quantum well structures.

A careful study of InGaAs/AlAs quantum well samples revealed the following facts: (1) Samples show many unidentified optical signals unless thick InGaAs or InGaAlAs buffer layers are used. (2) Dislocations due to strain relaxation are observed unless growth is performed at low-substrate temperature. (3) Transitions from the first to the second subband were observed. However, transitions from the first to the fourth subband were too weak to be detected. (4) Peak positions in the transmission spectra are difficult to predict so that simple effective mass approximation cannot be applied. A modified theory including other effects such as band bending or electron-electron exchange interactions cannot account for the results.

To realize a $1.55\text{ }\mu\text{m}$ intersubband transition, we have redesigned our quantum well structure using our previous experimental data. First observation of $1.55\text{ }\mu\text{m}$ intersubband transition will be in the near future. Theoretical work is also on going. To measure time resolved optical spectra, a new pump and probe system using white probe light is being built. In this system, strong optical pulses which are amplified in a NaCl color center crystal go into a nonlinear material and generate white light. It is expected that, with the use of this setup, the carrier dynamics in these new quantum well structures will become clear.

1.5 Growth and Characterization of High Quality InGaAlAs Multiple Quantum Wells

Sponsor

Joint Services Electronics Program
Contract DAAL03-92-C-0001

Project Staff

Woo-Young Choi, Yuzo Hirayama, Professor Clifton G. Fonstad, Jr.

Use of strained layers in heterostructure device research is one of the most significant developments in the past decade. Strained layers are now routinely utilized for enhancing the performance of optical and electrical devices, yielding lower threshold currents and faster modulation speeds for quantum well laser diodes and higher electron mobilities for heterostructure FET devices. However, this enhanced performance can be obtained only if the strained layers do not have any dislocation caused by strain relaxation. Consequently, understanding the strain relaxation mechanism and a careful control of epitaxial growth parameters are required for successful utilization of strained layers in heterostructure devices. With this in mind, we have performed intensive studies in which MBE-grown InGaAlAs strained multiple-quantum-wells on InP are characterized by double crystal x-ray diffraction, transmission, and photoluminescence measurements. The strained quantum wells under study have great potential for applications in laser diode and modulator devices.

Because the wavelength of x-rays is shorter than the lattice constants of materials being studied and the high beam quality obtained in the double crystal configuration, double crystal x-ray diffraction is the best characterization method for obtaining structural information of strained quantum wells. The degree of strain relaxation can be qualitatively determined by the sharpness of satellite peaks caused by the well and barrier periodicity. For coherent strained layers without major strain relaxation, we have developed a systematic method of determining layer composition and thickness in strained multiple quantum wells based on the amount of satellite peak separation and other growth information.

From the room temperature transmission measurements on strained multiple-quantum-well samples, we routinely observe excitonic transitions, indicating the high quality of strained quantum wells that are achieved in our lab. In addition, from the careful analysis of the spectra, we have estimated important parameters such as exciton binding energy and radius, in-plane reduced effective mass, etc.

From careful analyses of photoluminescence spectra, we have determined qualitative differences in the nature of luminescence peaks that are due to strain-relaxed quantum wells, bound or free excitons, and free carriers. These identifications and their characteristic dependence on temperature have enabled us to correctly interpret the photoluminescence spectra.

These characterization methods are exciting research techniques from which insight into the physics of strained multiple quantum wells can be obtained. Furthermore, they allow us to make an easy and early determination of quality of strained multiple quantum wells in actual device structures and provide material parameters that are of great importance in designing and analyzing devices.

1.6 New Three-Terminal Laser Diodes with Dynamic Control of Gain and Refractive Index

Sponsor

DARPA/NCIPT

Project Staff

Paul S. Martin, Professor Clifton G. Fonstad, Jr. in collaboration with Professor Hermann A. Haus

We are investigating a new class of devices in which the active region consists of two quantum wells with different widths and therefore different optical gain profiles. We call these devices independently addressable asymmetric quantum well laser diodes (IAADQW - LDs). By designing structures in which the current injection into these two quantum wells can be independently controlled, we are gaining a new, as yet unutilized, degree of freedom in controlling light output from the device.

Wavelength division multiplexing (WDM) is an area in which we believe this new class of devices can have an important impact. An alternative approach to a single very fast laser diode is to use many slower, and thus simpler, less expensive and more reliable laser diodes all transmitting down the same fiber but at slightly different wavelengths. Since the low loss region of currently installed silica fiber is very broad, this technique has the potential to dramatically increase single fiber data rates into the terabit per second range for the installed fiber base.

Essential for realizing practical WDM systems are dynamically tunable laser diodes for adjusting the wavelength of each signal channel and narrow linewidth channel. Simulations we have done show that InP-based IAADQW-LDs can have tuning ranges in excess of 20 nm (2 THz) within the 1.5 μ m low-loss window of Silica fiber. If realized, this would be a significant improvement over current multisection distributed Bragg reflector (DBR) type lasers which typically have usable tuning ranges of only a few nm. Also important for practical applications is the change in output power as the LD is tuned. Since the wavelength of the IAADQW is determined only by the ratio of the currents injected into the two active regions, the magnitude of current injection can be used to control power output, making it possible to keep power output constant over the entire tuning range. The ability to electrically tune output wavelength over a broad range while keeping output power constant makes the IAADQW device ideal for WDM.

To implement the IAADQW-LD we have developed a self-aligned process that uses a single metalization layer to define the ridge waveguide through SiCl_4 -based reactive ion etching (RIE). This layer defines the current injection region for the lower quantum well through H^+ ion implantation and contacts the upper quantum well. One subsequent photolithography step and metalization will then complete processing for the device.

Other applications for these devices include pure FM laser diodes with reduced AM noise, two-wavelength integrated but independently controlled laser diodes, and other non-laser devices like tunable narrow bandwidth filters and light modulators.

1.7 Laser Diode Modeling and Design for Narrow Linewidth Operation

Sponsor

Charles S. Draper Laboratories

Project Staff

Yakov Royter, Professor Clifton G. Fonstad, Jr. in collaboration with J.H. Hopps⁵

Many of the current laser applications require narrow linewidth output characteristics. Unfortunately, semiconductor lasers, possessing such advantages as small size, direct modulation capa-

⁵ Charles S. Draper Laboratories, Cambridge, Massachusetts.

bility, and integrability with other optical and electronic devices, have broad linewidths in comparison to almost all other kinds of lasers. The relatively broad linewidths are due to the low Q of the cavity and to the intrinsic effects specific to the semiconductor gain medium. Since most of the linewidth reduction methods have involved the increase of the cavity Q , our goal was to investigate and help in the reduction of intrinsic linewidth broadening effects. Reduction of these effects, in conjunction with the increase of the cavity Q , would produce semiconductor lasers with narrowest possible linewidths.

The first step in our research was to investigate theoretically the intrinsic linewidth broadening effects. In particular, we concentrate on the alpha parameter, the largest intrinsic linewidth broadening factor, which describes the coupling of gain and refractive index fluctuations in the gain medium via carrier density fluctuations. For this purpose, we calculated the carrier energy bands of the active region semiconductor material, using the $k \cdot p$ approximation. From the energy bands, we obtained gain and refractive index profiles and linewidth broadening parameter.

To test our models, we plan to compare the calculated laser characteristics, such as threshold current, gain, refractive index and linewidth, with experimental results obtained from measurements done in our laboratory, as well as those quoted in the literature. Measurements of the CW semiconductor laser subthreshold spectrum are being conducted from which gain profile can be deduced. The shifts in the mode spectrum due to the change in the pumping provide information on the gain-refractive-index coupling, and thus the alpha parameter. To reduce the effect of thermal variations, gain measurements of pulsed laser spectra will also be done. Finally, from the comparison between experimental and theoretical results, we will attempt to establish systematic ways of obtaining parameters for our semiconductor laser models.

As an extension of our modeling efforts, we will also investigate strain layer quantum well lasers. Furthermore, we intend to improve our models by including calculations of energy dependent carrier lifetimes, different loss mechanisms, and other sources of linewidth broadening.

1.8 Evaluation of GaAs MESFET VLSI Circuits as Substrates for III-V Heterostructure Epitaxy

Sponsors

DARPA/NCIPT
Hertz Foundation Fellowship
Vitesse Semiconductor

Project Staff

Krishna V. Shenoy, Professor Clifton G. Fonstad, Jr. in collaboration with J. Mikkelsen⁶

Commercially available VLSI GaAs metal semiconductor field effect transistors (MESFETs) are potentially very useful in optoelectronic integrated circuits (OEICs). Direct epitaxy of photonic devices on fully processed MESFET circuitry is a viable approach to realizing monolithic OEICs if MESFETs are thermally stable at elevated temperatures. Ohmic contact and Schottky gate degradation, caused by thermally induced interdiffusion to the source or drain and channel, respectively, are the major modes of failure in GaAs MESFETs with Au metallization. In this research, we are examining the performance of commercial refractory-metal VLSI GaAs MESFETs after 3 h, high-temperature anneals, which duplicate the molecular beam epitaxy (MBE) growth sequence for an in-plane surface-emitting laser (IPSEL).

Vitesse Semiconductor Corporation HGaAs2 technology, a self-aligned VLSI GaAs MESFET process with tungsten-based refractory-metal Schottky gates, nickel-based refractory-metal ohmic contacts, and aluminum interconnection metallization, was selected for this study. Enhancement mode MESFETs (EFETs), depletion mode MESFETs (DFETs), and transmission line model (TLM) structures were selected from standard production process control monitor test bars. Partially processed wafers (with neither aluminum interconnection nor passivation dielectric deposited), as well as fully processed wafers, were tested.

MESFET and TLM parameter trends as the maximum anneal temperature was increased from 400°C to 600°C are as follows: (1) The partially processed wafer trends are similar to the fully processed wafer trends but are less pronounced. (2) EFET and DFET parameter trends are in agreement. (3) V_T , Schottky diode ideality, Schottky barrier voltage, and R_{SH} show no significant trends while I_{B^*} and g_m decrease, and R_{GS} increases. (4)

⁶ Vitesse Semiconductor, Camarillo, California.

g_m and I_{DS} decrease significantly above $525^\circ\text{C} \pm 10^\circ\text{C}$; R_{GS} increases significantly above $525^\circ\text{C} \pm 10^\circ\text{C}$. Most significantly, Schottky gate and ohmic contact resistance degradation modes are absent. The increase in R_{GS} , which is the sum of the Schottky gate resistance, channel resistance, source implant sheet resistance, and ohmic contact resistance, can be attributed to an increase in the channel resistance component, and is responsible for the apparent decreases in g_m and I_{DS} .

These results indicate that if we can limit the temperature during the major portion of a growth sequence to 525°C or below, we will be able to grow heterostructures on pre-processed GaAs integrated circuits without effecting the performance of the underlying circuitry, and therefore not requiring any modification of existing design rules and circuit simulation models.

1.9 Low Temperature Growth of GaAlAs Laser Diodes

Sponsors

DARPA/NCIPT
GTE Laboratories
Hertz Foundation Fellowship
National Science Foundation Fellowship
Vitesse Semiconductor

Project Staff

Krishna V. Shenoy, Professor Clifton G. Fonstad, Jr. in collaboration with J. Mikkelsen⁶ and B. Elman⁷

Direct epitaxy of photonic devices on fully processed GaAs VLSI circuits to produce OEICs will require that lasers are grown at 525°C or less. The effect of lowered temperature AlGaAs epitaxial quality on laser performance is currently under investigation. Because conventional AlGaAs is grown at 700°C , which violates the thermal constraint imposed by the electronic circuitry.

To investigate lowered molecular beam epitaxy (MBE) growth temperatures on laser performance, single quantum well, step-confinement, strained-layer (Al,Ga,In)As laser diode heterostructures were optimized for growth at low temperatures. Low Al mole fraction cladding layers ($1.4\mu\text{m}$ of $\text{Al}_{0.22}\text{Ga}_{0.78}\text{As}$) were used to minimize oxygen incorporation at heterojunction interfaces and allowed ridge waveguide lasers to be fabricated using a

selective succinic acid etch and an AlAs etch-stop layer. 200 nm GaAs waveguide layers were used to maximize the optical confinement factor and optimize the quantum well-to-AlGaAs cladding layer separation which is critical with lowered temperature AlGaAs.

A 60 $\text{In}_{0.2}\text{Ga}_{0.8}\text{As}$ active region was used to minimize the threshold current; the corresponding emission is nominally at $0.98\mu\text{m}$. A strained layer quantum well active region yields lower threshold currents than unstrained quantum wells because compressively straining InGaAs decreases the effective mass in the parallel direction, thus reducing the density of states and number of carriers required to reach population inversion. Such laser diodes were MBE grown with a maximum substrate temperature of 530°C and had threshold current densities only 2.4 times higher than lasers grown under more optimal growth conditions. This demonstrates for the first time that practical laser diodes can be grown using standard MBE techniques at temperatures compatible with direct epitaxial growth on fully processed VLSI GaAs circuitry.

Further reduction in threshold currents are anticipated. More exploratory growth techniques, such as migration enhanced epitaxy (MEE), variable duty cycle As cell shuttering, and precisely controlled low As overpressure, are all being pursued to achieve high quality, low temperature ($< 600^\circ\text{C}$) AlGaAs. Phosphide based optoelectronic devices, grown by gas-source MBE, are also being considered because they provide both lower growth temperatures (typically $< 500^\circ\text{C}$) and shorter wavelength emission.

1.10 Optical Input and Output Circuitry for High Density, High Speed GaAs MESFET-based OEICs

Sponsors

DARPA/MOSIS
DARPA/NCIPT
Hertz Foundation Fellowship

Project Staff

Krishna V. Shenoy, Professor Clifton G. Fonstad, Jr. in collaboration with P. Nuytkens

Optoelectronic signal processors have become major components of advanced communication

⁷ GTE Corporation, Waltham, Massachusetts.

systems, real-time signal processors, and high-performance sensing systems. Integrated optics offers the potential to significantly advance these systems. To fully exploit the potential of optoelectronic devices, semiconductor processes and technology must be designed to integrate photodetectors, transimpedance amplifiers, laser diodes, and VLSI transistor circuits. Such integrated optoelectronic device technology results in lower cost, reduced power consumption, higher bandwidth, lower weight, increased reliability and increased performance of optoelectronic systems.

An optoelectronic integrated circuit (OEIC) transceiver has been designed, thoroughly simulated with HSPICE, and fabricated in the Vitesse HGaAs2 technology (MOSIS). The OEIC transceiver accepts either electrical or optical signal inputs and generates corresponding electrical or optical signal outputs. The OEIC incorporates an ECL electrical input receiver and output driver, MSM photodetector, with a companion transimpedance amplifier, laser diode driver, and opening to the substrate for epitaxial growth, cross point switch, and control logic. The OEIC transceiver demonstrates four possible signal conversions: (1) electrical signal at ECL level input, through intermediate DCFL electrical level, to ECL level output; (2) electrical signal at ECL level input through intermediate DCFL electrical level to optical signal output (via regrown in-plane surface emitting laser diode); (3) optical signal input through intermediate DCFL electrical level to electrical signal at ECL level output; and (4) optical signal input through intermediate DCFL electrical level to optical signal output.

Ninety-six processed chips 5 mm by 5 mm on a side, each with 24 OEIC transceiver cells, have been received through the MOSIS service. Each chip contains numerous 100 μ m by 400 μ m openings etched through to the substrate into which laser diode heterostructures are now being grown.

1.11 High Density GaAs MESFET-based OEIC Neural Systems

Sponsors

Hertz Foundation Fellowship
National Science Foundation Fellowship

Project Staff

Krishna V. Shenoy, Professor Clifton G. Fonstad, Jr. in collaboration with A. Grot^a and D. Psaltis^a

Two components required for implementation of a neural network are neurons and connections. In an optical implementation, neurons are typically arranged as two-dimensional arrays interconnected via the third dimension. The interconnections are realized with holograms or spatial light modulators. Use of GaAs optoelectronic circuits provides the flexibility of implementing complex neuron response functions and fine tuning properties of the neurons as required by the neural network algorithm that is being implemented.

LEDs and laser diodes are the choices for on-chip light sources. Laser diodes have higher quantum efficiency and a more directed beam than LEDs, which means a higher light efficiency. Unfortunately, electrical power dissipation is a limiting factor for high density circuits. For typical laser diode values of $V_D = 2$ Volts and $I_m = 500\mu A$ and a maximum power dissipation of 1 W/cm², the maximum integration density is 1000/cm². Because of the absence of a threshold current, LEDs can operate with very small currents allowing a density of up to 10⁵/cm². Thus, if one is interested in high density arrays that operate with relatively slow switching times then LEDs are the preferred choice.

A neuron calculates a simple nonlinear function, thereby mapping its input signals to the output signal. A commonly used nonlinearity is the "bump" function, simply the derivative of a sigmoidal function, which is used in backward error propagation algorithms for calculation of the interconnection weight updates. In the most simplistic approach to implementing the "bump" function, the output should be low whenever the two inputs are not equal and high when the two inputs are matched. In this realization, the input is a photodetector current, which is converted to a voltage in a differential input circuit, and the output is a current through an LED. This differential circuit acts as a thresholding circuit if the detectors have I-V characteristics where the current saturates quickly. An optoelectronic integrated circuit (OEIC) neural chip with arrays of GaAs MESFET neurons and photodetectors has been designed, simulated, fabricated by Vitesse, and tested by Grot and Psaltis at the California Institute of Technology. Monolithic integration of LEDs in dielectric windows is the final fabrication step.

^a California Institute of Technology, Pasadena, California.

The Vitesse refractory-metal GaAs MESFET circuitry can withstand three hour molecular beam epitaxy (MBE) growths at temperatures up to $525^{\circ}\text{C} \pm 10^{\circ}\text{C}$. GaAs-AlGaAs LEDs are being grown by MBE at MIT on fully processed neural chips in dielectric windows, regions where the interlevel and passivation dielectrics have been removed to expose the semi-insulating GaAs substrate. Processing of the LEDs is then completed at Caltech. After planarizing the neural chip by stripping the poly-crystalline material deposited everywhere but in the dielectric windows, LEDs are fabricated and metalically interconnected with the electronic neurons. The culmination of this research will be the demonstration of high-density, monolithic optoelectronic neural systems.

1.12 Applications of Resonant Tunneling Diodes in GaAs MESFET VLSI

Sponsors

Texas Instruments, Inc.
U.S. Army Research Office
Grant DAAL03-92-G-0251

Project Staff

Rajni J. Aggarwal and Professor Clifton G. Fonstad Jr. in collaboration with P. Nuykens

We are investigating the integration of resonant tunneling diodes (RTDs) with GaAs MESFETs. Our intent is to use epitaxial regrowth techniques to integrate RTDs with commercially available GaAs MESFET technology. We have considered both the development of a logic family as well as a SRAM. RTDs can provide stable, low current, voltage states, and both applications are designed to take full advantage of these properties. Additionally, the small area of tunnel diodes gives the potential for increasing integration densities. Using experimental techniques as well as HSPICE simulations to evaluate the circuits, we have concluded that only the SRAM presents a commercially viable technology.

We compared the performance of the RTD logic family to that of direct coupled FET logic (DCFL). We considered 23 stage ring oscillators using 1, 2, 3, and 4 input NOR gates. The RTD logic consistently dissipated an order of magnitude less power than DCFL, however, much of this advantage was lost when the delay per stage was considered. Overall, the power-delay product of the RTD logic was on average only a factor of four times smaller than that of DCFL. This does not represent enough of an improvement over DCFL to be a commercially viable logic family.

The SRAM cell consists of an enhancement mode FET connected to two RTDs. An integrated RTDs and FET static memory cell has two main advantages over present GaAs SRAMs. Using epitaxial regrowth, RTDs can be grown directly on top of the driver FET, reducing the memory cell size to that of a single transistor. This design has the possibility of obtaining DRAM densities in a static memory. Additionally, proper diode design will result in both the "1" and "0" states being low power states.

We have simulated the basic memory cell and are developing its driver circuitry. We have experimentally demonstrated the bistable nature of diode chains. Using both the experimental and simulation results, we have determined a series of design constraints for both RTDs and FETS. In the coming year we will be designing and growing suitable RTDs for these cells both in stand alone form as well as integrated with circuits. An integral part of the integration of these devices is the process flow required for manufacturing them, and these issues will also receive attention in the coming year.

1.13 Investigation of Infrared Intersubband Emission from InGaAs/AlAs/InP Quantum Well Heterostructures

Sponsors

National Science Foundation
U.S. Army Research Office
Grant DAAL03-92-G-0251

Project Staff

Jurgen H. Smet, Professor Clifton G. Fonstad, Jr. in collaboration with Professor Qing Hu

In this work, we are studying the possibility of achieving population inversion between two quantum well subbands, with an electrically pumped intersubband laser as the ultimate goal. A triple quantum well structure consisting of two narrow filter wells and a wide center well appears to be a promising structure to achieve this goal. To avoid fast relaxation through electron LO-phonon scattering, it is desirable to design a structure for a lasing frequency smaller than the LO-phonon frequency. In addition, the required population inversion imposed by the gain needed to overcome optical losses should be sufficiently low to prevent the energy difference between the quasi-Fermi level in the upper subband and the ground state from being larger than the LO-phonon energy. These stringent requirements can only be met in wide quantum well structures.

To test the feasibility of population inversion, the I-V characteristics at low temperature of triple quantum well structures with varying barrier thickness and well thickness are being studied to verify that injection and removal of the electrons from the inner well is not the current limiting factor, but that the intersubband relaxation processes determine the current and therefore that population inversion might be achieved.

As the width and the number of the quantum wells increases, and thus the characteristic energy scales reduce and the number of possible transmission channels increase, the assignment of various transmission channels to the currents peaks in the I-V characteristics becomes considerably more difficult and ambiguous. Of the techniques used to analyse the I-V characteristics, magneto-quantum oscillations observed in the tunnel current as a function of applied bias when sweeping the magnetic field have proven to be the most powerful. Using Fast Fourier Transform algorithms, we are able to determine the transmission channel responsible for a certain current peak, the energy separation between the lowest subbands, and the charge present in the subbands of the first well. We can also determine that the GaAs-like LO-phonon emission process is the dominant inelastic process over InAs-like inelastic scattering. This is in agreement with reports on bulk $\text{In}_{0.53}\text{Ga}_{0.47}\text{As}$.

Our interest in applying a magnetic field parallel to the current goes beyond its use as a diagnostic tool. The magnetic field reduces the dimensionality of the originally 2D quantum well to a 0D system and should suppress inelastic scattering processes if the spacing between Landau levels in different subbands differs from the LO-phonon energy and may thus aid in achieving population inversion. We are currently performing experiments to verify and demonstrate this suppression of inelastic scattering.

1.14 Infrared Characterization of InGaAs/AlAs/InP Quantum-Well Heterostructures

Sponsor

National Science Foundation

Project Staff

Lung-Han Peng, Professor Clifton G. Fonstad, Jr. in collaboration with R. Victor Jones and Victor Ehrenrich⁹

The application of III-V single quantum well (SQW) C1-to-C2 intersubband transitions for mid (2–5 μm) and far (8–10 μm) infrared (IR) detection, owing to their fast response speed, high detectivity, and reliance on more mature growth and process technologies, have advantages over conventional interband transition materials such as mercury cadmium telluride (MCT), which suffers serious problems of device uniformity and yield rate.

By devising angle- and polarization-resolved IR spectroscopy techniques, we have shown that conventional wisdom forbidding normal incidence (TE) quantum well intersubband transitions is incorrect. In fact, we have consistently measured equally strong TE- and TM-active intersubband QW absorption peaks and have seen a strain-dependent splitting between these peaks. These results enable us to develop a new theory that considers the symmetry effects on subband Bloch states, which leads to the explanation of polarization selection rules, absorption strength, and splitting in our experimental work (see next section).

By engineering the composition and width of InGaAs quantum well and the InAlAs barrier height, we have successfully measuring the intersubband absorption in the 2 to 5 μm wavelength region based on InGaAs/AlAs/InAlAs SQW the resonant tunneling diode structures. Future work involves using MQW structures to increase photocurrent and applying selective etches to contact the QW directly to realize high performance IR detectors.

1.15 Analysis of the Symmetry Properties of Quantum Well Subband Energy Levels

Sponsors

National Science Foundation
U.S. Army Research Office
Grant DAAL03-92-G-0251

⁹ Harvard University, Cambridge, Massachusetts.

Project Staff

Lung-Han Peng, Professor Clifton G. Fonstad, Jr. in collaboration with R. Victor Jones and Victor Ehrenrich⁹

$k \cdot p$ envelope function formalism, due to its computational simplicity, has been widely used for calculating the quantum well (QW) subband energies and predicting the polarization selection rules of interband and intersubband transitions. It has been assumed that the symmetry properties of high-lying conduction subband Bloch states are the same as in the ground state; however, closer examination of the first-order $k \cdot p$ correction to the high-lying subband Bloch states reveals this is an invalid assumption because the narrow width, highly confinement QW problem fails all the criteria that originally made in deriving the envelope function formalism which assumed a weak, slowly varying confinement potential and perturbed state energies close to the band edge.

We consider the irreducible representations of subband Bloch states in a [001] D2d symmetric QW structure for C_1 -to- C_2 intersubband transitions. Neglecting the QW in-plane crystal anisotropy along [1,1,0] and [1,-1,0] directions and the intersubband spin-orbit coupling, we have shown that the $C_1(n=1)$ state transforms as $\Gamma_6(\Gamma_1): S\uparrow$, and the $C_2(n=2)$ degenerate states transform according to $\Gamma_7(\Gamma_5): (X-iY)$, $\downarrow/\sqrt{2} \Gamma_6(\Gamma_5): (X+iY)\downarrow/\sqrt{2}$, and $\Gamma_7(\Gamma_4): Z$, and that they are of Kramers degeneracy in the absence of external magnetic field.

Our model leads us to the conclusions that C_1 -to- C_2 intersubband transitions are of equal absorption strength for polarization parallel and perpendicular to the QW plane; and that the $\Gamma_4(X,Y)$ and $\Gamma_5(Z)$ degenerate states split in the presence of strains, which explains the details of our recent experimental work.

1.16 Microwave Characterization, Analysis, and Modeling of Emitter-Down Heterojunction Bipolar Transistors

Sponsors

National Science Foundation/Northeastern University

TRW Systems

Project Staff

Sheila Prasad, Professor Clifton G. Fonstad, Jr. in collaboration with B. Meskoob¹⁰ and M. Kim¹¹

Emitter-down InGaAs/InAlAs/InP heterojunction bipolar transistors have been characterized at microwave frequencies and small-signal equivalent circuit models have been obtained using the commercial Touchstone software. The simulated annealing (SA) algorithm, which does not depend on good initial conditions, has been applied to the modelling problem and the results obtained with SA and Touchstone were consistent. However, continuous human intervention was required to obtain the results with Touchstone, whereas SA yielded the results automatically. SA was therefore proved to be the superior method for optimization because of its speed and convenience.

Small-signal s-parameter measurements were made by on-wafer probing of the transistors using a Hewlett-Packard 8510B automatic network analyzer and a Cascade Microtech probe station. These measurements were made for up to 39 different bias points. Consistent small-signal equivalent circuit models were obtained using both of the modeling methods described above. The bias dependence of the elements of the small-signal equivalent circuit was also determined, and it was found that five of the elements of the circuit were highly bias dependent.

These results were used for the large-signal modeling of the HBT. The model obtained was based on first-order device physics, and this was verified experimentally. When standard large signal modeling techniques such as the Harmonic Balance method are used, it is observed that the first-order model was sufficient accurate for medium power levels with respect to the particular device under consideration. At higher power levels where the transistor is driven into hard saturation and cutoff, a more elaborate model is necessary to obtain a high third-order intermodulation product (IP3) and hence device linearity. This investigation is now in progress.

¹⁰ Northeastern University, Boston, Massachusetts.

¹¹ TRW Systems, Redondo Beach, California.

1.17 Damage-Free In-Situ UHV Etching and Cleaning of III-V Heterostructures Using Molecular Beams

Sponsors

AT&T Bell Laboratories Fellowship
DARPA/NCIPT
National Science Foundation
Grant ECS 90-07745
TRW Corporation

Project Staff

Isako Hoshino, Professor Clifton G. Fonstad, Jr.

Development of damage-free ultra-high vacuum (UHV) etching, cleaning, and regrowth techniques compatible with molecular beam epitaxy (MBE) and ex-situ processing of III-V heterostructures is a major challenge facing device researchers. The ability to selectively pattern, etch, and overgrow quantum heterostructures is crucial to the effective realization of integrated optical circuitry and quantum effect electronic structures. Present techniques to do this involve relatively high energy (100 eV and above) ion beams which cause substantial sub-surface damage, much of which is impossible to remove.

As a solution to the problem of process-induced damage, we have begun a program investigating the use of UHV kinetic molecular beam techniques (widely used to study atomic interactions) to etch and clean III-V substrates and heterostructures with a minimum of surface damage and maximum flexibility. Depending on the etchant gas mixture established, it is anticipated that low energy (0.5 to 3.0 eV) kinetic beams can be used to (1) both directionally and isotropically etch-pattern III-V heterostructure wafers with no damage; (2) clean surfaces allowing epitaxial growth on wafers that have been removed from the UHV environment for external processing; and (3) selectively remove masking materials and clean surfaces suitable for subsequent overgrowth.

Currently, the UHV Kinetic Beam Etching (KBE) chamber construction designed to use a methane-hydrogen gas mixture in a supersonic beam source is near completion. The present design also allows the chamber to be connected to the existing Riber 2300 solid source MBE system through a transfer mechanism of special design.

The initial function tests of the KBE system are scheduled to be performed in the near future. Subsequently, a full-scale characterization of the ability of the KBE will be performed, mainly concentrating

on etch rate, etch profile, and surface damage assessment. The extent of any surface damage will be determined through photoluminescence and carrier mobility measurements using various III-V heterostructures grown by MBE.

1.18 Publications

Published Journal Articles

Broekaert, T.P.E., and C.G. Fonstad. "Novel Organic Acid-based Etchants for InGaAlAs/InP Heterostructure Devices with AlAs Etch-stop Layers." *J. Electrochem. Soc.* 139: 2306-2309 (1992).

Broekaert, T.P.E., and C.G. Fonstad. "Quantum Well Intersubband Relaxation in Resonant Tunneling Diodes and Transistors." *J. Appl. Phys.* 72: 746-752 (1992).

Broekaert, T.P.E., and C.G. Fonstad, "AlAs Etch-Stop Layers for InGaAlAs/InP Heterostructure Devices and Circuits." *IEEE Trans. Electron. Dev.* 39: 533-536 (1992).

Burns, G.F., and C.G. Fonstad. "Monolithic Fabrication of Stain-Free (Al,Ga)As Heterostructure Lasers on Silicon Substrates." *IEEE Photonics Tech. Lett.* 4: 18-21 (1992).

Burns, G.F., and C.G. Fonstad, "Complete Strain Relief of Heteroepitaxial GaAs on Silicon." *Appl. Phys. Lett.* 61: 2199-2201 (1992).

Harton, A.V., and C.G. Fonstad. "Implantation of Li⁺ and Na⁺ into PbTeSe for Current Confinement in PbTeSe/PbSnTe Ridge Waveguide Lasers." *J. Appl. Phys.* 72(7): 2575-2578 (1992).

Meskoob, B., S. Prasad, M. Vai, C.G. Fonstad, J.C. Vlcek, H. Sato, and B. Buluray. "A Small-signal Equivalent Circuit for the Collector-up InGaAs/InAlAs/InP Heterojunction Bipolar Transistor." *IEEE Trans. Electron. Dev.* 39: 2629-2632 (1992).

Meskoob, B., S. Prasad, M-K. Vai, J.C. Vlcek, H. Sato, and C.G. Fonstad. "Bias-dependence of the Intrinsic Element Values of InGaAs/InAlAs/InP Inverted Heterojunction Bipolar Transistors." *IEEE Trans. Microwave Theory Tech.* 40: 1012-1013 (1992).

Peng, L.H., J.H. Smet, T.P.E. Broekaert, and C.G. Fonstad. "Transverse Electric and Transverse Magnetic Polarization Active Intersubband Tran-

sitions in Narrow InGaAs Quantum Wells." *Appl. Phys. Lett.* 61: 2078-2080 (1992).

Peng, L.H., T.P.E. Broekaert, W.Y. Choi, B.R. Bennett, J.H. Smet, V. Diadiuk, S.H. Groves, S.C. Palmateer, N. Pan, and C.G. Fonstad, Jr.. "Mapping of the Localized Interface and Surface States of InGaAs Lattice Matched to Fe-doped InP by Infrared Spectroscopy." *J. Appl. Phys.* 72(8): 3664-3669 (1992).

Smet, J.H., T.P.E. Broekaert, and C.G. Fonstad. "Peak-to-valley current ratios as High as 50:1 at Room Temperature in Pseudomorphic $\text{In}_{0.53}\text{Ga}_{0.47}\text{As}/\text{AlAs}/\text{InAs}$ Resonant Tunneling Diodes." *J. Appl. Phys.* 71: 2475-2477 (1992).

Vlcek, J.C., W-Y. Coi, and C.G. Fonstad. "Techniques and Applications of Graded Composition InGaAlAs Alloys." *J. Vac. Sci. Technol. B* 10: 822-824 (1992).

Journal Articles Accepted for Publication

Choi, W.Y., T.P.E. Broekaert, and G.G. Fonstad. "MBE-grown InGaAlAs 1.5 μm MQW Ridge Waveguide Laser Diodes with AlAs Etch-Stop Layers." *Electronics Lett.*

Choi, W.Y., and C.G. Fonstad, "Photoluminescence and X-ray Diffraction Studies of Compressively Strained InGaAs and InGaAlAs Quantum Wells for 1.55 μm Laser Diode Applications." *J. Crystal Growth.*

Journal Articles Submitted for Publication

Choi, W.Y., and C.G. Fonstad. "Determination of the Layer Structure of Embedded Strained InGaAs Multiple Quantum Wells by High Resolution X-ray Diffraction." Submitted to *Appl. Phys. Lett.*

Hiriyama, Y., W.Y. Choi, L.H. Peng, and C.G. Fonstad. "Absorption Spectroscopy on Room Temperature Excitonic Transitions in Strained Layer InGaAs/InGaAlAs Multi-quantum-well Structures." Submitted to *J. Appl. Phys.*

McCann, P.J., and C.G. Fonstad. "Growth of $\text{PbSe}_{0.78}\text{Te}_{0.22}$ Lattice-Matched with BaF_2 ." Submitted to *Thin Solid Films.*

Peng, L.H., and C.G. Fonstad. "Normal Incidence Intersubband Transitions in Si-doped InGaAs Multiple Quantum Wells." Submitted to *Appl. Phys. Lett.*

Shenoy, K.V., C.G. Fonstad, and J.M. Mikkelsen. "High-Temperature Stability of Refractory-Metal GaAs VLSI MESFETs." Submitted to *IEEE Electron Dev. Lett.*

Meeting Papers Presented

Choi, W.Y., and C.G. Fonstad. "Photoluminescence and X-ray Diffraction Studies of Compressively Strained InGaAs and InGaAlAs Quantum Wells for 1.55 μm Laser Diode Applications." Seventh International Conference on Molecular Beam Epitaxy, Schwábisch Gmánd, Germany, August 24-28, 1992.

Peng, L.H., and C.G. Fonstad. "Strong TE-polarized Intersubband Absorption in InGaAs Single Quantum Well Waveguides." Device Research Conference, MIT, Cambridge, Massachusetts, June 22-24, 1992.

Shenoy, K.V., C.G. Fonstad, B. Elman, F.D. Crawford, and J. Mikkelsen. "Laser Diodes and Refractory-metal Gate VLSI GaAs MESFET's for Smart Pixels." LEOS '92 Annual Meeting, Boston, Massachusetts, November 16-19, 1992.

Theses

Broekaert, T.P.E. *Characterization of InGaAlAs Resonant Tunneling Transistors.* Ph.D. diss. Dept. of Electr. Eng. and Comput. Sci., MIT, 1992.

Shenoy, K.V. *VLSI GaAs MESFETs and Laser Diodes for Monolithic Optoelectronic Circuits.* S.M. thesis. Dept. of Electr. Eng. and Comput. Sci., MIT, 1992.

Singer, R. *Molecular Beam Epitaxial Growth of InGaAlAs Semiconducting Alloys on (III)B Zincblende Substrates for Optoelectronic Applications.* Ph.D. diss. Dept. of Electr. Eng. and Comput. Sci., MIT, 1992.

Chapter 2. High-Frequency InAlAs/InGaAs Metal-Insulator-Doped Semiconductor Field-Effect Transistors (MIDFETs) for Telecommunications

Academic and Research Staff

Professor Jesús A. del Alamo

Visiting Scientists and Research Affiliates

Dr. Yuji Awano¹

Graduate Students

Sandeep R. Bahl

Undergraduate Students

Michael H. Leary, Akbar A. Moolji

Technical and Support Staff

Charmaine A. Cudjoe-Flanders, Angela R. Odoardi

2.1 Introduction

Sponsors

Charles S. Draper Laboratories

Contract DL-H-441694

Fujitsu Laboratories

Joint Services Electronics Program

Contract DAAL03-92-C-0001

Texas Instruments

The goal of this project is to investigate InAlAs/n⁺-InGaAs Metal-Insulator-Doped channel Field-Effect Transistors (MIDFETs) on InP. These devices are of great interest for applications in long-wavelength lightwave communication systems and ultra-high frequency high-power microwave telecommunications.

InAlAs/InGaAs Modulation-Doped Field-Effect Transistors (MODFETs) on InP represent a prom-

ising choice for a variety of microwave and photonics applications. The outstanding transport properties of InGaAs have yielded devices with very low-noise and high-frequency characteristics.² Unfortunately, the low breakdown voltage of InAlAs/InGaAs MODFETs on InP (typically less than 5 V) severely restricts their use in medium- and high-power applications.² Additionally, in InP photonics receivers based on Metal-Semiconductor-Metal (MSM) photodiodes, one must use a separate high voltage supply to operate the photodetectors because they typically require several volts across them to achieve a high-quantum efficiency.³

A device strategy with great potential for power handling is the InAlAs/n⁺-InGaAs MIDFET featuring an undoped insulator and a thin, heavily-doped channel.⁴ Our research over the last few years at MIT on the physics and technology of this device has revealed that its breakdown voltage, V_B , is large and can be engineered using pseudomorphic

¹ Fujitsu Laboratories, Atsugi, Japan.

² L.D. Nguyen, L.E. Larson, and U.K. Mishra, "Ultra-High-Speed Modulation-Doped Field-Effect Transistors: A Tutorial Review," *Proc. IEEE* 80(4): 494-518 (1992).

³ J.H. Burroughes and M. Hargis, "1.3 μm InGaAs MSM Photodetector with Abrupt InGaAs/InAlAs Interface," *IEEE Phot. Tech. Lett.* 3(6): 532 (1991).

⁴ J.A. del Alamo and T. Mizutani, "An $\text{In}_{0.52}\text{Al}_{0.48}\text{As}/\text{n}^+\text{-In}_{0.53}\text{Ga}_{0.47}\text{As}$ MISFET with a Heavily-Doped Channel," *IEEE Electron Device Lett.* EDL-8(11): 534-536 (1987).

insulators⁵ and quantized channels.⁶ This is in addition to having a comparable frequency response to MODFETs of similar gate lengths.⁷

During 1992, we investigated the physics of breakdown in InAlAs/n⁺-InGaAs MIDFETs. We developed a hypothesis for the breakdown mechanism in this device that explains our experimental observations to date. We verified our hypothesis by carrying out detailed breakdown measurements as a function of temperature. Our work required the development of a breakdown measuring technique that was unambiguous, safe, and reliable. The following sections describe in greater detail our technical findings and conclusions.

2.2 Drain-current Injection Technique for the Measurement of Breakdown Voltage

Precise knowledge of the breakdown voltage, V_b , of a device, including an unambiguous definition of breakdown and a reliable and safe measuring technique, is essential for application of a device in a circuit environment. However, the FET literature contains many inconsistent definitions of breakdown. In addition, most measuring techniques are ambiguous, not amenable to automation, and can easily result in device destruction. In this section, a new technique of measuring the breakdown voltage of FETs is presented. Its application to InAlAs/n⁺-InGaAs MIDFETs is demonstrated.

This new technique, *drain-current injection technique*, uses a semiconductor parameter analyzer HP4145B with the device biased in a configuration schematically illustrated in figure 1. To measure breakdown, a fixed predefined current is injected into the drain, the gate-source voltage is ramped down from a strong forward bias to below threshold, and V_{DS} and I_G are monitored. In this manner, the device goes from the linear regime through the saturation region and into breakdown. This is analogous to tracing the locus of V_{DS} versus V_{GS} at a fixed I_D on the output I-V characteristics. As illustrated below, the *drain-source breakdown voltage* $V_{B(D-S)}$ is the peak drain-source voltage obtained in

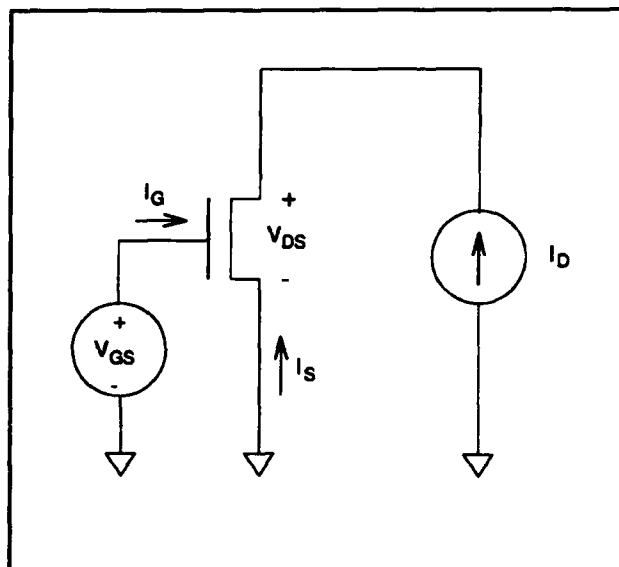


Figure 1. Schematic circuit diagram for implementation of the drain-current injection technique for measuring breakdown voltage in FETs.

this scan, and the *drain-gate breakdown voltage* $V_{B(D-G)}$ is the drain-gate voltage at $I_G = -I_D$.

We illustrate this technique on one of our devices in figure 2, which is a plot of V_{DS} , V_{DG} , and I_G versus V_{GS} for $I_D = 1$ mA/mm at room temperature. For values of V_{GS} above $V_t = -0.6$ V, both V_{DS} and V_{DG} are relatively small and $I_G = 0$. At V_{GS} around V_t , both V_{DS} and V_{DG} rise sharply and I_G starts becoming significant. At about $V_{GS} = -1$ V, V_{DS} peaks. This is the drain-to-source breakdown voltage of the device. At a more negative V_{GS} , I_G becomes 1 mA/mm, and the source current becomes zero. This defines the drain-to-gate breakdown voltage $V_{B(D-G)}$. Because of the well-defined nature of these two critical voltage points, they can be extracted using a computer, making this technique easily automatable.

Our drain-current injection technique also provides insight into the physics of breakdown. This is discussed in more detail in the next section of this chapter. Figure 2 shows that when this particular device reaches breakdown, the source current goes to zero and V_{DG} saturates. This shows that the device breakdown is being governed by a drain-to-

⁵ S.R. Bahl, W.J. Azzam, and J.A. del Alamo, "Strained-Insulator In_{0.15}As/n⁺-In_{0.53}Ga_{0.47}As Heterostructure Field-Effect Transistors," *IEEE Trans. Electron Dev.* 38 (9): 1986-1992 (1991).

⁶ S.R. Bahl and J.A. del Alamo, "Breakdown Voltage Enhancement from Channel Quantization in InAlAs/n⁺-InGaAs Heterostructure Field-Effect Transistors," *IEEE Electron Dev. Lett.* 13(2): 123-125 (1992).

⁷ S.R. Bahl, B.R. Bennett, and J.A. del Alamo, "Doubly-Strained In_{0.15}Al_{0.85}As/n⁺-In_{0.53}Ga_{0.47}As HFET with High Breakdown Voltage," *IEEE Electron Dev. Lett.* 14(1): 22-24 (1993).

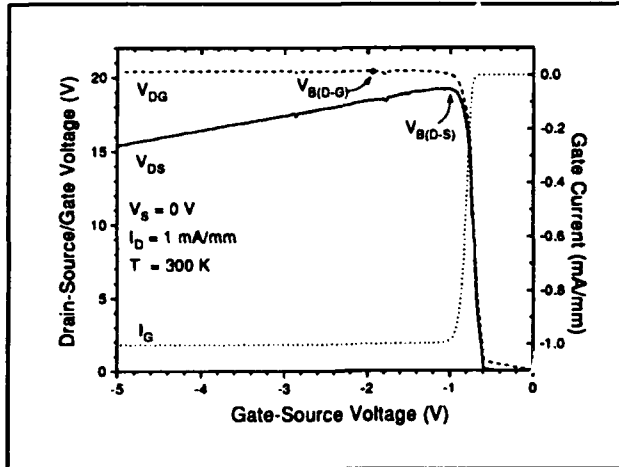


Figure 2. Illustration of drain-current injection technique in InAlAs/n-InGaAs HFET: V_{DG} , V_{DS} , and I_G versus V_{GS} . The peak of V_{DS} is $V_{B(D-S)}$, and the point at which $I_G = 1 \text{ mA/mm}$ is $V_{B(D-G)}$.

gate breakdown mechanism rather than by a channel or source-to-drain breakdown phenomenon. This is not always the case, and, in fact, at very low temperatures, most of our devices are governed by a channel breakdown mechanism.

To conclude this section, we have presented a new method of measuring the breakdown voltage in FETs. This simple technique provides unambiguous determination of $V_{B(D-S)}$ and $V_{B(D-G)}$. The current through the device is limited to a prespecified value so that risk to fragile devices is minimized.

2.3 Physics of Breakdown in InAlAs/n-InGaAs HFETs

We have performed a detailed study of the physics of breakdown of InAlAs/n-InGaAs MIDFETs. In brief, our research reveals that, similar to heterojunction avalanche photodiodes, breakdown in these devices is a two-step process (see figure 3). First, electrons are injected from the gate into the channel through thermionic emission or thermionic-field emission. Second, the electrons entering the channel are very hot and release their energy in an impact-ionization process which starts avalanche breakdown in the channel. This hypothesis explains our experimental observations to date and also the low breakdown voltage of InAlAs/InGaAs MODFETs.

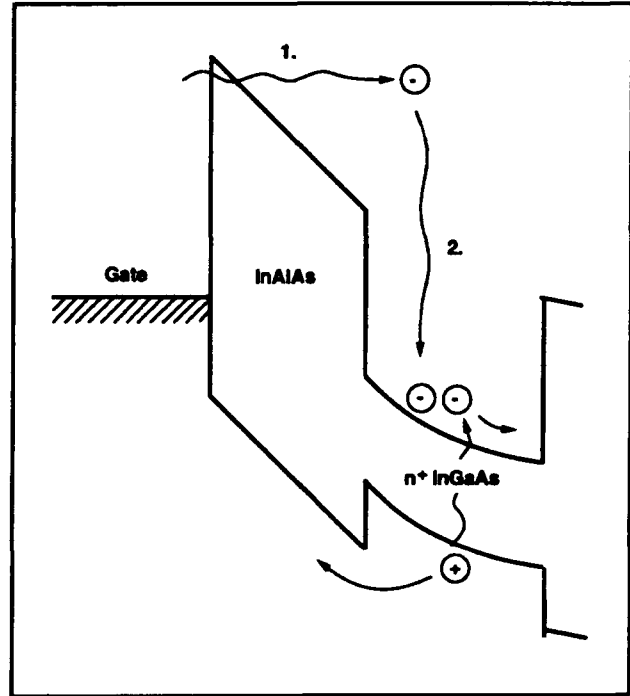


Figure 3. Schematic illustration of the postulated breakdown process in InAlAs/n-InGaAs MIDFETs. With a strong reverse bias between the gate and the drain, hot-electrons are injected from the gate to the channel (step 1), and, as they relax in the channel, they cause impact-ionization in the channel (step 2).

The devices used in this study are based on a MBE-grown heterostructure on S.I.-InP. As shown in figure 4, their structure consists of (bottom to top), a 1000 Å $\text{In}_{0.52}\text{Al}_{0.48}\text{As}$ buffer, a 75 Å $\text{In}_{0.53}\text{Ga}_{0.47}\text{As}$ subchannel, a 100 Å n^+ ($4 \times 10^{18} \text{ cm}^{-3}$) $\text{In}_{0.53}\text{Ga}_{0.47}\text{As}$ channel, a 300 Å undoped $\text{In}_{0.41}\text{Al}_{0.59}\text{As}$ insulator, and a 50 Å undoped $\text{In}_{0.53}\text{Ga}_{0.47}\text{As}$ cap.⁸ HFETs with $L_g = 1.9 \text{ } \mu\text{m}$ and $W_g = 30 \text{ } \mu\text{m}$ were studied. Both drain-source breakdown voltage, $V_{B(D-S)}$, and drain-gate breakdown voltage, $V_{B(D-G)}$, were measured using the drain-current injection technique presented in the previous section as a function of temperature.

At approximately room temperature, the breakdown voltages show a negative temperature coefficient with $V_{B(D-G)}$ increasing from 12.8 V at 360 K to 24.7 V at 260 K (see figure 5). $V_{B(D-S)}$ tracks $V_{B(D-G)}$, and increases from 11.1 V to 23.5 V. Measurements of I_G showed that for the temperature range 260 K-360 K at drain-source breakdown, all the

⁸ S.R. Bahl, B.R. Bennett, and J.A. del Alamo, "A High-Voltage, Doubly-Strained $\text{In}_{0.4}\text{Al}_{0.6}\text{As}/n\text{-In}_{0.53}\text{Ga}_{0.47}\text{As}$ HFET," paper presented at the Fourth International Conference on InP and Related Materials, Newport, Rhode Island, April 20-24, 1992, pp. 222-225.

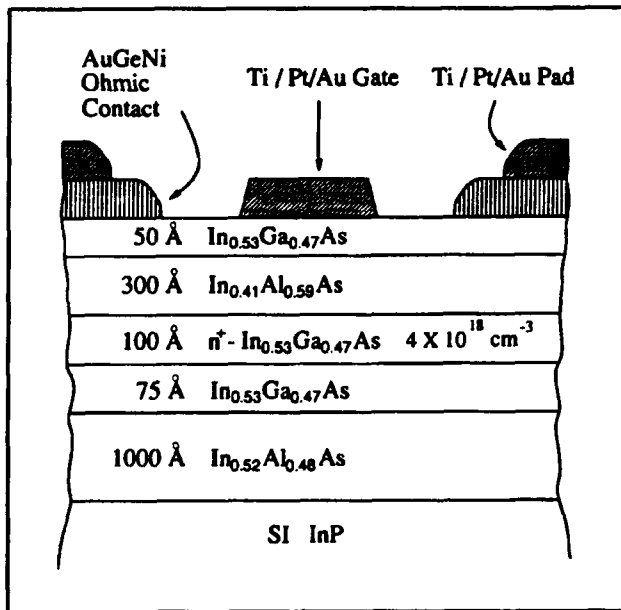


Figure 4. Schematic of device heterostructure used in our breakdown studies.

injected current flows from drain to gate (see figure 5). At these temperatures, drain-gate breakdown limits the value of the drain-source breakdown voltage. The temperature dependence that is measured is also incompatible with a simple impact ionization process in the channel.

To understand the relevant physics, we examined in detail the temperature dependence of I_G at the onset of breakdown. An Arrhenius plot of $\ln(I_G/T^2)$ was generated for V_{DG} steps from below V_T (-0.8 V) through $V_{B(D-G)}$ at 300 K (16 V), as shown in figure 6. Data from the locus of the drain-current injection technique ($I_D = 1$ mA/mm) was used. The gate current was found to be thermally activated with an activation energy of 0.41-0.46 eV, regardless of V_{DG} . This value is consistent with electron thermionic-field emission across the barrier as the breakdown limiting mechanism. The relatively constant activation energy exhibited from below threshold until breakdown implies that the voltage supported by the insulator does not change once the channel has been depleted. Instead, the excess voltage is supported by the lateral fields in the drain-gate gap. Measurements using a gated Hall-bar structure (essentially a long gate-length FET with taps directly into the channel) confirmed this hypothesis.

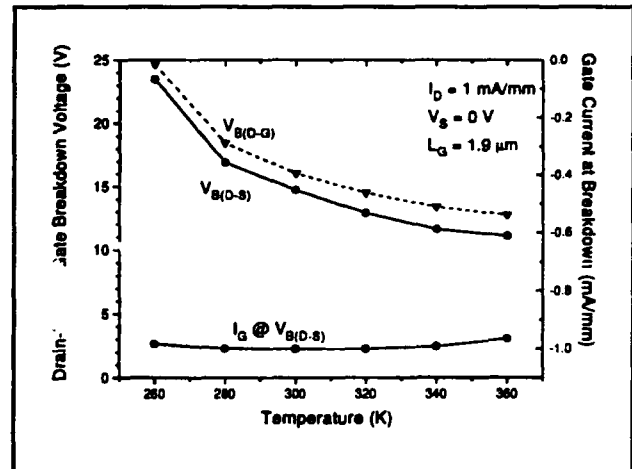


Figure 5. Drain-to-source breakdown voltage, drain-to-gate breakdown voltage, and gate current at drain-to-source breakdown versus temperature.

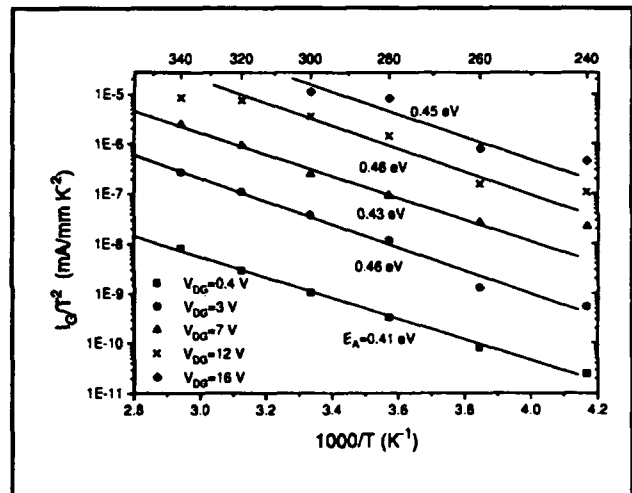


Figure 6. Arrhenius plot of gate current as a function of V_{DG} . The corresponding activation energy is indicated in the diagram.

The simultaneous occurrence of impact-ionization was established by detecting holes directly with a negatively biased sidegate in a specially designed structure, as shown in figure 7. The drain-current injection technique at $I_D = 1$ mA/mm was used, and the sidegate and gate currents monitored. The rise and saturation of the sidegate current coincides with the rise and saturation of the drain-gate voltage and drain-gate current. Since a very negative voltage has been applied to the sidegate, only holes can contribute to the sidegate current. This observation therefore verifies the occurrence of hole generation in the channel in an impact ionization process.

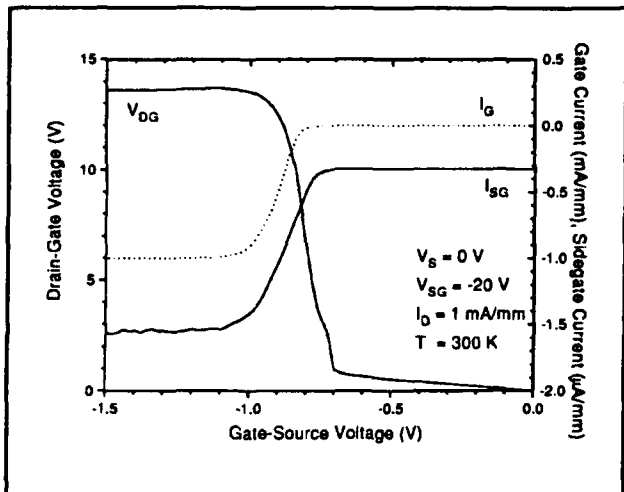


Figure 7. Sidegate current I_{SG} , gate current, and V_{DG} as a function of V_{GS} in a sidegate structure for $I_D = 1 \text{ mA/mm}$. The correlation between I_{SG} and I_G for $V_{SG} = -20 \text{ V}$ unmistakably indicates the existence of holes in the channel.

Our hypothesis, pictorially summarized in figure 3, explains our previously observed results which show that both the insulator and channel parameters affect V_B . V_B increases if (1) the Schottky barrier height of the insulator is enhanced⁹ (lower thermionic emission), (2) the channel bandgap is enlarged¹⁰ (lower multiplication), and (3) the channel doping is decreased¹¹ (decreased thermionic emission resulting from a higher voltage across the insulator at threshold). Now our hypothesis can be used as a guiding principle for further improvements of the breakdown voltage of InAlAs/n⁺-InGaAs MIDFETs.

A combination of thermionic (field) emission and impact-ionization is also likely to limit the breakdown voltage in InAlAs/InGaAs MODFETs, since in these devices, doping the insulator results in a reduced barrier to electron flow. This might pose a fundamental limit to the engineering of InAlAs/InGaAs MODFET breakdown voltages.

2.4 Publications and Conference Papers

Bahl, S.R., B.R. Bennett, and J.A. del Alamo. "Doubly-Strained InAlAs/n⁺-InGaAs HFETs." Paper presented at the 1992 Workshop on Compound Semiconductor Materials and Devices (WOCSEMMAD), San Antonio, Texas, February 16-19, 1992. Unpublished.

Bahl, S.R., B.R. Bennett, and J.A. del Alamo. "High Quality Heterostructures for Doubly-Strained InAlAs/InGaAs HFETs." Paper presented at the Seventh New England MBE Workshop, Cambridge, Massachusetts, May 13, 1992. Unpublished.

Bahl, S.R., B.R. Bennett, and J.A. del Alamo. "A High-Voltage, Doubly-Strained $\text{In}_{0.41}\text{Al}_{0.59}\text{As/n}^+\text{-In}_{0.65}\text{Ga}_{0.35}\text{As}$ HFET." Paper presented at the Fourth International Conference on InP and Related Materials, Newport, Rhode Island, April 20-24, 1992, pp. 222-225.

Bahl, S.R., and J.A. del Alamo. "Elimination of Mesa-Sidewall Gate-Leakage in InAlAs/InGaAs Heterostructures by Selective Sidewall Recessing." *IEEE Electron Dev. Lett.* 13(4): 195-197 (1992).

Bahl, S.R., and J.A. del Alamo. "Breakdown Voltage Enhancement from Channel Quantization in InAlAs/n⁺-InGaAs Heterostructure Field-Effect Transistors." *IEEE Electron Dev. Lett.* 13(2): 123-125 (1992).

Bahl, S.R., M.H. Leary, and J.A. del Alamo. "Mesa-Sidewall Gate-Leakage in InAlAs/InGaAs Heterostructure Field-Effect Transistors." *IEEE Trans. Electron Dev.* 39(9): 2037-2043 (1992).

del Alamo, J.A., S.R. Bahl, and D.R. Greenberg. "InP-Based High Breakdown Voltage HFETs." Paper presented at the Advanced Heterostructure Transistors Conference, Keauhou-Kona, Hawaii, November 29-December 4, 1992. Unpublished.

⁹ S.R. Bahl, W.J. Azzam, and J.A. del Alamo, "Strained-Insulator $\text{In}_{0.41}\text{Al}_{0.59}\text{As/n}^+\text{-In}_{0.65}\text{Ga}_{0.35}\text{As}$ Heterostructure Field-Effect Transistors," *IEEE Trans. Electron Dev.* 38 (9): 1986-1992 (1991).

¹⁰ S.R. Bahl and J.A. del Alamo, "Breakdown Voltage Enhancement from Channel Quantization in InAlAs/n⁺-InGaAs Heterostructure Field-Effect Transistors," *IEEE Electron Dev. Lett.* 13(2): 123-125 (1992); S.R. Bahl and J.A. del Alamo, "An $\text{In}_{0.52}\text{Al}_{0.48}\text{As/n}^+\text{-In}_{0.65}\text{Ga}_{0.35}\text{As}$ Heterostructure Field-Effect Transistor with an In-Enriched Channel," *Proceedings of the Second International Conference on InP and Related Compounds*, Denver, Colorado, April 23-25, 1990, p. 100.

¹¹ S.R. Bahl, B.R. Bennett, and J.A. del Alamo, "A High-Voltage, Doubly-Strained $\text{In}_{0.41}\text{Al}_{0.59}\text{As/n}^+\text{-In}_{0.65}\text{Ga}_{0.35}\text{As}$ HFET," paper presented at the Fourth International Conference on InP and Related Materials, Newport, Rhode Island, April 20-24, 1992, pp. 222-225.

Dumas, J.M., P. Audren, M.P. Favennec, S. Praquin, S.R. Bahl, and J.A. del Alamo. "Une Etude des Niveaux Profonds dans le Transistor a Effet de Champ de Puissance a Heterostruc-

ture InAlAs/n + -InGaAs." Paper presented at the Fourth Journees Microelectronique et Optoelectronique III-V, La Grande Motte, France, October 21-23, 1992. Unpublished.

Chapter 3. Chemical Beam Epitaxy of Compound Semiconductors

Academic and Research Staff

Professor Leslie A. Kolodziejski, Dr. Gale S. Petrich

Graduate Students

Christopher A. Coronado, Jay N. Damask, Philip A. Fisher, Easen Ho, Jody L. House, Kan Lu

Undergraduate Students

Kuo-yi Lim, Sang H. Park, Ayca Yuksel

Technical and Support Staff

Karen Chenausky, Charmaine A. Cudjoe-Flanders, Kelley S. Donovan, David S. Lee, Angela R. Odoardi

3.1 Introduction

Current state-of-the-art epitaxial growth techniques employ various metalorganic and hydride gases, particularly for high vapor pressure species such as phosphorus and sulfur, to deliver constituent species to the substrate surface. Chemical beam epitaxy (CBE) utilizes both metalorganic (MO) gases and hydride gas sources; metalorganic molecular beam epitaxy (MOMBE) uses MO gases; and gas source molecular beam epitaxy (GSMBE) combines hydride gas sources with the more typical solid elemental sources. The more conventional growth approach, molecular beam epitaxy (MBE), uses only molecular beams derived from the thermal evaporation of elemental or compound solid sources.

All the research objectives described in this chapter are concerned with layered structures composed of compounds containing As and P, or Se, S, and Te. The presence of these high vapor pressure species suggests that many advantages will be gained through fabrication of the device structures by the gaseous source epitaxy approach.

In the chemical beam epitaxy facility at MIT, epitaxial growth of both II-VI and III-V compound semiconductors is underway using all of the aforementioned growth techniques. The chemical beam epitaxy laboratory consists of two interconnected, fully operational gaseous source epitaxy systems along with several smaller chambers used for sample introduction and in-situ analysis/metalization. The multichamber epitaxy system allows various heterostructures to be grown in a continuous ultrahigh vacuum environment. The interconnection feature enables an additional

degree of freedom in device design by providing the ability to integrate the II-VI and III-V material families in a single device. The III-V GSMBE uses solid elemental sources of Ga, In, Al, Si and Be and gaseous hydride sources of arsenic and phosphorus. The II-VI reactor, on the other hand, is highly flexible, offering MO gas sources, hydride gas sources, and solid effusion cell type sources. Various constituent species available in the II-VI reactor include Zn, S, Se, Te, Cl, N, In, Ga, and As. Figure 1 highlights the many material systems, based on II-VI heterostructures, III-V heterostructures, or on a combination of II-VI and III-V semiconductors, which are available for exploration. Many of these are currently being fabricated in the epitaxy facility.

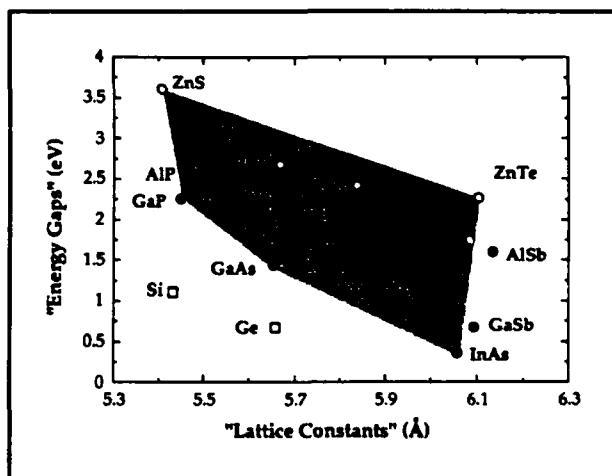


Figure 1. The shaded area highlights the many different II-VI and III-V semiconductors and the various heterostructure configurations which are available for investigation by fabrication in the MIT chemical beam epitaxy laboratory.

Wide bandgap II-VI materials have important technological potential, for example, as short wavelength (visible to ultraviolet) optical sources with applications in optical recording and bright emissive displays. A recent key advance in the area of Zn chalcogenides involves successful p-type doping of ZnSe-based semiconductors using nitrogen as acceptor species (first reported by Park et al.¹). This led to the achievement of a pn diode injection laser operating at blue/blue-green wavelengths by Haase et al.² and Jeon et al.³ These structures consisted of (Zn,Cd)Se narrow bandgap well layers with Zn(Se,S) cladding barrier layers, although more recent structures are composed of barrier layers of (Zn,Mg)(Se,S).⁴ To minimize defect generation within the active regions of the device, as well as to maximize the incorporation of the nitrogen acceptor species, the substrate temperatures have been reported to be extremely low (~150-250°C). By employing gas source epitaxy technologies for the growth of the aforementioned quantum well structures, control of the constituent species via precision mass flow controllers is anticipated to offer a solution to the difficulties encountered in the MBE of materials containing one or more high vapor pressure species. In addition, as the growth temperature is lowered, control of the flux ratio will become even more crucial.

The use of a beam-assisted growth approach in conjunction with metalorganic molecular beam epitaxy provides us with the capability of lateral patterning as well as composition modulation in the growth direction, which cannot be achieved by conventional MBE. To address some of these materials-related issues, we have embarked on a II-VI-based research program which emphasizes growth by the gas source epitaxy approach of various heterostructures which can be used for visible light emitters.

In section 4.2 we describe the progress that we have made in understanding the photo-assisted MOMBE growth of ZnSe using a combination of solid and gaseous MO sources with various energies of impinging photons. The laser-assisted growth technique was instrumental in aiding our understanding of the complex surface chemistry

which was occurring that limits the growth when using particular MO sources. The II-VI effort is complemented by a new research program with a research goal of fabricating lattice-matched epitaxial buffer layers of (In,Ga)P (section 4.3). The recently functioning III-V GSMBE is also being utilized to begin the investigation of very sophisticated (In,Ga)(As,P) waveguide devices for application as tunable filters operating at 1.55 μm which is the wavelength of interest for optical fiber communication (section 4.4).

3.2 Photo-Assisted Metalorganic Molecular Beam Epitaxy of ZnSe Using a Combination of Solid and Gaseous Sources

Sponsors

3M Company Faculty Development Grant
 Defense Advanced Research Projects Agency
 Subcontracts 216-25013 and 542383
 Joint Services Electronics Program
 Contract DAAL03-92-C-0001
 National Science Foundation
 Grant ECS 88-46919
 Grant ECS 89-05909

The use of photon illumination during the epitaxial growth of compound semiconductors enhances the capabilities of conventional growth techniques by modifying the surface chemistry and thus providing a potential tool necessary for in-situ selective area epitaxy. Photo-assisted epitaxy has been reported for the growth of both narrow and wide bandgap II-VI materials, as well as for a variety of III-V semiconductors. The effect of photons on the growth is dependent on the precursor selected for constituent materials (and/or the type of growth technology employed), as well as the energy and flux of illuminating photons.

The various physical mechanisms which have been either reported or verified experimentally to explain the effect of photon illumination include: (1) selective desorption of adsorbed surface species, (2) pyrolysis of source precursors at the surface via

¹ R.M. Park, M.B. Troffer, C.M. Rouleau, J.M. Depuydt, and M.A. Hasse, "P-Type ZnSe by Nitrogen Atom Beam Doping during Molecular Beam Epitaxial Growth," *Appl. Phys. Lett.* 57: 2127-2129 (1990).

² M.A. Hasse, J. Qui, J.M. Depuydt, and H. Cheng, "Blue-Green Laser Diodes," *Appl. Phys. Lett.* 59: 1272-1274 (1991).

³ H. Jeon, J. Ding, W. Patterson, A.V. Nurmikko, W. Xie, D.C. Grillo, M. Kobayashi, and R.L. Gunshor, "Blue-green Injection Laser Diodes in (Zn,Cd)Se/ZnSe Quantum Wells," *Appl. Phys. Lett.* 59: 3619-3621 (1991).

⁴ H. Okuyama, T. Miyajima, Y. Morinaga, F. Hiei, M. Ozawa, and K. Akimoto, "ZnSe/ZnMgSSe Blue Laser Diode," *Electron. Lett.* 28: 1798-1799 (1992).

increases in the substrate temperature, (3) direct photolysis of source precursors which are present in the gas phase, and (4) photo-catalysis of molecular species through the creation of free carriers present at the surface. Similar effects on the epitaxial growth process have been reported when the surface is illuminated with an electron beam. In the case of an electron beam, the physical mechanisms which have been postulated include kinetically-induced decomposition of adsorbed precursor molecules and/or the presence of charge carriers which interact with surface species.

In this program, the effect of "beam-assisted" growth during the metalorganic molecular beam epitaxy (MOMBE) of ZnSe is under investigation. By utilizing the wavelength-dependent laser-assisted growth technique and a combination of both gaseous metalorganic and solid elemental sources during the growth, we were able to identify the dominant surface reactions which result in significant enhancements in the growth rate, as well as a growth rate suppression.

ZnSe films were grown by MOMBE on GaAs(001) substrates. The Zn and Se precursors included elemental (6N) Zn and Se, diethylzinc (DEZn), dimethylzinc (DMZn), and diethylselenium (DESe). DEZn and DESe were initially chosen due to their lower thermal decomposition energies to enable the low temperature growth of ZnSe. The DEZn was typically utilized as a metalorganic gas, i.e. not thermally decomposed, with quadrupole mass spectroscopy of the gas beam indicating that thermal decomposition occurs near 300°C. In all cases, the DESe molecule was thermally decomposed at 800°C prior to impingement onto the substrate surface. The calibrated substrate temperature ranged from 150-475°C. Photo-assisted MOMBE was performed by illuminating a portion of the wafer's surface with laser radiation. The emission lines of an argon ion laser, a Ti:sapphire laser (7800 Å), and a dye (Coumarin 7) laser were all used to investigate the wavelength dependence of the photo-assisted growth. The power density of the lasers was kept very low (<200 mW/cm²), eliminating the possibility of photon-induced thermal pyrolysis of the metalorganic precursors.

The unilluminated growth rate using DEZn and DESe precursors was found to be abnormally low (several hundred angstroms per hour) for variations in the following growth parameters: substrate temperature, gas flow rate, the VI/II flow rate ratio, the

addition of hydrogen supplied by a gas injector, and the thermal pyrolysis of each gaseous species using a "cracking" gas injector. The growth parameter-independent low growth rate suggested that the growth rate was limited not by mass transport to the substrate surface, but rather that the Zn and Se atoms were unable to incorporate into the crystalline lattice. However, we found that illumination with photons having energy greater than the energy bandgap of the ZnSe, was found to significantly increase the growth rate under certain conditions. To verify that the resultant low growth rate and high illuminated growth rate was unique to the use of diethyl-based metalorganic sources, ZnSe was grown with all combinations of DEZn, DMZn, DESe, and elemental Zn and Se. Growth rates obtained using atomic Zn or DMZn and elemental Se were typical of that achievable with molecular beam epitaxy and limited only by mass transport to the substrate surface; however, when at least one diethyl metalorganic was used, the resultant unilluminated growth rate was very low. The experimental evidence thus suggested that the presence of ethyl radicals (or a byproduct of diethyl molecular decomposition) was responsible for the low unilluminated growth rate. The ethyl radicals are believed to be strongly chemisorbed to the ZnSe surface such that the incorporation sites for the metal atoms were not available. Relatively high substrate temperatures were investigated (up to 475°C) in an attempt to desorb the ethyl species responsible for surface site saturation. The measured growth rate was extremely low, ~100 Å/hour. We speculate that the desorption rate of the ethyl species was not significantly modified at the high substrate temperatures, whereas the desorption of Zn and Se became significant and dominated the growth. Work reported in the literature describing the chemical beam epitaxy of GaAs by Murrell et al.⁵ has indicated that a similar surface site blockage phenomenon was speculated to occur at relatively low substrate temperatures for GaAs.

The generation of free carriers at the growth front during MOMBE growth has been found to alleviate the site blockage phenomenon encountered using DEZn and DESe sources. In addition, new degrees of freedom are provided for the selection of the growth conditions. Depending on the degree of pyrolysis of the Zn source, the application of a laser was found to induce either an enhancement or a suppression of the growth rate. The influence of the laser on the growth rate for the various combinations of sources employed is summarized in table

⁵ A.J. Murrell, A.T.S. Wee, D.H. Fairbrother, N.K. Singh, J.S. Foord, G.J. Davies, and D.A. Andrews, "Surface Chemical Processes in Metal Organic Molecular-Beam Epitaxy: Ga Deposition from Triethylgallium on GaAs (100)," *J. Appl. Phys.* 68: 4053-4063 (1990).

Source of Zn	Source of Se	MOMBE Growth Rate*	Effect of Illumination on Growth Rate
DEZn	DESe	No Growth	None
DEZn	cracked DESe	Low	Enhancement
DEZn	elemental Se	Low	Enhancement
elemental Zn	cracked DESe	Low	Suppression
cracked DEZn	cracked DESe	Low	Suppression
elemental Zn	elemental Se	High (MBE)	Suppression
cracked DMZn	cracked DESe	Low	Enhancement
cracked DMZn	elemental Se	High	Suppression or Enhancement

* Low: 100 - 400 Å/hr. High: typical of MBE

Table 1. Comparison of the growth rate of ZnSe obtained for various source materials and with application of photons having energy sufficient to generate carriers.

1. An enhanced growth rate was observed for growth conditions which resulted in partially pyrolyzed DEZn at the surface. Thermal decomposition of the DEZn prior to delivery to the substrate surface resulted in the expected low unilluminated growth rate (as shown in table 1). However, in stark contrast to the results described for the unpyrolyzed DEZn molecule, a suppression of the illuminated growth rate was observed. From these qualitative observations, it is clear that the surface chemistry which dominated the laser-assisted MOMBE growth was the conversion of partially pyrolyzed DEZn into atomic Zn which leads to incorporation into the lattice. When using DMZn and solid Se, we have measured both growth rate enhancement and suppression depending on the growth conditions which result in various surface stoichiometries. A laser-assisted effect was also observed when a more "MBE-like" growth approach was used, i.e., both metalorganic sources were cracked and/or solid sources were employed. In these cases, however, the illuminated growth rate was measurably suppressed and was in agreement with earlier reports of laser-assisted MBE growth of ZnSe.⁶ We attributed the growth rate reduction to the desorption of excess Se on the surface. Variations of the energy of the impinging photons in the "MBE-like" growth approach also confirmed that the desorption phenomenon was related to the genera-

tion of electron/hole pairs and the presence of free carriers at the growth front.

Low temperature photoluminescence (PL) was used to assess the optical properties of the thin ZnSe films. Ultraviolet radiation from a He-Cd laser was used as the excitation source while keeping the sample temperature near 10K. Figure 2 shows the PL obtained from the illuminated (photons having $\lambda = 4579 \text{ Å}$) and unilluminated regions of the film when cracked DESe and uncracked DEZn were used as the source materials. The PL data demonstrates the effect that the laser has on the growth. The thin ZnSe film, which was not illuminated by the laser (upper curve), is dominated by deep level defects suggesting a highly nonstoichiometric layer. In contrast, the film grown with photon illumination (lower curve) shows practically no deep level luminescence and a remarkably more intense near bandedge feature, most likely a bound exciton with an energy of 2.796 eV. Identification of the impurity related to the formation of the exciton is complicated by the presence of strain and requires additional investigation. Figure 3 shows the PL for a film grown with solid Zn and cracked DESe, at a calibrated substrate temperature of 230°C. Comparison of the region illuminated by the laser (lower curve) to the unilluminated region (upper curve) is as expected for an "MBE-like" growth approach. In

⁶ R.L. Gunshor, L.A. Kolodziejewski, A.V. Nurmikko, and N. Otsuka, "Molecular Beam Epitaxy of II-VI Semiconductor Microstructures," in *Semiconductors and SemiMetals*, ed. T.P. Pearsall (Boston: Academic Press, 1990).

particular, the growth rate is not increased, but slightly decreased when illuminated with photons. The resultant effect of the laser illumination is to tune the surface stoichiometry. The PL reflects the tuning of the stoichiometry by eliminating the weak donor-to-acceptor pair band luminescence which may be attributed to electron-to-acceptor-like vacancy recombination. The photoluminescence measurements provide additional information suggesting that the photon-assisted growth affects primarily the metalorganic Zn molecule and contributes to converting the DEZn into metallic Zn allowing incorporation into the crystalline lattice.

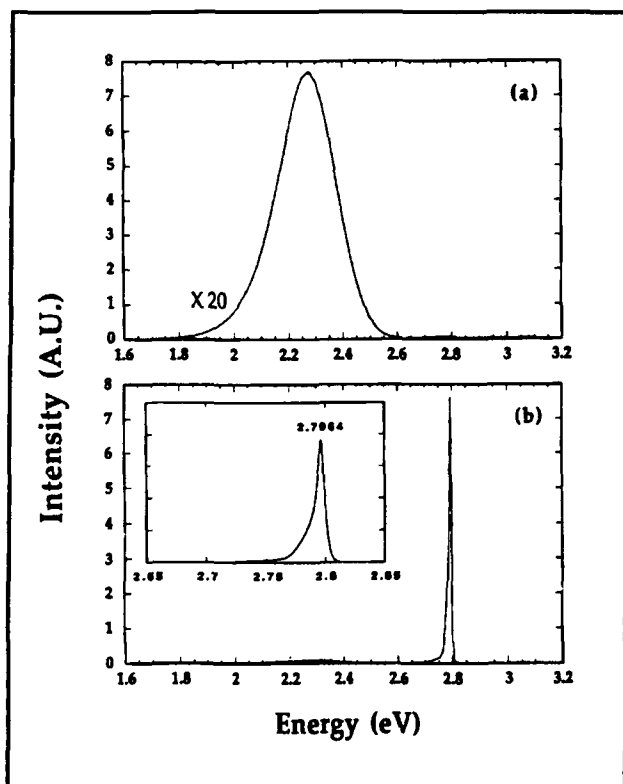


Figure 2. Photoluminescence of a ZnSe film grown using DEZn and DESe at a calibrated substrate temperature of 310°C (a) without laser illumination and (b) with $\lambda = 4579 \text{ \AA}$. Insert shows the energy of the dominant feature. Flow rates of 0.5 and 2.5 sccm were used for the DEZn and DESe, respectively.

3.3 Epitaxial Lattice-Matched III-V Buffer Layers for Wide Bandgap II-VI Visible Sources

Sponsors

Defense Advanced Research Projects Agency
Subcontract 216-25013
Joint Services Electronics Program
Contract DAAL03-92-C-0001

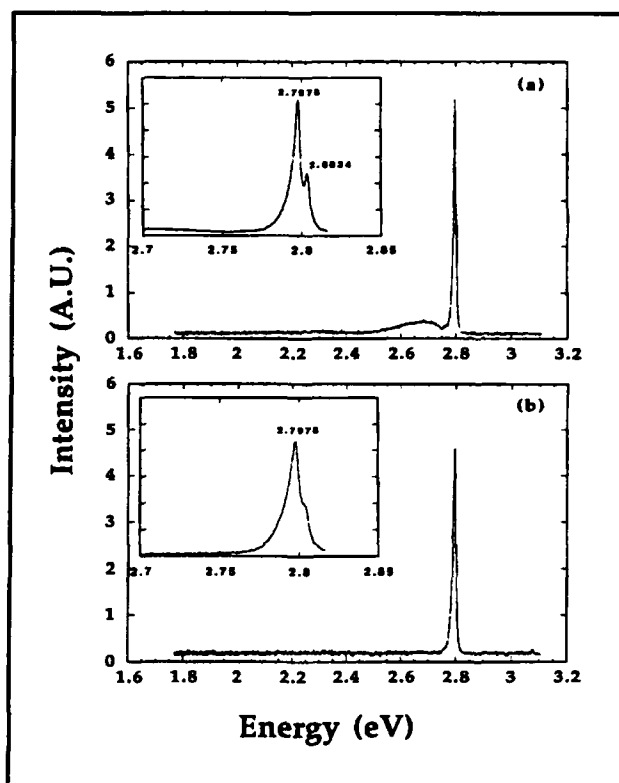


Figure 3. Photoluminescence of a ZnSe film grown using Zn and DESe (a) without laser illumination and (b) with $\lambda = 4579 \text{ \AA}$. Inserts show the energy of the dominant feature.

National Science Foundation
Grant DMR 92-02957

To take advantage of the numerous opportunities offered by long-lived, continuously operating, room temperature visible sources based on the wide bandgap II-VI semiconductors, several key technological barriers must be overcome. One very important difficulty is the lack of high quality II-VI substrate material. This particular limitation creates the need for the heteroepitaxy of II-VI layers onto III-V based substrates. If bulk substrates are employed, the only choice is to use GaAs which requires assessment of the effects of lattice mismatch (0.25%) strain on the resultant light emitting device (LED) structures. An additional consideration is the need for electronic confinement. Thus, the use of bandgap engineering and application of quantum wells is necessary for the design of the laser or LED device. Therefore, various II-VI ternary and quaternary layers are currently under investigation, with the resulting epilayer having a significantly varying lattice parameter. Issues of strain between both the substrate material and II-VI based active layer and between the well (narrow bandgap) and barrier (wider bandgap) II-VI alloy layers are crucial. The presence of strain contrib-

utes to the generation and propagation of defects which will ultimately affect the lifetime of any emitter.

Our interconnected epitaxy system provides the unique ability to investigate the growth of II-VI quantum well structures on III-V epitaxial surfaces where the lattice parameter ranges from that of GaP to InAs. These material systems cover the same lattice parameter range as Zn(S,Se,Te) and CdS, and all alloy combinations. The shaded region in figure 1 shows the range of lattice constants and energy bandgaps that can be grown in the CBE facility. We are presently investigating the growth of ZnSe on lattice-matched epitaxial (In,Ga)P buffer layers. As a first step, the growth conditions required to lattice match the (In,Ga)P to ZnSe are being determined. The epitaxial films are examined using double crystal x-ray diffraction and low temperature (10 K) photoluminescence. To date, the full width at half maximum (FWHM) of the (In,Ga)P peak (as determined by x-ray diffraction rocking curves) has been measured to be 34 arc seconds, whereas the GaAs substrate peak had a FWHM of 26 arc seconds. The photoluminescence spectra of the (In,Ga)P consists of a single peak corresponding to the near bandedge of the alloy. These (In,Ga)P films are typically grown at a substrate temperature of 470°C and with a growth rate between 0.25 and 1 μm per hour. Initial optical microscopy observations suggest that the starting surface morphology is featureless (unlike the cross-hatched surface of similarly strained (In,Ga)As which is typically used for buffer layers to ZnSe) and holds promise for the minimization of defect propagation into the active II-VI device layers and hence, enhancement of the performance of II-VI based optical sources.

3.4 Fabrication of Novel "Channel Dropping Filters" for Wavelength Division Multiplexed Photonic System Applications

Sponsor

Defense Advanced Research Projects Agency
Subcontract 542383

The fabrication of novel "channel dropping filters" for wavelength division multiplexed photonic system applications is currently underway. A channel dropping filter consists of three parallel, but coupled resonant waveguides, fabricated from (In,Ga)(As,P) to take advantage of the potential integration with the existing technology that is used in optical communication systems. The various (In,Ga)(As,P) layers

will be lattice-matched to InP substrates, but depending on the In and As mole fractions, will have various energy gaps and hence various indices of refraction. We are presently conducting experiments to determine the optimum growth conditions for the individual (In,Ga)(As,P) layers using in-situ reflection high energy electron diffraction, as well as ex-situ double crystal x-ray diffraction and photoluminescence. In addition, device simulations are underway to optimize the filter performance in order to determine (1) the appropriate mole fractions of quaternary layers necessary to vertically confine the optical signal, (2) the dimensions required to achieve the lateral waveguiding, and (3) the necessary coupling coefficient between the various waveguides. In this research program, a multi-investigator approach is required. Here, we will pursue the growth of the layered waveguide structure; the necessary gratings will be etched in the Submicron Structures Laboratory under the direction of Professor H.I. Smith (see part I, section 2, chapter 4), and the theory, device simulation, and measurements of filter performance are being carried out in the Optics and Devices Group with Professors H.A. Haus and E.P. Ippen (see part I, section 3, chapter 1).

3.5 Publications

Coronado, C.A., E. Ho, L.A. Kolodziejski, and C.A. Huber. "Photo-Assisted Molecular Beam Epitaxy of ZnSe." *Appl. Phys. Lett.* 61(5): 534-536 (1992).

Coronado, C.A., E. Ho, L.A. Kolodziejski, and C.A. Huber. "Laser-Assisted Growth of ZnSe by Metalorganic Molecular Beam Epitaxy." *Proceedings of the Material Research Society Symposium* 263: 181-186 (1992).

Coronado, C.A., E. Ho, and L.A. Kolodziejski. "Effect of Laser on MOMBE of ZnSe Using Gaseous and Solid Sources." *J. Cryst. Growth.* Forthcoming.

Ho, E., C.A. Coronado, and L.A. Kolodziejski. "Elimination of Surface Site Blockage due to Ethyl Species in MOMBE of ZnSe." *J. Electron. Mater.* Special Issue on Wide Bandgap II-VI Materials. Forthcoming.

Ho, E., C.A. Coronado, and L.A. Kolodziejski. "Photo-Assisted Chemical Beam Epitaxy of II-VI Semiconductors." *Proceedings of the Materials Research Society Symposium*, Boston, Massachusetts, November 28-December 4, 1992.

Chapter 4. Focused Ion Beam Microfabrication

Academic and Research Staff

Dr. John Melngailis, Professor Dimitri A. Antoniadis, Professor Carl V. Thompson, Dr. Xin Xu, Sergey Etchin

Visiting Scientists and Research Affiliates

Dr. Dominique Vignaud, Jane Sosonkina, Professor Guang-Sup Cho

Graduate Students

Mark A. Armstrong, Tony P. Chiang, Anthony D. Della Ratta, Henri J. Lezec, Christian R. Musil

Technical and Support Staff

Donna R. Martinez

4.1 Introduction

The focused ion beam research program at MIT has been mainly aimed at developing new applications. Our work can be divided into two areas: The first, served by a 150 kV system, is the high energy regime and includes implantation and lithography. The second is the lower energy regime and is aimed at developing repair processes for masks and integrated circuits. It is served by two machines, a 50 kV system mounted on a home built UHV chamber and an FEI 500D system which was donated by the FEI Company to MIT last year. This system produces Ga^+ ions between 5 and 25 keV at minimum beam diameters of 0.05 μm .

The high energy system includes automated patterning capability over wafers up to six inches in diameter. Alignment of the focused ion beam writing to within $\pm 0.1 \mu\text{m}$ of existing features on a wafer has been demonstrated. Software has been developed which permits patterns to be transferred from the layout system used in the Microsystems Technologies Laboratory to the focused ion beam machine. Accordingly, this permits flexible, mixed fabrication where standard steps have been carried out in the integrated circuits laboratory at MIT, and special implantation or lithography steps have been carried out on the focused ion beam system. Similar mixed fabrication has also been carried out on Si wafers partly fabricated at Ford Aerospace and on GaAs wafers at Raytheon Research Laboratory. The ion species available for implantation include the principal dopants of GaAs and Si. The

minimum beam diameter available is on the order of 0.1 μm at an ion current of 20 pA. In many of the implantation projects where the minimum diameter is not needed, a higher beam current can be used.

In the lower energy regime our work has mainly focused on the development of ion induced deposition. This technique uses a local ambient of a precursor gas, usually organometallic or metal halide, to permit deposition to be carried out with minimum linewidth of 0.1 μm . The local patterned deposition complements material removal by ion milling and is used to add missing absorber material in the repair of photomasks and x-ray lithography masks or to rewire local connections in integrated circuits. Our efforts have focused on (1) gold, tungsten, and copper deposition, (2) understanding the fundamentals of the process, and (3) deposition at non-normal incidence. Ga^+ ions in the range of 10-50 keV are mainly used.

4.2 Tunable Gunn Diodes - Optimization for Microwave Applications

Sponsor

Defense Advanced Research Projects Agency/
U.S. Army Research Office
Grant DAAL-03-92-G-0217

Project Staff

Christian R. Musil, Henri J. Lezec, Sergey Etchin, Leonard J. Mahoney,¹ Alex Chu,² Professor Dimitri A. Antoniadis, Dr. John Melngailis

Tunable Gunn diodes are two-terminal voltage controlled oscillators (VCOs). They are fabricated by using a focused ion beam to implant a gradient of doping in the direction of current flow. The best performance we have achieved so far is tunability over 20 GHz with a maximum frequency of 42 GHz. To optimize the performance, we have recently implanted a large array of devices (over 3000) varying the dose, geometry, and gradient as parameters. An immediate application of these simple VCOs is the built-in-test for monolithic microwave integrated circuits (MMICs). A tunable Gunn diode is coupled to the input, and a diode detector is coupled to the output. By switching these two elements into the circuit and applying a ramp bias signal to the Gunn diode, the circuit is tested by varying the frequency of the input signal over its entire range of operation.

4.3 Dose Rate Effects in the Implantation of Si in GaAs

Sponsor

Defense Advanced Research Projects Agency/
U.S. Army Research Office
Grant DAAL03-92-G-0217

Project Staff

Christian R. Musil, Tony E. Haynes,³ Sergey Etchin, Professor Dimitri A. Antoniadis, Dr. John Melngailis

The instantaneous current density of a focused ion beam is of order 0.1 to 1 A/cm². In normal, broad beam implantation the current density is 4 to 6 orders of magnitude lower. We have shown that this high instantaneous current density can lead to increased lattice damage in some cases of focused ion beam implantation. One way to mitigate these effects is to scan the beam over the sample so as to present a lower average current density. We have found surprising effects of a large variations in lattice damage as a function of the scan rate of the focused ion beam. At a given point on the substrate the scan schedule produces a pulsed implant

of a selected dwell time which is repeated after some period. We have measured the damage using Rutherford backscattering as well as electrical properties. At a given dwell time, for example, the amount of damage decreases for repetition periods up to times of order seconds. This implies that, contrary to one's intuition, after an ion (Si) has penetrated into the solid (GaAs), it does not come into equilibrium even after one second. In general, the lattice would be expected to be back in equilibrium in times of order nanoseconds.

4.4 Limited Lateral Straggle of Focused-Ion-Beam Implants

Sponsor

Defense Advanced Research Projects Agency/
U.S. Army Research Office
Grant DAAL03-92-G-0217

Project Staff

Dr. Dominique Vignaud, Christian R. Musil, Sergey Etchin, Professor Dimitri A. Antoniadis, Dr. John Melngailis

The lateral straggle of ions as they penetrate into a substrate limits the minimum lateral dimensions of implant profiles that can be defined in a substrate. This potential spreading of the profile has to be considered to fabricate devices at ultrasmall dimensions or confined carrier structures for quantum effect studies. The lateral distribution of focused-ion-beam implanted Si and Be atoms has been studied by measuring the electrical resistivity in grating structures. The gratings which were oriented perpendicular to the direction of the current flow were implanted with silicon and beryllium at 280 and 260 keV respectively. They were implanted into semi-insulating materials cut on- and off-axis, and then repaid-thermal-annealed. The lateral straggle was found to be less than 100 nm for Si and equal to 190 nm for the Be implants. The standard deviation of the lateral distribution was found to increase with the dose. This is attributed to a concentration-dependent diffusion which results in an anomalously high diffusion coefficient. Comparison of the experimental parameters of the implanted distribution with values found in standard tables or calculated by a Monte-Carlo TRIM code

¹ MIT Lincoln Laboratories.

² MITRE Corporation, Bedford, Massachusetts.

³ Oak Ridge National Laboratory.

seems to indicate that all simulations overestimate lateral straggle at the expense of penetration depth.

4.5 Focused Ion Beam Implantation in GaAs for Transistor Optimization

Sponsor

National Science Foundation
Grant ECS 89-21728

Project Staff

T.E. Kazior,⁴ M.H. Cobb,⁴ Sergey Etchin, Dr. John Melngailis

Focused ion beam implantation is a useful technique for optimizing channel implants in integrated circuits. The fact that the implants are done in a maskless, direct-write fashion permits the dose, ion energy, and ion species to be varied from device to device on the same wafer. Wafer to wafer variations do not obscure interpretation of the data. To demonstrate this, we have implanted the Be buried p-layer beneath the active Si-implanted channel in a GaAs MESFET. The Be and Si implant conditions were varied over a range of energies and doses. The optimum performance is expected for implant conditions which yielded the steepest gradient in the tail of the electron concentration profile without producing conducting holes. All implants were performed through a 50 nm SiN_x film and rapid thermal annealed at 900°C for 10 seconds. The transistor gates were 0.25 μm long with a T-shaped profile. Within the range of Be implant conditions explored, the gradient in the tail of the electron distribution was strongly dependent on the dose, but did not vary systematically with changes in energy. The experiments carried out on a single wafer indicate that a large process window exists for the Be implant parameters and this results in an improved 10 GHz noise performance. This type of optimization with conventional broad beam implants would require an unacceptable number of wafers and would be complicated by wafer to wafer variations.

These results also show that focused ion beam implantation could be useful as a production technique if a given integrated circuit required a large variety of implants, each one over a limited area. In conventional fabrication, each implant requires a complete sequence of steps (resist spinning, exposure, development, broad beam implantation, and resist stripping). These steps are eliminated by the

focused ion beam implant and, in some circumstances, may justify the cost in implantation time.

4.6 Confined Carrier Distributions in III-V Semiconductors Created by Focused Ion Beams

Sponsor

Defense Advanced Research Projects Agency/
U.S. Army Research Office (ASSERT Program)
Grant DAAL03-92-G-0305

Project Staff

Mark A. Armstrong, Professor Dimitri A. Antoniadis, Dr. John Melngailis

One way to obtain confined carrier distributions for quantum effect studies is to use focused ion beam implantation damage. In particular, the insulating region produced by the damage can be used to carve up the two-dimensional electron gas produced by modulation doping. One of the effects which may limit the resolution of this technique is the depletion of carriers around the implanted region. We are attempting to calculate the effect of this depletion by using analogies to the widely studied and modeled Si/SiO₂ interface in MOS structures. The width of the depletion will also be measured by writing different geometries to create planar capacitors and transistors in GaAs/AlGaAs mesas.

4.7 Focused Ion Beam Lithography for X-ray Mask Making

Sponsor

Semiconductor Research Corporation

Project Staff

Tony P. Chiang, Sergey Etchin, Dr. John Melngailis

Making an x-ray mask is a challenging task. The absorber material on the thin mask membrane must be fabricated of high Z material (e.g., Au or W) with high aspect ratio, (e.g., 0.25 to 0.5 μm thick at minimum dimensions down to 0.1 μm). Two techniques for writing the original pattern of the mask in resist are electron beam lithography and focused ion beam lithography. While electron beams have been extensively developed and applied, ion beams

⁴ Raytheon Research Laboratory, Lexington, Massachusetts.

have been used to write patterns down to $0.015\text{ }\mu\text{m}$ minimum linewidth and show no proximity effects even for resists over high Z material. The resist exposure times for the two techniques are comparable. Previously, we had fabricated x-ray masks at MIT with minimum linewidth of $0.05\text{ }\mu\text{m}$ in absorber $0.2\text{ }\mu\text{m}$ thick. One goal of this program is to fabricate x-ray masks for use at the Center for X-ray Lithography at the University of Wisconsin. The absorber material must be $0.5\text{ }\mu\text{m}$ thick because of the higher energy of the x-ray photons used. Thus the resist (PMMA) thickness in this case has to be of order $0.6\text{ }\mu\text{m}$, and the lithography is more challenging to accomplish. The masks are fabricated by exposing the PMMA over a thin gold plating base, writing the pattern with either Be^{++} or Si^{++} ions at 260 keV , developing the resist, and plating up the gold absorber features. We have determined the optimum ion exposure dose, developing conditions and plating conditions. In test structures we have succeeded in producing gold features with $0.1\text{ }\mu\text{m}$ lines $0.5\text{ }\mu\text{m}$ high. In the Prometrix test pattern which was successfully delivered to the University of Wisconsin the minimum lines written were $0.2\text{ }\mu\text{m}$ wide.

4.8 Focused Ion Beam Induced Deposition of Copper

Sponsors

National Science Foundation
Grant DMR 92-02633
U.S. Army Research Office
Grant DAAL03-90-G-0223

Project Staff

Anthony D. Della Ratta, Professor Carl V. Thompson, Dr. John Melngailis

Focused ion induced deposition is used in the repair of integrated circuits and masks. For the repair of circuits, a low resistivity of the deposited material is desirable. In the deposition process a local ambient of an organometallic gas is formed on the surface where the ion beam is incident. The incident ions cause the adsorbed molecules to be decomposed, leaving the metal, and usually some carbon, deposited on the surface. Typically the resistivity of the film is in the $100\text{-}1000\text{ }\mu\Omega\text{cm}$ range, compared to $1\text{-}10\text{ }\mu\Omega\text{cm}$ for pure metals. We have achieved the first focused ion beam deposition of copper from a novel organometallic precursor gas, $\text{Cu}(\text{hfac})\text{TMVS}$. Ga^+ ions at 35 keV

were used. Resistivity and yield have been measured as a function of temperature and average ion current density. Submicron copper lines deposited at room temperature from this precursor exhibit resistivities as low as $70\text{ }\mu\Omega\text{cm}$; a sharp drop in these values is noted for deposition at 70°C , and deposition on a substrate heated above about 100°C yields resistivities near those of pure bulk copper. Composition analysis by Auger Electron Spectroscopy shows the high temperature deposition to be nearly pure copper. Deposition yields of 25 copper atoms per incident Ga^+ ion have been obtained on both silicon and silicon dioxide substrates, with growth rates of up to $13\text{ }\text{\AA}$ per second at an average ion current density of $200\text{ }\mu\text{A}/\text{cm}^2$. The microstructure of the film will be examined by scanning electron microscopy (SEM) and transmission electron microscopy (TEM). The precursor shows special promise for the deposition of low resistivity submicrometer interconnects on integrated circuits.

4.9 Focused Ion Beam Induced Deposition and Ion Milling as a Function of Angle of Ion Incidence

Sponsors

U.S. Army Research Office
Grant DAAL93-90-G-0223
U.S. Navy - Naval Research Laboratory/Micrion
Contract M08774

Project Staff

Dr. Xin Xu, Anthony D. Della Ratta, Jane Sosonkina, Dr. John Melngailis

In the repair of integrated circuits, x-ray masks focused ion beam induced deposition and ion milling often have to be performed over quite nonplanar topography. Thus, the milling and the deposition as a function of the angle of ion incidence are important. The milling yield of Si , SiO_2 , Au , and W versus angle of incidence using 25 keV Ga^+ ions has been measured. In qualitative agreement with simulations, the yield rises with angle and then falls as grazing incidence is approached. Deposition yield versus angle was measured using dimethylgold hexafluoro-acetylacetonate and $\text{W}(\text{CO})_6$ as the precursor gases. The measurements were carried out using cylindrical quartz fibers $30\text{-}50\text{ }\mu\text{m}$ in diameter which automatically provide a range of angles. Rippling of the deposited material is observed at angles of incidence greater than 50° .

4.10 Publications

- Chu, A., H.M. Cronson, J.F. Devine, S. Soares, M.N. Solomon, H.J. Lezec, and C.R. Musil. "RF Built-In Test and Enabling Technologies for Integrated Diagnostics." Paper presented at the IEEE Systems Readiness and Automatic Testing Conference, Dayton, Ohio, September 21-24, 1992.
- Ehrlich, D.J., R.R. Kunz, M.A. Hartney, M.W. Horn, and J. Melngailis. "New Photoresist Processes at UV Wavelengths Less Than 200 nm." In *Irradiation of Polymeric Materials*. Eds. E. Reichmanis, O'Donnel, and Frank. ACS Symposium Series, vol. 527. Forthcoming.
- Kunz, R., D.J. Ehrlich, J. Melngailis, and M.W. Horn. "Selective Area Growth of Metal Oxide Films induced by Patterned Excimer Laser Surface Photolysis." *Proc. Mat. Res. Soc. Symp.* 236: 105 (1992).
- Lattes, A.L., S.C. Munroe, M.M. Seaver, J.E. Murguia, and J. Melngailis. "Improved Drift in Two-Phase, Long-Channel, Shallow-Buried-Channel CCDs with Longitudinally Nonuniform Storage-Gate Implants." *IEEE Trans. Electron Devices* 39: 1772 (1992).
- Melngailis, J. "Focused Ion Beam Lithography." Invited plenary paper at the International Conference on the Ion Beam Modification of Materials, Heidelberg, Germany September 1-11, 1992. *Nucl. Instrum. Methods Phys. Res.* Forthcoming.
- Vignaud, D., S. Etchin, K.S. Liao, C.R. Musil, D.A. Antoniadis, and J. Melngailis. "Lateral Straggle of Focused-Ion-Beam Implanted Be in GaAs." *Appl. Phys. Lett.* 60: 2267 (1992).
- Vignaud, D., C.R. Musil, S. Etchin, D.A. Antoniadis, and J. Melngailis. "Lateral Straggle of Si and Be Focused-Ion-Beam-Implanted in GaAs." *J. Vac. Sci. Technol.* Forthcoming.
- Xu, X., A.D. Della Ratta, J. Sosonkina, and J. Melngailis. "Focused Ion Beam Induced Deposition and Ion Milling as a Function of Angle of Incidence." Paper presented at the International Symposium on Electron, Ion, and Photon Beams, Orlando, Florida, May 26-31, 1992. *J. Vac. Sci. Technol. B* 10: 2675 (1992).

Thesis

- Lezec, H.J. *Tunable-Frequency Gunn Diodes Fabricated by Focused Ion-Beam Implantation*. Ph.D. diss., Dept. of Electr. Eng. and Comput. Sci., MIT, 1992.

Section 2 Quantum-Effect Devices

Chapter 1 Statistical Mechanics of Quantum Dots

Chapter 2 Single Electron Transistors

Chapter 3 Differential Resistance Through a Quantum Dot:
Signature of Kondo Correlation

Chapter 4 Submicron and Nanometer Structures Technology
and Research

Chapter 1. Statistical Mechanics of Quantum Dots

Academic and Research Staff

Professor Boris L. Altshuler, Dr. Richard Berkovits, Dr. Aaron Szafer

Graduate Students

Michael Faas

Technical and Support Staff

Imadiel Ariel, Kristine M. Bowring

1.1 Project Description

Sponsor

Joint Service Electronics Program
Contract DAAL03-92-C-0001

We are continuing to study equilibrium properties of quantum dots—isolated metallic systems with sizes smaller than a typical length of an electron dephasing. In contrast with the transport properties of these systems, their thermodynamics was relatively neglected by both theorists and experimentalists.

We are investigating theoretically the dielectric properties of quantum dots. We have considered a neutral grain with a positive uniform background and conduction electrons which are scattered by disordered impurity centers. Due to the fact that the grain is disordered, one should expect a nonuniform distribution of charge inside the grain. The electric field outside a grain is determined by the charge distribution inside the sample. Therefore, in principle, it is possible to measure electric field outside the grain, although the grain's net charge is equal to zero. This means that a neutral quantum dot without any external electric field possesses a finite dipole moment as well as higher-order multipole moments.

We have calculated the mean square electric potential far from the grain surface and determined its temperature and magnetic field dependence.¹ We have also considered the response of quantum dot to an external electric field and determined

mesoscopic (sample to sample) fluctuations of the electric polarizability.² The zero field (spontaneous) dipole moment, as well as the polarizability, depends significantly on the temperature and the magnetic field manifesting the quantum nature of the phenomena. Due to screening of the charge fluctuations in the bulk of the grain, both effects are rather weak, so that only the surface charge fluctuations are important. Nevertheless, for systems with relatively low-electron density (such as semiconductors), both effects are well within current experimental capabilities.

Modern experimental technique allows us to resolve single-electron energy levels in a quantum dot.³ In most cases the electrons within a dot are scattered irregularly by impurities and the surface. Even for a "clean" quantum dot with a size much smaller than the mean free path, the motion of electrons can be chaotic rather than integrable due to the particular shape of the grain. The electron energy spectrum of these chaotic systems turns out to be rather irregular.

We have started to develop a statistical approach to the description of chaotic energy spectra in the presence of external fields. First, we have considered a disordered mesoscopic ring with Aharonov-Bohm flux Φ . The energy of a given electron state ϵ_α (we will measure ϵ_α in units of mean energy level spacing Δ) is a periodic function of Φ with a period $\Phi_0 = hc/e$. At the same time, on the interval $0 < \Phi < \Phi_0$, this function $\epsilon_\alpha(\Phi)$ can be considered as a random one. We have found that the autocorrelation function of the derivatives $d\epsilon_\alpha/d\Phi$ (i.e., of

¹ R. Berkovitz and B.L. Altshuler, "Electric Field Outside a Neutral Mesoscopic Grain," *Europhys Lett.* 19: 115 (1992).

² R. Berkovitz and B.L. Altshuler, "Fluctuations of the Electrical Polarizability of a Thin Mesoscopic Film," *Phys. Rev. B* 46: 12526 (1992).

³ R.C. Ashoori, H.L. Stormer, J.S. Weiner, L.N. Pfeiffer, S.J. Pearton, K.W. Baldwin, and K.W. West, "Single-Electron Capacitance Spectroscopy of Discrete Quantum Levels," *Phys. Rev. Lett.* 68: 3088 (1992).

the currents carried by the level α at different fluxes) is determined as

$$C(\Phi) = \frac{\partial \varepsilon_{\alpha}(\Phi_1)}{\partial \Phi_1} \cdot \frac{d\varepsilon_{\alpha}(\Phi_1 + \Phi)}{d\Phi}.$$

In the interval $g^{1/2}\Phi_0 < \Phi < \Phi_0$ (where $g \gg 1$ is the conductance of the system in units e^2/h), this correlation function is universal, i.e., independent on the disorder and particular characteristics of the quantum dot:

$$C(\Phi) = -\frac{1}{\pi^2} \frac{\Phi_0}{\Phi}.$$

This result, though derived for the quantum dots with sufficiently strong disorder, is probably also valid for clean quantum dots with chaotic shape and perhaps also for much broader classes of quantum

systems including, for example, Rydberg atoms in an external magnetic field.

1.2 Publications

Altshuler, B.L., and L.B. Ioffe. "Motion of Fast Particles in Strongly Fluctuating Magnetic Fields." *Phys. Rev. Lett.* 69: 2979 (1992).

Berkovitz, R., and B.L. Altshuler. "Electric Field Outside a Neutral Mesoscopic Grain." *Europhys. Lett.* 19: 115 (1992).

Berkovitz, R., and B.L. Altshuler. "Fluctuations of the Electrical Polarizability of a Thin Mesoscopic Film." *Phys. Rev. B* 46: 12526 (1992).

Szafar, R., and B.L. Altshuler. "Universal Correlations in the Spectra of Chaotic Systems With an Aharonov-Bohm Flux." *Phys. Rev. Lett.* Forthcoming.

Chapter 2. Single Electron Transistors

Academic and Research Staff

Professor Marc A. Kastner

Visiting Scientists and Research Affiliates

Shalom Wind¹

Graduate Students

Paul A. Belk, Ethan B. Foxman

2.1 Project Description

Sponsors

Joint Services Electronics Program

Contract DAAL03-92-C-0001

National Science Foundation

Grant ECS 88-13250

Grant ECS 92-03427

Several years ago we discovered² that while conventional field-effect transistors turn from the off-state to the on-state only once as electrons are added to them, a very small transistor turns on and then off every time one electron is added. The near-term goal of our research is to understand why the single electron transistor works the way it does. Our long-term goal is to make the device characteristics useful for applications.

A sketch of our first single electron transistor³ is shown in figure 1a. We begin with a crystal of GaAs which has such a high density of impurities that it is metallic. This plays the role of the gate. On top of this we grow a layer of AlGaAs, which is an insulator, and a layer of pure GaAs, where the electrons reside. If a positive voltage is applied between the gate and the source or drain, electrons accumulate at the AlGaAs/GaAs interface. Because of the strong electric field at this interface,

each electron's energy for motion perpendicular to the interface is quantized, and at low temperatures the electrons move only in the two dimensions parallel to the interface. The special trick that makes this a single electron transistor is the creation by electron beam lithography of a pair of electrodes on the top surface of the GaAs. When negative voltage is applied between these and the source or drain, the electrons are repelled and cannot accumulate underneath the electrodes. Consequently, the electrons are confined in a narrow channel between the two electrodes. Constrictions sticking out into the channel repel the electrons and create potential barriers at either end of the channel. A plot of the potential is shown in figure 1b. For an electron to travel from the source to the drain, it must tunnel through these barriers. A "pool" of electrons accumulates between the two constrictions, separated from the leads by the tunnel barriers.

Figure 2 shows the current through the device⁴ as a function of the voltage V_g between the gate and the source. A very small amount of voltage is applied between the two leads, which is just large enough to measure the tunneling conductance between source and drain. The results are astounding. The conductance displays sharp resonances that are almost periodic in V_g . By calculating the capacitance between the pool of electrons and the gate,

¹ IBM Thomas J. Watson Research Laboratories, Yorktown Heights, New York.

² J.H.F. Scott-Thomas, S.B. Field, M.A. Kastner, H.I. Smith, and D.A. Antoniadis, "Conductance Oscillations Periodic in the Density of a One-Dimensional Electron Gas," *Phys. Rev. Lett.* 62: 583 (1989); M.A. Kastner, "The Single-Electron Transistor," *Rev. Mod. Phys.* 64: 849 (1992).

³ U. Meirav and S.J. Wind, "Single Electron Charging and Periodic Conductance Resonances in GaAs Nanostructures," *Phys. Rev. Lett.* 65: 771 (1990).

⁴ E.B. Foxman, P.L. McEuen, U. Meirav, N.S. Wingreen, Y. Meir, P.A. Belk, N.R. Belk, M.A. Kastner, and S.J. Wind, "The Effects of Quantum Levels on Transport Through a Coulomb Island," unpublished; M.A. Kastner, "Artificial Atoms," *Phys. Today*, 46(1): 24-31 (1993).

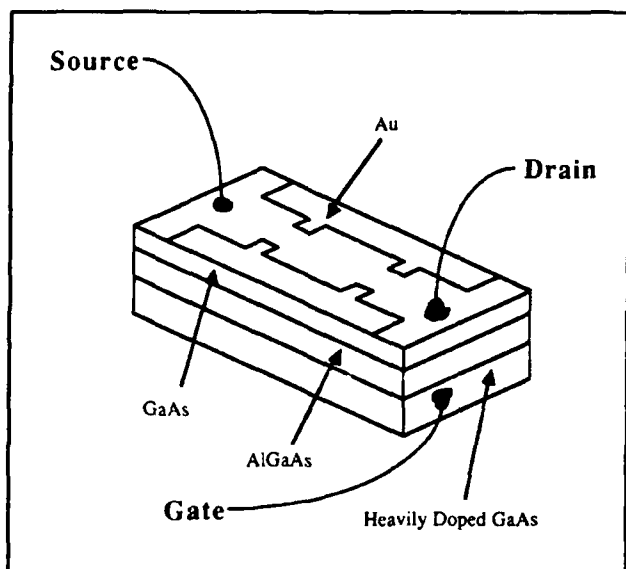


Figure 1a. (a) Schematic drawing of the single electron transistor.

we can show⁵ that the period is the voltage necessary to add *one electron* to the pool.

There is a simple way to explain the periodic conductance resonances;⁶ the theory is called the Coulomb blockade model. When an electron tunnels from one lead onto the pool of electrons and then onto the other lead, adding a charge Q to the pool requires energy $Q^2/2C$, where C is the total capacitance between the pool and the rest of the system; since you can add no less than one electron, the flow of current requires a Coulomb energy $e^2/2C$. A fancier way to explain this is that because of charge quantization there is an energy gap in the spectrum of states for tunneling: For an electron to tunnel onto the pool its energy must exceed the Fermi energy of the contact by $e^2/2C$, and for a hole to tunnel its energy must be below the Fermi energy by the same amount. Consequently, the energy gap has width e^2/C . If the temperature is low enough that $kT < e^2/2C$, neither electrons nor holes can flow from one lead to the other.

With the gate voltage V_g we can alter the energy required to add charge to the pool. V_g is applied between the gate and source, but if the drain-source voltage is very small, the source, drain and pool are all at almost the same potential. With V_g

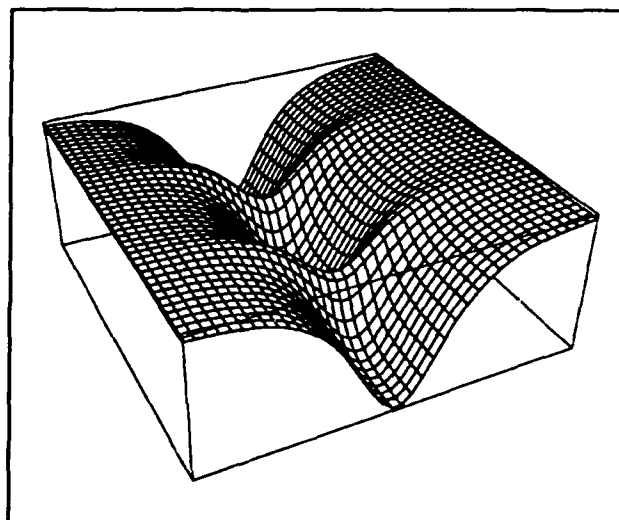


Figure 1b. (b) Potential similar to the one in the single electron transistor plotted as a function of position at the GaAs/AlGaAs interface.

applied the electrostatic energy of charge Q on the pool is

$$E = QV_g + Q^2/2C. \quad (1)$$

The first term is the attractive interaction between the positively charged gate electrode and the negative charge Q , and the second term is the repulsive interaction among the bits of charge in the pool. Equation 1 shows that the energy as a function of Q is a parabola with minimum at $Q_0 = -CV_g$.

By varying V_g , we can choose any value of Q_0 , the charge that would minimize the energy in equation 1 if the charge were not quantized. However, because the real charge *is* quantized, only discrete values of the energy E are possible. For all values of Q_0 except $Q_0 = -(N + 1/2)e$, there is a non-zero energy for adding or subtracting an electron. Under these circumstances, no current can flow at low temperature. However, if $Q_0 = -(N + 1/2)e$, the state with $Q = -Ne$ and that with $Q = -(N+1)e$ are degenerate; the charge fluctuates between the two values even at zero temperature. Consequently, the energy gap in the tunneling spectrum disappears, and current can flow. The peaks in conductance are, therefore, periodic, occurring whenever

⁵ U. Meirav and S.J. Wind, "Single Electron Charging and Periodic Conductance Resonances in GaAs Nanostructures," *Phys. Rev. Lett.* 65: 771 (1990); A. Kumar, "Self-consistent Calculations on Confined Electrons in Three-dimensional Geometries," *Surf. Sci.* 263: 335-340 (1992).

⁶ G. Grabert and M.H. Devoret, eds. *Single Charge Tunneling—Coulomb Blockade Phenomena in Nanostructures*, (New York: Plenum Press, 1992).

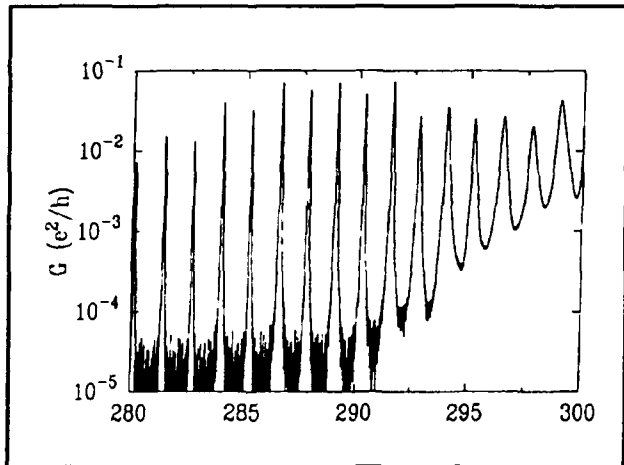


Figure 2. Conductance in units of the quantum of conductance e^2/h versus voltage on the n-GaAs substrate. On the logarithmic plot, it is clear that the transistor has an on-to-off conductance ratio that exceeds 10^3 for the lowest gate voltages.

the average charge on the artificial atom is $Q_0 = -(N + 1/2)e$, spaced in gate voltage by e/C .

The Coulomb blockade model accounts for charge quantization but ignores the quantization of energy resulting from the small size of the region in which the electrons are confined. If one thinks of the region between the potential barriers as a box, the lowest energy spacings are of the order $\hbar^2/2ma^2$ where a is the size of the box. Because the energy as well as the charge is quantized, we find it useful to think of the single electron transistor as an artificial atom.

The energy level spectrum of the atom can be measured directly by observing the tunneling current at fixed V_g as a function of the voltage (V_{ds}) between drain and source. The Fermi level in the source rises in proportion to V_{ds} relative to the drain, so it also rises relative to the energy levels of the artificial atom (see the inset to figure 3). Current begins to flow when the Fermi energy of the source is raised just above the first quantized energy level of the atom. As the Fermi energy is

raised further, higher energy levels in the atom fall below the Fermi energy, and more current flows because there are additional channels for the electron to use for tunneling onto the artificial atom. We measure the energies by measuring the voltage at which the current increases, or, equivalently, the voltage at which there is a peak in the derivative of the current dI/dV_{ds} . We show results of such a measurement⁷ in the upper part of figure 3.

Increasing the gate voltage lowers all the energy levels in the atom by $-eV_g$, so that the entire tunneling spectrum shifts with V_g . This effect can be observed by plotting the values of V_{ds} at which peaks appear in dI/dV_{ds} , as is done in the lower part of figure 3. You can see the gap in the tunneling spectrum shift lower with increasing V_g and then disappear at the charge-degeneracy point, just as predicted by the Coulomb blockade model. You can also see the discrete energy levels of the artificial atom. The charge-degeneracy points are the values of V_g for which one of the energy levels of the artificial atom is degenerate with the Fermi energy in the leads when $V_{ds} = 0$, because only then can the charge of the atom fluctuate.

During the past year, we have developed a thorough understanding of the energy spectrum of single electron transistors. In addition, we now know what limits their operating temperature. As shown in figure 3, the devices we have made so far have a Coulomb-blockade gap that is about 1 meV wide and energy level spacings that are about one-fifth to one-tenth of that. As the temperature is raised, the conductance resonances acquire a width of ~ 4 kT. Since $kT = 1$ meV is equivalent to $T = 12$ K, the peak-to-valley ratio becomes small above a few degrees K. Making the single electron transistor useful will require making its operating temperature much higher. This requires decreasing the size because both the Coulomb energy, which varies inversely with the capacitance, and the energy level spacings will get larger for smaller structures. This is the direction of our next research effort.

⁷ E.B. Foxman, P.L. McEuen, U. Meirav, N.S. Wingreen, Y. Meir, P.A. Belk, N.R. Belk, M.A. Kastner, and S.J. Wind, "The Effects of Quantum Levels on Transport Through a Coulomb Island," unpublished; M.A. Kastner, "Artificial Atoms," *Phys. Today*, 46(1): 24-31.

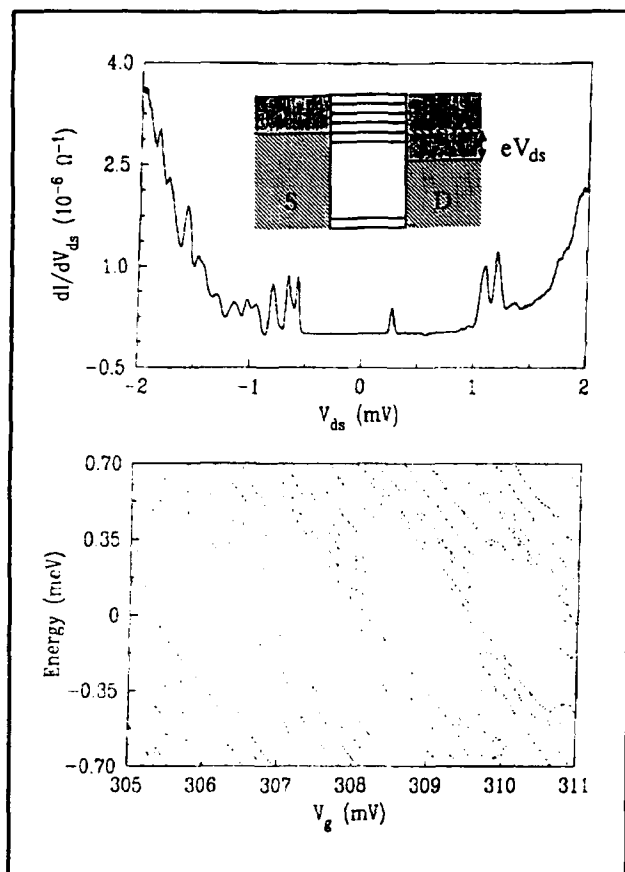


Figure 3. Discrete energy levels of a single electron transistor can be detected by varying the drain-source voltage. When a large enough V_{ds} is applied, electrons overcome the energy gap and tunnel from the source to the pool of electrons (see inset of upper panel). Upper panel: Every time a new discrete state is accessible, the tunneling current increases, giving a peak in dI/dV_{ds} . The Coulomb blockade gap is the region between about -0.5mV and $+0.3\text{mV}$ where there are no peaks. Lower panel: Plotting the positions of these peaks at various gate voltages gives the level spectrum. Note how the levels and the gap move downward as V_g increases.

2.2 Publications

Bagwell, P.F., S.L. Park, A. Yen, D.A. Antoniadis, H.I. Smith, T.P. Orlando, and M.A. Kastner. "Magnetotransport in Multiple Narrow Silicon Inversion Channels Opened Electrostatically into a Two-dimensional Electron Gas." *Phys. Rev. B* 45(16): 9214-9221 (1992).

Kastner, M.A. "The Single-Electron Transistor." *Rev. Mod. Phys.* 64(3): 849-858 (1992).

Kastner, M.A., E.B. Foxman, P.L. McEuen, U. Meirav, A. Kumar, and S.J. Wind. "Transport Spectroscopy of a Coulomb Island." In *Nanostructures and Mesoscopic Systems*. Eds. W.P. Kirk and M.A. Reed. San Diego, California: Academic Press, 1992.

McEuen, P.L., E.B. Foxman, J. Kinaret, U. Meirav, M.A. Kastner, N.S. Wingreen, and S.J. Wind. "Self-consistent Addition Spectrum of a Coulomb Island in the Quantum Hall Regime." *Phys. Rev. B* 45(19): 11419-11422 (1992).

Chapter 3. Differential Resistance Through a Quantum Dot: Signature of Kondo Correlation

Academic and Research Staff

Professor Patrick A. Lee

Graduate Students

Jari M. Kinaret, Dmitri B. Chklovskii

Technical and Support Staff

Imadiel Ariel

3.1 Project Description

Sponsor

Joint Services Electronics Program
Contract DAAL03-92-C-0001

The behavior of an atomic impurity coupled to conduction electrons has become one of the paradigms of condensed matter physics. Competition between on-site Coulomb interaction and band hybridization produces the Kondo effect: a crossover from weak to strong coupling between the localized and band electrons below the Kondo temperature, T_K . The study of the Kondo effect has been limited, however, by the nature of the impurity system. Since it is a daunting task to drive the host metal out of equilibrium, it is the *equilibrium* properties of Kondo impurities that have been explored.

In the study of transport through a quantum dot, we have a new Kondo system in which *non-equilibrium*—a semiconductor quantum dot weakly coupled to its leads—is routinely achieved. Anderson's model for a Kondo impurity—discrete, interacting levels coupled to a band—also describes quantum dots. The discrete spectrum of a single dot has been probed experimentally by transport and capacitance spectroscopy, and the strong on-site Coulomb interaction is observed in

Coulomb-blockade conductance oscillations.¹ Anderson's model has provided an excellent theoretical description of these experiments.² However, it is only the high temperature regime that has been explored experimentally, while it is below T_K that the Kondo effect emerges.

We have previously shown that below T_K , the Kondo resonance leads to perfect transparency of the quantum dot at the Fermi energy. This leads to dramatic effects on the lineshape of the conductance peaks as a function of gate voltage.³ We recently realized that a striking signature on the Kondo correlation appears in nonequilibrium properties, such as the differential conductance, even at a temperature higher than T_K .⁴ The requirement is that the temperature must be less than Γ , the intrinsic line width of the resonant transmission peak. This latter condition is much easier to realize experimentally. We have shown that if the gate voltage is set so that we are on the shoulder of a conductance peak and the source drain voltage V_{SD} is increased, the differential conductance would exhibit a peak around $V_{SD}=0$. Furthermore, if a magnetic field B is applied, the differential conductance peak will split into two peaks centered at the Zeeman energy $\pm g\mu_B B$. We believe that the observation of this conductance peak is a clean signature of the Kondo correlation in the quantum dot system.

¹ U. Meirav, M. Kastner, and S.J. Wind, "Single-Electron Charging and Periodic Resonances in GaAs Nanostructures," *Phys. Rev. Lett.* 65: 771 (1990).

² Y. Meir, N. Wingreen, and P.A. Lee, "Transport Through a Strongly Interacting Electron System," *Phys. Rev. Lett.* 66: 3048 (1991).

³ T.K. Ng and P.A. Lee, "On-site Coulomb Repulsion and Resonant Tunnelling," *Phys. Rev. Lett.* 61: 1768 (1988).

⁴ Y. Meir, N. Wingreen, and P.A. Lee, "Low Temperature Transport Through a Quantum Dot: The Anderson Model Out of Equilibrium," submitted to *Phys. Rev. Lett.*

3.2 Publications

Lee, P.A. "Few Electron Nanostructures: A New Laboratory for Studying Strongly Correlated Systems." *Proceedings of NATO Workshop*, Nordwig, Netherlands, 1992.

Meir, Y., N. Wingreen, and P.A. Lee. "Low Temperature Transport Through a Quantum Dot: The Anderson Model Out of Equilibrium." Submitted to *Phys. Rev. Lett.*

Chapter 4. Submicron and Nanometer Structures Technology and Research

Academic and Research Staff

Professor Henry I. Smith, Richard J. Aucoin, James M. Carter, Robert C. Fleming, Jr., Dr. Mark L. Schattenburg

Visiting Scientists and Research Affiliates

Dr. Khalid Ismail,¹ Yang Zhao,² Nubuyoshi Koshida³

Graduate Students

Martin Burkhardt, Mike T. Chou, William Chu, Jay N. Damask, Cristopher C. Eugster, Reza A. Ghanbari, Nitin Gupta, Scott D. Hector, Hang Hu, James J. Hugunin, Yao-Ching Ku, Arvind Kumar, Alberto M. Moel, George E. Rittenhouse, Lisa T.-F. Su, Farzam Toudeh-Fallah, Vincent V. Wong, Kenneth Yee, Anthony Yen

Undergraduate Students

Juan Ferrera, Julie C. Lew, Huiying Li, Michael H.Y. Lim, Kristine W. Ma, Chad H. Mikkelsen, Euclid E. Moon, Daniel B. Olster, Satyen N. Shah

Technical and Support Staff

Donna R. Martinez, Mark K. Mondol, Jeanne M. Porter, Robert D. Sisson

4.1 Submicron Structures Laboratory

The Submicron Structures Laboratory at MIT develops techniques for fabricating surface structures with feature sizes in the range from nanometers to micrometers and uses these structures in a variety of research projects. These projects, described briefly below, fall into four major categories: (1) development of submicron and nanometer fabrication technology; (2) nanometer and quantum-effect electronics; (3) crystalline films on non-lattice-matching substrates; and (4) periodic structures for x-ray optics, spectroscopy and atomic interferometry.

4.2 X-Ray Nanolithography

Sponsors

Defense Advanced Research Projects Agency
Contract N00019-92-K-0021
Joint Services Electronics Program
Contract DAAL03-92-C-0001

National Science Foundation
Grant ECS 90-16437

Project Staff

Richard J. Aucoin, James M. Carter, William Chu, Robert C. Fleming, Jr., Reza A. Ghanbari, Nitin Gupta, Scott D. Hector, Huiying Li, Alberto M. Moel, Dr. Mark L. Schattenburg, Professor Henry I. Smith, Vincent V. Wong

A large fraction of the applications pursued by the Submicron Structures Laboratory require a reliable lithographic technique capable of producing sub-100 nm features with broad process latitude and high throughput. Ideally, the technique should be simple, low-cost, and enable students to do their own lithography locally. For this reason, we have been developing x-ray nanolithography, exploring its limits, and making its various components (e.g., mask making, resists, electroplating, sources, alignment, etc.) reliable and "user friendly." Because of the critical importance of x-ray mask technology, we discuss this in a separate section (4.3).

¹ University of Cairo, Giza, Egypt, and IBM Corporation, Thomas J. Watson Research Center, Yorktown Heights, New York.

² Princeton University, Princeton, New Jersey.

³ Tokyo University of Agriculture and Technology, Tokyo, Japan.

Our sources for x-ray nanolithography are simple, low-cost electron-bombardment targets, typically Cu_L ($\lambda = 1.32 \text{ nm}$), separated by $1.4 \text{ }\mu\text{m}$ -thick SiN_x vacuum windows from the helium-filled exposure chambers. In 1993 we will greatly increase our throughput with a Hampshire Instruments 3500X laser-plasma x-ray source and exposure system. The 3500X will be located in a dedicated room adjacent to the Integrated Circuits Laboratory.

We have developed an apparatus for aligning an x-ray mask to substrates in X, Y and θ and controlling the mask-sample gap. Substrates ranging from 10 cm -diameter Si wafers to $1 \times 1 \text{ cm}$ GaAs chips are handled.

In earlier research we showed that for x-ray wavelengths longer than $\sim 1 \text{ nm}$, the range of the photoelectron emitted when an x ray is absorbed in resist does not limit resolution. Down to feature sizes $\sim 20 \text{ nm}$, diffraction is the only concern. By means of accurate electromagnetic calculations, taking into account the vectorial character of the electromagnetic field and the dielectric properties of the absorber, we have shown that when source spatial coherence is optimized, diffraction does not limit resolution as severely as had been predicted by simple Fresnel diffraction calculations. The results are summarized in figure 1.

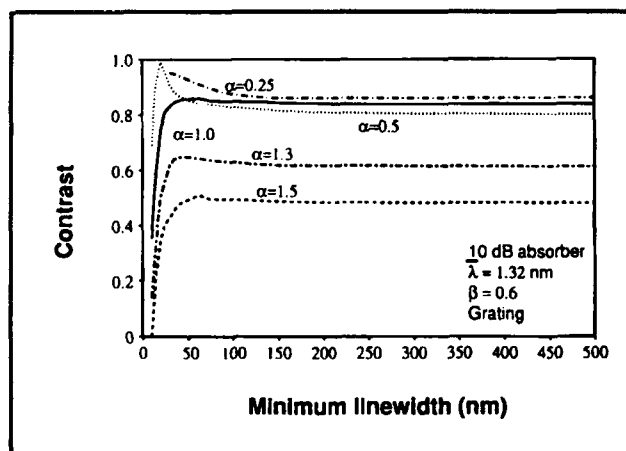


Figure 1. Plot of image contrast for a grating pattern of equal lines and spaces as a function of linewidth, W . The parameter α is related to gap G and wavelength λ via $G = \alpha W^2/\lambda$. β is the ratio of penumbral edge blur to linewidth $\beta = \delta/W$.

For the linewidth range from 70 to 20 nm , mask-substrate gaps must be below $5 \text{ }\mu\text{m}$. This is not a problem in research, but in manufacturing it may be unacceptable. For this reason we are investigating the feasibility of using arrays of zone plates for projection imaging with x rays of either 4.5 nm or $\sim 1.2 \text{ nm}$ wavelength.

Figure 2 shows the result of two aligned exposures with x-ray nanolithography. This quantum-effect device is an array of quasi-one-dimensional conductors with a crossing tunnel gate.

In the nanolithography range, the final profile obtained in resist depends on both the aerial image and the development characteristics of the resist. We have developed a model and simulation program that enable us to predict resist profiles given the input parameters. We are setting up an apparatus for checking experimentally the simulation.

Quasi-1D PRESTFET Device

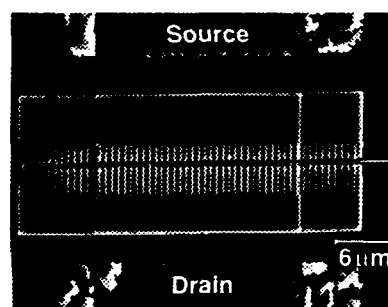


Figure 2. Scanning electron micrograph of a quantum-effect device structure fabricated using two separate, aligned x-ray nanolithography exposures. The master x-ray masks were fabricated at the Naval Research Laboratory (NRL). The device is an array of quantum wires with tunneling barriers in the middle.

4.3 Improved Mask Technology for X-Ray Lithography

Sponsors

Defense Advanced Research Projects Agency
Contract N00019-92-K-0021
National Science Foundation
Grant ECS 90-16437

Project Staff

James M. Carter, William Chu, Juan Ferrera, Robert C. Fleming, Jr., Reza A. Ghanbari, Michael H.Y. Lim, Mark K. Mondol, Dr. Mark L. Schattenburg, Professor Henry I. Smith, Vincent V. Wong

At feature sizes of 100 nm and below, the mask-to-sample gap, G , must be precisely controlled. The mesa mask shown schematically in figure 3 yields mask membranes that are flat to $< 250 \text{ nm}$. We are improving this technology with the flip-bonded

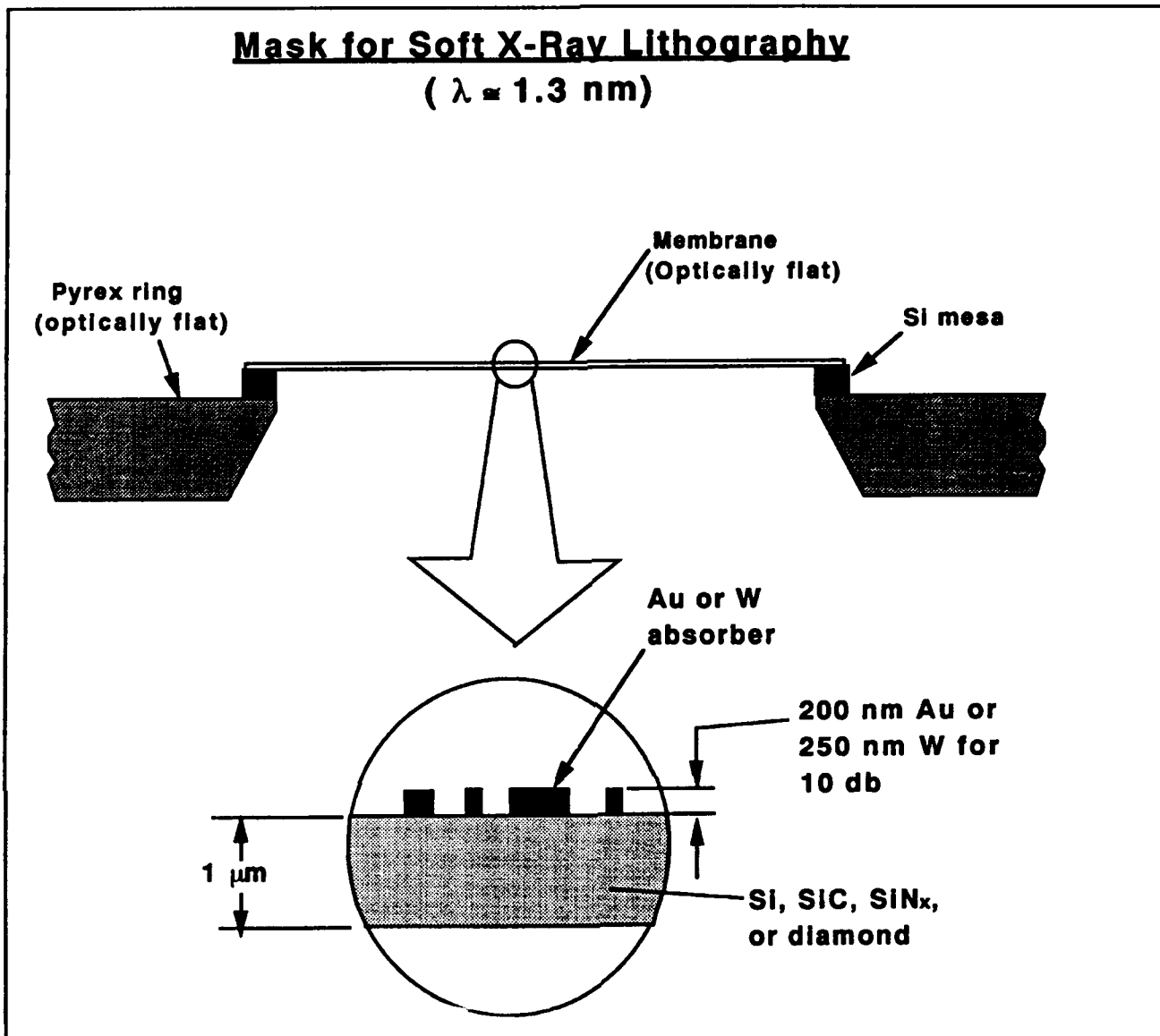


Figure 3. Mesa style mask suitable for x ray lithography at feature sizes from 500 to 20 nm. Membranes are flat to $< 250 \text{ nm}$.

scheme shown schematically in figure 4. With this technique, using polysilicon as the anodic bonding agent in place of Ni, we anticipate that x-ray mask blanks can be fabricated entirely with automated integrated circuit (IC) processing equipment.

Our mask technology is based on low-stress, Si-rich silicon nitride, SiN_x . This material is now produced in the IC Laboratory at MIT in a new, dedicated vertical LPCVD reactor. The resulting films are clean and uniform, and x-ray mask membranes made from them are extremely robust. They can be cleaned and processed in conventional stations. Radiation hardness remains a problem at dose levels corresponding to production (i.e., millions of

exposures) but for research the material is excellent.

For absorber patterns we use both gold, Au, and tungsten, W. Both can be obtained with near-zero stress (i.e., $< 10 \text{ MPa}$) which implies that pattern distortion should be negligible (i.e., $< 1 \text{ nm}$). The gold is electroplated onto the membrane after resist exposure and development using a specially designed apparatus. The W is sputter deposited and patterned by reactive-ion etching. We verify the achievement of stress $< 10 \text{ MPa}$ using a Linnik interferometer, which we have recently equipped with a CCD, a frame grabber, and special purpose software that improves sensitivity.

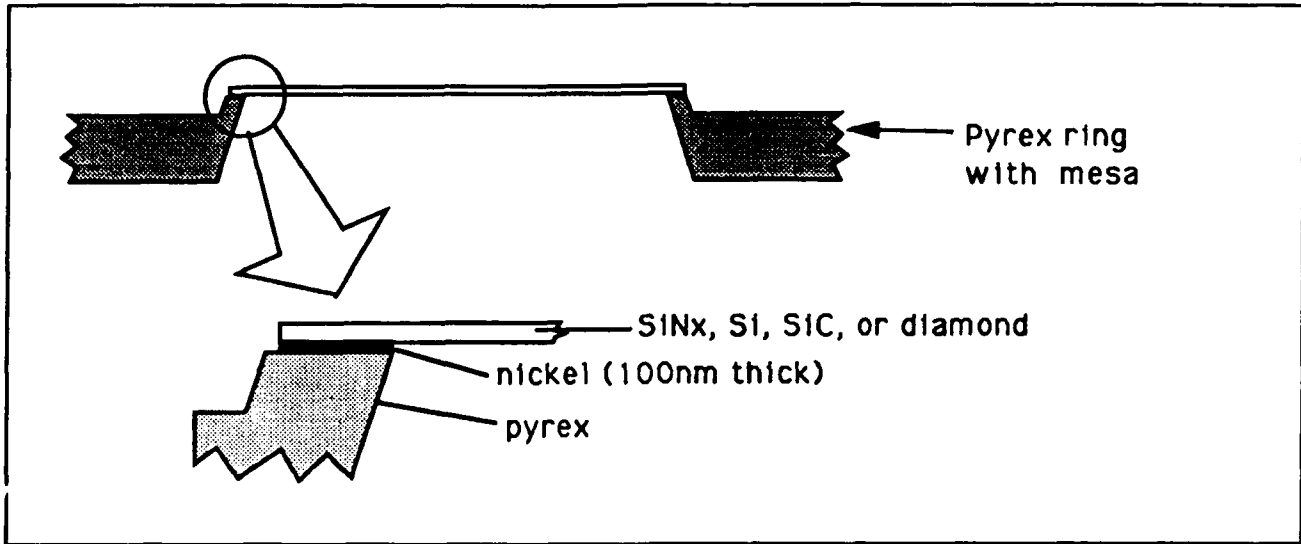


Figure 4. Flip-bonded mask structure in which the mesa rim is formed in the pyrex ring. Membrane flatness is < 100 nm.

In order to check that zero stress, as determined by Linnik interferometry, corresponds to zero in-plane distortion, we have developed a technique of holographic interferometry (HI) shown schematically in figure 5. We have shown a good correlation between Linnik and HI measurements, but we intend to further improve the sensitivity of the in-plane distortion measurements.

Patterning of x-ray masks is done by holographic lithography for periodic structures but, for patterns of arbitrary geometry, is done by e-beam lithography, in collaboration with the Naval Research Laboratory (NRL) and IBM. We use CAD tools at MIT to convert the data into formats compatible with the e-beam exposure systems. Data is shipped to NRL by electronic mail or IBM by express mail along with x ray mask blanks already coated with e-beam resist. After e-beam exposure, the masks are shipped back to MIT by express mail where development and Au electroplating are carried out. This collaboration has already demonstrated that x-ray mask patterning by e-beam can be done remotely, so that university researchers with limited facilities can have access to nanolithography via x ray alone without owning or visiting an e-beam lithography facility.

For the production of x-ray masks with W absorber, a reactive-ion-etching process is required, which puts considerable power into the membrane substrate. Since membranes have very low thermal mass and conductivity, we must heat sink the back side. We are constructing a new reactive-ion-etching system that will provide back-side He cooling. The cooling can be to temperatures as low

as -40°C. At such low temperatures the isotropic etching component is suppressed and high resolution directional etching on membranes should be possible.

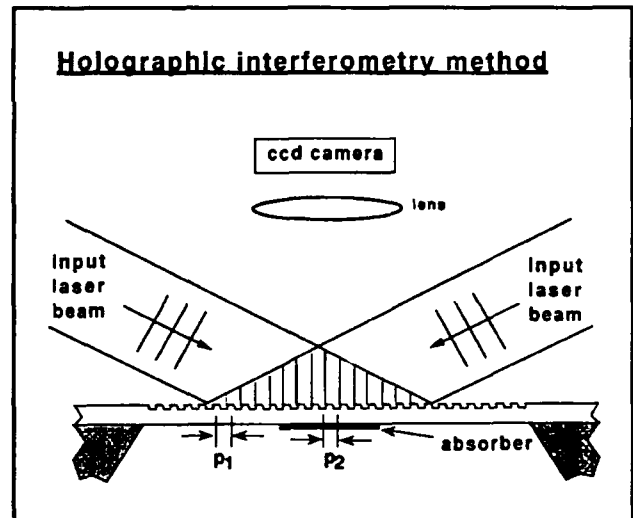


Figure 5. Holographic interferometer for detecting in-plane distortion in x-ray mask membranes.

4.4 Improved Scanning-Electron-Beam Lithography

Sponsors

Joint Services Electronics Program
Contract DAAL03-92-C-0001
U.S. Army Research Office
Grant DAAL03-92-G-0291

Project Staff

Juan Ferrera, Reza A. Ghanbari, Professor Henry I. Smith, Professor Mark L. Schattenburg, Vincent V. Wong

Conventional scanning-electron-beam lithography (SEBL) depends upon laser interferometry to achieve geometric integrity, such as axis orthogonality, accurate length scale, placement accuracy, etc. However, laser interferometry cannot solve all such geometric difficulties, in part because the e-beam location can drift due to thermal expansion, charging, and many other causes. This difficulty with conventional SEBL is particularly troublesome in the fabrication of optoelectronic devices which require spatial-phase fidelity over areas many times larger than a single scan field.

We have proposed a scheme called spatial-phase-locking in order to achieve high fidelity in SEBL. In this scheme, a spatially-coherent grating or grid, created by holographic lithography, is located on the substrate or, in the case of x-ray mask membranes, on a second substrate below. All e-beam writing is then done with reference to this grid using phase locking techniques. Preliminary work has been done in collaboration with IBM Corporation at Yorktown Heights, New York. Whereas in conventional SEBL stitching errors at the boundary of two fields is typically several times 10 nm, we achieved an error below 2 nm. We plan to expand this activity, and, in the long term, we expect to provide an entirely new paradigm for SEBL, which will also translate into lower capital costs.

In order to better predict the optimal SEBL exposure conditions, particularly when writing on x-ray mask membranes, we have implemented a Monte Carlo model for electron scattering and energy loss. A model developed earlier by Hawryluk et al. was modified to include the excitation of secondary electrons. The new model was employed successfully to show that the reduced proximity effect observed by Rhee et al. when SEBL was done over a thin SiO₂ layer on top of tungsten was due to the SiO₂ stopping the energetic secondary electrons from the W.

The new model has also been used to validate the experimentally observed reduction of the deleterious proximity effects due to backscattered electrons when SEBL is done on x-ray mask membranes rather than solid substrates. Figure 6

shows a simulation of resist development following e-beam exposure on (a) a membrane and (b) a solid Si substrate.

4.5 A High-Precision Mask Alignment Scheme

Sponsors

Joint Services Electronics Program
Contract DAAL03-92-C-0001
National Science Foundation
Grant ECS 90-16437

Project Staff

James M. Carter, Robert Frankel,⁴ Alberto M. Moel, Professor Henry I. Smith

In order for any lithographic technique to be of general utility, a compatible alignment technique must also be provided. This technique must be capable of superposition precision that is a small fraction of the minimum feature size.

We have demonstrated a novel alignment scheme that builds on the principles of an interferometric scheme we invented several years ago, but overcomes its shortcomings. Alignment marks are simple linear gratings with spatial periods around 1 micron so that the diffraction angle for visible light is around 30 degrees. The spatial periods of the mask and substrate marks differ by a few percent so that beams that are diffracted back onto the optical axis produce a moiré pattern that can be imaged on a CCD. The mask alignment mark also contains a fixed fiducial grating whose spatial period matches that of the moiré pattern. Alignment is defined as that condition wherein the spatial phase of the moiré (which moves as the mask is piezoelectrically displaced relative to the substrate) matches the spatial phase of the fiducial grating.

Using this scheme, a superposition precision with 1σ equal to 6 nm was achieved, as shown in figure 7. Analysis has shown that the theoretical limit is about 0.6 nm. Clearly, this would be compatible with minimum lithographic features ~ 20 nm, which we consider the practical limit of resist-based lithography.

We plan to work with Hampshire Instruments to develop a commercial version of this alignment scheme and install it in our 3500X x-ray lithography system.

⁴ Hampshire Instruments, Inc., Rochester, New York.

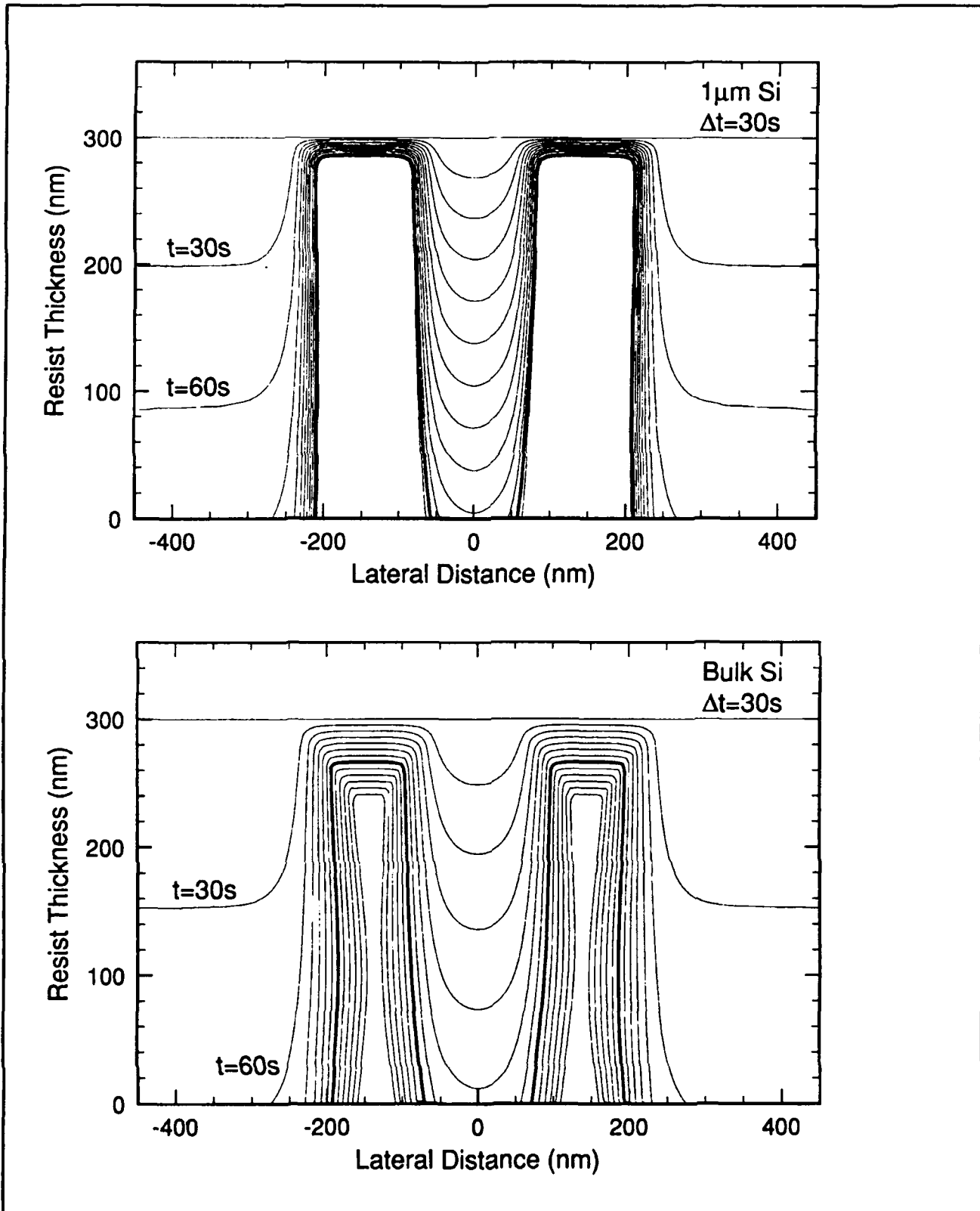


Figure 6. Electron-beam exposure and development simulation for a narrow line running between two large pads exposed at twice the clearing dose. (a) (top) For a 1 μm -thick Si membrane substrate, (b) (bottom) For a solid substrate. Successive contours represent 30 sec of additional development. Note the reduction of proximity effects for exposure on a membrane substrate.

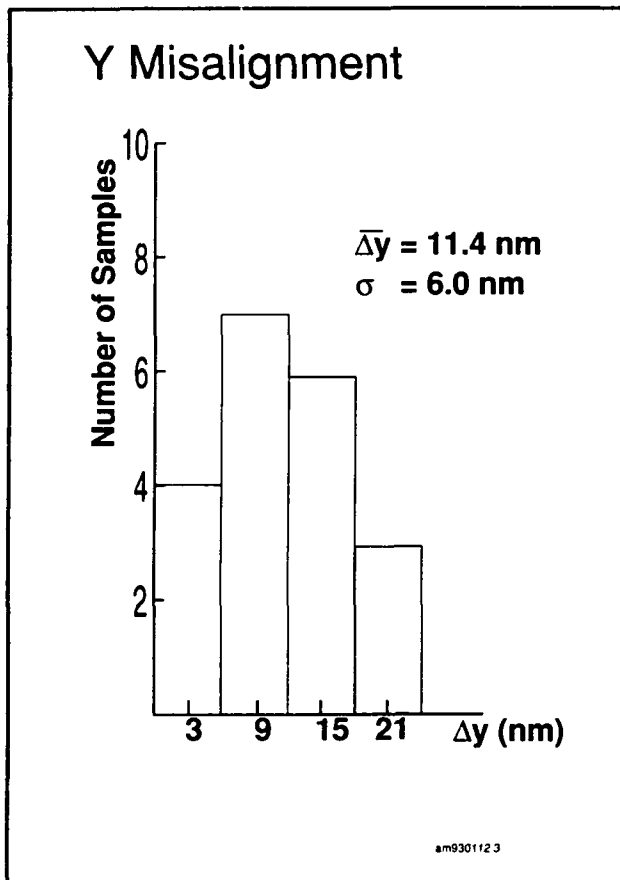


Figure 7. Histogram of 20 successive aligned x-ray exposures, showing $\sigma = 6$ nm. Offset of peak is not significant. A moiré method was used to measure misalignment.

4.6 Achromatic Holographic Lithography

Sponsor

Joint Services Electronics Program
Contract DAAL03-92-C-0001

Project Staff

Scott D. Hector, Satyen N. Shah, Professor Henry I. Smith

Holographic schemes are preferred for the fabrication of periodic and quasi-periodic patterns that must be spatially coherent over large areas and free of phase steps. For spatial periods below 200 nm light sources with wavelengths below 200 nm must be used. All such sources have limited temporal coherence, and thus one is forced to employ achromatic schemes such as shown in figure 8. Using this apparatus, we have achieved gratings of 100 nm period (i.e., 50 nm lines and

spaces). In order to make the apparatus more reliable the depth-of-focus has to be increased, which implies an improvement of the source spatial coherence. To this end, we have introduced a collimating lens and a slit scanning system. In order to enhance yield and area, it will be necessary to find the substrate location that provides maximum image contrast. Therefore, we have set up a white-light interferometer that utilizes optical paths through the quartz plates that closely approximate the paths of the exposing beams. A photodetector and lock-in amplifier will be used to find the optimum sample position.

Once the system is fully reliable, we plan to take the technique one step further to 50 nm periods (25 nm lines and spaces) using a 13 nm undulator as the light source.

4.7 Fabrication of T-gate Devices using X-ray Lithography

Sponsor

Defense Advanced Research Projects Agency
Contract N00019-92-K-0021

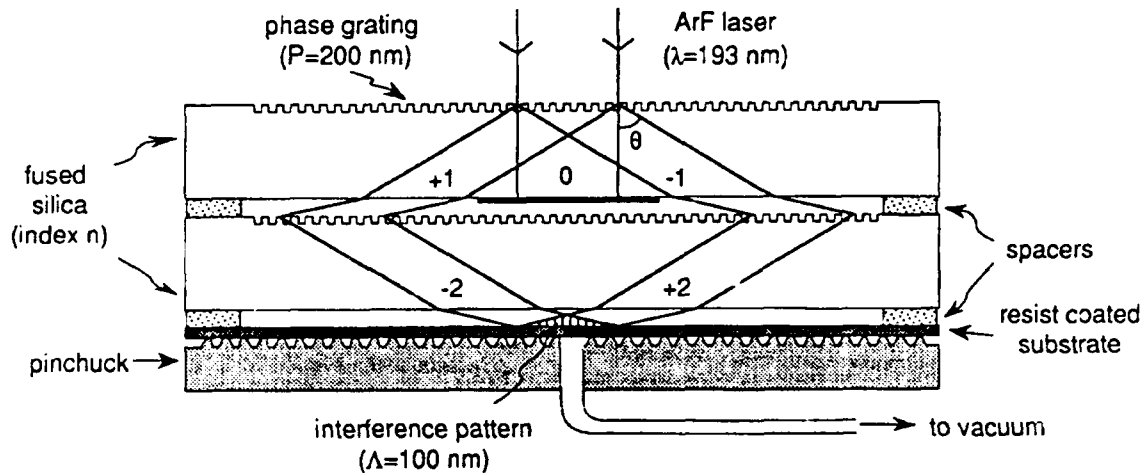
Project Staff

James M. Carter, Nitin Gupta, Professor Henry I. Smith

High-speed MODFET devices require very short gate lengths while preserving low resistance. Large gate widths are required for high current drive. To meet these conflicting demands, researchers have developed so-called "T-gate" and "gamma-gate" processes in which the base of the gate is very short (~ 100 nm) while the upper part is large and overlaps the short base, like a mushroom or the letters T or gamma. Such structures are readily achieved using direct-write electron-beam lithography. However, this technology is expensive, slow, and probably incompatible with mass production.

For these reasons, we are developing an x-ray lithography-based approach to making Tee and gamma gate devices. Several schemes are being pursued. The most straightforward involves a tri-layer resist. The first layer is an x-ray sensitive resist (e.g., PMMA or a chemically amplified novolak), the second is a barrier layer (e.g., photosensitive polyimide) between the x-ray resist and the upper layer, which is photoresist. The upper layer and the polyimide are exposed with UV light. This tri-level process provides maximum flexibility and a large process window, but requires two separate alignments and exposures. On the other

Achromatic Holographic Lithography



$$\sin\theta = \lambda/(nP),$$

$$\Lambda = \lambda/(2n \sin\theta)$$

$$= P/2$$

Figure 8. Achromatic holographic lithography configuration for generating 100-nm-period gratings.

hand, the photolithography does not have to be aligned as precisely as the x-ray exposure. Other approaches will also be investigated in which, for example, three different x-ray resist sensitivities are employed and only one alignment and exposure is needed.

4.8 Tenth-micron MOSFET Device Technology

Sponsors

IBM Corporation
Joint Services Electronics Program
Contract DAAL03-92-C-0001

Project Staff

Professor Dimitri A. Antoniadis, Professor James E. Chung, Dr. Hao Fang, Hang Hu, Professor Henry I. Smith

We have continued using x-ray lithography to fabricate both N- and P- channel MOSFET devices with effective channel lengths down to 80 nm. The emphasis is on investigating hot-carrier quasi-ballistic transport processes.

A new generation of x-ray masks capable of defining sub-0.1 μm polysilicon gates and compatible with conventional MOSFET device and circuit processing were successfully developed and tested. A portion of a ring oscillator circuit, patterned in Au on an x-ray mask, is shown in figure 9. A chemically amplified resist (PF-514) is used for the 0.1 μm gate definition, as shown in figure 10.

Self-aligned P-channel MOSFET devices were fabricated on N-type, 20 $\Omega\text{-cm}$ (100) silicon substrates. In order to maximize channel hole mobility and to control deep punchthrough down to L_{eff} of 0.1 μm , super-steep-retrograde (SSR) channel doping was used. It consists of phosphorus ion implantation with energy of 180 KeV and dose of $5.0 \times 10^{12} \text{ cm}^{-2}$, and arsenic ion implantation with energy ranging from 70 KeV to 94 KeV and dose ranging from $4.0 \times 10^{12} \text{ cm}^{-2}$ to $1.0 \times 10^{13} \text{ cm}^{-2}$. The 5.2 nm thick gate oxide was thermally grown at 800°C. In order to form the P-N source-drain junctions, germanium was first implanted to amorphize the source-drain area and a BF_2 implant with energy of 10 KeV and dose of $4.0 \times 10^{14} \text{ cm}^{-2}$ was carried out to form the shallow P - N junction extensions. A 10 nm thick oxide spacer was then formed. A second BF_2 implant with energy of 20 KeV and dose of $5.0 \times 10^{15} \text{ cm}^{-2}$ formed the P+ - N junctions in the area defined by the previously formed oxide spacer. The P+ - N junction annealing consisted of a 600°C, 30 min furnace diffusion followed by 10 sec RTA at 1000°C. Self-aligned cobalt silicide with thickness of about 40 nm was formed to reduce the sheet resistance of the source-drain junctions. Typical values of total source and drain resistance were about 850 $\Omega\mu\text{m}$. Finally, CVD oxide contact cuts and aluminum contacts were formed to the gates and the source-drain regions.

Two SSR channel doping profiles calculated by SUPREM-III are shown in figure 11. Two sets of P-MOSFETs with L_{eff} ranging from 0.1 μm to 10 μm obtained with these two SSR doping profiles all exhibit excellent punchthrough characteristics. The I - V characteristics of 0.1 μm P-MOSFET devices at 300 K and 77 K is shown in figure 12. The peak hole mobility at low longitudinal E - field was 92 $\text{cm}^2/\text{V}\cdot\text{s}$. The room temperature threshold voltage was -0.4 V. This shows that a good compromise between reducing short channel effects and maintaining practical device integrity is reached for 0.1 μm scale P-channel MOSFET devices with SSR channel doping profiles.

X-ray Mask for 0.1 μm Gate Length
NMOS Ring Oscillator
(Mask written by e-beam lithography at NRL)

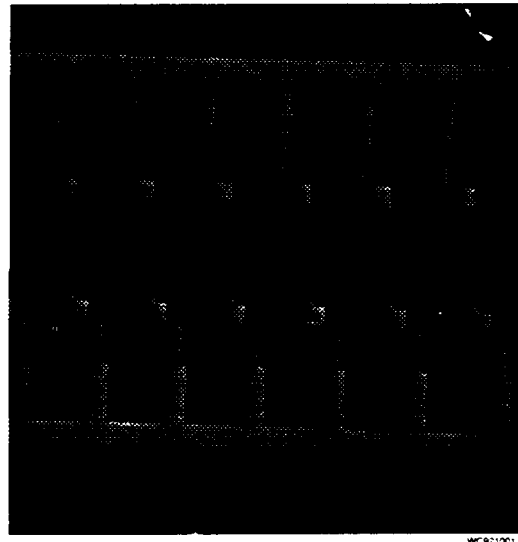


Figure 9. X-ray mask of a 0.1 μm gate-length NMOS ring oscillator (x-ray mask written by e-beam lithography at the Naval Research Laboratory).

Short-Channel MOSFET

Gate level exposed by x-ray lithography
(X-ray mask written at NRL)

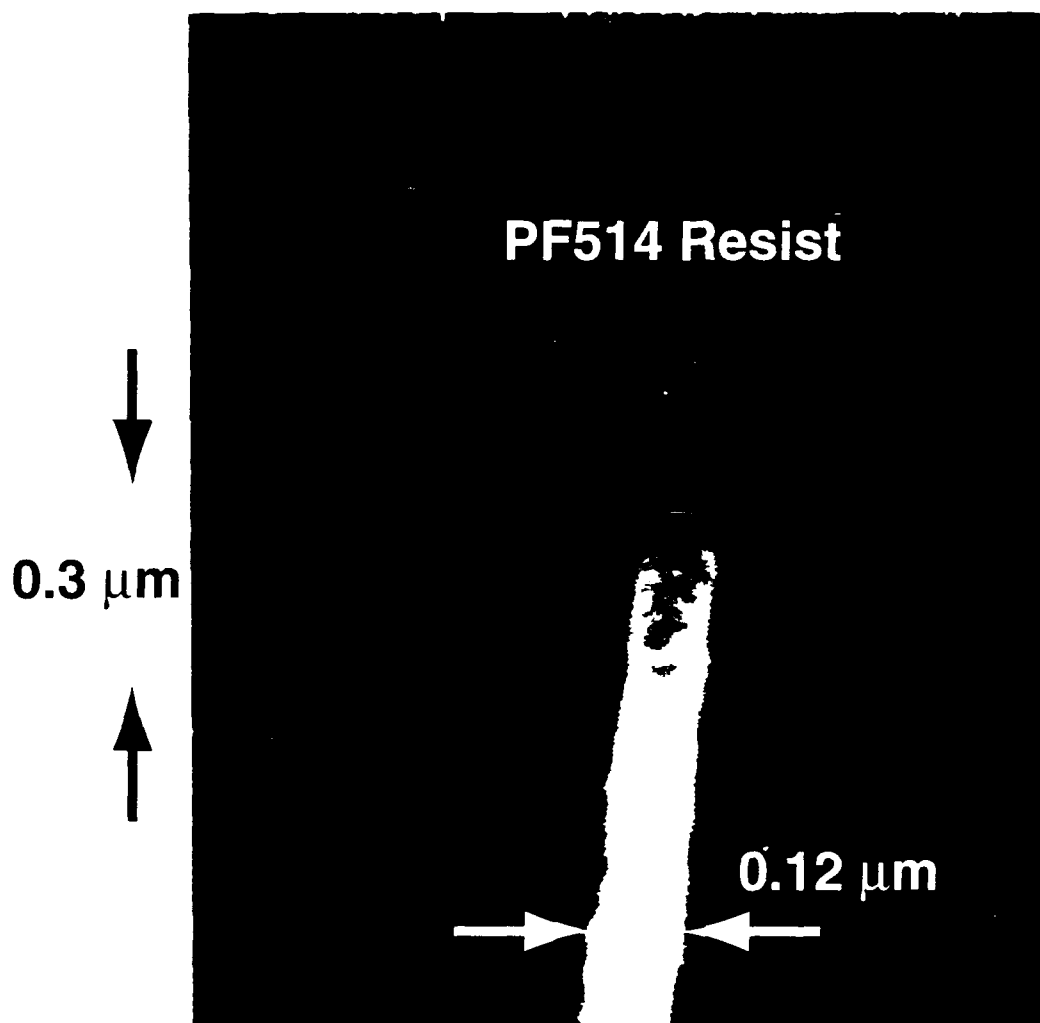


Figure 10. Resist pattern for a short-channel MOSFET exposed in the chemically amplified resist PF514 using x-ray lithography at $\lambda = 1.32 \text{ nm}$.

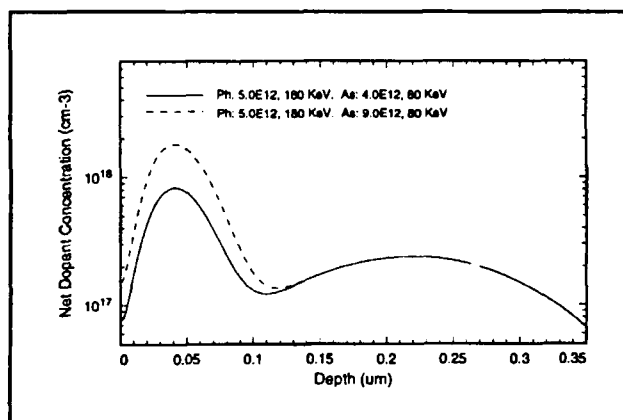


Figure 11. Dopant concentration as a function of depth as calculated by Supreme III.

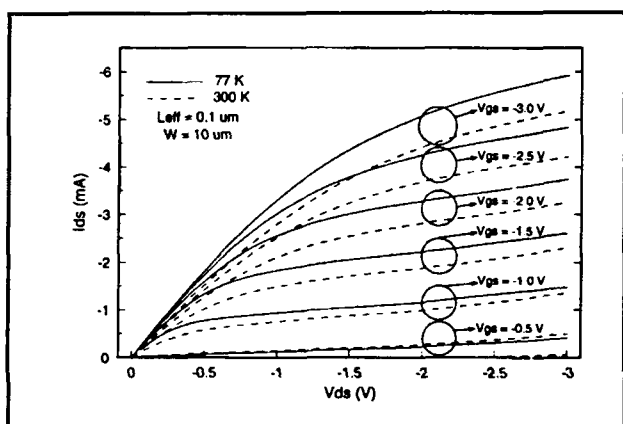


Figure 12. I-V characteristics of 0.1 μm PMOSFET devices at 77 K and 300 K.

4.9 Studies of Coulomb Charging Effects in Semiconductor Nanostructures

Sponsor

U.S. Air Force - Office of Scientific Research
Grant F49620-92-J-0064

Project Staff

Professor Dimitri A. Antoniadis, William Chu, Christopher C. Eugster, Arvind Kumar, Professor Terry P. Orlando, Michael Rooks⁵

Many novel effects have been observed in the transport properties of ultrasmall "quantum-effect" transistors whose feature size is comparable to the electron Fermi wavelength (about 50 nm in a typical

inversion layer). In addition to the prominent role played by these effects in solid-state physics, they have great potential in the technology of the electronics revolution.

In a "quantum dot" device, an electron gas is confined electrostatically in all three spatial dimensions, forming a small "puddle" of electrons bounded on all sides by a potential wall. This small electron "puddle" resembles an atom in that there can only be an integer number of electrons, and these electrons can occupy only certain discrete energy levels.

Recent low-temperature experiments on transport through a narrow electron channel interrupted by two tunnel barriers—forming an isolated electron "quantum dot"—have found that the conductance through the dot consists of a series of sharp maxima which occur periodically as the voltage on the transistor gate is varied. This remarkable conductance modulation arises from the condition of charge quantization inside the dot. Each successive conductance maximum corresponds to the discrete addition of a single electron to the dot. Between successive conductance peaks, the resistance increases by several orders of magnitude because there is a large energy cost for an electron in the contact to enter the dot. This energy cost can be removed by changing the gate voltage, resulting in the observed periodic dependence of the conductance on gate voltage.

This conductance modulation through an electron puddle has been studied extensively and is now well understood. We propose to study a device structure with two electron puddles which can interact with each other through a thin tunnel barrier. In addition to exploring new physics, we are motivated by the consideration that such a coupled system would represent the first step toward an architecture in which two elements could interact with each other without an interconnect. Figure 13 shows a scanning electron micrograph of the gate geometry of our device structure, fabricated by electron beam lithography at the National Nanofabrication Facility. A negative voltage applied to the gates depletes the high-mobility two-dimensional electron gas (2DEG) underneath, which is formed at the GaAs/AlGaAs interface, leaving behind two small electron puddles. Four ohmic contacts at the corners allow access to the 2DEG; both series and parallel combinations of the dots can be realized depending on the bias voltages.

⁵ Cornell University, Ithaca, New York.

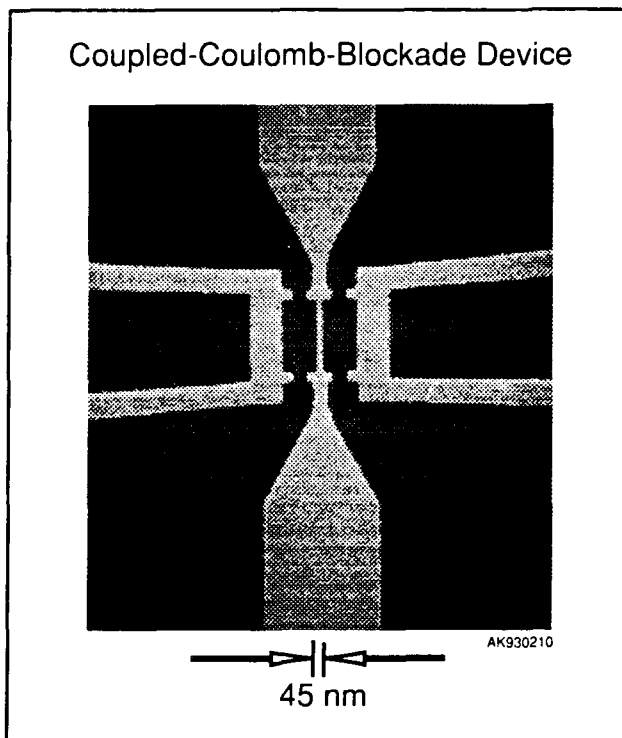


Figure 13. Gate electrodes fabricated by electron beam lithography and liftoff over a GaAs/AlGaAs heterostructure. A negative voltage on the gate electrodes depletes the 2DEG underneath, leaving behind two electron islands. Ohmic contacts at the four corners allow access to the 2DEG.

We are also working on studying Coulomb charging effects in devices fabricated by x-ray lithography. Figure 14 shows a scanning electron micrograph of an x-ray mask which will be used for patterning the gate geometry of a device with a single electron puddle. The corresponding device will offer independent control of the potential barriers confining the dot and the number of electrons occupying the dot. This independent control has been found in previous experiments to improve the yield of devices showing Coulomb blockade effects.

4.10 Study of Quasi-One-Dimensional Wires in GaAs/AlGaAs Modulation Doped Field-Effect Transistors

Sponsor

U.S. Air Force - Office of Scientific Research
Grant F49620-92-J-0064

Project Staff

Professor Dimitri A. Antoniadis, Martin Burkhardt, William Chu, Professor Jesús A. del Alamo, Reza

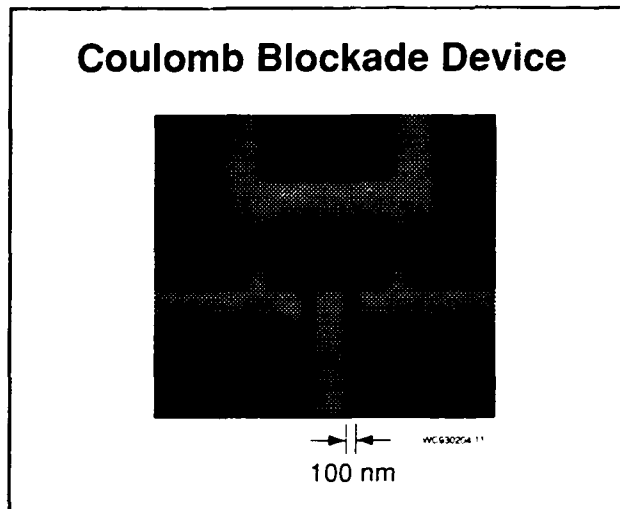


Figure 14. X-ray mask to pattern gate geometry of a quantum dot device with a single electron puddle. Note that the potential barrier at each constriction and the number of electrons in the dot can be controlled independently.

A. Ghanbari, Professor Terry P. Orlando, Professor Henry I. Smith

We have successfully fabricated quasi-one-dimensional (Q1D) wires using x-ray lithography and precise chemical etching. These devices were fabricated on a high quality GaAs/AlGaAs modulation-doped substrate. By first patterning the wires using x-ray lithography, then chemically etching the GaAs, the region under the etched areas become depleted of electrons, leaving behind many parallel quasi-one-dimensional wires. A schematic cross-section of this device is shown in figure 15.

Because the operation of this device depends critically on the shape of the confinement potential, control of the etch depth is crucial. Dry etching techniques have sufficient repeatability for this application, but they cause an unacceptable amount of damage to the substrate. Chemical etching minimizes damage but has a very unpredictable etch rate.

To overcome these difficulties, a high precision interferometric technique was developed that is capable of resolving depth changes of less than 1 nm. By capturing the image formed in a Linnik interferometer and using Fourier analysis techniques, we can monitor the etch depth with a precision < 1 nm, permitting the reliable fabrication of these devices.

When the Q1D devices are measured at cryogenic temperatures, the quantum confinement clearly manifests itself as a nonlinear conductance, as shown in figure 16. Each nonlinear bump in the

transconductance (shown in the insert in figure 16) corresponds to the Fermi level passing through different subbands of the Q1D confining potential. A schematic of the confinement potential, as seen by electrons traveling down the wire, is shown in figure 17.

Work is currently underway to harness these Q1D wires in a new type of planar resonant-tunneling device with Q1D emitter and collector (Q1D-PRESTFET) that has been predicted to show very strong non-linearities in conductance.

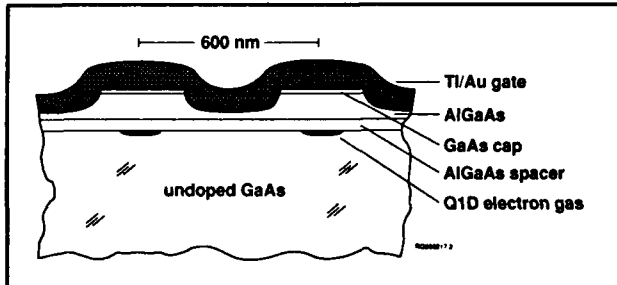


Figure 15. Schematic cross-section of completed quasi-one-dimensional device.

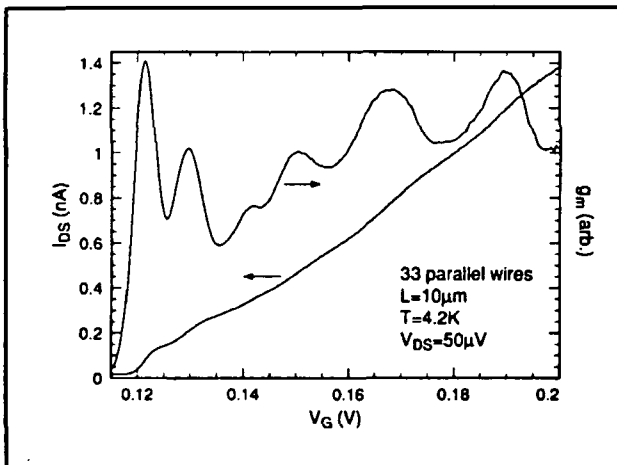


Figure 16. Measured conductance and transconductance for a multiple-parallel quasi-one-dimensional device.

4.11 Planar-Resonant-Tunneling Field-Effect Transistors (PRESTFET)

Sponsor

U.S. Air Force - Office of Scientific Research
Grant F49620-92-J-0064

Project Staff

Professor Dimitri A. Antoniadis, Mike T. Chou, William Chu, Martin Burkhardt, Professor Henry I. Smith

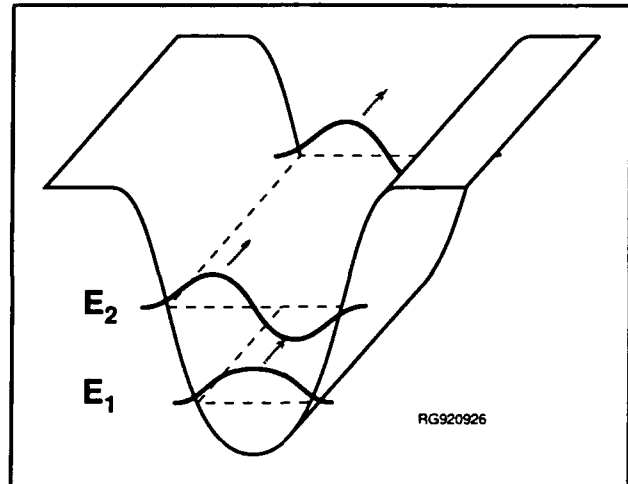


Figure 17. Schematic of potential seen by electrons traveling along a Q1D wire (arrows indicate direction of current flow).

Planar-resonant-tunneling field-effect transistors were built on modulation doped GaAs/AlGaAs substrates using x-ray lithography, making it possible to achieve good step coverage onto a 120 nm high mesa, as shown in figure 18. This device, with 200 nm gate pitch, showed good transistor characteristics but coherent resonant tunneling between source and drain was not observed. Efforts are underway to shrink the gate pitch to 150 and 100 nm. We expect to see resonant tunneling in these devices at liquid Helium temperature.

We are also investigating the feasibility of PRESTFETs in Si. Top and sideviews of the device are shown in figure 19. This device has a two-level gate structure. A very thin, high-quality layer of silicon dioxide (~10 nm) is grown on a p-type silicon substrate. Then, two parallel tunneling electrodes (lower level gates) will be patterned in polysilicon using x-ray lithography and liftoff. A thin layer (~10 nm) of insulating silicon nitride will be deposited over this structure. Finally, a large metal gate (the upper level gate) will be deposited over the silicon nitride. A two-dimensional electron gas (2-DEG) will be formed at the Si/SiO₂ interface by applying a positive bias to the upper gate. Tunnel barriers in the 2-DEG will be created directly underneath the lower gates by applying appropriate bias voltages.

This silicon PRESTFET offers the exciting possibility of potential modulations over extremely small distances (on the order of 10 nm). For the equivalent GaAs device, the distance between the gate electrodes and the 2-DEG is limited to the minimum thickness of the n-doped AlGaAs layer that is required to achieve a certain electron concentration at the 2-DEG (i.e., about 50 nm). The main disad-

vantage of the silicon system is its low mobility compared to GaAs. But, if we optimize the Si/SiO₂ interface quality by avoiding contamination and controlling the damage caused by processing steps, it is possible to obtain an interface defect/impurity concentration as low as $1 \times 10^{10} \text{ cm}^{-2}$. This implies an average spacing between defects of about 100 nm. Since our goal for the silicon PRESTFET is to fabricate a 50 nm-wide quantum well sandwiched between two 50 nm-wide barriers, carrier mobility, and hence scattering, should not be a fundamental limitation. We expect to observe quantum transport effects at 4.2 K.

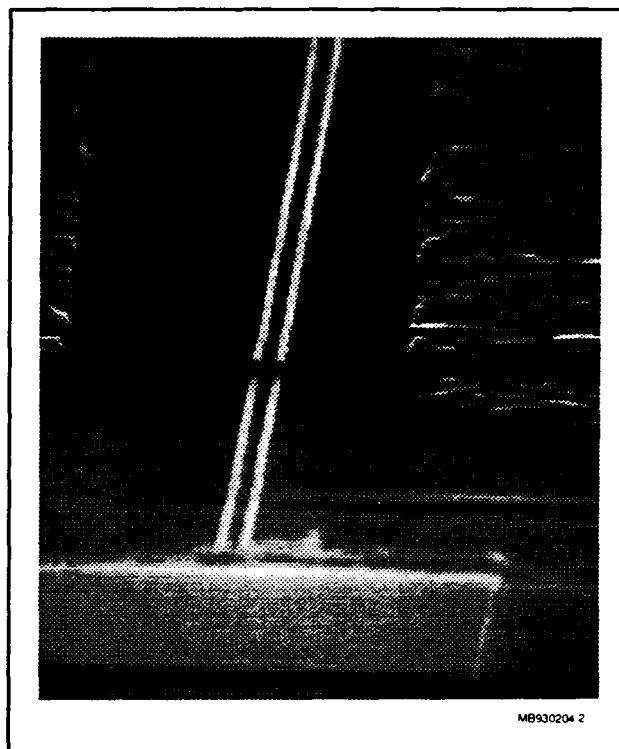


Figure 18. Electron micrograph of PRESTFET on GaAs fabricated using x-ray lithography, which enables good step coverage up onto the 120 nm-high mesa.

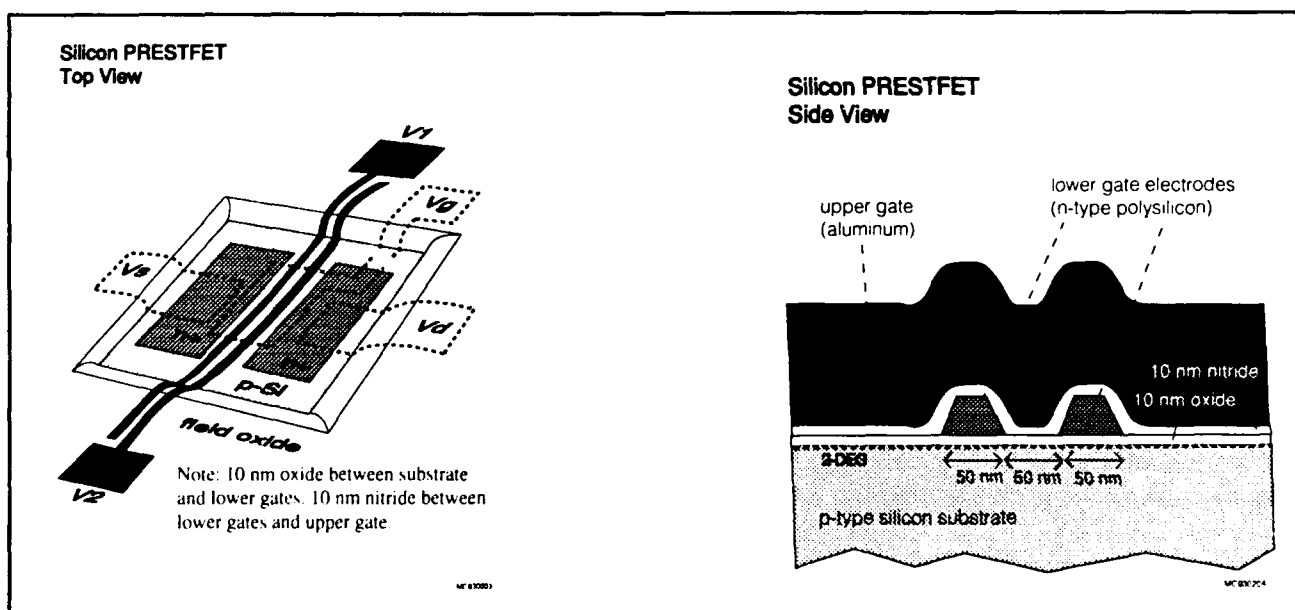


Figure 19. Schematic of Si PRESTFET.

4.12 Dual Electron Waveguide Device Fabricated using X-ray Lithography

Sponsor

National Science Foundation
Grant DMR 87-19217
Grant DMR 90-22933

Project Staff

Professor Jesús A. del Alamo, William Chu, Christopher C. Eugster, Professor Henry I. Smith.

We have recently fabricated a dual-electron-waveguide device, shown in figure 20, using x-ray nanolithography. An electron waveguide is essentially a one-dimensional channel which electrons can travel through without scattering. In our device, two such channels are electrostatically formed in close proximity of each other by depleting those electrons in an AlGaAs/GaAs modulation-doped heterostructure which reside underneath the three gates shown in figure 20. The x-ray mask used in the fabrication process was patterned using 50 keV e-beam lithography at the Naval Research Laboratory. We use x-ray lithography to replicate this mask to change its polarity. Then we align the new mask to the AlGaAs/GaAs sample and expose it using contact x-ray nanolithography.

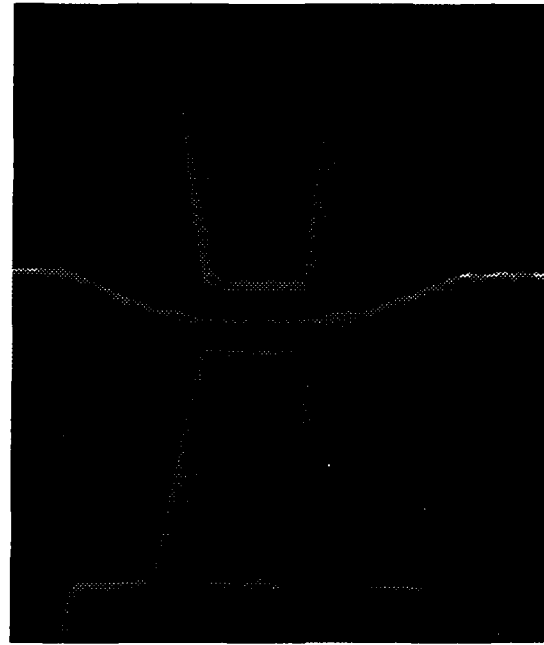
In an electron waveguide, similar to an optical waveguide, discrete transverse modes arise due to the lateral confinement. The conductance of each waveguide mode is equal to a fundamental constant $2e^2/h$. This results from the cancellation of the energy dependence in the product of the 1D density of states and the electron velocity. In recent experiments on x-ray fabricated dual electron waveguide devices, quantized conductance for each waveguide was observed as the number of occupied modes was electrostatically varied.

4.13 Far-Infrared Spectroscopy of Arrays of Quantum Dots and Wires

Sponsors

Joint Services Electronics Program
Contract DAAL03-92-C-0001
U.S. Air Force - Office of Scientific Research
Grant F49620-92-J-0064

Coupled Electron Waveguides



Middle gate: 60 nm linewidth

Figure 20. Electron micrograph of dual-electron-waveguide device fabricated using x-ray nanolithography.

Project Staff

Professor Dimitri A. Antoniadis, Martin Burkhardt, Reza A. Ghanbari, Professor Terry P. Orlando, Professor Henry I. Smith, Professor M. Shayegan,⁶ Song Sang-hun,⁶ Professor Daniel Tsui,⁶ Kenneth Yee, Yang Zhao

In collaboration with researchers at Princeton University, we have used x-ray lithography to fabricate devices for magneto-optic measurements of a two-dimensional electron gas (2DEG). Metal grids with spatial periods of 300-600 nm in both orthogonal directions and covering several square millimeters were placed on the surface of a modulation-doped AlGaAs substrate. The grids were used to periodically modulate far-infrared radiation (FIR) incident on the 2 DEG. Due to the close proximity of the grids to the heterointerface (~ 50 nm), it was possible to access an electron-electron interaction effect by the FIR radiation at the wave vectors of

⁶ Princeton University, Princeton, New Jersey.

the metal grid. These spectra were observed as a function of magnetic field. Results were in agreement with theoretical models.

Using similar lithographic techniques, metal gratings with spatial periods of 300-600 nm were placed on modulation-doped substrates (figure 21a), and a gate electrode was attached to the grating. Depending on the applied gate voltage, the potential seen by the electrons at the 2DEG can be varied from uniform (in which case the electrons behave as a normal 2 DEG) to weakly-coupled quantum wires (figure 21b), or to isolated quantum wires (figure 21c). These quantum-wire structures were measured using FIR cyclotron resonance. Mode softening due to quantum-mechanical coupling between wires was observed. The results were in agreement with theoretical models of coupled-quantum wires.

Arrays of etched quantum dots, quantum wires, and quantum anti-dots have also been fabricated, with typical spatial periods of 300-600 nm. The electronic subbands of these structures were also examined using FIR cyclotron resonance. Currently, we are continuing our study using extremely high-quality samples prepared by Professor Shayegan's group at Princeton.

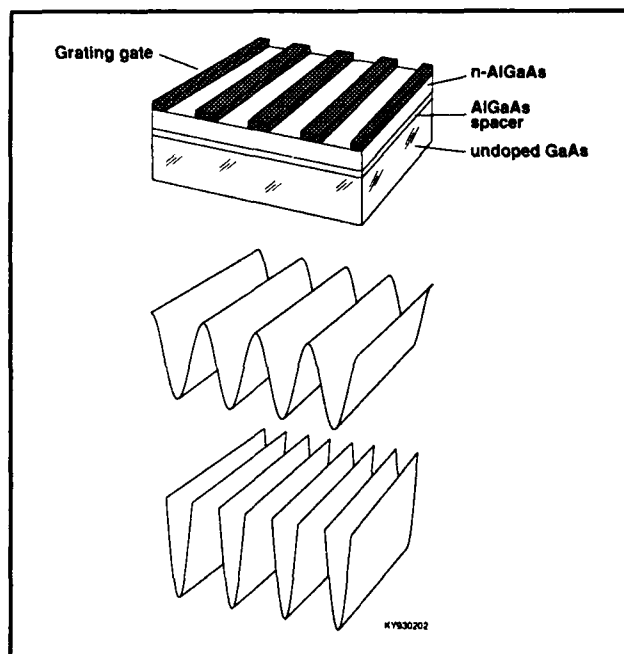


Figure 21. (a) Metal grating gate on a modulation-doped AlGaAs/GaAs substrate; (b) depiction of potential seen by electrons at the AlGaAs/GaAs interface for weakly coupled quantum wires; (c) potential for the case of isolated quantum wires.

4.14 Ridge-Grating Distributed-Feedback Lasers Fabricated by X-Ray Lithography

Sponsor

U.S. Army Research Office
Grant DAAL03-92-G-0291

Project Staff

James M. Carter, Woo-Young Choi, Juan Ferrera, Professor Clifton G. Fonstad, Jr., Professor Henry I. Smith, Vincent V. Wong

Distributed-feedback lasers (DFB) are essential components in optical communications systems because they operate in a single-longitudinal-mode and are easily integrable with electronic drive circuitry. In the fabrication of a typical DFB laser, an epitaxial regrowth step is carried out on top of the grating, which can be yield-limiting. In particular, because of etch back, the coupling constant after epi-growth can be difficult to predict. In the following paragraphs we describe a novel DFB laser that eliminates the need for regrowth and maximizes the utility of ridge-waveguide devices which are much simpler to fabricate.

To realize such a device structure, we have developed a fabrication process that utilizes x-ray lithography for the grating fabrication because it offers good process latitude, high throughput, long-range spatial-phase fidelity in the gratings, and large depth-of-focus, which is essential for sidewall patterning. A schematic of the ridge-grating DFB laser is shown in figure 22. After the epitaxial growth of a complete InGaAlAs graded-index, separate-confinement, multi-quantum-well-layer diode structure by molecular-beam epitaxy on an InP substrate, a 3-4 μm -wide ridge waveguide is formed by wet-etching. The wet-etching conditions are carefully controlled so that the desired side-wall profile is obtained. A first-order grating with a period of 230 nm for the target lasing wavelength of 1.55 μm is then patterned in resist using x-ray lithography. The Cu_L -line ($\lambda = 1.32 \text{ nm}$) of an electron-bombardment source is used in conjunction with SiN_x mask technology. The x-ray mask is patterned using holographic lithography, which guarantees excellent uniformity and long-range spatial-phase coherence in the grating, followed by gold electroplating. Dry-etching is used to transfer the grating into both sides of the ridge waveguide. With this ridge-grating, the optical feedback occurs via the interaction of the lateral fields with the index modulation introduced by the grating. Holographic lithography could not be used directly for the grating exposure because of troublesome coherent reflec-

tions from the ridge topography. For advanced optical communication systems (e.g., those implementing wavelength-division multiplexing), quarter-wave-shifted DFB lasers, hundreds of microns in length, are necessary. This will require e-beam lithography that is free of distortion and stitching errors for the x-ray mask making. As described in section 4.4, we are pursuing a technique based on a global-fiducial grid scheme which can potentially solve both of these problems. Once developed, this technique will be incorporated into the e-beam lithography process to define the appropriate DFB laser grating patterns onto a SiN_x x-ray mask.

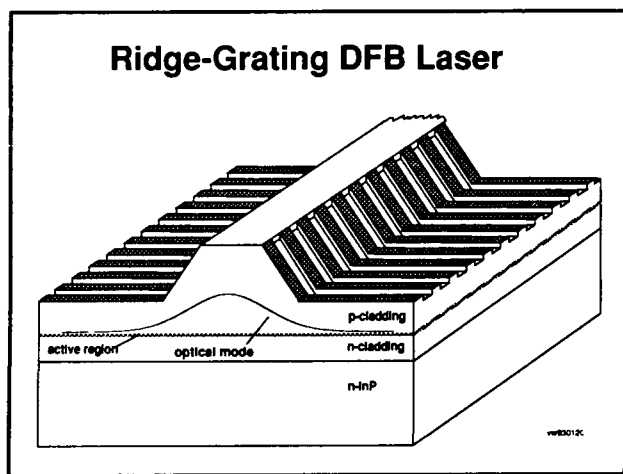


Figure 22. Schematic of ridge-grating DFB laser.

4.15 Channel-Dropping Filters Fabricated by X-Ray Lithography

Sponsor

U.S. Army Research Office
Grant DAAL0-92-G-0291

Project Staff

Jay N. Damask, Professor Hermann A. Haus, Professor Leslie A. Kolodziejski, Professor Henry I. Smith, Vincent V. Wong

Channel-dropping filters are novel optoelectronic devices that can extract a signal of a particular wavelength from an optical bus carrying multiple-signals. The extraction is achieved through the interaction of three coupled waveguides. A schematic of a channel-dropping filter (CDF) is shown in figure 23. The middle waveguide, which carries several signals, is side-coupled to two quarter-

wave-shifted grating resonators. These grating resonators are resonant at frequency f_2 and serve to extract this particular frequency component from the center waveguide.

For our initial demonstration of the CDF concept, we are working with a $\text{SiO}_2/\text{Si}_3\text{N}_4$ -layered system. For this materials system, grating periods tailored for a center optical wavelength of $1.55 \mu\text{m}$ will be approximately 515 nm. X-ray lithography will be used to transfer the grating pattern onto ridge waveguides fabricated by wet-chemical etching. The patterning of the necessary x-ray mask poses a significant challenge to existing mask-patterning techniques. In particular, the CDF requires spatially-coherent gratings spanning hundreds of microns, with precise control of pitch to $\sim 10^{-5}$ and appropriately placed phase steps of $(\pi/2) \pm 10^{-4}$ radians. As described in section 4.4, we are developing a spatial-phase-locked electron-beam lithography technique to achieve the required spatial fidelity in the x-ray masks.

4.16 Novel Superconducting Tunneling Structures

Sponsor

Defense Advanced Research Projects Agency
Consortium for Superconducting Electronics

Project Staff

Dr. Jack Chu,⁷ Professor John M. Graybeal, Dr. Bernard S. Meyerson,⁷ George E. Rittenhouse, Professor Henry I. Smith

In this project, we are studying the behavior of short-channel hybrid superconductor-degenerate semiconductor-superconductor (SSmS) Josephson devices, whose geometry is designed to display quantum electronic interference behavior. These studies include both theoretical and experimental examinations. This work represents the first examination of quantum interference effects for Cooper pairs via tunneling through extended resonant states. The characteristic energy scale for such a device would be set by the quantum confinement, and consequently may provide a new avenue for obtaining finite gains in Josephson three-terminal devices.

By numerically solving the Bogoliubov-deGennes equations for an SSmS junction, we have theoretically shown that the interference of ballistic

⁷ IBM Corporation Cambridge, Massachusetts.

CHANNEL-DROPPING FILTER

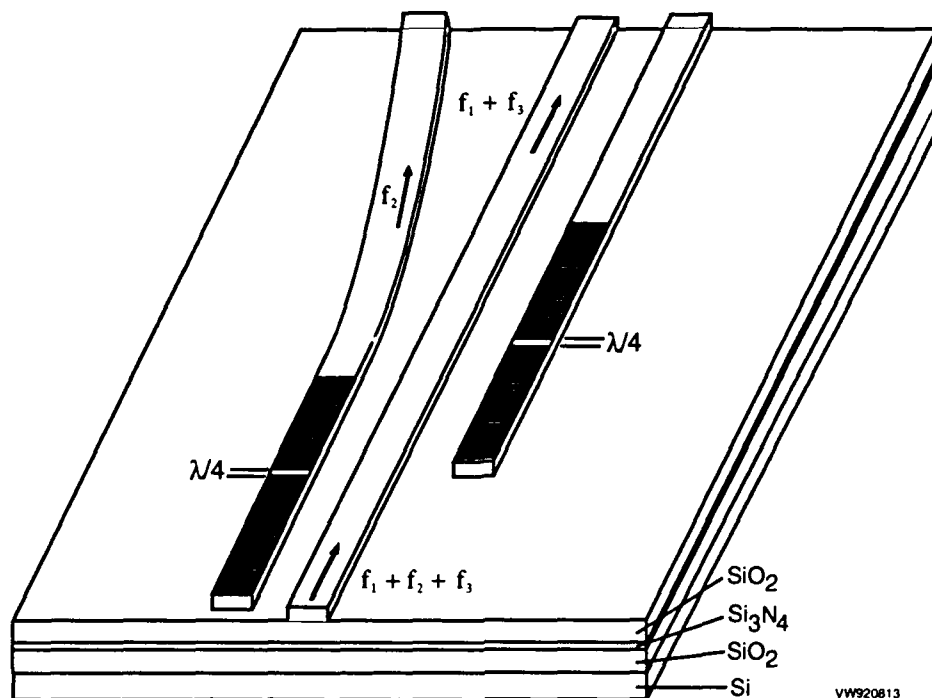


Figure 23. Structures of channel-dropping filter experiments on $\text{SiO}_2/\text{Si}_3\text{N}_4/\text{SiO}_2$.

Cooper pairs through spatially extended resonant states is indeed possible. As a function of the Fermi energy in the degenerate semi-conductor (i.e., as a function of electrostatic gate bias), we obtain striking cusp-shaped resonances in the Josephson critical current corresponding to the Fabry-Perot interference criteria. We find that such interference results regardless of how weakly coupled the quasi-bound states within the semiconductor layer are to the superconducting contacts. The coupling strength determines only the width and height of the cusp. Our calculations were performed assuming a one-dimensional system with a high-mobility semiconductor electron gas. The origin and nature of these resonances have been carefully analyzed, and differ markedly from those found in conventional non-superconducting resonant tunneling structures.

Note that our numerical solution to the Bogoliubov-deGennes equations can treat an arbitrary potential function within the semiconductor. We can thus consider a wide range of interesting and important junction geometries including con-

duction band mismatches, insulating interface or Schottky barriers, and intentionally introduced potentials within the N-layer which can enhance the quantum interferences. A key advantage of our technique is that it yields the full quasiparticle excitation spectrum within the Sm-layer as a function of the phase difference across the junction, thus providing important insight into the resultant physics.

We are exploring the fabrication of such a resonant tunneling Josephson junction using a high-mobility $\text{Si}:\text{Si}_{1-x}\text{Ge}_x$ two-dimensional electron gas (2DEG). A crucial and very demanding requirement of such a resonant SSmS structure is that the superconductor-semiconductor interface be clean and comparatively defect-free. The preferred electronic transport channel through the S-Sm interfaces is direct tunneling, as inelastic processes and/or tunneling through atomic localized states can be highly disruptive to the Cooper pair coherence. Presently, we are exploring superconductor-2DEG contacts using an intermediate phosphorous-implanted Si region. Optimizations of this contact

scheme are underway to improve their transmission of Cooper pairs.

4.17 Submicrometer-Period Transmission Gratings for X-ray and Atom-Beam Spectroscopy and Interferometry

Sponsor

Joint Services Electronics Program
Contract DAAL03-92-C-0001

Project Staff

James M. Carter, Julie C. Lew, Dr. Mark L. Schattenburg, Professor Henry I. Smith

Transmission gratings with periods of 100-1000 nm are finding increasing utility in applications such as x-ray, vacuum-ultraviolet, and atom-beam spectroscopy and interferometry. Over 20 laboratories around the world depend on MIT-supplied gratings in their work. For x-ray and VUV spectroscopy, gratings are made of gold and have periods of 100-1000 nm and thicknesses ranging from 100-1000 nm. They are most commonly used for spectroscopy of the x-ray emission from high-temperature plasmas. Transmission gratings are supported on thin (1 μ m) polyimide membranes or made self supporting ("free standing") by the addition of crossing struts (mesh). (For short x-ray wavelengths membrane support is desired, while for the long wavelengths a mesh support is preferred in order to increase efficiency.) Fabrication is performed by holographic lithography, x-ray lithography and electroplating. Progress in this area focuses on improving the yield and flexibility of the fabrication procedures.

Another application is the diffraction of neutral sodium beams (de Broglie-wavelength \sim 17 pm) by mesh-supported gratings. Professor David Pritchard's group at MIT has clearly demonstrated atomic diffraction and interference. Because good spatial coherence (low distortion) of the grating is critical to ensure measurable interference of the beams, efforts are concentrated on the use of holographic lithography and the reactive-ion etching of free-standing gratings in low stress and high stiffness materials such as silicon nitride. This process is continuously being improved via an undergraduate thesis project. We also will use holographic interferometry (figure 5, section 4.3) to

directly measure the spatial-phase fidelity of the free-standing nitride gratings.

4.18 High-Dispersion, High-Efficiency Transmission Gratings for Astrophysical X-ray Spectroscopy

Sponsor

National Aeronautics and Space Administration
Contract NAS8-36748

Project Staff

Professor Claude R. Canizares, Robert C. Fleming, Jr., Dr. Mark L. Schattenburg, Professor Henry I. Smith

This work involves a collaboration between the Center for Space Research and the Submicron Structures Laboratory (SSL), providing transmission gratings for the Advanced X-ray Astrophysics Facility (AXAF) x-ray telescope, currently scheduled for launch in 1998. Many hundreds of low-distortion, large-area transmission gratings of 200 nm period (gold) and 460 nm period (silver) are required. These will provide high resolution x-ray spectroscopy of astrophysical sources in the 100 eV to 10 keV band.

Because of the requirements of low distortion, high yield, and manufacturability, a fabrication procedure involving the replication of x-ray masks has been selected. Masks are made of high-stiffness silicon nitride membranes to eliminate distortion and patterned using a process involving holographic lithography, reactive-ion etching, and electroplating. The masks are then replicated using soft x-rays (1 - 1.5 nm) and the resulting patterns electroplated with gold or silver. An etching step then yields membrane-supported gratings suitable for space use. Flight prototype gratings have been fabricated and continue to undergo space-worthiness tests. Progress in this area focuses on increasing the yield and flexibility of the fabrication procedures, and the perfection of various mask and grating evaluation tests.

4.19 Submicron-Thickness X-ray Window Technology

Sponsor

National Aeronautics and Space Administration
Grant NAGW-2003
Contract NAS8-36748

Project Staff

Richard J. Aucoin, Nitin Gupta, Dr. Mark L. Schattenburg, Professor Henry I. Smith

We have been investigating various schemes for fabricating leak-free, large-area, ultrathin membranes to serve as vacuum isolation windows for the transmission of x-rays. Applications include gas-filled x-ray detector windows and high-vacuum isolation windows for x-ray lithography. Current window technology uses relatively thick beryllium windows which are opaque to x rays with wavelengths in the 0.5 - 1.5 nm band. However, this band is very useful for x-ray detector and x-ray lithography applications. Current efforts seek to perfect large-area polyimide windows which have a 1.0 micron thickness. When combined with tungsten or nickel meshes, these have been made leak free to the limit of He leak detector technology. Woven tungsten support meshes are used, and also advanced nickel meshes made by deep-etch x-ray lithography (so-called LIGA process), in collaboration with the MicroParts company in Germany. Future efforts will seek to reduce the membrane thickness still further, and also experiment with silicon nitride membranes which promise to be leak free and also bakeable for high vacuum applications. A silicon nitride isolation window is being used as a vacuum isolation window in our laboratory x-ray aligner. New high-strength nitrides, which we have developed using our dedicated in-house LPCVD system, promise to further improve window transmission.

4.20 GaAs Epitaxy on Sawtooth-Patterned Silicon

Sponsor

Joint Services Electronics Program
Contract DAAL 03-92-C-0001

Project Staff

Dr. Khalid Ismail, Nasser Karam,^a Professor Henry I. Smith, Kenneth Yee

The growth of GaAs on Si offers the possibility of combining high-speed and optoelectronic GaAs devices with Si integrated-circuit technology. Oriented gratings of 200 nm period are fabricated in Si₃N₄ on (100) Si substrates. Anisotropic etching in KOH is then used to produce sawtooth-profile gratings in the Si. Then these serve as substrates

for GaAs growth by MOCVD. The dislocation density in the grown GaAs films is orders of magnitude lower than the density in films formed on planar Si substrates.

4.21 Publications

Journal Articles

Bagwell, P.F., S.L. Park, A. Yen, D.A. Antoniadis, H.I. Smith, T.P. Orlando, and M.A. Kastner. "Magnetotransport in Multiple Narrow Silicon Inversion Channels Opened Electrostatically into a Two-Dimensional Electron Gas." *Phys. Rev. B* 45: 9214-9221 (1992).

Carter, J.M., D.B. Olster, M.L. Schattenburg, A. Yen, and H.I. Smith. "Large-Area, Free-Standing Gratings for Atom Interferometry Produced Using Holographic Lithography." *J. Vac. Sci. Technol. B* 10: 2909-2911 (1992).

Chu, W., H.I. Smith, S.A. Rishton, D.P. Kern, and M.L. Schattenburg. "Fabrication of 50 nm Line-and-Space X-ray Masks in Thick Au using a 50 keV Electron Beam System." *J. Vac. Sci. Technol. B* 10: 118-121 (1992).

Chu, W., C.C. Eugster, A. Moel, E.E. Moon, J.A. del Alamo, H.I. Smith, M.L. Schattenburg, K.W. Rhee, M.C. Peckerar, and M.R. Melloch. "Conductance Quantization in a GaAs Electron Waveguide Device Fabricated by X-ray Lithography." *J. Vac. Sci. Technol. B* 10: 2966-2969 (1992).

Ghanbari, R.A., M. Burkhardt, D.A. Antoniadis, H.I. Smith, M.R. Melloch, K.W. Rhee, and M.C. Peckerar. "Comparative Mobility Degradation in Modulation-Doped GaAs Devices after E-beam and X-ray Irradiation." *J. Vac. Sci. Technol. B* 10: 2890-2892 (1992).

Ghanbari, R.A., W. Chu, E.E. Moon, M. Burkhardt, K. Yee, D.A. Antoniadis, H.I. Smith, M.L. Schattenburg, K.W. Rhee, R. Bass, M.C. Peckerar, and M.R. Melloch. "Fabrication of Parallel Quasi-One-Dimensional Wires Using a Novel Conformable X-ray Mask Technology." *J. Vac. Sci. Technol. B* 10: 3196-3199 (1992).

Hector, S.D., M.L. Schattenburg, E.H. Anderson, W. Chu, V.V. Wong, and H.I. Smith. "Modeling and

^a Spire Corporation.

Experimental Verification of Illumination and Diffraction Effects on Image Quality in X-ray Lithography." *J. Vac. Sci. Technol. B* 10: 3164-3168 (1992).

Ku, Y.C., M.H. Lim, J.M. Carter, M.K. Mondol, A. Moel, and H.I. Smith. "Correlation of In-Plane and Out-of-Plane Distortion in X-ray Lithography Masks." *J. Vac. Sci. Technol. B* 10: 3169-3172 (1992).

Rhee, K.W., D.I. Ma, M.E. Peckerar, R.A. Ghanbari, and H.I. Smith. "Proximity Effect Reduction in X-ray Mask Making Using Thin Silicon Dioxide Layers." *J. Vac. Sci. Technol. B* 10: 3062-3066 (1992).

Rittenhouse, G.E., K. Early, B.S. Meyerson, H.I. Smith, and J.M. Graybeal. "Novel Vertical Silicon-Membrane Structure and Its Application to Josephson Devices." *J. Vac. Sci. Technol. B* 10: 2860-2863 (1992).

Smith, H.I., and M.L. Schattenburg. "X-ray Lithography, from 500 to 30 nm: X-ray Nanolithography." Submitted to *IBM J. Res. Dev.* as part of a special issue on X-ray Lithography (1993).

Yen, A., M.L. Schattenburg, and H.I. Smith. "A Proposed Method for Fabricating 50 nm-period Gratings by Achromatic Holographic Lithography." *Appl. Opt.* 31: 2972-2973 (1992).

Yen, A., E.H. Anderson, R.A. Ghanbari, M.L. Schattenburg, and H.I. Smith. "Achromatic Holographic Configuration for 100 nm Period Lithography." *Appl. Opt.* 31: 4540-4545 (1992).

Yen, A., H.I. Smith, M.L. Schattenburg, and G.N. Taylor. "An Anti-Reflection Coating for use with PMMA at 193 nm." *J. Electrochem. Soc.* 139: 616-619 (1992).

Zhao, Y., D.C. Tsui, M. Santos, M. Shayegan, R.A. Ghanbari, D.A. Antoniadis, and H.I. Smith. "Magneto-optical Absorption in a Two Dimensional Electron Grid." *Appl. Phys. Lett.* 12: 1510-1512 (1992).

Meeting Papers

Canizares, C.R., D. Dewey, E.B. Galton, T.H. Markert, H.I. Smith, M.L. Schattenburg, B.E. Woodgate, and S. Jordan. "The MIT High Resolution X-ray Spectroscopy Instruments on AXAF." Paper presented at AIAA Space Programs and Technologies Conference, Huntsville, Alabama, March 24-27, 1992.

Kumar, A. "Electron States and Potentials in Quantum Dot Structures." Paper presented at the American Physical Society Symposium on Charging Effects in Quantum Dots, Indianapolis, Indiana. *Bull. Amer. Phys. Soc.* 37: 429 (1992).

Smith, H.I., and D.A. Antoniadis. "Mesoscopic Devices: Will They Supersede Transistors in ULSI?" Paper presented at the International Conference on Solid State Devices and Materials, Tsukuba, Japan, August 26-28, 1992.

Smith, H.I. "History of X-ray Lithography." Paper presented at Optcon '92, Boston, Massachusetts, November 15-20, 1992.

Smith, H.I., and M.L. Schattenburg. "Proximity X-ray Nanolithography: P Current Performance and Theoretical Limits." Paper presented at the 39th National Symposium American Vacuum Society, Chicago, Illinois, November 9-12, 1992.

Smith, H.I., and M.L. Schattenburg. "Why Bother with X-ray Lithography?" Proceedings of the SPIE Symposium Microlithography, San Jose, California, March 8-13, 1992.

Zhao, Y., D.C. Tsui, K. Hirakawa, M. Santos, M. Shayegan, R.A. Ghanbari, D.A. Antoniadis, and H.I. Smith. "Far Infrared Magneto-Absorption by the 2DEG in GaAs/AlGaAs Heterostructures with Grid Gates." Paper presented at the 21st International Conference on the Physics of Semiconductors, Beijing, China, August 10-14, 1992.

Zhao, Y., D.C. Tsui, K. Hirakawa, M. Santos, M. Shayegan, R. Ghanbari, D.A. Antoniadis, and H.I. Smith. "Far Infrared Magneto-Absorption by the 2 DEG in GaAs/AlGaAs Heterostructures with Grid Gates." Paper presented at the American Physical Society Meeting, Indianapolis, Indiana, March 16-20, 1992.

Theses

Modiano, A.M. *An Aligner for X-ray Nanolithography*. Ph.D. diss. Dept. of Electr. Eng. and Comput. Sci., MIT, May 1992.

Olster, D.B. *Refining the Process of Achromatic Holographic Lithography*. S.B. thesis, Dept. of Electr. Eng. and Comput. Sci., MIT, May 1992.

MIT Patents

Smith, H.I., E.H. Anderson, and M.L. Schattenburg. "Holographic Lithography." Patent 5,142,385, August 25, 1992.

Smith, H.I., E.H. Anderson, and M.L. Schattenburg. "Energy Beam Locating." Patent 5,136,169, August 4, 1992.

Books/Chapters in Books

Bagwell, P.F., A. Kumar, and R. Lake. "Scattering and Quantum Localization of Electrons in a Waveguide by Static and Time-Varying Potentials." In *Quantum Effect Physics, Electronics and Applications*. Eds. Ismail, T. Ikoma, and H.I. Smith. Philadelphia: Institute of Physics Publishing, 1992, chapter 2, p. 45.

Ismail, K., T. Ikoma, and H.I. Smith, *Quantum Effect Physics, Electronics and Applications*. Institute of Physics Conference Series Number 127, Philadelphia: Institute of Physics Publishing, 1992.

Smith, H.I., and M.L. Schattenburg. "Lithography for Manufacturing at 0.25 Micrometer and Below." In *Crucial Issues in Semiconductor Materials and Processing Technologies*. NATO ASI Series E, 222: 153. Eds. S. Coffa, F. Priolo, E. Rimini, and J.M. Poate. 1992.

Section 3 Optics and Devices

Chapter 1 Optics and Quantum Electronics

Chapter 2 Optical Propagation and Communication

Chapter 3 High Frequency (> 100 GHz) Electronic Devices

Chapter 1. Optics and Quantum Electronics

Academic and Research Staff

Professor Hermann A. Haus, Professor Erich P. Ippen, Professor James G. Fujimoto, Professor Peter L. Hagelstein, Dr. Santanu Basu, Dr. Joseph A. Izatt

Visiting Scientists and Research Affiliates

Dr. Lucio H. Acioli, Yuzo Hirayama, Dr. Franz X. Kärtner, Dr. Charles P. Lin, Dr. Antonio Mecozzi, Dr. Jérôme M. Paye, Dr. Masataka Shirasaki, Dr. Fabrice Vallee

Graduate Students

Laura E. Adams, Keren Bergman, Luc Boivin, Jeffrey K. Bounds, Tak K. Cheng, Ali Darwish, Jay N. Damask, Ali M. Darwish, Christopher R. Doerr, David J. Dougherty, Siegfried B. Fleischer, James G. Goodberlet, Katherine L. Hall, Michael R. Hee, David Huang, Charles T. Hultgren, Joseph M. Jacobson, Sumanth Kaushik, Farzana I. Khatri, Gadi Lenz, Ilya Lyubomirsky, Martin H. Muendel, John D. Moores, Ann W. Morgenthaler, Lynn E. Nelson, Janet L. Pan, Lily Y. Pang, Malini Ramaswamy, Chi-Kuang Sun, Kohichi R. Tamura, Morrison Ulman

Undergraduate Students

Irfan U. Chaudhary, Darlene J. Ford, Akikazu Hashimoto, Jalil Kahn

Technical and Support Staff

Mary C. Aldridge, Donna L. Gale, Cynthia Y. Kopf, Lisbeth N. Lauritzen

1.1 Additive Pulse Modelocking

Sponsors

Joint Services Electronics Program
Contract DAAL03-92-C-0001
U.S. Air Force - Office of Scientific Research
Contract F49620-91-C-0091

Project Staff

Professor James G. Fujimoto, Professor Hermann A. Haus, Professor Erich P. Ippen, Dr. Antonio Mecozzi, Farzana I. Khatri, John D. Moores, Lynn E. Nelson

Additive Pulse Modelocking (APM) is a technique of modelocking that simulates saturable absorber action by transforming nonlinear phase modulation due to the Kerr effect into amplitude modulation. Since the Kerr effect has a very short response time, very fast absorption characteristics can be achieved. The Kerr effect is also responsible for

self-focusing, an effect used in the Kerr Lens Modelocking (KLM).

In order to compare the two modelocking schemes, we have developed an analytic theory of KLM.¹ With the analytic theory of APM already available, it was possible to make comparisons on the merits of the two schemes.¹

It has been observed by several researchers that achievable pulsewidths are critically dependent upon third order dispersion of the system (the dependence of the group velocity dispersion upon frequency). We have gained a good understanding of the process by extensive computer simulations and an analytic treatment that is capable of reproducing the main features of the simulation results.² Briefly stated, third order dispersion generates sidebands of the pulse spectrum because the dispersion characteristic provides phase matching of the main pulse phase velocity with the phase velocity of a spectral sideband of the pulse. This effect drains energy from the main pulse and

¹ H.A. Haus, J.G. Fujimoto, and E.P. Ippen, "Analytic Theory of Additive Pulse and Kerr Lens Mode Locking," *IEEE J. Quant. Elec.* 28: 2086-2096 (1992).

² H.A. Haus, J.D. Moores, and L.E. Nelson, "Effect of Third-order Dispersion on Passive Mode Locking," *Opt. Lett.* 18: 51-53 (1993).

reduces the saturable absorber action. A surprising outcome of the analysis is that, when third order dispersion effects are significant, the pulse can be shortened by filtering its spectrum. This filtering reduces the sideband generation and thus reduces its damaging effect.

Another theoretical investigation was triggered by observations of C. Doerr, a graduate student attempting to actively modelock an erbium fiber ring laser to produce high repetition rate pulse trains. It was hoped that the relatively short solitons (1 ps or less) in the laser with negative group velocity dispersion could be forced to circulate at a Gbit rate. Mr. Doerr found that he could achieve good steady state pulse generation with 100 ps pulses, but not shorter ones. The computer simulations made by L. Nelson, aided by analytic work, showed that this is consistent with theoretical predictions. The modelocked pulses can be shortened somewhat by the Kerr effect in the fiber, as already pointed out in our previous work.³ However, when much shorter pulses are attempted with increased Kerr effect, the system is forced to produce pulses closely resembling higher order solitons. These pulses, of course, change continuously and cannot lead to a steady state pulse train of constant amplitude. This work also provides a good physical interpretation for Haus and Silberberg,³ which did not provide a physical explanation of the results of its computer simulations. It is clear, however, that both very short pulses and pulse timing via active modelocking are achievable when APM components are introduced into the laser system. We shall pursue this problem both theoretically and experimentally.

1.2 Fiber Ring Laser

Sponsors

Charles S. Draper Laboratories
Contract DL-H-441629
Joint Services Electronics Program
Contract DAAL03-92-C-0001
U.S. Air Force - Office of Scientific Research
Contract F49620-91-C-0091

Project Staff

Professor Hermann A. Haus, Professor Erich P. Ippen, Christopher R. Doerr, Lynn E. Nelson, Kohichi R. Tamura

Work on all-fiber modelocked lasers is being pursued at several laboratories, e.g., the Naval Research Laboratory and the University of Southampton. We have concentrated on one particular realization, a simple unidirectional additively pulse modelocked (APM) ring erbium fiber laser. The gain fiber also acts as the nonlinear Kerr element. Fiber polarization transformers and fiber polarizer and isolator make this an all-fiber system.

K. Tamura was successful in obtaining stable operation of the laser⁴ with pulses at 42 MHz repetition rate (one pulse in the ring) of 452 fs duration. The system is truly self-starting because it breaks into pulse operation spontaneously when a 36 mw pump threshold is reached (cw operation is initiated at 11 mw pump power). The self-starting behavior is in agreement with our previously published theory⁵ that showed self-starting impeded by small backscatter in the laser resonator. The scatter displaces the resonator mode spectrum and thereby calls for increased injection signals into the individual modes. In the unidirectional ring only a combination of two backscatters (one backward, the other forward) displaces the resonator mode spectrum, and hence the effect is greatly reduced.

The very successful operation of this laser has encouraged us to intensify the work on this particular system. We will implement schemes to obtain stable operation with more than one pulse within the resonator, and we will work toward generation of even shorter pulses.

1.3 Long Distance Fiber Communications

Sponsors

MIT Lincoln Laboratory
National Science Foundation
Grant ECS 90-12787

³ H.A. Haus and Y. Silberberg, "Laser Mode Locking with Addition of Nonlinear Index," *IEEE J. Quant. Electron.* QE-22: 325-331 (1986).

⁴ K. Tamura, H.A. Haus, and E.P. Ippen, "Self-starting Additive Pulse Mode-locked Erbium Fibre Ring Laser," *Electron. Lett.* 28: 2226-2227 (1992).

⁵ H.A. Haus and E.P. Ippen, "Self-starting of Passively Mode-locked Lasers," *Opt. Lett.* 16: 1331-1333 (1991).

Project Staff

Professor Hermann A. Haus, Dr. Antonio Mecozzi,
Farzana I. Khatri, Yinchieh Lai

Last year we showed that the Gordon-Haus effect that sets a limit on long distance soliton communications could be overcome partially by filtering the pulse stream at every amplifier stage.⁶ The carrier frequency of a soliton that deviates from the filter center frequency is pushed by the filter toward the filter center frequency. Since the Gordon-Haus effect is a noise-induced random walk of soliton carrier frequency, filters help to reduce this effect. The filters also help in reducing background noise. Indeed, the net linear bandwidth of the transmission link is greatly reduced by the cascade of the filters so that linear high-bitrate communications are impossible. Fiber nonlinearity allows solitons to recover their spectral width when it has been reduced by filtering; thus high bit-rate soliton pulse trains can be transmitted. The same proposal was made independently by Hasegawa and Kodama at Bell Laboratories.⁷ The scheme permits wavelength multiplexing if the filters are the Fabry-Perot type with one multiple transmission peak per channel.

Nakazawa of NTT demonstrated a pulse train transmission that also extended the Gordon-Haus limit, using both filters and modulators.⁸ This scheme is not readily adaptable to wavelength multiplexed transmission. However, we have now shown that it eliminates the Gordon-Haus limit entirely.⁹ A pulse stream of ones and zeros can propagate indefinitely in a fiber ring with gain to compensate for the loss and with filters and modulators synchronized to the pulse stream. The zeros are maintained because the modulators spread the spectrum of the noise accumulating in the time slots occupied by zeros; then the filters absorb it. A fiber ring that operates on this principle can be used as a high bit-rate all-optical memory. We are now investigating how this memory can be used in conjunction with all-optical switches, delay lines, and frequency shifters for the conversion of Time Division Multiplexing (TDM) to Wavelength Division Multiplexing (WDM) and back again.

1.4 Squeezing

Sponsors

Charles S. Draper Laboratories
Contract DL-H-441629
Fujitsu Laboratories
National Science Foundation
Grant ECS 90-12787
U.S. Navy - Office of Naval Research
Grant N00014-92-J-1302

Project Staff

Professor Hermann A. Haus, Keren Bergman, Luc Boivin, Jeffrey K. Bounds, Christopher R. Doerr, Dr. Franz X. Kärtner, Ilya Lyubomirsky, Dr. Masataka Shirasaki

We are continuing our experiments on squeezing with optical fibers. Comparison of our results with those of the IBM group have shown that the degree of squeezing with pulses of 100 ps duration is critically dependent on the Guided Acoustic Wave Brillouin Scattering (GAWBS) in the fiber. The fiber used in our previous experiments had a "window" of low GAWBS within the frequency range in which we observed squeezing (40-80 kHz). We did not obtain squeezing with a fiber given to us by the IBM group which showed much higher GAWBS in the same frequency regime. This finding prompted us to look for ways to eliminate GAWBS. The IBM group has already proposed and demonstrated squeezing with reduced GAWBS using subpicosecond pulses; the shorter the pulses, the less GAWBS is excited. Another advantage presented by shorter pulses of a given energy is that squeezing can be achieved in short fibers (< 1 m), further reducing GAWBS. C. Doerr has reproduced these results in our laboratory. There are two other ways of reducing GAWBS:

1. A rapid phase modulation of the local oscillator (> 1 GHz) can cancel out the GAWBS upon detection.¹⁰

⁶ A. Mecozzi, J.D. Moores, H.A. Haus, and Y. Lai, "Soliton Transmission Control," *Opt. Lett.* 16: 1841-1843 (1991).

⁷ Y. Kodama and A. Hasegawa, "Generation of Asymptotically Stable Optical Solitons and Suppression of the Gordon-Haus Effect," *Opt. Lett.* 17: 31-33 (1992).

⁸ M. Nakazawa, E. Yamada, H. Kubota, and K. Suzuki, "10 Gbit/s Soliton Transmission over One Million Kilometres," *Electron. Lett.* 27: 1270-1272 (1991).

⁹ H.A. Haus and A. Mecozzi, "Long-term Storage of a Bit Stream of Solitons," *Opt. Lett.* 17: 1500-1502 (1992).

¹⁰ M. Shirasaki and H.A. Haus, "Reduction of Guided-acoustic-wave Brillouin Scattering Noise in a Squeezer," *Opt. Lett.* 17: 1225-1227 (1992).

2. A rapid repetition rate of the pulses (1 GHz) puts the GAWBS spectrum into a frequency regime that does not convolve to low frequencies upon detection.

We have demonstrated successfully scheme 1,¹¹ which was employed in conjunction with a phase measurement in a Mach-Zehnder interferometer achieving a noise floor 3 dB below the shot noise level. This is the first demonstration of the use of Kerr-squeezed vacuum for an improved phase measurement. We are presently working on scheme 2.

The theory of squeezing requires a self-consistent analysis of nonlinear optical processes. Every quantum measurement employs a nonlinear device. With a self-consistent, yet simple quantum theory of nonlinear devices, one can develop a self-consistent theory of quantum measurement. Taking advantage of this fact, we have analyzed some basic quantum measurements in which we have quantized not only the process to be measured, but also the measurement equipment. Paradoxes of quantum measurement, some of long standing, can be eliminated in this way.¹²

1.5 Integrated Optics Components: The Channel Dropping Filter

Sponsors

National Center for Integrated Photonics
National Science Foundation
Grant ECS 90-12787

Project Staff

Professor Hermann A. Haus, Jay N. Damask, Professor Leslie A. Kolodziejski, Professor Henry I. Smith, Gale S. Petrich, Vincent V. Wong

The Channel-Dropping Filter (CDF), proposed by Haus and Lai,¹³ is a novel narrow-band integrated optical filter highly suitable for wavelength-division demultiplexing of optically transmitted bitstreams. The novel architecture of the CDF allows "in-line" filtering of a WDM bitstream.¹⁴ This is in contrast

with other currently proposed filters, all of which require the termination of the entire bitstream to resolve the frequency components. Within the past year, we have shown the application of the CDF for phase control of optically controlled phased-array radars and wide area synchronous clock distribution.

The CDF is an integrated optical device that is constructed with three parallel waveguides and quarter-wave shifted distributed-feedback (DFB) gratings. The center guide, the bus, carries the WDM bitstream. On the two side guides, the receiver and mirror, spacially coherent DFB gratings are patterned.

Two prototypes of the CDF are being developed at MIT. One is based on the silica-on-silicon materials system, developed in the Integrated Circuits Laboratory at MIT. While this system is optically passive, its low loss will allow for the strong optical resonances required for proper operation. The other is based on the InGaAsP/InP semiconductor materials system, developed in the Photonic Semiconductors Laboratory in collaboration with Professor L.A. Kolodziejski. This optically active system will allow for optical amplification to overcome the intrinsic material loss as well as allow tuning of the filter frequency. In both cases, x-ray nanolithography is necessary to pattern the 5100 Å and 2300 Å period gratings for the two respective materials systems. The x-ray technology has been developed in the Submicron Structures Laboratory in collaboration with Professor H.I. Smith.

1.6 Tunable Semiconductor Lasers

Sponsor

National Center for Integrated Photonics

Project Staff

Professor Clifton G. Fonstad, Professor Hermann A. Haus, Paul S. Martin

Wavelength Division Multiplexing (WDM) applications such as the channel dropping filter proposed

¹¹ K. Bergman, C.R. Doerr, H.A. Haus, and M. Shirasaki, "Sub-shot Noise Measurement with Fiber Squeezed Optical Pulses," *Opt. Lett.*, forthcoming.

¹² F.X. Kärtner and H.A. Haus, "Quantum Nondemolition Measurements and the 'Collapse of the Wave Function'," *Phys. Rev. A*, forthcoming.

¹³ H.A. Haus and Y. Lai, "Quantum Theory of Soliton Squeezing: A Linearized Approach," *J. Opt. Soc. Am. B* 7: 386-392 (1990).

¹⁴ J.N. Damask and H.A. Haus, "Wavelength-division Demultiplexing Using Channel-dropping Filters," *IEEE J. Lightwave Tech.*, forthcoming.

by H.A. Haus and Y. Lai¹⁵ require tunable lasers and/or optical amplifiers. Simulations we performed have shown that the three terminal Independently Addressable Asymmetric Double Quantum Well (IAADQW) structure we proposed has a tuning range of more than 20 nm about a center wavelength of 1.5 μm . This is significantly larger than the continuous tuning range of both three-section Distributed Bragg Reflector (DBR) and Tunable Twin-Guide (TTG) lasers that are competing for use in WDM systems. In addition to wide tuning range, the IAADQW is a three-terminal device so light output power can be kept constant during tuning.

Fabrication of the IAADQW devices has begun using a self-aligned technique we developed. A single photolithography step defines a metal layer which we use as:

1. An etch mask for the definition of an optical waveguide using Reactive Ion Etching (RIE);
2. An ion implant mask that we use to confine the current injection in the lower quantum well;
3. A contact to the upper quantum well.

Use of this technique eliminates critical lithographic alignments that could make the fabrication of three terminal devices prohibitively complex.

1.7 Nonlinear Properties of InGaAsP Optical Amplifiers

Sponsors

Joint Services Electronics Program
Contract DAAL03-92-C-0001
National Center for Integrated Photonics
Technology
National Science Foundation
Grant EET 88-15834
U.S. Air Force - Office of Scientific Research
Contract F49620-91-C-0091

Project Staff

Professor Erich P. Ippen, Katherine L. Hall, Ali M. Darwish, Gadi Lenz

The nonlinear properties of semiconductor optical amplifiers are of interest because they 1) influence the modulation response and mode stability of diode lasers, 2) limit speed and produce cross-talk between multiplexed signals in optical amplifiers, and 3) may be useful for the design of nonlinear optical waveguide modulators and switches. We use femtosecond optical pulses, tunable near 1.5 μm , to characterize the optical nonlinearities in the gain and index of InGaAsP diodes and optical amplifiers.

During the past year, we measured for the first time the femtosecond gain dynamics of strained-layer multiple-quantum-well (SLMQW) amplifiers using the novel heterodyne pump-probe technique we had previously developed.¹⁶ The heterodyne technique is essential for studying SLMQW devices because their gain is highly anisotropic. This anisotropy is due to the polarization selection rules and the large energy separation between the light-hole and heavy-hole bands. The pump-probe results show a response consistent with spectral hole burning when the diode is biased in the absorption regime. In the gain regime, carriers are heated by free-carrier absorption, and there is a measurable delay (~ 200 fs) in the thermalization of the hot carrier distribution. Subsequent cooling to the lattice temperature follows with a time constant of ~ 1 ps, which is in good agreement with previous results on bulk and unstrained MQW InGaAsP optical amplifiers.

We have also extended the heterodyne pump-probe technique to measure ultrafast index nonlinearities in bulk and SLMQW amplifiers.¹⁷ For these experiments, we use a high-frequency (ham) radio receiver (instead of a spectrum analyzer) to detect the beat between reference and probe pulses because it has AM and FM reception at the same frequency. This new technique for measuring ultrafast index nonlinearities has many advantages over time division interferometer (TDI) techniques. It

¹⁵ H.A. Haus and Y. Lai, "Quantum Theory of Soliton Squeezing: A Linearized Approach," *J. Opt. Soc. Am. B* 7: 386-392 (1990).

¹⁶ K.L. Hall, G. Lenz, and E.P. Ippen, "Novel, Heterodyne Pump-Probe Measurement of Femtosecond Nonlinearities in Waveguides," *Conference on Lasers and Electro-optics Technical Digest*, Anaheim, California, 1992, paper no. JThF4; K.L. Hall, G. Lenz, E.P. Ippen, U. Koren, and G. Raybon, "Carrier Heating and Spectral Hole Burning in Strained-Layer Multiple Quantum Well Lasers at 1.5 μm ," *Appl. Phys. Lett.* 61: 2512 (1992).

¹⁷ K.L. Hall, A. Darwish, E.P. Ippen, U. Koren, and G. Raybon, "Femtosecond Index Nonlinearities in InGaAsP Optical Amplifiers," *Appl. Phys. Lett.*, forthcoming; K.L. Hall, A.M. Darwish, E.P. Ippen, U. Koren, and G. Raybon, "Subpicosecond Index Nonlinearities in InGaAsP Diode Laser Amplifiers," *Conference on Lasers and Electro-optics Technical Digest*, Baltimore, Maryland, 1993, paper no. JThA2, forthcoming.

requires no stabilization of the interferometer arms, no balanced detector to eliminate signals due to probe amplitude changes, and it can be used with either copolarized or cross-polarized pump-probe beams. Our results suggest that index nonlinearities are due to an ultrafast optical Kerr effect as well as to carrier heating. The measured n_2 in these diodes ranged from $-2 \times 10^{-12} \text{ cm}^2/\text{W}$ to $-6 \times 10^{-12} \text{ cm}^2/\text{W}$, depending on the pump-probe polarization orientation and the diode active structure (bulk vs. SLMQW). These are the first pump-probe measurements of index nonlinearities in InGaAsP diodes. Preliminary results for optical switching applications suggest that 150 fs pulses with only 3 pJ of pulse energy can be used to induce large gain ($\Delta T/T = 95\%$) and index ($\Delta\Phi = 0.75\pi$) changes in diodes biased at the transparency point. In this case, the gain and index nonlinearities have recovered completely after 5 ps.

1.8 Ultrafast Index Nonlinearities in Active Waveguides

Sponsors

National Center for Integrated Photonics
Technology
National Science Foundation
Grant EET 88-15834
U.S Air Force - Office of Scientific Research
Contract F49620-91-C-0091

Project Staff

Professor Erich P. Ippen, David J. Dougherty,
Charles T. Hultgren

Active optical waveguides exhibit large and potentially useful ultrafast nonlinearities. They are attractive structures for use in applications because the carrier density in the active region is easily varied, and thus, the magnitude and recovery time of a given nonlinearity can be controlled. For example, ultrafast index of refraction nonlinearities due to nonequilibrium carriers could become the basis for a controllable all-optical switch. The realization of such a device requires knowledge of how active waveguides respond to optical excitation.

With these ideas in mind, our aim for this project is to use short optical pulses to investigate and characterize the gain and refractive index nonlinearities

exhibited by active waveguides. The waveguides we study consist of bulk AlGaAs diode lasers (Hitachi HLP1400) with anti-reflection coatings deposited on the facets. Such a device functions as an active optical waveguide with gain provided by bias current injected into the device. Our previous pump-probe studies employed a dye laser system that produced optical pulses 400 femtoseconds in duration. These measurements revealed that transient carrier heating and the optical Stark effect are the dominant ultrafast refractive index nonlinearities in these devices.

We recently upgraded our source to a modelocked Ti:sapphire laser system that produces pulses as short as 70 femtoseconds. The short pulses and wide tuning range afforded by this new laser system have enabled us to perform detailed studies of above- and below-band gap dynamics in active waveguides.¹⁸ These recent studies have led to further interesting findings about refractive index nonlinearities. In a series of pump-probe measurements conducted with pulses tuned below the active region's band gap energy, we have observed a transient caused by carrier heating with a recovery time of ~ 1.3 picoseconds. The only method by which carriers can be heated by a below-band photon is through free carrier absorption. Thus, our results indicate that significant carrier heating can result from free carrier absorption. In addition, our below-band studies have also shown that there is a delay of about 0.12 picoseconds in the turn-on of the carrier heating dynamic. This indicates that it takes some finite amount of time for free carriers that have absorbed photons to heat up the sea of carriers sitting at the bottom of the band. We have also observed, in above- and below-band measurements, an instantaneous refractive index transient that we attribute to the optical Stark effect. Our measurements show that this instantaneous nonlinearity experiences a resonant enhancement as the pump wavelength is tuned toward an absorption edge. Finally, studies of above-band gain dynamics have revealed evidence for spectral-hole burning.

Our experiments reveal a great deal about fundamental physical processes and carrier relaxation mechanisms in an optically excited semiconductor. In addition, we are also learning about potentially useful nonlinearities in active waveguides. For instance, transient carrier heating and the optical Stark effect are the source of large, ultrafast

¹⁸ C.T. Hultgren, D.J. Dougherty, and E.P. Ippen, "Above- and Below-band Femtosecond Nonlinearities in Active AlGaAs Waveguides," *Appl. Phys. Lett.* 61: 2767 (1992); C.T. Hultgren, K.L. Hall, G. Lenz, D.J. Dougherty, and E.P. Ippen, "Spectral-hole Burning and Carrier Heating Nonlinearities in Active Waveguides," *Proceedings of the O.S.A. Topical Meeting on Ultrafast Electronics and Optoelectronics*, San Francisco, California, January 1993.

refractive index nonlinearities that may be useful in the development of practical photonic devices.

1.9 Femtosecond Pulse Generation and Amplification in F-center Systems

Sponsors

National Center for Integrated Photonics
Technology
National Science Foundation
Grant EET 88-15834
U.S Air Force - Office of Scientific Research
Contract F49620-91-C-0091

Project Staff

Professor Erich P. Ippen, Dr. Jérôme M. Paye, Gadi Lenz, Yuzo Hirayama

Modern lightwave communication systems use carrier wavelengths around 1.55 μm because optical fibers have minimum loss and can be tailored to have negligible dispersion in this spectral region. The characteristics of the semiconductor lasers, detectors, optical amplifiers, and modulators used in these systems depend strongly on material properties as well as device structure. High rates of information transmission will be limited in some cases by the nonlinearities and dynamic behavior of these components. At the same time, novel properties of these 1.5 μm materials and structures may make new device architectures possible. To investigate these limits and new possibilities, we have been developing a unique femtosecond laser system. Comprised of an F-center laser oscillator and high power amplifier, it will provide the broadly tunable source and continuum spectroscopic capability needed for such studies.

The cw femtosecond-pulse oscillator is an NaCl:OH⁻ laser with a center wavelength of 1.58 μm and a tuning range from 1.5 - 1.65 μm . Pulses with durations of about 100 fs are generated using the Additive Pulse Modelocking (APM) technique that was developed in our lab. With this particular laser, we have also discovered a self-starting mode of APM that exhibits highly stable operation and very low noise. This self-starting under cw pumping is particularly useful because it eliminates the noise associated with a modelocked pump laser.

Recently, we took advantage of this characteristic in an experiment involving the generation of squeezed light.¹⁹

Typical pulse energy at the output of our laser is ~1 nJ. This is sufficient for a variety of pump-probe experiments, but for many experiments, including continuum generation, higher pulse energies are required. This year, we built an optical amplifier for the purpose of reaching these energies. We have observed a gain of 10^4 and 10 μJ output pulses using this system. Our amplifier uses a long NaCl:OH⁻ crystal as the gain medium. The crystal is pumped by a Q-switched Nd:YAG at a rate of 1 KHz. The amplified pulse passes through the amplifier four times with a total transit time still much shorter than the pump pulse. To match oscillator pulses of the KHz pump repetition rate, we have set up a synchronized electro-optic pulse selection system. With further optimization we expect to achieve as much as 100 μJ per pulse. These energies will allow continuum generation making possible new time resolved spectroscopy experiments. These experiments will yield new information on the basic physics of optical devices.

1.10 Coherent Phonons In Electronic Materials

Sponsors

Joint Services Electronics Program
Contract DAAL03-92-C-0001
U.S Air Force - Office of Scientific Research
Contract F49620-91-C-0091

Project Staff

Professor Erich P. Ippen, Tak K. Cheng

Very large amplitude coherent optical phonons can be induced in semimetals and narrow-gap semiconductors and observed using pulses of light that are short in duration compared to the characteristic periods of lattice vibrations. The excitation mechanism for coherent phonons in these materials is attributed to a rapid displacement of the ion equilibrium coordinate induced by electronic excitation.²⁰ Our current interest in coherent phonons is two-fold: (1) using time-resolved femtosecond spectroscopy to further our understanding of lattice dynamics in

¹⁹ C.R. Doerr, I. Lyubomirsky, G. Lenz, J. Paye, H.A. Haus, and M. Shirasaki, "Optical Squeezing with a Short Fiber," paper presented at QELS '93, Baltimore, Maryland, May 1993.

²⁰ T.K. Cheng, J. Vidal, H.J. Zeiger, E.P. Ippen, G. Dresselhaus, and M.S. Dresselhaus, "Mechanism for Displacive Excitation of Coherent Phonons," *Appl. Phys. Lett.* 59: 1923 (1991); H.J. Zeiger, J. Vidal, T.K. Cheng, E.P. Ippen, G. Dresselhaus and M.S. Dresselhaus, "Theory for Displacive Excitation of Coherent Phonons," *Phys. Rev. B* 45: 768 (1992).

electronic materials, (2) exploiting the coherent phonon phenomena to modulate the physical characteristics of the material at THz frequencies. We are carrying out this work in collaboration with Professor M. Dresselhaus and her group in the Center for Materials Science and Engineering.

Our most recent experiments involving high excitation densities have shown that a solid, upon optical pulse excitation, can undergo coherent oscillation at frequencies which are shifted significantly (greater than 10 percent) from their low excitation values. Furthermore, we have studied the detailed dynamics of how the coherent phonon evolves from its initial frequency-shifted state back to the equilibrium state. These time-domain measurements provide information inaccessible via other spectroscopic techniques and reveal important non-equilibrium behavior of coherent phonons related to lattice anharmonicity and carrier screening.

A highlight of this past year is that we showed, for the first time, the possibility of coupling coherent phonon dynamics to electron dynamics in the limit of large vibrational amplitudes.²¹ For example, we investigated Ti_2O_3 , a narrow gap semiconductor which undergoes a semiconductor-semimetal transition as a function of temperature. On the basis of x-ray, Raman, and reflectivity measurements, we deduced that the coherent phonons we excite with femtosecond pulses can modulate the interatomic distances in Ti_2O_3 by as much as two percent. In principle, a three percent modulation is enough to modulate the entire semiconductor-semimetal transition. Experimental work in progress is directed at further developing this notion of modulating the physical characteristics of a solid at THz frequencies via optically induced coherent phonons.

1.11 Femtosecond Studies of Fullerenes

Sponsors

Joint Services Electronics Program
Contract DAAL03-92-C-0001
U.S Air Force - Office of Scientific Research
Contract F49620-91-C-0091

Project Staff

Professor Erich P. Ippen, Siegfried B. Fleischer

The soccerball-shaped molecule C_{60} with its high symmetry has generated considerable theoretical as well as experimental research. Some of this interest has been inspired by the discovery of superconductivity with a high transition temperature of 18 K and 28 K for this third form of carbon if doped with potassium and rubidium, respectively.

The high symmetry (I_h) of C_{60} imposes strong selection rules on phonon mediated excited states transitions. It is therefore interesting to study the processes of electronic and vibrational energy decay in the excited singlet and triplet states in C_{60} versus those for the C_{60}^- ions in doped samples which are metallic and of lower symmetry. A fundamental question is whether the fullerenes with their unusual structure present excited state features that are distinct from other aromatic molecules. Optical pump-probe experiments allow us to monitor the dynamics of the scattering between excited states and thus give information about the electronic structure as well as the strength of the coupling to phonons. We are performing such studies in collaboration with Professor M. Dresselhaus and with Professor P. Ecklund of the University of Kentucky.

The undoped (C_{60}) and doped (K_3C_{60} , Rb_3C_{60}) films used for our pump-probe measurements were thin homogeneous polycrystalline films deposited on quartz substrates with a typical film thickness of 2000 Å. To prevent oxygen contamination all the samples were sealed off in helium. Femtosecond dynamics were induced and observed, in reflectivity and transmission at $\lambda=625$ nm, using pulses from a colliding-pulse modelocked (CPM) dye laser. Both the K and Rb doped films show approximately the same fast decay on the order of 0.2 ps. This is much faster than the monitored response of C_{60} , which exhibits a decay rate on the order of 30 ps, with a fast initial component on the order of 1 ps.²²

The difference in these decay rates reflects the molecular character of C_{60} and the band-like character of M_3C_{60} ($\text{M}=\text{K}, \text{Rb}$). We attribute the measured nonexponential decay of the C_{60} films to the relaxation of excited state carriers from their initial singlet states to lower lying excited triplet states. This is a relatively slow process because the scattering is only on-ball via coupling to vibrational

²¹ T.K. Cheng, L. Aciofi, E.P. Ippen, J. Vidal, H.J. Zeiger, G. Dresselhaus, and M.S. Dresselhaus, "Modulation of a Semiconductor-to-Semimetal Transition at Seven Terahertz via Coherent Lattice Vibrations," *Appl. Phys. Lett.*, forthcoming.

²² S.B. Fleischer, E.P. Ippen, G. Dresselhaus, M.S. Dresselhaus, A.M. Rao, P. Zhou, and P.C. Ecklund, "Femtosecond Optical Dynamics of M_3C_{60} ," *Appl. Phys. Lett.*, forthcoming

modes. For the doped samples the half filled LUMO-derived conduction band gives rise to parity allowed pump-induced transitions of electrons to even higher lying bands. K_3C_{60} and Rb_3C_{60} are metallic and therefore exhibit properties related to narrow bands rather than vibrationally broadened molecular states (as in the case of C_{60}). Subsequent to their optical excitation, the carriers created in both the initial and final states undergo thermal equilibration within each band via Coulomb scattering and also on a slower or competing time scale via electron-phonon coupling. Both processes also scatter excited-state electrons out of their initial states into states with different symmetry and thus modulates the absorption cross section. For a more detailed understanding of the electronic structure and the scattering mechanisms in these materials, wavelength selective pump-probe investigations will be performed.

1.12 Ultrashort Pulse Generation in Solid State Lasers

Sponsors

Joint Services Electronics Program

Contract DAAL03-91-C-0001

National Science Foundation

Fellowship ECS-85-52701

U.S. Air Force - Office of Scientific Research

Contract F49620-91-C-0091

U.S. Navy - Office of Naval Research (MGH)

Contract N00014-91-C-0084

Project Staff

David Huang, Joseph M. Jacobson, Malini Ramaswamy, Morrison Ulman, Dr. Lucio H. Acioli, Dr. Joseph A. Izatt, Professor James G. Fujimoto

1.12.1 Fundamental Limits to Ultrashort Pulse Generation

The development of techniques for the generation of ultrashort laser pulses is essential for studies of ultrafast phenomena as well as high speed optical communications and signal processing applications. The problem of exploring the limits of short pulse modelocked laser performance is an important

issue in femtosecond optics. The time resolution of ultrafast measurements is limited only by the shortest laser pulse durations that can be generated. In addition, the bandwidths available from short pulses make possible the use of spectral shaping and synthesis techniques.

Recent advances have made it possible to generate pulse durations of less than 100 fs using third generation solid state laser technology. Solid state lasers feature high energy storage and high power operation and can be engineered into a compact and relatively low cost short pulse technology. The next milestone in ultrafast phenomena will be the development of solid state laser systems which can reliably generate pulse durations of a few femtoseconds. Advancing the performance of solid state laser technology will require fundamental studies of pulse generation and pulse shaping mechanisms as well as the development of new pulse generation techniques. During the past year our research has focussed on exploring the fundamental limits for short pulse generation in solid state lasers and developing techniques which have the potential for generating pulse durations of less than 10 fs.

The fundamental issue that underlies the development of sub 10 fs lasers is how can one achieve the minimum possible pulsewidth and utilize the full bandwidth that is available from a given laser gain media. $Ti:Al_2O_3$ is an especially attractive material for the study of femtosecond pulse generation because of its large gain bandwidth. The tuning range of $Ti:Al_2O_3$ is from 670 nm to greater than 1000 nm. From the energy time uncertainty relationship, the pulsewidth scales inversely with the bandwidth of the medium. More specifically, the analytic theory of Additive Pulse Modelocking (APM) as developed by Haus et al.²³ predicts that the shortest pulse scales inversely with the gain bandwidth multiplied by the square root of the saturable absorption. Assuming a saturable absorber loss modulation of 1 percent, the bandwidth of $Ti:Al_2O_3$ should support pulses of 10 fs. In addition, the use of intracavity self-phase-modulation and negative group velocity dispersion can further reduce the pulse width by a factor of three.²³ Thus, in theory, pulses of 3 fs should be achievable directly from a $Ti:Al_2O_3$ laser.

²³ H.A. Haus, J.G. Fujimoto, and E.P. Ippen, "Structures for Additive Pulse Modelocking," *J. Opt. Soc. Am. B* 8: 2068-2076 (1991).

1.12.2 Short Pulse Generation using Intracavity Dispersion Compensation

One central issue in the generation of extremely short pulse durations is the control of very broad bandwidth optical signals. The spectral width of a laser pulse is inversely proportional to its duration; in the 10 fs regime for a pulse in the near infrared, the pulse bandwidth will be more than 60 nm or almost ten percent of the carrier frequency. One approach for optimizing laser performance is to compensate intracavity dispersion. Previous results in pulse compression studies²⁴ and in laser modelocking²⁵ have shown that control of higher order dispersion is essential in short pulse generation. Second order, or group velocity, dispersion may be compensated with a pair of either prisms or gratings. The low loss of prisms inserted at Brewster's angle has allowed their use inside laser cavities; they are essential components of both colliding pulse modelocked dye lasers and Kerr lens mode locked solid state lasers. While the dominant effect of both prism and grating pairs is to correct second order dispersion, they simultaneously introduce third order effects. Luckily, the sign of the third order contribution of gratings is opposite to that of prisms. A combination of gratings and prisms was used in an extracavity pulse compression experiment to produce 6 fs pulses, the current world record.²⁴

Working in collaboration with CVI Inc., we have designed and built a thin film optical element that introduces only third order dispersion and has low loss necessary for intracavity use. Our device, a Gires-Tournois interferometer (GTI), is fabricated on a high reflecting mirror substrate and permits the independent control second and third order intracavity dispersion. The amount of third order dispersion may be selected by varying the number of bounces of the laser beam off the GTI. This technique has allowed us to reduce the pulse duration in a Kerr lens modelocked Ti:Al₂O₃ laser from 45 fs to 28 fs. We have performed detailed studies which characterize the intracavity dispersion in the Ti:Al₂O₃ laser in order to demonstrate the role of

third order dispersion compensation for the optimization of femtosecond laser performance.²⁶

Approaches for optimizing pulse duration performance have emerged as an active area of research in recent months. Since our demonstration of the GTI as a third order dispersion compensating device, a number of other approaches for controlling dispersion have also been investigated by us as well as other research groups. These techniques include the use of specialized glasses for prisms and multiple prism schemes. The current record for pulsewidth using this approach is 11 fs.²⁷ Further improvements in the pulse duration generated directly from a laser will probably require other pulse compression and shaping techniques as well as laser intracavity dispersion compensation.

In addition to optimizing laser performance, we are also investigating alternative strategies for generating short pulses. Our studies focus on exploiting the short pulse durations and high peak intensity of the pulses for external pulse compression. We are pursuing two approaches to achieve this compression and study its limits. We have recently built a Kerr lens modelocked Ti:Al₂O₃ laser which uses minimized third order dispersion to generate pulse durations of less than 30 fs. The high peak energies and short pulsewidths of these pulses suggest that good compression factors may be achieved using optical fiber pulse compression techniques to attain durations of 10 fs or less with pulse energies of 1 to 2 nJ at repetition rates of 100 Mhz. Investigation of these pulse compression techniques and factors which govern their performance are currently underway.

1.12.3 Cavity Dumped Femtosecond Laser Sources

Another complementary approach for short pulse generation is the development and investigation of techniques for cavity dumping modelocked femtosecond solid state lasers. These studies are important because they provide increased pulse energies without using amplification. These

²⁴ R.L. Fork, C.H. Brito-Cruz, P.C. Becker, and C.V. Shank, "Compression of Optical Pulses to Six Femtoseconds by Using Cubic Phase Compensation," *Opt. Lett.* 12: 483 (1987).

²⁵ R.L. Fork, C.H. Brito Cruz, P.C. Becker, and C.V. Shank, "Third-order Group Velocity Dispersion in a Colliding-pulse Mode-locked Dye Laser," *Opt. Lett.* 15: 1374-1376 (1990).

²⁶ J.M. Jacobson, K. Naganuma, H.A. Haus, J.G. Fujimoto, and A.G. Jacobson, "Femtosecond Pulse Generation in a Ti:Al₂O₃ Laser by Using Second- and Third-order Intracavity Dispersion," *Opt. Lett.* 17: 1608 (1992).

²⁷ M.T. Asaki, C.-P. Huang, D. Garvey, J. Zhou, H.C. Kapteyn, and M. Murnane, "Generation of 11 fs Pulses from a Self Mode-locked Ti:Sapphire Laser," *Opt. Lett.*, forthcoming.

increased pulse energies from this laser will make it ideal for pulse compression as well as for femtosecond studies of nonlinear processes.

In preliminary studies using the Kerr lens modelocked Ti:Al₂O₃ laser we have demonstrated cavity dumping using an intracavity acousto-optic Bragg cell. Pulse durations as short as 50 fs with 100 nJ pulse energies were generated at a 900 KHz repetition rate. In addition to the generation of high energy short pulses, cavity dumping provides an approach for studying the pulse formation dynamics in the laser. One of the surprising findings of our preliminary studies was that relatively high dumping rates can be achieved without significant disruption of the modelocking and pulse formation process.

Further studies are currently underway to extend these techniques to yield pulse durations of less than 30 fs with higher pulse energies. The development of a cavity dumped Kerr lens modelocked Ti:Al₂O₃ laser is significant because it represents a simpler and lower cost alternative approach to amplification for achieving increased pulse energies.

1.13 Studies of Ultrafast Phenomena in Materials

Sponsors

Joint Services Electronics Program
Contract DAAL03-91-C-0001
National Science Foundation
Fellowship ECS-85-52701
U.S. Air Force Office of Scientific Research
Contract F49620-91-C-0091
U.S. Navy - Office of Naval Research
Grant N00014-91-J-1956

Project Staff

Malini Ramaswamy, Chi-Kuang Sun, Dr. Lucio H. Acioli, Dr. Fabrice Vallee, Professor Erich P. Ippen, Professor James G. Fujimoto

1.13.1 Femtosecond Carrier Dynamics in AlGaAs

The design and optimization of high speed electronic and optoelectronic devices depends on knowledge of the dynamics of transient electron and hole populations in semiconductor materials. Carrier dynamics determine the fundamental limits of device speed. For example, intervalley electron scattering is largely responsible for the high field transport properties of GaAs and AlGaAs. For ideal device design it should be possible to predict the time and energy evolution of an excited carrier distribution in the bandstructure of a semiconductor. Electron-electron scattering times are as short as several femtoseconds. Therefore, an accurate model of carrier behavior must have the ability to predict transient effects on the femtosecond time scale.

Working in collaboration with solid state theoretical physicists at the University of Florida, we have developed a collaborative research program which combines state of the art experimental and theoretical techniques to perform detailed investigations of carrier dynamics in GaAs and AlGaAs on a femtosecond scale. Using femtosecond laser experimental studies at MIT and ensemble Monte Carlo computer simulations at the University of Florida, we have been able to experimentally measure and theoretically model the various scattering processes and relaxation mechanisms of excited carrier distributions. The result of our work is a model that may be extended to predict transient carrier dynamics in a variety of different excitation conditions in semiconductors.

Last year, we performed a series of experimental studies on AlGaAs using a tunable femtosecond laser system.²⁸ By systematic variation of the wavelength and spectrum of the femtosecond laser pulses, the evolution of optically excited carrier distributions initially generated in different regions of the band can be systematically investigated. The laser system used for these investigations is an amplified colliding pulse modelocked (CPM) laser. Optical pulses as short as 35 femtoseconds from the CPM are amplified to microjoule energies in a two stage dye amplifier pumped by a copper vapor laser. The amplified pulses are then focused on a flowing jet of ethylene glycol to produce a femtosecond white light continuum. A Fourier frequency filter is used to select the desired spectrum

²⁸ M. Ulman, D.W. Bailey, L.H. Acioli, F.G. Vallee, C.J. Stanton, E.P. Ippen, and J.G. Fujimoto, "Femtosecond Tunable Nonlinear Absorption Saturation Spectroscopy in Al_{0.1}Ga_{0.9}As," *Phys. Rev. B*, forthcoming.

from the continuum.²⁹ Fourier synthesized pulses may be generated with arbitrary spectral or temporal profiles; in our experiment we are primarily concerned with wavelength and bandwidth since they determine the initial state of carriers excited to the conduction band.

Using this laser source, pump probe studies were performed on AlGaAs samples. The mole fraction of Al in the AlGaAs sample was chosen to vary the bandstructure and isolate specific optical transitions. The result of the experimental part of our investigation is a comprehensive set of pump probe differential transmission traces. The data span a range of wavelengths and excited carrier densities, and are recorded for the first thousand femtoseconds after initial excitation.

In another study we investigated excited carrier dynamics in the presence of a cold carrier plasma.³⁰ This situation is analogous to the conditions found in a diode laser. We developed a novel three pulse pump probe technique to investigate the transient carrier dynamics after the generation of carriers with a pre-pulse. The first pulse excites carriers which relax to a quasiequilibrium, cold distribution before the pump probe measurement takes place. In this experiment we varied the bandstructure of the sample instead of tuning the femtosecond laser. With this technique we investigated effects above and below the cold plasma Fermi level and the role of intervalley scattering. The presence of the cold plasma induces only a small increase in the hot carrier thermalization rate even for high cold plasma densities. In fact, the thermalization of a low density, hot carrier distribution interacting with a cold, high density photoexcited plasma occurs on a time scale longer than intervalley scattering in GaAs.

While the femtosecond pump probe technique provides the highest temporal resolution available today, the interpretation of the experimental results

is often complex. We use state of the art computer simulations for two purposes: 1) to keep track of the large number of optical transitions and scattering channels in semiconductor experiments, and 2) to deduce fundamental physical information, such as the time dependent carrier distributions, from differential transmission data. Simple analytical models provide physical insight, but do not yield detailed correspondence with experimental results. Our theoretical model begins with a 30 band, full zone $\mathbf{k} \cdot \mathbf{p}$ calculation of the semiconductor bandstructure. Anisotropy and hole warping effects are included. An ensemble Monte Carlo simulation of 40,000 electrons and holes tracks the time development of the distribution functions.³¹ The final step is a calculation of the differential transmission which is then compared directly with the experimental traces. Fundamental parameters such as the deformation potential constant and carrier scattering rates are then deduced. A further advantage of the simulation technique is that the strengths of different scattering channels may be artificially varied and the sensitivity of the data to specific processes may be assessed.

1.13.2 Nonequilibrium Electronic Effects in Metals

Studies of interactions of free carriers between themselves and their environment constitute one of the major problems of solid state physics. This has been addressed directly in the time domain employing femtosecond techniques both in semiconductors and metals. Metals are especially interesting because they have a very high electron density and their behavior can be modeled relatively simply. The possibility of creating and probing a transient nonequilibrium electron population in metal with ultrashort laser pulses has been demonstrated by different groups.³² In previous experiments electron-electron interactions were assumed to be sufficiently fast to thermalize the

²⁹ A.M. Weiner, J.P. Heritage, and E.M. Kirschner, "High Resolution Femtosecond Pulse Synthesis," *J. Opt. Soc. Am. B* 5: 1563 (1988).

³⁰ L.H. Acioli, M. Uman, F. Vallee, and J.G. Fujimoto, "Femtosecond Carrier Dynamics in the Presence of a Cold Plasma in GaAs and AlGaAs," submitted to *Appl. Phys. Lett.*

³¹ D.W. Bailey, C.J. Stanton, and K. Hess, "Numerical Studies of Femtosecond Carrier Dynamics in GaAs," *Phys. Rev. B* 42: 3423 (1990).

³² G.L. Eesley, "Observation of Nonequilibrium Electron Heating in Copper," *Phys. Rev. Lett.* 51: 2140 (1983); H.E. Elsayed-Ali, T.B. Norris, M.A. Pessot and G.A. Mourou, "Time-resolved Observation of Electron-phonon Relaxation in Copper," *Phys. Rev. Lett.* 58: 1212 (1987); R.W. Schoenlein, W.Z. Lin, J.G. Fujimoto and G.L. Eesley, "Femtosecond Studies of Nonequilibrium Electronic Process in Metals," *Phys. Rev. Lett.* 58: 1680 (1987); R.H.M. Groeneveld, R. Sprik and A. Lagendijk, "Ultrafast Relaxation of Electrons Probed by Surface Plasmons at a Thin Silver Film," *Phys. Rev. Lett.* 64: 784 (1990); S.D. Brorson, A. Kazeroonian, J.S. Moodera, D.W. Face, T.K. Cheng, E.P. Ippen, M.S. Dresselhaus, and G. Dresselhaus, "Femtosecond Room-temperature Measurement of the Electron-phonon Coupling Constant λ in Metallic Superconductors," *Phys. Rev. Lett.* 64: 2172 (1990); S.D. Brorson, J.G. Fujimoto, and E.P. Ippen, "Femtosecond Electronic Heat transport Dynamics in Thin Gold Film," *Phys. Rev. Lett.* 59: 1962 (1987); H.E.

electron gas on a time scale of the order or shorter than the laser pulse duration, although some deviations from an instantaneous response were observed.³³ Recent investigations using transient photoemission have demonstrated the existence of non-Fermi electron distributions with thermalization times as long as 600 fs. These results were observed in gold film for large changes of the electron temperature (of the order of 400°K) with a limited time resolution.³⁴ Similar conclusions were drawn at lower laser fluence by analyzing the temperature dependence of the optically measured electron-phonon interaction time in gold and silver.³⁵

In order to analyze the effect of the non-instantaneous electron-electron interaction on the optical response of a metal film, recently we have performed transient reflectivity and transmissivity measurements of electron temperature dynamics.³⁶ Studies were performed in the perturbative regime where the measured changes in reflectivity and transmissivity can be directly connected to the electron distribution. In contrast to previous experiments, we use a multiple wavelength femtosecond pump-probe technique to excite the electron gas with a infrared pulse (from a mode-locked Ti:Al₂O₃ laser with 120 fs pulsewidth and 880-1065 nm wavelength) and probe changes in optical properties using frequency doubled wavelength in the visible (440-532.5 nm). This technique permits a more definitive measurement of electron dynamics by separating the effects of pump induced transitions from those monitored by the probe. Experiments were performed on thin gold films because the band structure of gold is relatively well known and band to band transition can be easily probed by a frequency doubled Ti:Al₂O₃ femtosecond laser.

Measurements show evidence for non-Fermi electron distributions with a electron thermalization time of ~500 fs and an electron-lattice cooling time of 1 ps, independent of the laser fluence in the range of 2.5 mJ/cm² - 200 mJ/cm² (corresponding to estimated peak temperature change 3-200°K).³⁶ A simple model based on carrier population changes and curved *d*-band was developed to describe the behavior of the system. The diffusion in the optically thin sample is neglected and the electron distribution change is simply separated to two parts: Fermi and non-Fermi, coupled by an electron gas thermalization term. Excellent qualitative correspondence between theory and experiment was obtained.

Our measured electron thermalization time is comparable to the previous estimations.³⁷ On the basis of the very high electron density of metals, one would expect very fast electron-electron interactions. However, the interaction efficiency is considerably reduced by phase space filling which blocks most of the energetically possible interaction channels and by screening which considerably reduces the efficiency of the Coulombic interaction. Our results are significant because they provide some of the first detailed information on non-Fermi electron dynamics in metals and demonstrate new experimental techniques for their investigation.

1.14 Time Domain Diagnostics of Waveguide Devices

Sponsors

Joint Services Electronics Program
Contract DAAL03-91-C-0001
National Science Foundation
Fellowship ECS-85-52701

Elsayed-Ali, T. Juhasz, G.O. Smith and W.E. Bron, "Femtosecond Thermorefectivity and Thermotransmissivity of Polycrystalline and Single-crystalline Gold Film," *Phys. Rev. B* 43: 4488 (1991).

³³ R.W. Schoenlein, W.Z. Lin, J.G. Fujimoto and G.L. Eesley, "Femtosecond Studies of Nonequilibrium Electronic Process in Metals," *Phys. Rev. Lett.* 58: 1680 (1987); S.D. Brorson, A. Kazerooni, J.S. Moodera, D.W. Face, T.K. Cheng, E.P. Ippen, M.S. Dresselhaus, and G. Dresselhaus, "Femtosecond Room-temperature Measurement of the Electron-phonon Coupling Constant λ in Metallic Superconductors," *Phys. Rev. Lett.* 64: 2172 (1990).

³⁴ W.S. Fann, R. Storz, H.W.K. Tom, and J. Bokor, "Direct Measurement of Nonequilibrium Electron-energy Distributions in Subpicosecond Laser-heated Gold Films," *Phys. Rev. Lett.* 68: 2834 (1992).

³⁵ R.H.M. Groeneveld, R. Sprik and A. Lagendijk, "Effect of a Nonthermal Electron Distribution on the Electron-phonon Energy Relaxation Process in Noble Metals," *Phys. Rev. B* 45: 5079 (1992).

³⁶ C.-K. Sun, F. Vallee, L. Acioli, E.P. Ippen, J.G. Fujimoto, "Femtosecond Investigation of Electron Thermalization in Gold," submitted to *Appl. Phys. Lett.*

³⁷ W.S. Fann, R. Storz, H.W.K. Tom, and J. Bokor, "Direct Measurement of Nonequilibrium Electron-energy Distributions in Subpicosecond Laser-heated Gold Films," *Phys. Rev. Lett.* 68: 2834 (1992); R.H.M. Groeneveld, R. Sprik and A. Lagendijk, "Effect of a Nonthermal Electron Distribution on the Electron-phonon Energy Relaxation Process in Noble Metals," *Phys. Rev. B* 45: 5079 (1992).

U.S. Air Force Office of Scientific Research
Contract F49620-91-C-0091
U.S. Navy - Office of Naval Research
Grant N00014-91-J-1956

Project Staff

Chi-Kuang Sun, Professor James G. Fujimoto

1.14.1 Studies of Gain Dynamics in Strained Layer Diodes

Nonlinear gain and transient carrier dynamics in diode lasers are important because they influence laser linewidth, modulation bandwidth, amplification, and short pulse generation. Previous investigators have performed picosecond and femtosecond pump probe measurements of nonlinear gain dynamics in bulk GaAs,³⁸ InGaAsP MQW,³⁹ and InGaAs/InGaAsP strained-layer MQW amplifiers.⁴⁰ These studies have shown that nonequilibrium carrier temperature effects play an important role in carrier dynamics. Carrier temperature changes are caused by a number of processes including state filling produced by stimulated transitions, free carrier absorption, and two photon absorption. Previous studies⁴⁰ have shown that free carrier absorption play a dominant role in carrier heating. A ~ 150 fs relaxation time had been observed which was attributed to either spectral hole burning or turn on delay of free carrier heating. In addition to nonlinear gain, carrier dynamics also produce nonlinear index effects such as self phase modulation.⁴¹

Recently we invented a new technique for performing independent multiple wavelength pump-probe measurement in waveguide devices.⁴² The output of a Kerr lens mode-locked Ti:Al₂O₃ laser was coupled to an optical fiber to produce a self phase modulation broadened spectral bandwidth ~ 50 nm FWHM. After the fiber, the beam was split into a pump and a probe, which were directed into two spectral windowing assemblies⁴³ to produce synchronous independent different-frequency pulses. This approach represents a powerful method for performing experimental studies since the pump and probe wavelengths can be varied independently and thus energy relaxation dynamics can be explicitly measured.

Working in collaboration with investigators at MIT Lincoln Laboratory, we have performed the first studies of carrier dynamics in InGaAs/GaAs strained layer quantum well diode lasers. Strained layer quantum well devices represent one of the most active and technologically promising areas of current optoelectronics device research. Strained layer materials provide an added degree of freedom by allowing the epitaxial growth of nonlattice-matched materials. High power, high efficiency, long lifetime, and low threshold current density⁴⁴ semiconductor lasers have been achieved in InGaAs strained layer devices.

Our studies were performed using a broad-area InGaAs/AlGaAs graded-index separate-confinement heterostructure single quantum well (GRIN-SCH

³⁸ M.S. Stix, M.P. Kesler, and E.P. Ippen, "Observations of Subpicosecond Dynamics in GaAlAs Laser Diodes," *Appl. Phys. Lett.* 48: 1722-1724 (1986); M.P. Kesler and E.P. Ippen, "Subpicosecond Gain Dynamics in GaAlAs Laser Diodes," *Appl. Phys. Lett.* 51: 1765-1767 (1987).

³⁹ K.L. Hall, J. Mark, E.P. Ippen, and G. Eisenstein, "Femtosecond Gain Dynamics in InGaAsP Optical Amplifiers," *Appl. Phys. Lett.* 56: 1740-1742 (1990); Y. Lai, K.L. Hall, E.P. Ippen, G. Eisenstein, "Short Pulse Gain Saturation in InGaAsP Diode Laser Amplifiers," *IEEE Photonics Tech. Lett.* 2: 711-713 (1990); K.L. Hall, Y. Lai, E.P. Ippen, G. Eisenstein, and U. Koren, "Femtosecond Gain Dynamics and Saturation Behavior in InGaAsP Multiple Quantum Well Optical Amplifiers," *Appl. Phys. Lett.* 57: 2888-2890 (1990).

⁴⁰ K.L. Hall, G. Lenz, E.P. Ippen, U. Koren, and G. Raybon, "Carrier Heating and Spectral Hole Burning in Strained-Layer Quantum Well Laser Amplifiers at 1.5 μ m," submitted to *Appl. Phys. Lett.*

⁴¹ N.A. Olsson and G.P. Agrawal, "Spectral Shift and Distortion Due to Self-phase Modulation of Picosecond Pulses in 1.5 μ m Optical Amplifiers," *Appl. Phys. Lett.* 55: 13 (1989); R.S. Grant and W. Sibbett, "Observations of Ultrafast Nonlinear Refraction in an InGaAsP Optical Amplifier," *Appl. Phys. Lett.* 58: 1119 (1989); P.J. Delfyett, Y. Silberberg, and G.A. Alphonse, "Hot-carrier Thermalization Induced Self-phase Modulation in Semiconductor Travelling Wave Amplifiers," *Appl. Phys. Lett.* 59: 10 (1990).

⁴² C.K. Sun, H.K. Choi, C.A. Wang, and J.G. Fujimoto, "Studies of Carrier Heating in InGaAs/AlGaAs Strained-Layer Quantum-Well Diode Lasers Using a Multiple Wavelength Pump-Probe Technique," *Appl. Phys. Lett.*, forthcoming.

⁴³ A.M. Weiner, J.P. Heritage, and E.M. Kirschner, "High Resolution Femtosecond Pulse Synthesis," *J. Opt. Soc. Am. B* 5: 1563 (1988).

⁴⁴ H.K. Choi, and C.A. Wang, "InGaAs/AlGaAs Strained Single Quantum Well Diode Lasers with Extremely Low Threshold Current Density and High Efficiency," *Appl. Phys. Lett.* 57: 321 (1990); R.L. Williams, M. Dion, F. Chatenoud, and K. Dzurko, "Extremely Low Threshold Current Strained InGaAs/AlGaAs Lasers by Molecular Beam Epitaxy," *Appl. Phys. Lett.* 58: 1816 (1991).

SQW) ridge waveguide diode laser⁴⁵ with a bandgap near 950 nm. Carrier heating was studied by tuning the pump pulse above and below the bandgap while keeping all the other conditions (including the probe) constant. The high sensitivity of the system allowed us to perform the experiment in the low perturbation regime. Different heating and cooling times were measured which reflect different thermalization mechanisms for above and below band pumping. This result shows that free carrier absorption is not always the dominant carrier heating process and stimulated transition induced heating plays an important role in the carrier heating process, at least in strained InGaAs/AlGaAs systems.⁴⁶ These studies represent the first pump-probe measurement in InGaAs/AlGaAs strained layer systems. This is also the first multiple wavelength time-domain diagnostics in waveguide structures.

Femtosecond gain dynamics was also investigated using multiple wavelength techniques.⁴⁷ Instead of shifting the pump pulse, the bias current was varied so that gain, transparency, and absorption was produced at the pump wavelength. The probe wavelength was in the gain region for all the cases. Carrier temperature changes mediated by both free-carrier absorption and stimulated transitions were observed. Stimulated transition induced carrier cooling was observed in the absorption region. This was the first observation of carrier cooling in GaAs based devices. An increased understanding of the physical mechanisms of gain dynamics from carrier temperature changes is important for the design of new devices. In particular, the reduction of carrier heating has important implications for reducing parasitic gain saturation effects in short pulse modelocked laser diodes and amplifiers.

1.15 Laser Medicine

Sponsors

National Institutes of Health
Grant NIH-5-R01-GM35459-08
U.S. Navy - Office of Naval Research (MGH)
Contract N00014-91-C-0084

Project Staff

Michael R. Hee, David Huang, Dr. Joseph A. Izatt,
Dr. Charles P. Lin, Professor James G. Fujimoto

1.15.1 The Ultrashort Pulse Scalpel

The objective of our program is to continue development of an optimized ultrashort pulse laser scalpel for precise intraocular microsurgery. Over the last ten years, short optical pulses have been successfully applied for non-invasive cutting of intraocular structures, for example in posterior capsulotomy and iridotomy. Through the mechanism of laser induced breakdown, photodisruption or cutting of intraocular structures is made possible without the need for intervening surgical incision. To date, the majority of clinical applications of laser induced optical breakdown have utilized nanosecond pulses in the millijoule energy range and single pulse exposures.⁴⁸ However, mechanical side effects of laser induced breakdown with nanosecond sources pose potential hazards to adjacent ocular structures and tissues. Our investigations have demonstrated that significant reduction of collateral tissue damage may be achieved through the use of ultrashort pulses. These studies are part of an ongoing collaboration between investigators at MIT, the New England Eye Center of New England Medical Center Hospitals, and the Wellman Laboratories of Photomedicine at Massachusetts General Hospital.

The physical processes which occur in laser induced breakdown include plasma formation, acoustic wave generation, and cavitation. We have

⁴⁵ C.K. Sun, H.K. Choi, C.A. Wang, and J.G. Fujimoto, "Studies of Carrier Heating in InGaAs/AlGaAs Strained-Layer Quantum-Well Diode Lasers Using a Multiple Wavelength Pump-Probe Technique," *Appl. Phys. Lett.*, forthcoming; C.K. Sun, H.K. Choi, C.A. Wang, and J.G. Fujimoto, "Femtosecond Gain Dynamics in InGaAs/AlGaAs Strained-Layer Quantum-Well Diode Lasers," submitted to *Appl. Phys. Lett.*

⁴⁶ C.K. Sun, H.K. Choi, C.A. Wang, and J.G. Fujimoto, "Studies of Carrier Heating in InGaAs/AlGaAs Strained-Layer Quantum-Well Diode Lasers Using a Multiple Wavelength Pump-Probe Technique," *Appl. Phys. Lett.*, forthcoming.

⁴⁷ C.K. Sun, H.K. Choi, C.A. Wang, and J.G. Fujimoto, "Femtosecond Gain Dynamics in InGaAs/AlGaAs Strained-Layer Quantum-Well Diode Lasers," submitted to *Appl. Phys. Lett.*

⁴⁸ F. Fankhauser, P. Roussel, J. Steffen, E. Van der Zypen, and A. Cherenkova, "Clinical Studies on the Efficiency of High Power Laser Radiation Upon Some Structures of the Anterior Segment of the Eye," *Int. Ophthalmol.* 3: 129 (1981).

studied and compared the mechanisms, scaling behavior, and tissue effects of single pulses in the nanosecond and picosecond ranges.⁴⁹ In general, nanosecond and picosecond optical breakdown results in comparable damage zones if the same amount of energy is deposited; however, the threshold energy for breakdown is much lower for picosecond pulses, and near-threshold picosecond pulses produce greatly reduced collateral damage zones. For example, we have demonstrated collateral damage ranges in a corneal endothelial cell model of only 100 microns with 40 picosecond duration pulses at 8 microjoules pulse energy. We have also studied tissue effects (corneal incisions) into the femtosecond domain.⁵⁰ Ultrashort pulses with high peak intensities can produce plasma-mediated ablation of transparent tissues, such as the cornea. Picosecond and femtosecond pulse durations have been demonstrated to produce much smoother excision edges and less damage to the adjacent tissue than nanosecond pulses.

Following these initial studies, we have developed a clinically viable picosecond laser scalpel based on a modelocked, Q-switched Nd:YAG laser with external pulse selection. This laser delivers single 100 picosecond duration pulses at a repetition rate variable from 3 to 1000 Hz; each pulse produces minimal collateral damage, while multiple pulses produce a cumulative incision effect. With this laser, we achieve optical breakdown in the deep vitreous with less than 70 microjoules pulse energy, compared to millijoules used in current clinical Q-switched systems. We have performed *in vitro* and *in vivo* studies of vitreous membrane surgery with the high repetition rate picosecond laser. Membrane surgery of the deep vitreous is a very challenging procedure because of the proximity of the retina and the sensitivity of the retina to thermal and/or mechanical injury. Using an *in vitro* vitreous membrane model, we have demonstrated that repetitive picosecond pulses can produce a fine linear incision with ~ 100 micron cut width. Mechanical disruption posterior to the laser focus is also confined to less than 200 microns. We have also performed picosecond laser microsurgery *in vivo* in experimental vitreous membranes in rabbit eyes. Cuts were successfully made through mem-

branes at distances varying from < 100 microns to 3 mm from the retina without causing vitreous hemorrhage and with only minor cell disruption visible upon histological examination. Based in part on these results, the FDA has approved an initial clinical trial of picosecond laser vitreous membrane surgery in human patients. We have also extended the use of picosecond lasers to glaucoma surgical procedures such as iridectomy and ab externo sclerostomy.

In addition to further clinical studies using our current picosecond laser system, we are also developing new laser technology designed specifically for optimizing highly localized photodisruption in transparent structures using laser induced breakdown. These studies are being performed using a flashlamp-pumped titanium-sapphire laser tunable from 700-1000 nm at 20 Hz repetition rate. Flashlamp pumped solid state lasers feature higher pulse energy and lower cost compared to cw laser pumped lasers. Using a combination of active modelocking and passive optical limiting for suppression of relaxation oscillations, we have obtained modelocked pulses of approximately 100 picoseconds duration with millijoule energy. Further studies should reduce the pulse duration to single picoseconds, using passive modelocking and new techniques for controlling pulse shaping and pulse energy using nonlinear intracavity elements. These new techniques employ refractive index nonlinearities and intracavity aperturing to achieve saturable absorption or saturable gain. If successful, the wavelength tunability and short pulse duration available from this laser system will outperform existing Nd:YAG and Nd:YLF laser technology for a wide range of laser medical applications.

In addition to direct modelocking we are also developing a variable pulse duration, regeneratively amplified titanium-sapphire laser. The 100 fs, 80 MHz, nJ energy Kerr-lens-modelocked oscillator described in a previous section is being incorporated as a seed laser for chirped-pulse regenerative amplification in the flashlamp-pumped titanium-sapphire rod. The completed laser will have variable pulse duration (100 fs - 300 ps), wavelength tunable (700 - 1000 nm) output. Using this source, studies will be performed to correlate tissue incision

⁴⁹ J.G. Fujimoto, W.Z. Lin, E.P. Ippen, C.A. Puliafito, and R.F. Steinert, "Time Resolved Studies of Nd:YAG Laser Induced Breakdown," *Invest. Ophthalmol. Vis. Sci.* 26: 1771 (1985); B. Zysset, J.G. Fujimoto, and T.F. Deutsch, "Time Resolved Measurements of Picosecond Optical Breakdown," *Appl. Phys. B.* 48: 139 (1989); B. Zysset, J.G. Fujimoto, C.A. Puliafito, R. Birngruber, and T.F. Deutsch, "Picosecond Optical Breakdown: Tissue Effects and Reduction of Collateral Damage," *Las. Surg. Med.* 9: 193 (1989); D. Stern, R. Schoenlein, C.A. Puliafito, E.T. Dobi, R. Birngruber, and J.G. Fujimoto, "Corneal Ablation by Nanosecond, Picosecond, and Femtosecond Lasers at 532 and 625 nm," *Arch. Ophthalmol.* 107: 587 (1989).

⁵⁰ D. Stern, R. Schoenlein, C.A. Puliafito, E.T. Dobi, R. Birngruber, and J.G. Fujimoto, "Corneal Ablation by Nanosecond, Picosecond, and Femtosecond Lasers at 532 and 625 nm," *Arch. Ophthalmol.* 107: 587 (1989).

and collateral injury effects with laser parameters (pulse duration, wavelength, and repetition rate). Studies will include time resolved measurements of the fundamental physical processes in optical breakdown, as well as tissue effects. Special emphasis will be placed on investigating pulse durations shorter than 100 picoseconds in order to reduce the pulse energy needed to achieve optical breakdown below the 70 microjoule level used in our previous study. This system will serve as a valuable and unique tool for optimizing the localizability and incision rate for ultrashort pulse intraocular laser surgery.

1.15.2 Optical Coherence Tomography

Optical coherence tomography (OCT) is a novel non-contact, non-invasive, high resolution tomographic imaging technology that we have developed for the measurement of microstructures in biological tissues.⁵¹ OCT can achieve a spatial resolution of 10 micrometers, which is more than a factor of 10 better than current clinical tomographic imaging modalities such as CT, MRI, or ultrasound B mode imaging. The operation of OCT is analogous to ultrasound imaging. An incident optical beam is reflected or backscattered from tissue structures. The roundtrip delay of the returned light is measured to derive the depth of the reflecting structure. This delay measurement is carried out using an interferometric ranging technique called optical coherence domain reflectometry (OCDR).⁵² By incorporating a lateral scanning mechanism to a high speed OCDR system, a two dimensional cross-sectional map of tissue backscattering magnitude is obtained. This data is presented in false-color or gray scale as an optical coherence tomograph. Our OCT studies have concentrated on the measurement of eye structures because the transparency of the ocular media permit easy optical access, and because OCT has the potential of obtaining clinical useful information in very thin eye structures such as the retina and the cornea that are not resolvable using other imaging methods.

This research project spans several different areas including technology development, physical studies, and studies in biological systems *in vitro* and *in vivo*. To address these issues, studies are performed in collaboration with investigators at the Optical Communications Group at MIT Lincoln Laboratory, and the New England Eye Center of the Tufts University School of Medicine.

Our initial results on OCT, published in Science,⁵³ demonstrated the application of OCT in ophthalmology by performing imaging of the retina *in vitro*. The problem of noninvasive measurement of the retinal thickness and morphology is relevant to the diagnosis of glaucoma and other retinal diseases. In addition, as an example of OCT imaging in a highly scattering system, we have performed studies in coronary arteries *in vitro*.

During the past year, we conducted our first *in vivo* studies of the retinal imaging in human subjects. These OCT images of the retina and the optic nerve head have at least ten times higher depth resolution than conventional ocular imaging methods such as ultrasound, laser scanning tomography, and x-ray computed tomography. These *in vivo* studies were made possible by the development of a high speed OCT system with image acquisition times of several seconds. The OCT system was coupled via a optical fiber and galvanometer driven transverse scanning mechanisms to a slitlamp biomicroscope, a commonly used instrument for clinical examination of the eye. We are continuing to improve the speed and robustness of the system in preparation for clinical studies on glaucoma and other vitreo-retinal diseases. We expect to upgrade the image acquisition time to 1-4 seconds in the near future to minimize patient efforts in clinical studies.

High-resolution imaging of retinal structures is clinically relevant to the diagnosis and management of a variety of retinal diseases such as glaucoma, macular degeneration, macular hole, and macular edema. Non-invasive OCT imaging of retinal structures in human subjects was demonstrated this

⁵¹ D. Huang, E.A. Swanson, C.P. Lin, J.S. Schuman, W.G. Stinson, W. Chang, M.R. Hee, T. Flotte, K. Gregory, C.A. Puliafito and J.G. Fujimoto, "Optical Coherence Tomography," *Sci.* 254: 1178 (1991).

⁵² R.C. Youngquist, S. Carr, and D.E.N. Davies, "Optical Coherence-domain Reflectometry: a New Optical Evaluation Technique," *Opt. Lett.* 12: 158 (1987); K. Takada, I. Yokohama, K. Chida, and J. Noda, "New Measurement System for Fault Location in Optical Waveguide Devices Based on an Interferometric Technique," *Appl. Opt.* 26: 1603 (1987); D. Huang, J. Wang, C.P. Lin, C.A. Puliafito and J.G. Fujimoto, "Micron-resolution Ranging of Cornea Anterior Chamber by Optical Reflectometry," *Lasers Surg. Med.* 11: 419 (1991); E.A. Swanson, D. Huang, M.R. Hee, J.G. Fujimoto, C.P. Lin, and C.A. Puliafito, "High-speed Optical Coherence Domain Reflectometry," *Opt. Lett.* 17: 151 (1992).

⁵³ D. Huang, E.A. Swanson, C.P. Lin, J.S. Schuman, W.G. Stinson, W. Chang, M.R. Hee, T. Flotte, K. Gregory, C.A. Puliafito and J.G. Fujimoto, "Optical Coherence Tomography," *Sci.* 254: 1178 (1991).

year. These tomographs have far higher resolution than other non-invasive imaging techniques and, to our knowledge, are the first images that actually allow one to delineate retinal layers *in vivo*.

In OCT images of the foveal region of the retina, the retina layers were identifiable from the previously known anatomy. The backscattering is very weak from the foveolar region, where the retina consists mainly of the photoreceptor layer and the Henle fiber layer. This contrasts with the surrounding region, where the brighter nerve fiber layer and the plexiform layers of the retina appear to gradually increase in thickness further from the center of the fovea. Other posterior eye structures such as the vitreous medium, the choroid, and the sclera, are also clearly identifiable. The ability of OCT to image these retinal structural details demonstrates its potential in the diagnosis and quantitative monitoring of retinal diseases such as macular degeneration, macular hole, and macular edema.

In OCT images of the retina around the optic nerve head, the retinal nerve fiber layer (RNFL), appear as a thick, highly scattering layer in the inner retina that contrasts with the subjacent retinal layers. Accurate RNFL thickness measurements are relevant to the diagnosis and management of glaucoma.⁵⁴ Glaucoma, where elevated intraocular pressure produces retinal nerve fiber atrophy, is a leading cause of blindness. The diagnosis of glaucoma is a difficult clinical problem. Intraocular pressure measurements do not reliably predict disease progression. Other diagnostic parameters such as visual field defects and optic disc cupping are detectable only after significant (~ 50 %) loss in the retinal nerve fiber layer (RNFL) has already occurred. Because both medical and surgical treatments for glaucoma can cause substantial adverse effects, there is a great deal of uncertainty and dilemma in making early treatment decisions. Early detection of optic nerve fiber atrophy with OCT could greatly reduce this uncertainty. Further trials in glaucoma patients and glaucoma animal models will determine whether OCT measurements can

provide early criteria by which to make treatment decisions in glaucoma patients.

1.15.3 Transillumination Imaging

Optical transillumination imaging of tissue offers the potential of a non-invasive diagnostic with non-ionizing radiation and the possibility of using spectroscopic properties to distinguish tissue pathology and probe metabolic function. Optical transillumination is analogous to x-ray imaging; however, optical radiation is relatively safe and can provide tissue contrast based on spectroscopic differences. Unfortunately, absorption and multiple light scattering severely limit optical image resolution in dense or thick tissue specimens. Recently, there has been interest in transillumination as an alternative or supplement to mammography for early breast tumor detection. Optical radiation may be capable of distinguishing malignant tissue without the hazards of x-ray imaging based on the optical properties of the surrounding tumor neovascularization.

Several time or spatially resolved optical imaging techniques have been proposed which reduce image degradation due to scattering by discriminating against the spatial or temporal characteristics of scattered light. Spatially resolved methods, based on the confocal imaging principle, require detected light to have a certain directionality or spatial phase coherence.⁵⁵ Time resolved techniques rely on the fact that multiply scattered light travels a longer path through tissue compared to unscattered light, and therefore may be rejected temporally. A short pulse propagating through a scattering media will be severely lengthened due to scattering, but a shadowgram of hidden objects may be reconstructed by temporally isolating the earliest arriving, least scattered component of the transmitted light from the later-arriving diffuse, or multiply scattered light. Any of a number of different incoherent or coherent imaging techniques may be used to time-gate early arriving light, including streak camera imaging,⁵⁶ photon

⁵⁴ H.A. Quigley and E.M. Addicks, "Quantitative Studies of Retinal Nerve Fiber Layer Defects," *Arch. Ophthalmol.* 100: 807 (1982).

⁵⁵ M. Toida, M. Kondo, T. Ichimura, and H. Inaba, "Two-Dimensional Coherent Detection Imaging in Multiple Scattering Media Based on the Directional Resolution Capability of the Optical Heterodyne Method," *Appl. Phys. B* 52: 391-394 (1991); D.S. Dilworth, E.N. Leith, and J.L. Lopez, "Imaging Absorbing Structures Within Thick Diffusing Media," *Appl. Opt.* 29: 691-698 (1990).

⁵⁶ K.M. Yoo, B.B. Das, and R.R. Alfano, "Imaging of a Translucent Object Hidden in a Highly Scattering Medium from the Early Portion of the Diffuse Component of a Transmitted Ultrafast Laser Pulse," *Opt. Lett.* 17: 958-960 (1992); J.C. Hebden, R.A. Kruger, and K.S. Wong, "Time Resolved Imaging Through a Highly Scattering Medium," *Appl. Opt.* 30: 788-794 (1991).

counting,⁵⁷ nonlinear gating,⁵⁸ and time-resolved interferometry⁵⁹ or holography.⁶⁰

In collaboration with MIT Lincoln Laboratory, we have developed a new technique for time-gated imaging through turbid media based on optical coherence tomography (OCT).⁶¹ In femtosecond transillumination optical coherence tomography, femtosecond pulses and coherent heterodyne detection time-resolve transmitted light based on its coherence properties.⁶² The operation principle of transillumination OCT is analogous to reflection-mode OCT; however, instead of depth resolving reflected light, the coherence properties of transmitted light are used to transversely resolve objects otherwise obscured by multiple scattering. Short pulses (50 to 400 fs) from a Kerr-lens modelocked Ti:Al₂O₃ laser are used in conjunction with a modified fiber-optic Mach-Zehnder interferometer. A fiber beamsplitter divides the incident pulses into a reference delay path and a sample transmission path. Light retroreflected from the variable delay reference mirror is recombined with temporally broadened light transmitted through the sample at another fiber splitter and is incident on a photodetector. Interference signal is created at the detector only for the coherent component of the transmitted pulse which temporally overlaps the reference pulse. Using dual balanced detectors to reduce excess laser noise in conjunction with lock-in amplification, we achieve the quantum shot noise detection limit. The transillumination system can resolve transmitted light as weak as 5 femtowatts, which is 10^{-13} of the incident optical power of 50 mW (a 130 dB dynamic range).

To study the basic characteristics of coherent photon migration through scattering media, we have used transillumination OCT to temporally profile the coherent constituent of the on-axis scattered pulse propagating through suspensions of uniform scattering microspheres. Similar to earlier studies of incoherent migration,⁶³ the coherent transmitted light consists of an unscattered ballistic component, and a later arriving, temporally broadened diffuse component. The arrival time and temporal profile of these components have been investigated as functions of scattering anisotropy and microsphere concentration, and have been qualitatively correlated with predictions from Mie scattering theory. Compared to previous studies of incoherent photon migration, the coherent diffuse component displays a reduced temporal extent due to loss of phase coherence with multiple scattering. The ballistic peak power attenuates exponentially as the number of scattering mean-free-paths (MFPs) contained in the scattering medium, or equivalent sample thickness. The transmitted diffuse power dominates ballistic light for sample thicker than about 25 scattering MFPs, fairly independent of scattering anisotropy. The diffuse power also attenuates about a factor of 10 more slowly in the exponential with increasing sample thickness.

Time-gated imaging of hidden objects embedded in scattering media is achieved by fixing the reference arm path length and raster scanning the sample to create a two-dimensional image of interference signal magnitude. High resolution (100 μm) images of an Air Force resolution chart placed in the center of a 1 μm diameter microsphere suspension 27 scattering MFPs thick have been obtained by using

⁵⁷ S. Andersson-Engels, R. Berg, S. Svanberg, and O. Jarlman, "Time-resolved Transillumination for Medical Diagnostics," *Opt. Lett.* 15: 1179-1181 (1990).

⁵⁸ L. Wang, P.P. Ho, C. Liu, G. Zhang, and R.R. Alfano, "Ballistic 2-D Imaging Through Scattering Walls Using an Ultrafast Optical Kerr Gate," *Sci.* 253: 769-771 (1991); K.M. Yoo, Q. Xing, and R.R. Alfano, "Imaging Objects Hidden in Highly Scattering Media Using Femtosecond Second-harmonic-generation Cross-correlation Time Gating," *Opt. Lett.* 16: 1019-1021 (1991); M.D. Duncan, R. Mahon, L.L. Tankersley, and J. Reintjes, "Time-gated Imaging Through Scattering Media Using Stimulated Raman Amplification," *Opt. Lett.* 16: 1868-1870 (1991).

⁵⁹ D. Huang, E.A. Swanson, C.P. Lin, J.S. Schuman, W.G. Stinson, W. Chang, M.R. Hee, T. Flotte, K. Gregory, C.A. Puliafito and J.G. Fujimoto, "Optical Coherence Tomography," *Sci.* 254: 1178 (1991).

⁶⁰ K.G. Spears, J. Serafin, N.H. Abramson, X. Zhu, and H. Bjelkhagen, "Chrono-Coherent Imaging for Medicine," *IEEE Trans. Biomed. Engr.* 36: 1210-1221 (1989); E. Leith, H. Chen, Y. Chen, D. Dilworth, J. Lopez, R. Masri, J. Rudd, and J. Valdmann, "Electronic Holography and Speckle Methods for Imaging Through Tissue Using Femtosecond Gated Pulses," *Appl. Opt.* 30: 4204-4210 (1991).

⁶¹ D. Huang, E.A. Swanson, C.P. Lin, J.S. Schuman, W.G. Stinson, W. Chang, M.R. Hee, T. Flotte, K. Gregory, C.A. Puliafito, and J.G. Fujimoto, "Optical Coherence Tomography," *Sci.* 254: 1178 (1991).

⁶² M.R. Hee, J.A. Izatt, J.M. Jacobson, E.A. Swanson, and J.G. Fujimoto, "Femtosecond Transillumination Optical Coherence Tomography," *Opt. Lett.*, forthcoming.

⁶³ Y. Kuga, A. Ishimaru, and A.P. Bruckner, "Experiments on Picosecond Pulse Propagation in a Diffuse Medium," *J. Opt. Soc. Am.* 73: 1812-1815 (1983); K.M. Yoo and R.R. Alfano, "Time-resolved Coherent and Incoherent Components of Forward Light Scattering in Random Media," *Opt. Lett.* 15: 320-322 (1990).

transillumination OCT to coherence-gate only the early arriving ballistic component of the transmitted light. Since ballistic light is unscattered, the spatial resolution of ballistic gated imaging is theoretically diffraction limited. However, imaging with ballistic light is virtually impossible through thick specimens due to the exponential attenuation of the ballistic component with sample thickness. We have derived a fundamental ballistic imaging thickness limit for any optical imaging technique based on quantum noise considerations and optical tissue damage thresholds. For parameters required for early breast tumor detection, this thickness limit evaluates to approximately 4 mm breast tissue.

The combined temporal and directional rejection of scattered light with transillumination OCT allows a comparison of time and spatially resolved imaging techniques. A purely spatial discrimination technique, such as confocal imaging, will be sensitive to the transillumination OCT interference signal integrated over all coherence-gate delays. Studies of time-resolved photon migration with confocal imaging show that ballistic imaging is impossible for spatially resolved methods because a substantial amount of late arriving diffuse light may be coherent at the detector when the sample is thicker than about 20 scattering MFPs.

Since ballistic imaging is restricted to relatively thin samples, medically relevant applications require gating the early arriving portion of the diffuse transmitted light. Spatial resolution is sacrificed for the wider coherence-gate delays necessary to image through thick samples. We characterized the degradation in resolution versus coherent photon arrival time for various sized opaque bars placed in 25 scattering MFPs of 1 μm diameter microspheres. The spatial resolution for a given transit delay was found to be bounded above by a simple square-root limit, obtained from geometric considerations, and below by an empirically derived linear limit. Consideration of these limits enabled us to design a transillumination OCT system capable of resolving a 1 mm width resolution chart embedded in 1.5 cm chicken breast *in vitro*. To our knowledge, this image represents the thickest biological sample with similar scattering characteristics through which submillimeter image resolution has been obtained.

The fundamental resolution and thickness limits we have identified in these basic studies should prove useful in the design of future time-domain imaging techniques for biomedical applications.

1.16 Observation of Gain in Ni-like Nb

Sponsors

Bose Corporation
Lawrence Livermore National Laboratories
Subcontract B160530
U.S. Department of Energy
Grant DE-FG02-89-ER14012

Project Staff

Professor Peter L. Hagelstein, Dr. Santanu Basu, James G. Goodberlet, Sumanth Kaushik, Martin H. Muendel

During the past four years, we have assembled an experimental facility suitable for testing various novel and low power approaches to EUV and soft x-ray lasers.⁶⁴ Our facility consists of a Nd:YLF oscillator and Nd:glass pre-amplifier (currently being upgraded to a Nd:YLF pre-amplifier), a zig-zag slab power amplifier, a 200-liter vacuum chamber with an internal target positioning and alignment system, and two EUV spectrometers. Various components of our facility have been described in previous annual *RLE Progress Reports*.

Last spring we began taking data, searching for the laser line in Ni-like Mo. The principal diagnostic for this work is a nearly stigmatic spectrometer which is based on a near-normal incidence spherical grating which images onto the cathode of a streak camera as illustrated below in figure 1. The grating was loaned by the National Research Laboratory (NRL); the streak camera was loaned by Lawrence Livermore National Laboratories.

The principal laser lines in mid-Z Ni-like ions have not been previously identified, and as a result we have relied on theory to a significant degree to guide our search. The computation of accurate line positions for the $3d^9 4d^1 S - 3d^9 4p^1 P$ transition is hindered by strong correlation effects due to mixing between the upper laser state and the $4d^{10} S$ ground state. For example, the results of a multi-configuration Hartree-Fock calculation gives the wavelength of the line in Ni-like Mo to be near 172 Å; the correlation corrections bring the wavelength near 190 Å, a correction of about ten percent. We first corrected the wavelength using data from Eu obtained by Lawrence Livermore National Laboratories, which led to an interpolated wavelength of 194

⁶⁴ P.L. Hagelstein, "Short Wavelength Lasers: Something Old Something New," *Proceedings of the OSA meeting on Short Wavelength Coherent Radiation: Generation and Applications*, ed. R.W. Falcone and J. Kirz, 1988.

Å. This value was updated using a low-Z measurement in As to provide a further correction to 191 Å. In the spring of 1992, a measurement of the analog line in Ni-like Sn was reported by the NRL at 119.1 Å; we were able to use this value to improve our prediction to 188.8 Å for Mo. When we finally found the laser line in Ni-like Mo, it appeared at 189.2 Å, as shown in figure 2.

The efficiency of the NRL grating becomes quite low at wavelengths below 200 Å, and this poor efficiency hindered our experiments; many shots would be required to find the nearby strong Cu-like lines, and the laser line would appear after only the most heroic efforts. As a result, we decided to shift the primary focus of our experiments to a study of gain in Ni-like Nb, which was predicted to occur at

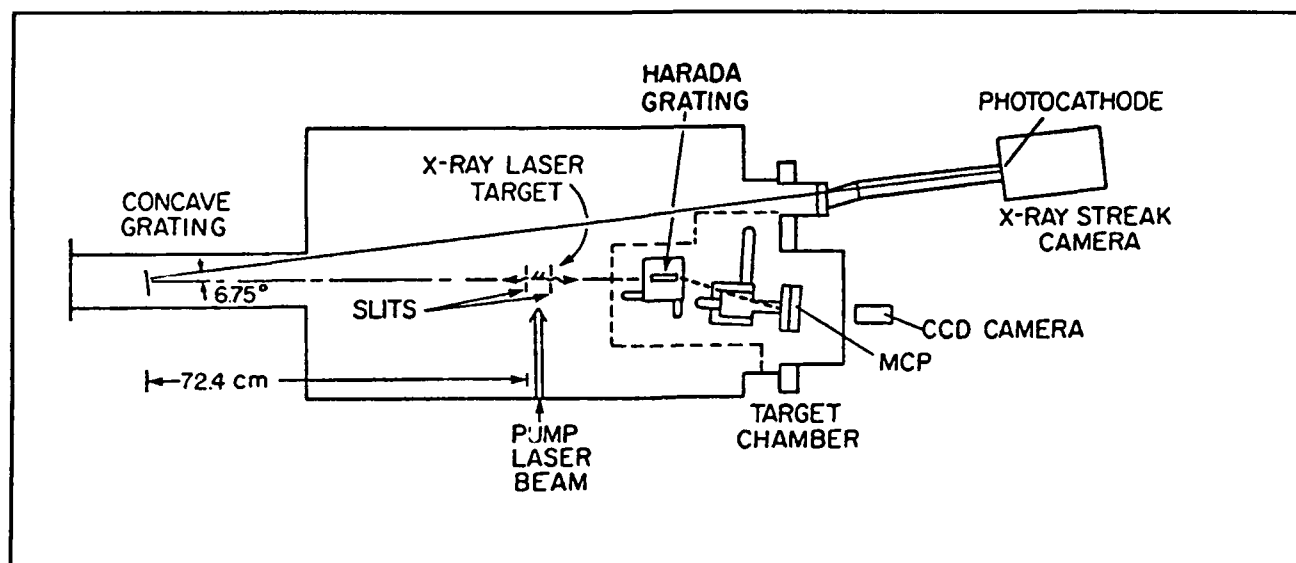


Figure 1. Schematic of the x-ray laser target chamber and spectrometers.

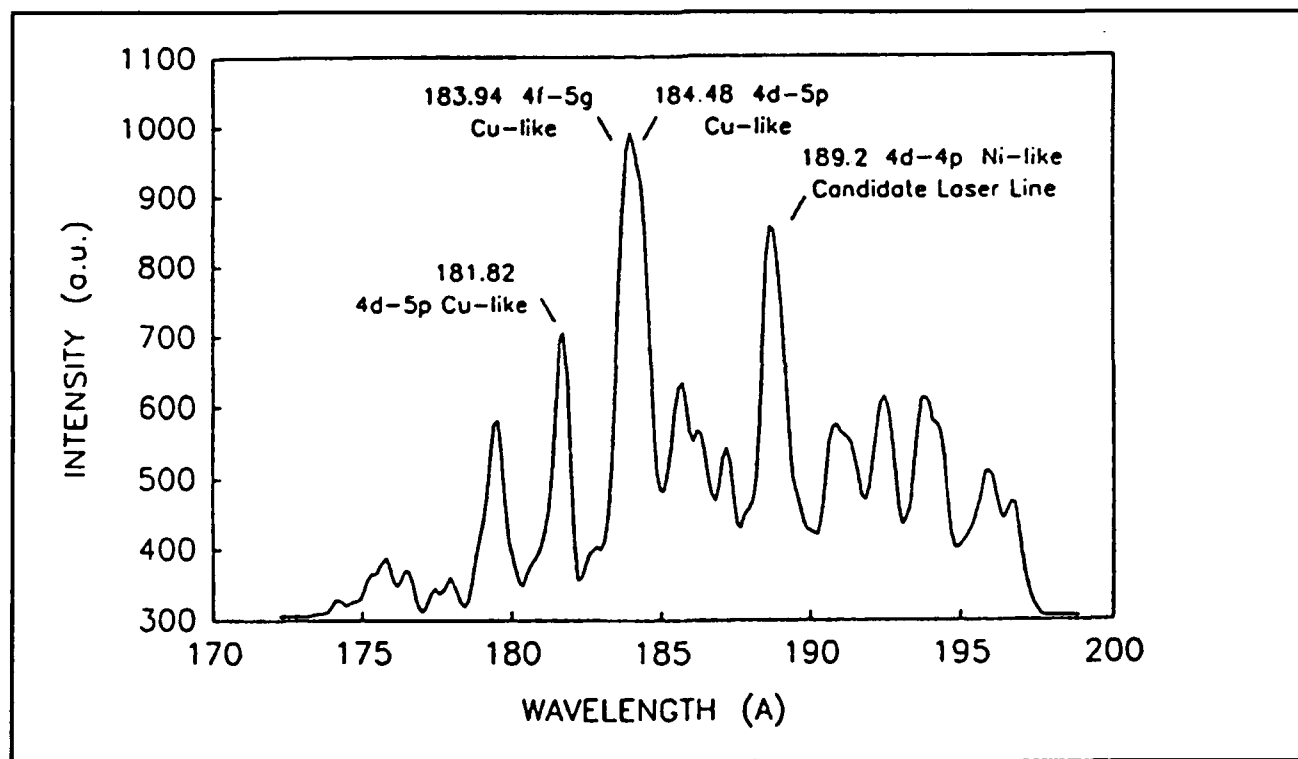


Figure 2. Spectrum of Mo in the vicinity of the Ni-like Mo $3d^4d^1S - 3d^4p^1P$ laser line.

203.7 Å. The transition in Nb was readily found, and it occurred at a wavelength of 204.2 Å.

The principal laser lines in Ni-like ions are quite weak if no gain is present. Since we observed the lines, and since we were able to make the candidate laser line dominate the spectrum locally, we knew that we had produced significant gain. This fact is important, because previously gain in Ni-like ions had only been produced at larger laser facilities in experiments involving kilojoules of incident laser pump energy; in our experiments we used less than 1 joule per pump pulse. Our result constituted a rather major breakthrough in the area of collisionally-driven EUV and soft x-ray lasers.

It remained to quantify the small signal laser gain. Experiments were conducted in which the beam was blocked to produce various plasma amplifier lengths, and the resulting measured intensity was plotted as a function of the amplifier length. The resulting curve shows exponentiation characteristic of laser gain, with a corresponding gain coefficient of about 3 cm^{-1} , as shown in figure 3. To date, our best data has been taken at a length of 9.1 mm, using about 1 joule per pulse of pump energy. The resulting spectra, shown in figure 4, is characteristic of between 3.0-3.5 total gain-lengths.

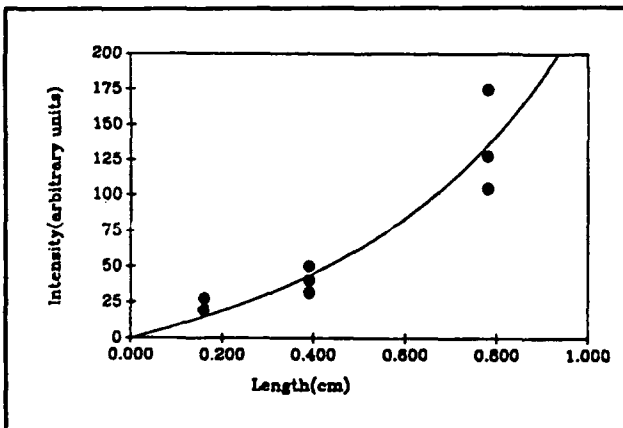


Figure 3. Intensity as a function of length for the Ni-like Nb $3d^4 4d^1 S - 3d^4 4p^1 P$ laser line.

Publications

Basu, S., et al, presented at LEOS, Boston, Massachusetts, November 1992.

Basu, S., P.L. Hagelstein, J.G. Goodberlet, M.H. Muendel, and S. Kaushik. "Amplification in Ni-like Nb at 204 Å Pumped by a Tabletop Laser." Submitted to *Appl. Phys. B*.

Hagelstein, P.L. "Short Wavelength Laser Studies at MIT: An Update." In *Solid State Lasers III*.

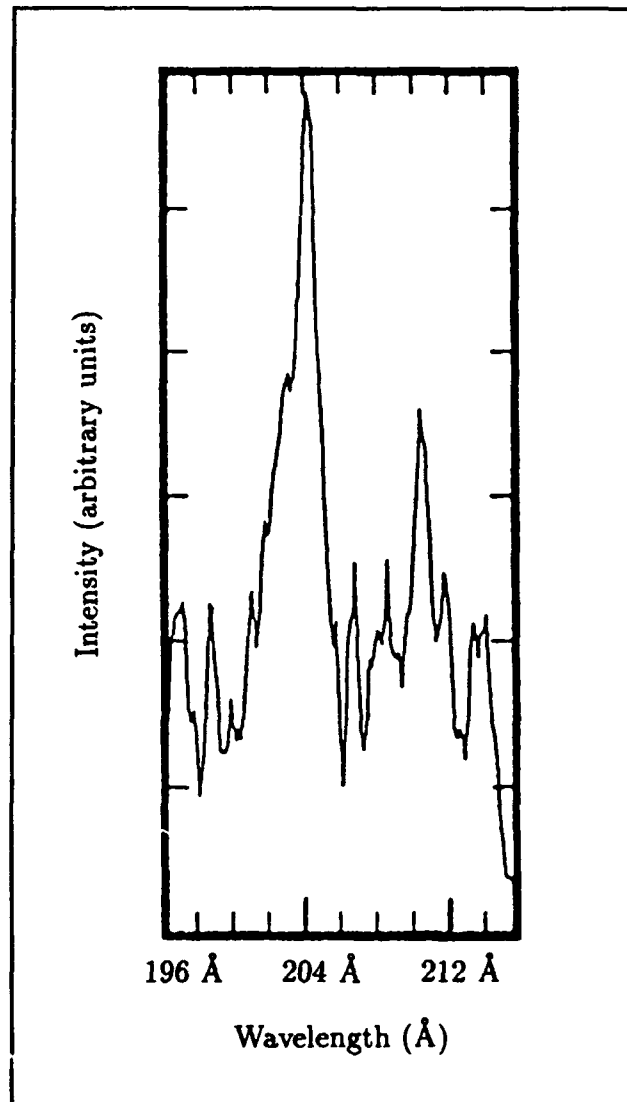


Figure 4. The $3d^4 4d^1 S - 3d^4 4p^1 P$ laser line (204.3 Å) in Ni-like Nb at 9.1 mm.

Ed. G.J. Quarles. *Proc. SPIE*. 1627: 340 (1992).

1.17 Pump Pulse Length

Project Staff

James G. Goodberlet, Professor Peter L. Hagelstein

We lost a Nd:glass preamplifier rod due to optical damage in November, and this loss has caused downtime. We took the opportunity to upgrade the preamplifier to a Nd:YLF rod, but before coming back up to run integral EUV laser experiments, we wanted to check the pulselength to make certain that the oscillator was not producing short pulses

spuriously. According to specifications, the Lumonics oscillator is supposed to provide 70 psec pulses; significantly shorter pulses at full energy could potentially damage the system.

To investigate this issue, autocorrelation of the electric field was accomplished using a Michelson interferometer with tilted mirrors to produce noncollinear interfering beams at the detector. If the pulses arrive at the detector coincidentally, they produce an interference pattern; additional path length in one arm produces a delay which can reduce or destroy the interference.

The initial results of the interferometry indicated that some of the pulses produced by the oscillator were as short as 25 psec. A weakness of an autocorrelator based on field rather than intensity is that it does not distinguish between a short pulse and a chirped pulse; inspection of the second harmonic signal from a KDP crystal indicated that indeed short pulses were present.

The large variation in pulse length was found to be due to an absence of pre-pulse signal before the oscillator Q-switched; the Lumonics laser was originally shipped and brought up at MIT with Lumonics staff to operate without pre-pulsing. We reset the oscillator to pre-pulse before Q-switching which stabilized the system.

Intensity autocorrelation was performed on the oscillator output, and the resulting pulses were determined to be near 60 psec; an etalon was acquired which results in 120 psec pulses.

In light of these results, some of the experimental difficulties which had been noted were likely due to the substantial pulse variability that was present in the system. A question now arises whether the best data that we obtained which showed gain occurred because the pump pulse was short, following from the increased intensity present. If so, this will limit how much more EUV laser total gain we will be able to obtain in the future. The dependence of gain on pulse length will be the focus of experiments to take place in the coming months.

1.18 End-pumped X-ray Lasers

Sponsors

Bose Corporation
Lawrence Livermore National Laboratories
Contract B160530
U.S. Department of Energy
Grant DE-FG02-89-ER14012

Project Staff

Professor Peter L. Hagelstein, Dr. Santanu Basu, Martin Muendel

Our research has recently led to a novel and very efficient EUV amplifier which is able to obtain 1 gain-length at 204 Å per 0.3 joules of incident 1μ pump energy; previous experimental work using collisional excitation schemes in this wavelength range has involved relative pumping efficiencies measured in gain-lengths per kilojoule.

The improvements which we have obtained are due primarily to: (1) the use of Ni-like ions, which has not previously been explored in this wavelength range; and (2) the use of a pulse train to create and then pump the plasma, which results in a very low ion temperature with an associated high gain due to a reduction in Doppler broadening.

The question arises as to whether further improvements might lead to still more gains in efficiency. For example, most of the laser energy which is absorbed goes ultimately into hydrodynamic kinetic energy or simply heats high density material far away from where gain is produced. Only about one part in 10^4 of the absorbed pump energy is ultimately utilized for the production of gain.

We have considered possible approaches towards improving the efficiency of EUV and soft x-ray laser amplifiers. If a pre-expanded low density (around 10^{19} electrons/cm³) plasma amplifier could be produced, then laser energy absorbed at low density would be used more efficiently to produce gain (the conversion efficiency of laser light to hydrodynamic energy in such a plasma is very poor). But such a scheme is ill-suited to current x-ray laser pumping arrangements since the absorption coefficient of a low density plasma is very low; less than one percent of the pump radiation would be absorbed in a 100 μ wide low density plasma pumped from the side under conditions where gain would be expected.

A potential solution to this problem is to modify the pumping geometry and to pump from the end instead of the side. Ideally, the pump radiation would in this case be absorbed where it does the most good, and the EUV beam builds up as it copropagates with the optical beam. The total number of gain lengths produced before the beam is completely absorbed will determine whether the approach is a good one.

The effectiveness of this approach can be seen by comparing the total number of EUV gain lengths gL with the number of inverse Bremsstrahlung absorption lengths $\kappa_{ib}L$. Interestingly enough, this ratio is maximized at low density. Normally, x-ray laser

designers seek to maximize the small signal gain in a laser design; in this case the total number of gain-lengths is maximized at a small signal gain which is less than the maximum possible small signal gain.

At an electron density which is low compared to the critical density ($N_e \ll N_c$), and also low compared to the characteristic density of the laser transition ($N_e \ll A_u / <\sigma v>_{uo}$), the ratio of the EUV gain to IR absorption becomes essentially independent of electron density. It can be shown that the low density limit is given by

$$\frac{gL}{\kappa_{ib}L} = \sigma_{SE} \frac{N_o}{N_e} \frac{<\sigma v>_{uo}}{A_u} \frac{4}{3} \sqrt{\frac{\pi}{2}} \frac{c^3 (mkT_e)^{3/2}}{Z^* e^6 \ln \Lambda \lambda^2} (1 - \zeta)$$

In this formula, σ_{SE} is the stimulated emission cross section, N_o is the ground state $3d^{10} 4s$ population, $<\sigma v>_{uo}$ is the rate coefficient for excitations from the ground state to the upper state, Z^* is the average ionization charge assuming a single element plasma, and $(1 - \zeta)$ is the ratio of the inversion density to the upper laser state density at low electron density. In the case of a low density Ni-like Mo EUV amplifier, this ratio can be larger than 100.

The implication of this result is that it should be possible in principle to obtain further very large improvements in the efficiency of EUV and soft x-ray lasers through the successful development of end-pumped lasers.

A primary technical drawback of such pumping schemes is that the pump laser will either refract or diffract out of the plasma amplifier before any significant fraction of the beam energy is absorbed in a real system unless some way can be found to keep the pump beam in the plasma. It is natural to consider a "soda-straw" type geometry; unfortunately, such a system by necessity brings high density plasma and the associated hydrodynamic losses in close proximity to the plasma amplifier.

We have therefore considered pumping schemes that involve segmented amplifiers wherein external optical components are used to help refocus the beam following transmission through individual segments. Examples of such schemes are shown in figures 5-7.

Publication

Hagelstein, P.L., S. Basu, and M. Muendel. "XRL Research at MIT: Recent Progress." *Proceedings of the Third International Conference on X-ray Lasers*, Schliersee, Germany, May 1992.

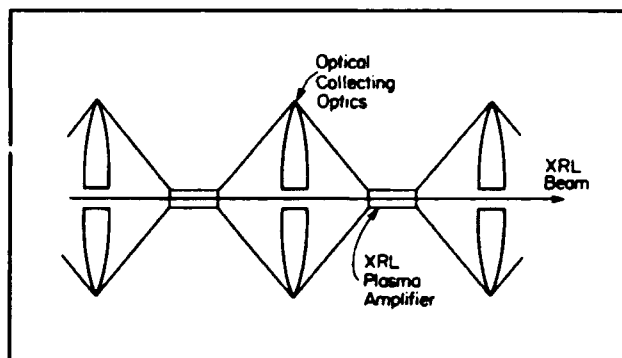


Figure 5. Schematic of a simple stable end-pumped laser.

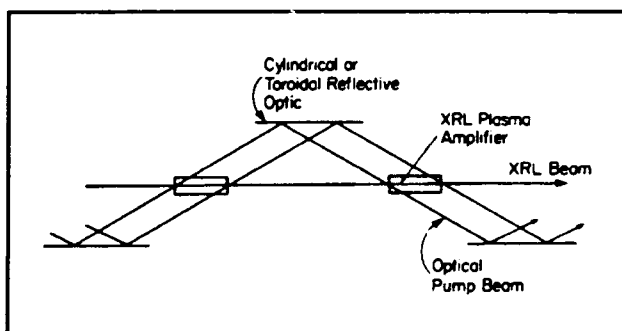


Figure 6. Schematic of a zig-zag end-pumped laser.

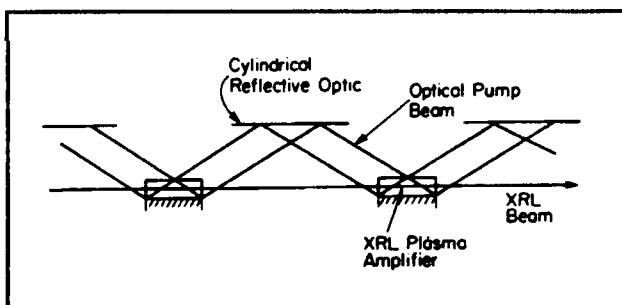


Figure 7. Schematic of solid surface targets pumped in sequence.

1.19 The Kinetics and Hydrodynamics of Laser-Generated Plasmas

Sponsor

MIT Lincoln Laboratory

Project Staff

Professor Peter L. Hagelstein, Ann W. Morgenthaler, Janet L. Pan

Laser-produced plasmas which are ablated from the surface of a solid are currently being used for x-ray laser amplifiers in a number of laboratories around

the world; our group at MIT has been focusing on the use of such plasmas primarily for collisional (Ni-like) x-ray lasers as described elsewhere in this report.

The success of the collisional scheme depends strongly on achieving a high electron temperature in the low-density coronal region of the plasma. The laser light is absorbed primarily near the critical surface (at 10^{21} electrons/cm³ for 1 μ m pump radiation), where the electron temperature is determined by a balance between inverse Bremsstrahlung absorption and flux-limited thermal conduction in other parts of the plasma. The thermal conductivity is a strongly increasing function of the electron temperature, and it is expected that once a high temperature is established near the critical surface, heating of the low density corona by conduction will quickly follow.

A basic understanding of electron thermal conduction in the plasma is therefore critical for making a quantitative prediction of the electron temperature as a function of the pump laser intensity, especially in regimes where significant flux limiting occurs. This has motivated our interest in the basic physics of electron transport in laser-produced plasmas. The approach which we have explored involves taking moments of the full, collisional Boltzmann equation, with Coulombic collisions described by the Landau operator as outlined in last year's *RLE Progress Report*. The treatment of collisions in the moment method is technically complicated, and we have recently reported a rather general solution to this problem that is amenable to numerical modeling.⁶⁵ Exact analytic coupling coefficients describing the interaction between identical particles during a collision are a central result of this paper, and this work has been extended to describe arbitrary collisions between unlike particles (e.g., electron-ion collisions) which are critical for describing plasma interactions.

The end result of the moment method is a set of coupled equations describing average plasma quantities such as density, mean velocity, temperature, and heat flux. The simplest useful set of such coupled equations are those describing electrons and ions in a 1 1/2 dimensional model (1-D space and 2-D velocity). The time-evolution equations for the lowest order moments are mass continuity equations:

$$\frac{\partial}{\partial t} N_e + \frac{\partial}{\partial z} (N_e v_e) = 0 \quad (1)$$

$$\frac{\partial}{\partial t} N_i + \frac{\partial}{\partial z} (N_i v_i) = 0 \quad (2)$$

where N_e and N_i are electron and ion densities, and v_e and v_i are average \hat{z} -directed electron and ion velocities. The first order moments give rise to momentum equations

$$\begin{aligned} mN_e \frac{\partial v_e}{\partial t} + mN_e v_e \frac{\partial v_e}{\partial z} \\ + eEN_e + \frac{\partial(N_e T_e)}{\partial z} \\ = - \frac{4\sqrt{2\pi} \ln \Lambda Z^2 e^4 N_e N_i m^{1/2}}{3T_e^{3/2}} (v_e - v_i) \end{aligned} \quad (3)$$

$$\begin{aligned} MN_i \frac{\partial v_i}{\partial t} + MN_i v_i \frac{\partial v_i}{\partial z} \\ - ZeEN_i + \frac{\partial(N_i T_i)}{\partial z} \\ = + \frac{4\sqrt{2\pi} \ln \Lambda Z^2 e^4 N_e N_i m^{1/2}}{3T_e^{3/2}} (v_e - v_i) \end{aligned} \quad (4)$$

Here, T_e and T_i are electron and ion temperatures, m and M are electron and ion masses, Z is the average ionic charge of the plasma, and $\ln \Lambda$ is the electron-ion Coulomb logarithm. A final set of equations describes the temperature evolution of this plasma:

$$\begin{aligned} 3N_e \frac{\partial T_e}{\partial t} + 3N_e v_e \frac{\partial T_e}{\partial z} \\ + 2N_e T_e \frac{\partial v_e}{\partial z} + \kappa \frac{\partial^2 T_e}{\partial z^2} \\ = - \frac{8\sqrt{2\pi} \ln \Lambda Z^2 e^4 N_e N_i m^{1/2}}{MT_e^{3/2}} (T_e - T_i) \end{aligned} \quad (5)$$

$$\begin{aligned} 3N_i \frac{\partial T_i}{\partial t} + 3N_i v_i \frac{\partial T_i}{\partial z} + 2N_i T_i \frac{\partial v_i}{\partial z} \\ = + \frac{8\sqrt{2\pi} \ln \Lambda Z^2 e^4 N_e N_i m^{1/2}}{MT_e^{3/2}} (T_e - T_i) \end{aligned} \quad (6)$$

⁶⁵ A.W. Morgenthaler and P.L. Hagelstein, "Kinetic Theory of a Non-Equilibrium Plasma: Evaluation of the Vectorized Collisional Boltzmann Equation," submitted to *Phys. Fluids B*.

where the linearized thermal conductivity κ can be derived to arbitrary accuracy from the higher-order moment equations for this simplest plasma. The heat conduction term in (5) is the place where the higher order moments couple to the temperature equation, and by considering sufficient numbers of higher-order moments, thermal flux limitation should appear quite directly.

It appears that the plasma hydrodynamic equations have many similarities with the equations governing drift and diffusion in semi-conductors; therefore, we will attempt to numerically solve the moment equations with efficient techniques such as Gummel's method. The equations governing electron and ion motion are not typically solved in this coupled form, and our goal is to produce numerical models of a laser-generated plasma which may be useful design tools for further developments of the x-ray laser. We are also interested in quasi-analytic models of plasma heating by intense electric fields, which can be found by considering fast and slow variations of all field quantities. A simple model describing the coupling of electromagnetic fields into the plasma is currently under investigation.

Because the "machinery" developed for understanding laser plasma kinetics is sufficiently general, we should be able to apply our techniques to other outstanding problems in plasma physics.

1.20 An Analytical Solution of the 2D Exciton-Phonon Matrix Element

Project Staff

Sumanth Kaushik, Professor Peter L. Hagelstein

Work has been on the development of analytical and numerical methods for the *ab initio* absorption lineshapes in two dimensional systems. We have focused our attention of multiple quantum well structures (MQW) for which considerable amount of experimental data exist in the literature. The in-plane confinement of the electron and hole due to the quantum wells enable these devices, even at room temperatures, to exhibit pronounced excitonic effects which can be strongly modified by optical and electro-optical modulation.

An important parameter that characterizes the strength of excitonic effects is the absorption linewidth. The sharper the linewidth, the more pronounced are the excitonic effects. At room temperatures, the dominant contribution to the linewidth is the interaction of the quasi two-dimensional excitons with optical phonons. Various theoretical models exist in the field to calculate the phonon

contribution to the absorption linewidth. However, in all these models, a fundamental quantity needed in the computation is the photon/phonon matrix element

$$\langle \lambda, m | \exp(i\mathbf{q} \cdot \mathbf{r}) | 0, 0 \rangle \sim 1$$

between the ground state and an arbitrary excited state of the exciton.

Often, for convenience, the exciton is modeled as a two-dimensional hydrogen atom where the parameters such as the Bohr radius and the binding energy are adjusted so as to reproduce more exact calculations. In the limit where the initial and final states are 2D hydrogen states, the above matrix element can be evaluated analytically. However, in evaluating this matrix element, one encounters an integral transform of the form

$$I = \int_0^\infty x(bx)^v \exp(-px) {}_1F_1(a, 2v+1, bx) J_v(\gamma x) dx$$

where a, b, p are complex and v, γ are real. In the particular case of the matrix element the parameters are defined to be $b=1/2\lambda$, $v=|m|$ and $p=1+1/4\lambda$ with m being an integer and λ being either real (for bound-bound transitions) or complex (for bound-free transitions).

We have managed to formulate an analytical solution to this matrix element which is written in the form

$$I = (\pm) \Gamma(2v+1) \left(\frac{z^3}{p^2} \right) \xi^{-a+v-1} \times$$

$$\left[(2v+1-2a) \xi P_{-a+v}^{-v}(p) - a \left(2 - \frac{b}{p} \right) P_{-a+v-1}^{-v}(p) \right]$$

where the a, b, p are arbitrary and complex and v, γ are arbitrary and real and the parameters. This matrix element, in addition to enabling rapid computation of lineshape, enables one to develop very useful and simple scaling relations for the linewidth in term of phonon coupling and well parameters.

Publications

Kaushik, S., and P.L. Hagelstein. "A Semi-empirical Line Shape Model of GaAs MQW Structures." Submitted to *IEEE J. Quantum Electron.*

Kaushik, S. "An Analytical Solution to the 2-D Exciton-Phonon Matrix Element." Submitted to *J. Math. Phys.*

1.21 Quantum Dot Diode Lasers

Sponsors

MIT Lincoln Laboratory
Rockwell International Corporation

Project Staff

Janet L. Pan

Lasers in the thermal infrared (2 to 10 micrometer) wavelength regime are useful for spectroscopy, medicine, and fiber optics. For medicinal purposes, these lasers take advantage of the large absorption of water in various windows in the thermal infrared. For spectroscopy, these lasers are useful because many substances (such as organic molecules or pollutants in the air) have characteristic vibrational frequencies in the thermal infrared.

We are interested in quantum dots for improving semiconductor lasers in the thermal infrared. In this wavelength regime, the Auger rate limits the performance of conventional semiconductor lasers,⁶⁶ such as the lead salt semiconductor lasers, to low temperatures. Quantum dots, with their discrete energy levels, could greatly reduce the Auger rate. We have calculated interband Auger processes in quantum dots,⁶⁷ and have shown that the use of large potential barriers surrounding quantum dots could greatly reduce the Auger rates in quantum dot lasers over those in conventional semiconductor lasers.

Figure 8 shows the temperature dependence of the CCCV and CVVV intraband Auger lifetimes for a 150 Å radius InSb quantum dot (with a bandgap at 4.8 micrometers (258 meV)) surrounded by CdTe barriers. We found that enough Auger processes were excluded by the large CdTe potential barriers so that our InSb quantum dot room temperature Auger lifetime was about 135 nanoseconds. This is to be compared with the calculated Auger rates for other semiconductors with band gaps in the infrared. For GaSb with a bandgap of 670 meV (1.8 micrometers), the Auger lifetime at 77 K for a carrier concentration in the bulk of $\frac{2}{\frac{4}{3}\pi R^3}$ was

calculated⁶⁸ to be about 0.01 nanoseconds and measured⁶⁸ to be about 1 nanosecond for our volume of $\frac{4}{3}\pi(150\text{\AA})^3$. A 4.5 nanosecond Auger lifetime⁶⁹ was found at liquid nitrogen temperature for a conventional 10 μm Pb_{0.82}Sn_{0.18}Te laser, whose active region injected carrier concentration is $0.8 \times 10^{17}\text{cm}^{-3}$ or our volume of $\frac{4}{3}\pi(150\text{\AA})^3$. Room temperature bulk InSb seems to have calculated Auger lifetimes between 0.1 and 1 nanosecond, depending⁷⁰ on how the atomic orbitals and nonparabolic energy bands are calculated.

We are now studying processes affecting the dynamics of bound carriers in quantum dots. We have estimated rates of collisions of quantum dot carriers via the Coulomb interaction and compared these rates to the competing interband and intraband radiative rates and phonon absorption/emission rates in quantum dots.

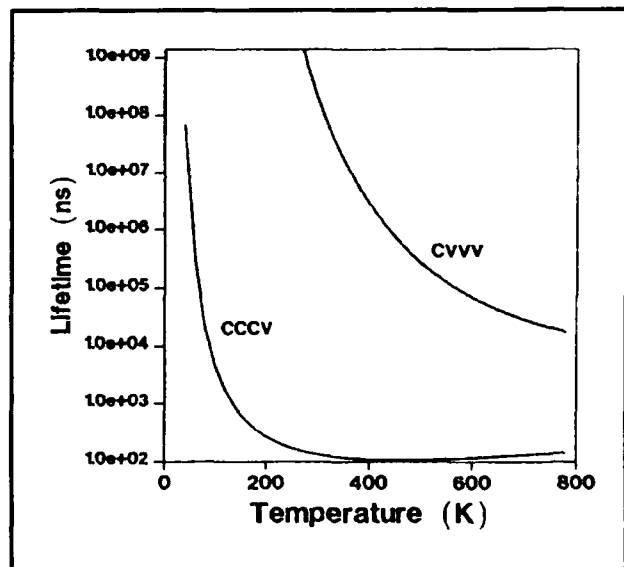


Figure 8. The temperature dependence of the CCCV and CVVV Auger lifetimes for a 150 Å radius InSb quantum dot surrounded by CdTe barriers. This is to be compared with the calculated Auger rates for other semiconductors with band gaps in the infrared.

⁶⁶ G.P. Agrawal and N.K. Dutta, *Long Wavelength Semiconductor Lasers*, (New York: Van Nostrand Reinhold Co., 1986).

⁶⁷ J.L. Pan, *Phys. Rev. B* 46: 3977 (1992).

⁶⁸ A. Haug, D. Kerkhoff, and W. Lochmann, *Phys. Stat. Solid B* 89: 357 (1978).

⁶⁹ R. Rosman and A. Katzir, *IEEE J. Quantum Electron.* QE-18: 814 (1982).

⁷⁰ H. Bruhns and H. Kruse, *Phys. Stat. Solid B* 97: 125 (1980).

We are interested in materials and fabrication methods necessary for realistic devices. We have suggested various possibilities, such as InSb dots in CdTe barriers, in a recent paper.⁷¹ Our long term goal is to fabricate and experimentally study quantum dots for use in lasers in the thermal infrared.

1.22 Coherent Fusion Theory

Project Staff

Professor Peter L. Hagestein, Irfan U. Chaudhary, Akikazu Hashimoto, Sumanth Kaushik

Three and a half years have now passed since the announcement of the observation of anomalies in deuterated metals that was made in March 1989. Excess heat was reported by Pons and Fleischmann, and evidence for low level neutron emission was presented by Jones. Efforts to reproduce the effects were largely unsuccessful in 1989, and the scientific community has generally rejected these claims.

Pons and Fleischmann have continued their experiments, and their current claims are far more dramatic than those made in 1989. The initial 1989 reports described a relatively weak heat effect that was observed with relatively poor reproducibility; the claims of 1992 describe a very dominant effect that is completely reproducible, although still not understood.

At the Third International Cold Fusion Conference in Nagoya, Japan, Pons and Fleischmann described reproducible observations of extreme excess heat production in electrolysis experiments,

with a specific power generation rate of more than 3kW/cm^3 of Pd cathode.⁷² This high level of heat production is sufficient to boil away the electrolyte (50 cc) completely in about 10 minutes. Energy production was monitored with their open-cell calorimeter, and gave a result that was consistent with an energy balance determination by multiplying the heat of vaporization of the electrolyte (about 41 kJ per mole) times the number of moles of electrolyte (2.5 moles), yielding about 100 kJ of energy output. The electrical energy input during this period was about 20 kJ, resulting in a power gain of about 4. The anomalous excess energy production during this period was close to 200 eV per atom of Pd.

We have continued to explore⁷³ theoretical mechanisms which could account for the heat anomaly, and for other anomalies (including tritium and ^4He production, and also gamma, neutron and fast ion emission) which continue to be reported by numerous laboratories.

We have considered several different types of possible nuclear reaction mechanism; fusion as a mechanism appears to be unlikely since there does not appear to be any practical way to get deuterium nuclei close enough to fuse at room temperature in a metal lattice. We have therefore proposed a new and speculative type of nuclear reaction involving the transfer of neutrons from "donor" nuclei to "acceptor" nuclei.

During the past year we have made progress towards understanding reactions in which a neutron is transferred from deuterium and then captured incoherently by a heavy metal nucleus, with no energy exchange with the lattice.⁷⁴

⁷¹ J.L. Pan, *Phys. Rev. B* 46: 3977 (1992).

⁷² M. Fleischmann and S. Pons, "Calorimetry of the Pd-D₂O system: from Simplicity via Complications to Simplicity," *Proceedings of the Third Annual International Cold Fusion Conference*, Nagoya, Japan, November 1992.

⁷³ P.L. Hagestein, "Coherent and Semi-Coherent Neutron Transfer Reactions I: The Interaction Hamiltonian," *Fusion Tech.* 22: 172 (1992); P.L. Hagestein, "Coherent and Semi-Coherent Neutron Transfer Reactions II: Transition Operators," *Fusion Tech.* forthcoming; P.L. Hagestein, "Coherent and Semi-Coherent Neutron Transfer Reactions III: Phonon Generation," *Fusion Tech.* 23: 353 (1993); P.L. Hagestein, "Coherent and Semi-Coherent Neutron Transfer Reactions IV: Two-step Reactions and Virtual Neutrons," submitted to *Fusion Tech.*; P.L. Hagestein, "Coherent and Semi-Coherent Neutron Transfer Reactions," *Proceedings of the Third Annual International Cold Fusion Conference*, Nagoya, Japan, November 1992.

⁷⁴ P.L. Hagestein, "Coherent and Semi-Coherent Neutron Transfer Reactions IV: Two-step Reactions and Virtual Neutrons," submitted to *Fusion Tech.*; P.L. Hagestein, "Coherent and Semi-Coherent Neutron Transfer Reactions," *Proceedings of the Third Annual International Cold Fusion Conference*, Nagoya, Japan, November 1992.

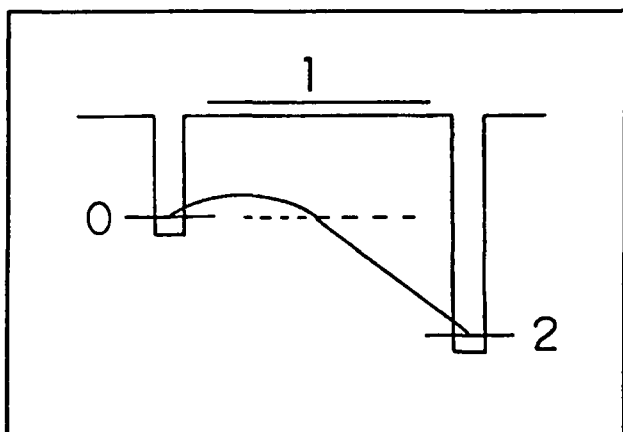


Figure 9. Schematic of a two-step reaction involving a virtual intermediate state.

This type of two-step reaction involves a virtual intermediate state that contains a free neutron. It is known that virtual neutrons in free space do not stray very far away from their point of origin. The Green's function for a virtual neutron in free space satisfies

$$[E - H_0]G(r|r_0) = \delta^3(r - r_0) \quad (1)$$

In this case $H_0 = -\hbar^2 \nabla^2 / 2M$, and the solution can be found analytically to be

$$G(r|r_0) = -\frac{1}{4\pi|r-r_0|} \frac{2M}{\hbar} \exp(-\alpha|r-r_0|) \quad (2)$$

where $\alpha = \sqrt{2M|E|/\hbar^2}$ for E negative. The Green's function is damped exponentially, with a decay constant that is on the order of an inverse fermi. Because of this, one would naively expect that a virtual neutron would never be able to go as far as a neighboring nucleus.

We have explored the modifications in the virtual neutron Green's function that would be brought about by the presence of a periodic produced by a lattice. In this case, the Green's function satisfies

$$[E - H_0 - V(r)]G(r|r_0) = \delta^3(r - r_0) \quad (3)$$

where the periodic potential $V(r)$ is due to neighboring nuclei in the lattice. We have shown that the presence of the periodic potential gives rise to a long range component of the neutron Green's function. In the case of a weak perturbation, we have found a very accurate approximate result for the

Green's function which exhibits explicitly long range effects that are on the scale of the characteristic Bragg extinction length (which can be on the order of a micron).

Unfortunately, the potential produced by nuclei in a lattice will normally be too weak to induce very much of an effect with being resonantly enhanced. Such a resonant effect has recently been identified: a virtual neutron that is transferred from a deuteron will be resonantly captured by a proton in an equivalent site to make another deuteron. By itself, this leads only to a weak correction of the Green's function; but if a rather specific type of phase correlation in space were to exist among the deuterons and protons in the lattice, then a rather dramatic enhancement of this new long range effect will take place.

We have conjectured that diffusion of hydrogen isotopes in the lattice would, in the quantum limit, produce the required coherence. Very recently we have obtained an existence proof of sorts that it is possible for a metal hydride to exhibit predominantly coherent tunneling near room temperature. It remains to be demonstrated that quantum diffusion produces Dicke states; this is an area of ongoing research.

One proposed model for heat production involves neutron transfer reactions in which the reaction energy is coupled into the lattice. In last year's RLE report we described an approach based on the Duschinsky operator which appears because the initial lattice phonon modes differ from the final state phonon modes due to the mass change at the site of the neutron transfer; the method proposed in that report was analyzed in detail and found to be incapable of significant energy transfer. It was found that the Duschinsky operator is not particularly efficient at creating phonons, but it appears to be capable of transferring energy through shifting the frequency of phonon modes.

Dilute impurities in a metal lattice can form reasonably precise phonon bands, termed impurity bands in the literature. If there are N_H interstitial hydrogen atoms and N_D interstitial deuterium atoms in a Pd lattice, then there will be $3N_H$ impurity modes at ω_H and $3N_D$ impurity modes at ω_D . If a neutron transfers off of a deuteron to make a proton, then the three highest deuterium impurity modes will be shifted to the hydrogen impurity band. The associated energy exchange with the lattice will be $\hbar(\omega_H - \omega_D)$. Since the impurity band modes are true continuum modes, the number of phonons in a

single mode can be quite large, and the energy transfer can be anomalously large.⁷⁵

The mechanism described above has the potential to couple energy even if the virtual neutron capture is incoherent. The anomalous energy transfer associated with neutron capture increases the energy available for possible nuclear reactions, which can increase the energy of reaction products and open new reaction channels. Such reactions may account for recent observations of copious emissions of gammas, alphas and neutrons from glow discharge experiments.⁷⁶

1.23 Deuterated Metal Experiments

Sponsors

Space Exploration Associates
Future Energy Applied Technology, Inc.

Project Staff

Professor Peter L. Hagelstein, Professor Louis D. Smullin, D. Farber, Akikazu Hashimoto, Martin H. Muendel, Q. Zheng

If anomalous effects actually do occur in metal-deuterium systems, then it should be possible to develop experiments at MIT which demonstrate one or more of the anomalies. A controversy has existed since 1989 as to whether there exist any anomalous effects at all, with the large majority of the scientific community being currently in agreement that no new effects exist at all. The demonstration at MIT of one or more of the anomalies (excess heat production, tritium production, or energetic nuclear products) would be expected to impact this controversy.

A primary goal of our experimental effort is therefore to develop an experiment that demonstrates at least one anomalous effect, for the express purpose of placing research in this area into the mainstream of science.

The experimental results that have been obtained to date in other laboratories have not clarified what reaction mechanisms are involved in any positive sense. A major goal of the present effort is to work towards a basic understanding of the underlying

reaction mechanism, and to provide experimental feedback for proposed theoretical mechanisms.

There are a number of experiments which have been done previously for which a confirmation at MIT would prove interesting. Additionally, there are new experiments that are motivated by theoretical considerations which could be attempted. The experimental program that we are currently pursuing includes both classes of experiment.

Our initial efforts towards developing experiments originated from theoretical ideas based on neutron transfer reaction model. As discussed above, the model is based on neutron transfers from donor nuclei (deuterium) to suitable acceptor nuclei. Heat production in the model follows from coherent neutron transfer from deuterium to lithium or boron; tritium production arises from coherent neutron capture on deuterium; gamma and alpha production follows from semi-coherent capture on metal nuclei; neutron and energetic ion emission would follow from neutron capture on nuclei accompanied by significant energy input from the lattice.

According to theory, significant relative phase coherence among pairs of interstitials in the lattice must be present before any anomalies can occur. For such relative phase coherence to be present, the interstitials must diffuse; the specifics of this process are under investigation theoretically. Metal deuterides are favored, since deuterium is the lightest interstitial that can donate a neutron. Palladium is favored since the diffusion coefficient of deuterium is one of the highest for an fcc lattice; but theory would suggest that V, Nb and Ta, which are bcc lattice and have lower diffusion barriers, may also prove interesting.

From theory, diffusion in the quantum limit will have the best chance of setting up the required phase coherence. A review of the experiments showing positive results indicate that most of them operate at temperatures somewhat (within a factor of 2) above where the diffusion is in the quantum limit. The faster the diffusion, the larger the coherence volume, hence the reactions should work better at higher temperatures up to a maximum temperature at which the phase differences accumulated between hydrogen and deuterium diffusion destroy the coherence. Where this occurs is unknown: the

⁷⁵ P.L. Hagelstein, "Coherent and Semi-Coherent Neutron Transfer Reactions III: Phonon Generation," *Fusion Tech.* 23:353 (1993).

⁷⁶ A.B. Karabut, Y.R. Kucherov, and I.B. Savvatimova, "Nuclear Product Ratio for Glow Discharge in Deuterium," *Phys. Lett. A* 170: 265 (1992).

early Karabut paper describes a cut-off at 500 K,⁷⁷ Fleischmann and Pons describe high heat generation with a temperature excursion up to about 600 K,⁷⁸ and Liaw reported excess heat in molten salt experiments near 700 K.⁷⁹ The solubility of Pd decreases markedly at higher temperature, which confuses the issue. In Nb, with higher solubility at elevated temperatures, effects have been reported at a temperature in excess of 1600 K.⁸⁰

Consequently, higher temperature appears to be favorable for the anomalies. Inasmuch as this leads to delocalization of the metal interstitials and maintains relative phase coherence, it is consistent with theory.

The first experiments which we set out to explore involved tritium production. From a mechanistic point of view, tritium production is simpler than heat production since only light hydrogen interstitials are diffusing. The diffusion of heavier interstitials such as Li and B in PdD is not well understood, but it is clear that the associated diffusion coefficients will be smaller. Tritium production is mechanistically more complicated than semicoherent alpha or gamma production, since the lattice has to participate in a nontrivial way; going into the experiment we are not guaranteed that the lattice will be correctly excited to take up the reaction energy.

Observations of tritium production have been reported in numerous metal deuterides in a variety of electrochemical, gas loading, and glow discharge experiments. One such experiment was developed at LANL by Tom Claytor.⁸¹ In this experiment, deuterium gas is absorbed by palladium that is part of a stack of alternating Si and Pd layers; a current is driven through the stack by pulses of high voltage. Tritium is reportedly produced under these conditions reproducibly at a rate of 10^6 – 10^7 tritium atoms per second. Tritium production was also studied by Lanza, who assessed the relative rates

for different metal host lattices.⁸² Tritium production was reportedly observed in Ti, Zr, Hf, Ta, Ti-Zr and in Zircaloy 2; the highest production figures were found for Ta.

A gas ionization gauge has been developed that is capable of detecting ionizing radiation at low levels; this instrument is sufficiently sensitive to detect about 10^{10} tritium atoms, which would be produced in about 20 minutes of operation at a rate of 10^7 atoms/second (the maximum rate reported by Claytor).

The first experiments completed to date involved a search for tritium evolved from gas-loaded Ta using the ionization gauge as a tritium detector; no tritium was observed in this experiment. Follow-on experiments are planned that will test for tritium production in V, Nb, Ta, and Pd under conditions in which (1) it can be verified that the metal loaded; (2) current flow is present; and (3) increased temperatures are maintained.

One confirmation experiment that is planned is a replication of the Claytor experiment, to be carried out in collaboration with the LANL team. Recently, Claytor has reported success in producing tritium in a PdD_x wire loaded in deuterium gas driven by a pulsed current source. We are modifying our system to operate in this mode.

A second type of experiment that we have been developing is an attempt to obtain excess heat in a gas-loading experiment. The basic idea is to assemble donor (deuterium) and acceptor (boron) nuclei in a host metal lattice that is gas loaded and at high temperature. If successful, this type of system would be better adapted for potential applications than excess heat-producing electrochemical systems, both because it is technically simpler and because energy conversion from a high temperature source is more efficient.

⁷⁷ A.B. Karabut, Y.R. Kucherov, and I.B. Savvatimova, "Nuclear Reactions at the Cathode in a Gas Discharge," *Sov. Tech. Phys. Lett.* 16: 463 (1990).

⁷⁸ M. Fleischmann and S. Pons, "Calorimetry of the Pd - D₂O System: from Simplicity via Complications to Simplicity," *Proceedings of the Third Annual International Cold Fusion Conference*, Nagoya, Japan, November 1992.

⁷⁹ B.Y. Liaw, P.-L. Tao, P. Turner and B.E. Liebert, "Elevated-temperature Excess Heat Production on a Pd + D System," *J. Electroanal. Chem.* 319: 161 (1991).

⁸⁰ V.A. Romodanov, V.I. Savin, and Y.M. Timofeev, "Nuclear Fusion in Condensed Matter," LUTCH report UDC:539.172.13; presented at the *Third Annual International Cold Fusion Conference*, Nagoya, Japan, November 1992.

⁸¹ T.N. Claytor, D.G. Tuggle, and H.O. Menlove, "Evolution of Tritium from Palladium in the Solid State Gas Cell," presented at the *Third Annual International Cold Fusion Conference*, Nagoya, Japan, November 1992.

⁸² F. Lanza, G. Bertolini, V. Vocino, E. Parnisari, and C. Ronsecco, "Tritium Production Resulting from Deuteration of Different Metals and Alloys," *Proceedings of the Second Annual Cold Fusion Conference* 151 (1991).

An experiment has been constructed to carry out this type of experiment. It consists of a heater that is surrounded by a deuterium gas filled annulus in which the metal sample is held and monitored. The central heater and annulus are surrounded by magnesium oxide thermally resistant bricks; due to the general appearance of the resulting structure, it has earned the moniker "Lenin's Tomb." As a calorimeter, Lenin's Tomb has been calibrated and has been found to be reproducible from day-to-day while heating; power excesses on the order of a watt would be detectable. In the initial trial runs of undoped vanadium (no boron) in deuterium, no excess heat has been observed to date.

From theory, gamma and alpha emission due to semi-coherent neutron capture on metal nuclei should occur as a precursor and during coherent reactions. This is of interest since the fully coherent reactions are difficult to diagnose unless they work at high levels. From a theoretical point of view, the semi-coherent reactions are simpler since they do not require any special degree of lattice excitation.

We have used a NaI gamma detector to search for excess gamma emission from gas loaded vanadium in Lenin's Tomb, as a signature of precursor activity. The background is very high, and no positive signals were identifiable.

A next step in the experiment is to arrange for current flow in the deuterated metal samples, and to diagnose for gamma emission in V, Nb, Ta and Pd. Some effort needs to be put into improving the signal to noise ratio in the gamma detection. The positive observation of a precursor signal would be a significant step forward experimentally, and would bode well for possible observations of an excess power anomaly. Experiments on boron-implanted gas loaded metals constitute the next phase of the experiments.

We had worked for about a year on the experiments described above when we learned of some closely related glow-discharge experiments that were reported at the International Cold Fusion Conference in Nagoya last November. In these experiments, various metals were loaded by glow discharge at high temperature and anomalies were observed. One group at the LUTCH Association in Moscow observed gammas, alphas and neutrons at very high levels $10^5 - 10^6$ per second in glow discharge experiments using a Pd cathode; very high levels of excess power (more than 1 kilowatt/cm³) were also observed.⁸³ Another experiment at LUTCH used a similar glow discharge to study tritium production at high temperature in a variety of metals; tritium production at the very high rate of 1.7×10^9 atoms/second was observed in Nb at 1170 K.⁸⁴ Glow discharge experiments in China gave intense neutron and gamma signals from a variety of metals, including Pt, Nb, W and Pd.⁸⁵

These experiments are closely related in that metal deuterides at high temperature exhibit positive precursor signals, as well as heat and tritium production. They differ from the experiments that we have been developing in that the cathodes are actively loaded by the discharge and achieve very high D/Pd loading ratios, and also that substantial current density is present in the cathodes. We decided to attempt a confirmation of one of the glow discharge experiments performed at LUTCH.

We have developed a glow discharge that runs under conditions similar to those reported by the LUTCH group, in terms of operating current, voltage and gas pressure. This discharge is unusual in that the cathode surface current density can reach several hundred milliamps/cm²; this high surface current level is accompanied by high cathode temperatures which appears to be important. This experiment will be carried out in collaboration with Y. Kucherov of the LUTCH group.

⁸³ A.B. Karabut, Y.R. Kucherov, and I.B. Savvatimova, "Nuclear Product Ratio for Glow Discharge in Deuterium," *Phys. Lett. A* 170: 265 (1992).

⁸⁴ V.A. Romodanov, V.I. Savin, and Y.M. Timofeev, "Nuclear Fusion in Condensed Matter," LUTCH report UDC:539.172.13; presented at the *Third Annual International Cold Fusion Conference*, Nagoya, Japan, November 1992.

⁸⁵ L. Heqing et al., presented at the *Third Annual International Cold Fusion Conference*, Nagoya, Japan, November 1992.

Chapter 2. Optical Propagation and Communication

Academic and Research Staff

Professor Jeffrey H. Shapiro, Dr. Robert H. Rediker, Dr. Ngai C. Wong

Visiting Scientists and Research Affiliates

Dr. Lance G. Joneckis¹

Graduate Students

L. Reginald Brothers, Christopher J. Corcoran, Boris Golubovic, Thomas J. Green, Jr., Suzanne D. Lau, Dicky Lee, Phillip T. Nee, Brian K. Pheiffer, Scott R. Shepard, Ke-Xun Sun, Peter T. Yu

Undergraduate Students

Kerry D. Rosenhagen

Technical and Support Staff

Barbara A. King

2.1 Introduction

The central theme of our programs has been to advance the understanding of optical and quasi-optical communication, radar, and sensing systems. Broadly speaking, this has entailed: (1) developing system-analytic models for important optical propagation, detection, and communication scenarios; (2) using these models to derive the fundamental limits on system performance; and (3) identifying and establishing through experimentation the feasibility of techniques and devices which can be used to approach these performance limits.

2.2 Squeezed States of Light

Sponsors

Maryland Procurement Office
Contract MDA 904-90-C-5070

Project Staff

Professor Jeffrey H. Shapiro, Dr. Ngai C. Wong, Dr. Lance G. Joneckis, Scott R. Shepard, Ke-Xun Sun, Kerry D. Rosenhagen

2.2.1 Experiments

We have employed optical parametric downconversion in a type-I phase-matched $\text{LiNbO}_3:\text{MgO}$ crystal in our efforts to generate nonclassical light. Our focus has been on the demonstration of squeezed amplification of a below-threshold optical parametric amplifier (OPA) in the gain-saturated regime.² Under gain saturation, the amplified output intensity of an injected coherent-state signal becomes amplitude squeezed, and the large-signal signal-to-noise ratio improves. Using a single-frequency diode-pumped YAG laser as the injection source, we have made extensive mean-field measurements: gain saturation and output lineshape have been studied as functions of the pump and signal powers, as well as the signal frequency, pump frequency and cavity detunings.³ We have found quantitative agreement between theory and experiment for the frequency spacings and widths of the key features in these measurements. We have observed an unsaturated signal-gain of 10^3 for an OPA pumped at 97 percent of threshold with a low level of signal injection. This gain is reduced to 13 at the same pump level when the signal injection is increased by

¹ Laboratory for Physical Sciences, College Park, Maryland.

² N.C. Wong, "Squeezed Amplification in a Nondegenerate Parametric Amplifier," *Opt. Lett.* 16(21): 1698-1700 (1991).

³ K.X. Sun, N.C. Wong, and J.H. Shapiro, "Squeezed Amplification with Cavity Detunings: Mean-Field Behavior," paper presented at the Optical Society of America Annual Meeting, Albuquerque, New Mexico, September 20-25, 1992.

33 dB. Potential applications of an injection-seeded gain-saturated OPA include master-oscillator output amplification and direct-detection digital communication.

2.2.2 Theory

A detailed analysis of the injection-seeded OPA including cavity detunings has been carried out.⁴ Both mean field and noise behavior of the gain-saturated OPA and their dependence on cavity detunings, pump power, and signal injection power have been obtained and used for comparison with our experiments. Direct-detection statistics have been obtained using the quantum analog of the Gaussian moment-factoring theorem, showing that the beat noise will be insignificant in our squeezed-amplification experiments.⁵ We have also developed a two-detector extension of the theory that permits efficient and insightful analysis of recent fourth-order interference experiments⁶ which use entangled photons from a parametric downconverter.

We have continued our study of the fundamental quantum limits on the measurement of phase. Our early work concentrated on the single-mode case,⁷ in which we showed that the Susskind-Glogower probability operator measure (SG-POM) provides the maximum-likelihood (ML) estimate of a c-number phase shift, and we explored a variety of quantum states for use in conjunction with this ML procedure. Recently, we have concentrated on the behavior of two-mode phase measurements which relieve the burden of the single-mode case's Paley-Wiener constraint. Here we have related quantum phase to angular momentum formalism⁸ and elucidated a system for error-free, phase-conjugate communication or finite-precision phase-sensing.⁹ The latter study casts new light on the two-mode

ML estimation problem, viz., it appears that there is no general ML phase-measurement POM for arbitrary input states.

Finally, we have continued and extended our theoretical work on quantum propagation in single-mode fiber.¹⁰ We now have a formalism which includes the Kerr effect, i.e., self-phase modulation (SPM), plus linear loss, and group-velocity dispersion. This construct reduces properly to the standard results of classical theory and linearized quantum theory. Moreover, we have already performed numerical studies which establish the validity limits of the linearized quantum theory for pure SPM, and for SPM plus loss, and we are proceeding with the richer case of SPM plus dispersion.

2.2.3 Publications

Joneckis, L.G., and J.H. Shapiro. "Quantum Propagation in a Kerr Medium: Lossless, Dispersionless Fiber." *J. Opt. Soc. Am. B*. Forthcoming.

Shapiro, J.H. "On the Performance of Optical Phase-Shift-Keying with Preamplified-Feedforward-Homodyne Reception." *IEEE Photon. Technol. Lett.* 4(6): 647-649 (1992).

Shapiro, J.H., and K.X. Sun. "Direct Detection of Gaussian-State Light." Paper presented at the Optical Society of America Annual Meeting, Albuquerque, New Mexico, September 20-25, 1992.

Shapiro, J.H., and N.C. Wong. "Optical Amplifiers, Phase-Shift Keying, and Signal-to-Noise Ratio." Paper presented at the Optical Society of

⁴ K.X. Sun, N.C. Wong, and J.H. Shapiro, "Squeezed Amplification with Cavity Detunings: Mean-Field Behavior," paper presented at the Optical Society of America Annual Meeting, Albuquerque, New Mexico, September 20-25, 1992; K.X. Sun and J.H. Shapiro, "Squeezed Amplification with Cavity Detunings: Noise Behavior," paper presented at the Optical Society of America Annual Meeting, Albuquerque, New Mexico, September 20-25, 1992.

⁵ J.H. Shapiro and K.X. Sun, "Direct Detection of Gaussian-State Light," paper presented at the Optical Society of America Annual Meeting, Albuquerque, New Mexico, September 20-25, 1992.

⁶ A.M. Steinberg, P.G. Kwiat, and R.Y. Chiao, *Phys. Rev. Lett.* 68(16): 2421-2424 (1992).

⁷ J.H. Shapiro and S.R. Shepard, "Quantum Phase Measurement: A System Theory Perspective," *Phys. Rev. A* 43(7): 3795-3817 (1991).

⁸ S.R. Shepard, *Phase of the Quantum Harmonic Oscillator*, Ph.D. diss., Dept. of Electr. Eng. and Comput. Sci., MIT, 1992.

⁹ J.H. Shapiro, "Phase Conjugate Quantum Communication with Zero Error Probability at Finite Average Photon Number," submitted to *Phys. Scripta*.

¹⁰ L.G. Joneckis and J.H. Shapiro. "Quantum Propagation in a Kerr Medium: Lossless, Dispersionless Fiber," *J. Opt. Soc. Am. B*, forthcoming.

America Annual Meeting, Albuquerque, New Mexico, September 20-25, 1992.

Shapiro, J.H. "Phase Conjugate Quantum Communication with Zero Error Probability at Finite Average Photon Number." Submitted to *Phys. Script*.

Shepard, S.R. *Phase of the Quantum Harmonic Oscillator*. Ph.D. diss., Dept. of Electr. Eng. and Comput. Sci., MIT, 1992.

Sun, K.X., N.C. Wong, and J.H. Shapiro. "Squeezed Amplification with Cavity Detunings: Mean-Field Behavior." Paper presented at the Optical Society of America Annual Meeting, Albuquerque, New Mexico, September 20-25, 1992.

Sun, K.X., and J.H. Shapiro. "Squeezed Amplification with Cavity Detunings: Noise Behavior." Paper presented at the Optical Society of America Annual Meeting, Albuquerque, New Mexico, September 20-25, 1992.

Wong, N.C. "Gravity-Wave Detection via an Optical Parametric Oscillator." *Phys. Rev. A* 45(5): 3176-3183 (1992).

2.3 Optical Frequency Division and Synthesis

Sponsors

Charles S. Draper Laboratories
Contract DL-H-441698
National Institute of Standards and Technology
Grant 60-NANBOD-1052
U.S. Army Research Office
Grant DAAL03-90-G-0128

Project Staff

Dr. Ngai C. Wong, L. Reginald Brothers, Dicky Lee, Phillip T. Nee

Frequency division and synthesis in the optical domain play an important role in modern optical precision measurements, optical frequency standards, and optical communication. We have demonstrated optical frequency division using an optical parametric oscillator (OPO) approach based on an

efficient, one-step parametric downconversion process.¹¹ An OPO converts an input pump into two intense, coherent subharmonic outputs whose frequencies are tunable and whose sum frequency equals the pump frequency. By phase locking the output frequency difference to a microwave source, the output frequencies are precisely determined, and the OPO functions as an optical frequency divider. OPO frequency dividers can be operated in series or in parallel to measure, compare, and synthesize frequencies from optical to microwave with high precision and resolution.

2.3.1 Demonstration of Optical Frequency Division

We have employed a type-II phase-matched KTP OPO for demonstrating the concept of optical parametric division. A three-element cavity design consisting of the KTP crystal and two cavity mirrors has been constructed. The mirrors are rigidly attached to a spacer block to provide excellent mechanical stability. This cavity design permits systematic and continuous frequency tuning of the outputs and stable operation of the OPO. We have successfully demonstrated frequency division in the optical regime by phase locking the two OPO subharmonic outputs at 1.06 μm to a microwave synthesized signal (2-25 GHz) with a residual beat-note linewidth of 25 mHz, limited by the resolution of the spectrum analyzer.¹² This indicates that the OPO has very low phase noise, which can be further suppressed by phase locking it to a microwave source. This exceptionally high spectral purity should also allow us to study the quantum phase diffusion noise of an OPO.

2.3.2 High-Frequency Phase-Velocity-Matched Electro-Optic Modulator

In order to facilitate phase locking of the OPO outputs with a difference frequency of ~ 1 THz or more, an optical frequency comb with a large frequency span is required. We have developed a new electro-optic modulator that is capable of generating hundreds of sidebands at a spacing of 20-40 GHz. By incorporating a microwave waveguide structure in a LiNbO_3 electro-optic modulator,

¹¹ N.C. Wong, "Optical Frequency Division using an Optical Parametric Oscillator," *Opt. Lett.* 15(20): 1129-1131 (1990); D. Lee and N.C. Wong, "Tunable Optical Frequency Division using a Phase-Locked Optical Parametric Oscillator," *Opt. Lett.* 17(1): 13-15 (1992).

¹² D. Lee and N.C. Wong, "Stabilization and Tuning of a Doubly Resonant Optical Parametric Oscillator," submitted to *J. Opt. Soc. Am. B*.

the phase velocities of the microwave and optical fields can be matched to maximize the interaction length.¹³ We have been able to obtain a single-pass modulation index of 0.4 with 1 W of rf power at a driving frequency of 17.2 GHz. Our next step is to place the modulator inside an optical resonator to increase the effective interaction length, thus making it possible to generate sidebands with a span of over 1 THz. Preliminary results in a 12.4 GHz modulator shows a one percent output power at the fifth order sideband at 62 GHz.¹⁴ In addition to optical frequency division, THz optical sideband generation is potentially useful for frequency identification in a wideband optical communication network.

2.3.3 Optical Frequency Counter

We have proposed an optical frequency counter that is capable of measuring any optical frequency from the UV to the near IR relative to a microwave frequency standard.¹⁵ The concept is to measure the frequency difference of two known ratios (1/2 and 2/3) of an optical frequency f relative to the cesium clock. By employing a parallel network of phase-locked OPOs and wideband modulators to link the $(1/2)f$ and $(2/3)f$ frequencies, a precise and accurate optical frequency comb can be provided in the ~ 1 -2- μm wavelength region. By using this comb, most optical frequencies from the UV to the near IR can be measured or synthesized. We have begun an experimental program to implement this frequency counter. Using a Ti:sapphire laser at ~ 775 nm ($f=387$ THz) as the pump source, our initial efforts will be to demonstrate a 2:1 OPO frequency divider with subharmonic outputs at 1.5 μm , which is also useful as an alternative source for fiber-optic communication.

2.3.4 Publications

Lee, D., and N.C. Wong. "High-Performance Optical Parametric Oscillator," *Proceedings of the SPIE Frequency Stabilized Lasers and Their Applications*, Boston, Massachusetts, November 1992.

Lee, D., and N.C. Wong. "Tunable Optical Frequency Division using a Phase-Locked Optical Parametric Oscillator." *Opt. Lett.* 17(1): 13-15 (1992).

Lee, D., and N.C. Wong. "Stabilization and Tuning of a Doubly Resonant Optical Parametric Oscillator." Submitted to *J. Opt. Soc. Am. B*.

Wong, N.C. "Gravity-Wave Detection via an Optical Parametric Oscillator." *Phys. Rev. A* 45(5): 3176-3183 (1992).

Wong, N.C. "Optical Frequency Counting from the UV to the Near IR." *Opt. Lett.* 17(16): 1155-1157 (1992).

Wong, N.C. "Proposal for a 10 THz, Precision Optical Frequency Comb Generator." *IEEE Photon. Technol. Lett.* 4(10): 1166-1168 (1992).

Wong, N.C., and D. Lee, "Optical Parametric Division," *Proceedings of the 1992 IEEE Frequency Control Symposium*, pp. 32-38, Hershey, Pennsylvania, May 27-29 1992.

2.4 Fiber-Coupled External-Cavity Semiconductor High Power Laser

Sponsor

U.S. Navy - Office of Naval Research
Grant N00014-89-J-1163

Project Staff

Dr. Robert H. Rediker, Christopher J. Corcoran

The experimental portion of this program ended in December 1991, and the program terminated officially when we submitted the final report to the Office of Naval Research in August 1992. During 1992, we expanded the theory of an optical maser first proposed by W.E. Lamb in 1964, using a traveling wave model to describe our experimental polarization results. The experimental results on spatial coherence were also more fully explained.

¹³ B.Y. Lee, T. Kobayashi, A. Morimoto, and T. Sueta, "Picosecond Electro-Optic Modulator/Deflector with Velocity Matching," paper presented at the Conference on Lasers and Electro-Optics, Baltimore, Maryland, May 12-17, 1991.

¹⁴ N.C. Wong and D. Lee, "Optical Parametric Division," *Proceedings IEEE Frequency Control Symposium*, Hershey, Pennsylvania, May 1992, p. 32; N.C. Wong, D. Lee, and L.R. Brothers, "Tunable Optical Frequency Division," *Digest of the International Quantum Electronics Conference*, Vienna, Austria, June 1992, p. 110.

¹⁵ N.C. Wong, "Optical Frequency Counting from the UV to the Near IR," *Opt. Lett.* 17(16): 1155-1157 (1992).

Because this program, which was considered a very long shot when started in 1980 under predecessor grant number N00014-80-C-0941, was becoming of commercial interest, in 1991 the principal investigator requested that the Navy project officer not renew the grant. The last sentence of the final report to the Navy reads, "It is hoped that ONR, by sponsoring this high-risk, long shot, has significantly contributed to the industrial competitiveness of our country."

Publications

Corcoran, C.J., and R.H. Rediker. "The Dependence of the Output of an External-Cavity Laser on the Relative Phases of Inputs from Five Gain Elements." *IEEE Photon. Tech. Lett.* 4(11): 1197-1200 (1992).

Corcoran, C.J. *Operation of Five Individual Laser Diodes as a Coherent Ensemble by Fiber Coupling into an External Cavity*. Ph.D. diss., Dept. of Physics, MIT, 1992.

2.5 Analog Processing of Optical Wavefronts Using Integrated Guided-Wave Optics

Sponsor

U.S. Air Force - Office of Scientific Research
Contract F49620-90-C-0036

Project Staff

Dr. Robert H. Rediker, Suzanne D. Lau, Brian K. Pheiffer, Boris Golubovic

In wavefront sensing and correction, it is envisioned that 10^3 - 10^4 basic modules would be used. In integrated optics as in integrated circuits, it is important to relax the requirements for individual components while requiring that operation of the integrated optics (circuits) is independent of significant component variations. The wavefront is sensed by interferometers between the multiplicity of through waveguides with the arms of the interferometers evanescently coupled to adjacent waveguides. The input powers to the interferometer arms will not be equal as a result of (1) the input power to the waveguide array being non-uniform

and (2) unequal coupling by the evanescent couplers.

In last year's *RLE Progress Report* (Number 134), we stated that the experimental results on the phase measurement and phase correction have been independent of the power difference between the interferometer arms up to ratios of greater than 10:1. It has since been experimentally determined that the phase measurement and the phase correction are independent of this power imbalance up to ratios of 50:1.

With this successful result and those from prior years, it was decided in 1992 to embark on building a complete basic optical module. The on-chip detector at the output of the interferometer is also incorporated in this planned module. In the previous work, the detector has been located off-chip. The semiconductor processing design we developed ensures that the components (e.g., waveguides, couplers and detectors) of the module are fabricated to be compatible. GaAs/AlGaAs epistuctures, which are used for making the module, have been specified and are on hand. Individual processing steps have been specified and optimized. We have received the photolithography masks, which we designed.

In 1992 the project dealt primarily with process definition and experimentation necessary for ongoing module fabrication. In the early part of 1993, we will complete the first basic modules, measure their performance, and compare their operation with theoretical predictions.

Publications

Lau, S.D., J.P. Donnelly, C.A. Wang, and R.H. Rediker. "Integrated AlGaAs Waveguide Components for Optical Phase Difference Measurements and Correction." Submitted to *IEEE J. Quantum Electron.*

Lau, S.D. *Optical Phase Difference Measurement and Correction Using AlGaAs Guided-Wave Components*. Ph.D. diss., Dept. of Electr. Eng. and Comput. Sci., MIT, 1992.

Pheiffer, Brian K. *Integrated AlGaAs Reduced-Confinement Tapered Waveguide Antennas*. S.M. thesis, Dept. of Electr. Eng. and Comput. Sci., MIT, 1992.



Professor Qing Hu

Chapter 3. High-Frequency (>100 GHz) Electronic Devices

Academic and Research Staff

Professor Qing Hu

Graduate Students

Edouard A. Garcia, Rajesh K. Gupta, Brian R. Jacobson, Zheny K. Lee, Jurgen H. Smet, Rolf A. Wyss

Undergraduate Students

Elliot E. Hui, Jason S. Kim

Technical and Support Staff

Barbara A. King

3.1 Facility for Millimeter-wave and THz Frequencies

Professor Hu's laboratory is equipped with various millimeter-wave and infrared sources which can generate coherent and incoherent radiation up to 30 THz. These include Gunn oscillators at W-band frequencies (75-110 GHz); a frequency doubler, tripler, and quadrupler using Schottky diodes at 200, 300, and 400 GHz; an optically pumped far-infrared laser which generates coherent radiation up to 8 THz; and an infrared Fourier transform spectrometer which is capable of performing linear spectroscopy from 45 GHz to 30 THz and beyond. The laboratory is also equipped with various cryogenic millimeter-wave and infrared detectors. These include Si composite bolometers, InSb hot-electron bolometers, SIS (superconductor-insulator-superconductor) receivers, and high- T_c Josephson detectors. There are many infrared cryostats which can cool the devices from 0.3 K to 77 K.

3.2 Millimeter-wave and Infrared Superconducting Focal-plane Receiver Arrays

Sponsors

MIT Lincoln Laboratory
National Aeronautics and Space Administration
Grant NAG2-693

Project Staff

Brian R. Jacobson, Edouard A. Garcia, Professor Qing Hu in collaboration with MIT Lincoln Laboratory

Although the range that includes millimeter-wave and far-infrared frequencies is one of the most

underdeveloped, these frequencies have great potential for applications in remote sensing and communication. The millimeter-wave and far-infrared frequency range falls between the two other frequency ranges in which conventional semiconductor devices are usually operated: (1) microwave frequency range and (2) near-infrared and optical frequency range.

Semiconductor devices which utilize the classical diffusive transport of electrons such as diodes and transistors have a high frequency limit. This limit is set by the time it takes for electrons to travel a certain distance. Currently, electron mobility and the smallest feature size which can be fabricated by lithography limit the frequency range to below 100 GHz. It is not likely that this limit can be pushed much higher. Semiconductor devices based on quantum mechanical interband transitions, however, are limited to frequencies higher than those corresponding to the semiconductor energy gap, which is higher than 10 THz for most bulk semiconductors. Therefore, a large gap exists from 100 GHz to 10 THz in which very few devices can operate.

The gap energies of conventional superconductors such as Nb are in the range of 100 GHz to 2 THz. This coincidence makes superconducting devices natural candidates for millimeter- and submillimeter-wave applications. At millimeter-wave frequencies, the superconducting video detectors have quantum efficiency $e/\hbar\omega$, that is, a transport of one electron for one incoming photon; while the superconducting coherent receivers have their sensitivities limited only by the zero-point fluctuation of vacuum. Such receivers have been used widely in astrophysical studies. Additional applications are feasible in space-based communication and far-infrared spectroscopy which requires the ultimate sensitivity.

We are currently developing a novel quasioptical scheme to couple the millimeter-wave and infrared signals to superconducting devices through a combination of an etched horn antenna and a planar antenna supported by a thin ($\sim 1\ \mu\text{m}$) membrane, as shown in figure 1. This scheme combines the advantages of the easy fabrication of lithographic thin-film structures and the high antenna efficiencies of horn antennas. Because of the absence of substrate losses in this scheme, it is expected that a THz receiver could be constructed using all-Nb superconductor-insulator-superconductor (SIS) junctions. More important, because of the cumbersome mechanical structures used in conventional waveguide technology, microwave receivers have been single-element devices, as opposed to CCD imaging arrays at optical frequencies. Spatial scan has been achieved mechanically. Using the novel quasioptical scheme mentioned above, focal-plane detector arrays can be fabricated lithographically on a single Si wafer, as shown in figure 2, so that far-infrared imaging becomes feasible.

The first step of this project is to demonstrate the feasibility of fabricating high-quality SIS devices on free-standing SiN membranes and then to demonstrate that these devices can survive thermal cycling. Using the microfabrication facilities in Group 86 at MIT Lincoln Laboratory, we have fabricated several wafers of SIS junctions with a critical current density of $4,000\ \text{A}/\text{cm}^2$. We then etched the Si wafer underneath anisotropically in a KOH solution. A view of an SIS junction with a log-periodic antenna on a $1\text{-}\mu\text{m}$ thick SiN membrane is shown in figure 3. Extreme care was taken to protect the SIS junctions from the KOH etchant during the anisotropic etching. Figure 4 shows the I-V curves of the SIS junction measured before and after the Si wafer was etched away. There are no noticeable changes in the I-V characteristics of the device. Clearly, our work has established the feasibility of building millimeter-wave SIS receivers using micro-machined horn antenna structures.

3.3 Photon-assisted Quantum Transport in Quantum Point Contacts

Sponsor

National Science Foundation
Grant ECS 91-09330

Project Staff

Rolf A. Wyss, Professor Qing Hu, in collaboration with Cristopher C. Eugster, Professor Jesús A. del Alamo

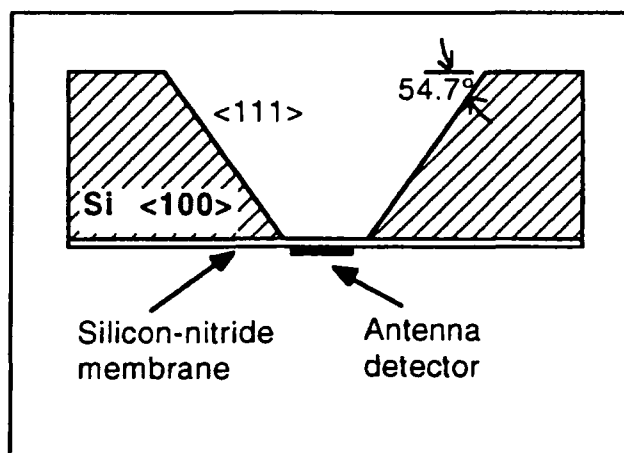


Figure 1. Example of anisotropic etching in a $\langle 100 \rangle$ silicon wafer. The opening of the wafer yields a pyramidal horn with a flare angle of 35.5° .

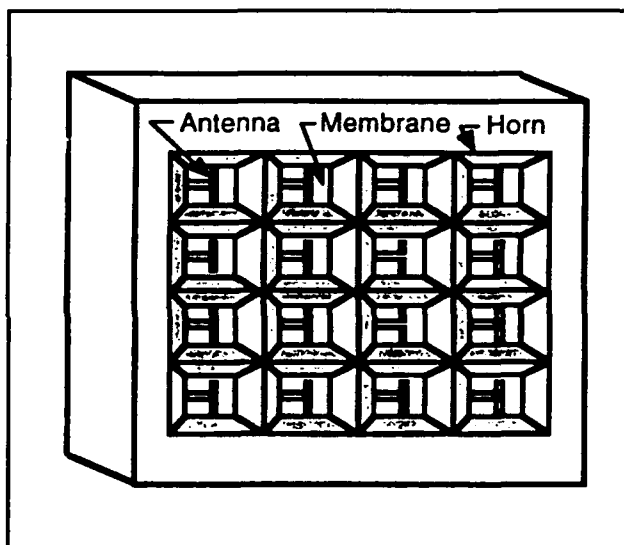


Figure 2. Perspective view of a two-dimensional horn imaging array.

Quantum transport has been one of the most active fields in solid-state physics in recent years. Advances in material preparation have made quantum phenomena profound in electron transport for many semiconductor quantum devices such as quantum point contacts, quantum dots, quantum wires, quantum wells, superlattices, etc. In clean samples and at low temperatures, electrons can travel through the whole sample without suffering phase-destructive scattering. Extensive work has been done to study various features of such phase-coherent quantum transport. However, so far the experiments reported are limited to dc transport measurements or far-infrared spectroscopy measurements.

It is well known in the field of superconducting tunneling that photons can assist the tunneling

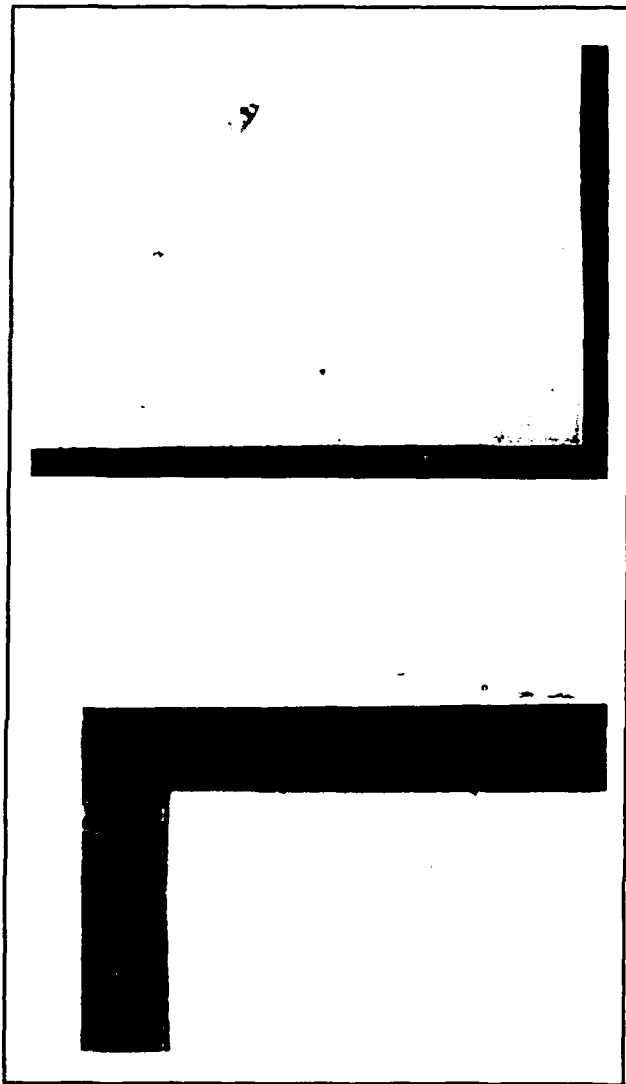


Figure 3. Perspectives on a silicon nitride membrane structure. (top) View of device seen through the membrane using backside illumination on microscope. (bottom) View of same device using top-side illumination; the 70° angle of the anisotropic etch can be made out by noticing the dark rim around the border of the device.

process, provided the tunneling is elastic so that electrons do not suffer inelastic scattering. In a broad sense, elastic tunneling is a phase-coherent quantum transport in a classically forbidden region. Therefore, all the results of photon-assisted tunneling can be applied to the study of photon-assisted quantum transport in semiconductor devices. This will provide a new dimension to study the exciting quantum transport phenomena. Novel long-wavelength optoelectronic devices may also emerge from this research.

In this NSF-sponsored project, we are studying the interaction between far-infrared photons and ballistic electrons in quantum point contact devices,

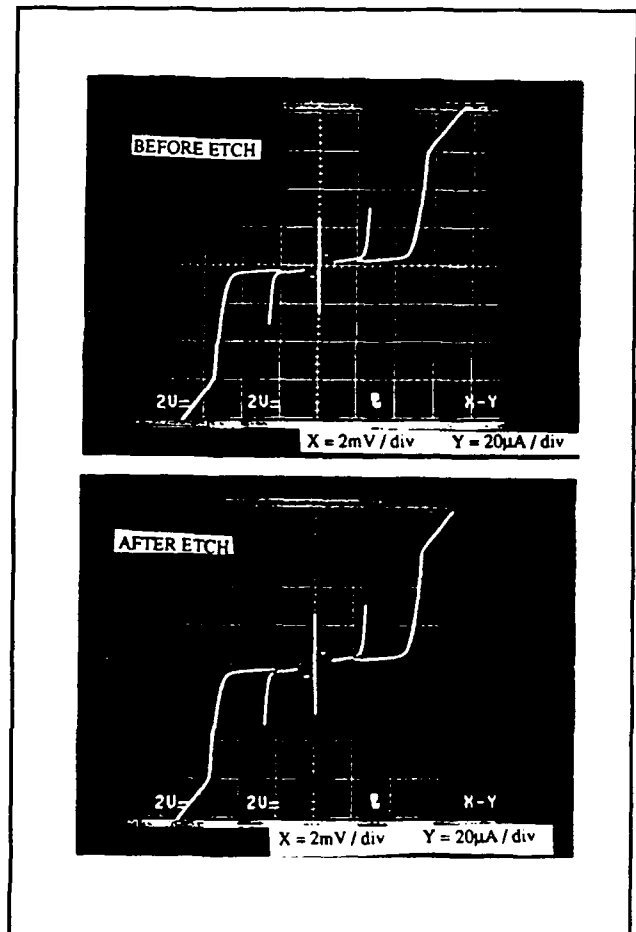


Figure 4. DC I-V curves for a device on SiN membrane (top) before etching, and (bottom) after etching the Si wafer in KOH.

whose schematic is shown in figure 5(a). We have fabricated several antenna-coupled quantum point contact devices using a combination of optical and electron-beam lithography. Figure 6 shows the SEM photographs of one of the devices. The split-gate electrodes (the vertical leads) also serve as the terminals of a log-periodic antenna, whose function is to couple the far-infrared radiation of millimeter wavelength to the point contact of submicron dimensions.

The dc transport measurement of the drain/source transport showed fifteen quantized conductance steps, indicating the high quality of the devices. Under a coherent far-infrared radiation (285 GHz), a profound photon-induced drain/source current is produced throughout a gate voltage range in which the device exhibits the behavior of a one-dimensional electron system. The amplitude of the photon-induced current is comparable to that corresponding to a quantized conductance step, and it oscillates with the gate voltage with a period corre-

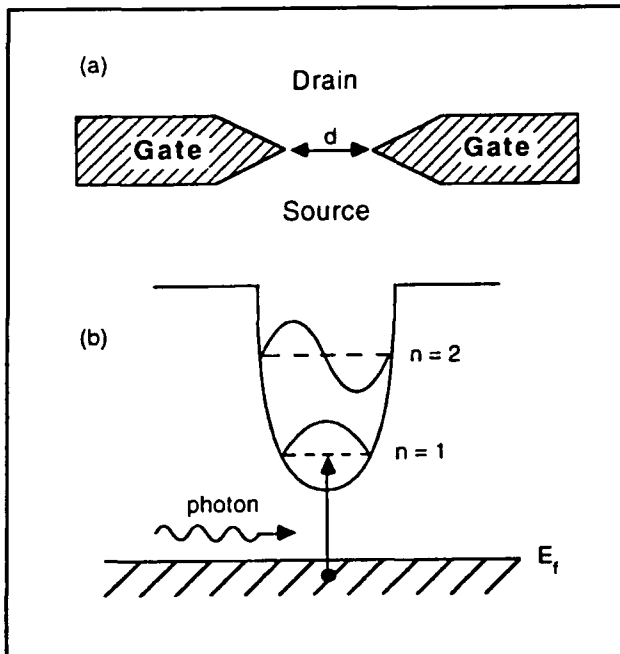


Figure 5. (a) Schematic of a quantum point contact. (b) Schematic of an electron waveguide which can be used to analyze the transport of electrons through the quantum point contact shown in (a).

sponding to the gate voltage between adjacent conductance steps, as shown in figure 7.

Our preliminary analysis suggests that the observed far-infrared photon-induced drain/source current is mainly due to heating (or a bolometric effect). Since the excitation in the two-dimensional electron gas is gapless, energy absorption can occur everywhere within the electron gas. Thus, the effect of photon-assisted quantum transport will always be accompanied by an effect due to heating. This aspect is quite different from photon-assisted tunneling in superconducting tunnel junctions in which the superconducting energy gap prevents energy absorptions in the leads. Our analysis also suggests several improvements must be made to enhance the effect of photon-assisted quantum transport and minimize the heating effect. According to the recently developed theory of photon-assisted quantum transport, the photon-assisted process mainly occurs near the classical turning points of the subbands under concern. Thus, to enhance the photon-assisted quantum process, it is crucial to concentrate the radiation field in the central region of the point contacts. This requires use of thick ($\sim 2000\text{\AA}$) antenna terminals made of good conductors. The quantum effect can also be enhanced by irradiating the devices at frequencies much higher than 300 GHz so that the photon energies are much greater than the thermal broadening of the Fermi surface.

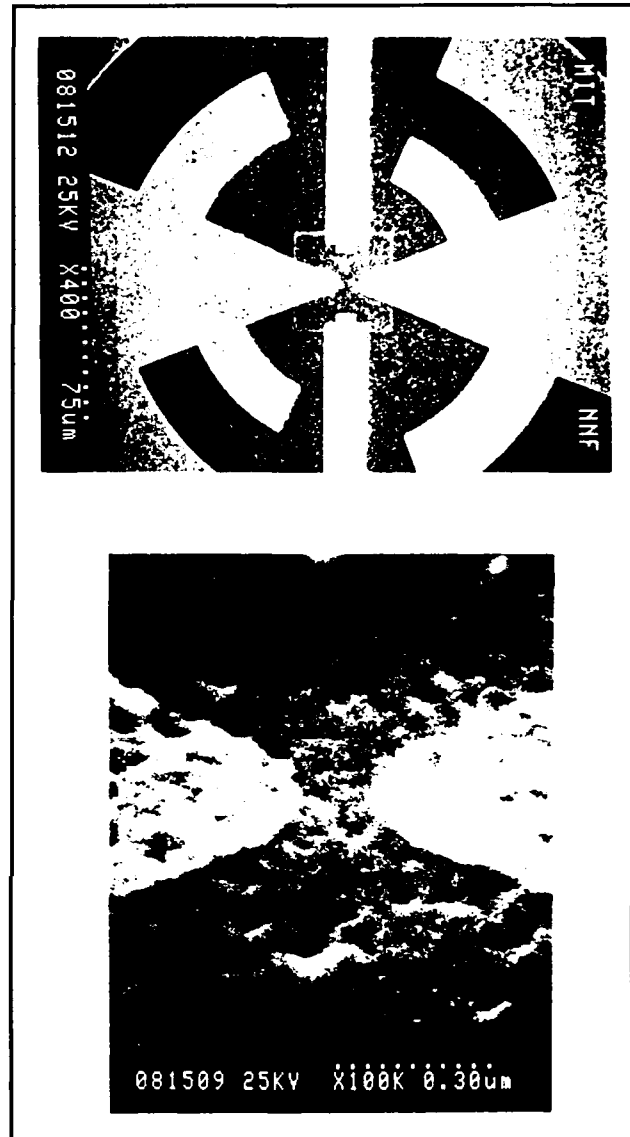


Figure 6. (a) SEM (with a magnification of 400) of a quantum point contact with log-periodic antenna. (b) Central region of the quantum point contact. The opening of the split-gate electrodes is $0.15\text{ }\mu\text{m}$.

3.4 High- T_c Superconducting Josephson Devices

Sponsor

Defense Advanced Research Projects Agency
Contract MDA972-90-C-0021

Project Staff

Rajesh K. Gupta, Professor Qing Hu, in collaboration with Twente University, The Netherlands

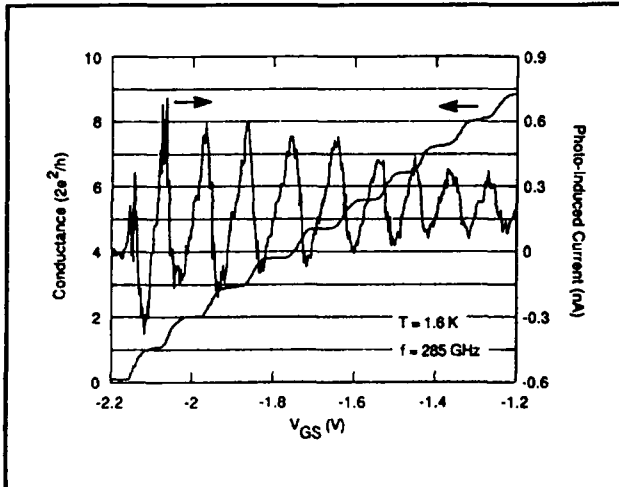


Figure 7. Drain/source conductance and the photon-induced drain/source current as functions of the gate voltage in a region where the conductance steps (measure without radiation) are well defined.

Many superconducting analog devices have been demonstrated to have higher sensitivities, higher speed and frequency limit, and lower power dissipation than competing semiconductor devices. Among them, the most successful ones are Superconducting QUantum Interference Devices (SQUIDS) and millimeter-wave detectors.

The discovery of superconductors with a superconducting transition temperature higher than liquid nitrogen temperature (high- T_c superconductors) has opened up new and exciting possibilities in electronic device technology. A high temperature version of the superconducting devices mentioned above will find a much wider range of applications wherever refrigeration is a problem. The key element of all superconducting analog and digital devices is the Josephson junction. This junction is formed by two superconductors weakly coupled together electrically. The supercurrent flowing through the Josephson junction oscillates at the Josephson frequency $f = 2eV/h$ (500 GHz/mV) when a voltage is applied across the junction. Most of the useful applications of Josephson devices result from this high-frequency oscillation. These devices include high-frequency and high-speed signal processors and high-sensitivity SQUID magnetometers whose high precision results from averaging over many cycles of the Josephson oscillations.

In collaboration with the Dutch group headed by Professor Horst Rogalla, which is the leading group in fabricating high-quality high T_c Josephson junctions, we have studied the response of a

YBCO/PBCO/YBCO ramp-type junction to coherent radiation at 176 GHz and 270 GHz. The I-V characteristic of the junction closely resembles the prediction of the resistively-shunted-junction (RSJ) model. The critical current and normal resistance product $I_c R_n$ of the junction is 0.25 mV at 5 K. The millimeter-wave radiation is coupled to the junction via a quasi-optical structure that focuses the radiation onto the junction through a yttrium-stabilized ZrO_2 substrate. At 176 GHz, we have observed as many as six Shapiro steps at the maximum power level of our Gunn Oscillator-pumped frequency doubler. This implies a Josephson oscillation up to 1 THz. Shapiro steps are still visible up to 65 K, as shown in figure 8.

The amplitudes of the zeroth, first, and second Shapiro steps, as functions of the square root of the radiation power, agree remarkably well with a Bessel function fit, as shown in figure 9. This Bessel-like behavior is an indication that the junction is voltage-biased at the radiation frequency. This is in great contrast to other experiments carried at lower frequencies, where a current-biased behavior is usually observed. For a voltage-biased RSJ-like junction, the detector response can be predicted analytically. The current responsivity of our device, defined as the induced dc current per unit RF power, is calculated to be 2×10^3 A/W, which is comparable to the quantum efficiency $e/h\omega \approx 1.4 \times 10^3$ A/W at this frequency.

We have also measured the response of the high- T_c Josephson junction to coherent radiation at 270 GHz. At this frequency, due to a combination of the heavy RF loss in the ZrO_2 substrate and the lack of radiation power, we have observed only the first Shapiro step.

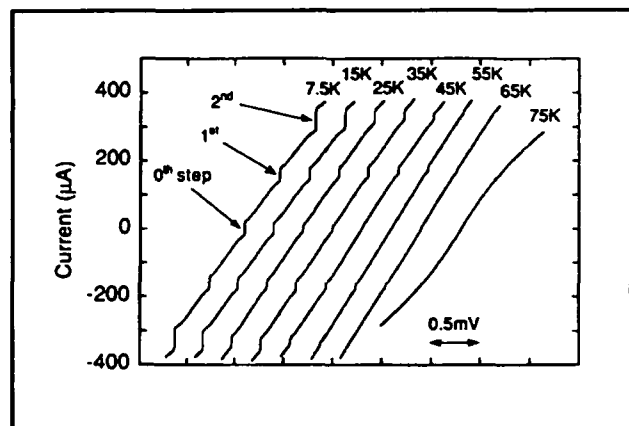


Figure 8. I-V curves of the high- T_c Josephson junction irradiated by coherent radiation at 176 GHz and taken at different temperatures. Shapiro steps are still visible at 65 K.

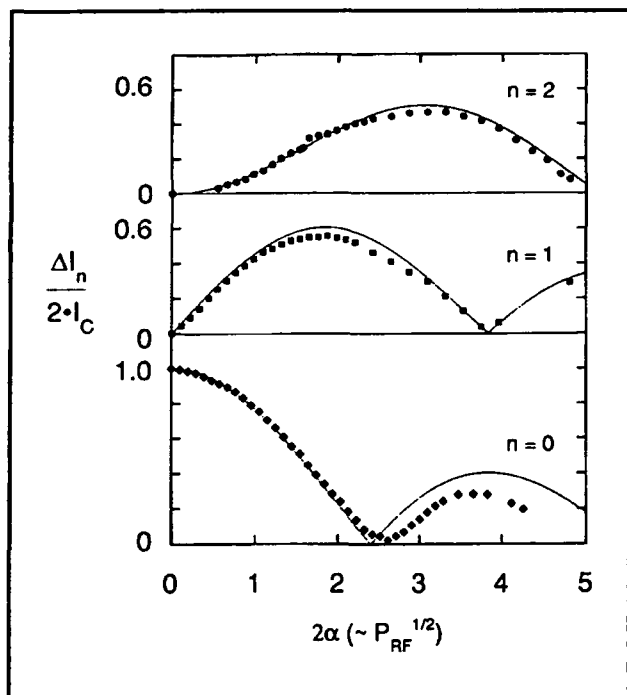


Figure 9. Measured amplitudes (normalized by the critical current in the absence radiation) of the zeroth, first, and second Shapiro steps as functions of the square root of radiation power at 176 GHz near 5 K. The solid lines are Bessel functions.

3.5 Far-infrared (THz) Lasers Using Multiple Quantum Wells

Sponsor

U.S. Army - Research Office
Grant DAAL03-92-G-0251

Project Staff

Jurgen H. Smet, Zachary K. Lee, Professor Qing Hu, in collaboration with Professor Clifton G. Fonstad, Jr.

Semiconductor quantum wells are man-made quantum mechanical systems in which the energy levels can be chosen by changing the sizes of the quantum wells. Typically, the frequency corre-

sponding to the intersubband transitions is in the far-infrared or THz range. Naturally, long-wavelength photoelectric devices, such as far-infrared lasers, which utilize the intersubband transitions have been proposed and subsequently studied.

Significant progress has been made recently toward this goal. Large oscillator strengths of intersubband transitions have been observed in far-infrared absorption spectroscopy experiments. An intersubband spontaneous emission with a power level of $\sim 10^{-7}$ W has been observed. Although these preliminary results are encouraging, two major challenges to building a quantum-well far-infrared laser still remain. One is to achieve a high degree of population inversion between two subband levels, and the other is the confinement of photons within the active region. Optical pumping suffers from low efficiency and low modulation speed. Thus, it will be difficult to achieve a sufficient gain to maintain a lasing oscillation, and, therefore, unsuitable for communication applications. As far as optical confinement is concerned, the usual dielectric waveguide confinement method, commonly used in optical and near-infrared laser systems, is not applicable at far-infrared frequencies because the confinement (on the order of a wavelength) is too large compared to the dimensions of the active region.

In this project, we will use a novel multiple quantum-well (MQW) device to circumvent these two problems. In this device, whose energy band diagram is shown in figure 10 with and without a dc bias voltage, electrons are injected selectively into an upper subband level of a wide lasing quantum well through a narrow filter quantum well. After relaxing into a lower subband in the lasing well, the electrons are then removed selectively to a collector through another narrow filter quantum well. This filter well prevents the electrons in the upper subband level from tunneling out to the collector. Using this method of selective injection and removal, a high degree of population inversion can be achieved, provided the tunneling rate of the electrons from the ground state to the collector is greater than the relaxation rate of the electrons from the upper subband to the ground state. Our calculation indicates that this should be achieved easily.

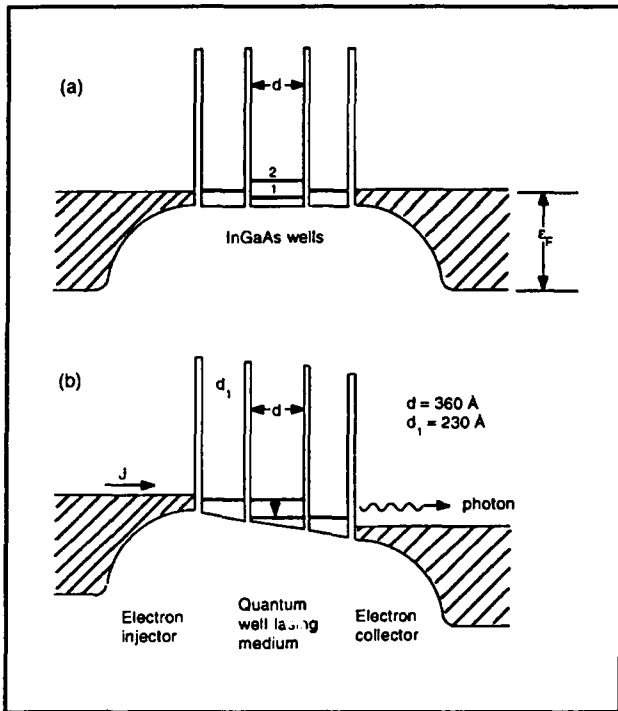


Figure 10. Band profiles (not drawn in proportion) of the proposed far-infrared laser device under (a) zero-bias, and (b) lasing condition in which $V_{\text{bias}} \sim (E_2 - E_1)/e E \approx 20$ mV. The device consists of one narrow quantum-well energy filter on both sides of the lasing quantum well. The width of the narrow filter wells (made of $\text{In}_{0.53}\text{Ga}_{0.47}\text{As}$) is approximately 230 Å so the energy of its first subband lies in between the first two subbands in the wide lasing well whose width is approximately 360 Å, and will have a radiation frequency of 5 THz due to the intersubband transitions.

In the proposed MQW laser device, a parallel-plate waveguide that confines the photons can be formed between a heavily doped semiconductor injector and collector. At a doping level of $2 \times 10^{18}/\text{cm}^3$, we can raise the plasma frequency in the injector and collector to about 17 THz. It has been reported that the electron mobility, μ , for such a high doping level is $5 \times 10^3 \text{ cm}^2/\text{Vs}$. This plasma is mostly reflective with a penetration depth as short as $0.8 \mu\text{m}$ for a lasing frequency in the range of 1-8 THz. This confinement is sufficiently tight so that the lasing threshold current density is on the order of several hundred A/cm^2 , which should be achievable.

The first step of this project is to fabricate multiple-quantum-well structures with different well widths and barrier thicknesses and to perform tunneling spectroscopy on them to determine the relative positions of the subbands in different quantum wells. Because of the small energy differences which are associated with the relatively wide quantum wells, the tunneling spectroscopy must be performed at liquid helium temperatures. Our initial

measurements on the tunneling I-V characteristics revealed many features which could be attributed to elastic tunneling and LO phonon-assisted inelastic tunneling.

To interpret the fine features of the I-V characteristics with a greater certainty, we have employed a powerful method, magnetotunneling spectroscopy, to study the relative positions of the subbands. In addition to spectroscopy, this study has a practical purpose for laser applications. The nonradiative intersubband relaxation rate due to phonon emissions is much greater than that of the radiative relaxation rate. This is mainly because the transverse motion of electrons in the lasing quantum well is unrestricted, so there is a large volume in the phase space into which the electrons can be scattered. Similar to the concept employed in a tokamak to confine plasmas, a strong magnetic field will restrict the electron motions in the transverse directions. This magnetic field-induced transverse confinement, along with the longitudinal confinement provided by the quantum well, will effectively reduce the dimensionality of the electron system to that of a zero-dimensional system, exactly like that of quantum dot systems. Therefore, the nonradiative relaxation rate can be substantially reduced. Because the magnetic field does not affect the longitudinal motion of electrons, electrical pumping is still possible. This is difficult to implement for quantum dot systems which are formed geometrically.

We have performed magnetotunneling spectroscopy on a double quantum-well structure which consists of 115-Å and 200-Å $\text{In}_{0.53}\text{Ga}_{0.47}\text{As}$ quantum wells, both are confined by 30 Å of $\text{In}_{0.52}\text{Al}_{0.48}\text{As}$ respectively on the top and bottom and separated by a 60-Å $\text{In}_{0.52}\text{Al}_{0.48}\text{As}$ middle barrier. When a longitudinal magnetic field is applied, the tunneling current is modulated by the field, as shown in figure 11(a). The magnetooscillation is periodic with the inverse of the magnetic field $1/B$. Thus, a Fourier transform of this magnetooscillation in $1/B$ gives a peak which centers at a characteristic field B_0 .

The physical origin of this magnetooscillation is scattering-mediated inter-Landau level tunneling. Suppose the energy in the first well is given by $E_1 + (n_1 + 1/2)\hbar eB/m^*$, and the energy in the second well is $E_2 + (n_2 + 1/2)\hbar eB/m^*$, where E_1 and E_2 are the energies of the subbands in the first and second well under concern. In the absence of LO phonon emissions, energy conservation requires that the two energies are equal. Thus, $(n_2 - n_1)/\hbar eB/m^* = E_1 - E_2$ or $1/B = (n_2 - n_1)/\hbar e/m^*(E_1 - E_2)$. This implies that whenever $1/B$ is an integer times the inverse of a characteristic field $1/B_0 = \hbar e/m^*(E_1 - E_2)$, the energy conservation is satisfied and the tunneling current will be enhanced,

which gives the oscillatory behavior of the tunneling current as a function of $1/B$, as shown in figure 11(a).

This magnetooscillation provides us with very important information about the relative positions of the subbands under concern. The energy difference between the two subbands is related to B_0 through $E_1 - E_2 = \hbar e B_0 / m^*$. Thus, the energy difference can be measured directly using the magnetotunneling spectroscopy. Since the energy difference $E_1 - E_2$ changes linearly with the bias voltage, so is the characteristic field B_0 . By measuring B_0 as a function of the bias voltage, we can determine the fraction of the total applied bias voltage dropped across the two wells.

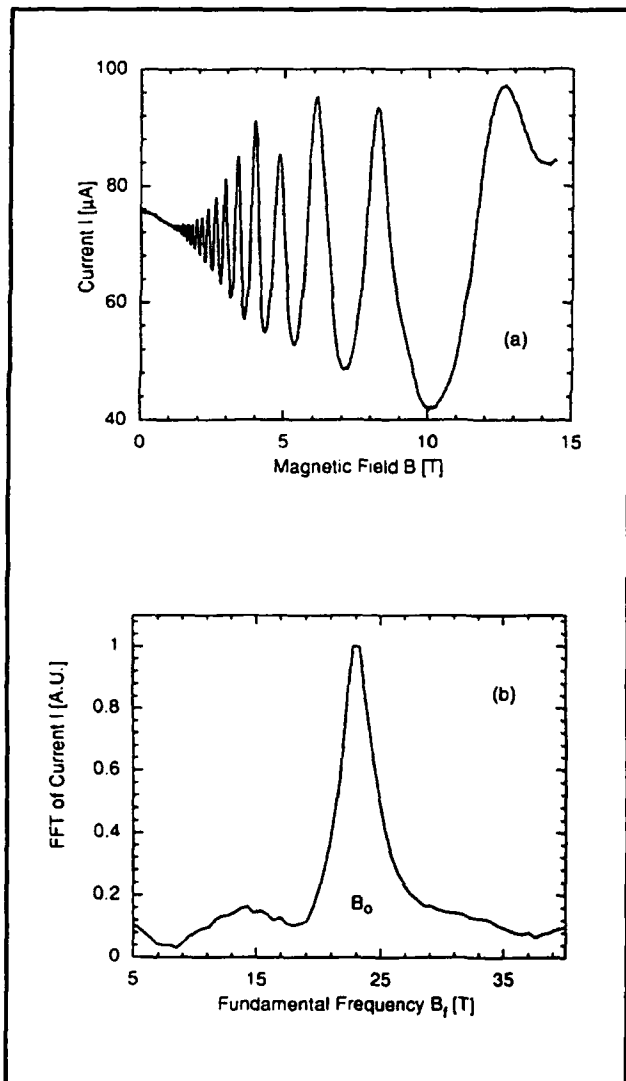


Figure 11. (a) Tunneling current (at a fixed bias voltage) as a function of the strength of a magnetic field applied in the same direction as that of the tunneling current. (b) Fourier transform of the tunneling current as a function of $1/B$.

3.6 Publications

Feng, S., and Q. Hu, "Far-infrared Photon-assisted Transport Through Quantum Point Contact Devices." Submitted to *Phys. Rev. B*, 1993.

Gupta, R., Q. Hu, D. Terpstra, G.J. Gerritsma, and H. Rogalla. "Near-millimeter-wave Response of High- T_c Ramp-type Josephson Junctions," Submitted to *Appl. Phys. Lett.*, 1993.

Hu, Q. "Photon-assisted Quantum Transport in Quantum Point Contacts." *Appl. Phys. Lett.* 62: 837 (1993).

Hu, Q., R.A. Wyss, C.C. Eugster, J.A. del Alamo, S. Feng, M.J. Rooks, and M.R. Melloch. "A Novel Submillimeter-wave Detector Using Quantum Point Contacts." *Proceedings of the Fourth International THz Conference*, University of California at Los Angeles, April 1993.

Wyss, R.A., C.C. Eugster, J.A. del Alamo, and Q. Hu. "Far-infrared Photon-induced Drain/Source Current in a Quantum Point Contact." Submitted to *Appl. Phys. Lett.*, 1993.

Thesis

Garcia, E.A. *Fabrication of All-Nb SIS Tunnel Junctions for Submillimeter-wave Detectors*. S.M. thesis. Dept. of Electr. Eng. and Comput. Sci., MIT, 1992.

Section 4 Surfaces and Interfaces

Chapter 1 Statistical Mechanics of Surface Systems and
Quantum-Correlated Systems

Chapter 2 Synchrotron X-Ray Studies of Surface Disordering

Chapter 3 Chemical Reaction Dynamics at Surfaces

Chapter 4 Semiconductor Surface Studies

Chapter 5 Epitaxy and Step Structures on Semiconductor
Surfaces

Chapter 1. Statistical Mechanics of Surface Systems and Quantum-Correlated Systems

Academic and Research Staff

Professor A. Nihat Berker

Graduate Students

Daniel P. Aalberts, Alexis Falicov, William C. Hoston, Jr., Roland R. Netz

1.1 Introduction

Sponsor

Joint Services Electronics Program
Contract DAAL03-92-C-0001

Our objectives are to develop, using renormalization-group theory and other methods of statistical mechanics, microscopic theories of quantum electronic systems and of semiconductor alloy systems that properly account for correlation effects. Our approach is particularly suited to systems with fluctuations due to finite temperatures, impurities, surfaces or other geometric constraints.

1.2 Renormalization-Group Approach to Electronic Systems

Project Staff

Alexis Falicov, Professor A. Nihat Berker

High- T_c superconductivity, metallic magnetism, the metal-insulator transition, and heavy fermion behavior are all phenomena produced by the strong correlations of electrons in narrow energy bands. It is therefore important to study theoretical models that incorporate the strong correlation effects of electrons. The tJ model is such a system. It is defined on a lattice with one spherically symmetric orbital per site by the Hamiltonian

$$\mathcal{H}_U =$$

$$P \left[-t \sum_{\langle ij \rangle, \sigma} (c_{i\sigma}^\dagger c_{j\sigma} + \text{h.c.}) \right. \\ \left. + J \sum_{\langle ij \rangle} (\vec{s}_i \cdot \vec{s}_j - n_i n_j / 4) \right] P,$$

where P is an operator that projects out all doubly occupied sites, $c_{i\sigma}^\dagger$ and $c_{i\sigma}$ are creation and annihilation operators for an electron in a Wannier state at site i with z -component of spin σ , n_i is the electron number operator that counts the total number of electrons at site i , and \vec{s}_i is the spin operator. This Hamiltonian can be interpreted in two ways: (1) In the case of small J , the system can be thought of as the large U limit of the single-band Hubbard model of electronic systems. The antiferromagnetic exchange comes as a result of a virtual process where one electron hops onto a singly occupied nearest-neighbor site and then hops back. The energy gain for such a process is of the order of t^2/U since a doubly occupied site has energy U . (2) The system can also be thought of as an electronic system with a "super" exclusion principle where no two electrons (like or unlike spins) are allowed on the same site. The second interpretation does not put any restriction on the size of J .

There are few rigorous results available on this system: (1) At half filling, the system reduces to a Heisenberg antiferromagnet; (2) At $2t = \pm J$, the model has been solved by the Bethe-ansatz technique; and (3) In one dimension and $J = 0$, the model has been solved also by the Bethe-ansatz technique. Other attempts to study this model have focused on the ground state and the first few excited states. We have decided, instead, to focus on the thermodynamic properties of this system. Our method, the renormalization-group approach, involves solving a statistical mechanics problem by a recursive elimination of the degrees of freedom. Since the Hamiltonian involves a regular lattice, this problem is well suited for the position-space renormalization-group method. The solution is obtained in an expanded space with Hamiltonian

$$\mathcal{H} =$$

$$P \left[-t \sum_{\langle ij \rangle, \sigma} (c_{i\sigma}^\dagger c_{j\sigma} + \text{h.c.}) \right. \\ \left. + \sum_{\langle ij \rangle} (\vec{J}_{ij} \cdot \vec{S}_i \vec{S}_j + V n_i n_j) + \mu \sum_i n_i \right] P.$$

Because of the non-commutativity of quantum operators, we had to develop new techniques of renormalization-group theory.

We have obtained the renormalization-group flows for the effective coupling constants for one-, two-, and three-dimensional systems. The flows determine the phase diagrams and all thermodynamic properties. In one dimension, we find, as expected, no finite-temperature phase transition. In two dimensions, we find a single finite-temperature critical point, as previous researchers conjectured but were unable to derive.

In three dimensions, we find a global finite-temperature phase diagram that is richly structured. Disordered, antiferromagnetic, and conducting phases are separated by first- and second-order phase boundaries, which are themselves delineated by lines of tricritical points, critical points, and critical endpoints. Complicated structures with multiple reentrances occur. We have also calculated, using our renormalization-group transformation, electronic densities and nearest-neighbor correlations as a function of electronic chemical potential. These yield a microscopic understanding of the different phases. We have also completed small-cluster calculations which cannot yield phase transitions, but which support the densities and correlations of the renormalization-group theory.

1.3 Suzuki-Trotter Approach to Electronic Systems

Project Staff

Daniel P. Aalberts, Professor A. Nihat Berker

It is possible to rigorously map d-dimensional quantum mechanical spin systems onto (d+1)-dimensional classical systems with more complicated interactions. This method, introduced by Suzuki, uses the Trotter formula and is the analog for statistical mechanics of the Feynman-path approach to particle propagators.

We are investigating the possibility of adapting this approach to electronic systems where, in more than

one dimension, fermion statistics complicates the classical problem. By numerical simulation, the resulting classical models will be used to confirm the renormalization-group results mentioned above.

1.4 Phase Diagrams of Semiconductor Alloys

Project Staff

William C. Hoston, Jr., Professor A. Nihat Berker

We are conducting a study of ternary compounds on face-centered-cubic lattices. Our aim is to elucidate the phase behavior of ternary and quaternary semiconductor alloys. These alloys could exist in the zincblende, chalcopyrite, or possibly stannite structures, involving two interpenetrating fcc lattices on which up to four atomic species exist. One atomic species occupies one of the fcc lattices while three other atomic species may (chalcopyrite, stannite) or may not (zincblende) order on the other fcc lattice. At present, the chalcopyrite structure is seen experimentally in the III-V compounds. The ranges of stability of these structures are of interest.

In previous work by K.E. Newman and collaborators, the Blume-Emery-Griffiths model has been adopted for the study of the zincblende to chalcopyrite or stannite transitions. This model is a spin-1 Ising model with Hamiltonian

$$\mathcal{H} = J \sum_{\langle ij \rangle} s_i s_j + K \sum_{\langle ij \rangle} s_i^2 s_j^2 \\ - \Delta \sum_i s_i^2, \quad s_i = 0, \pm 1.$$

The three spin values are each associated with a different species of atom, A, B, or C, which exist on one of the fcc lattices. The other fcc lattice is considered occupied by atomic species D. The systems under consideration have the composition $[(AB)_{1-x}C_{2x}]D_2$. The model includes interactions between the A, B, and C atoms. The parameters J and K in the Hamiltonian above are fixed as combinations of these interaction energies. They are chosen to give the chalcopyrite structure at low temperature ($J < 0$) and to control the phase transition between the chalcopyrite and the zincblende. Δ controls the relative densities of the species (AB) and C.

These systems contain competing, frustrated interactions, which necessitate a renormalization-group treatment. We have been able to develop a renormalization-group transformation that yields both the

ferromagnetic and, in contrast with previous work, the (fully frustrated) antiferromagnetic phase transitions on the fcc lattice in the spin-1/2 limit obtained by taking Δ to negative infinity. We are now pursuing the global phase diagram in thermodynamic field (interaction constant) space, which will be followed by a study of density space.

1.5 Renormalization-Group Theory of an Internal Critical Endpoint Structure

Project Staff

Roland R. Netz, Professor A. Nihat Berker

A prefaced renormalization-group study has been completed, indicating that all three new features of the Blume-Emery-Griffiths model with repulsive biquadratic interaction survive fluctuations in three dimensions but not in two dimensions. These features are: (1) a critical endpoint structure occurring inside the ferromagnetic phase; (2) disordered-ferromagnetic-disordered reentrance; and (3) a ferrimagnetic phase sandwiched between the ferromagnetic and antiquadrupolar phases. The renormalization-group mechanism for a critical endpoint structure inside the ordered phase is shown to be the same as that originally found for a critical endpoint structure inside the disordered phase, namely a distinct hybrid fixed point, contrary to a previous claim. This critical-endpoint structure may have been seen experimentally in the analogous alloy system of FeBr_2 .

1.6 Phase Diagrams of the Ising Model on the Square Lattice with Crossed Diagonal Bonds

Project Staff

Professor A. Nihat Berker

The global phase diagram of the spin-1/2 Ising model with nearest- and next-nearest-neighbor interactions on the square lattice has been considered, including the fully anisotropic cases. A closed-form expression has been deduced that accurately represents the phase boundaries when the crossed next-nearest-neighbor interactions are not of opposite signs. The phase diagram includes disordered, ferromagnetic, antiferromagnetic, axially single-striped, and diagonally double-striped phases.

1.7 Publications

Berker, A.N. "Critical Behavior Induced by Quenched Disorder." *Physica A*. Forthcoming.

Berker, A.N., R.G. Caflisch, and M. Kardar. "Statistical Mechanics of Phase Transitions with a Hierarchy of Structures." In *Hierarchically Structured Materials*. Ed. I.A. Aksay. Pittsburgh: Materials Research Society, 1992.

Berker, A.N., and K. Hui. "Phase Diagram of the Ising Model on the Square Lattice with Crossed Diagonal Bonds." Submitted to *Phys. Rev. B*.

Netz, R.R. "Microscopic Theory of the Ripple Phase." In *The Structure and Conformation of Amphiphilic Membranes*. Eds. R. Lipowsky, D. Richter, and K. Kremer. Berlin: Springer-Verlag, 1992.

Netz, R.R. "New Phases and Multiple Reentrance of the Blume-Emery-Griffiths Model with Repulsive Biquadratic Coupling: Monte Carlo Renormalization-Group Theory." *Europhys. Lett.* 17(4): 373-377 (1992).

Netz, R.R. "Symmetry-Breaking Fields in Frustrated Ising Systems on Square and Cubic Lattices." *Phys. Rev. B* 46(2): 61-64 (1992).

Netz, R.R., and A.N. Berker. "Microscopic Liquid Crystal Theory of Nematic Reentrance, Smectic C Ordering, and In-Plane Domain Formation." In *Phase Transitions in Liquid Crystals*. Eds. S. Martellucci and A.N. Chester. New York: Plenum Press, 1992.

Netz, R.R., and A.N. Berker. "Renormalization-Group Theory of an Internal Critical Endpoint Structure: The Blume-Emery-Griffiths Model with Biquadratic Repulsion." *Phys. Rev. B*. Forthcoming.

Netz, R.R., and A.N. Berker. "Smectic C Order, In-Plane Domains, and Nematic Reentrance in a Microscopic Model of Liquid Crystals." *Phys. Rev. Lett.* 68(3): 333-336 (1992).

Meeting Papers

Aalberts, D.P., and A.N. Berker. "Hard-Spin Mean-Field Theory: Variational Free Energy and First-Order Phase Transitions." Paper presented at the American Physical Society Meeting, Indianapolis, Indiana, March 16-20, 1992.

Berker, A.N. "Critical Behavior Induced by

Quenched Disorder." Paper presented at the International Conference on Thermodynamics and Statistical Mechanics, Berlin, Germany, August 2-8, 1992.

Berker, A.N. "Phase Transitions in Disordered Systems." Paper presented at the Summer School on Recent Developments in Statistical Physics, Istanbul, Turkey, July 26-August 6, 1993.

Berker, A.N., and K. Hui. "Closed-Form Expression for the Global Phase Diagram of the Ising Model on the Square Lattice with Crossed Diagonal Bonds." Paper presented at the American Physical Society Meeting, Seattle, Washington, March 22-26, 1993.

Berker, A.N., and R.R. Netz. "Smectic C Order, In-Plane Domains, and Nematic Reentrance in a Frustrated Microscopic Model of Liquid Crystals." Paper presented at the American Physical Society Meeting, Indianapolis, Indiana, March 16-20, 1992.

Netz, R.R. "Multiple Reentrance and New Phases from the Blume-Emery-Griffiths Model in Three Dimensions: Monte Carlo Renormalization-Group Theory." Paper presented at the American Physical Society Meeting, Indianapolis, Indiana, March 16-20, 1992.

Netz, R.R. "Symmetry-Breaking Fields in Frustrated Ising Systems on Square and Cubic Lattices." Paper presented at the American Physical Society Meeting, Indianapolis, Indiana, March 16-20, 1992.

Netz, R.R., and A.N. Berker. "Renormalization-Group Theory of the Blume-Emery-Griffiths Model with Repulsive Biquadratic Coupling." Paper presented at the General Conference of the Condensed Matter Division of the European Physical Society, 13th, Regensburg, Germany, March 29-April 2, 1993.

Netz, R.R., and A.N. Berker. "Renormalization-Group Theory of an Internal Critical Endpoint Structure: The Blume-Emery-Griffiths Model with Biquadratic Repulsion." Paper presented at the American Physical Society Meeting, Seattle, Washington, March 22-26, 1993.

Netz, R.R., and A.N. Berker. "Smectic C/A₂ Order, Domains, Reentrance in a Microscopic Model of Liquid Crystals." Paper presented at the International Conference on Thermodynamics and Statistical Mechanics, Berlin, Germany, August 2-8, 1992.

Chapter 2. Synchrotron X-ray Studies of Surface Disordering

Academic and Research Staff

Professor Robert J. Birgeneau, Dr. Kenneth I. Blum, Dr. Do-Young Noh

Graduate Students

William J. Nuttall, Monte J. Ramstad

Technical and Support Staff

Elizabeth M. McCaffery

2.1 Introduction

Sponsor

Joint Services Electronics Program
Contract DAAL03-92-C-0001

In this research program we use modern x-ray scattering techniques to study structures and phase transitions in thin films and on surfaces. We have two principal experimental facilities, one at MIT and the other at the National Synchrotron Light Source at Brookhaven National Laboratory. At MIT, we have four high-resolution computer-controlled x-ray spectrometers. The angular resolution can be made as fine as 1.8 seconds of arc, which enables us to probe the development of order from distances of the order of the x-ray wavelength $\sim 1\text{\AA}$, up to 30,000 \AA . The sample temperature can be varied between 2 K and 500 K with a relative accuracy of 2×10^{-3} K. At the National Synchrotron Light Source, in collaboration with IBM, we have three fully instrumented beam lines. Two of these beam lines allow us to make studies with photons varying in energy between 3 and 12 keV; the third has a fixed energy of 17 keV. These facilities make possible high-resolution scattering experiments with a flux of more than three orders of magnitude larger than that of a rotating anode x-ray generator.

Several years ago, as part of this JSEP program, we built an x-ray-compatible, high-vacuum single crystal apparatus. This enabled us to use synchrotron radiation to study the structures and transitions occurring at a single surface, and such experiments are now becoming routine. In collaboration with Professor Simon G.J. Mochrie, we have now designed, built and commissioned a second-generation x-ray surface facility which is extremely versatile allowing a wide range of surface scattering experiments.

Our basic scientific objective is to understand the morphologies and microscopic structures of simple semiconductor and metal surfaces at high temper-

ature. Possible phase changes include surface roughening, surface reconstruction, melting, amorphization and dilution. These phenomena are particularly interesting on stepped surfaces, where there may be an interplay between step structures, faceting, reconstruction, and roughening.

2.2 Metal Surface Studies

Step interactions play a central role in determining the equilibrium morphology of a crystalline surface. Different interactions are known to result in such diverse phenomena as step pairing, surface faceting, and surface roughening. A small density of steps may be incorporated onto a metal surface by deliberately cutting the crystal at an angle slightly off from a high symmetry direction. If the high symmetry surface does not reconstruct, the theory of equilibrium crystal shapes (ECS) predicts that at low temperatures the steps should either cluster together or spread uniformly across the surface. In the former case, a "hill and valley" structure of densely stepped rough regions coexisting with flat, high symmetry facets will result. The fraction of the surface comprised of flat facets should decrease with increasing temperature, falling to zero at some temperature below the roughening transition temperature of the facet. In the latter case, the surface is predicted to be rough at all temperatures. That is, entropically wandering steps should result in a logarithmic divergence of the mean square height fluctuations as a function of lateral distance across the surface. X-ray scattering, low energy electron diffraction and atom scattering studies have reported surface roughening of numerous metal crystalline facets, including Cu(110), Ag(110), Cu(113) and Ni(113). In addition, studies of vicinally miscut Cu(110) and Ag(110) have reported low temperature surface phase separation into a hill and valley structure.

The situation for Ag(110) is, however, controversial. In 1987 we carried out a high resolution x-ray scat-

tering study of a vicinal Ag(110) surface using a crystal which had been inadvertently miscut by $\sim 0.5^\circ$; we interpreted the data on the basis of a roughening transition of the flat (110) facets at ~ 725 K. More recently, Robinson and coworkers have re-addressed this problem using a Ag(110) crystal miscut by $\sim 0.2^\circ$. They assert that, in equilibrium, their 0.2° vicinal Ag(110) surface phase separates into flat (110) facets together with stepped regions for temperatures below 790 K and that a uniform step structure is only stable above that temperature. In order to resolve this controversy and to understand generally the behavior of stepped Ag(110) surfaces, we have carried out x-ray scattering and scanning tunneling microscopy (STM) studies of a Ag(110) sample miscut 1° from the (110) axis along the (110) direction. The STM measurements have been performed at IBM by R.M. Feenstra and G.A. Held.

For a clean and well annealed surface, we find that at all temperatures above 300 K, the surface is comprised of a uniform density of single atomic height meandering steps. That is, we find no evidence for vicinal phase separation. However, as the surface is annealed to sufficiently high temperatures, we find that impurities are driven to the surface and that this, in turn, results in the formation of large, flat (110) terraces. The latter is the behavior reported by Robinson and coworkers although they interpreted their data assuming a clean surface. For the clean surface we observe diffraction characteristic of uniform, albeit meandering, steps at all temperatures between 300 K and 875 K. With increasing temperature, the step peaks lose intensity and undergo an evolution in lineshape consistent with a decrease in step-step correlations, most noticeably in the (001) direction. While our data above 670 K are consistent with a rough surface, the peak evolution is not consistent in detail with the simplest model of entropically repulsive steps.

2.3 Semiconductor Surface Studies

As discussed above, vicinal surfaces, that is, surfaces of crystals cut close to a high symmetry direction, exhibit remarkably rich and diverse physical behavior. At equilibrium, such surfaces may exhibit roughening, faceting, and/or reconstruction transitions. Novel non-equilibrium phenomena also may occur. One of the most interesting and well-studied systems is vicinal Si(111). At temperatures immediately above the 1×1 to 7×7 reconstruction transition at 1100 K, this surface can be described by flat (111) terraces separated by uniformly spaced single Si(111) bilayer steps. In recent synchrotron x-ray experiments we demonstrated that the "uni-

formly" stepped surface is in fact rough with logarithmically divergent height fluctuations. Below 1100 K the $1 \times 1 \rightarrow 7 \times 7$ transition drives a faceting transition in which the steps phase-separate yielding flat, reconstructed (111) terraces and well-ordered but higher-angle stepped regions.

We have determined the temperature dependence of the surface roughness above 1100 K, a regime where significant numbers of atoms sublime. Remarkably, the surface height fluctuations exhibit a logarithmic divergence up to 1275 K even under significant sublimation. This is best represented by a power-law line shape diffraction profile of the step lattice characterized by the exponent η . Representative power law diffraction profiles are shown in figure 1. At ~ 1275 K, the surface undergoes a sharp morphological transition to one characterized by large uniform (111) terraces plus highly disordered stepped regions. This faceting was apparently observed previously, although on a Si(111) surface with a very small miscut ($8'$) compared with a 3° miscut on our Si(111) sample.

Our x-ray experiment reveals that the faceting is accompanied by a step disordering transition in which the step correlations change drastically. Above the disordering transition the height fluctuations of the surface diverge much faster than the thermal logarithmic divergence. Data on the stepped region diffraction peak position and width are shown in figure 2. We speculate that the "transition" is a non-equilibrium phenomenon driven by a combination of sublimation and electromigration. Our results are consistent with theoretical predictions for growing stepped surfaces. The discovery of this new transition on thoroughly studied and structurally perfect silicon surfaces should cast light on the general problems of surface morphology at high temperatures.

2.4 Model Surface Overlayers

Much of the basic physics of surface systems, including both clean surfaces and surfaces with physisorbed or chemisorbed overlayers, is determined by general structural and symmetry considerations. For this reason, experiments on model systems such as rare gas overlayers on graphite can provide important insights with implications for all surface systems. An important illustration of this is the chiral 3-states Potts model description of the melting of the 1×3 reconstruction of Si(113) as described by Simon G.J. Mochrie in this report. The theory for this semiconductor surface transition was originally developed to describe the melting of the $\sqrt{3} \times \sqrt{3}$ structure of monolayer krypton on graphite.

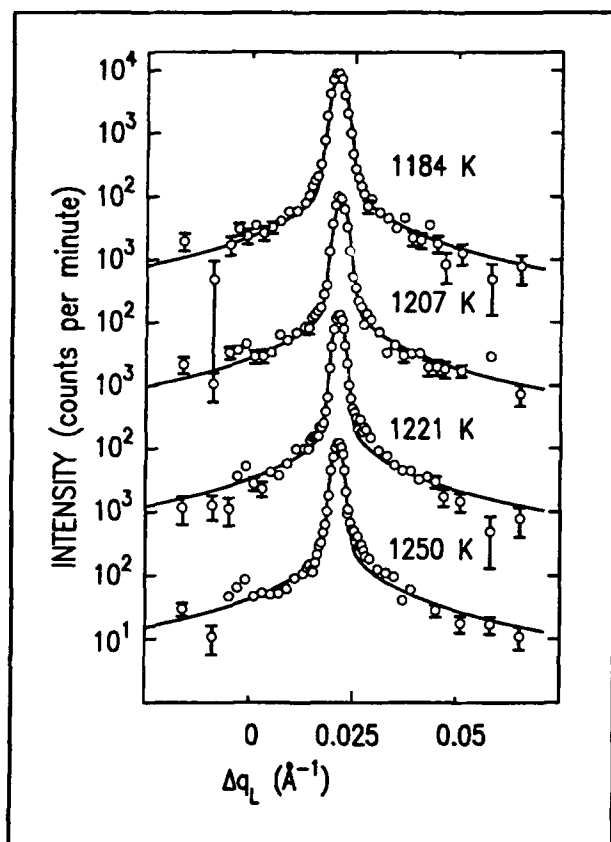


Figure 1. Longitudinal scans of the primary step superlattice peak for a 3° miscut Si(111) crystal below 1270 K with background subtracted. The scans are plotted relative to the integer order peak position of the (111) facets. The solid curves are the results of fits to a power law singularity form for the step correlations. There is no change in the lineshape in this temperature range other than sharpening due to annealing.

Recently, we have carried out a series of experiments on xenon overlayers physisorbed onto single crystal graphite. These experiments have focused on two issues: (1) the evolution of the structure as a function of temperature for one, two, three and six layers; and (2) the nature of the melting transition for coverages in the monolayer region. Results of both sets of experiments are still being analyzed.

The essential features of the multilayer studies may be summarized as follows. Monolayer xenon exhibits a commensurate-incommensurate transition at about 65 K. Bilayer xenon exhibits more elaborate behavior. For temperatures above 60 K, the two layers have the same lattice constant with a value incommensurate with respect to the substrate. At ~ 60 K the layer of xenon closest to the graphite locks into registry with the substrate while the second layer remains incommensurate. On the

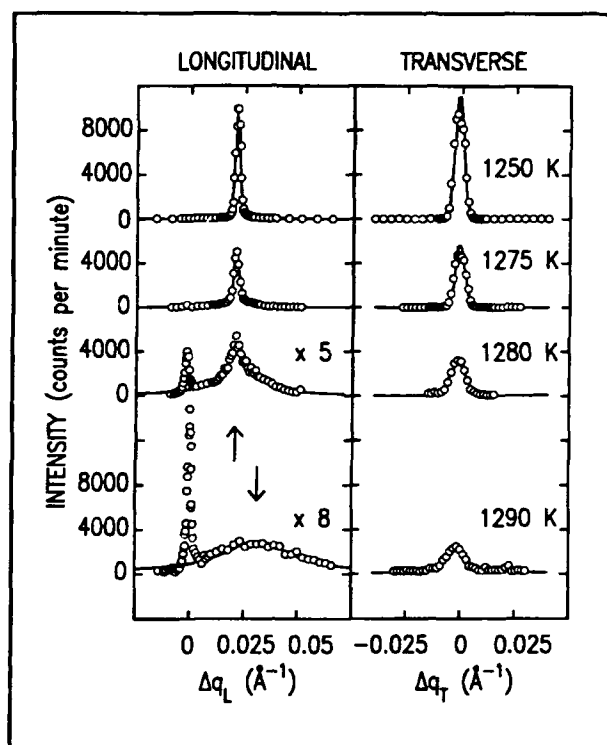


Figure 2. Longitudinal and transverse scans of the step superlattice peak across the disordering transition near 1275 K. The solid curves are the results of fits of the step peak to an anisotropic displaced Lorentzian. Note the drastic change in the width of the longitudinal scans.

other hand, the three- and six-layer xenon systems remain uniform and incommensurate at all temperatures.

Monolayer xenon on graphite has been viewed as a model system for studying melting in two dimensions. There is, however, disagreement in the interpretation of thermodynamic and scattering data on the order of the melting transition at various coverages. Specifically, scattering studies suggest a continuous melting process whereas thermodynamic data have been interpreted on the basis of first order melting transition for coverages near but below one monolayer. We have studied the melting as a function of pressure and hence chemical potential at fixed temperatures of 121 K, 140 K, and 146 K. At the two higher temperatures, we find that the solid diffraction peak decreases progressively in intensity with decreasing pressure evolving continuously into the diffraction pattern characteristic of a strongly correlated fluid with well-developed orientational order. This necessitates that the melting transition is at least nearly continuous. We are currently carrying out a detailed line-shape analysis of the diffraction profiles to obtain quantitative information on the melting transition.



Professor Sylvia T. Ceyer

Chapter 3. Chemical Reaction Dynamics at Surfaces

Academic and Research Staff

Professor Sylvia T. Ceyer, Dr. Yulin Li, Dr. David P. Pullman, Dr. Athanassios A. Tsekouras, Dr. Arthur L. Utz

Graduate Students

Sean P. Daley, David B. Gosalvez, Theodore R. Trautman, Julius J. Yang

Technical and Support Staff

Anne Stollerman

3.1 A New Mechanism for Dissociative Chemisorption on Si: Atom Abstraction

Sponsor

Joint Services Electronics Program
Contract DAAL03-92-C-0001

Project Staff

Professor Sylvia T. Ceyer, Dr. Yulin Li, Dr. David P. Pullman, Dr. Athanassios A. Tsekouras, David B. Gosalvez, Julius J. Yang

F_2 is known to adsorb on Si(100) at 300 K with close to unit probability in the zero coverage limit. We have shown that the adsorption mechanism involves both the common mechanism for dissociative adsorption, whereby both fluorine atoms of the molecule adsorb, and a new mechanism, fluorine atom abstraction. In the abstraction mechanism, the Si surface captures one of the fluorine atoms from the incident F_2 molecule, while the other F atom scatters back into the gas phase.

This observation was made in a UHV molecular beam surface scattering apparatus by monitoring the directly scattered F atom signal with a triply differentially pumped quadrupole mass spectrometer. The scattered F atom signal is readily distinguishable from the F^+ signal due to cracking of the unreacted F_2 in the electron bombardment ionizer by its time of flight spectrum. The directly scattered F atoms are significantly more energetic, indicating that some of the exothermicity of this reaction is channeled into translation.

We have also taken measurements of the abstraction mechanism as a function of the incident F_2 energy, incident angle, surface temperature, and fluorine coverage. In addition, we have shown that the Si dangling bonds are the sites for fluorine

adsorption and are probably responsible for the abstraction mechanism. This was accomplished by directing a well-characterized, monoenergetic beam of He atoms at the surface covered with a monolayer of fluorine and monitoring the angular distribution of diffracted atoms. The results of He diffraction measurement show that the fluorine does not break the dimer bond characteristic of (2x1) reconstruction. While the binding of fluorine to the dangling bonds along with the maintenance of the surface Si dimer bond is not surprising, this study represents the experimental evidence for these adsorption sites.

The reaction of F_2 with Si(100) ceases after the dangling bonds are saturated at one monolayer of coverage. This lack of additional reactivity precludes build up of a sufficient layer of fluorine to produce the volatile etch product SiF_4 and therefore the use of F_2 as an etchant of Si. However, we have shown that if the kinetic energy of the incident F_2 molecule is increased above a threshold value of 4-5 kcal mol⁻¹ (0.2 eV), the dissociation probability of F_2 with a fluorinated surface increases linearly with the normal component of the kinetic energy.

This additional reactivity at higher translational energies, which results in fluorine coverages greater than one monolayer, is the result of surmounting a barrier to dissociation on the fluorinated surface. Measurements of the He atom diffraction spectra as a function of the incident F_2 kinetic energy indicate that the barrier is associated with dissociative chemisorption on the second layer of Si atoms as well as on Si dimer atoms. These conclusions are based on the identical rate of linear decay for all diffraction features with increasing F_2 normal energy above the threshold. There is no preferential cleavage of the Si dimer atoms. These observations may represent the first experimental correlation of the barrier for dissociation with the sites for dissociation.

Publications

- Ceyer, S.T., D.J. Gladstone, M. McGonigal, and M.T. Schulberg. "Molecular Beams: Probes of the Dynamics of Reactions on Surfaces." In *Physical Methods of Chemistry, Vol. IX A, Investigations of Surfaces and Interfaces*. 2nd ed. Eds. B.W. Rossiter and R.C. Baetzold. New York: Wiley, 1993. pp. 83-452.
- Li, Y.L., D.P. Pullman, J.J. Yang, A.A. Tsekouras, D.B. Gosalvez, K.B. Laughlin, M.T. Schulberg, D.J. Gladstone, M. McGonigal, and S.T. Ceyer. "Observation of a New Mechanism for Dissociative Chemisorption: F Atom Abstraction on Si(100)." Submitted to *Phys. Rev. Lett.*
- Li, Y.L., J.J. Yang, D.P. Pullman, and S.T. Ceyer. "Reaction Dynamics of F₂ on Si(100)." Paper presented at the Physical Electronics Conference, Irvine, California, June 20-25, 1992.
- Pullman, D.P., Y.L. Li, J.J. Yang, and S.T. Ceyer. "Reaction Dynamics of F₂ on Si(100)." Paper presented at the American Chemical Society Meeting, Washington, DC, August 24-28, 1992.
- Pullman, D.P., Y.L. Li, J.J. Yang, and S.T. Ceyer. "Reaction Dynamics of F₂ on Si(100)." Paper presented at the American Vacuum Society Meeting, Chicago, Illinois, November 9-13, 1992.

3.2 New Mechanisms for Surface Processes

Sponsor

National Science Foundation
Grant CHE 90-20623

Project Staff

Professor Sylvia T. Ceyer, Dr. Arthur L. Utz, Sean P. Daley, Theodore R. Trautman

We have recently shown that hydrogen can be embedded in the bulk of Ni by a new mechanism, collision induced absorption. A beam of monoenergetic Ar, Kr, or Xe atoms, produced by the supersonic expansion of the inert gas seeded in He, is directed at a monolayer of atomic hydrogen chemisorbed on Ni(111). We observed that impacts of the incident inert gas atoms induce absorption of chemisorbed hydrogen. The hydrogen absorbed is identified by appearance of a vibrational mode at 800 cm⁻¹ and appearance of a feature at 180-220 K in the thermal desorption

spectrum. This is consistent with our previous study of atomic hydrogen absorption into this crystal.

We have extended this work to include a study of the dynamics of collision induced absorption. We probe these dynamics by measuring the cross section for absorption of chemisorbed H induced by the impact of Ar, Kr, or Xe atoms as a function of their incident energy and angle. The cross section is calculated from measurements of absorption rate in the limit of zero absorbance.

The absorption rate is measured in the following manner. An inert gas atom beam is directed at the crystal covered with a H monolayer. A partial pressure of 2x10⁻⁵ torr of H₂ is present in the chamber during exposure to the inert gas atom beam. The pressure of H₂ is necessary to replace the H lost from the surface as the result of absorption and a competing process, collision induced recombinative desorption. In addition, maintenance of a layer of surface H blocks the exchange between surface and bulk H that is observed to be also induced by collisions of the inert gas atoms. At the end of the exposure to the inert gas atom beam, the ambient H₂ is pumped away, and a thermal desorption measurement is carried out. The amount of H absorbed is determined by the integrated area of the low temperature feature. This measurement is made for Ar, Kr, and Xe atoms incident over a wide range of angles and total kinetic energies.

The collision induced absorption cross section is observed to depend linearly on the normal component of the kinetic energy of the incident Ar, Kr, and Xe atoms. Strict normal energy scaling of the cross section is observed, and the cross section for absorption induced by Xe is significantly larger than that for Kr or Ar. These two observations suggest that the cross section for collision induced absorption is directly proportional to the energy transfer to the Ni lattice:

$$\Sigma(E_i, \phi_i, m) = A \Delta E(E_i, \phi_i, m)$$

where ΔE is the energy transferred from the inert gas atom to the lattice, E_i is the incident energy, ϕ_i is the incident angle, m is the mass of the inert gas atom and A is a proportionality constant.

To test whether the absorption cross section does correlate with energy transfer to the lattice, the incident energy, incident angle, and mass dependence of the energy transferred from the inert gas atom to the Ni lattice is calculated and compared to that of the experimentally determined cross section. The energy transfer is calculated within a hard sphere-hard cube impulsive collision model which has been modified to include the multiple collisions that take

place when a heavier gas atom is incident on a lighter substrate atom. The mass of the Ni atom is taken as its atomic mass. Motion of the Ni atom is only allowed normal to the macroscopic plane of the surface, which is known to be an excellent approximation in an atom-surface collision. Once the Ni atom has suffered its first collision with the inert gas atom, it is assumed to recoil instantaneously back toward the incoming inert gas atom. However, the Ni atom recoils with only a fraction (0.8) of its momentum acquired by collision with the inert gas atom. The rest of the momentum is lost to the lattice and in this way energy is dissipated to the lattice in this calculation. A second collision of the recoiling Ni atom and the incoming inert gas atom occurs, and their new momenta are calculated. Again, the Ni atom is assumed to recoil instantaneously with a fraction (0.8) of its momentum after the second collision. A third collision may occur, depending on the mass of the incoming inert gas atom. The total energy transferred is calculated by summing the energy lost to the lattice by the recoiling Ni atom after each collision and the final energy of the Ni atom.

The energy transferred to the lattice by Xe, Kr, and Ar is plotted as a function of their normal energy on the same plot as the experimental cross sections. The energy transferred by Xe is scaled to the experimental cross section for Xe, allowing the proportionality factor A to be determined. The proportionality factor is then used to predict the cross sections for absorption by Ar and Kr based on the energy transferred to the lattice by Ar and Kr. The experimental dependence of the cross sections on the mass and normal energy agrees very well with that of the cross sections predicted on the basis of the amount of energy transferred to the lattice. The one adjustable parameter in this model, the fraction of momentum with which the Ni atom recoils away from the lattice, is set at 0.8, but this parameter gives good agreement with the data over a wide range of values between 0.1 to 0.95 for a Ni mass of 58.7. This excellent correlation between the cross section for collision induced absorption and the energy transferred to the Ni lattice suggest a surface deformation mechanism. The incident atom collides with the surface either directly on top of or close to the adsorbed H atom. The impact of the collision transfers energy to the surface which momentarily distorts it to open up channels or holes into which the hydrogen can readily diffuse and enter the bulk.

Publications

Maynard, K.J., A.D. Johnson, S.P. Daley, and S.T. Ceyer. "A New Mechanism for Absorption: Collision Induced Absorption." *Faraday Discuss. Chem. Soc.* 91: 437 (1991).

3.3 The Chemistry of Bulk Hydrogen

Sponsor

U.S. Department of Energy
Grant DE-FG02-89-ER14035

Project Staff

Professor Sylvia T. Ceyer, Dr. Arthur L. Utz, Sean P. Daley, Theodore R. Trautman

Using molecular beam techniques coupled with high resolution electron energy loss spectroscopy, we have recently demonstrated the synthesis and detection of hydrogen embedded in the bulk of Ni under low pressure, UHV conditions. These capabilities have enabled the chemistry of bulk hydrogen to be probed unambiguously for the first time. We have found that the bulk hydrogen atom has unique chemistry. In particular, we have shown that the species reactive with adsorbed CH_3 is not a surface bound H atom but a bulk H atom.

The experiment is performed as follows. Exposure of the Ni(111) crystal to atomic hydrogen not only results in hydrogen embedded within the Ni lattice but also in a monolayer of hydrogen adsorbed on the surface. The surface-bound hydrogen blocks sites necessary for the second reactant, adsorbed CH_3 that we synthesize by the dissociative chemisorption of CH_4 . Therefore, the H adsorbed on the surface must be removed. The removal of the surface-bound H cannot be effected thermally because it is more stable than bulk H, recombining and desorbing between 340-390 K. Therefore, removal of the surface-bound H by the non-thermal process, collision induced recombinative desorption, is necessary. A 100 kcal/mol Xe atom beam is directed at the surface at a glancing angle. The impacts of the Xe atoms deform the surface and allow the hydrogen to recombine and desorb as H_2 . In this manner, the surface is swept clean of hydrogen while the bulk hydrogen remains. The clean surface is then exposed to CH_4 incident at 17 kcal/mol. The CH_4 dissociatively adsorbs, producing adsorbed CH_3 and adsorbed hydrogen. With the reactants now synthesized, the surface temperature is ramped at 2K/s and the partial pressures of hydrogen and methane are measured. At exactly the same temperature at which hydrogen

desorbs from the bulk, 180 K, there is very intense desorption of CH_4 . We have also carried out this reaction with a deuterium isotope embedded in the Ni lattice. In this case, the sole product observed is CH_3D . There is no formation of CH_4 or higher deuterated methanes. In the absence of bulk hydrogen, no CH_4 is observed to desorb.

Methane is formed solely by the reaction with bulk hydrogen. The surface bound hydrogen is unreactive with CH_3 . The reaction likely proceeds by the direct recombination of a bulk H atom with CH_3 because the interstitial octahedral site in which the hydrogen atom is bound is directly beneath the threefold hollow site on which the CH_3 is bound. As the surface temperature is raised, the bulk hydrogen atom moves up toward the surface where it encounters the methyl radical. Because the

hydrogen atom now has the correct orientation required by the transition state for sp^3 hybridization, it reacts with CH_3 and immediately desorbs as CH_4 . The reaction of CH_3 with an adsorbed H atom probably does not occur because access of the H atom to the $\text{Ni}_3\text{-C}$ bond is blocked. This result documents a new mechanism for a surface reaction—a reaction between an adsorbed and a bulk species—and it unambiguously demonstrates the importance of bulk hydrogen as a reactant in a heterogeneous catalytic reaction.

Publications

Johnson, A.D., S.P. Daley, A.L. Utz, and S.T. Ceyer. "The Chemistry of Bulk Hydrogen: Reaction of H Embedded in Ni with Adsorbed CH_3 ." *Sci.* 257: 223 (1992).

Chapter 4. Semiconductor Surface Studies

Academic and Research Staff

Professor John D. Joannopoulos, Dr. Arnaldo Dal Pino, Dr. Robert D. Meade

Graduate Students

Tomas A. Arias, Kyeongjae Cho, Andrew M. Rappe, Jing Wang

Technical and Support Staff

Imadiel Ariel

4.1 Introduction

Sponsor

Joint Services Electronics Program
Contract DAALO3-92-C-0001

Understanding the properties of surfaces of solids and the interactions of atoms and molecules with surfaces has been of extreme importance both from technological and academic points of view. The recent advent of ultrahigh vacuum technology has made possible microscopic studies of well-characterized surface systems. The way atoms move to reduce the energy of the surface, the number of layers of atoms involved in this reduction, the electronic and vibrational states that result from this movement, and the final symmetry of the surface layer are of utmost importance in arriving at a fundamental and microscopic understanding of the nature of clean surfaces, chemisorption processes, and the initial stages of interface formation.

The theoretical problems associated with these systems are quite complex. However, we are currently at the forefront of solving the properties of real surface systems. In particular, we are continuing our efforts in developing new techniques for calculating the total ground-state energy of a surface system from "first principles," so that we can provide accurate theoretical predictions of surface geometries and behavior. Our efforts in this program have concentrated in the areas of surface growth, surface reconstruction geometries, structural phase transitions, and chemisorption.

4.2 Surface Reconstruction

The (7x7) reconstruction of Si(111) is perhaps the most complex and widely studied surface of a solid. Since its discovery through low-energy electron diffraction (LEED) more than thirty years ago, an enormous amount of effort has been expended to elucidate the properties of this important surface. Based on this work, it is now generally accepted that the geometry of the (7x7) reconstruction is described by the dimer-atom-stacking-fault (DAS) model as proposed by Takayanagi et al. The complexity of this geometry, however, has defied any complete and realistic theoretical treatment of its properties. The only progress that could be made theoretically was by isolating and modeling bits and pieces of the surface. The only attempt at a complete work used an empirical tight-binding model to study the Si(111)-(7x7) reconstruction in a supercell geometry with 196 atoms.

In this work, we have exploited the power of the state of the art in parallel computation to demonstrate the feasibility of performing *ab initio* calculations with supercells approaching 1000 atoms. Specifically, we have performed the first *ab initio* calculation of the Si(111)-(7x7) using a supercell geometry with 700 effective atoms. These calculations predict the fully relaxed atomic geometry of this system, allow construction of theoretical scanning tunneling microscope (STM) images as a function of bias voltages, and predict the energy difference between the (7x7) and (2x1) reconstructions.

The DAS model for the Si(111)-(7x7) surface reconstruction is shown in figure 1. The unit-cell boundary is outlined by a dashed line. The largest solid circles denote the twelve atoms. The smaller solid circles denote six rest atoms that lie one layer below the surface and are threefold coordinated. There is also a single corner hole in each unit cell. Together, these 19 atoms account for the 19 unbonded electrons on the reconstructed surface.

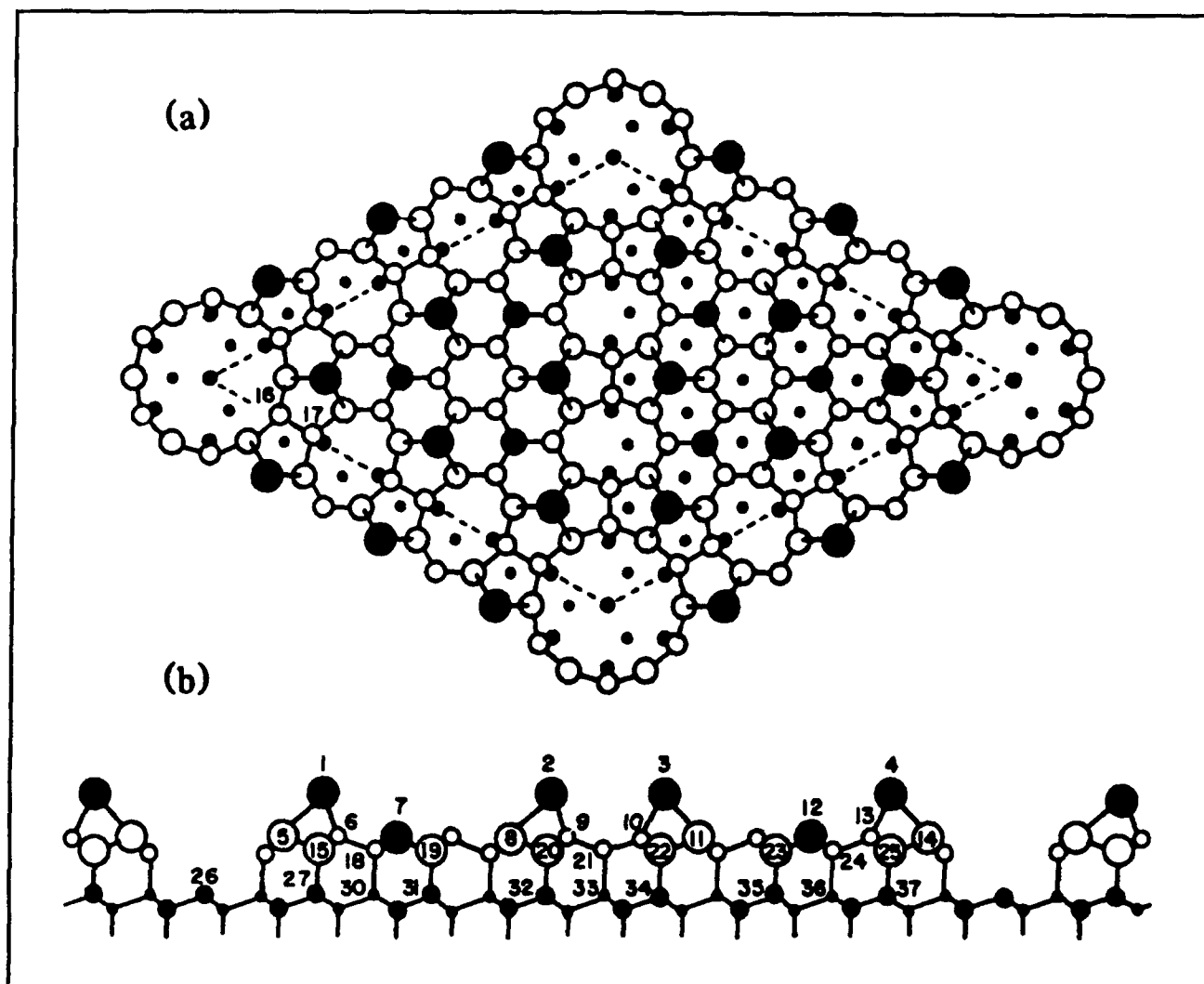


Figure 1. (a) Top view of the DAS model for the Si(111)-(7x7) surface reconstruction. The (7x7) unit cell is outlined. Atoms at increasing distances from the surface are indicated by circles of decreasing size. The large solid circles denote the twelve adatoms, the smaller solid circles represent the rest atoms. The faulted half of the unit cell is on the left. Small open circles denote the dimers, while small solid circles and dots represent atoms in the unreconstructed layers. (b) Side view. Atoms on the lattice plane along the long diagonal of the surface unit cell are shown with larger circles than those behind them. The numbers label the 37 unique atoms in the four-layer slab. All others are related by symmetry operations.

The smallest solid circles denote the fourth layer of atoms below the surface on the unfaulted half of the unit cell. Nine dimers are present two layers below the surface. One dimer is labeled by atoms with the number 16 and 17. The side view shows that the stacking sequence in the right half of the unit is the same as in bulk Si, while the stacking sequence in the left half is faulted.

Our model system consists of a supercell with a slab geometry containing vacuum on both sides. Periodic boundary conditions are applied in all directions. The slab contains the adatom layers and four surface layers shown in figure 1(b) plus a mirror image reflection in the vertical direction.

Thus, the supercell consists of eight layers of atoms with adatom layers on both slab surfaces and a region of 10 Å of vacuum. The 400 silicon atoms and the vacuum layer make this supercell equivalent to a 700-atom system. Unit-cell dimensions are 22 Å x 2 Å x 26 Å.

All atoms were allowed to move freely except the innermost layer, which was frozen in its bulk position. Thus, our model of the surface includes the relaxation of three surface layers in addition to the adatom layer. The atoms were assumed to be in their fully relaxed positions when the forces on the ions were converged to 0.15 eV/Å.

Table 1 shows the relaxed ionic positions. The computed positions in the surface plane are nearly identical with those from the tight-binding calculations. The most significant differences involve expansion of the surface layers away from the bulk layer. Compared to the tight-binding calculations, the adatoms move ~ 0.03 Å away from the bulk layer. The rest atoms move ~ 0.02 Å toward the bulk layer. Most of the remaining atoms move ~ 0.05 Å away from the bulk layer. However, atoms directly below adatoms move only ~ 0.03 Å,

	Atom	X	Y	Z
Adatoms	1	1.500	1.500	1.662
	2	4.492	4.491	1.594
	3	6.002	6.002	1.555
	4	9.005	9.005	1.603
First-layer atoms	5	1.033	1.033	-0.057
	6	1.958	0.993	-0.058
	7	2.481	2.481	0.348
	8	4.021	4.022	-0.155
	9	4.974	4.050	-0.099
	10	5.980	5.057	-0.135
	11	6.478	6.478	-0.163
	12	8.019	8.019	0.345
Second-layer atoms	13	9.029	8.059	-0.104
	14	9.472	9.472	-0.111
	15	1.504	1.504	-1.512
	16	1.162	0.006	-1.057
	17	1.800	0.007	-1.042
	18	2.492	1.499	-0.867
	19	2.969	2.969	-0.863
	20	4.494	4.495	-1.561
Third-layer atoms	21	5.403	4.780	-1.046
	22	6.004	6.004	-1.567
	23	7.532	7.532	-0.871
	24	8.505	7.510	-0.874
	25	8.998	8.998	-1.537
	26	0.001	0.001	-3.986
	27	1.500	1.500	-4.416
	28	1.006	-0.002	-3.989
	29	1.990	0.000	-3.964
	30	2.499	1.499	-3.946
	31	2.997	2.997	-3.951
	32	4.499	4.499	-4.460
	33	5.496	4.512	-3.973
	34	5.999	5.999	-4.440
	35	7.497	7.497	-3.933
	36	8.505	7.496	-3.930
	37	9.001	9.001	-4.414

Table 1. Relaxed atomic positions for the adatom layer and the first three surface layers for the *ab initio* (7x7) calculation. The coordinate system is the same as in reference 10. All reduced coordinates (X, Y, Z) are with respect to the Cartesian system indicated in figure 1, where the x axis is along the cubic [110] direction, and the y axis is along the [111] direction outward normal to the surface. The actual atomic coordinates (x, y, z) are related to (X, Y, Z) by the scaling relations $x = aX$, $y = aY/\sqrt{3}$, $z = aZ/\sqrt{24}$, where $a=3.85$ Å is the (1x1) surface hexagonal lattice constant.

resulting in a more distorted adatom configuration. The atoms two layers directly below move the most compared to the tight-binding calculations, relaxing ~ 0.10 Å away from the bulk layer. The relative heights of adatoms 1, 2, 3, and 4 are 0.085, 0.031, 0.000, and 0.038 Å, respectively. Experimental LEED values are 0.120, 0.080, 0.0, and 0.040.

Having generated the electronic wave functions in our pseudopotential calculation, we proceeded to make theoretical STM figures. In figure 2, we compare the theoretical results (top) with corresponding experiments at a tip voltage of 2 V (bottom) for both occupied and unoccupied states.

The theoretical STM probe was placed 3.8 Å above the surface adatom layer. The probe height is limited by the presence of a second surface layer above the probe due to the periodic replication of the unit cell. The theoretical grey scale was matched to the experimental grey scale at the tops of the adatoms and bottoms of the corner holes, and linearly interpolated in between. Experiments show a variation of 2-3 Å corresponding to this scale. The corresponding theoretical variation is 5 Å. Depths greater than 3 Å are set to minimum intensity in order to match the experimental grey scale.

The most fundamentally interesting part of this calculation is the comparison of formation energies of the (7x7) reconstruction and the (2x1) surface. Cleavage of Si to create the (111) surface results in a (2x1) metastable structure. This surface must then be annealed to generate the stable (7x7) structure. We find that the (7x7) reconstruction is energetically favorable over the metastable (2x1) surface by 60 meV per (141) cell. Our absolute values are 1.179 eV for the (7x7) surface and 1.239 eV for the (2x1).

The calculations discussed in this section were made possible because of the considerable computational power associated with massively parallel architectures. The calculations elevate *ab initio* investigations to a new echelon and demonstrate that studies of complex material systems with supercells containing nearly an order of magnitude more atoms than previously possible are now feasible.

4.3 Computation at Large Length Scales

As we discussed in the previous section, with recent advances in highly parallel computer architecture, calculations on systems with hundreds of atoms are now tractable. This not only permits more comfortable extraction of the thermodynamic

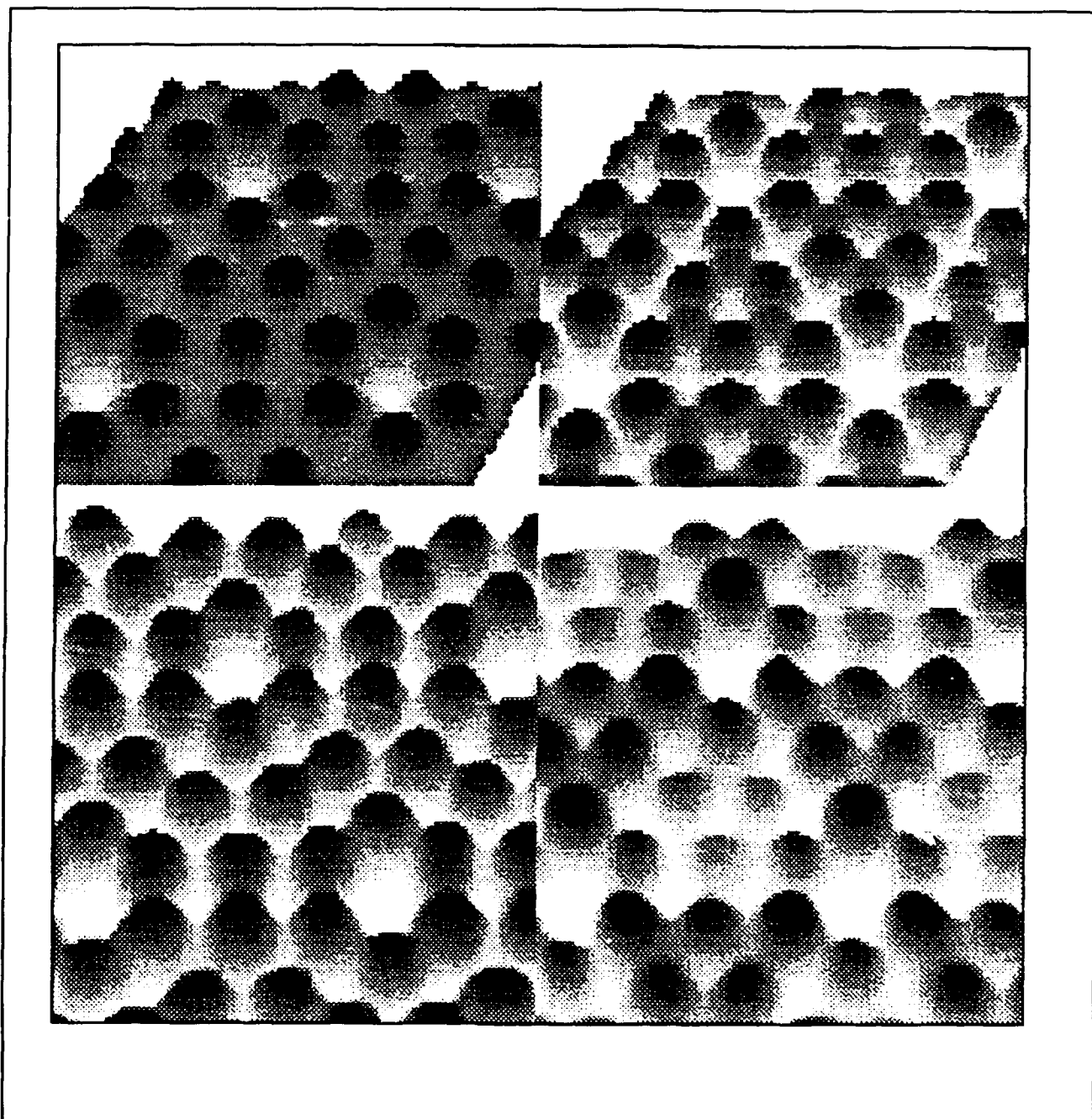


Figure 2. STM images of the Si(111)-(7x7) surface reconstruction based on the results of this calculation (top panels) and the experimental results of Avouris and Wolkow (bottom panels). Shown are unoccupied (left panel) and occupied (right panel) state contributions. The determination of the grey scale in the top panels is described in the text.

limit but also extends the qualitative level of complexity in accessible problems. However, with growing interest in calculations involving larger systems, it has been demonstrated that as the longest physical length scale in a calculation increases, integration of the fictitious electronic equations of motion becomes dominated by fluctuations in the electronic Hartree energy ("charge sloshing"). These fluctuations force the time step

for integration of the equations of motion to approach zero as the system size increases. While the onset of this instability depends on the physics of the system under study, the effect has been demonstrated dramatically in a silicon system of six primitive cells (~ 46 Å long) at 8 Ry. To fully benefit from the next generation of computer technologies, an approach free of charge sloshing is needed.

Recently, conjugate-gradient procedures introduced by Teter, Payne, Allan, and Gillan for relaxing the electronic wave functions at fixed atomic arrangements have been shown not to exhibit the aforementioned instability and to consume an order of magnitude less CPU time than the best fictitious electronic dynamics schemes. Despite this improvement, performing a dynamics calculation with conjugate-gradient techniques is very costly because of the tight tolerances to which the electronic problem must be solved (typically 10 μ V/atom) to yield stable atomic trajectories.

Very recently we have overcome these difficulties and introduced a new technique for performing finite-temperature *ab initio* total-energy calculations at long length scales. The method involves the introduction of a new class of energy functionals and an efficient scheme for performing iterative solutions.

To demonstrate the practicality of the new technique for long-length-scale systems, we have performed tests using a system that is well over 50 Å long. In particular, we have determined the phonon spectrum of Si through the velocity-velocity autocorrelation function of the ions in our calculation. After projecting the ionic displacements from our calculation onto the allowed k states and the known purely longitudinal and transverse polarization vectors, we then determine the frequencies present in the time of autocorrelation functions of these spatial *Fourier coefficients* with the maximum entropy method. Taking the frequencies of the peak values of the resulting spectra, we compare our parameter-free results with the experimentally measured phonon frequencies in figure 3 and find excellent agreement. Our spectra clearly and accurately reproduce not only the celebrated flattening of the lower acoustic (TA) modes as one moves away from the Γ point but also the delicate splitting of the optic modes along Δ . Note that the calculation also accurately reproduces the lowest frequency acoustic mode despite its period of nearly 1 ps and manifests the delicate splitting of the optic modes, which beat against each other with even longer periods. This illustrates that our dynamics technique produces reliable ionic trajectories even over periods of picoseconds and is thus very precise.

4.4 Publications

Arias, T., M. Payne, and J.D. Joannopoulos. "Ab-Initio Molecular Dynamics at Large Length-Scales." *Phys. Rev. B* 45: 1538 (1992).

Arias, T., M. Payne, and J.D. Joannopoulos, "Ab-Initio Molecular Dynamics: Analytically Con-

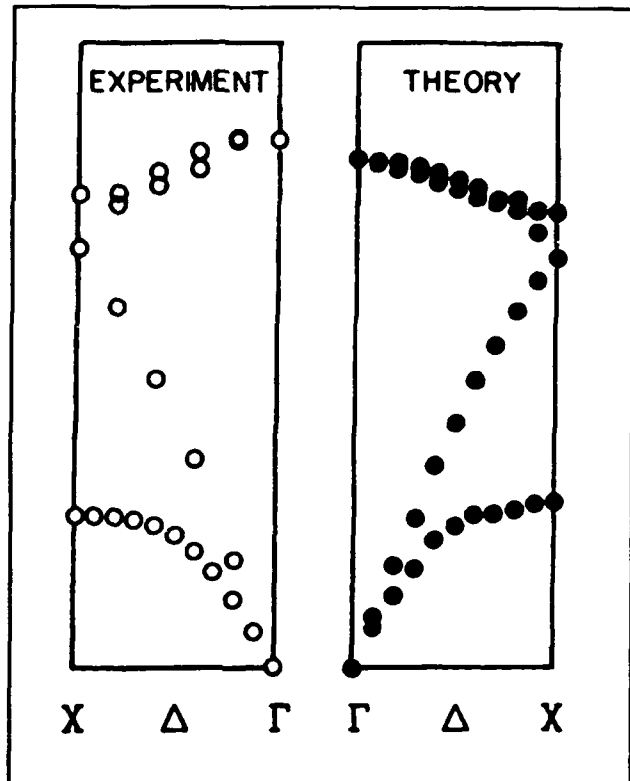


Figure 3. Phonon spectrum as determined from maximum peak values of MEM fits. These values are completely *ab initio* with no free parameters. The left-hand panel displays experimental data (13, 14) and the right hand panel displays frequencies from our dynamically determined trajectories.

tinued Energy Functionals and Insights into Iterative Solutions." *Phys. Rev. Lett.* 69: 1077 (1992).

Brommer, K., B. Larson, M. Needels, and J.D. Joannopoulos. "Implementation of the Car-Parrinello Algorithm for Ab-Initio Total Energy Calculations on a Massively Parallel Computer." In *Computers in Physics*.

Brommer, K., M. Needels, B. Larson, and J.D. Joannopoulos. "Ab-Initio Theory of the Si(111) (7x7) Surface Reconstruction - A Challenge for Massively Parallel Computation." *Phys. Rev. Lett.* 68: 1355 (1992).

Kaxiras, E., O. Alerhand, J. Wang, and J.D. Joannopoulos. "Theoretical Modelling of Heteroepitaxial Growth Initiation." *Mat. Sci. Eng. B* 14: 245 (1992).

Payne, M., G. Francis, M. Needels, E. Tarnow, P. Dallot, P. Bristowe, and J.D. Joannopoulos. "Ab-Initio Investigations of Surfaces and Grain Boundaries in Germanium." In *Ordering at Sur-*

faces and Interfaces. New York: Springer Verlag, 1992, p. 169.

Rappe, A., A. Dal Pino, M. Needels, and J.D. Joannopoulos. "Mixed Basis Pseudopotential Method for Iterative Diagonalization Techniques." *Phys. Rev. B* 46: 7353 (1992).

Rappe, A., J.D. Joannopoulos, and P. Bash. "A Test of the Utility of Planewaves for the Study of Molecules from First Principles." *J. Am. Chem. Soc.* 114: 6466 (1992).

Chapter 5. Epitaxy and Step Structures on Semiconductor Surfaces

Academic and Research Staff

Professor Simon G.J. Mochrie

Graduate Students

Douglas L. Abernathy

5.1 Structure and Phase Behavior of the Si(113) Surface

Sponsor

Joint Services Electronics Program
Contract DAAL03-92-C-0001

Over the last year, we have pursued a comprehensive x-ray scattering study of the structure and phase behavior of the Si(113) surface in collaboration with Professor R.J. Birgeneau. The results will allow us to determine the atomic structure of the (3×1) reconstructed Si(113) surface. Moreover, it is already clear that our results represent an important advance for our basic understanding of order-disorder transformations in model two-dimensional systems.

In theoretical models of an overlayer on a substrate, it is possible to identify four generic phases. (1) Commensurate (C) solids are characterized by long-range translational order and a wavevector which is commensurate with the substrate lattice. (2) C-fluids are also characterized by a commensurate wavevector, but their translational correlation length is finite. (3) Incommensurate (IC) floating solids exhibit a wavevector which is incommensurate with the substrate and an infinite correlation length. (4) Finally, IC-fluids show an incommensurate wavevector and a finite correlation length.

The critical behavior at the phase transformations between these different structures is largely known: C-solid-to-fluid transformations are described by p -state Potts models, where p is the order of the commensurability (which is defined as the period of the overlayer measured in units of the substrate lattice constant).¹ IC-solid-to-fluid melting is Kosterlitz-Thouless melting.² The transformation between a C-solid and an IC-solid is a Pokrovski-Talapov transformation for uniaxial phases³ and discontinuous in the hexagonal case.⁴ C-fluids and IC-fluids are separated by so-called disorder lines.⁵

Each of the above mentioned transformations is well understood theoretically. The situation is more complicated for the transformation from a C-solid into an IC-fluid, where the order of the commensurability (p) is key in determining the expected behavior. For $p \geq 4$, there is general agreement that an IC-solid phase always separates the C-solid and IC-fluid phases. For $p=2$, there is agreement that near the critical temperature for the C-solid-to-IC-fluid transformation the correlation length, incommensurability, susceptibility, and order parameter show power-law behavior. This behavior is characterized by the same critical exponents ($\nu, \bar{\beta}, \gamma, \beta$, respectively) as found for the C-solid-to-fluid transformation, i.e., the universality class of the transformation is that of the 2-state Potts model. In contrast, for $p=3$ the character of the transformation from a C-solid into an IC-fluid phase remains unresolved. There are three possible scenarios. The first is that a direct C-solid-to-IC-fluid transformation cannot occur;

¹ M. Schick, *Surf. Sci.* 11: 245 (1981).

² J.M. Kosterlitz and D.J. Thouless, *J. Phys. C* 6: 1181 (1973).

³ V.L. Pokrovski and A.L. Talapov, *Phys. Rev. Lett.* 42: 65 (1979).

⁴ J. Villain, *Surf. Sci.* 97: 219 (1980).

⁵ V.J. Emery and I. Peschel, *Z. Phys. B* 43: 241 (1981).

instead, an IC-solid phase inevitably intervenes.⁶ The second possibility is that there is a direct transformation, which falls in the same universality class as the C-solid-to-fluid transformation (3-state Potts universality class).⁷ Finally, Huse and Fisher⁸ have suggested that there may be a direct transformation, but that it is in a new *chiral melting* universality class, with as-yet-unknown critical exponents.

The signature of a chiral transformation is that the product of the incommensurability and the correlation length approaches a constant near the critical temperature (T_c), i.e., $\bar{\beta} = \nu$.⁸ In contrast, according to den Nijs, the product of the incommensurability and the correlation length goes to zero near T_c . Specifically, he predicts $\bar{\beta} = 2\nu$. It is clear that careful studies of experimental realizations of a system such as the Si(113) surface, which determine critical behavior, are particularly valuable. Below $T_c = 959$ K, Si(113) exhibits a (3×1) commensurate reconstruction ($p=3$) and a transformation into a disordered IC structure for temperatures above T_c .⁹ For Si(113), the reconstructed surface layer plays the role of the overlayer, while subsequent layers with bulk periodicity constitute the substrate.

Figures 1 and 2 show x-ray diffraction profiles obtained at the National Synchrotron Light Source near the surface $(5/3, 1)$ position in reciprocal space for several different temperatures. This experiment employed our new JSEP-funded UHV surface x-ray scattering apparatus. Below T_c the scattering profile consists of a narrow profile located at the $(5/3, 1)$ -position ($\sigma=\tau=0$). For temperatures increasing above T_c , the peak of the scattering shifts away from $\sigma=0$ (y -direction) and broadens in both σ and in τ (x -direction). The peak shift reflects the formation of discommensurations in the erstwhile commensurate reconstruction, so that the surface layer is now incommensurate. The peak broadening indicates that the translational correlation length in the incommensurate phase is finite, i.e., it is an IC-fluid. Figure 3 shows results for the dependence of the incommensurability (ϵ), the inverse correlation lengths (κ_y and κ_x), the square of the order parameter (I_0), and the wavevector dependent susceptibility (χ) versus reduced temperature $((T - T_c)/T_c)$.

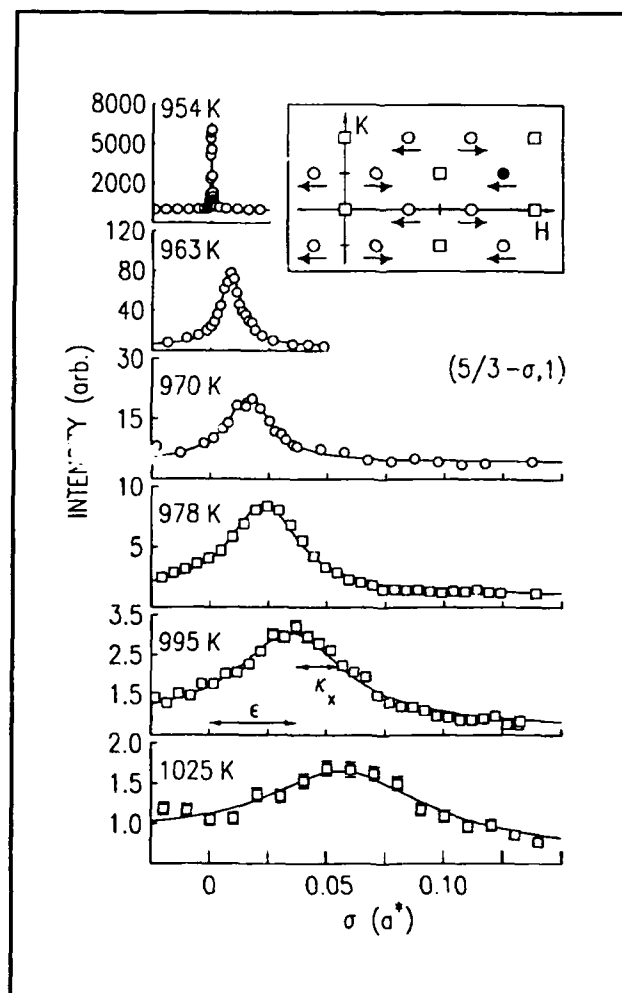


Figure 1. Scans along the x -direction through the $(5/3, 1)$ position in the reciprocal space of the reconstructed Si(113) surface versus temperature. The solid lines are least-mean-squares fits of a Lorentzian scattering function plus a smoothly-varying background to the data, which determine the peak shift from the commensurate position, i.e., incommensurability (ϵ), peak width (κ_x) and peak intensity (χ).

Each of these quantities shows power-law behavior over approximately two decades of reduced temperature with exponents $\bar{\beta} = 0.63 \pm 0.05$ for the incommensurability, $\nu_x = 0.65 \pm 0.07$ for the inverse correlation length in the incommensurate direction,

⁶ F.D.M. Haldane, P. Bak, and T. Bohr, *Phys. Rev. B* 28: 2743 (1983).

⁷ S.F. Howes, *Phys. Rev. B* 27: 1762 (1983); M. den Nijs, *Phase Transitions and Critical Phenomena*, eds. C. Domb and J. Lebowitz (London: Academic Press, 1987).

⁸ D.A. Huse, and M.E. Fisher, *Phys. Rev. Lett.* 49: 793 (1982).

⁹ Y.N. Yang, E.D. Williams, R.L. Park, N.C. Bartelt, and T.L. Einstein, *Phys. Rev. Lett.* 64: 2410 (1990); B.Z. Olshanetsky and V.I. Mashanov, *Surf. Sci.* 111: 414 (1981).

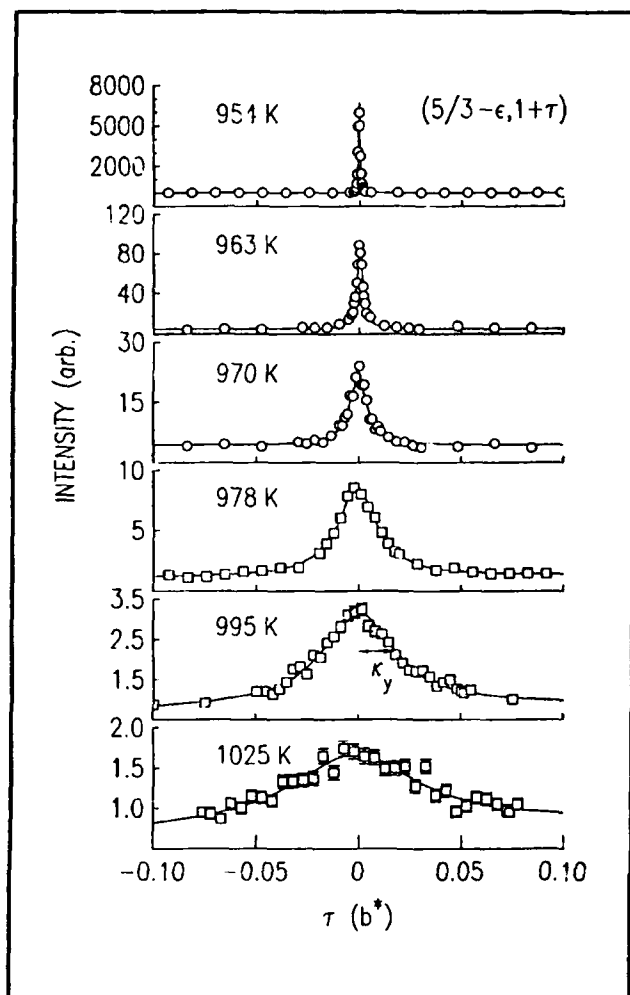


Figure 2. Scans along the y-direction through the $(5/3-\epsilon, 1+\tau)$ position in the reciprocal space of the reconstructed Si(113) surface versus temperature. The solid lines are least-mean-squares fits of a Lorentzian scattering function plus a smoothly varying background to the data, which determine peak width (κ_y), and peak intensity.

$\nu_y = 1.05 \pm 0.07$ for the inverse correlation length in the transverse direction, $2\beta = 0.23 \pm 0.03$ for the square of the order parameter, and $\gamma = 1.56 \pm 0.10$ for the susceptibility.

These results are striking for several reasons. First, we believe that the data presented in figures 1, 2, and 3 represent the highest quality measurements to date of surface critical exponents. The results are particularly impressive when one considers that the scattering emanates from relatively high-index Si surface and that Si is not a strong

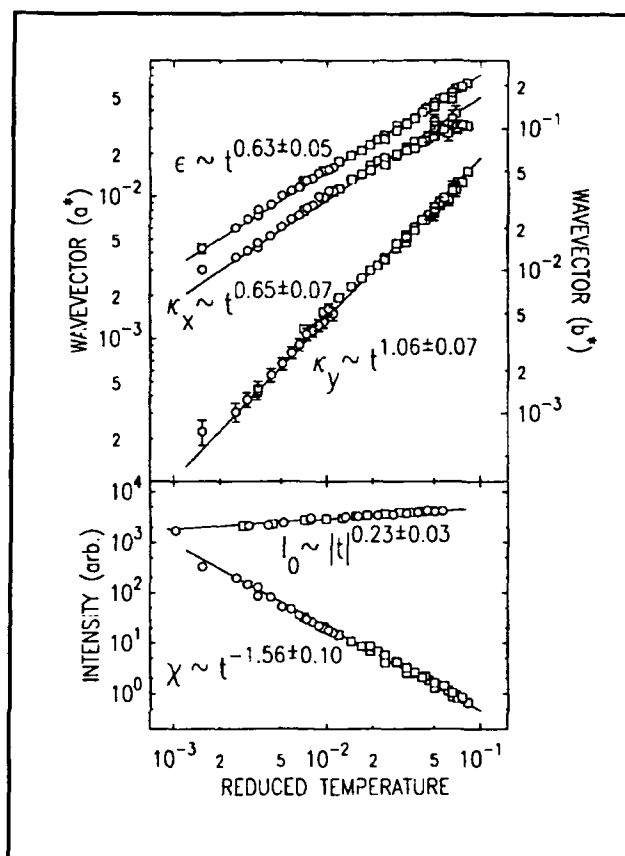


Figure 3. Dependence of the incommensurability (ϵ), inverse correlation lengths (κ_x and κ_y), susceptibility (χ), and square of the order parameter (I_0) versus reduced temperature $((T - T_c)/T_c)$. Note the log-log scales.

x-ray scatterer. They demonstrate that our apparatus teamed with an intense synchrotron x-ray source constitutes the world's premier facility for surface x-ray diffraction studies. Only with such high quality data is it possible to accurately determine critical exponents. Second, it is clear that the exponent for the correlation length along the x-direction is different from that for the correlation length along the y-direction, i.e., there is *anisotropic scaling*. Such behavior is unusual, although one instance in which it occurs is the uniaxial C-solid-to-IC-solid transformation, where exact results give $\nu_x = \beta = 1/2$ and $\nu_y = 1$.¹⁰ Furthermore, Howes¹¹ has suggested that $\nu_y = 1$ and $\nu_x = 2/3$ at the special point in the phase diagram (Lifshitz point) where the line of direct C-solid-to-IC-fluid transformations ends and is replaced by successive C-solid-to-IC-solid and IC-solid-to-IC-fluid transformations. Third, the measured exponent values are

¹⁰ V.L. Pokrovski, and A.L. Talapov, *Phys. Rev. Lett.* 42: 65 (1979).

¹¹ S.F. Howes, *Phys. Rev. B* 27: 1762 (1983).

consistent with the hyperscaling relation: $\nu_x + \nu_y = \gamma + 2\beta$. A final important observation is that the product of the incommensurability and the correlation length along the incommensurate direction is constant ($\beta = \nu_x$) as expected for chiral melting.

A direct C-solid-to-IC-fluid transformation indicates that the phase diagram proposed by Haldane et al. is incorrect. Furthermore, the observation of anisotropic scaling informs us that the disordering transformation of Si(113) is not in the universality class of the 3-state Potts model. It follows that these data imply that the C-solid-to-IC-fluid transformation of Si(113) lies in a chiral melting universality class as proposed by Huse and Fisher. Moreover, the previously unknown exponents which characterize the chiral melting universality class have been determined.

We are confident that these results will stimulate and guide further theoretical work aimed at finally

understanding the critical behavior at the C-solid-to-IC-fluid transformation with $p=3$. This would complete our understanding of phase transformations in this type of *model* two-dimensional system.

5.2 Publications

Abernathy, D.L., S.G.J. Mochrie, D.M. Zehner, G. Grübel, and D. Gibbs. "Thermal Roughness of a Close-Packed Metal Surface: Pt(001)." *Phys. Rev. Lett.* 69: 941 (1992).

Abernathy, D.L., S.G.J. Mochrie, D.M. Zehner, G. Grübel, and D. Gibbs. "Orientational Epitaxy and Lateral Structure of the Hexagonally-Reconstructed Pt(001) Surface." *Phys. Rev. B* 45: 9272 (1992).

Part II Applied Physics

Section 1 Atomic, Molecular and Optical Physics

Section 2 Plasma Physics

Section 3 Electromagnetics

Section 4 Radio Astronomy

Section 1 Atomic, Molecular and Optical Physics

Chapter 1 Quantum Optics and Photonics

Chapter 2 Basic Atomic Physics

Chapter 3 Neutrality of Molecules by the Pulsed Gas
 Flow Method

Chapter 1. Quantum Optics and Photonics

Academic and Research Staff

Professor Shaoul Ezekiel, Dr. M. Selim Shahriar

Visiting Scientists and Research Affiliates

Dr. Philip R. Hemmer,¹ Dr. Mara G. Prentiss,² Dr. Farhad Zarinetchi,² John D. Kierstead¹

Graduate Students

John J. Donoghue,³ Daniel Katz,² Juliet Mervis,² Stephen P. Smith

Undergraduate Students

Arthur Chu²

1.1 Optical Data Storage with Raman Excited Spin Echoes

Sponsor

U.S. Air Force - Electronic Systems Division
Contract F19628-92-K-0013

There has been much recent interest in the use of optical photon echoes for information storage and processing.⁴ So far, however, the most successful demonstrations have been restricted to doped crystals operating at liquid helium temperatures, and homogeneous decay of the excited state limits performance. Here we demonstrate, theoretically as well as experimentally, that optical data can be stored and retrieved using spin echoes which are excited and detected by the optical resonance Raman interaction. The advantage is that spin echoes contain no contribution from the optical excited state and therefore are not limited by excited state decay. Moreover, since Raman spin echoes are optically excited and detected, full optical holographic spatial resolution is available. Finally, it might be possible to develop high temper-

ature optical memories and processors, since spin echo data storage has been demonstrated at room temperature.⁵

The ability of Raman excited spin coherence to store optical temporal and phase information is based on the fact that this coherence is sensitive to the relative phases of the optical fields.⁶ When inhomogeneous broadening is present, the differential optical phase sensitivity permits the storage of optical temporal variations, just as in conventional optical (or microwave) echo storage schemes.

Experimental realization of the three-part storage and recall scheme is accomplished with a sodium atomic beam that has three spatially separated interaction zones and uses an off-resonant optical-Raman beam as the rephasing field. The experimental setup is illustrated in figure 1. Here, the Raman transition is the

$$3^2S_{1/2}(F=1, m=1) \leftrightarrow$$

$$3^2P_{1/2}(F=2, m=2) \leftrightarrow 3^2S_{1/2}(F=2, m=1)$$

¹ Rome Laboratory, Hanscom, Massachusetts.

² Harvard University, Cambridge, Massachusetts.

³ Tufts University, Medford, Massachusetts.

⁴ M.K. Kim and R. Kachru, "Storage and Phase Conjugation of Multiple Images Using Backward-stimulated Echoes in $\text{Pr}^{3+}:\text{LaF}_3$," *Opt. Lett.* 12: 593 (1987).

⁵ S. Fernbach and W.G. Proctor, "Spin-echo Memory Device," *J. Appl. Phys.* 26: 170 (1955).

⁶ M.S. Shahriar and P.R. Hemmer, "Direct Excitation of Microwave-spin Dressed States Using a Laser-excited Resonance Raman Interaction," *Phys. Rev. Lett.* 65: 1865 (1990).

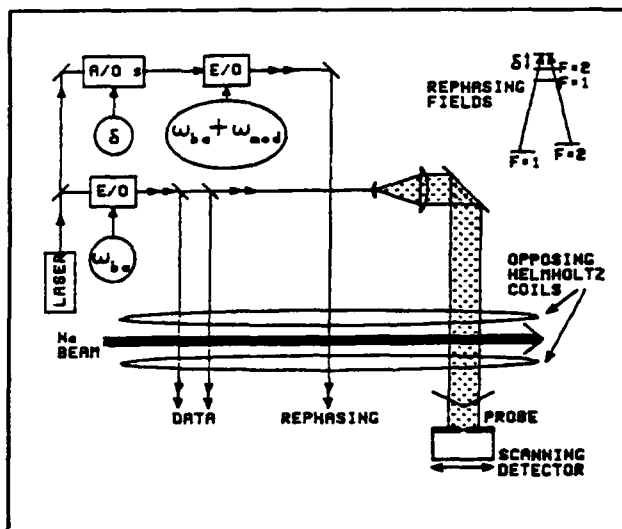


Figure 1. Experimental setup for optical data storage and recall using optical-Raman excited spin echoes, in a sodium atomic beam.

transition at 589.7 nm optical frequency, where the ground state splitting is 1.772 GHz and the excited state decay time is 16 nsec. Ground state inhomogeneous broadening is produced using the linear Zeeman shift and an applied magnetic field gradient of 1 Gauss/cm, to give a total ground state inhomogeneous broadening of 450 kHz.

The optical pulse sequence is shown in figure 2a. The first two Raman pulses interfere to store the optical temporal information via spectral hole-burning. The rephasing is accomplished with an off-resonance Raman π -pulse. The Raman probe beam senses the echo via changes in absorption. Figure 2b shows the experimentally observed echo signals. The echo amplitude is about 50% of the maximum demodulated signal obtained when a single, saturating Raman data pulse is applied in the absence of a magnetic field gradient (no dephasing). Figure 2c shows the theoretical echo signal calculated using a numerical solution of the optical Bloch equations for input parameters that approximately correspond to experimental conditions of figure 2c. Good qualitative agreement between theory and experiment is achieved, both in the width and peak amplitude of the echo signals.

Although the present optical data storage experiment employs optical data pulses that are longer than the excited state homogeneous decay time, this is not a fundamental requirement. In fact, Raman resonant optical pulses shorter than the optical homogeneous decay time can also be stored. The new fundamental limit on optical storage capacity, using Raman-optical echoes, is given by the ratio of the spin homogeneous lifetime to the optical inhomogeneous lifetime. This is typi-

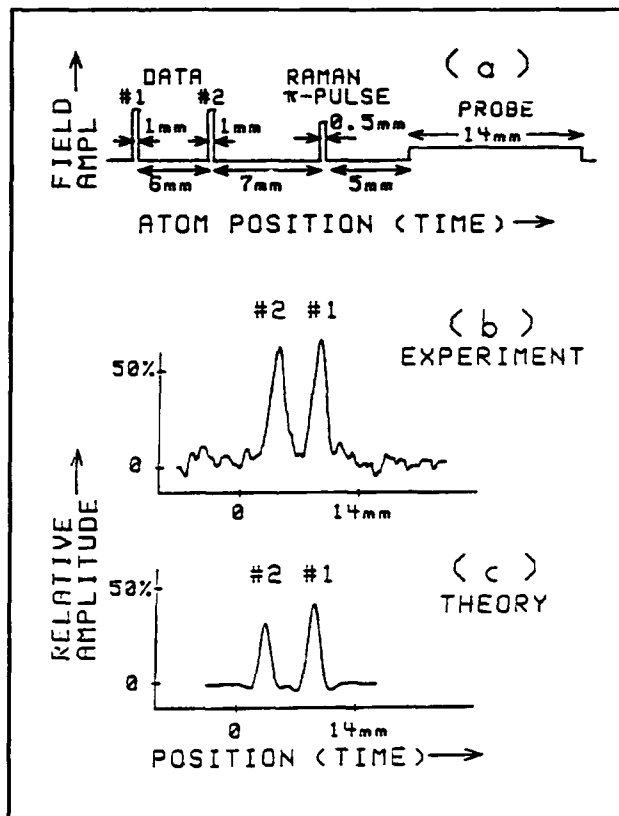


Figure 2. (a) Pulse sequence for data storing and retrieval. (b) Experimentally observed echo signals. (c) Corresponding theoretical echoes.

cally several orders of magnitude larger than for optical two-level echoes. Furthermore, if the rephasing microwave π -pulse is split into two temporally separated $\pi/2$ -pulses, then archival storage is possible.

In summary, we have experimentally demonstrated that the Raman transparent states can store and retrieve optical temporal and phase information via a ground state spin echo process. This opens up the possibility of enhancing the performance of optical photon echo memories. Future work includes demonstration of this type of data storage in cryogenic doped crystals as well as a search for higher temperature materials.

1.2 Phase-dependent Velocity Selective Coherent Population Trapping in a Folded Three-level Λ System under Standing Wave Excitation

Sponsors

U.S. Air Force - Electronic Systems Division
Contract F19628-92-K-0013

U.S. Navy - Office of Naval Research
Grant N0014-91-J-1808

Recently, there has been a great deal of interest in the forces experienced by a folded three-level Λ atom. Aspect et al.⁷ first demonstrated that such an atom can be cooled below the recoil limit via velocity selective coherent population trapping (VSCPT) when excited by a pair of counter-propagating traveling waves. Here, we show theoretically that VSCPT occurs in a Λ atom excited by a pair of Raman resonant standing waves, and its efficiency depends on the relative phase, ϕ , between the standing waves. Finally, we describe briefly the generalization of this process to three dimensions.

The importance of VSCPT in Raman resonant standing waves stems from our earlier experimental observation of deflection and cooling of Λ sodium atoms in an atomic beam.⁸ This experiment suggests that these standing wave forces could be used to design a stimulated force trap. In addition, our theory predicts that the cooling can be made to have characteristics very similar to those of conventional polarization gradient cooling (see next section), so that such a trap should have a sub-Doppler temperature. The theory presented here suggests that it may be possible to reach a sub-recoil temperature in a Raman force trap.

In analogy to the traveling wave VSCPT, we are interested in finding a state (the dark state) which satisfies the following conditions: (1) it does not contain any excited states so that it is completely decoupled from the vacuum fields, and (2) the net amplitude for coupling this state to any of the excited states must vanish. Let us denote the linear momentum of the atom by p and the wavenumber of the optical field by k . It can be shown that if $p = 0$ and/or $\phi = 0$ then the state:

$$|NC(p)\rangle = \frac{1}{2}$$

$$[|a, p - \hbar k\rangle \exp(-i\phi) + |a, p + \hbar k\rangle$$

$$\exp(i\phi) - |b, p - \hbar k\rangle - |b, p + \hbar k\rangle]$$

does not couple to any excited state, as illustrated in figure 3. Here, the square boxes represent the

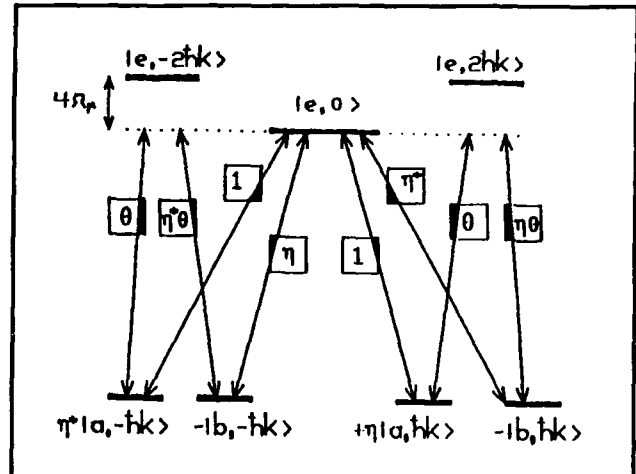


Figure 3. Illustration of the dark state, $|NC(0)\rangle$. Here, $\eta = \exp(i\phi)$, and $\theta = \exp(i\Omega t)$. The numbers in the boxes represent the relative weights of the matrix element. Here, we have chosen $\delta = -\Omega_r$.

relative transition matrix elements. Summing over the allowed transitions we find, for an atom starting in $|NC\rangle$ at $t = 0$, that the amplitude of being in the excited state after a time dt is given by $dA_e = -2i(dt)^2 gk(p/m) \sin \phi$, where g is the Rabi frequency, and m is the mass of the atom. Thus, for $p = 0$ and/or $\phi = 0$, $|NC\rangle$ is a dark state. For $\phi \neq 0$, we therefore have a single, zero velocity dark state, and VSCPT occurs. The efficiency of VSCPT would vary as $\sin^2 \phi$, being maximum at $\phi = (2n+1)\pi/2$ and vanishing at $\phi = n\pi$. We also find that for $\phi = (2n+1)\pi/2$, the standing wave VSCPT is nearly as efficient as the traveling wave.

The existence of VSCPT corresponds to the absence of diffusion for zero velocity atoms in the trapped state. However, Chang et al.⁹ have previously computed a non-zero diffusion coefficient in Raman resonant standing waves by a perturbative numerical solution of the Wigner density matrix equation of motion. This disagreement with Chang et al. seems to stem from the fact that they assumed, *a priori*, that the distribution of atoms in momentum space is smooth, which is in sharp contrast with the result of VSCPT. We should also point out that VSCPT observed by Aspect et al. for a variable angle between the planes of polarization of two counterpropagating traveling waves can be interpreted in terms of the theory of standing wave VSCPT as developed here, thus validating our

⁷ A. Aspect, E. Arimondo, R. Kaiser, N. Vansteenkiste, and C. Cohen-Tannoudji, *Phys. Rev. Lett.* 61: 826 (1988).

⁸ P. Hemmer, M. Shahriar, M. Prentiss, D. Katz, K. Berggren, J. Mervis and N. Bigelow, *Phys. Rev. Lett.* 68: 3148 (1992).

⁹ S. Chang, B. Garraway, and V. Minogin, *Opt. Comm.* 77: 19 (1990).

result. Finally, we have found that this process can be generalized to three dimensions employing a $j = 1 \leftrightarrow j' = 1$ transition, with three mutually orthogonal pairs of Raman resonant standing waves.

In summary, we have shown theoretically that phase sensitive VSCPT takes place when a Λ system is excited by a pair of Raman resonant standing waves. This corresponds to absence of diffusion for zero velocity atoms in the trapped state, in disagreement with predictions made by Chang et al. We also find that previous experimental observations reported by Aspect et al. agree with our predictions. Finally, we outline the generalization to three dimensions. Given our prior observation of stimulated trapping and cooling forces and our theoretical prediction of strong pol-grad cooling in Raman resonant standing waves, the simultaneous existence of VSCPT may make it possible to design a subrecoil temperature trap for Λ atoms.

1.3 Continuous Pol-Grad Pre-Cooling for Loading a Subrecoil Temperature Trap

Sponsors

U.S. Air Force - Electronic Systems Division
Contract F19628-92-K-0013
U.S. Navy - Office of Naval Research
Grant N0014-91-J-1808

As discussed in the preceding section, there has been increasing interest in multilevel atoms that undergo velocity selective coherent population trapping (VSCPT) into a zero velocity dark state. However, since VSCPT takes place via a random walk in momentum space, in three dimensions the efficiency would fall off rapidly as a function of velocity, with a capture range of the order of the recoil velocity. Therefore, in order to significantly populate the 3D dark state, it is necessary to pre-cool atoms to the recoil limit. It is advantageous for this pre-cooling to occur simultaneously with VSCPT; otherwise the random walk causes most of the atoms to heat up to velocities beyond the capture range. This type of pre-cooling does not exist in the various VSCPT schemes considered so far.

Here, we present a new mechanism under which polarization-gradient cooling efficiently slows atoms from a sample at the Doppler limit to the recoil limit. Unlike other methods of cooling to the recoil limit, this cooling occurs under the same conditions as required for VSCPT. We illustrate the basic mech-

anism in one dimension using a Sisyphus model. The predictions of this model are consistent with numerical results obtained from continued fractions as well as from numerical integrations of the optical Bloch equations. We also discuss the generalization of this scheme to three dimensions. This new mechanism opens the possibility of continuously cooling a large number of atoms to a subrecoil temperature.

The basic features of this cooling technique are well demonstrated in one dimension by a Λ system excited by a pair of Raman resonant standing wave fields. Efficient cooling is obtained in the case where the common mode detuning δ is positive and the phase difference ϕ between the standing waves is $\pi/4$. We have developed a Sisyphus type model to interpret this process physically. This model is illustrated in figure 4, using the non-absorbing ($| - \rangle$) and absorbing ($| + \rangle$) superposition states. Figure 4a shows the Rabi frequencies, figure 4b shows the population of $| + \rangle$, and figure 4c shows the Stark shifts of $| + \rangle$ and $| - \rangle$. As can be seen, the atoms on average climb energy hills, thus experiencing cooling.

Figure 5a (thick line) shows a plot of the averaged force in natural units as a function of velocity obtained from a continued fraction solution. The parameters used here are $\phi = \pi/4$, $g_c = 0.3$ and $\delta = 1.0$. We fit this plot to a function of the form $f(v) = -\zeta_0 \cdot v / (1 + v^2/v_c^2)$, which is maximum at $v = v_c$. We find $v_c \approx 5.5 \times 10^{-3}$ and $\zeta_0 \approx 0.81$.

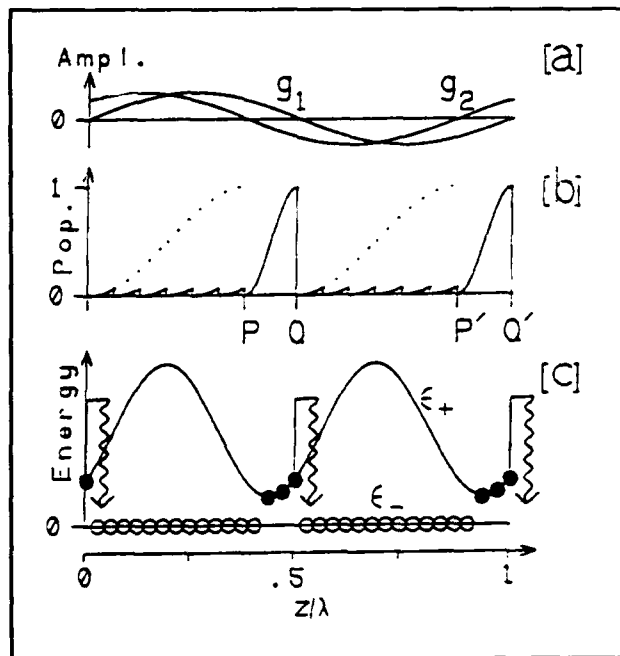


Figure 4. (a) Rabi frequencies for $\chi = \pi/4$. (b) Population of the $|W\rangle$ state for a moving atom. (c) Sisyphus cooling.

The Sisyphus type model predicts $v_c = 3.4 \times 10^{-3}$ and $\zeta_0 \approx 0.97$, with reasonable agreement. For equivalent values of parameters, these numbers are comparable ($\zeta_0 = 3.0$, $v_c = 4.0 \times 10^{-3}$) to the ones estimated by Dalibard et al.¹⁰ for a $J = 1/2 \leftrightarrow J' = 3/2$ transition. The dashed line superimposed on figure 5a shows the corresponding values of the Doppler cooling force, calculated for the $|a\rangle \leftrightarrow |e\rangle$ transition, in the absence of $|b\rangle$, for the same parameters. As can be seen, the pol-grad cooling coefficient (slope) is about a factor of 30 larger than the Doppler cooling coefficient. Figure 5b shows how the force varies as a function of ϕ , for $v = 5.5 \times 10^{-3}$.

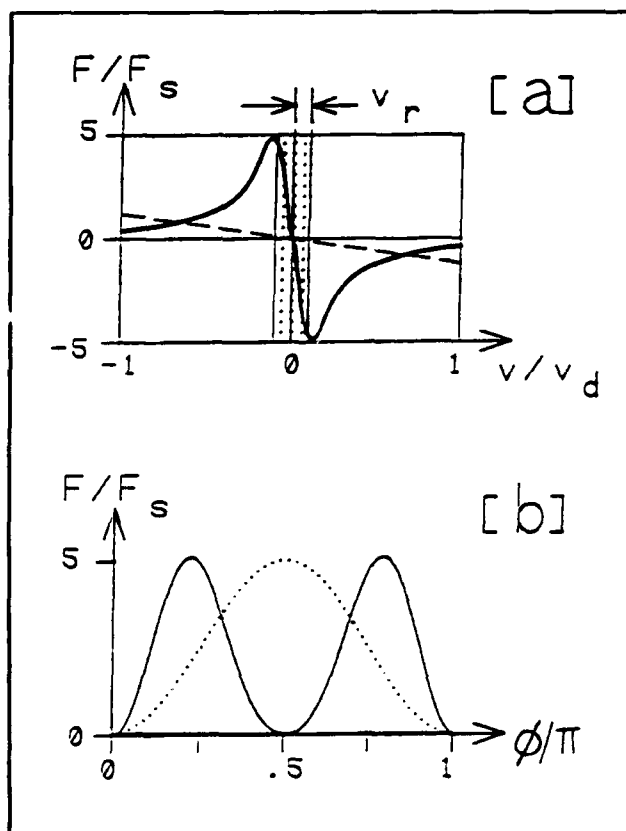


Figure 5. (a) The thick line shows the averaged pol-grad cooling force for sodium as a function of velocity, in units of $F_s = 10^{-3} \times \hbar k \Gamma / 2$. The dashed line shows the corresponding Doppler cooling force, and the dotted area represents the capture range for VSCPT. (b) The solid line shows the pol-grad cooling force as a function of ϕ . The dotted line shows the efficiency of VSCPT.

As discussed above, this system undergoes VSCPT into a zero velocity dark state, so that the equilibrium temperature is limited only by the interaction time and can be substantially below the recoil limit. The efficiency of VSCPT into this state varies as $\sin^2 \phi$, as illustrated by the dotted line in figure 5b. We have also found how to generalize this scheme to three dimensions, following the approach of Ol'shanii et al.¹¹

We have estimated the enhancement of the efficiency of VSCPT in three dimensions due to the pol-grad pre-cooling. Consider, for example, a sample of sodium atoms cooled to the Doppler limit. In the presence of the pol-grad cooling mechanism, the atoms would be pre-cooled to a velocity spread of the order of v_r , so that the time needed for all the atoms to end up in the dark state would be much less than that needed in the absence of such pre-cooling. Preliminary calculations suggest nearly three orders of magnitude enhancement in efficiency from pol-grad pre-cooling.

In summary, we show that pol-grad cooling occurs in the Λ system simultaneously with VSCPT. This process may continuously and efficiently transfer atoms from a Doppler temperature sample to near-recoil velocities that are within the capture range of VSCPT, which would then continuously cool the atoms to below the recoil limit. This pol-grad pre-cooling is estimated to enhance the VSCPT pumping rate by nearly three orders of magnitude compared to the rate achievable from Doppler pre-cooling alone. We present results from a Sisyphus model, along with numerical results obtained from continued fractions. Experimental efforts are in progress for realizing this scheme in three dimensions.

1.4 Raman Gain in a Λ Three-level System with Closely Spaced Ground States

Sponsor

U.S. Air Force - Electronic Systems Division
Contract F19628-92-K-0013

Recently, there has been much interest in the Raman gain observed in a Λ system with closely spaced ground states such that both ground states are initially equally populated and are both coupled

¹⁰ J. Dalibard and C. Cohen-Tannoudji, *J. Opt. Soc. Am. B* 6: 2023 (1989).

¹¹ M. Ol'shanii and V. Minogin, In *Proceedings of the International Workshop on Light Induced Kinetic Effects on Atoms, Ions, and Molecules*, ed. L. Moi et al. (Pisa, Italy: ETS Editrice, 1991), p. 99.

to the excited state by a single frequency pump.¹² This system is of interest for applications such as frequency shifting,¹³ self phase conjugation,¹⁴ and high precision laser magnetometry.

We have studied the mechanism of this gain and found qualitative agreement with experimental results.¹⁵ Briefly, a single frequency pump interacts with both legs of the system, as shown in figure 6a. Figure 6b shows a typical gain lineshape. The vertical rectangle superimposed on this plot indicates a resonance frequency of the dressed states of the

atom and the pump. As can be seen, gain is peaked at this resonance frequency. Thus, we are able to interpret the gain spectrum in terms of the energy intervals of the dressed states of the pumped system.

The gain mechanism is analogous to the process of sideband amplification in a strongly driven two-level system. However, the width of gain is not limited by the linewidth of the excited state. This is illustrated in figure 6c, where the linewidth is plotted as a function of pump Rabi frequency. As can be

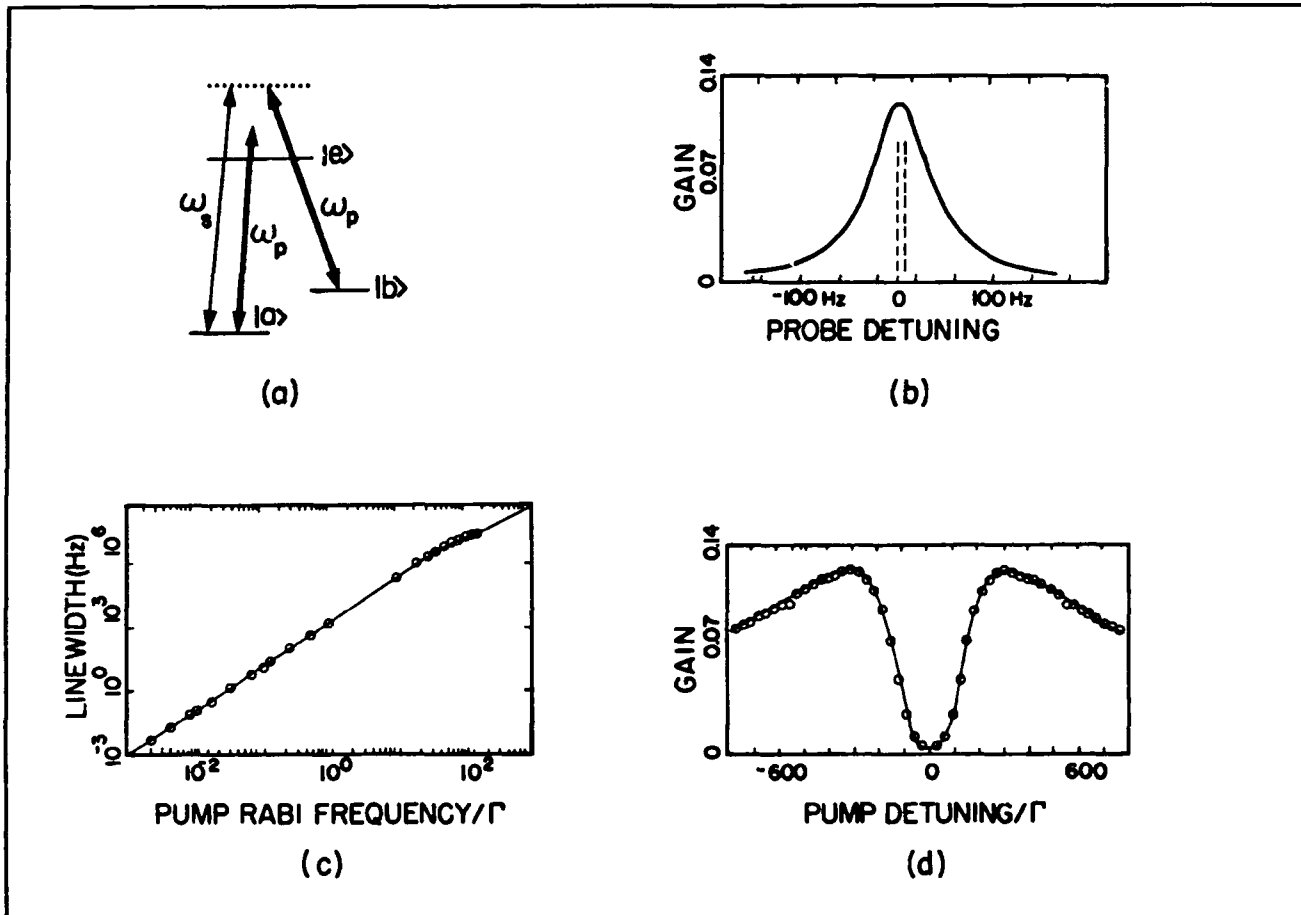


Figure 6. (a) Doubly pumped Raman gain scheme. (b) A typical gain lineshape, centered at a resonance frequency of the dressed states. (c) Linewidth of gain as a function of pump Rabi frequency. (d) Gain as a function of pump detuning. The gain is expressed in arbitrary units.

¹² J. Donoghue, M. Cronin-Golomb, J.S. Kane, and P.R. Hemmer, *Opt. Lett.* 16: 1313 (1991); M. Poelker and P. Kumar, *Opt. Lett.* 17(6): 399 (1992); M.S. Shahriar, P.R. Hemmer, J. Donoghue, M. Cronin-Golomb, and P. Kumar, *OSA Annual Meeting Tech. Dig.* 23: 127 (1992).

¹³ M. Poelker and P. Kumar, *Opt. Lett.* 17(6): 399 (1992).

¹⁴ J. Donoghue, M. Cronin-Golomb, J.S. Kane, and P.R. Hemmer, *Opt. Lett.* 16: 1313 (1991).

¹⁵ M. Poelker and P. Kumar, *Opt. Lett.* 17(6): 399 (1992); M.S. Shahriar, P.R. Hemmer, J. Donoghue, M. Cronin-Golomb, and P. Kumar, *OSA Annual Meeting Tech. Dig.* 23: 127 (1992).

seen, linewidth falls off linearly with the Rabi frequency. In practice, linewidth is limited only by additional factors such as transit time. This is consistent with extremely narrow gains (less than 1 kHz) observed in sodium vapor. In addition, we have found that gain amplitude becomes a constant below a certain intensity. Thus, this gain mechanism is in principle thresholdless (if not limited by transit time). This is because the dressed states population inversion needed for this gain is created via optical pumping. Thus, for a long enough transit time, optical pumping saturates even for a very low pump intensity.

In summary, we have studied the Raman gain mechanism for a doubly pumped Λ system. For a low intensity, the gain amplitude and width are limited by transit time only. These observations are in qualitative agreement with previous experimental observations. One of the various applications of this process is high resolution laser magnetometry. We have performed preliminary experiments for this application, with encouraging results.

1.5 Brillouin Laser Fiberoptic Gyroscope

Sponsor

Charles S. Draper Laboratory
Contract DL-H-418522

Research is in progress on a new fiberoptic ring laser gyroscope based on two counter-propagating stimulated Brillouin scattering (SBS) lasers which are generated in the same fiberoptic ring resonator.¹⁶ The use of SBS is crucial to the operation of this gyro because a conventional solid-state gain medium cannot support simultaneous bidirectional lasing due to gain competition. It is the directional property of the SBS gain medium that prevents gain competition and thus allows stable, simultaneous, bidirectional lasing.

In the presence of an inertial rotation normal to the plane of the resonator, a difference frequency is automatically generated between the counterpropagating SBS lasers which is directly proportional to the rotation rate,¹⁷ as predicted by the Sagnac effect. The operation of this gyro is very similar to that of the bulkoptic ring laser gyroscope (RLG) based on the He-Ne gain medium. It should be

noted that gain competition in a gaseous medium is avoided by using two partially overlapping, Doppler broadened gain media.

In contrast with the passive interferometer or resonator gyroscope, the SBS fiber RLG, as in the bulkoptic RLG, does not require external means to measure the nonreciprocal phase shift that is induced by rotation.

Figure 7 shows a simplified schematic of a SBS ring laser gyroscope. Light from a 1 mW He-Ne laser at $1.15 \mu\text{m}$ is split into two pump beams, P1 and P2, shifted by acousto-optic modulators, and coupled into counterpropagating directions of the same ring resonator. For maximum effective pump power inside the resonator, the pump lasers are held at the center of a cavity resonance, using a servo not shown in the figure, and are matched to the polarization of the cavity resonance.

With the pump lasers P1 and P2 above the $60 \mu\text{W}$ Brillouin threshold, two SBS lasers, B1 and B2, are generated simultaneously in directions opposite to those of their respective pumps. The two SBS lasers are then combined via a coupler and fall onto detector D.

Figure 8 shows the difference frequency between B1 and B2 when a sinusoidal rotation is applied to the gyroscope. As predicted by the Sagnac effect, the frequency difference varies linearly with the applied rotation rate, which is 90 degrees out of phase with the rotation angle in figure 8b.

However, it is important to note that, in figure 8, for a range of low rotation rates the frequency differ-

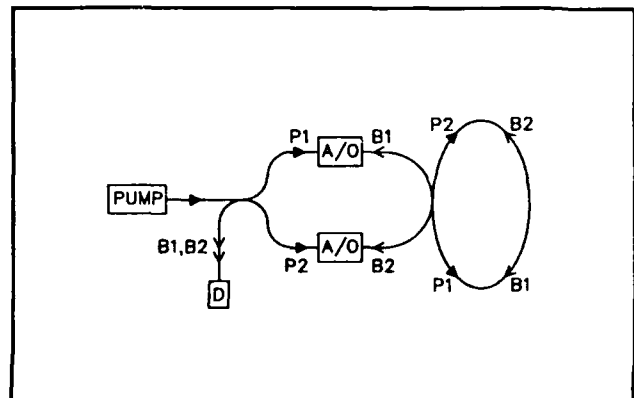


Figure 7. Simplified schematic diagram for a SBS ring laser gyroscope.

¹⁶ S.P. Smith, F. Zarinetchi, and S. Ezekiel, "Fiberoptic Ring Laser Gyroscope," *Proceedings of OFS '89*, Paris, France, 1989, post deadline paper.

¹⁷ F. Zarinetchi, S.P. Smith, and S. Ezekiel, "Stimulated Brillouin Fiber Optic Laser Gyroscope," *Opt. Lett.* 16: 229 (1991).

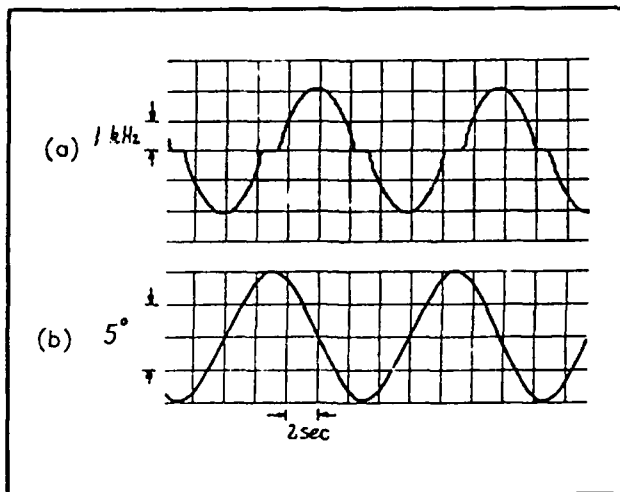


Figure 8. Simultaneous recording of (a) difference frequency between SBS lasers as a function of rotation and (b) angle of the applied rotation.

ence between the SBS lasers is zero. This "lock-in" zone is similar to that observed in the bulkoptic RLG and is caused by the coupling of the counterpropagating lasers through backscattering within the cavity. In the bulkoptic RLG, the lock-in effect has been thoroughly studied and is removed by mechanical dither.¹⁸

Mechanical rotation dither minimizes the amount of time that the gyro spends in the lock-in zone, thus reducing the errors due to lock-in. Mechanically dithering the fiber RLG would be much simpler than dithering the bulkoptic RLG because of its very small mass.

Another promising method for the removal of lock-in, which is being investigated here and elsewhere,¹⁹ is optical dither. In this case, instead of mechanically rotating the cavity, the optical path length of the cavity is modulated to generate a nonreciprocal phase shift between the SBS lasers. The optical path length of the cavity can be modulated using two phase shifters, PS1 and PS2, symmetrically located on the cavity, as shown in figure 9. With the phase shifters driven 180 degrees out of phase, there is no net change in the optical length of the cavity. However, due to the finite time it takes the light to go from one modulator to the other, a small nonreciprocal phase shift is generated. By appropriately adjusting the phase modulations, the

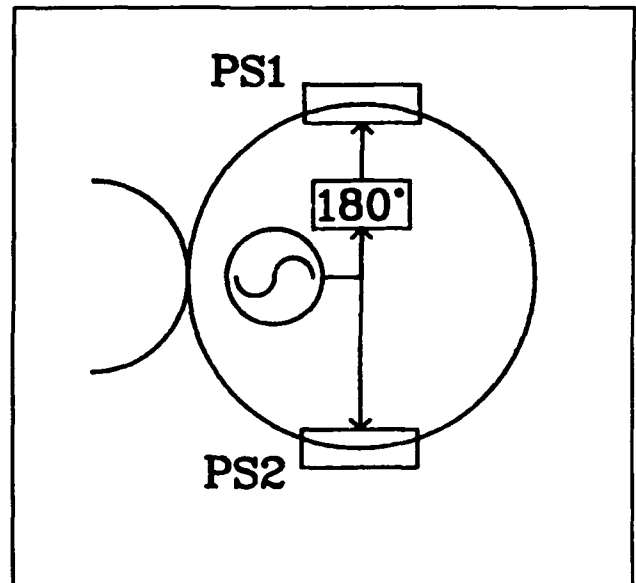


Figure 9. Simplified schematic diagram of a fiber resonator with optical dither.

coupling between the lasers can be greatly suppressed or completely eliminated.

Figures 10 and 11 demonstrate the effect of adjusting optical dither in a fiber cavity with high backscattering. Figure 10a shows the difference in frequency between the SBS lasers for a peak rotation equivalent to a Sagnac frequency of approximately 9 kHz and a lock-in zone of about 1 kHz, with Figure 10b indicating the corresponding rotation angle. Figure 11 shows the response to the same rotation with reduced optical dither, thus increasing the size of the lock-in zone to approximately 2 kHz. In practice, the maximum achievable lock-in suppression is limited by several factors including errors in modulator location, misadjustment of modulation parameters, and modulation distortion.

Another method for removing the lock-in is by generating the SBS lasers with a large frequency difference between them to prevent the lasers from locking. It is possible to generate a separation in frequency between the SBS lasers by either frequency shifting one of the pump lasers or by using separate pumps. In this way, the counterpropagating SBS lasers can be generated in different longitudinal modes of the cavity. Figure 12

¹⁸ F. Aronowitz, "The Laser Gyro," in *Laser Applications*, ed. M. Ross (New York: Academic Press, 1971), vol. 1, pp. 133-200.

¹⁹ S. Huang, K. Toyama, P.A. Nicati, L. Thevenaz, B.Y. Kim, and H.J. Shaw, "Brillouin Fiber Optic Gyro with Push-pull Phase Modulator and Synthetic Heterodyne Detection," *Proc. SPIE* 1795 (1992), Fiber Optic and Laser Sensors X, Boston, Massachusetts, September 8-11, 1992.

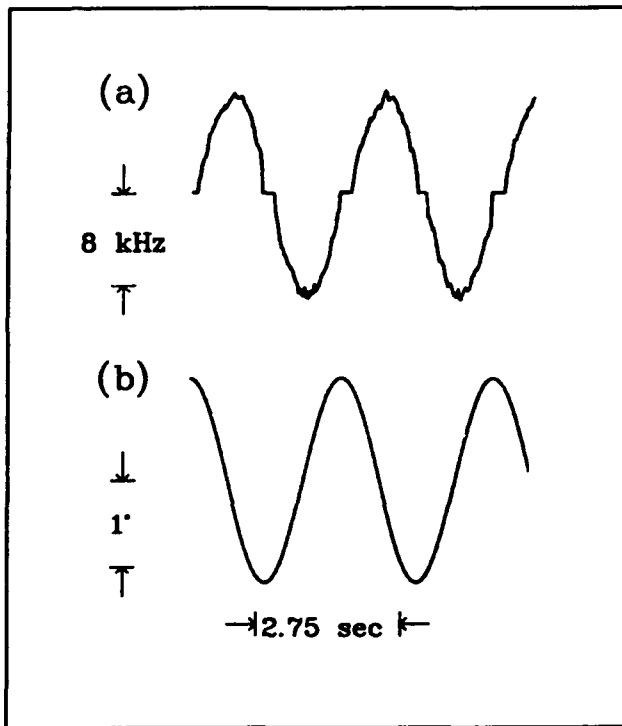


Figure 10. (a) Recording of SBS laser difference frequency and (b) the corresponding rotation angle with applied optical dither.

shows the lock-in free output beat frequency with rotation for such a configuration.

Aside from the temperature sensitivity of this mode of operation, there are a number of additional error sources that are unique to such an SBS gyro. One such error is due to bias variations caused by SBS dispersion pulls. In this case, the backscattering of pump laser P1, for example, generates a very small SBS gain in the same direction as P1. This new SBS gain, however, is also in the same direction as SBS laser B2 and will pull the frequency of B2, causing a bias variation. Further, since the backscattering in the cavity is highly variable, the size of the new SBS gain and hence the size of this frequency pull will also be highly variable.

In addition to lock-in, there are other error sources that are unique to any type of fiber resonator gyro. These include fiber birefringence and the nonlinear optical Kerr effect,²⁰ both of which have been observed and must be appropriately controlled.

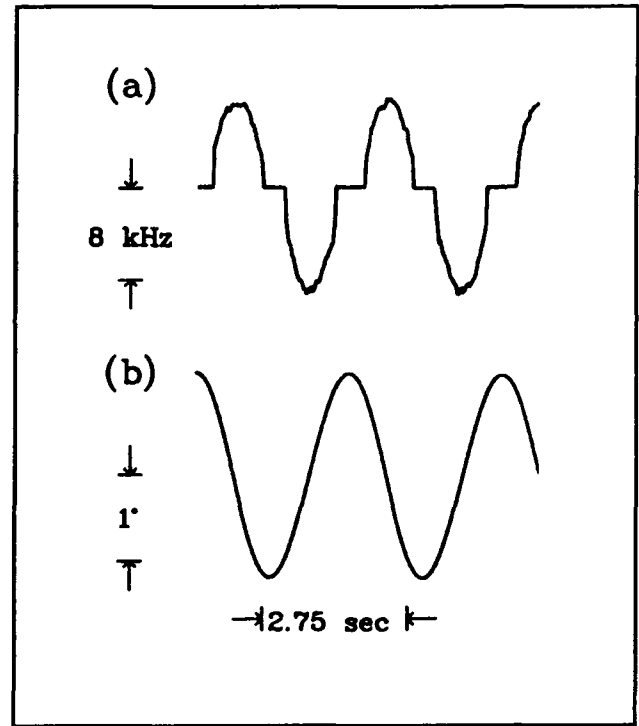


Figure 11. (a) SBS laser difference frequency and (b) the corresponding rotation angle with reduced optical dither.

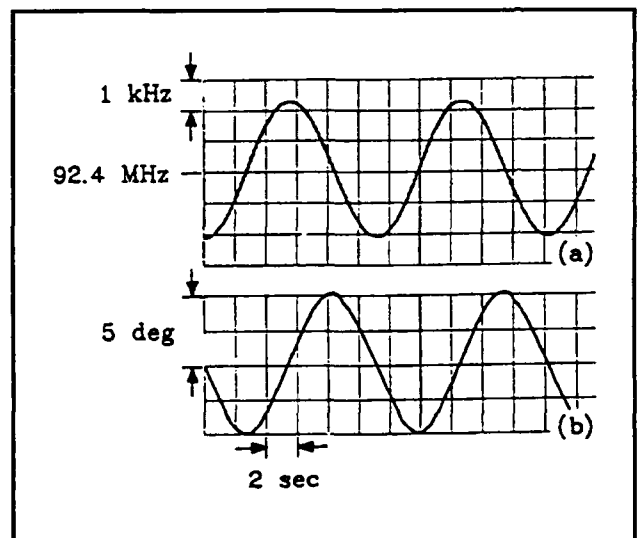


Figure 12. (a) SBS laser difference frequency with applied rotation and (b) the corresponding rotation angle for SBS gyro using SBS lasers with widely separated frequencies.

²⁰ S. Ezekiel, J.L. Davis, and R.W. Hellwarth, "Observation of Intensity-Induced Nonreciprocity in a Fiber Optic Gyroscope," *Opt. Lett.* 7: 457 (1982)



Professor Daniel Kleppner

Chapter 2. Basic Atomic Physics

Academic and Research Staff

Professor Daniel Kleppner, Professor David E. Pritchard, Dr. Wolfgang Ketterle, Dr. Alexander Martin

Visiting Scientists and Research Affiliates

Pin P. Chang,¹ Dr. Theodore W. Ducas,² Scott N. Paine,³ Dr. H. Joerg Schmiedmayer

Graduate Students

Michael P. Bradley, Kevin R. Boyce, Michael S. Chapman, Michael W. Courtney, Kendall B. Davis, Frank DiFilippo, Christopher R. Ekstrom, Troy D. Hammond, Jeffrey R. Holley, Hong Jiao, Michael A. Joffe, Robert P. Lutwak, Marc O. Mewes, Vasant Natarajan

Undergraduate Students

John E. Berberian, Tracie M. Drew, Matthew J. Marjanovic, J. David Pelly, Eliot J. Quataert, Alexis P. Silitch, Abraham D. Stroock, Bridget E. Tannian, John J. Wu, Peter Yesley

Technical and Support Staff

Carol A. Costa

2.1 Millimeter-Wave Frequency Measurement of the Rydberg Constant

Sponsors

Joint Services Electronics Program
Contract DAAL03-92-C-0001
National Science Foundation
Grant PHY 89-19381

Project Staff

Pin P. Chang, Dr. Theodore W. Ducas, Jeffrey R. Holley, Robert P. Lutwak, Scott N. Paine, Professor Daniel Kleppner

The Rydberg constant, R_∞ , relates the wavelengths of the spectrum of atomic hydrogen to practical laboratory units. As such, R_∞ is the natural unit for measurements of many atomic properties. Recent advances in optical wavelength metrology have enabled experiments using laser spectroscopy to measure R_∞ with accuracy approaching 2 parts in 10^{11} .⁴

While R_∞ remains the most accurately measured fundamental constant, other high-precision experiments, which depend on R_∞ as an auxiliary constant, demand even more accurate measurement. The accuracy of optical wavelength measurements is approaching the practical limitations of wavelength metrology. Further progress in the measurement of R_∞ will require frequency measurements making use of the modern definition of length in terms of time intervals and the defined speed of light.

We are attempting to advance the measurement of R_∞ by directly measuring cR_∞ , the "Rydberg frequency." By initially preparing highly excited "Rydberg" states of atomic hydrogen around $n=30$, we are able to measure millimeter-wave transitions to nearby states with the full precision of frequency metrology.

The goal of our experiment is three-fold: First is the reevaluation of R_∞ itself, providing an independent check, in a different regime, on concurrent developments in optical wavelength metrology. Second is the measurement of the ground state

¹ National Measurement Laboratory, Taiwan.

² Physics Department, Wellesley College, Wellesley, Massachusetts.

³ Smithsonian Astrophysical Observatory, Cambridge, Massachusetts.

⁴ T. Andreae et al., *Phys. Rev. Lett.* 69: 1923 (1992); F. Nez et al., *Phys. Rev. Lett.* 69: 2326 (1992).

Lamb shift. Because our measurements involve high angular momentum states for which the Lamb shift is extremely small, our results may be compared with optical measurements of transitions between low-lying states to yield an improved measurement of the Lamb shift. Third is the frequency calibration of the spectrum of hydrogen, which may eventually lead to a single frequency standard extending from the radio-frequency regime to the ultraviolet.

Our experiment is performed with an atomic beam in order to suppress the Doppler effect and to avoid collisional perturbations. Atomic hydrogen is excited to a low angular momentum $n=29$, $m=0$ state by two-photon stepwise absorption. The hydrogen atoms are then transferred to the longer lived $n=29$, $m=28$ "circular" state by the method of crossed electric and magnetic fields.⁵ The atoms enter a region of uniform fields in which the frequency of the resonant transition $n=29$, $m=28 \rightarrow n=30$, $m=29$ is measured. The atoms interact with the millimeter-wave radiation at two locations in a Ramsey separated oscillatory fields geometry. The final state distribution of the atoms is measured by

a state-selective electric field ionization detector. The resonance signal is observed as a transfer of atoms from the $n=29$ state to the $n=30$ state as the millimeter-wave frequency is tuned across the transition.

Figure 1 illustrates the main features of the apparatus. Atomic hydrogen or deuterium is produced by dissociation of H_2 or D_2 in a radio frequency discharge. The beam is cooled by collisions with the walls of a cryogenically cooled thermalizing channel in order to slow the beam and thereby increase the interaction time. The atoms are excited to the $n=29$, $m=28$ state by two-photon stepwise excitation in the circular state production region. The development of the hydrogen beam and optical systems was described in a previous *Progress Report*. The magnetic field necessary to transfer the atoms to the circular state is provided by permanent magnets. The electric field is produced by an arrangement of strip electrodes which allows the direction of the field to be rotated. A detector in the circular state production region monitors the efficiency of the laser excitation and momentum transfer processes.

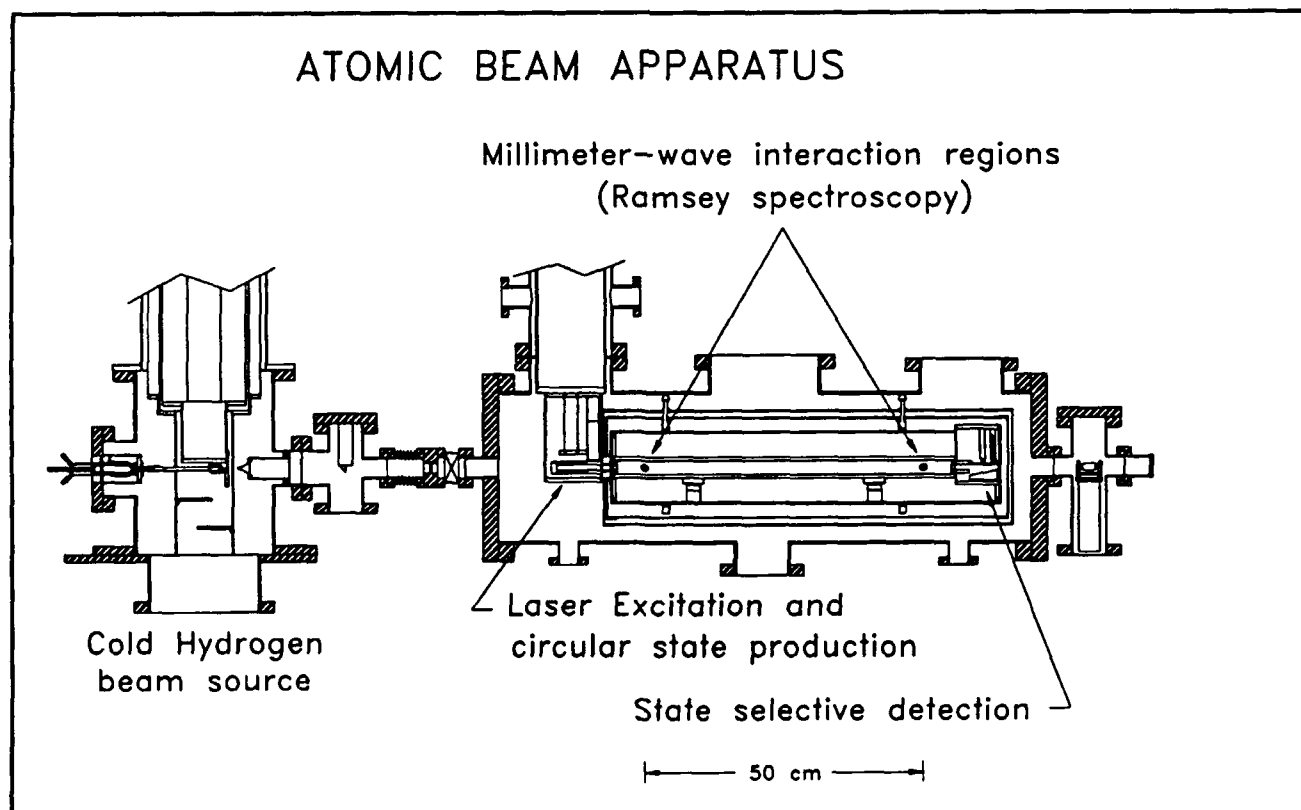


Figure 1. Schematic of the atomic beam apparatus.

⁵ D. Delande and J.C. Gay, *Europhys. Lett.* 5: 303 (1988).

After the atoms are prepared in the $n=29$ circular state, the beam enters the interaction region. Because Rydberg atoms interact strongly with external fields, accurate measurement of the energy level structure requires careful control of the interaction environment. Thermal radiation is reduced by cooling the interaction region to ~ 10 K by a liquid helium flow system. The ambient magnetic field is shielded out by a double-wall high-permeability shield. A small electric field, which defines the quantization axis of the atoms, is applied with high uniformity by field plates with corrective strip electrodes along the sides. The millimeter waves intersect the atomic beam at two locations separated by 50 cm. The millimeter-wave optics were described in a previous *Progress Report*.

The state distribution of the atoms emerging from the interaction region is analyzed by an electric field ionization detector. The atoms enter a region of increasing electric field produced by a ramped plate held at constant potential. The atoms in the $n=30$ state, which ionize at lower field, are collected in the first detector, while the $n=29$ atoms, which ionize at higher field, are collected at the second detector.

In the past year we have begun making measurements. Some typical time-resolved Ramsey fringe data is presented in figure 2. The accuracy with which we can currently extract R_∞ from the data is limited by our understanding of the systematics of the experiment to about 1 part in 10^9 . In order to extract all the necessary systematic information, it will be necessary to increase the signal-to-noise ratio of the experiment by a factor of at least 1000. Towards this end, efforts are underway to increase the duty cycle of the experiment and to decrease signal loss due to blackbody radiation. We have acquired a 120 Hz excimer pump laser to replace our aging 10 Hz YAG laser and have begun development of a new ultraviolet dye laser system. In addition to the improvement in signal from the increased repetition rate, we expect the new system to provide a narrower UV linewidth and, hence, improved efficiency of atomic excitation. We are also investigating alternative methods of circular state production which may lead to better radiation

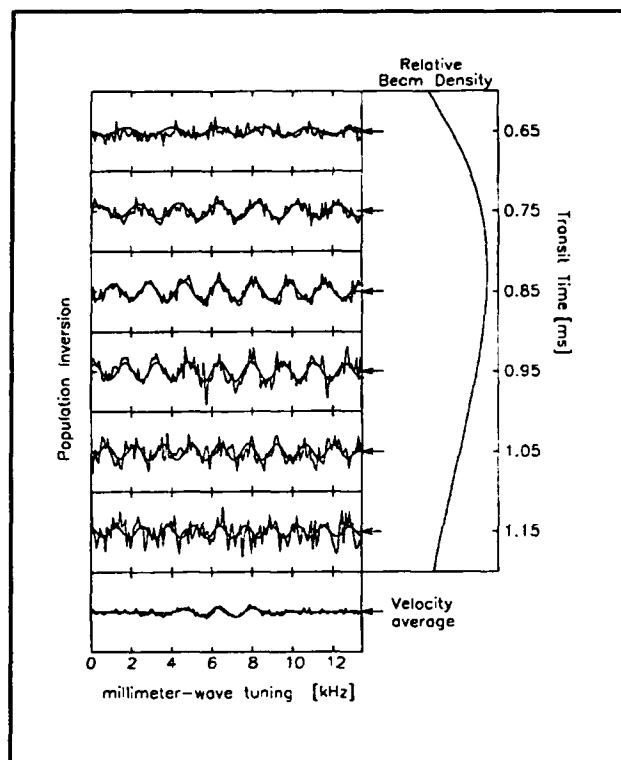


Figure 2. Preliminary data displaying narrow linewidth "Ramsey" fringes. The deuterium $n=29$, $m=28 \rightarrow n=30$, $m=29$ circular transition is shown. The time resolution of the detection system allows each velocity group to be studied independently. The velocity-averaged data is presented, along with the theoretical model, at the bottom of the page. Further refinement of these experiments will yield a measurement of R_∞ with accuracy of 1 part in 10^{11} .

shielding and simpler evaluation of the magnetic field strength in the interaction region.

2.1.1 Publications

Chang, P. *Measurement of the Rydberg Frequency Using Circular Rydberg States of Atomic Hydrogen*. Ph.D. diss., Dept. of Physics, MIT, 1992.

Paine, S. *High Precision Millimeter-Wave Spectroscopy of Atomic Hydrogen*. Ph.D. diss., Dept. of Physics, MIT, 1992.

2.2 The Diamagnetic Rydberg Atom

Sponsors

National Science Foundation
Grant PHY 89-19381
U.S. Navy - Office of Naval Research
Grant N00014-90-J-1322

Project Staff

Michael W. Courtney, Hong Jiao, Professor Daniel Kleppner

A highly excited hydrogen atom in a strong magnetic field, the so-called "diamagnetic hydrogen atom," is among the simplest nonseparable systems in quantum mechanics. Understanding this atom could provide a key to the more general aspects of nonseparable systems. The problem is also attracting attention in the context of nonlinear dynamics because its classical behavior displays a transition from orderly to disorderly motion as the energy is increased in a fixed magnetic field. One can study the quantum structure of the system in this regime both theoretically and experimentally. Thus, the diamagnetic hydrogen atom provides an ideal testing ground for studying the relation between quantum structure and disorderly classical motion, a subject sometimes called "quantum chaos."

We have developed techniques for carrying out high resolution laser spectroscopy on the lithium atom in a strong magnetic field. The difference between lithium and hydrogen is minor for Rydberg atoms.

The experiment uses a lithium atomic beam which is excited by two c.w. lasers. The first laser excites the atoms from the 2S state to the 3S state by a two-photon transition and the second laser excites the atoms to Rydberg states. The excited atoms are detected by electric field ionization. We typically operate in magnetic fields near 6T. We can determine the energy within 10^{-3} cm^{-1} , the magnetic field within 5 gauss. Figure 3 shows the atomic beam apparatus and superconducting magnet.

The Hamiltonian for the diamagnetic hydrogen atom, in atomic units, is

$$\mathcal{H} = \frac{p^2}{2} - \frac{1}{r} + \frac{1}{2} L_z B + \frac{1}{8} B^2 \rho^2 \quad (1)$$

There are no general solutions to this problem and perturbation theory is inapplicable in the positive energy regime. In previous years, our experimental results⁶ have helped to stimulate theoretical advances, but an obsolete superconducting magnet made further progress difficult. The apparatus has been rebuilt using a new superconducting magnet.

The new magnet employs a split coil configuration. The four-inch bore allows a significantly larger interaction region and more convenient optical access than previously possible. Rydberg atoms are very sensitive to stray electric fields, which was a limiting factor in our previous work. Figure 4 shows the new interaction region in which stray electric fields are greatly reduced because surfaces are farther from the interaction volume. In addition, any stray electric field parallel to the magnet axis can be cancelled out by field plates, or an electric field can be applied as an additional probe of the system. Another improvement in the interaction region is the collection of light from fluorescence decay of the 3S state. One mirror focuses light onto a light pipe. Another doubles the area of collection by focusing light back to the point of interaction.

A scintillator and light pipe have replaced the surface barrier diode for detection of Rydberg atoms. After atoms are ionized, they are accelerated into the scintillator by a 15 KV potential. Light produced is carried to a photomultiplier by the light pipe. This detection method has the advantage of being able to count single ions. As a result, our signal is linear to the number of Rydberg atoms produced, and we detect nearly all the Rydberg atoms produced.

In certain regimes the system displays one-dimensional behavior. It is useful to write the Hamiltonian for the diamagnetic hydrogen atom as

$$\mathcal{H} = \mathcal{H}_\rho + \mathcal{H}_z + \mathcal{H}', \quad (2)$$

where

$$\mathcal{H}_\rho = \frac{p_\rho^2}{2} + \frac{1}{2} L_z B + \frac{1}{8} B^2 \rho^2, \quad (3)$$

$$\mathcal{H}_z = \frac{p_z^2}{2} - \frac{1}{|z|}, \quad (4)$$

⁶ D. Delande, A. Bommier, and J.C. Gay, *Phys. Rev. Lett.* 66: 141 (1991); C. Lu, G.R. Welch, M.M. Kash, D. Kleppner, D. Delande, and J.C. Gay, *Phys. Rev. Lett.* 66: 145 (1991).

and

$$\mathcal{H}' = \frac{1}{|z|} - \frac{1}{r}. \quad (5)$$

\mathcal{H}_0 is the Hamiltonian of an electron in a magnetic field, \mathcal{H}_z is the Hamiltonian of one-dimensional Hydrogen, and \mathcal{H}' is a perturbation to the otherwise trivial Hamiltonian. Although the perturbing potential is not small (in fact it is singular for the entire $z=0$ plane), it has been shown⁷ that parts of the experimental spectrum can be understood simply in terms of the unperturbed Hamiltonian as a superposition of the spectra of one-dimensional Hydrogen and an electron in a magnetic field.

Using the stray electric field in the old apparatus, we have studied the Stark splitting of the one-dimensional hydrogen atom that is approximated by magnetic confinement of the electron transverse to

the magnetic field. The measured field is in reasonable agreement with the splitting predicted by the one-dimensional model. However, it is more desirable to measure the Stark splitting at a variety of electric fields by using the electric field as a controlled probe to check how closely our system resembles one-dimensional Hydrogen. The new magnet and interaction region allow this to be done.

Using a program written by Dominique Delande of E.N.S. Paris, we have calculated the spectra in many regions below the ionization limit. One result of these calculations suggests that there are energy levels which correspond to wavefunctions localized near the $z=0$ plane. These levels can be connected with eigenvalues of a simple one dimensional model, and they produce the smallest anticrossings in the system. This suggests yet another undiscovered approximate symmetry. It also shows that in spite of the chaotic nature of the corresponding classical motion, the trivial periodic

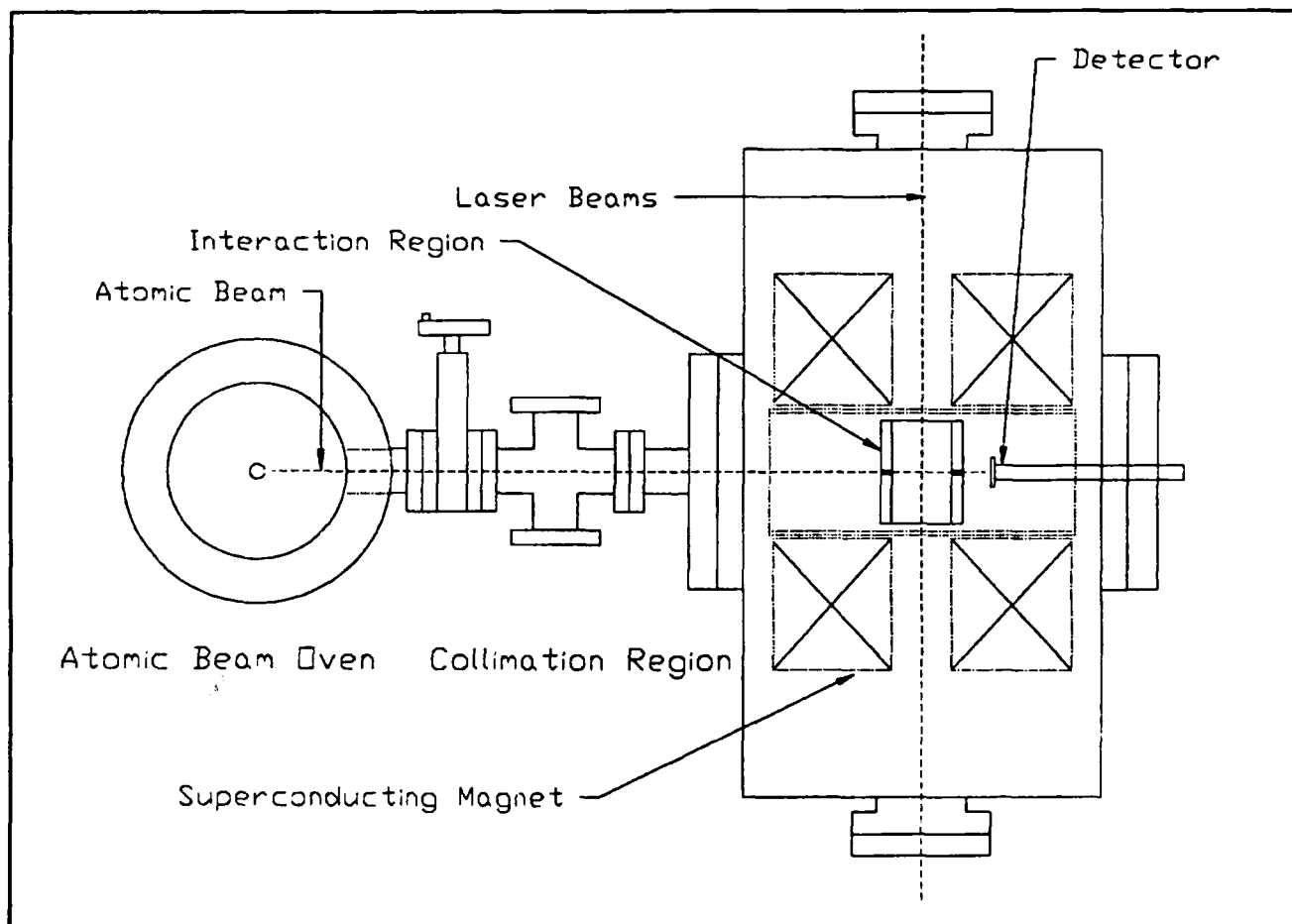


Figure 3. Superconducting magnet and atomic beam apparatus.

⁷ C. Lu, G.R. Welch, M.M. Kash, L. Hsu, and D. Kleppner, *Phys. Rev. Lett.* 63: 1133 (1989).

orbits in the $z=0$ plane have a strong influence on the quantum spectrum. This has been shown previously in the quasi-Landau modulations (periodic modulations in the oscillator strength of 1.5 times the cyclotron frequency⁸), but ours is the first work connecting these orbits with individual energy levels.

There is a growing interest in periodic orbit spectroscopy. Periodic orbit spectroscopy is a technique that relates the quantum mechanical spectrum to the periodic orbits of the corresponding classical system.⁹ Classically chaotic systems possess a proliferation of periodic orbits. The clas-

sical dynamics of diamagnetic hydrogen follow a simple scaling rule, and the Fourier transform of the constant-scaled-energy spectrum gives the scaled classical actions of periodic orbits. This has been shown experimentally,¹⁰ but many peaks in the Fourier transform were unresolved. A better technique is needed to study quantum processes corresponding to classical bifurcations of periodic orbits. Classical bifurcation theory describes the manner in which new periodic orbits can be created out of old ones or "out of nowhere" as the energy changes.

We have shown that the results of Delande's program can be used to calculate the constant-

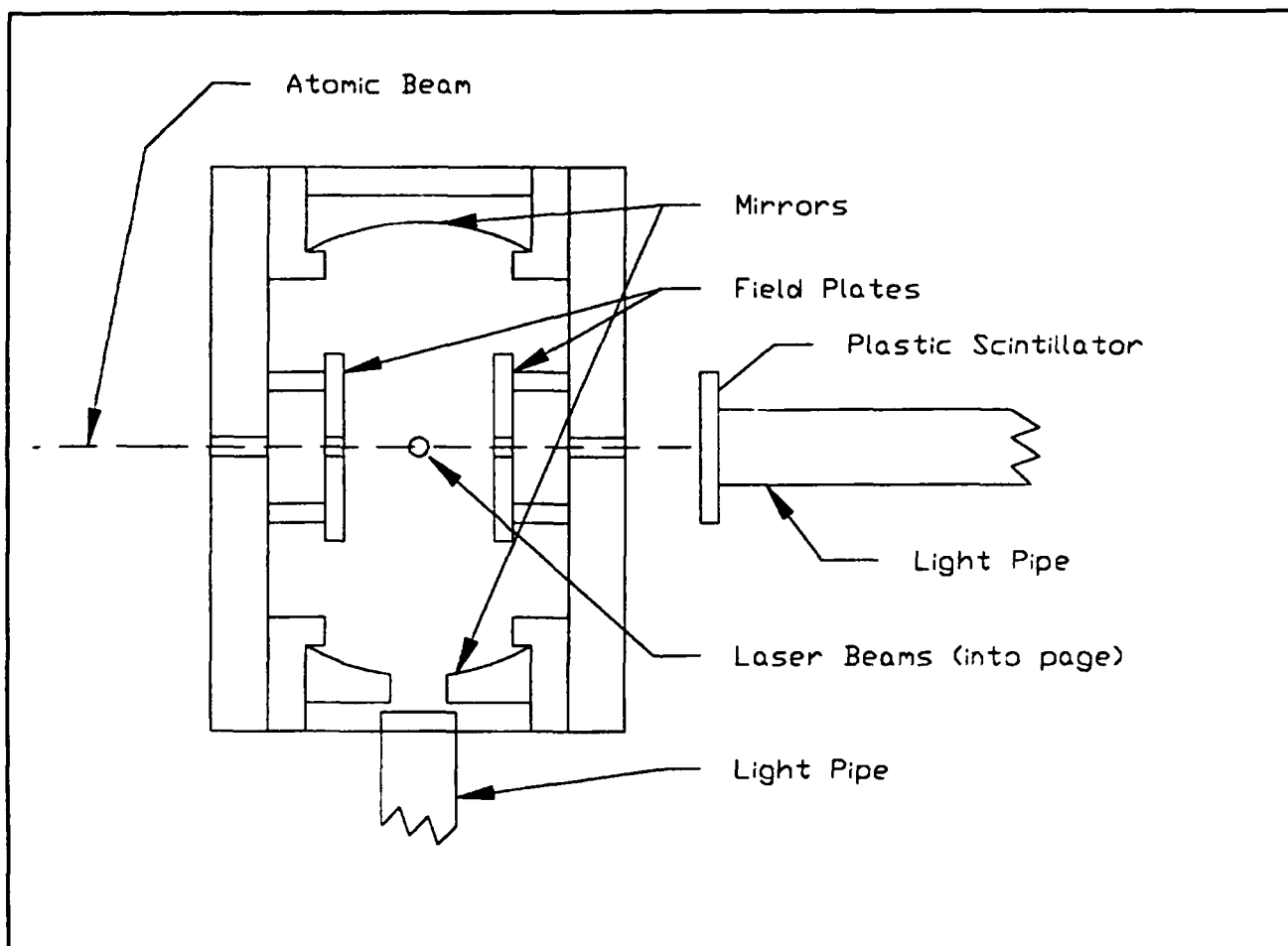


Figure 4. Interaction region.

⁸ J.C. Castro, M.L. Zimmerman, R.G. Hulet, and D. Kleppner, "Origin and Structure of the Quasi-Landau Resonances," *Phys. Rev. Lett.* 45: 1780 (1980).

⁹ A. Holle, J. Main, G. Wiebusch, H. Rottke, and K.H. Welge, "Quasi-Landau Spectrum of the Chaotic Diamagnetic Hydrogen Atom," *Phys. Rev. Lett.* 61: 161 (1988); J.-M. Mao and J.B. Delos, "Hamiltonian Bifurcation Theory of Closed Orbits in the Diamagnetic Kepler Problem," *Phys. Rev. A.* 45: 1746 (1992).

¹⁰ A. Holle, J. Main, G. Wiebusch, H. Rottke, and K.H. Welge, "Quasi-Landau Spectrum of the Chaotic Diamagnetic Hydrogen Atom," *Phys. Rev. Lett.* 61: 161 (1988).

scaled-energy spectrum. One constant-scaled-energy spectrum and a series of Fourier transforms is shown in Figure 5. Each peak in the Fourier transform corresponds to the scaled classical action of a periodic orbit. These results are currently being compared with the semi-classical results of J.B. Delos.

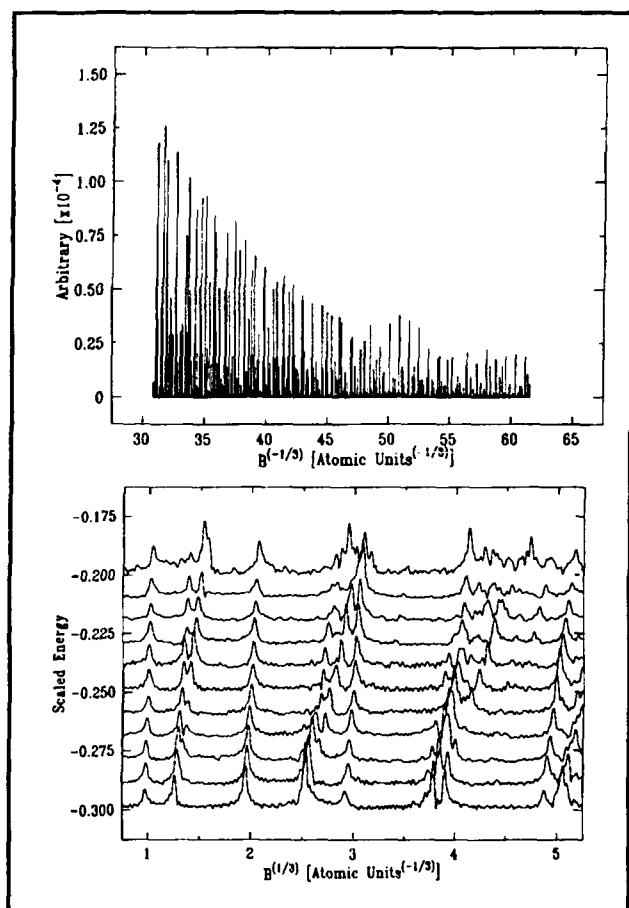


Figure 5. a) Constant-scaled-energy spectrum for a scaled energy of -0.3. b) Fourier transforms. Each peak corresponds to a periodic orbit of the classical system.

2.3 Precision Mass Spectroscopy of Ions

Sponsors

Joint Services Electronics Program
Contract DAAL03-92-C-0001
National Science Foundation
Grant PHY 89-21769

Project Staff

Michael P. Bradley, Kevin R. Boyce, Frank DiFilippo, Tracie M. Drew, Matthew J. Marjanovic,

Vasant Natarajan, Abraham D. Stroock, Professor David E. Pritchard

In 1992, we undertook a program of measurement of the atomic masses of some key atoms important for the improvement of the nuclear mass table. Through major improvements in our experiment, we have increased our precision by a factor of 5 to less than 10^{-10} and performed several checks on our sources of error. This capability will allow us to do a variety of experiments in both fundamental and applied physics, including:

- The $^3\text{H}^+ - ^3\text{He}^+$ mass difference, important in ongoing experiments to determine the electron neutrino rest mass;
- Determination of Avogadro's number N_A , by weighing γ -rays—and combined with the Rydberg, gives an independent value of α ; Determining the Avogadro's number accurately would permit the replacement of the "artifact" mass standard by an atomic mass standard.
- Improvement of many traditional applications of mass spectroscopy by orders of magnitude improvement in both accuracy and sensitivity and,
- Determination of excitation and binding energies of atomic and molecular ions by weighing the small decrease in energy, $\Delta m = E_{\text{bind}}/c^2$ (we must reach our ultimate goal of a few $\times 10^{-12}$ to make this a generally useful technique).

Our experimental approach is to measure ion cyclotron resonance on a single molecular or atomic ion in a Penning trap, a highly uniform magnetic field with axial confinement provided by weaker electric fields. We monitor the ion's oscillation along the magnetic field lines by detecting the currents induced in the trap electrodes. Working with only a single ion is essential because space charge from other ions leads to undesired frequency shifts. This work in trapping and precision resonance draws on techniques developed by Hans Dehmelt at the University of Washington and Norman Ramsey at Harvard University, for which they shared the Nobel Prize in 1989.

We have developed techniques for driving, cooling, and measuring the frequencies of all three normal modes of Penning trap motion. Thus, we can reproduce our manipulation of the ion position to within 30 microns of the center of the trap, correcting for electrostatic shifts in the cyclotron frequency to great accuracy. We use a π -pulse method to coherently swap the phase and action of

the cyclotron and axial modes.¹¹ Therefore, although we detect only the axial motion directly, we can determine cyclotron frequency by measuring the phase accumulated in the cyclotron motion in a known time interval (figures 6a and 6b).

In the past two years we have rebuilt our apparatus with a new Penning trap and quieter rf SQUID detector. We have implemented a new signal processing algorithm to improve our phase estimation by a factor of 2-3, resulting in a precision of 1×10^{-10} for a one-minute measurement. Our entire ion-making process has been automated, and the computer can cycle from an empty trap to having a cooled single ion in about 3 minutes. This has been partly due to a new broadband white noise generator that is used to expel unwanted ions.¹² In addition, we have built an external ion source and associated optics that can produce and select ions with a resolution of 0.1. When this comes on line, we should be able to greatly reduce the percentage of "bad" ions and also alleviate the problem of residual neutral gas when using volatile species such as helium.

We have also developed a new measurement technique that enables us to extend our precision comparison to non-doublets of mass (actually mass to charge ratio). This has allowed us to perform stringent checks on systematics using such known ratios as N_2/N^+ and Ar^+/Ar^{++} . This represents a significant advance in precision mass spectrometry since it allows us to obtain absolute masses by direct comparison to carbon. Indeed, we have compared CD_2 and CD_3 to C to obtain two determinations of the absolute mass of deuterium. Mass ratios of doublets cannot be inverted to obtain absolute masses in general without comparing some species to carbon (C_6H_4/C_7H_2 to obtain H or C_3D_8/C_4D_2 to obtain D, for example). But we have developed a scheme involving only doublet comparisons that uses the known Ar^+/Ar^{++} ratio to obtain the absolute masses of several light atoms—H, D, N, O, Ne, Ar—to about an order of magnitude better than the current standard mass table. The value of the deuterium mass obtained using this method is consistent with the value from the direct non-doublet comparisons, giving us confidence in our error estimates. With H and D thus known, we can obtain the mass of any ions by comparison with a suitable organic compound of the same nominal mass.

With the field imperfections (both magnetic and electric) shimmed as well as we can, our systematic errors are well below 5×10^{-11} . In one night of quiet magnetic time, we can get between 20 and 30 switches of the two ion species. The lowest statistical noise we have obtained thus far is 2.4×10^{-10} per shot (over the smooth drift in the field) and 6×10^{-11} for the night (see figure 6). We feel that this precision is perhaps the limit with the alternate ion scheme that we use now, but this is already quite a useful precision for the $^3H-^3He$ and the N_{Ar} measurements described above. We plan to improve our precision either by shielding field fluctu-

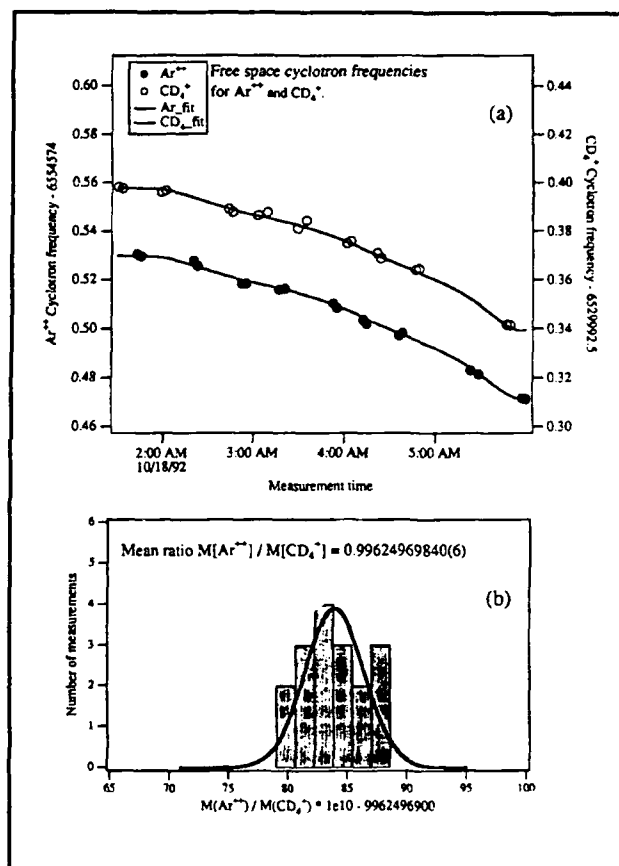


Figure 6. (a) Cyclotron frequency as a function of time for alternate CD_2 and Ar^{++} ions in our Penning trap. The frequencies are obtained after a 50s integration of cyclotron phase (see text). The solid line is a polynomial fit to the drift in the field common to both ions. (b) A histogram of the individual ratios obtained between neighbouring points. Solid line is a gaussian distribution with a standard deviation of 2.4×10^{-10} .

¹¹ E.A. Cornell, R.M. Weisskoff, K.R. Boyce, and D.E. Pritchard, "Mode Coupling in a Penning Trap: π and a Classical Avoided Crossing," *Phys. Rev. A* 41: 312 (1990).

¹² K.R. Boyce, *Improved Single Ion Cyclotron Resonance Mass Spectroscopy*, Ph.D. diss., Dept. of Physics, MIT, 1992.

ations better or having two ions in the trap at the same time.¹³

If we can get the shot to shot fluctuation below 1×10^{-10} , the primary source of measurement noise will be the special relativistic mass shift due to thermal fluctuations in cyclotron amplitude. We have proposed a scheme of classical squeezing with parametric drives to reduce amplitude fluctuations.¹⁴ We hope to demonstrate its ability in reducing these fluctuations by a factor of 3 to 5. These techniques should help us in reaching our ultimate goal in precision of a few parts in 10^{12} , necessary for weighing chemical bonds.

Publications

Boyce, K.R. *Improved Single Ion Cyclotron Resonance Mass Spectroscopy*. Ph.D. diss. Dept. of Physics, MIT, 1992.

Cornell, E.A., K.R. Boyce, D.L.K. Fyngenson and D.E. Pritchard. Two Ions in a Penning Trap: Implications for Precision Mass Spectroscopy." *Phys. Rev. A* 45: 3049-3059 (1992).

DiFilippo, F., V. Natarajan, K.R. Boyce, and D.E. Pritchard. "Classical Amplitude Squeezing for Precision Measurements." *Phys. Rev. Lett.* 68: 2859-2862 (1992).

2.4 Atom Interferometry

Project Staff

John E. Berberian, Michael S. Chapman, Christopher R. Ekstrom, Troy D. Hammond, Eliot J. Quataert, Dr. H. Joerg Schmiedmayer, Bridget E. Tannian, Professor David E. Pritchard

Sponsors

Joint Services Electronics Program

Contract DAAL03-92-C-0001
U.S. Army - Office of Scientific Research
Contract DAAL03-89-K-0082
U.S. Navy - Office of Naval Research
Grant N00014-89-J-1207

During 1992, we refined our atom interferometer¹⁵ and began performing experiments with spatially separated beams. The interferometer is now operating with smaller period gratings,¹⁶ providing greater beam separation. The experiments were performed with the aid of an interaction region that inserts a thin metal foil between the beams. This allowed us to manipulate the atomic wave function in only one arm of the interferometer.

Atom interferometers will make possible qualitatively new types of experiments involving inertial effects, studies of atomic and molecular properties, and tests of fundamental physics. In addition, they may ultimately open the way for making ultra-small structures using atom holograms.

- The relatively large mass and low velocity of atoms make atom interferometers especially sensitive to inertial effects such as rotation, acceleration, and gravity. Sagnac rotation has been observed in accord with theoretical predictions¹⁷ and sensitivity to gravitational acceleration at the 3×10^{-6} level has been demonstrated.¹⁸ Atom interferometers may become the best absolute accelerometers and gravimeters in the next few years.
- Atom interferometers can be applied to a number of experiments in fundamental physics: tests of quantum mechanics such as the Aharonov-Casher effect,¹⁷ geometric phases and the measurement process, measurement of the equality of proton and electron charges, and a precise measurement of the momentum of a photon. This latter measurement should produce a new high precision value for the fundamental constants $N_A \hbar$.

¹³ E.A. Cornell, K.R. Boyce, D.L.K. Fyngenson and D.E. Pritchard, Two Ions in a Penning Trap: Implications for Precision Mass Spectroscopy." *Phys. Rev. A* 45: 3049-3059 (1992).

¹⁴ F. DiFilippo, V. Natarajan, K.R. Boyce, and D.E. Pritchard, "Classical Amplitude Squeezing for Precision Measurements." *Phys. Rev. Lett.* 68: 2859-2862 (1992).

¹⁵ D.W. Keith, C.R. Ekstrom, Q.A. Turchette, D.E. Pritchard, "An Atom Interferometry for Atoms," *Phys. Rev. Lett.* 66: 2693 (1991).

¹⁶ C.R. Ekstrom, D.W. Keith, and D.E. Pritchard, "Atom Optics Using Microfabricated Structures," *Appl. Phys. B* 54: 369 (1992).

¹⁷ F. Riehle, T. Kisters, A. Witte, J. Helmcke, and J. Borde, "Optical Ramsey Spectroscopy in a Rotating Frame: Sagnac Effect in a Matter Wave Interferometer," *Phys. Rev. Lett.* 67: 177 (1991).

¹⁸ M. Kasevich and S. Chu, "Atomic Interferometry Using Stimulated Raman Transitions," *Phys. Rev. Lett.* 67: 181 (1991).

- Interferometers for atoms and molecules will offer more accurate ways to measure intrinsic properties of these particles, like their polarizability. They will also open up new areas of study, such as measurements of the "index of refraction" of a gas for a particle beam which passes through it.

The key component of our interferometer is the set of three matched transmission diffraction gratings which we constructed at the National Nanofabrication Facility (NNF) at Cornell University. The process allows fabrication of precisely positioned openings in thin silicon nitride membranes mounted in silicon frames. The pattern created in the membrane is determined by an electron beam writer, making the process quite versatile. This process was used to create a variety of diffraction gratings used in the interferometer. In addition, several zone plates (atom lenses) were also built, and were later successfully demonstrated.¹⁹

Our present interferometer consists of three 200 nm period transmission gratings, mounted 0.66 m apart on separate translation stages inside the vacuum envelope. During operation, the 0th and 1st order beams from the first grating strike the middle grating (which is 140 μm wide) where they are diffracted in the 1st and -1st orders so that they converge at the third grating. At the second (middle) grating the beams have widths of 30 μm (FWHM) and are separated by 55 μm . The first two gratings form an interference pattern in the plane of the third grating, which acts as a mask to sample this pattern. The detector, located 0.30 m beyond the third grating, records the flux transmitted by the third grating. An interaction region, consisting of a stretched metal foil positioned symmetrically between two side electrodes, is inserted in the interferometer so that the atom wave in the two sides of the interferometer went on opposite sides of the foil. The foil was 10 cm long and 10 microns thick and the gap between the foil and each electrode, where the separated atom beams traveled, was 2 mm. Figure 7 shows the design of the interferometer.

The data necessary to determine the interferometer phase and contrast are acquired by modulating the position of one grating relative to the other two and simultaneously recording the signal from the atom counting electronics as well as the signal from an optical interferometer used to measure the relative position of the gratings. After removing data obscured by noise spikes from the hot wire, the

atom count rate data are averaged into bins according to relative grating position, resulting in the fringe pattern shown in figure 8. The peak to peak amplitude of our interference signal is 1600 Hz, which enables us to determine the interferometer phase to a precision of 15 milliradians in 1 minute.

By putting an electric field on one side of the interaction region, the interference pattern is shifted. This phase shift is caused by the DC Stark shift of the atom. The Stark shift is $-\alpha E^2/2$, where α is the electric polarizability and E is the electric field. The measured phase shift was quadratic with the applied field, allowing us to determine the polarizability of the ground state. Figure 9 shows the phase shifts versus applied electric field. By observing the reduction of the interference contrast with increasing phase shift, we can measure the longitudinal coherence length of the atomic beam. Our coherence length is 1.6 \AA , consistent with the measured velocity distribution.

In another experiment, we apply a uniform magnetic field along the beam axis to determine the quantization direction. By running a current down the metal foil, perpendicular to the plane of the interferometer, we increase the field magnitude on one side of the interaction region (thus on one beam) and decrease it on the other. This gives a differential Zeeman energy, and therefore phase, for the two paths that is proportional to the septum current and the projection of the magnetic moment along the beam axis.

The interference pattern of each of the eight sodium ground states shifts independently. There are five different values of the angular momentum projection (one each $m_F \pm 2$, two each $m_F = \pm 1, 0$). The different interference patterns superpose to produce an interference pattern whose contrast depends on the differential Zeeman shifts. This is shown in figure 10. The first revival of contrast is the point where the phase shifts are: $\pm 4\pi$ for the $|m_F| = 2$ states, $\pm 2\pi$ for the $|m_F| = 1$ states, and 0 for the $m_F = 0$ states.

The scientific future of atoms interferometers looks bright: atom beam sources are inexpensive and intense relative to other particle beams/sources (e.g., neutrons, electrons); several techniques have now been demonstrated to make interferometers for them; and the atoms which may be used in them come with a wide range of parameters such as polarizability, mass, and magnetic moment. This assures the applicability of these instruments to a

¹⁹ C.R. Ekstrom, D.W. Keith, and D.E. Pritchard, "Atom Optics Using Microfabricated Structures," *Appl. Phys. B* 54: 369 (1992).

wide range of measurements of both fundamental and practical interest.

Publications

Berberian, J. *Measuring the Isotropic Polarizability of the Sodium Ground State*. S.B. thesis, Dept. of Physics, MIT, 1992.

Ekstrom, C.R., D.W. Keith, and D.E. Pritchard. "Atom Optics Using Microfabricated Structures," *Appl. Phys. B* 54: 369-374 (1992).

Turchette, Q.A., D.E. Pritchard, and D.W. Keith. Numerical Model of a Multiple Grating Interferometer, *J. Opt. Soc. Am. A* 9: 1601-1606 (1992).

Pritchard, D.E. "Atom Interferometers." In *Proceedings of the 13th International Conference on Atomic Physics*, Munich, Germany, August 3-7, 1992, Eds. T.W. Hansch and H. Walther.

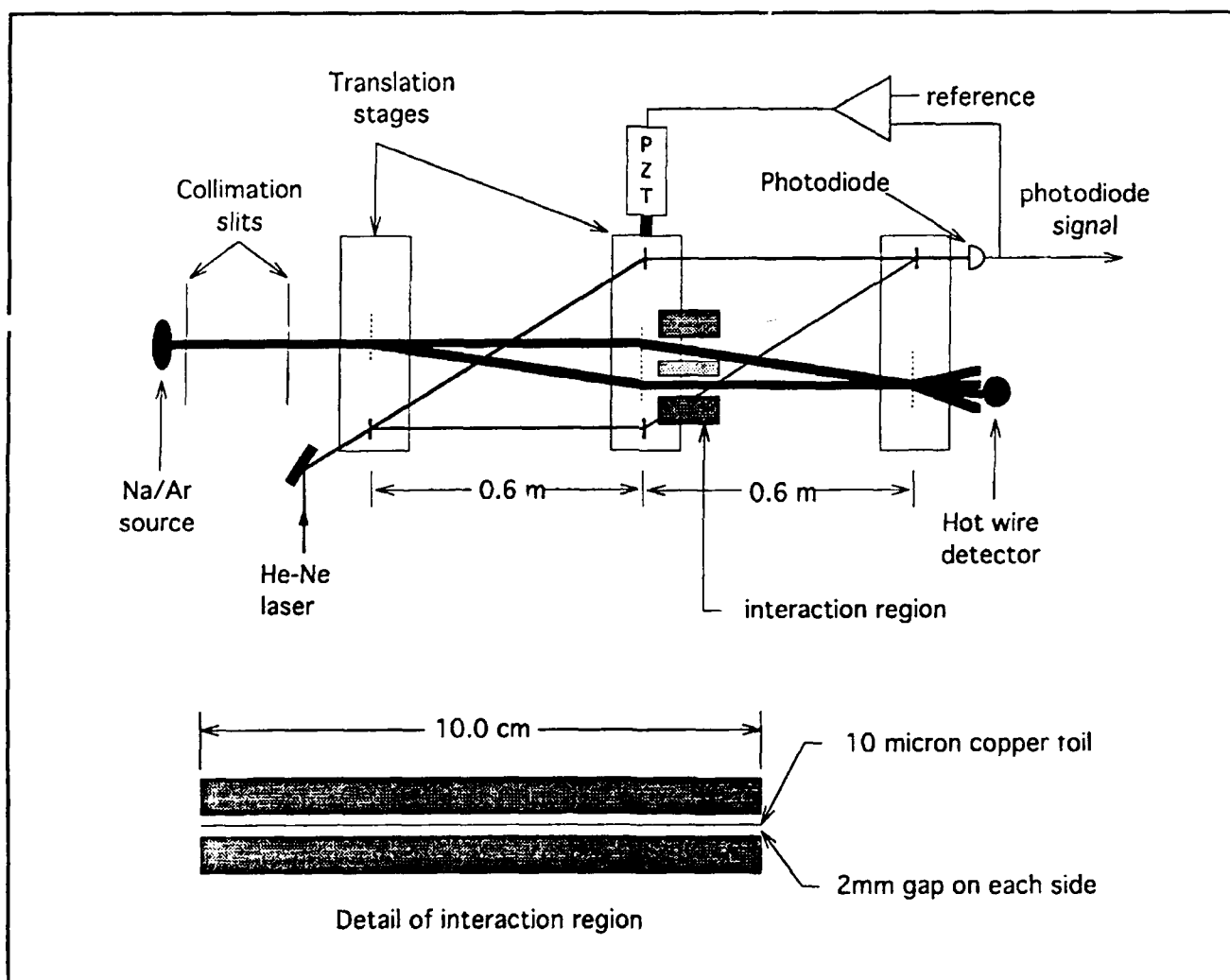


Figure 7. A schematic, not to scale, of our atom interferometer showing the active vibration isolation system and the interaction region. The 10 μm copper foil is shown between the two arms of the interferometer (thick lines are atom beams). The optical interferometer (thin lines are He-Ne beams) is used for active vibration isolation. The 200-nm period atom gratings are indicated by a vertical dashed line, and the 3.3- μm period optical gratings by a vertical solid line.

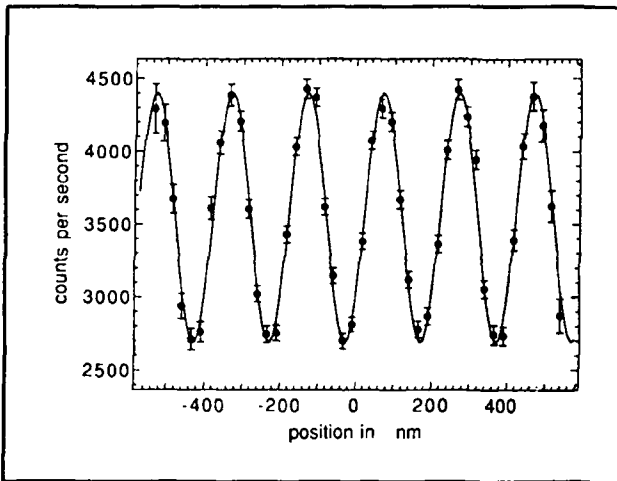


Figure 8. Interference pattern from 40 seconds of data. The interference signal is 860 counts per second with a contrast of 25%, which allows us to determine the phase to 15 milliradians in 1 minute. A background of 120 counts per second has been subtracted.

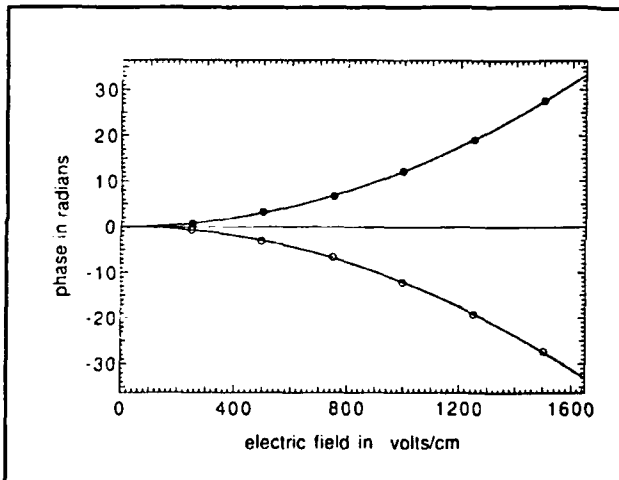


Figure 9. Stark phase shifts for voltages applied to the right (open circles) and the left (filled circles) sides of the interaction region. Phase shift per applied electric field in $(\text{volt/cm})^2$ is $1.220(7) \times 10^{-5}$ for the left side and $1.224(7) \times 10^{-5}$ for the right side. This measurement statistically determines the dc polarizability of sodium to 0.4%.

2.4.1 Cooling and Trapping Neutral Atoms

Sponsors

Joint Services Electronics Program
Contract DAAL03-92-C-0001
U.S. Navy - Office of Naval Research
Grant N00014-90-J-1642

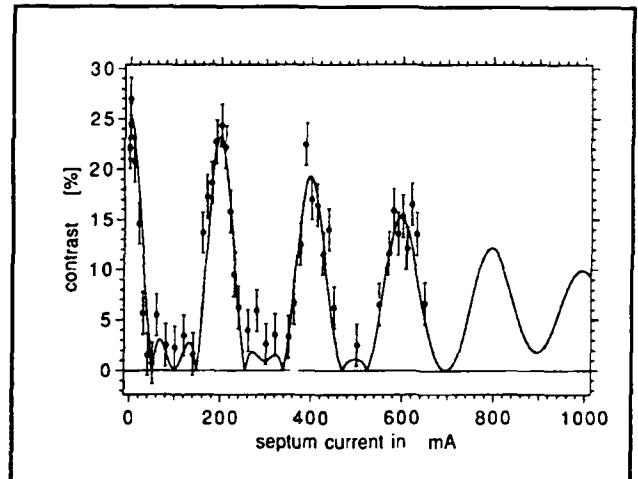


Figure 10. Contrast revival from the independent precession of the 8 different internal ground states of sodium. A current flows down the septum, altering the size of an axial magnetic guide.

Project Staff

Dr. Alexander Martin, Dr. Wolfgang Ketterle, Kendall B. Davis, Michael A. Joffe, Marc O. Mewes, J. David Pelly, Alexis P. Silitch, John J. Wu, Professor David E. Pritchard

Our current objective is to obtain samples of atoms at very high density and ultra-low temperatures. This goal is pursued by using a high flux slower for atoms, a dark light trap to stop and compress the atoms, and a magnetic trap for the final confinement and cooling.

Experiments with dense samples of cold neutral atoms promise exciting new discoveries in basic and applied physics. Due to the considerably reduced thermal motion of atoms, they are ideal for high resolution spectroscopy and for more accurate atomic frequency standards.

- Collisions of ultra-cold atoms in such samples are characterized by a long deBroglie wavelength and are dominated by weak long-range interactions. Since the collision duration for slow atoms greatly exceeds the radiative decay time, stimulated and spontaneous radiative transitions can take place during the collision. Slow collisions are therefore radically different from fast collisions studied so far and will

become an exciting new field of atomic physics.²⁰

- High density samples of atoms open possibilities for observing quantum collective effects such as Bose-Einstein condensation and collectively enhanced or suppressed radiative decay.

In 1992, we completed work on an inverse Zeeman slower, which produced the highest flux of cold atoms obtained to date. We demonstrated that further enhancement is possible by transverse collimation of the slow atom beam inside the slower. The slow atoms were captured in a novel light trap, a "dark SPOT" (dark spontaneous force optical trap), which enabled us to confine more than 10^{10} atoms at densities one to two orders of magnitude higher than achieved to date. In addition, two theoretical papers were published on possibilities (and impossibilities) of trapping and cooling atoms by external fields.

Inverse Zeeman Slower

In a Zeeman slower the changing Doppler shift as an atom slows is compensated by the Zeeman shift in an inhomogeneous magnetic field. This method has the advantage of producing a continuous beam of slow atoms and has a practically unlimited velocity capture range. In the original implementation of Zeeman slowing, however, one encountered difficulties in producing beams of atoms with velocities lower than 200 m/s. The major problems were off-resonant slowing of atoms after they left the slower and substantial spreading of the slow atomic beam due to transverse heating.

To solve the first problem we chose the recently demonstrated inverse Zeeman slower which slows atoms using σ^- light.²¹ This type of slower requires a magnetic field increasing along the atom's trajectory until the atoms are slowed to the desired final velocity. The magnetic field drops off rapidly after reaching this maximum, thus quickly shifting atoms out of resonance and reducing off-resonant slowing (figure 11). The atomic densities in the slow beam were high enough so that the longitudinal velocity distributions could be determined directly from

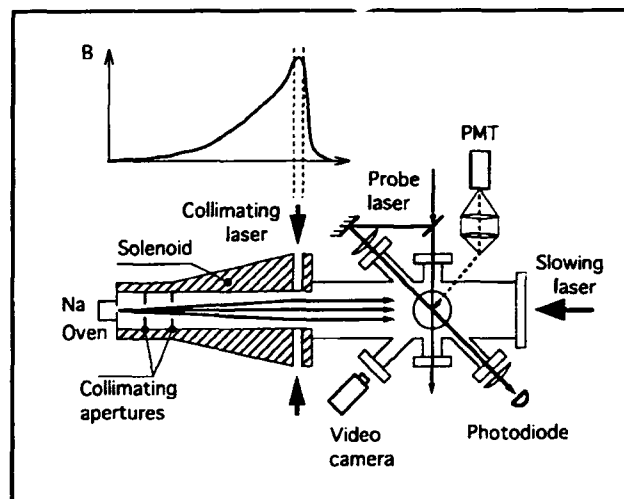


Figure 11. Experimental setup for the inverse Zeeman slower: A beam of sodium atoms is slowed by counter-propagating laser light inside a solenoid with a parabolically increasing magnetic field. The slow atomic beam is collimated and deflected inside the slower by transverse two-dimensional optical molasses.

absorption spectra for the first time. This allowed the unambiguous measurement of absolute flux—values of 2×10^{11} atoms/sec at 40 m/sec and 10^{12} atoms/sec at 100 m/sec through a 4 cm^2 cross section were obtained. The observed drop in flux for small velocities showed an approximate v^2 dependence, consistent with spreading of the slow beam due to transverse heating during the slowing process.

The problem of transverse spreading of the slow atoms has been reduced by application of transverse cooling with red molasses. This was applied inside the slower, at the stationary field point where the atoms have essentially completed their slowing, but have not yet had time to spread transversely. The transverse velocities were reduced from ~ 2.5 m/s to ~ 1 m/s, resulting in a sixfold increase in the density of the slow atoms. Furthermore, deflection of the slow atomic beam by imbalancing the molasses beams resulted in complete separation of the slowed beam from both the original thermal beam and the slowing laser beam; this is important for experiments requiring slow atoms unperturbed by laser beams or collisions with thermal atoms.

²⁰ P.S. Julienne and J. Vigue, "Cold Collisions of Ground- and Excited-state Alkali-metal Atoms," *Phys. Rev. A* 44: 4464 (1991).

²¹ T.E. Barrett, S.W. Daport-Schwartz, M.D. Ray, and G.P. Lafyatis, "Slowing Atoms with σ^- Polarized Light," *Phys. Rev. Lett.* 67: 3483 (1991).

A Dark Light Trap for Neutral Atoms

The most common method of obtaining high density samples of cold atoms is to use a magneto-optical trap (MOT) to collect, cool and confine the atoms. However, the maximum density achieved in a MOT has been limited so far to $\sim 10^{11}$ atoms/cm³ by two processes: (1) trap loss due to collisions between ground- and excited-state atoms,²² and (2) repulsive forces between the atoms caused by reabsorption of scattered photons (radiation trapping).²³

We have demonstrated a dark SPontaneous-force Optical Trap ("dark SPOT"), in which all the above-mentioned limitations are mitigated by confining the atoms mainly in a ("dark") hyperfine ground state which does not interact with the trapping light. The key idea is "shelving" atoms, i.e., cooling and trapping forces are only exerted on the small fraction of atoms in the "bright" state. In such a trap, more than 10^{10} sodium atoms have been confined to densities approaching 10^{12} atoms cm⁻³ (figure 12). A similar number of atoms have been previously trapped by light forces only at densities 20 times lower.

The high densities achieved in a dark SPOT are promising for the observation of evaporative cooling after transferring the atoms into a magnetic trap. At densities of 10^{12} cm⁻³, the estimated elastic collision rate is already 100 s^{-1} , much larger than the trap loss rate due to collisions with the background gas.

Trapping and Cooling Atoms by External Fields

In a theoretical paper we have studied possibilities of using electric, magnetic and gravitational fields to trap atoms in the ground state. A trap for particles in the lowest internal state is highly desirable since loss by two-body collision is endothermic and thus suppressed. However, we were able to prove that it is impossible to trap ground state particles at rest using arbitrary combinations of electric, magnetic, and gravitational fields, a result which is a considerable generalization of a previous theorem. Confinement of ground state particles is possible if they are in motion (dynamic equilibrium). Our analysis showed that axially symmetric storage rings with electric or magnetic fields are possible and should be experimentally feasible.

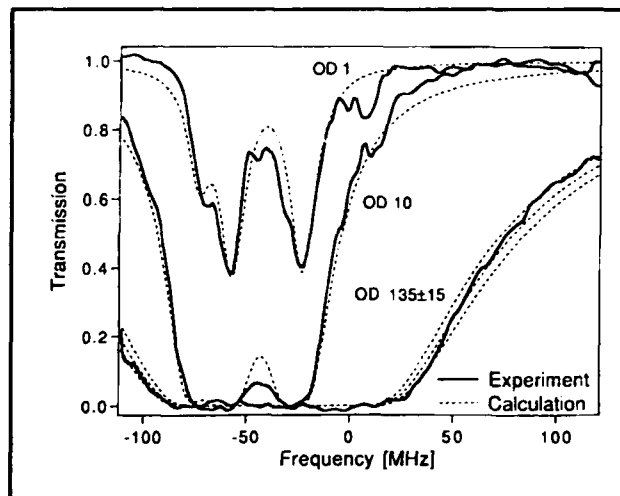


Figure 12. Absorption spectrum of a 4-mm diameter cloud of sodium atoms trapped in a dark SPOT. The best fit yields an optical density (OD) of 135 which corresponds to an atomic density of 7×10^{11} cm⁻² and $\sim 5 \times 10^{10}$ trapped atoms. Traces with lower OD were recorded with a reduced number of atoms. The dashed lines are calculated spectra for OD = 1, 10, 120, 135, and 150, respectively.

Recently, cooling schemes for atoms have been suggested which rely solely on time-dependent conservative forces. We were able to devise a theorem showing that time-dependent potentials cannot increase the phase-space density of atoms, even if the motion is nonclassical. "Real cooling" or "brightening" of atoms is only possible if the time evolution is non-unitary, e.g., by spontaneous emission of photons or loss of atoms (evaporative cooling).

Publications

Joffe, M.A., W. Ketterle, A. Martin, and D.E. Pritchard, "Transverse Cooling and Deflection of an Atomic Beam Inside a Zeeman Slower." Submitted to *J. Opt. Soc. Am. B*

Ketterle, W., K.B. Davis, M.A. Joffe, A. Martin, and D.E. Pritchard, "High Densities of Cold Atoms in a Dark Spontaneous-force Optical Trap." *Phys. Rev. Lett.* 70: 2253 (1993).

Ketterle, W., A. Martin, M.A. Joffe, and D.E. Pritchard. "Slowing and Cooling Atoms in

²² M. Prentiss, A. Cable, J.E. Bjorkholm, S. Chu, E.L. Raab, and D.E. Pritchard, "Atomic-density-dependent Losses in an Optical Trap," *Opt. Lett.* 13: 452 (1988).

²³ T. Walker, D. Sesko, and C. Wieman, "Collective Behavior of Optically Trapped Neutral Atoms," *Phys. Rev. Lett.* 64: 408 (1990).

Isotropic Laser Light." *Phys. Rev. Lett.* 69: 2843-2846 (1992).

Ketterle, W., and D.E. Pritchard. "Atom Cooling by Time-dependent Potentials." *Phys. Rev. A* 46: 4051-4054 (1992).

Ketterle, W., and D.E. Pritchard. "Trapping and Focusing Ground State Atoms with Static Fields." *Appl. Phys. B* 54: 403-406 (1992).

Pritchard, D.E., and W. Ketterle. "Atom Traps and Atom Optics." In *Lecture Notes of the International School of Physics Enrico Fermi*, Varenna, 1991.



Professor John G. King

Chapter 3. Neutrality of Molecules by the Pulsed Gas Flow Method

Academic and Research Staff

Professor John G. King

Visiting Scientists and Research Affiliates

Joseph A. Jarrell, Stanley J. Rosenthal

Undergraduate Students

Daniel I. Goldman, Adam P. London, Michael S. Mermelstein

3.1 Introduction

Sponsor

F.L. Friedman Chair

Determining whether the magnitude of the charge of a proton differs from that of an electron or whether neutrons, neutrinos, or photons are charged presents a significant and fundamental problem. Verifying the existence of these charge differences would be very important to our fundamental understanding of (1) electric charge quantization and conservation and (2) the standard model and grand unified theories.

Because these hypothetical small charges or differences in charges have no observable effect on the world, we could only verify them using specially designed experiments. Since there is no definite theoretical prediction for these hypothetical small charges, we simply carry out improved bench-top experiments that are feasible with our limited resources. (This is in contrast to studies of neutron dipole moment, proton lifetime, missing neutrinos, etc., which justified a large scale effort and commitment of resources.)

Experiments dating back 70 years have virtually guaranteed that these charges or charge differences are less in magnitude than 10^{-20} of the fundamental electron charge, 1.6×10^{-19} C. So far the results of our experiments have further reduced the limit of magnitude difference of proton-electron charge and the neutron charge by three orders of magnitude.

3.2 Project Description

The electric charge of any object, material, or system is measured by bringing a suitable sample near other charges or other charges near it so that electric forces would produce observable effects. The materials or systems that have been studied or are currently being studied by various groups around the world include: (1) beams of single atoms, which if not neutral, would experience a velocity change in an electric field and be deflected, change deBroglie wavelength, or interact with Doppler-shifted light; (2) small aggregates, like Millikan oil drops, which if not neutral, would be deflected by electric fields; (3) bulk fluids from which ordinary charges (ions or electrons) can be removed. This includes many gases and superfluid helium, which would transfer charge when moved by flow whether at low frequency, when simply let out of an electrically insulated container, or, in the case of liquid He II, sloshing in a U-tube, or at higher frequency such as in a standing sound wave; and (4) the inverse of the last method—an applied alternating electric field would induce sound waves in the material if it is not neutral.

While many of these methods suffer from difficulty with controlling, reversing, and otherwise characterizing applied electric fields, the gas efflux method we are using has problems with flow-induced charge separation, drift and noise problems of essentially dc charge measurements in the attoampere range, and comparatively small throughput of molecules (about 10^{21} /second). The pulsed flow method would raise the throughput by a factor of 500, and the fact that the signal sought is at 1 kHz, i.e., above the 1/f-noise range, should make long term correlation feasible to yield an additional factor of 100.

In the gas efflux method a siren-like chopper releases 0.5 ms gas pulses at a one kHz rate into a chamber where a background pressure of the same

gas is maintained by suitable pumps. This pressure must be such that the pulses travel a substantial distance with minimum diffusion neither stopping from viscous retardation nor coming apart by free molecule flow. We calculate that 0.5 kPa is approximately the correct pressure. These pulses, if charged, induce charge on cylindrical electrodes through which they travel. The resulting potential changes can be detected with a suitable electro-

meter, which might take the form of an array of paralleled, cooled FETs to take advantage of Shannon's theorem.

At present, we are using a crude apparatus assembled from pipe fittings with a pneumatically operated shutter to investigate the dynamics of single pulses in background gas in order to design the pumping system needed to handle 1000 of these pulses per second.

Section 2 Plasma Physics

Chapter 1 Plasma Dynamics

Chapter 1. Plasma Dynamics

Academic and Research Staff

Professor George Bekefi, Professor Abraham Bers, Professor Bruno Coppi, Professor Miklos Porkolab, Professor Jonathan S. Wurtele, Dr. Chiping Chen, Dr. Shien-Chi Chen, Dr. Paolo Detragiache, Dr. Stefano Migliuolo, Dr. Abhay K. Ram, Dr. Barrett Rogers, Dr. Linda E. Sugiyama, Edward W. Fitzgerald, Ivan Mastovsky

Visiting Scientists and Research Affiliates

Dr. Gregory A. Benford, Dr. Carson C. Chow,¹ Dr. Vladimir Fuchs,² Dr. Eli Jerby, Dr. Pallavi Jha, Dr. Cesar Meirelles-Filho,³ Dr. Marco Nassi,⁴ Dr. Leonid E. Zakharov⁵

Graduate Students

Neer R. Asherie, Palmyra E. Catravas, Manoel E. Conde, David S. Gloss, Wen Hu, Alexander Matusis, Michael C. Moldoveanu, Gregory E. Penn, Caterina Riconda, Todd H. Rider, Steven D. Schultz, Jared P. Squire, Richard E. Stoner, Luigi Vacca, Jesus Noel Villaseñor, Pavel S. Volfbeyn

Undergraduate Students

Jonathan C. Doan, Todd A. Hay, Hana Ohkawa, Vladislav Portnoy, Kenneth N. Ricci

Technical and Support Staff

Felicia G. Brady, Laura B. Doughty, Kerry L. Gafney, Catherine Lorusso

1.1 Relativistic Electron Beams

Sponsors

National Science Foundation
Grant ECS-89-02990
U.S. Air Force - Office of Scientific Research
Grant AFOSR 89-0082-C
U.S. Army - Harry Diamond Laboratories
Contract DAAL02-89-K-0084
Contract DAAL02-92-K-0037
U.S. Department of Energy
Contract DE-AC02-90ER-40591
U.S. Navy - Office of Naval Research
Grant N00014-90-J-4130

Project Staff

Professor George Bekefi, Professor Jonathan S. Wurtele, Ivan Mastovsky, Dr. Chiping Chen, Dr. Shien-Chi Chen, Dr. Eli Jerby, Dr. Pallavi Jha, Dr. Gregory A. Benford, Palmyra E. Catravas, Manoel E. Conde, Wen Hu, Alexander Matusis, Richard E. Stoner, Pavel S. Volfbeyn, Jonathan C. Doan, Todd A. Hay, Kenneth N. Ricci

1.1.1 Frequency Shifting Phenomena In Free Electron Lasers - Experiment

Frequency upshifting of an electromagnetic wave incident on a rapidly time varying plasma medium is of considerable interest recently. Such upshifting can occur as a result of a time-dependent dielectric

¹ University of Colorado, Boulder, Colorado.

² Centre Canadien de Fusion Magnétique (CCFM), Quebec, Canada.

³ Universidade de São Paulo, Brazil.

⁴ Politecnico di Milano, Milan, Italy.

⁵ Kurchatov Institute of Atomic Energy, Moscow, Russia.

coefficient caused by changes in plasma density,⁶ or as a result of a rapidly moving plasma-vacuum boundary.⁷ Prior studies have been confined to cases in which the dielectric is essentially a passive medium; that is, the amplitude of the wave propagating through it is constant in time and space. In this paper we report what we believe are the first frequency shift measurements in an active, lasing medium in which the wave amplitude exhibits exponential growth. Here, the time-varying dielectric medium is modeled as an interaction between the pulsed relativistic electron beam of the free electron laser (FEL), the magnetic wiggler, and the copropagating electromagnetic wave launched into the system. The detailed theoretical and computational modeling by Shvets and Wurtele is described elsewhere.⁸

A schematic of the FEL⁹ amplifier is shown in figure 1a. A mildly relativistic electron beam (750 keV) is generated by a Marx capacitor bank (Physics International Pulserad 110 Å). The electrons are emitted from a hemispherical graphite cathode by an explosive field-emission process. The graphite anode acts as an emittance selector, allowing only a small fraction of the current (90 Å) to propagate through its 2.54-mm radius and 62-mm-long aperture.

The 50-period bifilar helical wiggler produced by current-carrying helical wires has a period of 3.18 cm and provides a magnetic field of uniform amplitude whose magnitude on axis is adjustable up to 1.8 kG. The wiggler field intensity is slowly increased over the initial six periods, providing an adiabatic input for the electron beam. The system, including the gun, is immersed in a uniform axial guide magnetic field generated by a solenoid. The intensity of this field can be varied up to a maximum of 11.6 kG.

The 2-m-long stainless-steel drift tube has an internal radius of 0.51 cm and acts as a cylindrical waveguide whose fundamental TE_{11} mode has a cutoff frequency of 17.2 GHz. The system is designed to operate in this lowest waveguide mode.

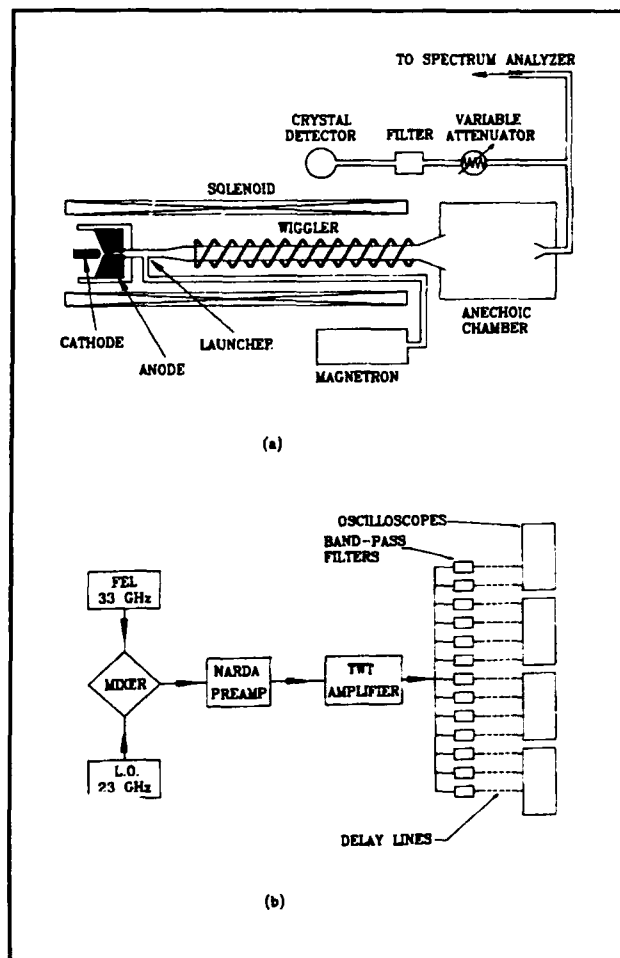


Figure 1. (a) Free electron laser set-up (b) schematic of the spectrum analyzer.

A high-power magnetron operating at 33.39 GHz is the input power source for the FEL amplifier. The wave launcher consists of a short section of circular waveguide of radius 0.31 cm into which ~12 kW of power is coupled from a standard Ka-band rectangular waveguide. This section of circular waveguide supports only the fundamental TE_{11} mode for the operating frequency. Its radius is then adiabatically increased to the radius of the drift tube. A linearly polarized wave is thereby injected into the interaction region. Half of the incident

⁶ S.C. Wilks, J.M. Dawson, and W.B. Mori, *Phys. Rev. Lett.* 61: 337 (1989); C.J. Joshi, C.E. Clayton, K. Marsh, D.B. Hopkins, A. Sessler, and D. Whitum, *IEEE Trans. Plasma Sci.* 18: 814 (1990); V.R. Goteti and D.K. Kalluri, *IEEE Trans. Plasma Sci.* 17: 828 (1989); D.K. Kalluri, *IEEE Trans. Antennas Propag.* 37: 1638 (1989).

⁷ W.B. Mori, *Phys. Rev. A* 44: 5118 (1991); P. Sprangle, E. Esarey, and A. Ting, *Phys. Rev. A* 41: 4463 (1990); H.C. Kapteyn and M.M. Murnane, *J. Opt. Soc. Am. B* 8: 1657 (1991); R.L. Savage Jr., W.B. Mori, C. Joshi, T.W. Johnston, and G. Shvets, Dept. of Electr. Eng., UCI, Report No. PPG-1422 (1992).

⁸ G. Shvets and J. Wurtele, submitted to *Phys. Fluids*.

⁹ M.E. Conde and G. Bekefi, *Phys. Rev. Lett.* 67: 3082 (1991); M.E. Conde and G. Bekefi, *IEEE Trans. Plasma Sci.* 20: 240 (1992).

power, with the correct rotation of the electric-field vector of the amplified circularly polarized wave, participates in the FEL interaction.

The output power from the FEL is transmitted by means of a conical horn into a reflection free "anechoic chamber." A small fraction of the radiation is then collected by a receiving horn, passes through precision calibrated attenuators, and a 1.7-GHz-wide band-pass filter. The power level is finally determined from the response of a calibrated crystal detector.

The spatial growth of the electromagnetic wave intensity is determined from the measurement of the output power as a function of the length of the interaction region. This length is varied by changing the distance that the electron beam is allowed to propagate in the drift tube. Application of a strong transverse magnetic field locally is sufficient to deflect the electrons into the waveguide wall and thereby terminate the interaction at that point. The results of such measurements are illustrated in figure 2 which shows an initial exponential growth of the signal intensity, followed by nonlinear saturation at a power level of ~ 6 MW.

The frequency spectrum of the output power is determined by a heterodyne technique. A crystal rectifier is used as a mixer for the 33 GHz FEL radiation and for radiation from a variable frequency 23 GHz local oscillator. The resulting beat wave is amplified and sent to an array of band-pass waveguide filters. Thus, the calibrated response of the various channels provides, on a single shot basis, a direct histogram of output power in terms of radiation frequency.

A schematic of the experimental setup used to measure the frequency spectrum is shown in figure 1b. An Alfred 650 sweep oscillator is used as a local oscillator, generating ~ 6 mW at 23.39 GHz. This signal is combined in a magic tee with the FEL signal (previously attenuated to the appropriate milliwatt level) and then sent to a crystal rectifier (HP R422A). The nonlinear response of this crystal gives rise to the beat wave of the two signals, with a frequency of 10 GHz. This beat wave is then amplified by a Narda 60164 solid state amplifier and by a Logimetrics TWT, and finally sent to the filter bank. The bank consists of 32 waveguide band-pass filters adjacent in frequency and each one 80 MHz wide. These channels are fed in parallel and each one has its own rectifier crystal (HP 33330B). Thus, the calibrated response of this array of rectifiers gives, on a single shot basis, the frequency spectrum of the output power.

There are two factors limiting the number of channels that can actually be used. The first one is the

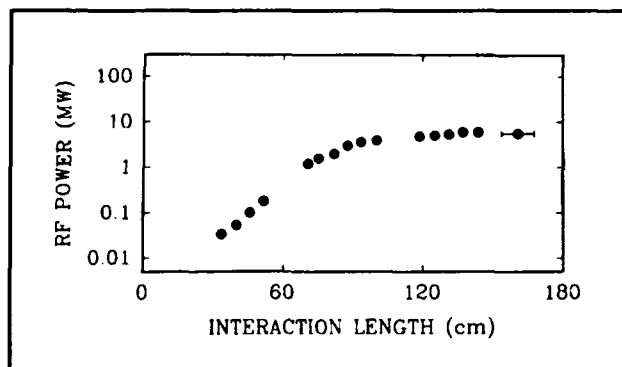


Figure 2. FEL output power as a function of the interaction length. Beam energy 750 keV; beam current 90 A; axial guide magnetic field 4.06 kG; wiggler magnetic field 0.63 kG.

bandwidth of the TWT amplifier, from 9.5 to 10.5 GHz, allowing only 13 channels to be used. The other limitation is the number of available oscilloscopes to monitor the filter bank channels. This second problem is solved by using delay lines to give temporal separation between channels, such that four of them can be added in a single oscilloscope. The measured attenuation of each of these delay lines has to be taken into account in the analysis of the data.

The frequency spectrum in the saturation region, corresponding to a measurement with a full length wiggler of ~ 180 cm (see figure 2) is shown in figure 3a. We observe that the spectrum is shifted from the input magnetron frequency. Its full width at half maximum (FWHM) is less than 160 MHz. The 80 MHz width of each band-pass filter does not allow a resolution better than this, and, as a matter of fact, the short duration of the radiation pulse (~ 20 ns) limits the resolution to no better than ~ 50 MHz (dictated by $\Delta f \Delta t \sim 1$).

To see if the frequency shift occurs at all power levels, that is, in the exponential growth regime and in the saturated regime, we scan the output power as a function of interaction length and observe any frequency shifts. Figure 3b shows a scan of power versus interaction length (using the kicker magnet) from two adjacent channels of the filter bank, namely, the channel corresponding to the driver frequency and its higher frequency neighbor. The driver channel initially has the higher power, but it is surpassed by the other channel for longer interaction distances. From these measurements and measurements of the total power integrated over the 1.7 GHz frequency band (figure 2), we conclude that for short interaction lengths, that is, in the exponential growth regime, the RF power is predominantly at the channel centered around the input magnetron frequency of 33.39 GHz. However, when one reaches the nonlinear satu-

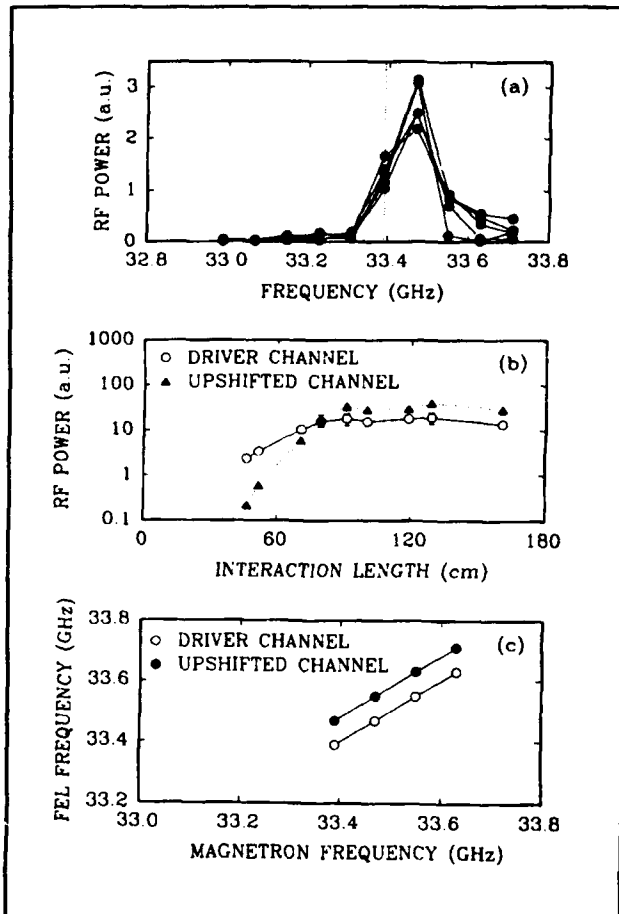


Figure 3. (a) Frequency spectrum of the FEL output power for five successive shots, for an interaction length of 180 cm; the dotted vertical line shows the input magnetron frequency. (b) RF power as a function of interaction length for two adjacent channels of the filter bank. (c) FEL frequency as a function of magnetron input frequency for an interaction length of 180 cm.

ration regime, the power is predominantly in the frequency upshifted channel centered around 33.47 GHz.

When the input magnetron frequency is varied, the frequency spectrum moves in proportion to the input frequency, but it is always shifted towards higher frequencies, as is shown in figure 3c.

In summary, we have observed frequency shifts in a pulsed free electron laser amplifier. One possible cause could be the presence of nonlinear excitation of side-band¹⁰ instabilities which are often observed in the saturated regime of FELs. Since we observe frequency upshifting in both the exponential growth and saturation regimes (figure 3b) we rule this out as a cause of our observations. Another cause could be the presence of self-amplification of spontaneous emission (SASE) which occurs even in the absence of the magnetron driver. We rule out this effect for two reasons. First, our measurements¹¹ of SASE have shown that the intensity of the emission is about an order of magnitude lower than the intensity of the amplified signal (figure 2). Secondly, when we vary the magnetron frequency, the FEL emission frequency tracks the input magnetron frequency as illustrated in figure 3c.

Our observations are in qualitative agreement with computations modeled on the premise that the frequency shifting is the result of the rapid temporal variations, typically ~ 10 ns, of the voltage and current pulses of our FEL. This leads to temporal variations of the effective dielectric coefficient associated with the FEL interaction. The contributions to Δf are shown¹² to consist of two components. One can be attributed to "dielectric beam loading", that is, the temporal behavior of the right circularly polarized wave propagating through the relativistic electron beam. This is present even in the absence of the magnetic wiggler and leads to frequency downshifting. The other component is associated with the temporal variations of the slow ponderomotive wave excited by the presence of the magnetic wiggler, and yields a frequency upshift. The net of the two effects is a frequency upshift of ~ 100 MHz.

We note that the magnitude of the frequency upshifting or downshifting depends sensitively¹² on the relative temporal voltage and current histories of the relativistic electron beam. These may differ for different regimes of FEL operation. The aforementioned experiments were carried out in an FEL operating in the Group I regime. Frequency shifting was not seen in the Group II or in the Reversed Field regimes¹³ which occur at much higher guide magnetic fields. To fully understand the differences in the observed frequency characteristics requires

¹⁰ W.B. Colson, *Nucl. Instrum. Methods A* 250: 168 (1986); F.G. Yee, J. Masud, T.C. Marshall, and S.P. Schlesinger, *Nucl. Instrum. Methods A* 259: 104 (1987).

¹¹ M.E. Conde and G. Bekefi, *IEEE Trans. Plasma Sci.* 20: 240 (1992).

¹² G. Shvets and J. Wurtele, submitted to *Phys. Fluids*.

¹³ M.E. Conde and G. Bekefi, *Phys. Rev. Lett.* 67: 3082 (1991); M.E. Conde and G. Bekefi, *IEEE Trans. Plasma Sci.* 20: 240 (1992).

monitoring the temporal beam voltage and current characteristics to a precision of the order of 1-2 ns, a task that has not been carried out to date.

Our frequency shift measurements were carried out in a Raman FEL amplifier. However, frequency shifts may also be important¹² in FEL oscillators. They could also be of practical interest in frequency chirping using carefully shaped voltage and current pulses of the relativistic electron beam.

1.1.2 Frequency Shifting Phenomena In Free Electron Lasers - Theory

The frequency shifting of light by a moving dielectric front and bulk ionization of gases has been extensively investigated both theoretically and experimentally. These studies have been restricted to passive dielectric systems—those which induce phase shifts but have negligible gain. An electromagnetic wave in an underdense plasma, with

$$\text{dielectric } \epsilon = 1 - \frac{\omega_p^2}{\omega^2},$$

being the typical example. Similar physics can be expected in an active medium which exhibits both gain and phase shifts, such as the FEL. Since any frequency shift creates a phase shift, these shifts must be fully understood if the FEL is used as a driver for high gradient accelerators. They will place limits on the tolerable shot-to-shot jitter in system parameters. The frequency shifting mechanism also provides the first explanation of the way in which an FEL oscillator can adjust its frequency to changes in beam energy.

Two distinct parameter regimes, a high-power high-gain microwave amplifier and a low-gain infrared oscillator, have been studied in detail. A brief description of the amplifier analysis is given below; a detailed study is provided elsewhere. The theory is consistent with recent experiments¹⁴ which report frequency upshifting in a FEL microwave amplifier.

The wave equation for the vector potential of the transverse EM wave including the FEL and plasma coupling is

$$\left(\frac{1}{c^2} \frac{\partial^2}{\partial t^2} - \frac{\partial^2}{\partial z^2} + k_{\perp}^2 \right) \vec{A} = \frac{4\pi}{c} (\vec{J}_{nr} + \vec{J}_{fel}), \quad (1)$$

where the source term has two distinct contributions: \vec{J}_{nr} , from the usual (nonresonant) cold beam response to the EM wave which is present in the absence of the wiggler, and a second term from the resonant FEL interaction. The resonant current \vec{J}_{fel} is produced by the ponderomotive force of the EM wave beating with the magnetic field of the wiggler.¹⁵ The beam is bunched in the ponderomotive wave, and the wiggling bunches produce the current which synchronously drives the EM wave. In the linear analysis (to which we restrict ourselves in this paper), this results in an exponentially growing instability. Since the parameters of the electron beam can be time-dependent, this can potentially lead to frequency-changing phenomena. The FEL is subject to frequency shifts when the driving terms \vec{J}_{nr} and \vec{J}_{fel} are time-dependent.

It is instructive to briefly summarize frequency shifting in passive media, such as occurs when radiation propagates through a moving inhomogeneous medium¹⁶ with no FEL interaction. The wave equation, when used together with the canonical momentum conservation, becomes:

$$\left(\frac{1}{c^2} \frac{\partial^2}{\partial t^2} - \frac{\partial^2}{\partial z^2} + k_{\perp}^2 \right) \vec{a} = - \frac{\omega_p^2(z,t)}{c^2} \vec{a}, \quad (2)$$

where we have introduced the normalized vector potential of the radiation field $\vec{a} = eA/mc^2$, e is the electron charge, m is the electron mass and c is the speed of light in vacuum. It is convenient to transform to the set of variables

$$s = t - \frac{z}{v_g}, \quad (3)$$

$$z = z,$$

where s is the distance from the head of the pulse, which propagates with group velocity v_g .

Using the eikonal approximation, which in our notation requires that variations in z are much slower than in s , results in:

$$\frac{\partial a(s,z)}{\partial z} = - \frac{-i\omega_p^2(s,z)v_g}{2\omega c^2} a(s,z). \quad (4)$$

¹⁴ M.E. Conde, C.J. Taylor, and G. Bekefi, submitted to *Phys. Fluids*.

¹⁵ C.W. Roberson and P. Sprangle, *Phys. Fluids B* 1: 3 (1989).

¹⁶ M. Lampe, E. Ott, and J.H. Walker, *Phys. Fluids* 21: 42 (1978); E. Esarey, A. Ting, and P. Sprangle, *Phys. Rev. A* 42: 3526 (1990).

While it is straightforward to integrate equation 4 by quadratures, further insight can be obtained by assuming that the density gradient is moving with constant velocity, v_b . Here, for a prescribed density profile $\omega_p^2(t - z/v_b)$,

$$a(s, z) = a(s, 0) \exp(-i\Phi(s, z)), \quad (5)$$

and the frequency change, $\delta\omega = \partial\Phi/\partial s$, is now given by

$$\delta\omega(s, z) = \frac{\beta_b \beta_g}{2\omega(1 - \beta_b/\beta_g)} \times \left[\omega_p^2(s) - \omega_p^2\left(s - \frac{z(1 - \beta_b/\beta_g)}{v_b}\right) \right]. \quad (6)$$

It is instructive to analyze this equation in two limits.

First, expanding the term $\omega_p^2\left(s - \frac{z(1 - \beta_b/\beta_g)}{v_b}\right)$ in equation 6 results in an

expression for the frequency change of a pulse that has propagated a distance z with the moving plasma:

$$\delta\omega(s, z) = \beta_g \frac{1}{\omega} z \frac{\partial \omega_p^2}{\partial (cs)}. \quad (7)$$

This expression is well behaved for $v_g = v_b$, and our subsequent analysis of the FEL amplifier will be carried out under this "zero slippage" assumption. Secondly, the opposite limit, that of a step profile electron beam, where finite slippage generates the frequency shift, can also be recovered from equation 6. Radiation starts inside the electron beam and eventually slips out of the beam, because $v_g > v_b$, is frequency upshifted by

$$\delta\omega = \frac{\beta_b \beta_g}{1 - \beta_b/\beta_g} \frac{\omega_p^2}{2\omega}. \quad (8)$$

This effect is important in understanding the spectral characteristics of FEL oscillators.

Unfortunately, when the FEL interaction is included, the differential equation for the vector-potential is no longer first-order, and a simple integration, similar to the one above, is no longer possible.

We now restrict our analysis to the "zero slippage" approximation, which neglects the difference between group velocity of radiation and the velocity of an electron beam. This is reasonable for many microwave FELs which have long pulse-lengths, moderately relativistic energies and a reduction of the group velocity in the waveguide. For instance, in a recent studies of a Raman FEL,¹⁷ the slippage parameter

$$S = \frac{L_{\text{slip}}}{L_{\text{beam}}} \quad (9)$$

is less than 5 percent. The FEL equations, which have temporal and spatial derivatives in the field equation, then become ordinary differential equations.

As is well known, a FEL with a helical wiggler and axial magnetic field, can be described, in the coordinates of equation 3, by

$$\begin{aligned} \frac{\partial \gamma(z, s)}{\partial z} = & \\ iC \frac{\beta_{\perp}}{2\beta_{\parallel}} a(z, s) \exp(i\theta) - & \\ i \frac{\omega_p^2(s) p_1^2}{c^2(k_z + k_w)} \exp(i\theta) < \exp(-i\theta) > & \end{aligned} \quad (10)$$

$$\frac{\partial \theta(z, s)}{\partial z} = k_z + k_w - \omega/v_{\parallel} \quad (11)$$

$$\begin{aligned} \frac{\partial a}{\partial z} + & \\ iF \frac{\omega_p^2(s)}{2\gamma\omega v_b} \frac{\omega - k_z v_b}{\omega - k_z v_b - \Omega_0/\gamma} a = & \\ 2\pi iC \frac{I(s)}{I_A} < \frac{\beta_{\perp}}{\beta_{\parallel}} \exp(-i\theta) >, & \end{aligned} \quad (12)$$

where $v_{\parallel} = \beta_{\parallel}c$ is the longitudinal electron velocity, $\theta = (k_z + k_w)z\omega t$ the slow varying ponderomotive phase, v_b is the unperturbed beam velocity, γ is the beam relativistic factor, $\Omega_0 = eB_0/mc$ is the cyclotron frequency due to the axial field B_0 , F is a dimensionless filling factor, C is a geometric factor which depends on the waveguide and mode. The factor C is defined in Wurtele, Chu and Fajans

¹⁷ M.E. Conde, C.J. Taylor, and G. Bekefi, submitted to *Phys. Fluids*.

(1990)¹⁸ and roughly equals the inverse of the waveguide radius. A nonresonant beam-loading term, which is not present in earlier work,¹⁸ has been included in equation 12. Equations 10-12 were linearized¹⁸ with the approximation that force bunching and wave perturbation of the equilibrium orbits is negligible. The dispersion relation thereby obtained (including the beam-loading term) can be written

$$\left(\Gamma + F \frac{\omega_p^2(s)}{2\gamma\omega v_b} \frac{\omega - k_z v_b}{\omega - k_z v_b - \Omega_0/\gamma} \right) \times$$

$$\left((\Gamma + \Delta K)^2 - \frac{1}{\beta_{||0}} \frac{\partial \beta_{||0}}{\partial \gamma} \frac{p_1^2 \omega_p^2}{c^2} \right)$$

$$= - \frac{\pi C^2 \beta_{||0}^2 \omega}{\beta_{||0}^4 c l_A} \frac{\partial \beta_{||0}}{\partial \gamma} \quad (13)$$

Equation 13 can be solved explicitly for the real part of Γ , the s derivative of which is easily related to the frequency shift. Frequency shifts are seen to occur because of two distinct mechanisms: the usual cold beam dielectric shift (from the beam density) and the coupling to the slow space-charge wave, which is due to the FEL interaction. The beam dielectric shift is physically equivalent to that of a cold plasma and is extensively described in the literature,¹⁹ the FEL term, which has time-dependence from changes in beam voltage and current, has not been analyzed until now. Numerical evaluation of this expression for the frequency shift from physically realizable pulse forms for the voltage and current is in agreement with the observed shifts in reference 12.

Further investigations to determine the effect of frequency shift phenomena on the performance of FEL user facilities and power sources for high gradient structures are ongoing.

This work was supported by the Air Force Office of Scientific Research, Department of Energy, National Science Foundation, and Lawrence Livermore

National Laboratories. We thank Paul Woskov for lending us the frequency filter bank.

1.2 Plasma Wave Interactions—RF Heating And Current Generation

1.2.1 Introduction

Sponsors

Lawrence Livermore National Laboratories
Subcontract B-160456
National Aeronautics and Space Administration
Grant NAGW-2048
National Science Foundation
Grant ECS-88-22475
U.S. Department of Energy
Grant DE-FG02-91-ER-54109

Project Staff

Professor Abraham Bers, Dr. Abhay K. Ram, Dr. Carson C. Chow, Dr. Vladimir Fuchs, Michael C. Moldoveanu, Steven D. Schultz, Luigi Vacca

The work of this research group is concerned with studies on the electrodynamics of plasmas. Attention is directed toward understanding the nonlinear dynamics of plasmas driven by high-frequency electromagnetic fields (as in RF heating and current drive of magnetically confined plasmas, or in laser-plasma interactions) and the generation and propagation of unstable radiations from laser-plasma interactions and anisotropic electron distributions in space and astrophysical plasmas

In the following we report on two studies of chaotic dynamics: the first in stimulated Brillouin scattering with particular application to optical fibers and the second in plasma ion-cyclotron orbits driven by electrostatic wave fields. The third report is on our progress in modeling and understanding of the observed current drive efficiency enhancement in the Joint European Torus (JET) through the synergistic use of ion-cyclotron range of frequency (ICRF) waves with lower-hybrid current drive (LHCD). The last report describes our recent study of the double stream cyclotron maser amplifier.

¹⁸ J.S. Wurtele, R. Chu, and J. Fajans, *Phys. Fluids B* 2: 1626 (1990).

¹⁹ E. Esarey, A. Ting, and P. Sprangle, *Phys. Rev. A* 42: 3526 (1990).

1.2.2 Chaotic Stimulated Brillouin Scattering (SBS) in an Optical Fiber

Sponsors

Lawrence Livermore National Laboratories
Subcontract B160456
National Science Foundation
Grant ECS-88-22475

As part of our studies on chaotic wave dynamics in spatially extended media, we have considered in some detail the SBS three-wave-interaction (3WI).

The dynamics of stimulated Brillouin scattering in a homogeneous medium of finite extent has captured considerable interest both in laser-plasma interactions²⁰ and optical fibers.²¹ Nonstationary and chaotic behavior had been previously reported in SBS with external feedback such as reflection at the boundaries²² or with models involving more than one pump.²³ Harrison et al.²⁴ have observed chaotic SBS experimentally in an optical fiber without feedback. Gaeta and Boyd²⁵ have performed similar experiments and obtained similar results. However, these scientists propose that the experimentally observed aperiodic behavior is due to amplification of noise.

We have shown²⁶ that with the addition of resonance detuning and without feedback, the spatio-temporal 3WI modeling SBS can be chaotic in a restricted parameter regime. The model we propose appears to be one of the simplest SBS models exhibiting chaos in spatially extended media. We utilize the nonlinear 3WI equations²⁷ in

one dimension and time for the fields of the waves involved, including resonance detuning (δ).

In a typical experiment with fused silica optical fibers and a single-mode argon-ion laser operating at $\lambda=514.5$ nm, the parameters are: index of refraction $n=1.46$; acoustic velocity $c_a = 5.96 \times 10^3$ ms⁻¹; acoustic damping rate $\gamma_a \approx 270$ MHz; nonlinear coupling constant $K = 66$ ms⁻¹V⁻¹; and ratio of laser (or Stokes) to acoustic damping rate $\gamma_0/\gamma_a = 10^{-3}$.²⁸ Since the damping length of the acoustic wave (c_a/γ_a) is much smaller than the typical interaction length $\sqrt{c_a c/n/Ka_0}$ ($x=0$), we can ignore the convective term in the acoustic equation. Also, the damping on the laser and Stokes em waves are weak and can be ignored. Length and time scales can be rescaled with $\gamma_a t \rightarrow t$, $x\gamma_a(n/c) \rightarrow x$, $\Delta = \delta/\gamma_a$, and the wave amplitudes can be rescaled with $E_0 = a_0 K/\gamma_a$, $E_s = a_s K/\gamma_a$, $E_a = (a_a K/\gamma_a) \exp(-i\Delta t)$. The SBS equations become

$$\partial_t E_0 + \partial_x E_0 = -E_s E_a, \quad (1)$$

$$\partial_t E_s - \partial_x E_s = E_0 E_a^*, \quad (2)$$

$$\partial_t E_a + (1 + i\Delta)E_a = E_0 E_s^*, \quad (3)$$

with the boundary conditions $E_0(x=0,t) = a_0(x=0)K/\gamma_a = A$, $E_s(x=L,t) = \epsilon$. The scattered wave is assumed to grow from a small amplitude (noise) ϵ at the right boundary. The laser wave E_0 is referred to as the pump, the scattered light wave E_s is often called the Stokes wave. In terms of a

²⁰ C.J. Randall and J.R. Albritton, *Phys. Rev. Lett.* 52: 1887 (1984); K. Sauer and K. Baumgärtel, *Phys. Rev. Lett.* 52: 101 (1984); R. Blaha, E.W. Laedke, A.M. Rubenchik, and K.H. Spatschek, *Europhys. Lett.* 7: 237 (1988); S. Hüller, P. Mulser, and A.M. Rubenchik, *Phys. Fluids B* 3: 3339 (1991).

²¹ D. Cotter, *J. Opt. Commun.* 4: 10 (1983); I. Bar-Joseph, A.A. Friesem, E. Lichtman, and R.G. Waarts, *J. Opt. Soc. Am. B* 2: 1606 (1985); J. Coste and C. Montes, *Phys. Rev. A* 34: 3940 (1986); J. Botineau, C. Leycuras, C. Montes, and E. Picholle, *J. Opt. Soc. Am. B* 6: 300 (1989); R.G. Harrison, J.S. Uppal, A. Johnstone, and J.V. Moloney, *Phys. Rev. Lett.* 65: 167 (1990); A.L. Gaeta and R.W. Boyd, *Phys. Rev. A* 44: 3205 (1991).

²² C.J. Randall and J.R. Albritton (1984); K. Sauer and K. Baumgärtel (1984); S. Hüller, et al. (1991).

²³ P. Narum, A.L. Gaeta, M.D. Skeldon, and R.W. Boyd, *J. Opt. Soc. Am. B* 5: 623 (1988); A.L. Gaeta, M.D. Skeldon, R.W. Boyd, P. Narum, *J. Opt. Soc. Am. B* 6: 1709 (1989).

²⁴ R.G. Harrison, et al. (1990).

²⁵ A.L. Gaeta and R.W. Boyd (1991).

²⁶ C.C. Chow, *Spatiotemporal Chaos in the Nonlinear Three Wave Interaction*, Ph.D. diss., Dept. of Physics, MIT, 1991; C.C. Chow and A. Bers, "Chaotic Stimulated Brillouin Scattering in a Finite Length Medium," *Phys. Rev. A*, forthcoming 1993.

²⁷ A. Bers, "Linear Waves and Instabilities," in *Plasma Physics—Les Houches 1972*, eds. C. DeWitt and J. Peyraud (New York: Gordon and Breach Publishers, 1975), pp. 113-215.

²⁸ D. Cotter (1983); R.G. Harrison, et al. (1990); A.L. Gaeta and R. Boyd (1991); D. Cotter, *Opt. Quantum Electron.* 19: 1 (1987).

typical optical fiber experiment, $L=1$ corresponds to 0.75 m, $\Delta=1$ corresponds to 270 MHz, and $A=\epsilon=1$ corresponds to 4 MVm^{-1} .

Equations (1) to (3) were numerically simulated.²⁹ The system has four free parameters A , Δ , ϵ , and L . However, a numerical survey of the parameter space indicated that a two-dimensional surface could capture the unfolding behavior. The Δ - A parameter plane for fixed L and ϵ was chosen. Figure 4 shows the numerically determined unfolding diagram in the Δ - A plane for $L=40$ and

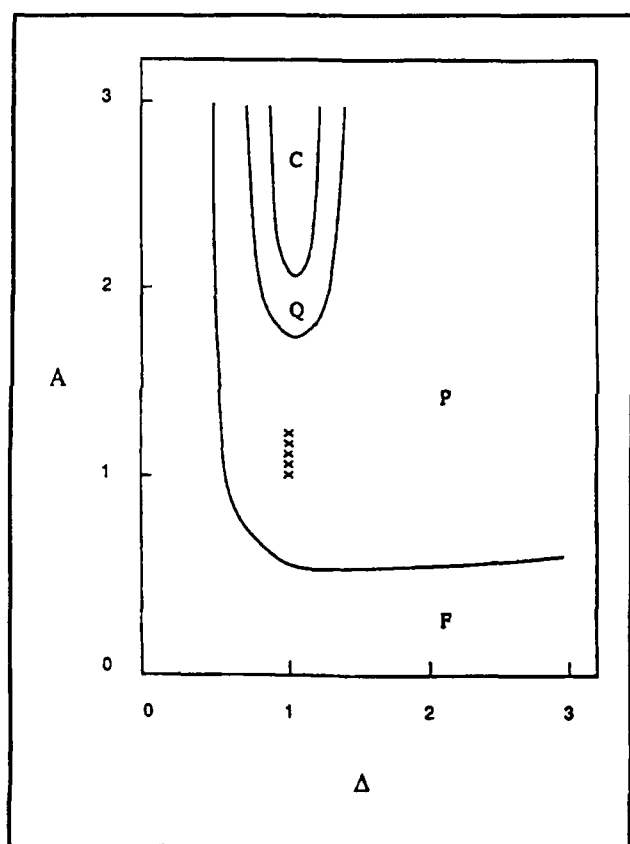


Figure 4. Bifurcation diagram in the Δ - A plane for $L = 40$ and $\epsilon = 0.0025$. There are four different phases: F denotes the fixed state, P denotes the periodic orbit, Q denotes quasi-periodicity and C denotes chaos. The line of x's indicate a region of phase coexistence between a periodic and a quasi-periodic orbit.

$\epsilon=0.0025$. Parameters L and ϵ were chosen so that the bifurcation diagram in the Δ - A plane contained all the observed dynamics. For small Δ and A there is a stable fixed state. It becomes unstable through a Hopf bifurcation to a periodic state. Then there is a transition to quasi-periodicity and to chaos. Each region is discussed in detail in Chow's thesis and in a forthcoming publication.³⁰ There it is shown that the system described by equations (1) to (3) has one fixed state (figure 5) which is stable when there is no resonance detuning, $\Delta = 0$. For $\Delta \neq 0$, there is a phase twist over the distance, in both the pump (laser) and Stokes waves, which depends on both Δ and A . When the phase twist exceeds a certain threshold, the fixed state becomes unstable and Hopf-bifurcates to a periodic state (figure 6). For the chaotic regime (figure 7) to occur, the reflectivity must be high and the medium must be larger than the growth length of the Stokes wave. Note that the coherence length of the pump structures is on the order of the growth length of the Stokes wave. Thus the resulting chaos is low-dimensional and does not exhibit spatiotemporal chaos.³¹

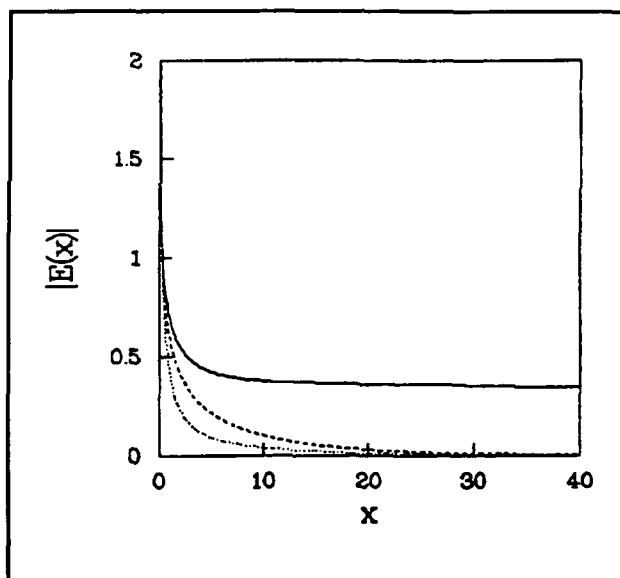


Figure 5. Fixed state spatial profiles of the pump (solid line), Stokes wave (dashed line) and acoustic wave (dotted line) for the parameters $\Delta = 0$, $A = 1.6$, $L = 20$, $\epsilon = 0.0025$.

²⁹ C.C. Chow, Ph.D. diss., Department of Physics, MIT, 1991.

³⁰ C.C. Chow, Ph.D. diss., Department of Physics, MIT, 1991; C.C. Chow and A. Bers, *Phys. Rev. A*, forthcoming 1993.

³¹ C.C. Chow, Ph.D. diss., Dept. of Physics, MIT, 1991; C.C. Chow, A. Bers, and A.K. Ram, "Spatiotemporal Chaos in the Nonlinear Three Wave Interaction," *Phys. Rev. Lett.* 68: 3379 (1992).

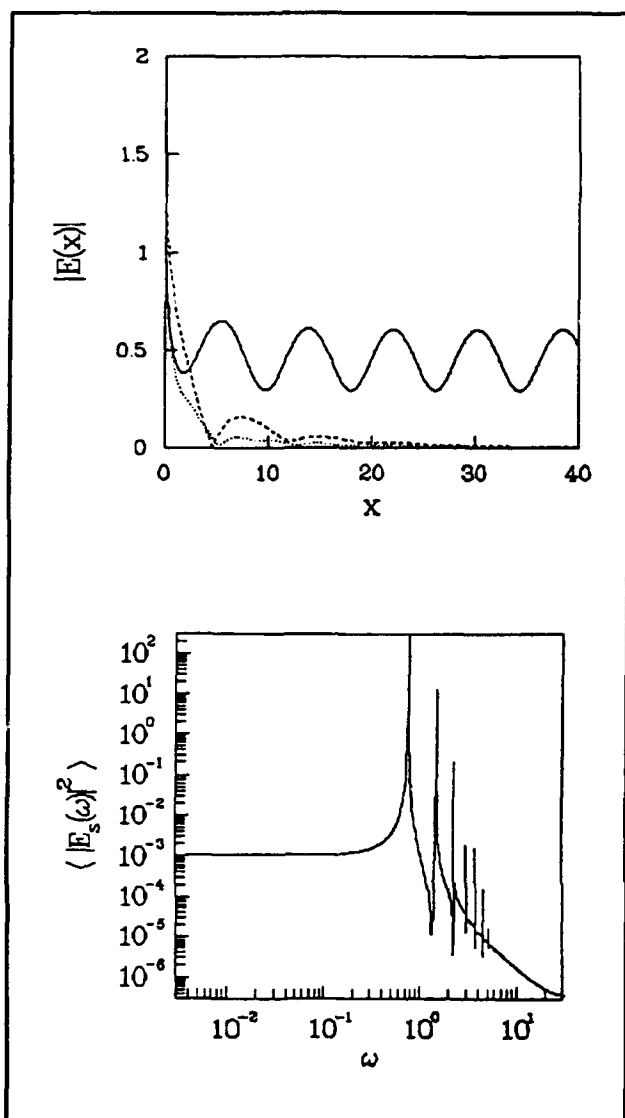


Figure 6. (a) Periodic state: Spatial profile of the amplitudes at a fixed time at $(\Delta = 1, A = 1)$. (b) Periodic state: Power spectrum of pump at $(\Delta = 1, A = 1)$.

1.2.3 Chaotic Webs in Ion-orbit Chaos Induced by Waves

Sponsors

National Aeronautics and Space Administration
Grant NAGW-2048
National Science Foundation
Grant ECS 88-22475
U.S. Department of Energy
Contract DE-FG02-91-ER-54109

The motion of a charged particle in a steady magnetic field and acted upon by an electrostatic wave, propagating in a direction perpendicular to the magnetic field, can be written as:

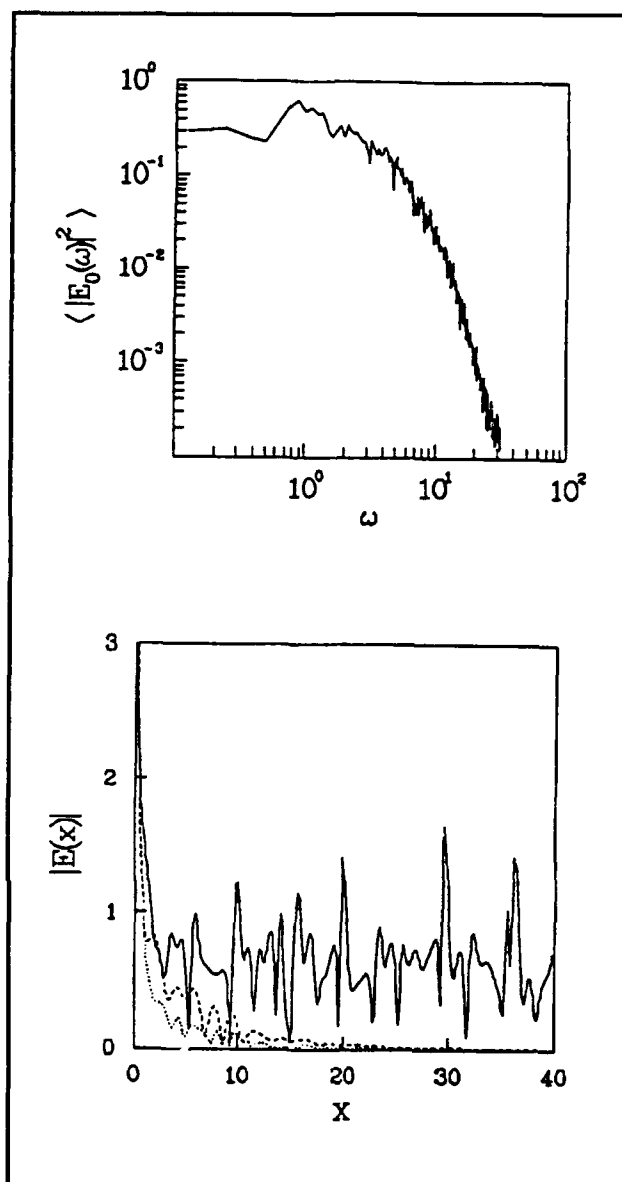


Figure 7. (a) Chaotic state: Spatial profile at $(\Delta = 1, A = 5)$. (b) Chaotic state: Power spectrum of the pump at $(\Delta = 1, A = 5)$.

$$\ddot{x} + \omega_c^2 x = \frac{eE_0}{m} \sin(kx - \omega t) \quad (1)$$

where e is the charge of a particle of mass m , ω_c is the cyclotron frequency of the particle in the constant magnetic field, E_0 is the amplitude of the electrostatic wave with wavenumber k and frequency ω . By using the normalized variables $\tau = \omega t$, $q = kx$, $p = k\dot{x}/\omega$, and $\Omega = \omega/\omega_c$, the Hamiltonian corresponding to the above equation of motion can be written as:

$$H(q, p, \tau) = \frac{p^2}{2} + \frac{\Omega^2}{2} q^2 + \varepsilon \cos(q - \tau) \quad (2)$$

where $\varepsilon = eE_0 k / (m\omega^2)$ is the normalized amplitude of the electric field. By defining the action-angle, (I, ψ) , coordinates:

$$I = \frac{\Omega}{2} \left(q^2 + \frac{p^2}{\Omega^2} \right)$$

$$\psi = \tan^{-1} \left(\frac{\Omega q}{p} \right)$$

the above Hamiltonian can be transformed to:

$$\begin{aligned} H &= \Omega I + \varepsilon \cos \left(\sqrt{\frac{2I}{\Omega}} \sin \psi - \tau \right) \\ &= \Omega I + \varepsilon \sum_{-\infty}^{\infty} J_n \left(\sqrt{\frac{2I}{\Omega}} \right) \cos(n\psi - \tau) \quad (3) \end{aligned}$$

This Hamiltonian has been examined in a variety of regimes by several authors. The case when $1/\Omega \approx$ integer (the non-resonant case) has been examined in detail by Karney.³² There it was found, using an analysis similar to the Chirikov resonance overlap criterion, that the motion of the ions became chaotic for amplitudes $\varepsilon > \Omega^{4/3}$; the chaotic region in p -space being limited from below by trapping condition: $p \geq 1 - \sqrt{\varepsilon}$, and from above by $p \leq (10n^2\varepsilon^2/\Omega)^{1/3}$ (where n is the closest integer to $1/\Omega$). From these conditions, it is clear that the threshold amplitude goes down as the frequency of the wave becomes much higher than the cyclotron frequency and, correspondingly, the extent of the region in p -space becomes wider as the amplitude is increased.

For $1/\Omega = n$, an integer (i.e., the wave frequency is an integer multiple of the particle cyclotron frequency; this will be referred to as the resonant case), the motion of the charged particle was first examined by Fukuyama et al.³³ and later by Chernikov, et al. and Zaslavsky.³⁴ The former found conditions for attaining wide-spread chaos, when $p \gg n$, using the Chirikov resonance overlap criterion, while the latter showed the existence of chaotic "webs." The importance of the web is twofold: first, the chaotic web has no amplitude threshold condition, although the chaotic region is very thin at low

amplitudes; second, the chaotic web exists over all phase space extending down to zero energies. These characteristics could obviously have important new applications for such wave induced chaos. The crucial problem is to determine the parameter regime for which the web is sufficiently thick to have a significant part of phase space chaotic, and, of course, the relationship between, and transition from, web chaos to the Chirikov-type global, but limited range, chaos which we already know for this problem. Below, we present some sample calculations illustrating the intriguing aspects of web chaos.

In the resonant case all the particle orbits are confined to islands. For small amplitudes, ε , the islands lie between the zeros of the Bessel function $J_n(\sqrt{2I})$, where $1/\Omega = n$. The separatrices of these islands are connected in a web structure, and a particle started on this web will diffuse along the web (figure 8). As ε is increased, the web widens occupying a larger fraction of the phase space. This increases the region of phase space for which the motion of the particle is chaotic (figure 9). Since the web is connected over the entire range of I , a particle starting on the web can, in principle, diffuse over the whole range of I . Note, however, that the lower energy region tends toward global chaos, while the web extension to higher energies remains rather thin.

In the slightly nonresonant case, and for small ε , there appear untrapped particle orbits which separate (in I) the islands mentioned above (figure 10). Even though the islands occupy most of the phase space, the web structure does not connect all the islands as in the resonant case. However, there exists a periodic web structure which is separated in I by untrapped particle orbits. The particle orbits can diffuse along this web structure bounded in I . Increasing ε does not restore the web structure of the resonant case. However, it does lead to local regions of chaotic motion which are formed by the widening of the webs (figures 11a and 11b).

As the wave frequency and the particle cyclotron frequency get farther off resonance, for small ε a larger region of phase space is occupied by untrapped particle orbits (figure 11a), until eventually, when the frequencies are sufficiently non-resonant, the entire phase space is occupied by

³² C.F.F. Karney and A. Bers, *Phys. Rev. Lett.* 39: 550 (1977); C.F.F. Karney, *Phys. Fluids* 21: 1584 (1978).

³³ A. Fukuyama, H. Momota, R. Itatani, and T. Takizuka, *Phys. Rev. Lett.* 38: 701 (1977).

³⁴ A.A. Chernikov, M. Ya. Natenzon, B.A. Petrovichev, R.Z. Sagdeev, and G.M. Zaslavsky, *Phys. Lett. A* 129: 377 (1988); G.M. Zaslavsky, *Chaos* 1: 1 (1991).

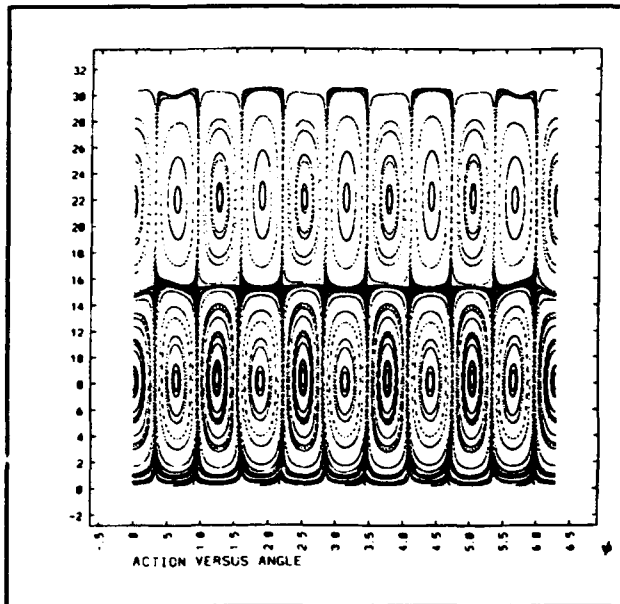


Figure 8. Action I versus angle ψ for $\Omega = 1/5 (\omega = 5 \omega_0)$ and $\epsilon = 10^{-2}$.

untrapped particle orbits. In this case, as ϵ is increased, there again appear islands in phase space where the particle orbits are trapped.

We are presently examining these puzzling features of web chaos, a new type of chaos, and its relation to the more commonly encountered Chirikov resonance overlap chaos.

1.2.4 Lower Hybrid Current Drive in the Presence of Waves in the Ion Cyclotron Range of Frequencies

Sponsor

U.S. Department of Energy
Contract DE-FG02-91-ER-54109

In a set of recent experiments on the Joint European Tokamak (JET),³⁵ it was observed that the lower hybrid (LH) current drive (CD) efficiency was significantly enhanced when the current driving lower hybrid waves (LHW) were launched in the presence of waves in the ion cyclotron range of frequencies (ICRF). The experiments were performed in a deuterium plasma with a hydrogen minority; an asymmetric (current drive mode) LHW k_{\perp} -spectrum and a symmetric (heating mode) ICRF k_{\perp} -spectrum

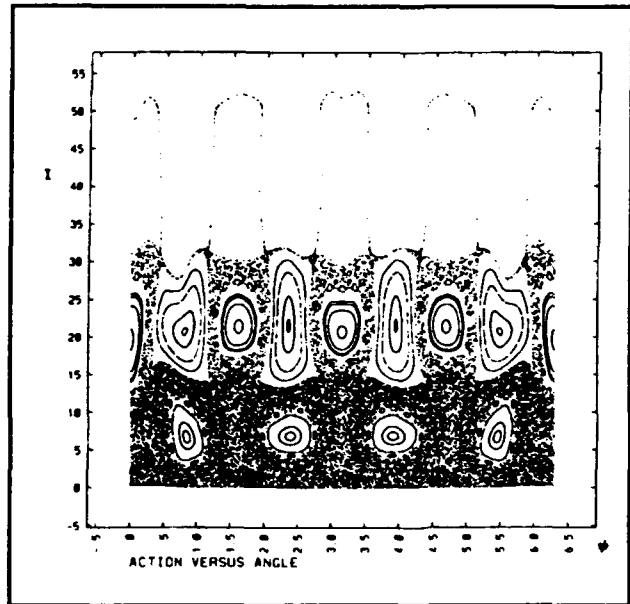


Figure 9. Action I versus angle ψ for $\Omega = 1/4 (\omega = 4 \omega_0)$ and $\epsilon = 10^{-1}$.

were applied externally. The experimental conditions for the enhancement in CD efficiency required that the ICRF antenna be in a monopole configuration and that the ion cyclotron and ion-ion hybrid resonance layers be located near the center of the plasma. In fact, if any of these two conditions were not satisfied, no enhancement in the CD efficiency was observed.

The initial ICRF power is carried from the antenna into the center of the plasma by fast Alfvén waves (FAW). At the resonance layers located inside the plasma some of this power is mode converted to ion-Bernstein waves (IBW). These IBWs then propagate away from the plasma core. The mode conversion is most efficient for small k_{\perp} 's (k_{\perp} is the component of the total wave vector along the toroidal magnetic field).

The FAWs can directly and indirectly heat the electrons. The direct heating is through electron Landau damping and transit time magnetic pumping. The indirect heating is by the slowing down of the energetic minority ion tails, generated by FAWs, on the electron distribution. This heating of electrons is known to lead to an enhancement in the LHCD efficiency and was first observed on the Japanese tokamak JT-60 (and, hence, known as the JT-60

³⁵ C. Gormezano, M. Brusanti, A. Ekedahl, P. Froissard, J. Jaquinot, and F. Rimini, *Proceedings of the IAEA Technical Meeting on Fast Wave Current in Reactor Scale Tokamaks (Synergy and Complementarity with LHCD and ECRH)*, Arles, France, September 23-25, 1991, eds. D. Moreau, A. Bécoulet, and Y. Peysson, pp. 244-259.

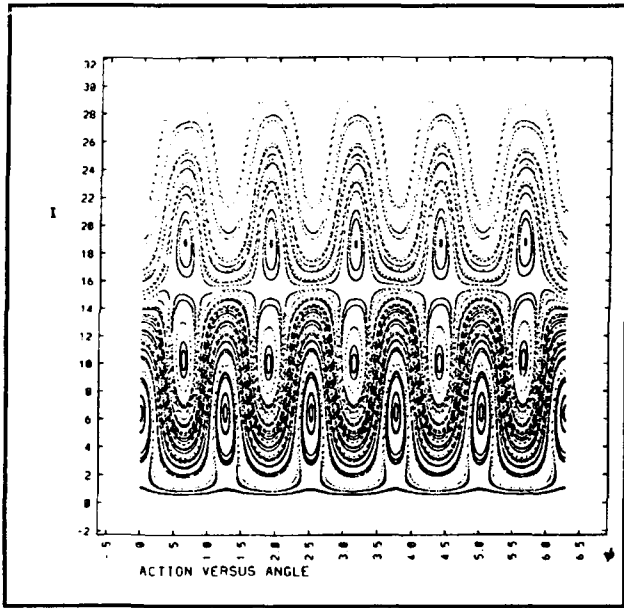


Figure 10. Action I versus angle ψ for $\Omega = 1/5.02 (\omega = 5.02 \omega_0)$ and $\epsilon = 10^{-2}$.

effect).³⁶ The FAWs can also interact with the electron tail pulled out by the LHWs.

For the IBWs, the initial mode converted spectrum has parallel (to the toroidal magnetic field) phase velocities which are much larger than the parallel electron thermal velocity. Thus, the IBWs cannot, initially, interact with the electron distribution function unless it has a runaway tail. The IBW spectrum also cannot interact with the ion distribution function as the mode conversion point is sufficiently far away from the ion cyclotron resonance. However, as the IBWs propagate away from the mode conversion region, toroidal effects upshift the $|k_{\parallel}|$'s so that eventually the IBW spectrum can interact with the LHCD electron distribution function.³⁷ The interaction is in the form of Landau damping. Thus, the IBWs can interact with the energetic electron tail pulled out by the LHWs.

Although several models have been proposed, the JT-60 effect remains largely unexplained. Since JET observed enhancements in the CD efficiency beyond those due to the JT-60 effect, we have concentrated our efforts toward understanding the direct interaction of the FAWs and IBWs with the

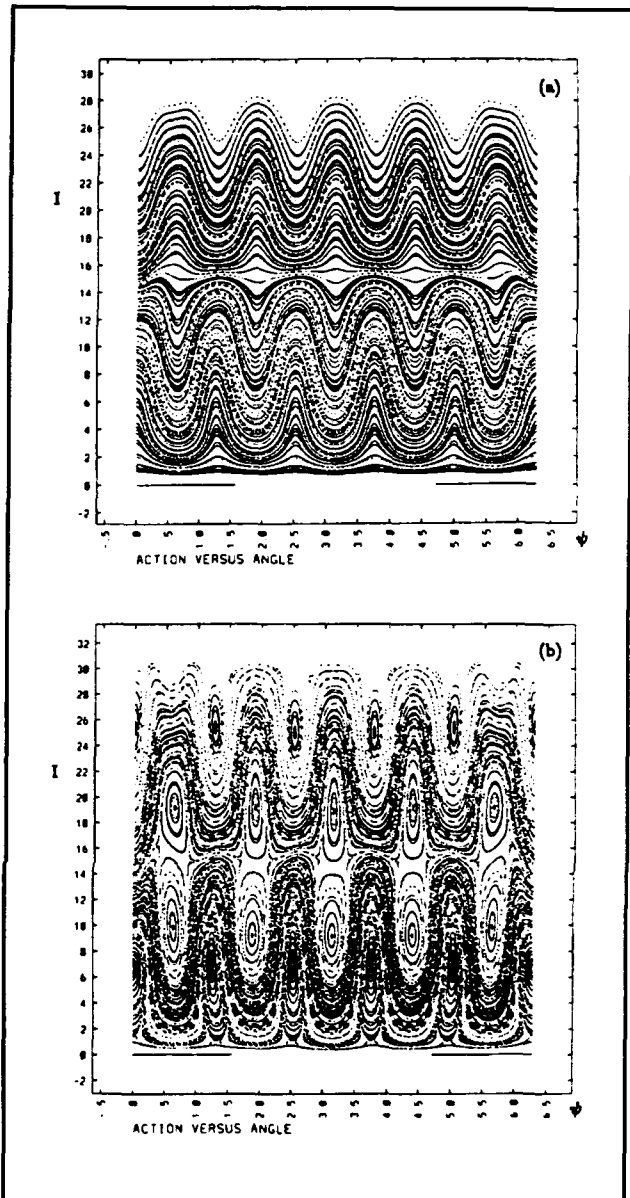


Figure 11. Action I versus angle ψ for $\Omega = 1/5.05 (\omega = 5.05 \omega_0)$: (a) $\epsilon = 10^{-2}$; (b) $\epsilon = 3 \times 10^{-2}$.

LH generated asymmetric electron distribution function. Toward this end, we have studied solutions of the relativistic Fokker-Planck equation describing the evolution of the electron distribution function, on a given flux surface, when acted upon by LHWs

³⁶ T. Imai and JT-60 Team, IAEA, 13th International Conference on Plasma Physics & Contributions to Nuclear Fusion Research, Washington, D.C., October 1-6, 1990, paper CN-53/E-1-3.

³⁷ A.K. Ram and A. Bers, "Propagation and Damping of Mode Converted Ion-Bernstein Waves in Toroidal Plasmas," *Phys. Fluids B* 3: 1059 (1991).

and either FAWs or IBWs.³⁸ The evolution of the flux surface averaged electron distribution function, in a uniform magnetic field and for wave frequencies ω below the electron cyclotron frequency ω_{ce} , is given by:

$$\frac{\partial}{\partial t} f_0 = \frac{\partial}{\partial p_{\parallel}} D^{\text{LHW}} \frac{\partial}{\partial p_{\parallel}} f_0 +$$

$$\frac{\partial}{\partial p_{\parallel}} D^{\text{FAW/IBW}} \frac{\partial}{\partial p_{\parallel}} f_0 + \left(\frac{\partial}{\partial t} f_0 \right)_{\text{collisional}}$$

where the D s are the appropriate quasilinear

diffusion coefficients and p_{\parallel} is the component of the electron momentum along the total magnetic field. Following the usual procedures,³⁹ we express the quasilinear diffusion coefficients in the following forms:

$$D^{\text{LHW}} = \pi e^2 |E_{kz}|^2 \delta\left(k_{\parallel} - \frac{\omega}{v_{\parallel}}\right) D_0^{\text{LHW}}$$

$$D^{\text{FAW/IBW}} = \pi e^2 |E_{ky}|^2 \delta\left(k_{\parallel} - \frac{\omega}{v_{\parallel}}\right) D_0^{\text{FAW/IBW}} \quad (1)$$

where

$$D_0^{\text{LHW}} = \frac{1}{|v_{\parallel}|} \left[\left\{ J_0 - \frac{v_{\perp}}{v_{\parallel}} J_1 \text{Im} \left(\frac{E_{ky}}{E_{kz}} \right) \right\}^2 + \left\{ \frac{v_{\perp}}{v_{\parallel}} J_1 \text{Re} \left(\frac{E_{ky}}{E_{kz}} \right) \right\}^2 \right]$$

$$D_0^{\text{FAW/IBW}} = \frac{1}{|v_{\parallel}|} \left[\left\{ \frac{v_{\perp}}{v_{\parallel}} J_1 + J_0 \text{Im} \left(\frac{E_{kz}}{E_{ky}} \right) \right\}^2 + \left\{ J_0 \text{Re} \left(\frac{E_{kz}}{E_{ky}} \right) \right\}^2 \right] \quad (2)$$

e is the electron charge, v 's are the velocities (with the component perpendicular to the magnetic field having the subscript \perp), E_k 's are the appropriate components of the Fourier transformed electric field spectrum, and the argument of the Bessel functions, J_0 and J_1 , is $(k_{\perp} v_{\perp})/\omega_{ce}$. The purpose of expressing the diffusion coefficients in different forms for the LHWs and the FAW/IBWs is that the factor multiplying D_0 in equation (1) is essentially determined by the input power spectrum. Meanwhile, D_0 in equation (2) depends only on the local plasma properties and polarizations of the fields. For typical JET-type parameters, we find that $D_0^{\text{FAW}}/D_0^{\text{LHW}} = (k_{\perp} \rho_e)^2$ where ρ_e is the electron Larmor

radius. Then, from equation (1), one can see that the diffusion coefficient for the FAW will be small compared to the LHW diffusion coefficient for similar powers. Then, on the basis of this comparison between the FAW and LHW diffusion coefficients, one expects that the FAW should not have a significant effect on the LH generated electron tails. Indeed, numerical solutions of the Fokker-Planck equation confirm this fact.

Meanwhile, since there is no easy way to evaluate the electric field polarizations for the IBW, a similar type of analytical analysis comparing the IBW diffusion coefficient with the LHW diffusion coefficient is not practical. However, numerical evaluations

³⁸ A. Bers and A.K. Ram, "Lower Hybrid and Fast Wave Current Drive—Status of Theory," *Proceedings of the IAEA Technical Meeting on Fast Wave Current in Reactor Scale Tokamaks (Synergy and Complementarity with LHCD and ECRH)*, Arles, France, September 23-25, 1991, eds. D. Moreau, A. Bécoulet, and Y. Peysson, pp. 2-34; Ram, A.K., A. Bers, V. Fuchs, R.W. Harvey, and M.G. McCoy, "Effects of Fast Alfvén Waves in Lower Hybrid Current Drive," *Proceedings of the Europhysics Topical Conference on RF Heating and Current Drive of Fusion Devices*, Brussels, Belgium, July 7-10, 1992, pp. 201-204; A.K. Ram, A. Bers, V. Fuchs, R.W. Harvey, and M.G. McCoy, "Current Drive by Lower Hybrid Waves in Presence of Fast Alfvén Waves," *Bull. Am. Phys. Soc.* 37(6): 1605 (1992); A.K. Ram, A. Bers, V. Fuchs, R.W. Harvey, and M.G. McCoy, "Effect of ICRF Waves on Lower Hybrid Current Drive," *Proceedings of the US-Japan Workshop on Non-Inductive Current Drive and Profile Control*, Princeton Plasma Physics Laboratory, 14-16, 1992.

³⁹ C.F. Kennel and F. Engelmann, *Phys. Fluids* 9: 2377 (1966); I. Lerche, *Phys. Fluids* 11: 1720 (1968).

show that the D^{IBW} is small compared to D^{LHW} but larger than D^{FAW} . Although the mode converted power to the IBW is smaller than the input power on the FAW, the electric field amplitude along the IBW increases by almost an order of magnitude as the IBWs propagate in a tokamak plasma. This increase is due to the IBWs group velocities slowing down as they propagate away from the mode conversion region. Numerical solutions of the Fokker-Planck equation then show that the IBWs can significantly affect the electron distribution function and, consequently, lead to an enhancement in the current drive efficiency.

Another important aspect of the IBWs is that they interact with electrons on the same flux surfaces on which the LHWs generate currents. It is well known that the LHCD generally occurs well off-axis in a tokamak. In experiments the ion resonances for ICRF waves are located near axis. So the FAW, which would interact with electrons near the ion resonances, is not interacting with the electrons on the flux surfaces where LHCD is generated. However, IBWs propagate away from the mode conversion region until there is sufficient enhancement in $|k_{\parallel}|$'s for the IBWs to interact with the electron distribution function. This interaction generally takes place well off-axis in the region where LHWs produce electron tails. This analysis is in general agreement with the experimental conditions required for an enhancement in the current drive efficiency.

1.2.5 Linear Analysis of the Double Stream Cyclotron Maser Instability

Sponsors

National Aeronautics and Space Administration
Grant NAGW-2048

National Science Foundation
Grant ECS-88-22475

The double stream cyclotron maser in which two copropagating electron beams with different beam velocities gyrate in a uniform axial magnetic field has been proposed as a source of millimeter wavelength radiation.⁴⁰ The interaction which leads to the

radiation is between the slow cyclotron space charge of one beam and the fast cyclotron space charge of the other beam. This interaction leads to high frequency bunching of the electrons and subsequent radiation.

We have carried out a linear instability analysis of the linear, uniform medium dispersion relation describing the interaction of two such beams.⁴¹ The dispersion relation describes the propagation of electrostatic waves, and, thus, is strictly valid for waves with phase velocities smaller than the speed of light. The analysis shows that electrostatic instabilities can be generated at frequencies lying near the doppler shifted electron cyclotron frequencies and also, approximately, half way between doppler shifted electron cyclotron frequencies. These instabilities exist for large k_{\parallel} (the wave vector component along the magnetic field) with $\omega_r/k_{\parallel} < c$ (ω_r is the real part of the frequency and c is the speed of light). For low beam densities, typical of those under consideration, the calculations point out the distinct advantage of the two electron beam system. For a single beam of electrons, the slow cyclotron space charge wave near a harmonic of the electron cyclotron frequency does not interact with the fast space charge wave at a neighboring harmonic. The only instabilities in this case are near the electron cyclotron frequency and its harmonics, and for small k_{\parallel} such that $\omega_r/k_{\parallel} > c$; this is the domain where the electrostatic approximation used to obtain the dispersion relation breaks down. Thus, the two beam system is important for generating emission at very high frequencies. In figure 12 we plot $(\omega_r - \bar{v}_{\parallel}k_{\parallel})/\Omega$ (where \bar{v}_{\parallel} is the average of the parallel velocities of the two beams and Ω is the average of the electron cyclotron frequency of the two beams) versus ck_{\parallel}/Ω . The regions instability are easily identifiable.

We have extended our linear analysis to include parallel temperature spreads in the beams. It has been found that the growth rates of the instabilities decreases as the temperature goes up. However, for parameters relevant to experiments, the growth rate is not substantially reduced so that instabilities exist for high frequencies and short parallel wavelengths.

⁴⁰ G. Bekefi, *J. Appl. Phys.* 71: 4128 (1992).

⁴¹ G. Bekefi, A.K. Ram, A. Bers, and C. Chen, *SPIE Proceedings of the 1992 OE LASE Conference*, Los Angeles, California, January 1992; A.K. Ram, C. Chen, A. Bers, W. Hu, and G. Bekefi, "Linear and Nonlinear Analysis of the Double Stream Cyclotron Maser," *Conference Record of the 19th IEEE International Conference on Plasma Science*, Tampa, Florida, 1-3 June 1992; A. Bers, A.K. Ram, and G. Bekefi, "Linear Analysis of the Double Stream Cyclotron Maser," *Bull. Am. Phys. Soc.* 37(6): 1536 (1992).

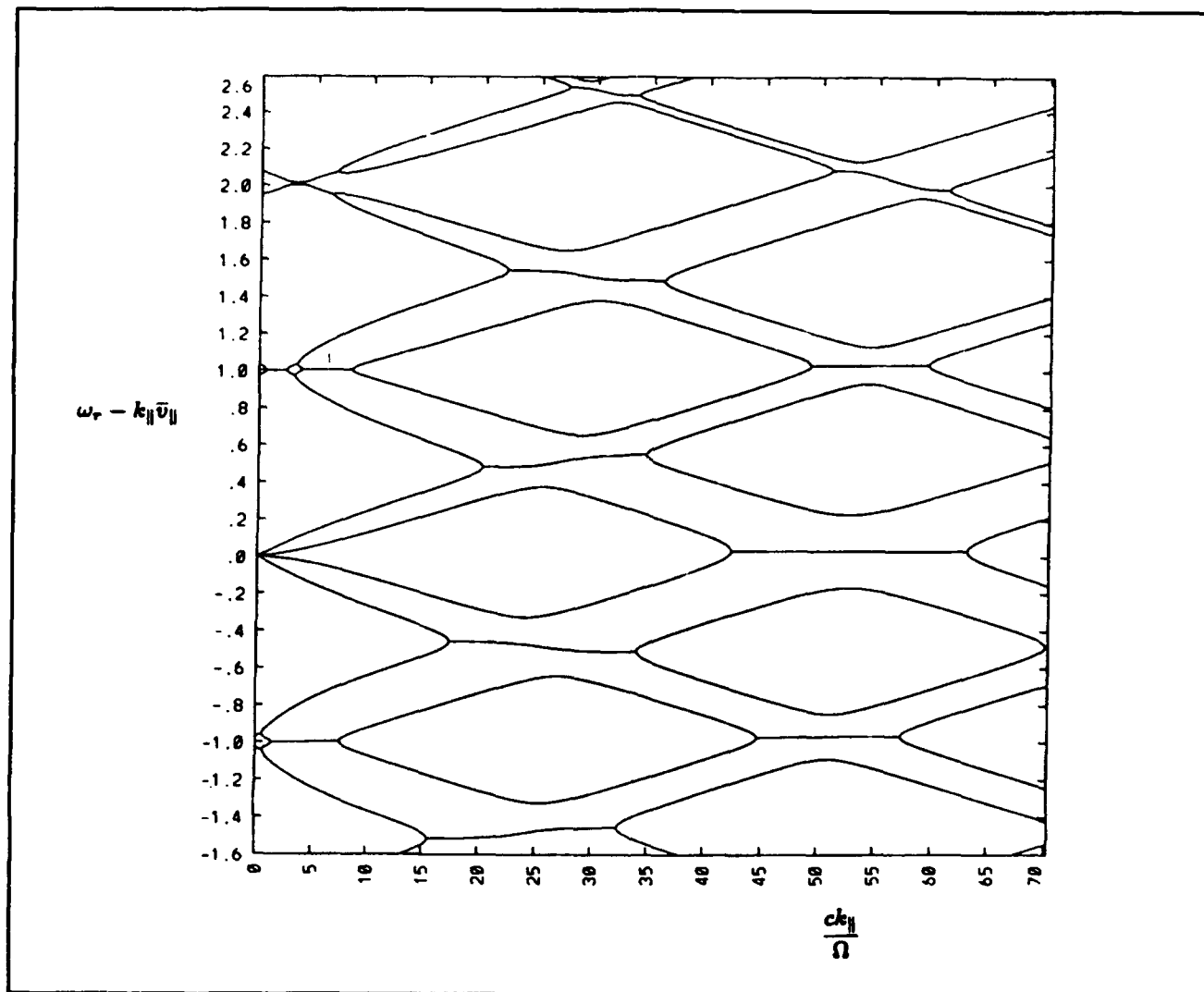


Figure 12. $\omega_r - \tilde{v}_1 \frac{k_{||}}{\Omega}$ versus $c \frac{k_{||}}{\Omega}$ for two beams whose parallel velocities are separated by 0.038c.

1.2.6 Publications

Bekefi, G., A.K. Ram, A. Bers, and C. Chen. *SPIE Proceedings of the 1992 OE LASE Conference*, Los Angeles, California, January 1992.

Bers, A., and A.K. Ram. *Lower Hybrid and Fast Wave Current Drive—Status of Theory*. PFC/JA-92-3. Cambridge: MIT Plasma Fusion Center, January 1992.

Bers, A., and A.K. Ram. "Lower Hybrid and Fast Wave Current Drive—Status of Theory." *Proceedings of the IAEA Technical Meeting on Fast Wave Current in Reactor Scale Tokamaks* (Synergy and Complementarity with LHCD and ECRH), Arles, France, September 23-25, 1991. Eds. D. Moreau, A. Bécoulet, and Y. Peysson, pp. 2-4.

Bers, A., A.K. Ram, and G. Bekefi. "Linear Analysis of the Double Stream Cyclotron Maser." *Bull. Am. Phys. Soc.* 37(6): 1536 (1992).

Chow, C.C. *Spatiotemporal Chaos in the Nonlinear Three Wave Interaction*. Ph.D. diss., Department of Physics, MIT, 1991.

Chow, C.C., and A. Bers. *Chaotic Stimulated Brillouin Scattering in a Finite Length Medium*. PFC/JA-92-36. Cambridge: MIT Plasma Fusion Center, December 1992.

Chow, C.C., and A. Bers. "Chaotic Stimulated Brillouin Scattering in a Finite Length Medium," *Phys. Rev. A*. Forthcoming.

- Chow, C.C., A. Bers, and A.K. Ram. "Spatiotemporal Chaos in the Langmuir Decay and its Implications on the Saturation of SRS." *Proceedings of the 22nd Anomalous Absorption Conference*, Lake Placid, New York, July 12-17, 1992.
- Chow, C.C., A. Bers, and A.K. Ram. *Spatiotemporal Chaos in the Nonlinear Three Wave Interaction*. PFC/JA-92-2. Cambridge: MIT Plasma Fusion Center, January 1992.
- Chow, C.C., A. Bers, and A.K. Ram. "Spatiotemporal Chaos in the Nonlinear Three-Wave Interaction." *Phys. Rev. Lett.* 68: 3379 (1992).
- Chow, C.C., A. Bers, and A.K. Ram. "Spatiotemporal Chaos in Three Wave Interactions." *Plasma Phys. Contr. Fusion*, 34(13): 1945 (1992). Special Issue: Invited papers for the 1992 ICPP, Innsbruck, Austria, June 29-July 3, 1992.
- Chow, C.C., A. Bers, and A.K. Ram. *Spatiotemporal Chaos in Three Wave Interactions*. PFC/JA-92-27. Cambridge: MIT Plasma Fusion Center, September 1992.
- Chow, C.C., A. Bers, and A. K. Ram. "The Three Wave Interaction and Spatiotemporal Chaos." *Physics of Space Plasmas* (1991), SPI Conference Proceedings and Reprint Series, Number 11. Eds. T. Chang, G.B. Crew, and J.R. Jasperse. Cambridge: Scientific Publishers, 1992, pp. 179-195.
- Chow, C.C., A. Bers, and A.K. Ram. *The Three Wave Interaction and Spatiotemporal Chaos*. PFC/JA-92-1. Cambridge: MIT Plasma Fusion Center, January 1992.
- Chow, C.C., A.K. Ram, and A. Bers. "Spatiotemporal Chaos in the Nonlinear Three Wave Interaction," *Research Trends in Physics: Chaotic Dynamics and Transport in Fluids and Plasmas*. Eds. I. Prigogine, et al. New York: American Institute of Physics. Forthcoming.
- Friedland, L., and A. Bers. *Hermitian Description of Interacting Inhomogeneous Electron Beams*. PFC/JA-92-15. Cambridge: MIT Plasma Fusion Center, April 1992.
- Friedland, L., and A. Bers. "Hermitian Description of Interacting Inhomogeneous Electron Beams," *Phys. Fluids B (Plasma Physics)* 4: 1457 (1992).
- Harvey, R.W., M.G. McCoy, A.K. Ram, A. Bers, and V. Fuchs. "Scaling of Lower Hybrid Current Drive with Temperature." *Proceedings of the Europhysics Topical Conference on RF Heating and Current Drive of Fusion Devices*, Brussels, Belgium, July 7-10, 1992, pp. 205-208.
- Lashmore-Davies, C.N., A. Bers, and A.K. Ram. "Enhanced Electron Power Absorption of the Fast Wave in the Vicinity of the Two Ion Hybrid Resonance." *Bull. Am. Phys. Soc.* 37(6): 1583 (1992).
- Ram, A.K., and A. Bers, "Comments on Absolute and Convective Instabilities." *Geophys. Res. Lett.* 19: 143 (1992).
- Ram, A.K., A. Bers, V. Fuchs, R.W. Harvey, and M.G. McCoy. "Current Drive by Lower Hybrid Waves in Combination with Fast Alfvén Waves." *Proceedings of the International Sherwood Fusion Conference*, Santa Fe, New Mexico, April 6-8, 1992.
- Ram, A.K., A. Bers, V. Fuchs, R.W. Harvey, and M.G. McCoy. "Current Drive by Lower Hybrid Waves in Presence of Fast Alfvén Waves." *Bull. Am. Phys. Soc.* 37(6): 1605 (1992).
- Ram, A.K., A. Bers, V. Fuchs, R.W. Harvey, and M.G. McCoy. "Effects of Fast Alfvén Waves in Lower Hybrid Current Drive." *Proceedings of the Europhysics Topical Conference on RF Heating and Current Drive of Fusion Devices*, Brussels, Belgium, July 7-10, 1992, pp. 201-204.
- Ram, A.K., A. Bers, V. Fuchs, R.W. Harvey, and M.G. McCoy. *Effects of Fast Alfvén Waves in Lower-Hybrid Current Drive*. PFC/JA-92-33. Cambridge: MIT Plasma Fusion Center, November 1992.
- Ram, A.K., A. Bers, V. Fuchs, R.W. Harvey, and M.G. McCoy. "Effect of ICRF Waves on Lower Hybrid Current Drive." *Proceedings of the US-Japan Workshop on Non-Inductive Current Drive and Profile Control*, Princeton Plasma Physics Laboratory, 14-16, 1992.
- Ram, A.K., C. Chen, A. Bers, W. Hu, and G. Bekefi. "Linear and Nonlinear Analysis of the Double Stream Cyclotron Maser." *Conference Record of the 19th IEEE International Conference on Plasma Science*, Tampa, Florida, June 1-3, 1992.

1.3 Physics of Thermonuclear Plasmas

Sponsor

U.S. Department of Energy
Contract DE-FGO2-91ER-54109

Project Staff

Professor Bruno Coppi, Neer R. Asherie, Dr. Paolo Detragiache, David S. Gloss, Dr. Cesar Meirelles-Filho, Dr. Stefano Migliuolo, Dr. Marco Nassi, Hana Ohkawa, Gregory E. Penn, Vladislav Portnoy, Caterina Riconda, Todd H. Rider, Dr. Barrett Rogers, Dr. Linda E. Sugiyama, Dr. Leonid E. Zakharov

As our primary activity in this research program, we study the theory of magnetically confined plasmas in regimes relevant to present-day advanced experiments and to future thermonuclear devices. In the future, these devices will probably ignite the plasma ("thermonuclear fuel") within toroidal magnetic confinement configurations and will involve either first generation fuels, a deuterium-tritium mixture (Ignitor, ITER), or more advanced fuels such as deuterium-deuterium or deuterium-helium mixtures (Candor).

The Ignitor-Ult machine is now in the early stages of construction in Europe. At MIT, the Alcator C-MOD experiment has recently begun operation. Alcator C-MOD combines the favorable features of an elongated plasma cross section with a high magnetic field to produce high plasma currents. This machine is in fact very similar to Megator, an experiment we proposed in the early 1970s as a logical continuation of the Alcator program.

Currently, our research program follows two major avenues. First, we are studying the basic physical processes of thermonuclear plasmas (equilibrium, stability, transport, etc.) as they apply to existing or near-term future systems. In this effort, we closely collaborate with our experimental colleagues and with theorists from other research groups (e.g., Columbia University, JET, Phillips Laboratory, Princeton University, University of Texas, Lawrence Livermore National Laboratories). This work also involves time-dependent simulations of plasma discharges in the Ignitor-Ult experiment. We focus particular attention on the evolution of spatial profiles of plasma current and temperature. Collaboration with our colleagues at the Italian laboratories, Energia Nucleare e Energie Alternative

(E.N.E.A.), as well as inhouse code development by scientists "on loan" from Italy and the former Soviet Union, plays a major role in this endeavor.

Second, we explore advanced regimes of thermonuclear burning, including those employing low neutron yield fuels (D-³He, and "catalyzed" D-D). We consider both the design of machines that will contain these very high temperature plasmas as well as the physics that govern their behavior. Below, we discuss some of the salient results of work completed or presently being carried out by members of our research group.

1.3.1 Theory of Reconnecting Modes in Collisionless Plasmas

We have investigated plasma processes capable of producing new magnetic field topologies (so-called magnetic reconnection) in collisionless, high temperature regimes.

In particular, we have developed a theory⁴² of $m = 1$ modes based on a kinetic description of the plasma dynamics inside the reconnection layer of width δ_R about the $q(r = r_1) = 1$ resonant surface where the parallel electric field $E_{\parallel} \neq 0$. At high temperatures, two scale distances characterize the plasma dynamics: the collisionless skin depth $d_e = c/\omega_{pe} \propto n^{-1/2}$ and the ion sound Larmor radius $\rho_s = (T_e/m_i)^{1/2}/\Omega_{ci} \propto T_e^{1/2}/B$. Here $T_{e,i}$ are the electron and ion temperatures, and Ω_{ci} is the ion gyrofrequency. Typically, experiments operate in regimes where $\rho_s > d_e$. A third scale distance of the problem is given by $\lambda_H r_1$, where λ_H is the ideal-MHD stability parameter (a functional of the global equilibrium profiles). We have focused on the case of ideal-MHD marginal stability $\lambda_H = 0$. In this case, $\delta_R \sim \rho_s$ and the parallel current density J_{\parallel} is confined to a sub-layer of width $\sim d_e$. By numerically solving the relevant mode equation, we find a mode growth rate $\gamma/\omega_A \sim (d_e/r_1) [1 + 1/(2\sqrt{\pi}) (1 + T_e/T_i)^{1/2} \rho_s/d_e]$ (ω_A is the shear Alfvén wave frequency) that can be quite fast, in particular for the parameters of the JET experiment when additional heating is used to enhance the plasma temperature.) In fact, we have proposed that the crash phase of the "sawtooth oscillations" in these experiments may be caused by the excitation of these modes.

At high temperatures, another effect that needs to be included in the analysis is that of the "drift" fre-

⁴² B. Coppi and P. Detragiache, *Phys. Lett. A*, 168: 59 (1992); B. Coppi and P. Detragiache, RLE PTP-Report 92-9, MIT, submitted to *Ann. Phys.* (1992).

quencies $\omega_j \propto T_j/B$ (j denotes the species: electrons or ions), related to the local equilibrium density (L_n) and temperature (L_T) gradient scale lengths, that is strongly stabilizing for $\omega_e > \gamma$. Now, since $\omega_e/\omega_A = \alpha \cdot (1 + L_n/L_T)(\rho_s/d_e)^2 d_e/r_0$, where $\alpha = (m_e/m_i)^{1/2} L_s/L_n$ and L_s is the magnetic shear length, ω_e -effects become dominant at large ρ_s/d_e . By numerically solving the relevant mode equation,⁴² we have verified that, for realistic values of L_s/L_n , there is only a small interval in ρ_s/d_e in which an enhancement of the growth rate by high temperature effects can be achieved, with a further increase in temperature (i.e., in ρ_s/d_e) leading to a strong stabilization of the mode.

1.3.2 Linear and Nonlinear Kink-Tearing Modes

A linear, two fluid model of the collisionless reconnecting mode in tokamaks has also been formulated, leading to a stability condition, which is in qualitative agreement with experimental observations of sawtooth activity in contemporary, high temperature experiments. In contrast to the predictions of the ideal MHD $m = 1$ mode theory, the density and temperature gradients $n'(r_1)$, $T'_{e,i}(r_1)$ (associated with the so-called ω_e -effects⁴³) play a stabilizing role in this condition while the magnetic shear $q'(r_1)$ is a destabilizing factor. Here, $q(r) = rB_z/(RB_\theta)$ is the "safety factor", B_z and B_θ are the toroidal and poloidal magnetic fields, r and R are the minor and major plasma radii, and r_1 is the radius where $q(r_1) = 1$. An approximate form of this stability condition may be written as

$$0.04\mu^{1/6} \left| \frac{(T_e + T_i)|n'|R}{B_z^2} \left[\frac{(T'_e + T'_i)n}{(T_e + T_i)n'} \right]^{1/3} \right|_{r=r_1} > q'(r_1)r_1, \quad \mu = \frac{m_i}{2m_p} \quad (1)$$

in terms of practical units: keV, 10^{13} cm^{-3} , Tesla, are used for $T_{e,i}$, n and B .

We have also considered the nonlinear evolution of the sawtooth crash in tokamaks. Specifically, our

study addressed the early nonlinear stage of the crash, when the plasma central core displacement $\xi_0(t)$ is still small with respect to the radius $r = r_1$, but exceeds the characteristic width of the narrow layer in which the magnetic reconnection occurs. First, the helically symmetric magnetic geometry of the nonlinear reconnecting mode was determined by solving Waelbroeck's equations.⁴⁴

Waelbroeck's equations are essentially approximate forms of the MHD equilibrium equation and the global flux conservation condition, which are valid when the crash time is slow compared to the relevant Alfvén time $\tau_A = 1/\omega_A$, but fast when compared to the resistive diffusion time. A typical result is plotted in figure 13, which shows a poloidal cross section of constant helical flux surfaces for a particular central core displacement. Combining this solution with the estimate of the reconnection layer width appropriate to current experiments, $\Delta \sim \rho_r = \sqrt{(T_e + T_i)/m_i}/\Omega_{ci}$, exponential growth of the mode was found with a rate $\gamma \sim q'(r_1)\rho_r\omega_A$. This result is also in good agreement⁴⁵ with experimental observations of the "fast" crash.

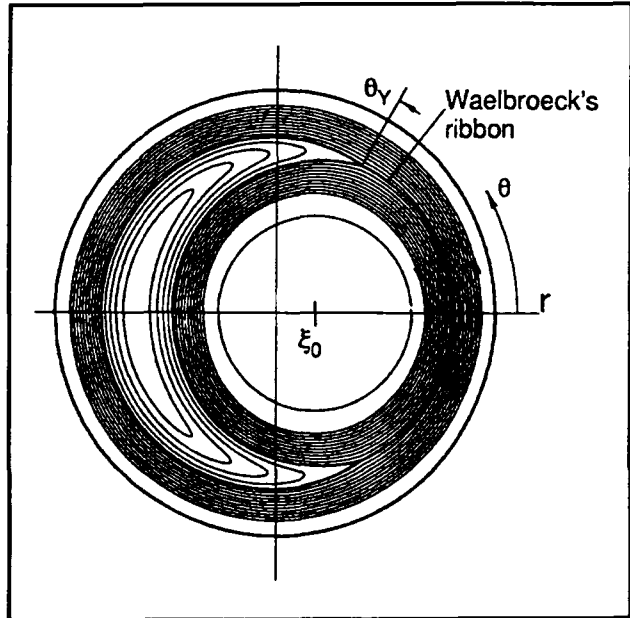


Figure 13. Magnetic configuration during the early nonlinear stage.

⁴³ G. Ara, B. Basu, B. Coppi, G. Laval, M.N. Rosenbluth, and B.V. Waddell, *N.Y. Ann. Phys.* 112: 443 (1978).

⁴⁴ F.L. Waelbroeck, *Phys. Fluids B* 1: 2372 (1989).

⁴⁵ L.E. Zakharov, B.N. Rogers, and S. Migliuolo, *Phys. Fluids B* 5, forthcoming.

1.3.3 Impurity Effects on Ion Temperature Gradient Microturbulence

The role played by impurities in influencing the linear stability properties of ion temperature gradient (ITG) modes has been considered with the intent to elucidate the role played by this turbulence in producing anomalous transport at the plasma edge. As is well-known, conventional gyro-Bohm transport models predict thermal diffusivities that scale as $T^{3/2}$, thereby becoming small in the outer plasma. (This is contrary to observed trends.)

The addition of one or more impurity (ion) species has one effect that may be termed beneficial in terms of transport: it leads to a dilution in the primary ion concentration ($n_i = n_0 - Z_i n_{i_1}$, for a hydrogenic primary, where Z_i is the charge of the impurity ion) and, thus, a tendency to stabilize the standard ITG mode. Indeed, calculations⁴⁶ done in shearless slab geometry for collisionless plasmas indicate that the critical value of the ion temperature gradient parameter, $\eta_i = d \ln T_i / d \ln n$ can increase by factors of 2-8 when an impurity species is present. The effect is stronger for higher ionization states and larger impurity mass.

This study was then carried out⁴⁷ for shaped plasmas in toroidal geometry, which is subject to the restriction that the mode frequency must be greater than the ion transit frequency. A collisionless, electrostatic, kinetic model was employed, and a considerable trend toward stabilization due to the impurity was found again. Of interest is the fact that three geometrical factors associated with the toroidal geometry and noncircular cross section of the plasma also contribute to smaller growth rates. The Shafranov shift has a strong stabilizing influence on the odd-parity mode and moderate stabilizing influence on the even-parity mode. Parity here refers to the property of the perturbed electrostatic potential when acted upon by a mirroring operator in the poloidal angle, $\theta \rightarrow -\theta$, where $\theta = 0$ corresponds to the outside of the torus farthest from the axis of symmetry).

Ellipticity tends to strongly stabilize the even-parity mode and only moderately weaken the growth of the odd-parity mode. The situation is reversed for triangularity (odd-mode affected more strongly), which has a weaker stabilizing effect overall than ellipticity.

While impurities tend to stabilize the collisionless plasma, which is typically found in the center of high temperature present-day experiments, they can trigger their own brand of drift-wave type microinstability in collisional regimes (e.g., at the plasma edge). This type of mode is driven unstable by the temperature gradient of the primary ion species (like the ITG mode), but requires the presence of an impurity (preferably massive in comparison to the primary ions) and dissipation (e.g., a parallel thermal conductivity). It propagates in the electron diamagnetic direction for peaked impurity density profiles ($d \ln n_i / d \ln n_0 \geq 1$). First discussed in the context of collisionless plasmas with reversed density profiles ($d \ln n_i / d \ln n_0 < 0$),⁴⁸ its properties were elucidated later for collisional regimes.⁴⁹ Our recent analysis⁵⁰ has concentrated on properties in sheared slab geometries. This mode has been found to be robustly unstable, relatively impervious to magnetic shear, with an extended linear eigenfunction (more than 10 ion Larmor radii wide). Thus, it is a good candidate for the anomalous energy transport in the outer region of the plasma.

1.3.4 Emissions at the Harmonics of the Helium Gyro-Frequency

In recent experiments carried out with D-T plasmas in JET,⁵¹ emissions were detected with a spectrum that showed distinct peaks at multiples ($l = 1 \rightarrow 8$) of the ^4He cyclotron frequency. An analysis⁵² of the linear stability of collective modes indicates that these emissions are likely to arise because of the presence of an anisotropic (in velocity space) population of high-energy α -particles. These particles occur naturally as by-products of D-T thermonuclear fusion reactions. The relevant modes are shown to

⁴⁶ S. Migliuolo, *Nucl. Fusion* 32: 1331 (1992).

⁴⁷ S. Migliuolo, *Nucl. Fusion* 33: 3 (1993).

⁴⁸ B. Coppi, H.P. Furth, M.N. Rosenbluth, and R.Z. Sagdeev, *Phys. Rev. Lett.* 17: 377 (1966).

⁴⁹ B. Coppi, G. Rewoldt, and T. Schep, *Phys. Fluids* 19: 1144 (1976).

⁵⁰ S. Migliuolo, *Phys. Lett. A*, forthcoming.

⁵¹ JET Team, *Nucl. Fusion* 32: 193 (1992).

⁵² B. Coppi, submitted to *Phys. Lett. A*, 1992.

be spatially localized in a narrow layer centered on a surface near the edge of the plasma column. The position of this surface is consistent with that inferred from the value of the magnetic field that corresponds via the cyclotron frequency to the observed radiation. The width of the layer is compatible with the relatively narrow width of the peaks in the emitted spectrum. The outermost portion of the plasma is reached by α -particles that are trapped in orbits with relatively large values of v_{\perp}/v_{\parallel} . Work is underway⁵³ to determine the characteristics of the α -particle velocity space distribution function that are "optimal" for linear growth of these cyclotron harmonics, so that, in the future, emission spectra in other experiments can be used as a diagnostic tool. One additional issue being explored⁵⁴ is the effect of impurity ions on the emitted radiation: they may play an important role in determining some of the finer features in the observed spectrum.

1.3.5 Deuterium-Tritium Ignition Experiments with High Magnetic Fields

High magnetic field experiments have been designed to investigate deuterium-tritium fusion ignition conditions, on the basis of known experimental and theoretical understanding of plasma behavior. Our group has long maintained a strong effort in pioneering the practical use of such configurations. We have shown that the most advantageous and least expensive designs incorporate an interlocking set of characteristics: aspect ratio, relatively small size with significant vertical elongation, high toroidal and poloidal magnetic fields, large plasma currents, high plasma densities, good plasma purity, strong ohmic heating, good plasma and α -particle confinement, and robustness against ideal MHD and resistive plasma instabilities.⁵⁵ We have investigated the physical basis for these plasma properties, while also constructing the design and engineering solutions for attaining the necessary parameters in the Ignitor Ult machine⁵⁵ presently being built in Italy. Since ignition depends upon many spatially and temporally varying processes, many of our studies are based upon the numerical simulation of a free boundary plasma from the current ramp through ignition, using the

MHD evolution and plasma flux surface transport code (TSC).⁵⁶

The ignition of a 50:50 deuterium-tritium plasma requires a minimum value of the parameter $n_0\tau_E \approx 4 \times 10^{20} \text{ sec/m}^3$ in order to achieve ignition with $T_{eo} \approx T_{io} \leq 15 \text{ keV}$, where n_0 is the peak plasma (electron) density, T_{eo} the peak temperature, and τ_E the energy replacement time. Here ignition is defined as the point when the plasma heating due to fusion α -particles, P_{α} , equals the plasma thermal losses P_L . Relatively high values of the plasma density, $n_0 \approx 10^{21} \text{ m}^{-3}$, then require only moderate values of τ_E , whose magnitude is less easy to predict with certainty. Both these values should be achievable, based on the favorable confinement properties of high density plasmas that have been demonstrated by a series of high field experiments, the Alcator A and C at MIT and the FT/FTU devices at Frascati, Italy. Experimentally, the maximum plasma density n_0 that can be supported correlates with the ratio B_T/R_0 , where B_T is the toroidal magnetic field at the center of the plasma column, at major radius $R = R_0$. On the basis of the Alcator C machine, where $n_0 \approx 2 \times 10^{21} \text{ m}^{-3}$ was achieved with $B_T \approx 12.5 \text{ T}$ and $R_0 = 0.64 \text{ m}$, and the TFTR machine at Princeton, where even larger ratios of n_0R_0/B_T were achieved, a configuration with $R_0 \approx 1.3 \text{ m}$ and $B_T \approx 13 \text{ T}$ should be able to sustain reliably densities of 10^{21} m^{-3} .

A strong toroidal magnetic field also supports a high poloidal field B_p and correspondingly large plasma current I_p . A significant vertical elongation, e.g., $\kappa \approx 1.8$, substantially increases the plasma current that can be carried for a given B_T and R . If the density correlates with the (volume) averaged toroidal current density, $\langle J_{\phi} \rangle$, then experimental results suggest that somewhat less than 1 kA/cm^2 should offer considerable margin to attain the desired peak density $n_0 \approx 10^{21} \text{ m}^{-3}$. High values of B_p produce a strong rate of ohmic heating, while large currents I_p tightly confine the fast α -particles produced by the fusion reactions, so that they deposit their energy in the center of the plasma. The degradation of the plasma energy confinement that is commonly observed when injected (nonohmic) heating is applied, is reduced at higher plasma current. In addition, the poloidal plasma beta β_p can be kept small at ignition, to improve the

⁵³ B. Coppi and N. Asherie, *Bull. Am. Phys. Soc.* 37: 1475 (1992).

⁵⁴ N. Asherie, in preparation (1993).

⁵⁵ B. Coppi, M. Nassi, and L.E. Sugiyama, *Physica Scripta* 45: 112 (1992).

⁵⁶ S.C. Jardin, N. Pomphrey, and J. Delucia, *J. Comp. Phys.* 66: 481 (1986).

plasma stability, and, in particular, to stabilize the ideal MHD modes with mode numbers $m = 1$, $n = 1$ that are associated with sawtooth oscillations. Large plasma density combined with good ohmic heating allows ignition at low plasma temperatures. This reduces the fusion power, and therefore the thermal wall loads. The low beta increases the overall margin of plasma stability.

The plasma purity has been shown to improve with increasing plasma density, that is, the effective charge $Z_{eff} = \sum n_i Z_i^2 / n_e$ decreases monotonically with n_e in an extensive series of experiments starting with the Alcator A. The major effect of impurities is to dilute the concentration of fusing nuclei, while a secondary effect is the increase of power loss due to bremsstrahlung radiation. If auxiliary heating is not used, Z_{eff} cannot exceed about 1.6 for D-T ignition in the Ignitor, as indicated by our analyses.

Relatively high plasma edge densities also help to confine impurities to the scrape off layer, where the induced radiation helps to distribute the thermal wall loading more uniformly over the plasma chamber surface. The low ignition temperatures associated with high density further help to keep the plasma clean by reducing the thermal wall loading that result in sputtering.

Peaked plasma density profiles should be maintained by external means such as pellet injectors if necessary. Peaked profiles maintain stability to ion temperature gradient modes that enhance the ion thermal transport. Since the neoclassical (Ware) inward particle pinch is relatively strong in a tight aspect ratio, high field configuration and an anomalous inflow are also present. Therefore, pellets that penetrate partway into the plasma can be successfully used to raise the plasma density and produce peaked profiles near ignition.

Plasma configurations such as X-points that concentrate the thermal (particle) heat flux on localized areas of the vessel wall limit the amount of fusion power that can be handled. In addition, an even more limited plasma current can be sustained. However, X-points and detached plasmas can be obtained with relatively little sacrifice in the plasma and magnet parameters. By creating the conditions known to produce "H-mode" operation, X-points and detached plasmas may prove desirable in limiting degradation of the plasma confinement caused by nonohmic heating.

Divertors represent a more severe compromise, since they alter the design of the plasma chamber

and the toroidal magnet. The major radius must be increased to accommodate a reliable divertor, reducing the ratio B_T/R and therefore the maximum plasma density. The magnetic fields are also reduced, lowering the plasma current and the ohmic heating, and increasing β . A large injected heating system becomes necessary to replace the ohmic heating and the resulting degradation of the plasma confinement makes low temperature ignition difficult. The divertor plates must then handle large thermal heat fluxes. There is no demonstrated advantage to using divertors in high density plasmas, while the cumulative disadvantages make ignition difficult to attain. Their use would remove much of the rationale for using a compact, high field machine.

1.3.6 Time-dependent Ignition

The transient nature of ignition has important consequences. The initial current ramp, when I_p , n_e , B_T , and the plasma cross section are increased simultaneously, to their maximum values, has important effects on the plasma energy balance and stability at ignition.⁵⁷ These effects arise from the relatively slow inward diffusion of the plasma current, which is added at the outer surface of the plasma by the current ramp, compared to the growth of the central temperature due to plasma heating. The current ramp generates an inhomogeneous toroidal electric field in the plasma that is peaked near the plasma edge and allows large values of ohmic heating at high central temperature. The magnetic safety factor q can be easily maintained above unity or held to a very small $q < 1$ region during the current ramp. A more careful study,⁵⁷ shows that the magnetic safety factor can also be kept small after the ramp, at least until the central temperature reaches high values and fusion α -particles begin to appear, both of which are stabilizing effects for $m = 1$ modes. Furthermore, small amounts of injected heating (e.g., $P_{inj} < P_{oh}/2$) during the current ramp can maintain a very small size (or nonexistence) for the $q < 1$ region until well past ignition, if central temperatures approach 10 keV by the end of the current ramp, through the freezing-in of the central current density at low resistivity. Injected heating also reduces the magnetic flux consumption required to reach ignition, particularly if ignition occurs during the current ramp. These characteristics are illustrated in table 1 (reference case for the maximum Ignitor design parameters, peak $B_T = 13.5$ T, $I_p = 12$ MA, $R = 1.3$ m, $a = 0.48$ m,

⁵⁷ B. Coppi, M. Nassi, and L.E. Sugiyama, *Physica Scripta* 45: 112 (1992); L. Sugiyama, and M. Nassi, *Nucl. Fusion* 32: 387 (1992).

$\kappa = 1.8$, and $n_{eo} = 1.1 \times 10^{21} \text{ m}^{-3}$, at 50:50 D:T ratio and $Z_{eff} = 1.2$).

It is possible to simultaneously maintain monotonically increasing q profiles without large low shear regions and with edge values $3 < q_{va} < 4$ during the current ramp, to beyond ignition. These conditions should prevent instabilities associated with internal plasma modes (e.g., "locked" or quasistationary modes) that can be triggered during the current ramp and often lead to serious disruptions, in which the confinement of the plasma can be lost. Since hollow q profiles are usually associated with the excitation of internal macroscopic modes and enhanced, "anomalous" current penetration, while ignition is aided by a slow current penetration that keeps $q_0 > 1$ for as long as possible, these precautions are not superfluous.

A major question for all ignition experiments is the degree of degradation expected in the plasma energy confinement near ignition, since D-T ignition is easily achieved if the confinement remains at the optimal ohmic heating level. One strategy for a high field experiment is to maintain a high level of

ohmic heating up to ignition, $P_{\alpha} \leq 2P_{OH}$, to reduce the degree of degradation. Since α -particle heating possesses two important characteristics of ohmic heating that are not shared by any presently available form of injected heating—axisymmetric deposition and generation in the center of the plasma column—we expect that the degradation should not be as severe.

The requirement that the edge q is between 3 and 4 (high plasma current) means that special care must be devoted to maintaining $q > 1$ up to ignition. If only ohmic heating is contemplated, the steadily increasing size of the $q < 1$ region after the end of the current ramp imposes a more severe limit on the time in which the plasma can ignite and on the required energy confinement level than the energy balance alone. This assumes that sawtooth oscillations large enough to destroy the central peaking of the temperature cannot be avoided. Then ignition in the Ignitor reference case, at $T_e \sim 11 \text{ keV}$, requires $\tau_E \sim 0.66$ seconds and must occur within approximately 1.5 seconds of the end of the current ramp (table 1). Our theoretical analysis, on the

Table 1. Reference Discharge for the Ignitor Ult. Maximum parameters at the End of Ramp $I_p = 12 \text{ MA}$, $B_T = 13.5 \text{ T}$, $R = 1.3 \text{ m}$, $a = 0.48 \text{ m}$, $b = 0.87 \text{ m}$, $\delta = 0.4$, $n_{eo} = 1.1 \times 10^{21} \text{ m}^{-3}$, $n_{eo}/\langle n_e \rangle \% = 2.2$, $Z_{eff} = 1.2$.

	End Ramp	Ignition	
t	3.0	4.3	time (sec)
$\ell/2$	0.32	0.38	internal inductance
β_p	0.08	0.13	poloidal beta
β	0.8	1.26	toroidal beta (%)
q_{va}	3.3	3.6	edge magnetic safety factor
W	7.5	11.7	plasma kinetic energy (MJ)
T_{eo}	4.0	11.0	peak electron temperature (keV)
τ_E	710	660	energy confinement time (msec)
P_{OH}	13.0	9.5	ohmic heating (MW)
P_{α}	2.0	17.8	α -particle heating (MW)
$n_{\alpha o}$	1.5	12.0	peak α -particle density (10^{17} m^{-3})
P_B	3.2	4.1	bremsstrahlung radiation (MW)
P_{IC}	0.4	0.5	cyclotron and impurity radiation (MW)
$V_{q=1}$	1.4	5.8	volume where $q \leq 1$ (% of total)
$\Delta\Phi$	29.2	31.4	magnetic flux variation (V sec)
I_{BS}	0.6	1.0	bootstrap current (MA)

other hand, indicates that Ignitor remains, in all regimes, within the stability limits of the ideal MHD and resistive $m = 1$, $n = 1$ modes. In addition, moderate amounts of auxiliary heating, $P_{ICRH} \sim 10$ -15 MW, started during the current ramp, allow ignition down to the limits predicted by $n_0\tau_E$, i.e., $\tau_E \leq 0.4$ sec, while maintaining very small $q = 1$ regions well beyond ignition. Similarly, in the ohmic case, if the requirement of small $q < 1$ region is dropped, either on the basis of the theoretical analysis or by externally stabilizing the sawtooth oscillations, ignition can also occur at this τ_E and at times of $t_i \sim 5$ -5.5 seconds.

The importance of ohmic heating during the ignition sequence at high field and density means that a model for the electron thermal transport should, similar to the one used here, simulate ohmic regimes and reproduce typical toroidal loop voltages in steady state ohmic experiments that are observed to be an almost "universal" constant. In addition, the total diffusion coefficient should increase with injected heating and reproduce the degraded confinement observed in present experiments that are dominated by injected heating.

A second major question for ignition is the effect of variation in the plasma density and its profile, since pellets injected to raise the density are unlikely to fully penetrate a high density plasma. For a given level of thermal transport, there is an optimum density for fastest ignition. A higher density is more favorable under degraded conditions. Higher density, however, accelerates the toroidal current penetration at a given time by lowering the T_e , producing larger $q < 1$ regions earlier than at lower density. This effect also operates in the outer part of the plasma radius when density profiles are broadened. Thus, for $n_{e0} = 1.1 \times 10^{21} \text{ m}^{-3}$, profile peaking factors $n_{e0}/\langle n_e \rangle \geq 1.9$ where $\langle n_e \rangle$ is the volume average give relatively similar results for ignition. Broader profiles rapidly lead to degraded ignition, e.g., $n_{e0}/\langle n_e \rangle = 1.5$ requires longer t_i and higher τ_E and yields a significantly larger $q = 1$ radius. Lower central density, e.g., $n_{e0} = 6.5 \times 10^{20} \text{ m}^{-3}$ at the end of the current ramp increasing to 8 - 9×10^{20} by ignition, allows broader profiles, $n_{e0}/\langle n_e \rangle = 1.5$. For related reasons, increasing the plasma density after the current ramp is more advantageous than increasing the density during the ramp. At high density, a region of low magnetic shear develops in the mid-region of the minor radius. This region becomes seriously unstable when its value of q approaches unity, since ideal MHD instabilities with $m = 1$ can occur. This is one of the major limits on the broad density profile cases.

1.4 Versator II Tokamak Research Program

Sponsor

U.S Department of Energy
Contract DE-FG02-91-ER-54109

Project Staff

Professor Miklos Porkolab, Edward W. Fitzgerald,
Jared P. Squire, Jesus Noel Villaseñor

Versator II is a small tokamak facility (major radius $R = 40$ cm, minor radius $a = 13$ cm) with modest plasma parameters (magnetic field $B_0 \sim 1.3$ Tesla, density $n_0 \sim 3 \times 10^{13} \text{ cm}^{-3}$, and plasma current $I_p \sim 10$ -80 kA) which is used for fundamental studies of the interaction of electromagnetic waves with a fully ionized, nearly collisionless plasma. For this purpose, we use several high power ($P_r \sim 100$ kW) microwave sources to launch waves at frequencies near the electron-gyro frequency ($f_{ce} \sim 28$ -35 GHz) and the lower hybrid (ion-plasma) frequency ($f_{lh} = 800$ MHz or 2.45 GHz). In the sections below, we describe two different experimental projects which were carried out during the past year.

1.4.1 High Beta-Poloidal Experiments with Advanced X-Ray Diagnostics

High poloidal beta ($\epsilon\beta \sim 1$) plasma equilibria have been produced by both toroidally asymmetric (current drive, LHCD) and symmetric (heating, LHH) lower hybrid RF injection in the Versator II tokamak. (Here β_p is the ratio of the plasma pressure to the poloidal magnetic field pressure, and $\epsilon = a/R_0$ is the inverse aspect ratio). In both cases, the plasma current was fully sustained by the RF, with the loop voltage negligibly small ($V_{loop} < 0.03$ V). The RF-created energy electron distribution function, which provides a large fraction of the plasma current and pressure in these plasmas, is studied by means of x-ray spectroscopy of the electron-ion bremsstrahlung plasma emission. Profile measurements of the emission perpendicular to the toroidal magnetic field and emission measurements at a full range of angles to the toroidal magnetic field have been carried out.

For low plasma current equilibria, β_p is enhanced, and an outward shift in major radius of the x-ray emission profile peak was observed, corresponding to a Shafranov shift ($\Delta_0/a \sim 0.33$) of the magnetic axis. The LHCD equilibrium current profile was determined from the x-ray emission profile. The safety factor on axis is calculated as $q_0 = 3 \pm 1$ and is nearly independent of the total current. The normal-

ized internal inductance increases slightly with lower plasma current, $I_p/2 = 0.8 \rightarrow 1.2$. From $\beta_p + I_p/2 \approx 4$, the poloidal beta is calculated, $\epsilon\beta_p \approx 0.9$. The LHCD x-ray data indicate a highly anisotropic energetic electron distribution function with a density approximately 1 percent of the bulk electron density at the center. The stored energy of this distribution is much larger than the bulk energy and the global energy confinement time scales in agreement with the Kaye-Goldston L-mode scaling ($\tau_E \propto I_p^2$).

At high values of $\beta_p \sim 3$, LHH generates nearly the same plasma current as LHCD. The LHH equilibria has a reduction of up to a factor of four in the high energy (> 30 keV) x-ray emission flux, as compared to LHCD. Modeling of the electron distribution function in the LHH case indicates that only one third of the current is carried by the high energy electrons. At lower values of $\beta_p \sim 1.5$, LHH requires the assistance of a small applied loop voltage ($V_{loop} \sim 0.2V$) to maintain the plasma current. The high energy electrons carry a majority of the plasma current. Soft x-ray data indicates the presence of an enhanced intermediate energy electron population with a temperature of $T_{int} = 15$ keV. Calculations show that for the high $\beta_p \sim 3$ equilibria, the intermediate energy electrons could carry a majority of the current ($\sim 70\%$) in the form of bootstrap current.

Thesis

Squire, J.P. *An Experimental Study of Lower Hybrid Wave-driven High-Poloidal Beta Plasmas in the Versator II Tokamak*. Ph.D. diss., Dept. of Physics, MIT, 1993.

1.4.2 Fast Wave Current Drive Experiments

Previously we had discussed a combined fast wave-slow lower hybrid wave current drive experiment where two traveling waves are launched. Slow lower hybrid waves launched at 2.45 GHz by a conventional grill form a suprathermal electron tail, which is then expected to absorb an 800 MHz fast wave spectrum launched by a specially built dielectric-loaded waveguide array. This is expected

to enhance the current driven by the 2.45 GHz slow wave, and raise the current drive efficiency at high densities where slow wave current drive efficiencies are degraded.

We have built and successfully tested the 800 MHz antenna, and showed that its coupling to the plasma corresponds well with theory. However, high power experiments ($P_{rf} < 25$ kW) using the fast wave antenna in conjunction with the 2.45 GHz launcher have failed to produce any form of current drive or central heating, as shown by measurements using tangential and perpendicular hard x-ray detectors. Further, only edge parameters appear to be affected with the application of RF power. Our code calculations indicate that according to linear wave theory, a significant fraction of the power should have penetrated the plasma interior and also should have been absorbed by fast electrons. We conclude that the fast waves must be absorbed on the plasma surface, possibly by non-linear effects such as parametric decay or scattering by low frequency edge density fluctuations.

Miniature retarding potential energy analyzer probes have been installed at different edge locations on Versator II. A thin region where electrons are heated from 5-10 eV to as high as 100 eV was detected. This region has a radial extent of approximately 1 cm, and a height of 2 cm, which corresponds to the antenna height. The region of hot electrons is located just behind the limiter edge and along the midplane of the tokamak (coplanar with the antenna array). This phenomena appears to be well localized in that region; no heating was seen in top or bottom probes. The heating also begins when the applied RF power exceeds 200 W.

We have also installed several electrostatic probes to measure the parametric decay spectra at different toroidal and poloidal locations. Parametric decay activity was clearly seen when the fast wave power is applied. We note asymmetric broadening of the pump frequency with more activity occurring on the lower frequency side of the pump. This phenomena has a measured threshold of $P_{rf} = 200$ W, which corresponds with the threshold of the edge electron heating.

Section 3 Electromagnetics

Chapter 1 Electromagnetic Wave Theory and Applications

Chapter 1. Electromagnetic Wave Theory and Applications

Academic and Research Staff

Professor Jin Au Kong, Professor Terry P. Orlando, Dr. Robert T. Shin, Dr. Y. Eric Yang, Dr. Yi Yuan, Qizheng Gu

Visiting Scientists and Research Affiliates

Dr. Sami M. Ali, Dr. Arthur K. Jordan,¹ Dr. Che Y. Kim,² Dr. Kevin O'Neill,³ Dr. Soon Y. Poh,⁴ Dr. Michael Tsuk,⁵ Dr. Herre S.J. van der Zant, Dr. Rongqing Xu,⁶ Masanori Yamaguchi⁷

Graduate Students

David V. Arnold, Robert G. Atkins, William W. Au, Philippe Berisset, David Berman, Pierre Coutu, Derek R. Curd, K.A. Delin, Hong-Tat Ewe, Hsiu C. Han, Chih-Chien Hsu, Gregory T. Huang, Joel T. Johnson, Arvind Kumar, Cheung-Wei Lam, Hongsing Lee, Laurence H. Lee, Kevin Li, Harold H. Lim, Derek S. Linden, Michael C. Moldoveanu, Alex Mou, John H. Oates, Joel R. Phillips, Leonard M. Rubin, M. Ali Tassoudji, Murat E. Veysoglu, Li-Fang Wang, Shih-Jih Yao, Jiqing Xia

Undergraduate Students

Robert D. Bock, Upanishad K. Chakrabati, Joseph H. Kang, Jerome S. Khohayting, William K. Lee, Yong Liu, Katherine Tso, Elaine C. Yiu

Technical and Support Staff

Margery E. Brothers, Karen Chenausky, Charmaine A. Cudjoe-Flanders, Kit-Wah F. Lai, Angela R. Odoardi, Barbara A. Roman

1.1 Remote Sensing of Earth Terrain

Sponsors

National Aeronautics and Space Administration
Grant NAGW-1617
Agreement 958461
Grant NAGW-1272
U.S. Army Corp of Engineers
Contract DACA39-87-K-0022
U.S. Navy - Office of Naval Research
Grant N00014-89-J-1107
Grant N00014-92-J-1616

Project Staff

Professor Jin A. Kong, Dr. Robert T. Shin, Robert G. Atkins, David V. Arnold, William W. Au, Pierre Coutu, Hong-Tat Ewe, Hsiu C. Han, Chih-Chien Hsu, Joel T. Johnson, Harold H. Lim, Michael C. Moldoveanu, Alex Mou, Murat E. Veysoglu

Polarimetric radar calibration algorithms using a combination of point targets and reciprocal distributed targets are developed. From a distributed target, a matrix equation is derived which can be converted into an equivalent point target response. The equivalent point target corresponds physically to a 90-degree polarization rotator which is non-

¹ U.S. Navy, Naval Research Laboratory, Washington, D.C..

² Department of Electronics, Kyungpook National University, Taegu, Korea.

³ Civil and Geotechnical Engineering, Department of the Army, Hanover, New Hampshire.

⁴ Digital Equipment Corporation, Andover, Massachusetts.

⁵ Digital Equipment Corporation, Tewksbury, Massachusetts.

⁶ Department of Radio Engineering, Harbin Institute of Technology, Harbin, Peoples Republic of China.

⁷ Tsukuba Research Laboratory, Hitachi Chemical Company, Tsukuba, Ibaraki, Japan.

reciprocal and rotation-invariant. Due to this equivalent-point-target interpretation, the cases of polarimetric calibration using two point targets and one distributed target then reduce to those using three point targets, which have been solved in previous research. Regarding the calibration using one point target and one reciprocal distributed target, two cases are analyzed with the point target being a sphere (triheral reflector) or a polarimetric active radar calibrator (PARC). For both cases, the general solutions of system distortion matrices are written as a product of a particular solution and a matrix with one free parameter, and then an additional assumption about the distributed target is made to determine the free parameter. For the triheral-reflector case, when the particular solution is applied for calibration, the measured polarimetric data can be calibrated to the level that only rotation errors remain. When azimuthal symmetry is assumed for the distributed target, an iterative scheme is devised to solve the rotation parameter. For the PARC case, the residual error is similar to the channel imbalance after the data are calibrated by the particular solution, and the free parameter can be determined by knowing one ratio of two covariance matrix elements of the distributed target. Numerical results were simulated to demonstrate the validity of the algorithms developed.

A branching model is proposed for the remote sensing of vegetation. The frequency and angular responses of a two-scale cylinder cluster are calculated to demonstrate the significance of vegetation architecture. The results indicate that it is necessary for theoretical models to take into account the architecture of vegetation which plays an important role in determining the observed coherent effects. A two-scale branching model is implemented for soybean with its internal structure and the resulting clustering effects considered. Furthermore, at the scale of soybean fields, the relative location of soybean plants is described by a pair of distribution functions. The polarimetric backscattering coefficients are obtained in terms of the scattering properties of soybean plants and the pair distribution function. Theoretical backscattering coefficients evaluated using the hole-correction pair distribution are in good agreement with extensive data collected from soybean fields. Compared with the independent-scatterer pair distribution, it is found that the hole-correction approximation, which prevents two soybean plants from overlapping each other, is more realistic and improves the agreement between the model calculation and experimental data near normal incidence. Extension to a multi-scale branching model can be achieved by recursion.

Fully polarimetric scattering of electromagnetic waves from snow and ice is studied with a multilayered random medium model and applied to interpret experimental data obtained under laboratory controlled conditions such as CRRELEX. The snow layer is modeled as an isotropic random medium. The sea ice is described as an anisotropic random medium due to the nonspherical shape of brine inclusions. The underlying sea water is considered as a homogeneous half-space. The random media in both layers are characterized by three-dimensional correlation functions with variances and correlation lengths corresponding to the fluctuation strengths and the physical geometries of the inhomogeneities, respectively. The strong fluctuation theory is used to calculate the effective permittivities of the random media. The distorted Born approximation is then employed to obtain the covariance matrix which represents the fully polarimetric scattering properties of the snow-ice media. It has been shown that the polarimetric covariance matrix contains more information than the conventional scattering coefficients on the remotely sensed media.

In a saline ice sheet under quiescent condition, the background ice grows in columnar form and saline water is trapped between ice platelets in the form of brine inclusions which are usually ellipsoidal. The ice tends to grow vertically downward rendering the *ellipsoidal inclusions* aligned preferably in the vertical direction and the crystallographic C axes parallel to the horizontal plane. In this case, the C axes are, however, random in the azimuthal direction. The strong fluctuation theory is extended to account for vertically aligned ellipsoidal brine inclusions with C axes randomly oriented in the horizontal direction. The brine inclusions are described by three-dimensional local correlation functions. The configuration average over the azimuthal orientation angles is carried out in the process of deriving the global correlation tensor. The distorted Born approximation is applied to obtain the covariance matrix for the multilayered snow-ice configuration. The theoretical results show non-zero cross-polarized returns under the first-order distorted Born approximation. We have also compared the results with experimental data obtained by the U.S. Army Cold Regions Research and Engineering Laboratory (CRREL).

A multivariate K-distribution has been developed to model the statistics of fully polarimetric radar data from earth terrain with polarizations HH, HV, VH, and VV. In this approach, correlated polarizations of radar signals, as characterized by a covariance matrix, are treated as the sum of N n -dimensional random vectors; N obeys the negative binomial distribution with a parameter α and mean \bar{N} . Subse-

quently, an n -dimensional K-distribution, with either zero or nonzero mean, is developed in the limit of infinite N or illuminated area. The probability density function (PDF) of the K-distributed vector normalized by its Euclidean norm is independent of the parameter α and is the same as that derived from a zero-mean Gaussian-distributed random vector. The above model is well supported by experimental data provided by MIT Lincoln Laboratory and the Jet Propulsion Laboratory in the form of polarimetric measurements. The results are illustrated by comparing the higher-order normalized intensity moments and cumulative density functions (CDF) of the experimental data with theoretical results of the K-distribution.

Among the various theoretical models applied to study the electromagnetic wave scatterings from geophysical terrain, such as snow and ice, the radiative transfer theory has drawn intensive attention in the microwave remote sensing community during the past years. In most of the scattering models, the volume scattering and the surface scattering effects have been investigated separately. Recently, there has been a growing interest in the construction of composite models which can take into account both types of scattering. We derived the first order iterative solution to the vector radiative transfer equations for a two-layer medium with a diffuse top boundary and an irregular bottom boundary of Gaussian roughness. The Kirchhoff approximation and the geometrical optics approach with shadowing correction are used in formulating the boundary conditions. To demonstrate the utilities of the theory, randomly oriented spheroidal discrete scatter model is used to calculate the backscattering coefficients from a soybean field in different growing stages and then compared to the experimental measurements. Good agreement has been achieved for both the co-polarized and the cross-polarized data. It is observed that the presence of the rough surface can significantly enhance the backscattering at small incident angles and increase the cross-polarized returns. The polarization signatures calculated based on the Mueller matrix show a straight distortion track and an observable pedestal. Numerical comparison to the backscattering coefficients calculated by using planar bottom boundary conditions with or without the incoherent addition of the rough surface effects are also made.

The concept of polarimetry in active remote sensing is extended to passive remote sensing. The potential use of the third and fourth Stokes parameters U and V , which play an important role in polarimetric active remote sensing, is demonstrated for passive remote sensing. It is shown that, by the use of the

reciprocity principle, the polarimetric parameters of passive remote sensing can be obtained through the solution of the associated direct scattering problem. In particular, the full polarimetric information, including the corresponding brightness temperatures of U and V , can be obtained from the solution of the direct scattering problem for four different polarizations of the incident wave. These ideas are applied to study polarimetric passive remote sensing of periodic surfaces. The solution of the direct scattering problem is obtained by an integral equation formulation. Incidence on a penetrable, lossy medium is considered. Since the kernels of the integral equations are the periodic Green's functions and their normal derivatives on the surface, rapid evaluation of the slowly convergent series associated with these functions is critical for the method to be feasible. The study has shown that the brightness temperature of the Stokes parameter U can be significant in passive remote sensing. Values as high as 50 K are observed for certain configurations.

To demonstrate the use of polarimetry in passive remote sensing of azimuthally asymmetric features on a terrain surface, an experiment was designed and implemented. A triangular corrugation pattern was made on the sandy soil surface. Polarimetric brightness temperatures are measured with horizontal, vertical, and 45° polarization orientations for various observation angles. From the measured temperatures, absolute values as high as 30-40 K of the third Stokes brightness temperatures are observed. A theoretical analysis of the data indicates that the high values of U are caused by the azimuthal asymmetry on the remotely sensed soil surface. It is also observed from the experiment that the brightness temperatures for all three Stokes parameters vary as the observation direction varies from being parallel to the surface row structure to being perpendicular to the row structure. The significant implication of this experiment is that the surface asymmetry can be detected with a measurement of U at a single azimuthal angle.

1.2 Electromagnetic Waves in Multilayer Media

Sponsors

Digital Equipment Corporation
Joint Services Electronics Program
Contract DAAL03-92-C-0001
U.S. Navy - Office of Naval Research
Grant N00014-90-J-1002
Grant N00014-89-J-1019

Project Staff

Professor Jin Au Kong, Dr. Robert T. Shin, Dr. Y. Eric Yang, Dr. Soon Y. Poh, David V. Arnold, Robert G. Atkins, Pierre Coutu, Hong-Tat Ewe, Hsiu C. Han, Chih-Chien Hsu, Gregory T. Huang, Joel T. Johnson, Cheung-Wei Lam, Hongsing Lee, Kevin Li, Michael C. Moldoveanu, John H. Oates, M. Ali Tassoudji, Murat E. Veysoglu, Li-Fang Wang, Jiqing Xia

Recent studies on electromagnetic emissions have identified the significance of resonance in the radiation and re-radiation of printed wiring board (PWB) components such as transmission lines and heatsinks. This has drawn attention to other components within a computer system which are of larger dimensions and which are likely candidates to resonate within the frequency range of emissions tests. An arrangement in computer systems which falls into this category is the modules-on-backplane configuration. Discussions with DEC engineers have identified the voltage fluctuations across the relatively high impedance reference connections, between a reference plane within a module and that on the backplane, as a likely energy source for electromagnetic emissions. The array arrangement of multiple modules on a backplane raises the possibility of parallel plate resonances where the resonance frequencies, to leading order, are inversely proportional to the dimensions of the module planes. The large dimensions of the module planes relative to the signal etch runs, heatsink dimensions, etc., imply that any resonance effects may be manifested at lower frequencies.

There is common perception that in the printed wiring board (PWB) environment stripline configurations will generate lower emission levels than microstrip structures. In previous years, the radiation properties of both microstrip and stripline structures of finite size were quantitatively compared. The examination of conducting structures which may model shielding enclosures on the radiating properties of the two structures is of interest, as these configurations correspond to the case where modules are placed in close proximity to the shielding enclosure common in computer systems.

Metallic enclosures are commonly used to house computer systems. The electromagnetic field distribution and intensities which result from sources within the enclosure are of concern because of the possibility of strong fields existing due to the resonator structure formed by the metallic enclosure. The effects of adding resistive material of varying dimensions, resistivities, and positions to the enclosure is also examined. The study will attempt to

determine the optimum parameters for the resistive material which will minimize the electromagnetic field intensity within the enclosure. Perforations (holes, slots) in the metallic enclosure and the corresponding radiated power are also considered.

For each configuration, field strengths, radiated power levels, and resonance frequencies (which are crucial for the radiation mechanism) are being investigated. This study will benefit the design of integrated circuit interconnections to meet regulatory limits on electromagnetic emission levels. It reflects the progression from examining module interconnect and component radiation in relative isolation (performed in the last two contract years) to more realistic situations which incorporate interaction with other conducting structures in close proximity, as is the case at the system level.

The finite difference-time domain (FD-TD) technique is applied to the solution of Maxwell's equations. A computer program, which can be used to simulate and study numerous electromagnetic phenomena, is developed and implemented on an IBM 386-compatible personal computer. The FD-TD technique is a useful tool for students in electromagnetics. The technique is flexible and can be applied to many basic EM scattering and radiation problems. Because field solutions are found as a function of time, visualization of the propagation of the EM fields is possible. The FD-TD technique is implemented for a two-dimensional rectangular grid in conjunction with a second-order absorbing boundary condition. Both E- and H-field polarizations are analyzed. Finite objects consisting of dielectric, magnetic and conducting materials, and perfectly conducting infinite ground planes are modeled. Plane wave and line current sources are implemented. In addition to the capability of animating the propagation of the EM fields, radiation and scattering patterns can be generated.

A methodology developed to handle dispersive materials in the time domain is extended to model the dispersive characteristics of the impedance boundary condition used for a thin layer coating over perfect conductors. The impedance boundary condition is first approximated as a rational function of frequency. This rational function is then transformed to a time domain equation, resulting in a partial differential equation in space and time. Discretization of the time domain model to efficiently handle the thin layer coating is presented in the context of the finite-difference time-domain (FD-TD) technique. The methodology is verified by solving a one-dimensional problem using the FD-TD technique and comparing it with the analytical results.

1.3 Aircraft Landing Systems: ILS, MLS, GPS, and SVS

U.S. Department of Transportation
 Agreement DTRS-57-88-C-00078TTD13
 Agreement DTRS-57-88-C-00078TTD30
 Agreement DTRS-57-92-C-00054TTD1

Project Staff

Professor Jin Au Kong, Dr. Robert T. Shin, Dr. Y. Eric Yang, Dr. Yi Yuan, Hong-Tat Ewe, Qizheng Gu, Chih-Chien Hsu, Jerome Khohayting, Yong Liu, Barbara A. Roman, M. Ali Tassoudji, Katherine Tso, Li-Fang Wang, Elaine C. Yiu

Precision landing system plays an important role in continuing air travel services during adverse weather conditions. Instrument Landing System (ILS) has been in service for the past five decades, and microwave landing system (MLS) will be gradually replacing ILS within the next decade. These two systems require ground equipments to work properly; therefore, their usage is limited to where such setup is available. Two alternative technologies that do not require ground setups have been proposed as the future replacement for ILS and MLS: the synthetic vision (SV) sensors and the global positioning system (GPS).

In this project we have developed a computer simulation tool EMSALS which uses the databases of navigational and commercial radiowave transmitters to calculate the strengths of desired and undesired signals, and generates an EM interference assessment based on user-selected assumptions. The first part of the software EMSALS/I (for ILS) has been used to analyze the frequency congestion and electromagnetic interference problems in the continental United States given the assumptions of the current FAA standard interference protections. Emphasis was first placed on ten complex metropolitan areas with high densities of runways. Then the less densely populated regions were analyzed to determine ILS capacity across the entire continental United States (CONUS).

The second part of the software, EMSALS/M (for MLS), was used to evaluate channel availability and to generate a frequency assignment plan given the assumptions of the current ICAO MLS channel assignment rules and interference protection standards. The channel assignments had to be carried out for ILS-to-MLS conversion sites as well as new candidates, including heliports which cannot be sited with ILS. The total number of candidate sites is over 1800.

The instrument landing system (ILS) is the standard precision landing aid used by thousands of airline carriers and general aviation aircraft. In recent years, there have been growing concerns over potential hazards from FM-broadcast interference. The ILS localizer, which provides lateral guidance during the aircraft landing phase, has its frequency band (108-112 MHz) located right above the commercial FM-broadcasting stations (88-108 MHz). Because the effective radiated power of a localizer transmitter is typically around 15 W, as compared to 10-100 kW for an FM station, it is possible for FM signals to overload the airborne receiver front-end or to drive it out of specifications and cause intermodulation interference.

We developed a scheme to link the interference immunity with the risk allowance for instrument landing operations. The risk allowance is derived as a function of the aircraft position. By the very nature of landing, the allowable risk from interference decreases or becomes more stringent as the aircraft approach the decision height. We also establish the composite probability of interference from the statistical models of systems involved, including the localizer transmitter power, FM station power, propagation factors, antenna directivity, and variations in airborne receivers. By comparing the composite probability of interference with the risk allowance at each point within the service volume of ILS localizer, we can then determine whether there is harmful interference from the FM stations. A computer program has been developed for the model.

Electromagnetic interference is one of the factors that can adversely affect GPS receiver functioning during the critical phase of final approach and landing. Although no actual incidence has been reported, in theory the threat from a moderately low power interference source does exist. In this study, we conducted experimental investigation of SPS GPS receiver susceptibility to electromagnetic interference. An aviation-grade GPS receiver mounted on the roof of a six-story building was subject to on-channel and off-channel CW and narrow-band noise with varying power levels. The interfering signal was transmitted over the open space to reach GPS antenna. We used a combination of IBM PC and receiver front-panel display to continuously record GPS data and warning flag for the cases with and without jammers. Taking the receiver front-end as the reference point, we obtained the interference power level that causes the GPS receiver to lose lock and become unable to provide accurate position data. This level is then converted to antenna receiving power, from which we estimate the effective radiation power level required for interferers at a distance.

1.4 Publications

- Borgeaud, M., J.A. Kong, R.T. Shin, and S.V. Nghiem. "Theoretical Models for Polarimetric Microwave Remote Sensing of Earth Terrain." In *Direct and Inverse Methods in Radar Polarimetry*. The Netherlands: Kluwer Academic Publishers, 1992, Part 2, pp. 1139-1190.
- Chu, N.C., J.A. Kong, H.A. Yueh, and S.V. Nghiem. "Variance of Phase Fluctuations of Waves Propagation Through a Random Medium." *J. Electromag. Wave Appl.* 6(2): 169-197 (1992).
- Ding, K.H., C.E. Mandt, L. Tsang, and J.A. Kong. "Monte Carlo Simulations of Pair Distribution Functions of Dense Discrete Random Media with Multiple Sizes of Particles." *J. Electromag. Wave Appl.* 6(8): 1015-1030 (1992).
- Lee, C.F., R.T. Shin, and J.A. Kong. "Time Domain Modeling of Impedance Boundary Condition." *IEEE Trans. Microwave Theory Tech.* 40(9): 1847-1850 (1992).
- Li, K., M.A. Tassoudji, R.T. Shin, and J.A. Kong. "Simulation of Electromagnetic Radiation and Scattering using a Finite Difference-Time Domain Technique." *Comput. Appl. Eng. Ed.* 1(1): 45-63 (1992).
- Tsang, L., C.H. Chan, J.A. Kong, and J. Joseph. "Polarimetric Signatures of a Canopy of Dielectric Cylinders Based on First and Second Order Vector Radiative Transfer Theory." *J. Electromag. Wave Appl.* 6(1): 19-51, (1992).
- Tsang, L., and J.A. Kong. "Scattering of Electromagnetic Waves from a Dense Medium Consisting of Correlated Mie Scatterers with Size Distributions and Applications to Dry Snow." *J. Electromag. Wave Appl.* 6(3): 265-286 (1992).
- Xia, J., A.K. Jordan, and J.A. Kong. "Inverse Scattering View of Modal Structures in Inhomogeneous Optical Waveguides." *J. Opt. Soc. Am. A* 9(5): 740-748 (1992).
- Yueh, S.H., J.A. Kong, J.K. Jao, R.T. Shin, and T. Letoan. "Branching Model for Vegetation." *IEEE Trans. Geosci. Remote Sens.* 30(2): 390-402 (1992).
- Yueh, S.H., J.A. Kong, and R.T. Shin. "External Calibration of Polarimetric Radars using Point and Distributed Targets." *J. Electromag. Wave Appl.* 6(7): 921-941 (1992).
- ## Meeting Papers
- Beaudoin, A., T. Le Toan, C.C. Hsu, H.C. Han, J.A. Kong, and R.T. Shin. "Simulation of Forest Backscatter as a Function of Forest and Ground Parameters." Paper presented at the International Geoscience and Remote Sensing Symposium, Houston, Texas, May 26-29, 1992.
- Han, H.C., J.A. Kong, R.T. Shin, S.V. Nghiem, and R. Kwok. "Application of Theoretical Models to Active and Passive Microwave Measurements of Saline Ice." Paper presented at the International Geoscience and Remote Sensing Symposium, Houston, Texas, May 26-29, 1992.
- Hsu, C.C., H.C. Han, R.T. Shin, J.A. Kong, A. Beaudoin, and T. Le Toan. "Radiative Transfer Theory for Polarimetric Remote Sensing of Pine Forest." Paper presented at the International Geoscience and Remote Sensing Symposium, Houston, Texas, May 26-29, 1992.
- Hsu, C.C., Y.E. Yang, R.T. Shin, J.A. Kong, C. Kohler, T. Nguyen, H. Nguyen, and J. Ho. "Applications of EMSARS Background Model to MMW Vegetation Scattering Simulation." Paper presented at the Ground Target Modeling and Validation (GTMV) Conference, Marquette, Michigan, August 17-19, 1992.
- Kong, J.A. "Progress in Electromagnetics and Future Developments." Paper presented at the International Electromagnetic Compatibility Symposium, Singapore, December 7-9, 1992.
- Kong, J.A. "Theoretical Modeling for Passive Microwave Remote Sensing of Earth Terrain." Paper presented at the URSI Specialists Meeting on Microwave Radiometry and Remote Sensing, Boulder, Colorado, January 24-26, 1992.
- Kong, J.A. "Characterization of Earth Terrain Material as Random Media Applied to Remote Sensing." Paper presented at the International Electromagnetic Compatibility Symposium, Singapore, December 7-9, 1992.
- Nghiem, S.V., R. Kwok, J.A. Kong, R.T. Shin, A.J. Gow, and S.A. Arcone. "Effective Permittivity of Saline Ice Under Thermal Variation." Paper presented at the International Geoscience and Remote Sensing Symposium, Houston, Texas, May 26-29, 1992.
- Xia, J., and J.A. Kong. "Electromagnetic Profile Reconstruction using the Riccati Equation Approach." Paper presented at the IEEE APS

International Symposium, Chicago, Illinois, July 18-25, 1992.

Xia, J., T.M. Habashy, R.T. Shin, and J.A. Kong. "The Renormalized STIE Approach Applied to Inversion of Soil Moisture Profiles." Paper presented at the National Radio Science Meeting, Boulder, Colorado, January 7-10, 1992.

Xia, J., and J.A. Kong. "Electromagnetic Inverse Scattering in Remote Sensing." Paper presented at the Optical Society of America Topical Meeting on Signal Recovery and Synthesis, New Orleans, Louisiana, April 14-15, 1992.

1.5 Superconducting Transmission Lines

1.5.1 Simulations of Vortices in Arrays of Josephson Junctions

Sponsors

DARPA/Consortium for Superconducting Electronics
Contract MDA972-90-C-0021
National Science Foundation
Fellowship MIP 88-58764

Project Staff

Joel R. Phillips, Herre S.J. van der Zant, Robert Bock, Professor Terry P. Orlando, Professor Jacob K. White

Vortices play a central role in determining the static and dynamic properties of two-dimensional (2D) superconductors. Artificially fabricated networks of superconducting islands weakly coupled by Josephson junctions are model systems for studying the behavior of vortices. These arrays have also been used to study the superconducting-insulator transition, Giant Shapiro steps, and the Kosterlitz-Thouless-Berezinskii (KTB) transition.

Studies of vortices in Josephson junction arrays generally neglect magnetic fields induced by currents flowing in the array. It is assumed that the penetration depth for flux λ is much larger than the size of the array. With the present SNAP technology, all niobium arrays have been made with λ of the order of the cell size; therefore, effect of induced fields must be considered for an accurate description of these systems.

We use numerical simulation to investigate how a variety of vortex static properties are affected by

finite penetration depth λ , and we calculate for the first time the self-consistent current and magnetic fields from a vortex in a 2D array. We find that in order to calculate the correct current and field distributions, the full 3D behavior of the magnetic fields must be accounted for by including nearly all mutual inductance terms. However, to calculate the energy barrier for cell to cell vortex motion, which was first shown by Lobb, Abraham, and Tinkham (LAT) to be $0.2 E_J$, where E_J is the Josephson coupling energy, including only self and nearest neighbor inductances is sufficient. The LAT calculation neglected induced magnetic fields. We show that induced fields may increase the energy barrier substantially above $0.2 E_J$. Our calculations also show that the thermodynamic lower critical field of the array is enhanced when the computation self-consistently accounts for induced magnetic fields. By using only a self-inductance term to model the induced fields, the lower critical field is overestimated.

Self-consistently determining the currents and fields in a Josephson junction array is a difficult numerical problem. This is because the fields induced by a junction current affect the current through every junction in the array. This dense interaction implies that for an array having N cells, on the order of N^2 words of computer memory are required just to store the mutual inductance matrix. If a direct approach is used to compute the self-consistent solution by factoring the inductance matrix, on the order of N^3 operations are required. For example, the inductance matrix of a 100×100 array requires more than 400 megabytes of memory to store and on the order of 10^{12} operations to factor.

To make the computation tractable, we derive a novel simulation algorithm which combines several numerical techniques with an appropriate problem formulation. When used to simulate an N -cell array, this approach reduces the storage required to order N and decrease the computation time to order $N \log N$. This approach makes it possible to compute self-consistent array currents and fields in a 100×100 array in a minute or so using a scientific workstation (IBM RS6000).

1.5.2 NonLinear Effects in Superconducting Transmission Lines

Sponsors

DARPA/Consortium for Superconducting Electronics
Contract MDA972-90-C-0021

Project Staff

Cheung-Wei Lam, Dr. Sami M. Ali, and Professor Terry P. Orlando in collaboration with Daniel E. Oates⁸

The Ginzburg-Landau theory has been applied to model the nonlinear behavior of superconducting transmission lines, including striplines and microstrip lines.

The Ginzburg-Landau differential equations are solved numerically inside the signal line where high current density exists. The resulting distribution of the magnetic penetration depth and conductivity is then used to calculate the nonlinear inductance and resistance of the superconducting transmission lines. Numerical results are compared with measurements on NbN and YBCO stripline resonators. Good agreement is obtained for the nonlinear shift of resonant frequency. However, the measured Q factor appears to be much more nonlinear than predicted by the numerical model. It is believed that some other nonlinear loss mechanism is dominating over that caused by pair-breaking.

This observation motivates us to investigate the nonlinear loss caused by vortex motions. A nonlinear diffusion equation for the magnetic flux is formulated for the flux flow dynamics. Appropriate models for the nonlinear diffusion coefficient will be adopted for the numerical calculation of flux flow in a superconducting slab.

1.5.3 Superconducting Transmission Lines

Sponsor

DARPA/Consortium for Superconducting Electronics
Contract MDA972-90-C-0021

Project Staff

Laurence H. Lee, Dr. Sami M. Ali, Professor Terry P. Orlando in collaboration with W. Gregory Lyons⁸

A full-wave spectral-domain volume-integral-equation method has been developed to analyze various configurations of superconducting transmission lines: microstrip lines, striplines, coplanar strips, and coplanar waveguides. In the formulation, a spectral-domain Green's function for isotropic, layered media is used to set up an inte-

gral equation for the electric field inside the superconducting strips. Galerkin's method with roof-top basis functions is employed to solve for the complex propagation constant and current distribution. The characteristic impedance of the structures is then obtained from transmission line theory. This method rigorously accounts for the anisotropy and the finite thickness of the superconducting films, yielding accurate characterization for the loss and kinetic effect of the superconductors. However, this technique is computationally inefficient.

To implement an efficient method, an equivalent surface impedance is used to transform the superconducting strip with finite thickness to an infinitely thin strip. This equivalent surface impedance accounts for the loss and kinetic inductance of the superconductors. An empirical formula for the current distribution in a thin superconducting film is determined for the derivation of the equivalent surface impedance. To include effects of anisotropic substrates, a 2D dyadic Green's function for anisotropic, layered media is used to formulate an integral equation for the surface current. Galerkin's method with entire-domain basis functions is used to solve for the complex propagation constant and the surface current. The characteristic impedance is then calculated using the power-current definition. This method has been used to analyze superconducting single and coupled microstrip lines on anisotropic substrates.

We have been successfully measuring the long wavelength infrared quantum well (LWIR) intersubband absorption in 2 to 5 μm wavelength region based on InAs/InGaAs/AlAs resonant tunneling diode structures for the IR detectors application. Over 40 percent intersubband absorption can be achieved from a doped single quantum well through our dedicated designed waveguiding system, where IR is focused upon the sample edge and makes 20 times total internal reflection while it propagates along the samples and dramatically increases the absorption strength. We also demonstrate both theoretically and experimentally that TE as well as TM modes can excite the intersubband absorption. We also pointed out the interface Fe interband absorption at 0.3 eV could seriously obscure the IR absorption spectra and have shown how they can be avoided. These results, applied in concert with recently developed selective etches that allow us to make electrical contact to the quantum well directly and open the way to realizing high performance LWIR detectors.

⁸ MIT Lincoln Laboratory.

1.5.4 Publications

Book Chapters

Delin, K.A., and T.P. Orlando. "Superconductivity." In *The Electrical Engineering Handbook*. Ed. R.C. Dorf. Boca Raton, Florida: CRC Press, 1993.

Published Journal Articles

Delin, K.A., T.P. Orlando, E.J. McNiff, Jr., S. Foner, R.B. van Dover, L.F. Schneemeyer, and J.V. Waszczak. "High-Field Magnetization Scaling Relations for Pure and Ni-Substituted Single-Crystal $\text{YBa}_2\text{Cu}_3\text{O}_7$," *Phys. Rev. B* 46: 11092 (1992).

Juang, J.Y., D.A. Rudman, and T.P. Orlando. "On the Fermi Liquid Effects in the Upper Critical Field of NbN Thin Films." *Appl. Phys. Lett.* A172: 91 (1992).

Kucera, J.T., T.P. Orlando, G. Virship, and J.N. Eckstein. "Magnetic-field and Temperature Dependence of the Thermally Activated Dissipation in Thin Films of $\text{Bi}_2\text{Sr}_2\text{CaCu}_2\text{O}_{8-x}$," *Phys. Rev. B* 45: 11004 (1992).

Lam, C.-W., D.M. Sheen, S.M. Ali, and D.E. Oates. "Modeling the Nonlinearity of Superconducting Strip Transmission Lines." *IEEE Trans. Appl. Superconduct.* AS-2(2): 58-66 (1992).

Lee, L.H., S.M. Ali, and W.G. Lyons. "Full-wave Characterization of High- T_c Superconducting Transmission Lines," *IEEE Trans. Appl. Supercond.* 2(2): 49-57 (1992).

Luo, J., T.P. Orlando, J.M. Graybeal, X.D. Wu, and R. Muenchausen. "Comparison of the Longitudinal and Hall Resistivities from Vortex Motion in YBCO." *Phys. Rev. Lett.* 68: 690 (1992).

Phillips, J.R., H.S.J. van der Zant, J. White, and T.P. Orlando. "Influence of Induced Magnetic Fields on Static Properties of Josephson-junction Arrays." *Phys. Rev. B* 47: 5219-5229 (1993).

Rubin, L.M., T.P. Orlando, J.B. VanderSande, G. Gormer, R. Savoy, R. Swope, and R. Beyers. "Phase Stability Limits and Solid-State Decomposition of $\text{Bi}_2\text{Sr}_2\text{CaCu}_2\text{O}_{8-x}$ and $\text{Bi}_2\text{Sr}_2\text{Ca}_2\text{Cu}_3\text{O}_{10-x}$ in Reduced Oxygen Pressures." *Appl. Phys. Lett.* 61(16): 1977 (1992).

van der Zant, H.S.J., F.C. Fritschy, T.P. Orlando, and J.E. Mooij. "Vortex Dynamics in Two-dimensional Underdamped, Classical Josephson-junction Arrays." *Phys. Rev. B* 47: 295 (1993).

Journal Articles Accepted for Publication

Lee, L.H., S.M. Ali, W.G. Lyons, D.E. Oates, and J.D. Goettee. "Analysis of Superconducting Transmission-line Structures for Passive Microwave Device Applications." *Applied Superconductivity Conference*, Chicago, Illinois, August 1992; *IEEE Trans. Appl. Supercond.* 3(1): 2782 (1993).

van der Zant, H.S.J., E.H. Visscher, D.R. Curd, T.P. Orlando, and K.A. Delin. "Vortex Dynamics in One-dimensional Parallel Arrays of Underdamped Josephson Junctions." *IEEE Trans. Appl. Superconduct.* 3(1): 2658 (1993).

Journal Articles Submitted for Publication

van der Zant, H.S.J., F.C. Fritschy, T.P. Orlando, and J.E. Mooij. "Massive Vortices in Underdamped Josephson-junction Arrays." Submitted to the *Proceedings of the Workshop on Tunneling Phenomena in High and Low- T_c Superconductors*, Capri, Italy, 1992.

Meeting Papers Presented

Lam, C.-W., D.M. Sheen, S.M. Ali, and D.E. Oates. "Nonlinear Model of Superconducting Strip Transmission Lines." *IEEE MTT-S International Microwave Symposium Digest*, June 1992, pp. 197-199.

Lam, C.-W., S.M. Ali, and D.E. Oates. "Modeling of the Nonlinear Resistance of Superconducting Striplines." *Applied Superconducting Conference*, Chicago, Illinois, August 1992.

Lee, L.H., G. Arjavalingham, S.M. Ali, and T.R. Dinger. "Hybrid-mode Analysis of Coplanar Strips and Coplanar Waveguides." *Topical meeting on Electrical Performance of Electronic Packaging*, Tucson, Arizona, April 1992.

Lee, L.H., S.M. Ali, W.G. Lyons, R.S. Withers, and T.P. Orlando. "Full-wave Analysis of Superconducting Microstrip Lines on Sapphire Substrates." *IEEE MTT-S International Microwave Symposium*, Atlanta, Georgia, June 1993. Forthcoming.

Lee, L.H., S.M. Ali, W.G. Lyons, D.E. Oates, and J.D. Goettee. "Analysis of Superconducting Transmission-line Structures for Passive Microwave Device Applications." *Applied Superconductivity Conference*, Chicago, Illinois, 1992; *IEEE Trans. Appl. Supercond.* 3(1): pages (1993). Forthcoming.

Theses

Delin, K.A. *Transport and Magnetic Properties of High T_c Superconductors*. Ph.D. diss., Dept. of Electr. Eng. and Comput. Sci., MIT, 1991.

Kucera, J.T. *Thermally Activated Dissipation in Superconducting Thin Films of Bi-Sr-Ca-Cu-Oxide*. Ph.D. diss., Dept. of Electr. Eng. and Comput. Sci., MIT, 1992.

Lam, C.-W. *Modeling of Superconducting Transmission Lines and Three-dimensional High Speed Interconnects*. Ph.D. diss., Dept. of Electr. Eng. and Comput. Sci., MIT, 1993.

Rubin, L.M. *Growth of Superconducting Bi-Sr-Ca-Cu-O Films by Reactive Sputtering: A Thermodynamic Approach*, Ph.D. diss., Dept. of Electr. Eng. and Comput. Sci., MIT, 1993.

Section 4 Radio Astronomy

Chapter 1 Radio Astronomy

Chapter 1. Radio Astronomy

Academic and Research Staff

Professor Bernard F. Burke, Professor David H. Staelin, Professor Jacqueline N. Hewitt, Dr. Philip W. Rosenkranz, John W. Barrett

Visiting Scientists and Research Affiliates

Dr. Alan Wright¹

Graduate Students

Ashraf S. Alkhairy, Ian M. Avruch, Deborah J. Becker, Carlos R. Cabrera, Grace H. Chen, Kevin G. Christian, Samuel R. Conner, Sheperd S. Doeleman, John D. Ellithorpe, Paul W. Fieguth, André B. Fletcher, Matthew K. Gray, Mark R. Griffith, Lori K. Herold, Charles A. Katz, Pauline McMahon, Mark D. Messier, Christopher B. Moore, Michael J. Schwartz, Jie Sun

Technical and Support Staff

Wendy E. Hunter, Clare F. Smith

1.1 Extragalactic Radio Source Studies

Sponsor

National Science Foundation
Grant AST 90-22501

Project Staff

Professor Bernard F. Burke, Jacqueline N. Hewitt, John W. Barrett, Ian M. Avruch, Deborah J. Becker, Samuel R. Conner, Sheperd S. Doeleman, André B. Fletcher, Mark R. Griffith, Lori K. Herold,

Three major areas of research were covered by the program under Professor Burke's direction. Two of these were in the field of radio astronomy: the search for gravitational lenses (two new examples have been discovered by our group) and a survey of radio sources in the Southern Hemisphere that increased the number of known radio sources there by nearly an order of magnitude. The third is the opening of a new field of research: the search for and study of planets of other stars known as "exoplanets."

1.1.1 Gravitational Lens Studies

The study of the gravitational lensing phenomenon, which occurs when a distant object such as a quasar has its image distorted by a foreground mass such as a galaxy, presents a new tool for investigating gravitational interaction and cosmology. In particular, the distribution of all matter in a galaxy can be studied, whether it is luminous or dark, baryonic or non-baryonic. Two new examples of gravitational lensing were discovered during the past two years of the program. In the course of this work, it has become clear that there are systematic classes of lensing which may be called "Einstein rings" and "Einstein quads." (The first example of an Einstein ring was discovered earlier by Professor Jacqueline Hewitt of the MIT Physics Department and RLE.)

The work uses the MIT-Green Bank (MG) Survey as a finding list, mapping a large number of these radio sources at high angular resolution with the Very Large Array (VLA) and then pursuing promising examples with further optical and radio studies. In our program, over 6000 radio sources have been mapped with the VLA. This collection is the largest sample of sub-arcsecond radio source maps in the world, and it can be used for numerous astronomical investigations.

¹ Australian National Telescope Facility, Parkes, Australia.

Publications

Burke, B.F. "Introduction to Orbiting VLBI." *Adv. Space Res.* 11(2): 349-353 (1991).

Burke, B.F., D.H. Roberts, J. Lehar, and J.N. Hewitt. "The Hubble Constant from VLA Measurement of the Time Delay in the Double Quasar 0957+561." *Nature*. July 1991.

Burke, B.F., M.B. Heflin, M.V. Gorenstein, and C.R. Lawrence. "First and Second Epoch VLBI Observations of the Gravitational Lens System 2016+112." *Astrophys. J.* 378: 519-536 (1991).

Burke, B.F. "Summary of the Issues." In *Frontiers of VLBI: Proceedings of the International VSOP Symposium and the mm-Wave VLBI Workshop*, Eds. H. Hirabayashi, M. Inoue, and H. Kobayashi. Chapter 5: Management Plan. Tokyo: University Academy Press, 1991.

Burke, B.F. "A View of the Universe Through Imperfect Lenses: A Tribute to David Heesch." Talk presented at the Heesch Retirement party, December 16, 1991.

Burke, B.F., J. Lehar, and S. Conner. "Einstein Rings and Related Phenomena." Paper presented at the International Conference on Gravitational Lenses, Hamburg, Germany, September 1991.

Burke, B.F., J. Lehar, J.N. Hewitt, and D.H. Roberts. "The Radio Time Delay in the Double Quasar 0957+561." *Astrophys. J.* 384:453-466 (1992).

Burke, B.F., S.R. Conner, and J. Lehar. "Reconciling the Image Brightness Ratios in the Gravitational Lens System 0957+561." *Astrophys. J. Lett.* 387 LC: 61-64 (1992).

Griffith, M., G. Langston, M. Heflin, and S. Conner. "The Fourth MIT-Green Bank 5 GHz Survey." *Astrophys. J. Suppl.* 75: 801-833 (1991).

Invited Talks

Burke, B.F. "Gravitational Lenses." Arecibo Radio Observatory, Puerto Rico, March 1992.

Burke, B.F. "Gravitational Lenses in the Ultraviolet." University College, London, June 1992.

Burke, B.F. "Einstein Rings and Einstein Quads." IAU Colloquium, Manchester, England, July 1992.

1.1.2 The Parkes-MIT-NRAO Southern Hemisphere Survey

The Parkes-MIT-NRAO survey of radio sources was concluded. The work was carried out with the Parkes 210-foot radio telescope using the National Radio Astronomy Observatory (NRAO) 14-channel 6 cm receiver by Dr. Alan Wright of Australia and Mr. Mark Griffith, an MIT graduate student. We have published a first general overview paper, and a detailed technique paper will be published in May 1993.

The detailed catalogue is ready for submission and contains a list of approximately 60,000 radio sources in the southern sky. This is an increase by nearly an order of magnitude in the number of known Southern Hemisphere radio sources, and follow-up work is continuing with our Australian colleagues.

1.2 The Study of Exoplanets

Sponsor

National Aeronautics and Space Administration
Grant NAGW 1386

Project Staff

Professor Bernard F. Burke, Ian M. Avruch, Deborah J. Becker, Samuel R. Conner, André B. Fletcher, Mark R. Griffith, Lori K. Herold

The search for and study of exoplanets, including the study of their origin and evolution, is a new research area that has become a NASA program known as the Toward Other Planetary Systems (TOPS) program. In 1988, Professor Burke was appointed Chair of the NASA science working group that formulated this program. In 1992 NASA published the report *TOPS: Toward Other Planetary Systems*. During the past decade, Professor Burke published several papers that treated the possibility of searching for exoplanets.

Publications

Burke, B.F. "Concluding Remarks: Prospects for the Study of Planetary Radio Emission." Third International Workshop on Radio Emissions from Planetary Magnetospheres, Graz, Austria, September 1991.

Burke, B.F. "Searching for Exoplanets." In *ESA Publications for the Symposium on Targets for*

Space-Based Interferometry, Beaulieu, France, October 1992.

Meetings and Talks

Burke, B.F. "Searching for Exoplanets." University of Massachusetts, Amherst, Massachusetts, April 1992, and University of Manchester, Manchester, England, November 1992.

Burke, B.F. "The Search for Other Planetary Systems." Talk presented at the Royal Astronomical Society, London, December 1992.

Burke, B.F. "The TOPS Program." California Institute of Technology Summer School, Pasadena, California, August 1992.

1.3 Studies of Gravitational Lenses

Sponsors

National Science Foundation
Presidential Young Investigator Award
David and Lucile Packard Fellowship
for Science and Engineering

Project Staff

Professor Jacqueline N. Hewitt, Grace H. Chen, John D. Ellithorpe, Matthew K. Gray, Charles A. Katz, Pauline McMahon, Mark D. Messier, Christopher B. Moore, Jie Sun

Gravitational lenses provide radio astronomers with the opportunity to reexamine many long-standing problems in astrophysics. Two of these problems, addressed by the work described here, are the nature and distribution of dark matter in galaxies and the calibration of the age and scale of the universe (i.e., determination of the Hubble constant). Both applications require that the distribution of gravitating matter be inferred from the observed imaging properties of the lens. This, in turn, requires detailed measurements of the brightness distribution of the image. Extensive radio maps of

two gravitationally lensed extragalactic radio sources, MG1131+0456 and MG0414+0534, are being compiled from data taken with a Very Large Array radio telescope. Figure 1 shows high-frequency images that highlight the multiple images of the active galactic nuclei in the two systems. The configuration of these images provides constraints on models of the mass distribution in the lens; other information is derived from mapping at lower frequencies where other structure is evident.² There are differences in the propagation time, of order days to months, for the different ray paths associated with the images of the active galactic nucleus. Monitoring programs aimed at measuring these time delays are being carried out with the Very Large Array telescope. Preliminary plots of 15 GHz flux density as a function of time for the four images of MG0414+0534 are shown in figure 2. Simulations of time delay estimation techniques indicate that, with the variability displayed by the data of figure 2, the time delays in this system should be measurable.

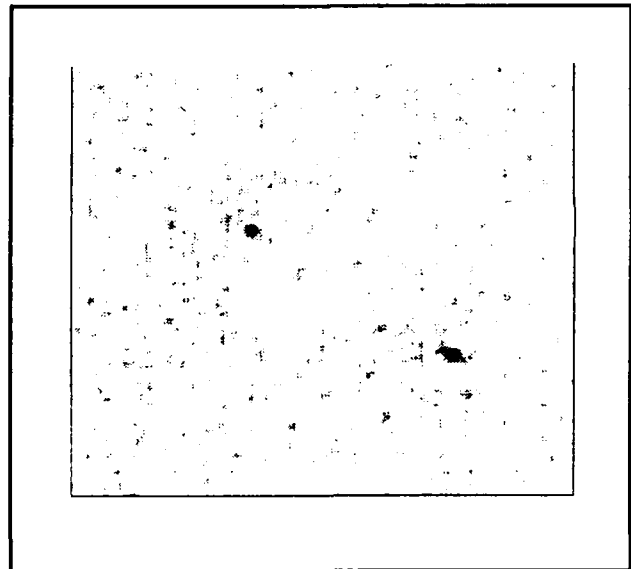


Figure 1a. 22 GHz radio image of the gravitational lens MG1131+0456. The two bright sources are two images of the same background galactic nucleus.

² C.A. Katz and J.N. Hewitt, *Astrophys. J. Lett.*, forthcoming; G.H. Chen and J.N. Hewitt, "Multifrequency Radio Images of MG1131+0456," in *Sub-Arcsecond Radio Astronomy*, ed. R.J. David and R.S. Booth (Manchester, England: CVP), forthcoming.

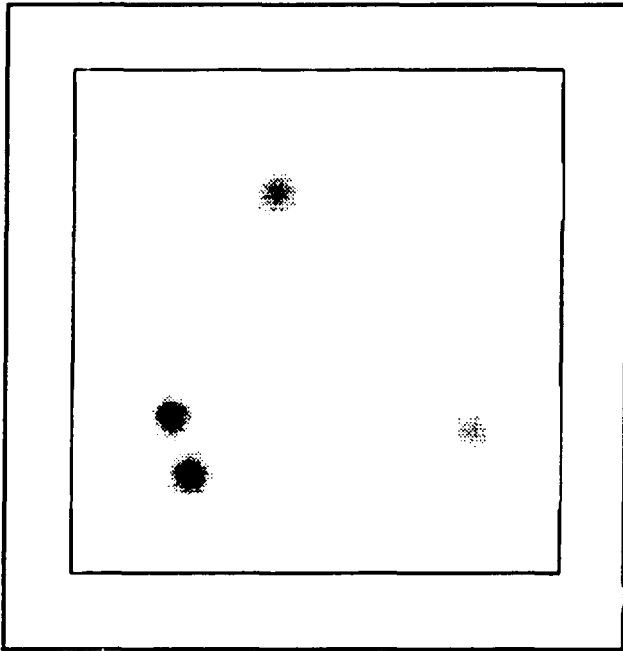


Figure 1b. 15 GHz radio image of the gravitational lens MG0414+0534. In this case, there are four images of the background active galactic nucleus.

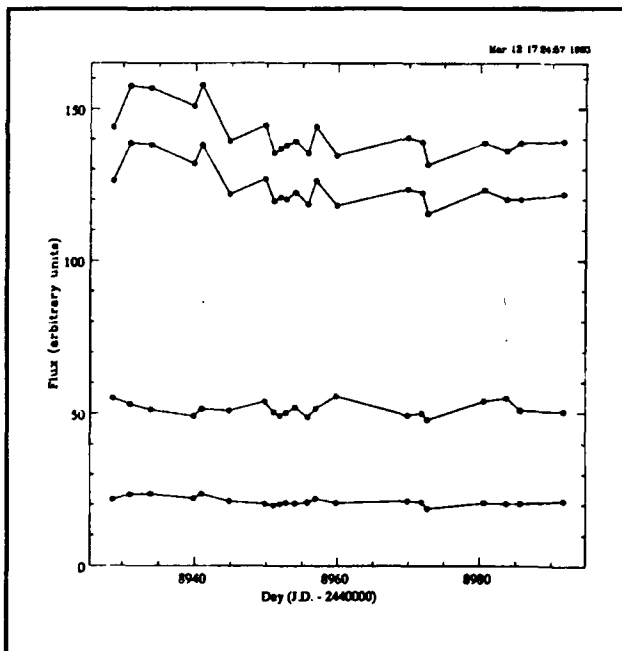


Figure 2. Plots of radio flux density at 15 GHz as a function of time for the four components of MG0414+0534. All four components display variability at a level not uncommon in active galactic nuclei.

1.4 Radio Interferometry of Nearby dMe Stars

Sponsors

National Aeronautics and Space Administration
Grant NAGW-2310
David and Lucile Packard Fellowship
for Science and Engineering

Project Staff

Professor Jacqueline N. Hewitt, John D. Ellithorpe,
Christopher B. Moore

dMe stars are dwarf M stars that show evidence of surface activity. For some time these dwarf stars have been known to flare strongly at optical and radio wavelengths. More recently, it has been demonstrated that many dMe stars exhibit low-level quiescent emission that is detectable in Very Long Baseline Interferometry (VLBI). The detection of dMe stars on VLBI baselines makes possible measurement of the position of these stars with high precision. In addition, it shows that astrometric detection of planetary companions may be feasible. The astrometric monitoring program has continued with third epoch measurements of dMe stars.

1.5 Algorithms for Advanced Microwave Sounding Unit Operational Use

Sponsors

MIT Lincoln Laboratory
SM Systems and Research Corporation

Project Staff

Professor David H. Staelin, Dr. Philip W. Rosenkranz

This project provides scientific support to the National Oceanic and Atmospheric Administration (NOAA) for the Advanced Microwave Sounding Unit (AMSU). The AMSU is scheduled for launch on NOAA polar-orbiting weather satellites in the mid-1990s and also for follow-on instruments. Our effort emphasizes development of line-by-line atmospheric transmittance algorithms,³ estimation of

³ P.W. Rosenkranz, "Emission and Absorption of Microwaves by Atmospheric Oxygen and Water Vapor," paper presented at the Specialist Meeting on Microwave Radiometry and Remote Sensing Applications, Boulder, Colorado, January 14-16, 1992; H.J. Liebe, P.W. Rosenkranz, and G.A. Hufford, "Atmospheric 60-GHz Oxygen Spectrum: New Laboratory Measurements and Line Parameters," *J. Quant. Spectrosc. Radiat. Transfer* 48(5/6): 629-643 (1992).

surface emissivity and precipitation, issues related to instrument design and specification, and general retrieval methods.

Measurements from the MIT aircraft-based Microwave Temperature Sounder and from present satellite radiometers such as the Special Sensor Microwave Imager⁴ and the Microwave Sounding Unit are used to develop and test prototype parameter-retrieval algorithms.

1.6 Earth Observing System: Advanced Microwave Sounding Unit

Sponsor

National Aeronautics and Space Administration/
Goddard Space Flight Center
Contract NAS 5-30791

Project Staff

Professor David H. Staelin, Dr. Philip W. Rosenkranz, John W. Barrett, Michael J. Schwartz, Carlos R. Cabrera

The Advanced Microwave Sounding Unit (AMSU) will provide microwave-band measurements to the Atmospheric Infrared Sounder (AIRS), which will be a facility instrument on NASA's planned Earth Observing System (EOS). This effort is directed toward developing algorithms for the retrieval of temperature and humidity profiles, precipitation, sea ice, land snow cover, and other parameters.⁵ According to our present plans, the temperature and humidity profiles obtained from AMSU will provide initial conditions for the AIRS infrared cloud-correction and profile retrieval algorithms. Current work is focused on simulation efforts and on a rapid (as distinguished from line-by-line) microwave transmittance algorithm.

1.7 High-Resolution Passive Microwave Imaging of Atmospheric Structure

Sponsor

National Aeronautics and Space Administration/
Goddard Space Flight Center
Grant NAG 5-10

Project Staff

Professor David H. Staelin, John W. Barrett, Dr. Philip W. Rosenkranz, Michael J. Schwartz, Paul W. Fieguth

The MIT Microwave Temperature Sounder (MTS) is a dual-band radiometer, incorporating an imaging spectrometer at 118 GHz and a tunable fixed-beam radiometer at 52-54 GHz. This instrument is flown on the NASA ER-2 high-altitude aircraft. In February and March 1992, we participated in the STORM Fronts Experiment Systems Test (STORM-FEST), which was a national field experiment to provide research background and experience with new weather observing systems. Several winter storms in the Kansas-Oklahoma region were overflown. These measurements will be used to study the response of microwave radiometer measurements to precipitation and weather fronts.

In May, July, and August 1992, the MTS was flown along with the Microwave Imaging Radiometer, a NASA instrument, under the orbital track of a satellite carrying the new DMSP SSMT-2 instrument, a microwave humidity profiler. These flights will be used to validate satellite measurements.

On other flights, upward-observing profiles of atmospheric brightness temperature were obtained. These will be used to test recently developed atmospheric transmittance algorithms.

1.8 Rapid Precision Net-Form Manufacturing

Sponsor

MIT Leaders for Manufacturing Program

⁴ P.W. Rosenkranz, "SSM/I Measurements as Predictors of the Response of AMSU-A to Surface and Atmospheric Phenomena," paper presented at the First NMC/NESDIS/DOD Conference on DMSP Retrieval Products, Washington, DC, April 14-15, 1992; P.W. Rosenkranz, "Rough-Sea Microwave Emissivities Measured with the SSM/I," *IEEE Trans. Geosci. Remote Sens.* 30(5): 1081-1085 (1992).

⁵ D.H. Staelin, "Passive Microwave Observations of Atmospheric Parameters from Space," paper presented at the Specialist Meeting on Microwave Radiometry and Remote Sensing Applications, Boulder, Colorado, January 14-16, 1992.

Project Staff

Professor David H. Staelin, Paul W. Fieguth

Algorithms were improved for estimating the shape of manufactured objects with a precision of microns at very high data rates.⁶ The technique is to estimate in optimum fashion the distance at which minimum defocusing blur is encountered at each point on the object; multiple images are viewed (typically four or five) at different ranges while the object is illuminated with a fine grid of illuminated points of light (approximately 600 were observed). The experiment involves use of a previously developed four-axis stage with a simultaneously scannable volume of ~20 cubic inches. A 512² pixel CCD camera is employed with an adjustable field of view down to 0.5 mm². The system is fully computer controlled and can receive up to 30 frames per second.

Rms accuracies of 50 nm were obtained for ideal mirror surfaces for the 0.5-mm field and a stand-off distance of a few mm; this accuracy degraded to 100 nm when faster and simpler algorithms were employed. These accuracies were higher than those expected, partly because the nature of the blur function is strikingly asymmetric, as can be seen from thick lens ray tracing (but not thin lens or diffraction optics). For rougher materials—chalk, black plastic, and copper—accuracies of 1000-2000 nm were obtained. Chalk and plastic are difficult to test because light diffuses inside them on this spatial scale; copper exhibits strong glint from its microcrystalline surface. The system scaling laws derived reveal that these results might be useful in applications to much larger systems.

1.9 Conformal Experiment Design

Sponsor

MIT Leaders for Manufacturing Program

Project Staff

Professor David H. Staelin, Ashraf S. Alkhairy, Paul W. Fieguth

Optimization of operating parameters for products and manufacturing processes are often determined by experiment in cases where theoretical analysis is inadequate. The performance of these products and processes is often limited because of the high cost of such experiments; experimentation simply ceases when the allocated budget or time ends. Using most conventional techniques for experiment design, such as those of Taguchi and Box, on the order of N^2 experiments are required, where N is the approximate number of important parameters. Using newly developed techniques, Dr. Ashraf Alkhairy⁷ has shown that in many cases of practical interest, on the order of $2N$ experiments are sufficient to yield excellent results.

The coined phrase "conformal experiment design" suggests the way in which these new techniques probe the complexity of the product or process space and guide definition of efficient sets of experiments. This new approach conforms to the process or product of interest by taking advantage of any intrinsic simplicity and a priori knowledge and by matching more closely the chosen quality cost functions and statistical models to the problem at hand. This involves performing a series of experiments which ends when those experiments suggest that enough or all unaccounted second-order interactions are negligible; the implication is that all higher-order interactions are then probably negligible too. Other methods often overlook some of these interactions even with N^2 experiments, and thus can yield inferior results.

The impact of these new, more efficient methods for experiment design can be substantial when studying processes and products that are characterized by so many significant parameters that N^2 experiments are not practical. Therefore, experimental optimization can be employed now for larger and more complex systems or subsystems with larger values of N . This could lead to significantly superior performance in cases where sequential optimizations of subsets of N parameters must otherwise be performed.

Initial comparisons of these methods with more traditional Taguchi and response-surface methods

⁶ P.W. Fieguth, *Range Estimation Accuracy Using Depth-from-focus Methods—Theory and Experiment*, S.M. thesis, Dept. of Electr. Eng. and Comput. Sci., MIT, 1992.

⁷ A.S. Alkhairy, *Optimal Product and Manufacturing Process Selection—Issues of Formulation and Methods for Parameter Design*, Ph.D. diss., Dept. of Electr. Eng. and Comput. Sci., MIT, 1991. Also RLE TR No. 572.

(RSM) by J.E. Glancy⁸ and F.J. MacDonald, Jr.,⁹ revealed that the conformal design technique yielded both better performance and process characterization and required fewer experiments for these cases (MacDonald did not test RSM). Glancy obtained a 68% increase in mean process performance for a heat sealing manufacturing operation and tripled process capacity with only eight conformal experiments. After 16 experiments, MacDonald reduced marginal manufacturing costs for a fiber drawing process by 30% and more than doubled the capacity of the existing drawing equipment while improving quality sufficiently to establish a new premium product line.

Our recent work has been directed toward generation of a simple user-friendly program to assist engineers with both experiment design and analysis of the results. This program accepts a list of control parameters and another of the most likely nonlinear interactions between them. The program then recommends sets of 8, 16, 32, 64 or more experiments, as selected by the user. These experiment sets are orthogonal arrays designed to evaluate preferentially those interactions of greatest concern. The analysis portion of the initial version will accept the experiment results, expressed as a user-chosen quality metric that incorporates errors in both mean and variance. It outputs an equation relating the input parameters to the quality and a list of parameter values that should yield maximum quality; this recommendation can readily be checked with only one or a few more experiments using these values. Once its development is complete, the program will be tested in industry and then improved further.

1.10 Recognition of Natural Nearly Repetitive Signals

Sponsor

MIT Leaders for Manufacturing Program

Project Staff

Professor David H. Staelin, Kevin G. Christian

Dolphins (and some machinery) emit nearly repetitive whistles resembling bird song. This project is exploring methods for compressing such signals so that the repetitious elements might be rapidly identified. The challenge is to maximize performance with minimal (perhaps zero) training with the system.

This year a broad class of robust measures of whistle parameters was applied to a database of approximately 1160 dolphin whistles collected for 22 animals. We used contact hydrophones to reduce the effects of environmental noise and propagation variations. Our current research involves developing methods for compact representation of the whistles and their efficient recall from a computer database. Preliminary search algorithms for a 16-dimension space require searching roughly five percent of the total data base, and sometimes more, to find the best Euclidian match. The reductions in search time obtained by less perfect searches are being explored. These same algorithms should also be useful for diagnosing acoustic and other signals produced by machinery, manufacturing processes, and other environments.

Studies of these dolphin whistles using these same whistle metrics have revealed a dolphin has much better control over frequency when reproducing its own signature whistles than when copying that of another dolphin.

⁸ J.E. Glancy Jr., *Manufacturing Cost Modeling and Robust Process Design*, S.M. thesis, Dept. of Mech. Eng. and Dept. of Manage., MIT, 1992.

⁹ F.J. MacDonald, Jr., *An Integrative Approach to Process Parameter Selection in Fused-Silica Capillary Manufacturing*, S.M. thesis, Dept. of Electr. Eng. and Comput. Sci. and Dept. of Manage., MIT, 1992.

Part III Systems and Signals

Section 1 Computer-Aided Design

Section 2 Digital Signal Processing

Section 1 Computer-Aided Design

Chapter 1 Custom Integrated Circuits

Chapter 2 Computer-Integrated Design and Manufacture
of Integrated Circuits

Chapter 1. Custom Integrated Circuits

Academic and Research Staff

Professor Jonathan Allen, Professor John L. Wyatt, Jr., Professor Jacob K. White, Professor Srinivas Devadas, Professor Dimitri A. Antoniadis, Professor William J. Dally, Professor Berthold K.P. Horn, Professor Hae-Seung Lee, Professor Terry P. Orlando, Professor Martin A. Schmidt, Professor Stephen D. Senturia, Professor Charles G. Sodini, Dr. Sami M. Ali, Dr. Robert C. Armstrong, Dr. John G. Harris

Visiting Scientists and Research Affiliates

Dr. Ichiro Masaki,¹ Jose C. Monteiro, Dr. Filip J. Van Aelten, Dr. Herre S.J. van der Zant

Graduate Students

Mazhar M. Alidina, Kelly S. Bai, Donald G. Baltus, Vishal L. Bhagwati, Xuejun Cai, Steven J. Decker, Lisa G. Dron, Ibrahim M. Elfadel, Kamyar Eshghi, J. Mikko Hakkarainen, Frederick P. Hermann, Mattan Kamon, Craig L. Keast, Songmin Kim, Steven B. Leeb, Stan Y. Liao, Andrew Lumsdaine, David R. Martin, Ignacio S. McQuirk, Keith S. Nabors, Gene T. Osgood, Joel R. Phillips, Lisa A. Pickelsimer, Khalid Rahmat, Mark W. Reichelt, Mark N. Seidel, Gideon P. Stein, Chin Hwee Tan, Amelia H. Shen, Luis M. Silveira, Ricardo Telichevsky, Christopher B. Umminger, Paul C. Yu

Technical and Support Staff

Susan E. Chafe, Dorothy A. Fleischer

1.1 Custom Integrated Circuits

Sponsors

Analog Devices, Inc.
IBM Corporation

Project Staff

Professor Jonathan Allen, Robert C. Armstrong, Donald G. Baltus, Lisa A. Pickelsimer, Mark W. Reichelt, Chin Hwee Tan, Filip J. Van Aelten

The overall goal of VLSI CAD research is to provide the means to produce custom integrated circuits quickly, correctly, and economically. Traditionally, correctness has been verified at several representational levels of abstraction, such as layout (via design rule checking), and circuit and logic representations (both via simulation). These techniques for checking correctness are usually local to the particular representational level involved and, while these techniques are important components of the overall design testing procedure, they do not attempt to provide for the alignment and consistency checks between the different abstract representational levels and an input behavioral

specification. In addition, they do not characterize the set of possible designs at each representational level corresponding to the initial functional specification in a way that ranges over the wide variety of possible performance levels. For this reason, there is an increasing need to provide CAD tools that serve as a framework for design exploration, thus providing the desired performance together with consistently aligned representations at all levels.

This research group studies a variety of topics with an emphasis on performance-directed synthesis of custom VLSI designs. An overview of the viewpoint that motivates these projects has recently been provided in a major survey paper² in which the need for coordinating the design optimization process over the several levels of representation is emphasized. Since design exploration is so central to the production of high-performance designs, emphasis is placed on how performance can be characterized at the several levels of representation and how overall optimal performance can be achieved in an integrated way.

In addition to the basic issues of circuit optimization, architectures for digital signal processing have been studied because of the highly parallel nature

¹ Computer Science Department, General Motors Research Laboratory, Warren, Michigan.

² J. Allen, "Performance-Directed Synthesis of VLSI Systems," *Proc. IEEE* 78(2): 336-355 (1990).

of the algorithms involved and the need for a very high level of real-time performance in these systems. Emphasis on developing formally specified systems has increased so that the design space can be comprehensively searched, and verification of the resultant design can be confirmed in terms of the initial behavioral specification. Current projects focus on design methodologies for very high-speed clocked circuits, the trade-offs between power dissipation and circuit delay with transistor sizing as a parameter, design of highly optimized array architectures for digital signal processing, and provision of a VLSI design database that provides for incremental consistency maintenance.

There has been a continuing evolution of circuit styles to provide high performance in a minimal space. For example, in CMOS technology, static designs are utilized, but precharge-evaluate methodologies have also been employed to provide speed, minimize the number of transistors, and increase utilization of n-channel devices (rather than slower p-channel devices). In recent years, examples of a new circuit style called *True Single-Phase Clocking* (TSPC) have been published.³ This style provides for clock speeds of several hundred megahertz in modest CMOS technologies. While these results have been confirmed, an analysis that explains the speed has not been provided, and no overall design methodology for these circuits has been demonstrated. In her master's thesis research project, Pickelsimer⁴ has analyzed the performance of TSPC circuits as well as other precharge-evaluate forms, in the context of a ripple-carry binary adder. A library of basic TSPC circuit elements has been provided, as well as a comprehensive design methodology for the optimal structuring of TSPC and TSPC-related circuits for minimal delay. In this way, it is possible to systematically derive an optimal circuit form from an input logical specification through the appropriate combination of matched circuit forms. All of these circuits require only a single-phase clock, without the need for clock waveform inversion, and hence avoid the problems of clock skew and waveform overlap.

It has frequently been observed that sizing of transistors (i.e., variation of MOSFET channel widths) can significantly improve the speed of many circuit forms. In particular, optimal procedures have been provided to examine the trade-off of circuit delay with aggregate transistor channel width. Even more recently, techniques have been devised to probabilistically characterize switching activity on circuit nodes in terms of the logic function being performed and hence deriving power estimates for the circuit, which can be modified through logical transformations.⁵ Tan, in her master's thesis work, is studying the trade-off between circuit delay and power dissipation (as characterized by probabilistic power estimates) with transistor channel width size as a parameter. The results of this study will be useful in maximizing the performance of low-power circuitry or minimizing the power of circuits designed to meet a given delay specification.

In a doctoral dissertation project by Baltus, comprehensive optimization of array logic designs is being achieved over all design representations from the input function specification to the final layout. The goal is to generate a custom layout specification from an input functional description using a language called FLASH, which is well suited to functionally characterizing signal processing algorithms, and can be viewed as an extension of the SILAGE language.⁶ FLASH designs are converted to data dependence graphs, where some elements of these graphs are reused and indexed to provide a compact representation that does not grow with the size of the array. Since algorithms are mapped onto a class of architectures with well-defined structural and interconnection characteristics, important implementation-level costs can be accurately modeled at the architectural level. More specifically, the structured nature of the target architecture allows the temporal and spatial relationships between computations to be seen at the architectural level.

The availability of an abstract model which accurately predicts implementation-level characteristics allows the process of performance-directed synthesis to be formalized. Powerful techniques from

³ J. Yuan and E. Svensson, "High-Speed Circuit Technique," *IEEE J. Solid-State Circ.* 24(1): 62-70 (1989).

⁴ L.A. Pickelsimer, *A Structured Design Methodology for Speed-Optimized True Single-Phase-Clock Dynamic CMOS*, S.M. thesis, Dept. of Electr. Eng. and Comput. Sci., MIT, 1992.

⁵ A. Shen, A. Ghosh, S. Devadas, and K. Keutzer, "On Average Power Dissipation and Random Pattern Testability of CMOS Combinational Logic Networks," *Digest of Technical Papers, IEEE/ACM International Conference on Computer-Aided Design*, Santa Clara, California, November 1992, pp. 402-407.

⁶ P.N. Hilfinger, "A High-Level Language and Silicon Compiler for Digital Signal Processing," *Proceedings of the IEEE 1985 Custom Integrated Circuits Conference*, Portland, Oregon, May 1985, pp. 213-216.

graph theory, optimization theory, and linear algebra can be used to allow the space of possible implementation architectures to be efficiently, comprehensively, and systematically explored. A systolic array synthesis method has been developed which exploits these techniques. The space of possible implementation architectures is efficiently explored, and a set of provably optimal register-transfer-level implementations is generated. The exhaustive nature of the design exploration process ensures that all optimal designs are generated. Compared to other work in this area, the developed technique is applicable to a wider class of algorithm and is the only system of its kind which incorporates exhaustive architectural exploration.

Armstrong has built a multirepresentation VLSI database that provides for incremental consistency maintenance.⁷ The goal of this system is to automatically, incrementally, and continuously provide for consistent alignment of all levels of design abstraction. The system provides a design environment which maintains these consistency linkages while allowing the designer to initiate changes at any level of representation. Alignment is achieved through the introduction of explicit correspondence zones between the adjacent representation levels. Some of the necessary translation rules to maintain correspondence are built into the system, but there is also provision for the user to introduce new relationships between levels of design representation. The initial implementation of this system has required over 60,000 lines of code, written in C, but database schemas that are written in C++ will now be introduced to vastly compress the size of the code, increase the speed of the database, and minimize errors and the need for debugging. In addition, the ability to explore designs at a given level of representation is being coupled to the basic database structure. A circuit simulator is being connected at the circuit-level of representation, and a transistor-sizing algorithm is also being used at that level. Since there will always be design requirements that have not been contemplated in the existing design, a default capability is being provided that will indicate structural regions that must be changed in a design in response to a user-initiated change at another level without automatically providing the translation rule that maintains correspondence. In this way, users will not be restricted to a system-provided set of correspondences, but may continuously introduce new translations that

may eventually be assimilated into the overall system.

There is increasing interest in overall CAD systems where the database is central and surrounded by specific applications for design and verification at a variety of different levels of representation, such as in the database just described. This research group is currently using a network of workstations that provides an implicit client-server architecture together with coupling to a mainframe and its attached large tape and disk capabilities interconnected with high-speed fiberoptic switching. Scalable, parallel architectures, particularly useful for highly parallel simulation codes, are now being studied for introduction into this framework. They will also support multiple client utilization of the database with extremely fast communication between the contributing processors. This system will serve as a test bed for the combined utilization of high-performance workstations and mainframe-based storage for high-speed, reliable database access. This environment also provides a structure in which distributed parallel algorithms can run coherently within an overall environment that supports other specialized, nonparallel CAD algorithms.

1.2 Analog VLSI Systems for Integrated Image Acquisition and Early Vision Processing

Sponsor

National Science Foundation
Grant MIP 91-17724

Project Staff

Professor John L. Wyatt, Jr., Professor Berthold K.P. Horn, Professor Hae-Seung Lee, Dr. Ichiro Masaki, Professor Charles G. Sodini, Professor Jacob K. White

1.2.1 Project Summary

In real-time machine vision the sheer volume of image data to be acquired, managed and processed leads to communications bottlenecks between imagers, memory, and processors, and also to very high computational demands. We are designing and testing experimental *analog* VLSI

⁷ R.C. Armstrong and J. Allen, "FICOM: A Framework for Incremental Consistency Maintenance in Multi-Representation, Structural VLSI Design Databases," *Digest of Technical Papers, IEEE/ACM International Conference on Computer-Aided Design*, Santa Clara, California, November 1992, pp. 336-343.

systems to overcome these problems. The goal is to determine how the advantages of analog VLSI—high speed, low power and small area—can be exploited, and its disadvantages—limited accuracy, inflexibility and lack of storage capacity—can be minimized. The work is concentrated on *early* vision tasks, i.e., tasks that occur early in the signal flow path of animal or machine.

The next section details substantial progress on eleven different designs, including systems for camera motion estimation, edge detection, automatic alignment to calibration marks, brightness adaptive imaging, and other tasks. Perhaps the most exciting news concerns the stereo vision system, the initial portion of which was completed by J. Mikko Hakkarainen in his doctoral work with Professor Hae-Seung Lee last May. This project has attracted the attention of General Motors, which sent a vision systems engineer, Dr. Ichiro Masaki, to Boston for a year to work with us and investigate the possibilities of this type of design for future use in automobiles. He has made a real contribution to this project in directing our attention to practical automotive applications.

1.2.2 Vision Chip Designs

Real-Time Stereo Vision System in CCD/CMOS Technology

J. Mikko Hakkarainen completed, for his doctoral thesis under Professor Hae-Seung Lee, the design of an analog VLSI design for a high-speed binocular stereo vision system used for the recovery of scene depth. In this context he has attempted to exploit the principal advantages of analog VLSI—small area, high speed, and low power—while minimizing the effects of its traditional disadvantages—limited accuracy, inflexibility, and lack of storage capacity. A CCD/CMOS stereo system implementation was proposed, capable of processing several thousand image frame pairs per second for 40×40 pixel binocular images, which should yield approximately frame rate operation on 256×256 pixel image pairs. A shift-and-compare module of the stereo system has been fabricated and characterized.

The algorithmic focus of this research was on binocular stereopsis and the stereo correspondence problem in particular. Three stereo algorithms (Marr-Poggio-Drumheller, Pollard-Mayhew-Frisby, and Prazdny) were considered in detail as solutions to this problem and as candidates for VLSI implementation. The most crucial step in the recovery of stereo correspondence was found to be the correlation of left and right images through candidate

matches and local support scores. The Marr-Poggio-Drumheller (MPD) algorithm was shown to be best suited for an efficient VLSI implementation. A detailed simulation study of this algorithm was presented. The simulations were specifically designed to address issues related to analog VLSI implementation.

A full MPD stereo system consists of seven modules: two imagers (left and right views), two image filters, a shift-and-compare module ("correlator"), a local support filter, and a vote taker. The shift-and-compare module together with the local support filter perform the largest number of operations per pixel in the stereo system, and thus they present the speed bottleneck. Of the two modules, the shift-and-compare function is more demanding for hardware implementation, particularly because the local support filter has a simple low-pass characteristic that has already been demonstrated previously using the CCD/CMOS approach. For these reasons the shift-and-compare circuit was selected for design and fabrication. A 40×40 pixel absolute-value-of-difference (AVD) array, the core processor of the shift-and-compare function, was fabricated through MOSIS in a 2 μ m CCD/CMOS process. The array can perform the AVD operation between two arrays a programmable number of times. At a 10 MHz clock rate for the CCD processor, approximately 1000 array (image frame) pairs can be processed per second for a total disparity range of 11 pixels. Special purpose test circuits were designed that are compatible with such high speed processing requirements. Individual AVD processors as well as the full array were characterized. Array functionality was demonstrated in the stereo algorithm context by running the MPD stereo system with actual data from the AVD chip. Upon comparison, the chip output was seen to correspond closely with fully computerized stereo simulations for both artificial and real input image pairs.

A Dynamic-Wires Chip for Pixel Clustering

Dr. John G. Harris, working in collaboration with Shih-Chii Liu from the Rockwell Science Center, has continued to develop the *dynamic wires* paradigm for solving a new class of computer vision problems with analog hardware. This methodology provides dedicated lines of communication among groups of pixels of an image which share common properties. In simple applications, object regions can be grouped together to compute the area or the center of mass of each object. Alternatively, object boundaries may be used to compute curvature or contour length. These measurements are useful for higher level tasks such as object recognition or structural saliency. The dynamic wire meth-

odology is efficiently implemented in fast, low-power analog hardware. Switches create a true electrical connection among selected pixels—dynamically configuring wires or resistive networks on the fly. Dynamic wires provide a different processing approach from that of present vision chips, which are limited to pixel-based or image-based operations. Using this methodology, they have successfully designed and demonstrated a custom analog VLSI chip which computes contour length.

Single-Chip CMOS Imager and Smoothing and Segmentation System Using Resistive Fuses

Paul Yu, working with Professor Hae-Seung Lee, has designed, built, and tested an integrated CMOS resistive-fuse processor capable of smoothing out noise while preserving the edges of a 32x32 image. The on-chip photo-transistor imager converts the optical image into electrical currents. Through a system-level optimization, a single-pixel processing element using only 15 transistors for the horizontal resistive fuses and only one transistor for the vertical resistor was realized. The processed output is read out using a row decoder and a column MUX. Since the on-resistance and off-voltage of the resistive fuses can be electronically controlled, one can vary the degree to which the image is smoothed and segmented electronically. The chip was fabricated through MOSIS and tested; it works well. The chip contains over 19,000 transistors and occupies a 9.2 mm x 7.9 mm area. Operating from a single 5-V supply, it typically dissipates only 10 mW.

Novel Operational Amplifier for Video Rate Analog-to-Digital Conversion

Paul Yu is working with Professor Hae-Seung Lee on novel operational amplifiers to serve as key components in a video-rate pipelined analog-to-digital converter. A new gain-enhancement technique, using a replica amplifier, is being studied. Although this technique is general and can be applied to any conventional op-amp topologies such as folded-cascode, class-AB, differential, or single-ended, a two-stage topology without any cascode was chosen to maximize the available output swing and input common-mode range. Experimental results show that the gain enhancement technique improves the open-loop gain by a factor of 13 without adversely affecting the output swing or the settling behavior. The amplifier achieves an effective open-loop gain of 10,800 using only minimum-length transistors in the signal path and no cascode. Even with a 1 K ohm load resistor, an

effective open-loop gain of over 10,000 is maintained. The output swings within 100 mV from either rail. The gain-bandwidth product is 63 MHz with a 27 pF load capacitance and 9 mW power dissipation. These results are obtained using only a 2-V supply. The chip was fabricated in a 1.2 μ m CMOS technology.

CMOS/CCD Imager and Focus-of-Expansion Chip for Camera Motion

Ignacio McQuirk, working with Professors Berthold Horn and Hae-Seung Lee, has continued development of a chip that determines the direction of camera translation directly from a time-varying image sequence with a real-time analog VLSI system. His approach assumes a camera moving through a fixed world with only translational velocity. Also, the surfaces in the environment must have some spatial variations in reflectance. The focus of expansion (FOE) is the projection of the camera translation vector onto the image plane and hence gives the direction of camera motion. The FOE is the image of the point towards which the camera is moving and the point from which other image points appear to be receding. Knowledge of the location of the FOE in the case of pure translation also allows coarse calculation of the depth map of the imaged world up to a scale factor ambiguity, as well as the associated time to impact.

Previously, various possible algorithms for estimating the FOE were compared in terms of accuracy, robustness, and feasibility for single-chip analog VLSI implementation with on-chip imaging circuitry. As a result of these studies, an algorithm based on minimizing the sum of squares of the differences at stationary points between the observed time variation of brightness and the predicted variation was chosen for implementation. Additionally, several system architectures and circuit designs were explored, and one was chosen for realization in analog VLSI. Mr. McQuirk designed a preliminary CMOS/CCD version of the FOE chip using on-chip CCD imaging circuitry and a row-parallel processing scheme. Several components of this design were fabricated through MOSIS and tested with excellent results.

During the period covered by this report, the design of the FOE chip was revised, and a preliminary version of the complete chip was also fabricated through MOSIS. He is currently in the process of designing and fabricating a test printed circuit board for the FOE system consisting of pattern generators, CCD clock drivers, FOE chip bias circuitry, I/O drivers, and an interface to the Vision Chip Test System. This will allow for stand-alone operation of the FOE system as well as operation with the

Vision Chip Test System for algorithmic, system, and circuit level testing.

Robust Analog Image Segmentation Chip for Edge Detection and Camera Motion

Lisa Dron, working with Professor Horn, has invented a robust method of image segmentation that has been shown to work well in computer simulations. The basic idea is to segment an image between two nodes of a grid wherever the difference in intensities at the two nodes exceeds a threshold at *all of several different scales* of spatial low-pass filtering. (The threshold can vary with the scale.) The method is *robust* in the sense that local noise spikes in the image are averaged out with filtering and do not contribute false edges, and it is *accurate* in the sense that the unfiltered image plays a role, since threshold must be exceeded there as well. Bandwidth compression is achieved by retaining intensity values only at nodes adjacent to edges. Intensities elsewhere are obtained by spatial averaging using a resistive grid.

A preliminary design has been studied for the segmentation circuit using a two-dimensional CCD array with added circuitry for computing differences and performing threshold tests. The structure of the array uses the same principles developed by Dr. Craig Keast for *smoothing and segmentation*; however, it has been modified to implement the multi-scale veto (MSV) algorithm. In addition, several improvements suggested by Dr. Keast to improve the performance of the CCD circuits have been incorporated. A test chip containing a one-dimensional array, as well as its isolated subcircuits, has been fabricated through MOSIS and tested. A second chip with a two-dimensional array has now been designed and fabricated and is currently being tested.

The two primary applications of the multi-scale veto (MSV) chip are image reconstruction and edge detection. Ms. Dron has chosen to pursue the second application in order to design a system for computing general camera motion in real-time with analog processing. The binary edge signals produced by the MSV chip can be used to obtain correspondences between successive frames by matching patches of the edge maps in the two images. It is well known that it is possible to compute the relative camera motion between frames from as few as five correspondences, provided the internal camera parameters are known; although in practice, several more than five are used in order to obtain a more reliable estimate of the motion.

Conventional digital methods for estimating camera motion typically utilize special purpose DSP chips to find point correspondences by matching gray levels over small patches in the two images using either cross-correlation or mean absolute value of difference. Due to the complexity of the computations with 8-bit gray-level data, the maximum displacement which can be computed at video rate with a single chip is currently limited on commercially available chips to around ± 8 pixels in any direction. In addition, the displacement estimates obtained from matching gray levels are in general less reliable than those which can be obtained by matching edges. It is possible to define functions on two patches of binary edges which have a large non-zero value only when there is a good match between their edge patterns. Robust displacement estimates are obtained by identifying patches which produce a well-peaked unimodal response when tested against all like-sized patches within a large search area in the other image. An analog processor can be designed to effectively implement such a matching function because it is not necessary to accurately compute the exact value of the function, but only to find the location of its peak value and to determine if it is significantly greater than zero.

Ms. Dron has recently completed a study of different matching functions which can be computed by *analog methods using the binary edge signals* produced by the MSV chip. She has designed several test structures which will eventually form the basis of the analog matching circuit and has sent these out for fabrication by MOSIS. In addition to designing the circuits, she has also developed the algorithms needed to use the point correspondences in a real-time system. She has derived a robust least-squares method suitable for implementation on a digital processor to compute camera motion, as well as an algorithm to determine the internal camera calibration parameters, required for motion computation, from point matches in a sequence of images for which the translational motion is known.

Content-Addressable Parallel Digital Image Processor

Massively parallel associative processors may be well suited as coprocessors for accelerating machine vision applications. They achieve very fine granularity, as every word of memory functions as a simple processing element. A dense, dynamic, content-addressable memory cell supports fully-parallel operation, and pitch-matched word logic improves arithmetic performance with minimal area cost. An asynchronous reconfigurable mesh network handles interprocessor communication and

image input/output, and an area-efficient pass-transistor circuit counts and prioritizes responders.

Frederick P. Herrmann has completed the design of a 16K-trit associative processing chip, under the supervision of Professor Charles Sodini. The chip integrates 256 processing elements, each with 64 trits of memory. A 16 x 16 mesh network connects the processing elements, and larger meshes may be constructed using several chips.

The chip has been submitted for fabrication in MIT's 1.5 μm CCD/CMOS process. Fabrication is complete, and testing will begin in January 1993.

Single-Chip Alignment Sensor

Christopher Umminger, working with Professors Sodini and Horn, has been researching implementations of single-chip sensors to measure alignment error for tasks in automated manufacturing. The sensor will optically acquire an image of the alignment marking and output a measure of the misalignment. Currently they have settled on two methods for the task of aligning a mark to the sensor. The first is based on the surveyor's mark. The sensor consists of a four quadrant photodiode combined with an edge detection circuit to provide extra alignment accuracy in the face of nonuniform illumination. The second sensor design uses a square grating mark. A position sensitive Moiré fringe pattern formed between the sensor and the marking is used to achieve accurate alignment.

The first sensor design using the surveyor's mark was finished in June and submitted for fabrication. The completed chips were received in mid-September and preliminary tests show that the circuits are working as expected. Characterization of the sensor in an alignment system awaits the construction of a prototype aligner. Design of the Moiré fringe sensor will begin in November and will be submitted for fabrication at the end of the year.

Switched-Capacitor System for Merging Depth and Slope Estimates

Mark Seidel, working with Professor John Wyatt and Principal Research Scientist Thomas Knight, has been designing and fabricating a switched-capacitor chip to robustly compute the depth of a scene by merging depth estimates (possibly from a stereo algorithm) with surface slope estimates (possibly from a shape-from-shading algorithm). This multi-sensor image fusion design uses the least-squares properties of certain switched-capacitor systems to compute a dense depth map given noisy or sparse depth and slope input. Testing of a 1-D version fabricated through the MOSIS system

revealed a shorting problem that inhibits further testing. Laser "surgery" done at MIT Lincoln Laboratory failed to resolve the origin of the problem. A MOSIS Tinychip containing some subcircuits has also been fabricated, but not tested. The architecture of the chip was presented at ISCAS 1992 in San Diego. In the final two months of the year, the MOSIS Tinychip will be tested.

Brightness Adaptive CCD Imager with Analog and Digital Output

Steven Decker, working with Professor Sodini, has been designing an imager to act as the front end of a modular vision system. It will feature a 64x64 array of pixels, large fill factor, operating speed on the order of 1000 frames/sec, column parallel output, a brightness adaptation capability, and user selectable analog or 10-bit digital output.

A CCD-based algorithmic A/D converter has been developed which requires only CCD gates and one operational amplifier. It avoids the need for subtraction of charge packets required by a similar previous design, a step which severely limited the attainable accuracy. Analog output can also be obtained by shifting the charge onto an integrating capacitor in a feedback loop around an operational amplifier. The linearity of the analog output is much better than for a conventional CCD output because the poly-poly capacitor in the feedback loop is much more linear than the diffusion capacitance of a conventional CCD output.

The brightness adaptive imaging element is based on a design that was previously patented elsewhere. Each pixel is composed of an MOS capacitor biased in deep depletion and an overflow gate. The overflow gate establishes a barrier to the flow of imaged charge from the main potential well to a sink. During the integration period, the height of the barrier $\phi(t)$ is varied as a function of time. A relationship between the light intensity and final imaged charge can be derived for a given $\phi(t)$. In particular, it is possible to obtain a logarithmic compression curve so that, ideally, any light intensity can be sensed without saturating the imager. The advantages of this technique over other schemes which have been considered are simplicity, flexibility, and small size.

Efforts have been directed towards designing a practical realization of the brightness adaptive imager. In the original patent, $\phi(t)$ is assumed to be a continuous, infinitely precise function of time. The implications of approximating $\phi(t)$ with a digital signal have been examined. Using the digital generation scheme and digital output, reconstruction of the original light intensity from the imaged charge is

easy since this can all be done digitally. A layout scheme which allows column parallel output while maintaining a fill factor exceeding 50 percent has been achieved.

1.2.3 Mixed Circuit/Device Simulation for CMOS/CCD Systems

Andrew Lumsdaine and Mark Reichelt, under the supervision of Professor Jacob K. White, are working on algorithms for accelerating mixed circuit/device simulation, as this kind of analysis is required to properly simulate the performance of CCD-based analog vision circuits. Initially, they have focused on developing parallelizable algorithms for semiconductor device transient simulation, and are investigating waveform relaxation (WR), a natural candidate. They found experimental evidence that accelerating WR convergence using standard overrelaxation can produce oscillatory results and have recently developed methods for eliminating this phenomenon. In particular, they have developed two new techniques for accelerating WR convergence, one based on a generalized conjugate-direction method and the other based on a frequency-dependent successive over-relaxation (SOR) algorithm. Proofs of the optimality of the SOR algorithm and the guaranteed convergence of the C-D method have been completed, and experimental results indicate that both methods can reduce the number of waveform iterations as much as an order of magnitude.

1.2.4 Vision Chip Test System

In order to test VLSI early vision processors that are being developed by this project, it is important to input synthetic data or real image data to the chip and study processed image output from the chip. Kamyar Eshghi and Professor Sodini have constructed a Demonstration System for Early Vision processors (DSEV) that will perform this high-level testing. DSEV can capture images from video cameras and transmit them to a device under test (DUT). Processed images retrieved from the DUT are stored by DSEV and may be displayed for visual comparison to the input image. Also, the same images that were input to the DUT may be processed by software algorithms on a workstation and compared with the DUT output, allowing the sensitivities of the integrated circuit design to be studied. DSEV has been standardized in such a way that a minimum of effort is required to interface various vision chips to it.

The hardware of DSEV consists of a camera, display monitor, frame grabber, display interface,

image memory, SUN workstation, S-bus to VME adapter, MaxBus interface, DUT interface, and DUT board. A MaxVideo20 module was purchased from DataCube Incorporated, which includes a frame grabber, display interface and image memory. Software has been written to control MaxVideo20, and the MaxBus interface board and DUT interface boards were designed, built and tested.

Each student will have to design and build his or her own DUT board specifically for the chip to be tested, but the rest of the system is shared, at a substantial savings in overall group effort. Ignacio McQuirk is now modifying and altering the system for use in testing his motion chip. He is currently moving the level-shifting and scaling circuitry from the DUT board to the A/D and D/A converter boards and building more of those boards.

1.2.5 Novel Camera Calibration Method Using Images of Lines and Spheres

A stereo vision system and two systems for camera motion determination were described earlier in this report. Both these tasks require accurate knowledge of camera parameters, specifically, principal point, focal length and distortions such as horizontal scaling and radial distortion, for any analog or digital implementation.

Although camera calibration is important for 3D measurements, it is often neglected because it is a laborious process and requires special apparatus and skill. The aim of this project is to devise a method for calibration which will be simple to perform and accurate to better than one percent error in camera parameters.

Most of the techniques currently used in the field of robotics use images of a 3D object whose world coordinates are accurately known and then proceed to find both the camera parameters and the position and orientation of the camera relative to the 3D object. These methods have a few inherent weaknesses. It is often hard to decouple the camera parameters from the camera orientation parameters (external parameters). To have any chance of success, a very precise 3D object is required with easily identifiable calibration points. These objects are relatively hard to obtain, and the number of calibration points in the object is small (on the order of 100).

Gideon Stein has been working with Professors Wyatt and Horn to develop new techniques for calibration of internal camera parameters which will not require finding all the external calibration parameters.

The first method finds the radial distortion parameters. The image of straight lines under perspective projection are straight lines. In real images these lines are curved due to radial distortion. By correcting for the radial distortion the lines can be made straight. This is an adaptation of the "plumb line" method known in the literature.

The second method finds the focal length and the principal point. It assumes the image has been corrected for radial distortion. The image of a sphere under perspective projection is an ellipse whose major axis is on a line which passes through the principal point. The eccentricity of the ellipse is a function of the focal length. By taking the image of a number of spheres the intersection of the lines passing through the major axis gives the principle point. The focal length can be found from the eccentricity. This method finds the principal point to within one pixel but so far does not provide accurate estimates of the focal length.

The third method involves rotating the camera around the y-axis through a known angle. By tracking points in the scene the focal length and radial distortion can be recovered. Currently the estimates are repeatable to within 0.5 percent. To a lesser degree of accuracy, the principal point can also be recovered. This method is suitable for self calibration of autonomous robots working in unstructured outdoor environments.

Future work involves refining these three methods and evaluating their performance compared to the more traditional methods.

1.2.6 Analog versus Digital Approaches to Machine Vision Hardware

Recent technical progress in analog vision chips has stimulated comparisons of analog and digital processing schemes through case studies. The analog vision chips have demonstrated their small cost in silicon area and high speed characteristics for some applications. The goal of this project is to identify the capabilities and limitations of the analog chips and to find what application areas would be suitable for analog, digital, and hybrid chips, respectively.

In collaboration with Professors Charles Sodini, Berthold Horn, and John Wyatt, David A. Martin, under the supervision of Professor Hae-Seung Lee, and Ichiro Masaki, visiting scientist from General Motors, chose direct image correlation and three-dimensional stereo vision algorithms as the cases. These algorithms are frequently used in various applications including intelligent vehicles and flexible manufacturing systems.

As the first step, two algorithms were compared at a conceptual level: a binary algorithm for digital implementation and a multi-valued algorithm for analog chips. The computer simulation is being developed for this algorithm level comparison. The chip implementation level comparison is also underway. Currently a Multi-Instruction Multi-Data Array Processor architecture, implemented in both analog and digital, is being studied. Each processing element includes an arithmetic unit, a data flow control unit, and a system control unit which includes program memory.

Our next goals include finalization of the chip architecture, design of the chips, and performance comparisons based on simulations of the designed chips. The criteria for the comparisons will include cost in silicon area, processing speed, manufacturing and development costs, testability, and other related issues.

1.2.7 Solutions of Theoretical Problems in Analog Hardware and Machine Vision

Gibbs Random Field Models

Gibbs random fields (GRFs) are probabilistic models inspired by statistical mechanics and used to model images in computer vision and image processing. In this research, conducted by Ibrahim Elfadel under the supervision of Professors John Wyatt, Berthold Horn and Alan Yuille, the analytical methods of statistical mechanics are brought to bear on these models. Specifically, the following fundamental problems have been addressed and contributions have been made to their solutions:

1. Mean-field estimation of a constrained GRF model: The configuration space of a GRF model is often constrained to produce "interesting" patterns. Mr. Elfadel has developed mean-field equations for estimating the means of these constrained GRFs. The novel feature of these equations is that the finiteness of graylevels is incorporated in a "hard" way in the equations.
2. Correlation-field estimation of a GRF model: GRF correlation functions are generally hard to compute analytically and expensive to compute numerically. Mr. Elfadel has used the mean-field equations developed above to propose a new procedure for *estimating* these correlation functions. His procedure, which is valid for both unconstrained and constrained models, is applied to the quadratic interaction model, and a new closed-form approximation for its corre-

lation function in terms of the model parameters is derived.

3. Network representation: Mr. Elfadel has shown how the mean-field equations of the GRF model can be mapped onto the fixed point equations of an analog winner-take-all (WTA) network. The building block of this network is the *generalized sigmoid mapping*, a natural generalization of the sigmoidal function used in artificial neural networks. This sigmoidal mapping has a very simple VLSI circuit implementation with desirable circuit-theoretic properties such as reciprocity and local passivity.
4. Solution algorithms: Iterated map methods and ordinary differential equations (ODEs) are proposed to solve the network fixed-point equations. In the former, Mr. Elfadel has shown, using Lyapunov stability theory for discrete systems, that the worst that could happen during synchronous iteration is an oscillation of period 2. In the latter, he has shown that the ODEs are the gradient descent equations of energy functions that can be derived from the mean-field approximation. One of his gradient descent algorithms can be interpreted as the generalization to analog WTA networks of Hopfield's well-known algorithm for his analog network.
5. Temperature dependence: The GRF temperature parameter reflects the thermodynamic roots of the model. Using eigenstructure analysis, he has studied the temperature effect on the stability of the WTA network fixed points. In particular, he derived new closed-form formulas for the *critical temperature* of a large class of models used in grayscale texture synthesis. The stability study is used to gain insight into the phase transition behavior of GRFs.

The technical details of these results will appear in Ibrahim Elfadel's Ph.D. thesis titled *From Random Fields to Networks*, which was submitted in February 1993.

In future work, Mr. Elfadel will investigate the implications of these results in the fields of image modeling, optimization, and analog hardware implementation of image processing and computer vision algorithms.

Switched-Capacitor Network Theory

Mark Seidel, working with Professor John Wyatt, has been studying general networks of switches, capacitors, and sources. These networks are important in the implementation of computational and image processing problems formulated as minimization algorithms. For nonpathological networks, conditions for stability during each clock phase have been proven. Stability for the discrete time system has been proven for a large subclass of these networks. We also expect to prove stability for general networks.

Under constant input conditions, the switched-capacitor networks can be shown to be equivalent to networks comprised of, in general, nonreciprocal passive resistive multiports and multiterminal elements. Each such element is associated with exactly one of the capacitors in the network. The transformation to these resistive networks is equivalent in the sense that all node voltages are the same, and all currents are equal to the corresponding average transferred charge over the period. This equivalence indicates certain rules for the reverse problem of synthesizing a switched capacitor network from a resistive network. This synthesis can always be accomplished for networks of two-terminal resistors and lossy two-port transformers. It has also been shown that even if the resistive network to be implemented includes only the nonreciprocal passive resistive elements discussed earlier, clock phase assignment is sometimes impossible. We will be generating several examples and writing a journal article.

Finally, additional work has been completed on bounding the discrete time system settling time of large switched capacitor networks. The bounds have been completely inverted and can be shown to be equivalent to the continuous time bounds in the appropriate limit. We will be generating several examples.

Generating a Uniformly Spaced Set of 3-D Rotations for Object Recognition Purposes

In some pattern recognition tasks, e.g., vehicle identification from aerial photography, one wishes to decide which object from a finite, previously determined set is represented in some portion of a single image. One seeks the best match by rotating each of the known objects to various positions, creating 2-D images in various sizes, and finding the best match. One problem is that there is no known way of writing down closed form expressions for a uniformly spaced set of N rotations in three dimensions, except for very special values of N corresponding to the number of faces on a regular

polyhedron. (The solution in two dimensions is trivial—the rotations are through angles of $(K/N) \cdot 360^\circ$, where $K = 1, 2, \dots, N - 1$.)

Gene Osgood, working with Professors Wyatt and Horn, has explored an iterative method for producing uniformly spaced rotations using the quaternion number system. In this system each rotation in three dimensions is represented abstractly as a point on the three-dimensional sphere in four dimensions. Gene represents each point as a positive point charge and simulates the movement of these charges under mutual repulsion as they spread apart on the surface of the sphere. The method yields a substantial savings in computer time over conventional approaches that use unevenly spaced points.

1.2.8 Publications

Journal Articles

- Dron, L. "The Multi-Scale Veto Model: A Two-Stage Analog Network for Edge Detection and Image Reconstruction." *Int. J. Comput. Vision*. Forthcoming.
- Elfadel, I.M., and A.L. Yuille. "Mean-Field Phase Transitions and Correlation Function for Gibbs Random Fields." *J. Math. Imag. Vision*. Forthcoming.
- Elfadel, I.M., and R.W. Picard. "Gibbs Random Fields, Co-Occurrences, and Texture Modeling." *IEEE Trans. Pattern Anal. Mach. Intell.* Forthcoming.
- Herrmann, F., and C. Sodini. "A Dynamic Associative Processor for Machine Vision Applications." *IEEE Micromag.* 12(3): 31-41 (1992).
- Liu, S.C., and J.G. Harris. "Dynamic Wires: An Analog VLSI Model for Object Processing." *Int. J. Comput. Vision* 8(3): 231-239 (1992).
- Picard, R.W., and I.M. Elfadel. "Structure of Aura and Co-occurrence Matrices for the Gibbs Texture Model." *J. Math. Imag. Vision* 2: 5-25 (1992).
- Umminger, C.B., and C.G. Sodini. "Switched Capacitor Networks for Focal Plane Image Processing Systems." *IEEE Trans. Circuits Syst. Video Technol.* 2(4): 392-400 (1992).
- Wyatt, J.L., Jr., C. Keast, M. Seidel, D. Standley, B. Horn, T. Knight, C. Sodini, H-S. Lee, and T. Poggio. "Analog VLSI Systems for Image Acquisition and Fast Early Vision Processing." *Int. J. Comput. Vision* 8(3): 217-230 (1992).
- Yu, P.C., S.J. Decker, H-S. Lee, C.G. Sodini, and J.L. Wyatt, Jr. "CMOS Resistive Fuses for Image Smoothing and Segmentation." *IEEE J. Solid-State Circuits* 27(4): 545-553 (1992).

Meeting Papers

Dron, L. "System-Level Design of Specialized VLSI Hardware for Computation Relative Orientation." *Proceedings of the IEEE Workshop on Applications of Computer Vision*, Palm Spring, California, November 30 - December 2, 1992.

Dron, L. "Dynamic Camera Self-Calibration from Controlled Motion Sequences." Submitted to the 1993 *Conference on Computer Vision and Pattern Recognition*.

Elfadel, I.M., and A.L. Yuille. "Mean-Field Phase Transitions for Gibbs Random Fields." *SPIE '92 Proceedings*, San Diego, California, July 1992.

Hakkarainen, J.M., and H-S. Lee. "A 40x40 CCD/CMOS AVD Processor for Use in a Stereo Vision System." *1992 European Solid-State Circuits Conference*, Copenhagen, Denmark, September 1992, pp. 155-157.

Keast, C.L., and C.G. Sodini. "A CCD/CMOS Based Imager with Integrated Focal Plane Signal Processing." Paper presented at the 1992 *Symposium on VLSI Circuits*, Seattle, Washington, June 1992, pp. 38-39.

Lumsdaine, A., and J.K. White. "Accelerating Dynamic Iteration Methods with Application to Semiconductor Device Simulation." *Proceedings of the Copper Mountain Conference on Iterative Methods*, Copper Mountain, Colorado, April 1992.

Masaki, I. "Function-oriented Vision Chips for Factory Automation." *1992 International Conference on Industrial Electronics, Control, and Instrumentation*, San Diego, California, November 1992.

Masaki, I. "Vision-based Vehicle Guidance." *1992 International Conference on Industrial Electronics, Control, and Instrumentation*, San Diego, California, November 1992.

Reichelt, M., J. White, and J. Allen. "Frequency-Dependent Waveform Overrelaxation for Transient Two-Dimensional Simulation of MOS

Devices." *Proceedings of NUPAD IV*, Seattle, Washington, May 1992.

Seidel, M.N. "Analysis and Synthesis of Steady-State SC Networks." Submitted to *IEEE International Symposium on Circuits and Systems*, Chicago, Illinois, 1993.

Wyatt, J.L., Jr., C. Keast, M. Seidel, D. Standley, B. Horn, T. Knight, C. Sodini, H-S. Lee, and T. Poggio. "Analog VLSI Systems for Early Vision Processing." *Proceedings of the 1992 IEEE International Symposium on Circuits and Systems*, San Diego, California, May 1992, pp. 1644-1647.

Wyatt, J.L., Jr., C. Keast, M. Seidel, D. Standley, B. Horn, T. Knight, C. Sodini, and H-S. Lee. "Small, Fast Analog VLSI Systems for Early Vision Processing." Paper presented at the Conference on *Intelligent Vehicles '92*, Detroit, Michigan, June 1992, pp. 69-73.

Yu, P.C., and H-S. Lee. "A CMOS Resistive-fuse Processor for 2-D Image Acquisition, Smoothing and Segmentation." *1992 European Solid-State Circuits Conference*, Copenhagen, Denmark, September 1992, pp. 147-149.

Yu, P.C., and H-S. Lee. "A High-Swing 2-V CMOS Operational Amplifier with Gain Enhancement Using a Replica Amplifier." *1993 International Solid-State Circuit Conference*, San Francisco, California, February 1993.

Theses

Eshghi, K. *A System Demonstration of VLSI Early Vision Processors*. S.M. thesis, Dept. of Electr. Eng. and Comput. Sci., MIT, 1992.

Hakkarainen, J.M. *A Real-Time Stereo Vision System in CCD/CMOS Technology*. Ph.D. diss., Dept. of Electr. Eng. and Comput. Sci., MIT, 1992.

Keast, C.L. *An Integrated Image Acquisition, Smoothing and Segmentation Focal Plane Processor*. Ph.D. diss., Dept. of Electr. Eng. and Comput. Sci., MIT, 1992.

Lumsdaine, A. *Theoretical and Practical Aspects of Parallel Numerical Algorithms for Initial Value*

Problems, with Applications. Ph.D. diss., Dept. of Electr. Eng. and Comput. Sci., MIT, 1992.

Osgood, G.T. *Evenly Sampling a Rotation Space*. S.B. thesis, Dept. of Electr. Eng. and Comput. Sci., MIT, 1992.

1.3 Parallel Algorithms for Device Simulation

Sponsors

IBM Corporation
National Science Foundation
Grant MIP 91-17724
U.S. Navy - Office of Naval Research
Grant N00014-91-J-1698

Project Staff

Andrew Lumsdaine, Khalid Rahmat, Mark W. Reichelt, Professor Jacob K. White, Professor Jonathan Allen

Enormous computational expense and the growing importance of mixed circuit/device simulation, as well as the increasing availability of parallel computers, suggest that specialized, easily parallelized algorithms should be developed for transient simulation of MOS devices. In earlier work on the WORDS program (Waveform Overrelaxation Device Simulator), the easily parallelized waveform relaxation (WR) algorithm was shown to be a computationally efficient approach to device transient simulation even on a serial machine. However, the WR algorithm typically requires hundreds of iterations to achieve an accurate solution.

In order to use WORDS in a mixed circuit/device simulator, we have been investigating ways of making WORDS more robust and efficient. We determined how to compute the terminal currents accurately using different timepoints at different mesh nodes. We also improved the timestep selection procedure by determining how to refine the timesteps as WR iterations proceed (reducing the total computation by as much as a factor of 2 by using only a few coarse timesteps in early iterations). The more accurate, electric field dependent mobility model was also implemented. Recent work on theoretical aspects of these methods have answered several long-standing questions about multirate stability.⁸

⁸ M. Reichelt, F. Odeh, and J. White, "A-Stability of Multirate Integration Methods, with Application to Parallel Semiconductor Device Simulation," (Invited paper) *Proceedings of the SIAM Meeting on Parallel Processing for Scientific Computing*, Norfolk, Virginia, March 1993.

Through experiments, we found evidence that WR, using standard overrelaxation acceleration, can produce oscillatory results and are investigating methods for eliminating this phenomenon. A frequency-dependent overrelaxation algorithm using lowpass filtering was developed⁹ as well as a waveform conjugate-direction approach.¹⁰ Experimental results indicate that both approaches reduce the number of waveform iterations required by more than a factor of seven. Finally, experimental results using a parallel computer show that, although the accelerated WR methods are only competitive with the best of the standard algorithms for device transient simulation on a serial machine, the WR algorithms are substantially faster on a parallel machine.¹¹

1.4 Numerical Simulation of Short Channel MOS Devices

Sponsors

IBM Corporation
National Science Foundation
Fellowship MIP 88-58764
U.S. Navy
Contract N00174-92-Q-0133

Project Staff

Khalid Rahmat, Professor Dimitri A. Antoniadis,
Professor Jacob K. White

The model used in conventional device simulation programs is based on the drift-diffusion model of electron transport, but this model does not accurately predict the field distribution near the drain in small geometry devices. This is of particular importance for predicting oxide breakdown due to penetration by "hot" electrons. There are two approaches for more accurately computing the electric fields in MOS devices, one is based on adding an energy equation to the drift-diffusion model, and the second is based on direct solution of Boltzman's equation.

In the first approach, an energy balance equation is solved along with the drift-diffusion equations so that the electron temperatures are computed accurately. This combined system is numerically less tame than the standard approach and must be solved carefully. We have developed a two-dimensional device simulator in which an energy balance equation is solved for electron temperature along with the usual drift-diffusion equations. The program avoids temperature instabilities produced by previous discretization approaches through the use of a careful application of exponential-fitting to the energy equation. Drain currents for silicon MOSFETs predicted by the simulator, using one set of model parameters, match well with experimental data for devices over a range of channel lengths from 0.90 μm to 0.16 μm . Also, a method to compute substrate current has been derived which uses the electron temperature provided by the simulator. The computed substrate currents match well with measured data, for the regime above sub-threshold, for MOSFET's with channel lengths as short as 0.16 μm .¹²

The limited ability to accurately predict hot-electron effects from an energy-balance based simulator has led to our current investigation. We are now trying to solve the full Boltzman equation, using a spherical harmonics based approach in portions of the MOS device which are likely to create hot carriers.

1.5 Circuit Simulation Algorithms

Sponsors

IBM Corporation
National Science Foundation
Fellowship MIP 88-58764

Project Staff

Luis M. Silveira, Steven B. Leeb, Professor Jacob K. White

A challenging problem in the area of analog circuits is the simulation of clocked analog circuits like

⁹ M. Reichelt, J. White, and J. Allen, "Frequency-Dependent Waveform Overrelaxation for Transient Two-Dimensional Simulation of MOS Devices," *Proceedings of NUPAD IV*, Seattle, Washington, May 1992, pp. 161-166.

¹⁰ A. Lumsdaine and J. White, "Accelerating Dynamic Iteration Methods with Application to Semiconductor Device Simulation," (Third place, best student paper competition) *Proceedings of the Copper Mountain Conference on Iterative Methods*, Copper Mountain, Colorado, April 1992.

¹¹ A. Lumsdaine and M. Reichelt, "Waveform Iterative Techniques for Device Transient Simulation on Parallel Machines," Invited paper, *Proceedings of the SIAM Meeting on Parallel Processing for Scientific Computing*, Norfolk, Virginia, March 1993.

¹² K. Rahmat, J. White, and D. Antoniadis, "Simulation of Very Short Channel MOSFETs Including Energy Balance," *IEEE Trans. Comput.-Aided Des.*, forthcoming.

switching filters, switching power supplies, and phase-locked loops. These circuits are computationally expensive to simulate using conventional techniques because these kinds of circuits are all clocked at a frequency whose period is orders of magnitude smaller than the time interval of interest to the designer. To construct such a long time solution, a program like SPICE or ASTAP must calculate the behavior of the circuit for many high frequency clock cycles. The basic approach to making simulation of these circuits more efficient is to exploit only the property that the similar behavior of such a circuit in a given high frequency clock cycle, but not identical, to the behavior in the preceding and following cycles. Therefore, by accurately computing the solution over a few selected cycles, an accurate long term solution can be constructed. Such approaches are known as "envelope-following" algorithms.

In our recent work, we are trying to make the envelope-following algorithm more robust and efficient by exploiting the fact that the envelope of "quasi-algebraic" components in the solution vector need not be computed. An automatic method for determining the quasi-algebraic solution components has been derived, and experimental results demonstrate that this modified method reduces the number of computed clock cycles when applied to simulating closed-loop switching power converters.¹³

1.6 Parallel Circuit Simulation Algorithms

Sponsor

U.S. Navy - Office of Naval Research
Grant N00014-91-J-1698

Project Staff

Luis M. Silveira, Ricardo Telichevsky, Professor
William J. Dally, Professor Jacob K. White

We are taking an application-oriented approach to developing parallel numerical algorithms and focusing on circuit and device simulation. Application programs and techniques are being developed for both massively parallel machines SIMD machines like the Connection Machine or MIMD machines like the Intel hypercube. In addition, we

are also trying to understand fundamental aspects of the interaction between architecture and certain numerical algorithms.

For example, the direct solution of circuit simulation matrices is particularly difficult to parallelize, in part because methods like parallel nested dissection are ineffective due to the difficulty of finding good separators. For that reason, general sparse matrix factorization techniques are being studied and, in particular, the interaction between sparse matrix data structures, computer memory structure, and multiprocessor communication is being investigated. To focus this work, a special-purpose processor for circuit simulation, the Numerical Engine (NE), is under development. Preliminary design is complete, and register-transfer level simulation results indicate that the specialized processor can achieve up to 80% of its peak floating-point performance for sparse matrix factorization and nearly 90% of its peak performance on model evaluation.

Explicit integration methods avoid matrix solution and, therefore, are also interesting algorithms to use on parallel processors. For this reason, we investigated some properties of the recently developed explicit exponentially-fit integration algorithms. The results were not very encouraging, although our theoretical investigation yielded several new insights about these methods.¹⁴

1.7 Microelectromechanical CAD (MEMCAD)

Sponsors

Federal Bureau of Investigation
Contract J-FBI-92-196
National Science Foundation
Fellowship MIP 88-58764

Project Staff

Xuejun Cai, Mattan Kamon, Professor Martin A. Schmidt, Professor Stephen D. Senturia, Professor Jacob K. White

High fabrication costs and increasing microsensor complexity is making computer simulation of the realistic geometries necessary, both to investigate design alternatives and to perform verification before fabrication. At MIT, we are developing a

¹³ M. Silveira, J. White, and S. Leeb, "A Modified Envelope-Following Approach to Clocked Analog Circuit Simulation," *Proceedings of the International Conference on Computer-Aided Design*, Santa Clara, California, November 1991, pp. 20-23.

¹⁴ H. Neto, L.M. Silveira, J. White, and L.M. Vidigal, "On Exponential Fitting For Circuit Simulation," *IEEE Trans. Comput.-Aided Des.* 11(5): 566-574 (1992).

MicroElectroMechanical Computer-Aided Design (MEMCAD) system to make it possible for micro-sensor designers to easily perform realistic simulations. Carefully selected commercial software packages have been linked with specialized database and numerical programs to allow a designer to easily enter a three-dimensional microsensor geometry and quickly perform both mechanical and electrical analyses. The system currently performs electromechanical analyses, such as calculating the capacitance versus pressure (or force) curve for a square diaphragm deformed by a differential pressure and can be used to calculate levitation forces in structures as complicated as a comb drive.¹⁵

1.8 Numerical Techniques for Simulating Josephson Junction Arrays

Sponsors

National Defense Science and Engineering
Graduate Fellowship
National Science Foundation
Fellowship MIP 88-58764

Project Staff

Joel R. Phillips, Herre S.J. van der Zant, Professor
Terry P. Orlando, Professor Jacob K. White

Vortices play a central role in determining the static and dynamic properties of two-dimensional (2D) superconductors. Artificially fabricated networks of superconducting islands weakly coupled by Josephson junctions are model systems to study the behavior of vortices. Through simulation, we have discovered that the static properties of vortices in an array of Josephson junctions can be significantly influenced by magnetic fields induced by vortex currents. The energy barrier for vortex motion is enhanced, nearly doubling for penetration depths on the order of a cell size. Moreover, we have found that correct calculation of the vortex current distribution, the magnetic moment, and the lower critical field require modeling mutual inductance interactions between all cell pairs in the array.

To make numerical simulation of the system with all inductive effects computationally feasible, a novel FFT-accelerated integral equation solver was derived. This algorithm is sufficiently efficient to allow study of large (500 x 500 cells) arrays.¹⁶

1.9 Efficient 3-D Interconnect Analysis

Sponsors

Digital Equipment Corporation
IBM Corporation
National Science Foundation
Fellowship MIP 88-58764
U.S. Navy - Office of Naval Research
Contract N00014-91-J-1698

Project Staff

Mattan Kamon, Songmin Kim, Keith S. Nabors, Joel R. Phillips, Professor Jacob K. White

We have developed multipole-accelerated algorithms for computing capacitances and inductances of complicated 3-D geometries and implemented these algorithms in the programs FASTCAP and FASTHENRY. The methods are accelerations of the boundary-element or method-of-moments techniques for solving the integral equations associated with the multiconductor capacitance or inductance extraction problem. Boundary-element methods become slow when a large number of elements are used because they lead to dense matrix problems which are typically solved with some form of Gaussian elimination. This implies that the computation grows as n^3 , where n is the number of panels or tiles needed to accurately discretize the conductor surface charges. Our new algorithms, which use generalized conjugate residual iterative algorithms with a multipole approximation to compute the iterates, reduces the complexity so that accurate multiconductor capacitance and inductance calculations grow nearly as nm where m is the number of conductors. For practical problems which require as many as 10,000 panels or filaments, FASTCAP and FASTHENRY are more than two orders of magnitude faster than standard boundary-element

¹⁵ S.D. Senturia, R.M. Harris, B.P. Johnson, S. Kim, K. Nabors, M.A. Shulman, and J.K. White, "A Computer-Aided Design System for Microelectromechanical Systems (MEMCAD)," *IEEE J. Microelectromech. Syst.* 1(1): 3-13 (1992); J. R. Gilbert, P.M. Osterberg, R.M. Harris, D.O. Ouma, X. Cai, A. Pfajfer, J. White, and S.D. Senturia, "Implementation of a MEMCAD System for Electrostatic And Mechanical Analysis of Complex Structures From Mask Descriptions," *Proceedings of the IEEE Micro Electro Mechanical Systems Conference*, Fort Lauderdale, Florida, February 1993.

¹⁶ J. Phillips, H. van der Zant, J. White, and T. Orlando, "Influence of Induced Magnetic Fields on the Static Properties of Josephson-Junction Arrays," *Phys. Rev. B*. Forthcoming.

based programs.¹⁷ Manuals and source code for FASTCAP and FASTHENRY are available directly from MIT.

1.10 Techniques for Logic Synthesis, Formal Verification and Testing

Sponsors

Defense Advanced Research Projects Agency/
U.S. Navy - Office of Naval Research
Contract N0014-91-J-1698
IBM Corporation Grant/Fellowship

Project Staff

Professor Srinivas Devadas, Mazhar M. Alidina,
Vishal L. Bhagwati, Kelly S. Bai, Stan Y. Liao, Jose
C. Monteiro, Amelia H. Shen, Dr. Filip J. Van Aelten

1.10.1 Introduction

The design of microelectronic integrated circuits is a complex process because the final product must meet many different requirements and specifications. Specifications concerning the size and performance of a circuit are invariably placed on the design process. For example, reliability restrictions requiring that a circuit be testable for a chosen fault model place limitations on the design process. With an increasing number of transistors being fabricated within a small area on a silicon substrate, the power consumption of a circuit has become a very important design parameter. Indeed, within the next decade, the power consumed by a circuit may soon become the fundamental constraint limiting the density, i.e., transistors per unit area, of integrated circuits. At MIT, we are working on various aspects of the problem of designing integrated circuits for low power consumption. Some solutions include efficient power estimation methods as well as automated methods for logic optimization directly targeting low power consumption in the optimized circuit.

In addition, a circuit being designed must be checked for correct functionality and must meet performance goals. Formal verification methods can guarantee correctness of the design—however, a successful and practical method must be efficient and use a realistic circuit model. We are addressing various verification problems at the architectural, logic, and circuit levels. These problems include verification of pipelines, combinational logic verification, and asynchronous circuit verification. Verifying asynchronous circuits is particularly difficult since a sequential circuit must be directly checked for correct functionality, while in the synchronous case one can separate the combinational logic of the synchronous circuit from the memory elements. For instance, verifying the functionality of an asynchronous circuit requires timing simulation on the combinational logic to identify the presence of hazards that might cause its malfunction.

In the following sections, we will describe our recent work in the areas of design for low power consumption and formal verification techniques.

1.10.2 Design for Low Power Consumption

Probabilistic Power Estimation

We have addressed the problem of estimating the average switching activity of VLSI sequential circuits under random input sequences. We have developed a model that can be used to gauge the power dissipation of the sequential circuit and to make architectural or design-style decisions during the VLSI synthesis process.

Because switching activity is strongly affected by gate delays, we have used a general delay model in estimating switching activity. This model considers glitching at gate outputs in the circuit while modeling the inertial delay of a gate. Our method considers correlation caused at internal gates in a circuit due to reconvergence of input signals. In combinational circuits, uncorrelated input patterns with uniform switching rates are typically assumed, simplifying the problem of switching activity esti-

¹⁷ K. Nabors, S. Kim, and J. White, "Fast Capacitance Extraction of General Three-Dimensional Structures," *IEEE Trans. Microwave Theory Tech.* 40(7): 1496-1507 (1992); K. Nabors, T. Korsmeyer, and J. White, "Multipole Accelerated Preconditioned Iterative Methods for Three-Dimensional Potential Integral Equations of the First Kind," *SIAM J. Sci. Stat. Comp.* Forthcoming; K. Nabors, and J. White, "Multipole-Accelerated 3-D Capacitance Extraction Algorithms for Structures with Conformal Dielectrics," *Proceeding of the 29th Design Automation Conference*, Anaheim, California, June 1992, pp. 710-715; M. Kamon, M. Tsuk, C. Smithisler, and J. White, "Efficient Techniques for Inductance Extraction of Complex 3-D Geometries," *Proceedings of the International Conference on Computer-Aided Design*, Santa Clara, California, November 1992, pp. 438-442; J.R. Phillips, M. Kamon, and J. White, "An FFT-Based Approach to Including Non-ideal Ground Planes in a Fast 3-D Inductance Extraction Program," *Proceedings of the Custom Integrated Circuits Conference*, San Diego, California, May 1993; M. Kamon, K. Nabors, and J. White, "Multipole-Accelerated 3-D Interconnect Analysis," (Invited paper) *Proceedings of the International Workshop on VLSI Process and Device Modeling (VPAD)*, Nara, Japan, May 1993.

mation. However, in sequential circuits the input sequence applied to the combinational portion of the circuit is highly correlated because some of the inputs to the combinational logic are flip-flop outputs representing the state of the circuit. We have developed approximate methods to probabilistically estimate switching activity in sequential circuits that automatically compute switching rates and correlations between flip-flop outputs.

Ongoing work includes relaxing our current assumptions in sequential circuit power estimation and improving the efficiency of our algorithms.

Combinational Logic Synthesis

We are also investigating the use of retiming methods to improve power dissipation. In our experiments with probabilistic power analysis, we noted that power consumption depended significantly on the gate-level structure of a combinational or sequential circuit. Then we became interested in gauging exactly what logic structures corresponded to low power realizations. With this information we can tailor a logic optimization strategy to produce circuit topologies that consume the least amount of power.

We have developed several strategies to optimize a combinational circuit to lower its power consumption: (1) timing optimization and V_{DD} scaling, (2) selective collapsing, (3) don't-care-based minimization, and (4) implementation as a disjoint cover.

In Method 1, the circuit is restructured for maximum speed, and then the power supply voltage V_{DD} is lowered while increasing the delay of the circuit to the maximum allowed delay. Power consumption for the reduced V_{DD} circuit is lowered because power is proportional to V_{DD}^2 . In Method 2, the delay of the circuit is maintained constant, but portions of the circuit that are not on the critical path are collapsed into two levels of logic, reducing power dissipation. In Method 3, observability don't-cares are used to minimize the internal gates in the circuit. Minimization alters the signal probabilities at the gate outputs in a manner such that power consumption is reduced. In Method 4, the circuit is implemented as a disjoint two-level cover, where each AND gate is disjoint from all other AND gates—this is a minimal power realization.

Experimental results on a variety of examples are extremely encouraging. Method 2 resulted in the circuits with the lowest power dissipation.

Sequential Logic Synthesis

We are exploring methods to optimize sequential circuits for low power consumption. In particular, we are developing methods for the state assignment of finite state machines that result in low power dissipation. For instance, if a state s_2 can be reached by many input vectors from state s_1 , to minimize power, a good heuristic is to assign s_1 and s_2 uni-distant codes. The combinational logic of the state-encoded machine can be optimized using techniques described in the previous section to obtain a minimal power circuit realization.

1.10.3 Formal Verification Techniques

Pipeline Verification

It is difficult to verify a behavioral specification against a logic-level implementation since the logic-level implementation can be serial, parallel, or pipelined implementation of the behavioral description. We are investigating automatic methods for verifying pipelined implementations against unpipelined specifications. These methods ensure that each data transfer taking place upon the execution of any instruction in the unpipelined circuit also occurs in the pipelined circuit. In the case where data dependence hazards exist, verification requires checking that pipelined circuit contains bypass logic, as well as checking that this logic results in data transferring correctly. Similarly, branch instructions may require purging of the pipeline or disabling of register/memory writes.

A symbolic simulation method is being developed that will efficiently verify pipelined μ -processors against instruction set specifications.

Free Binary Decision Diagrams

We are developing a set of algorithms for (1) the probabilistic construction of free Binary Decision Diagrams from multilevel combinational logic circuits and (2) the Boolean manipulation of free Binary Decision Diagrams.

With the aid of a previously shown result, namely that the equivalence of two free Binary Decision Diagrams can be decided probabilistically in polynomial time, we have developed a set of polynomial-time algorithms to reduce, i.e., remove redundant nodes and subfunctions from a free Binary Decision Diagram. The algorithms have a time complexity of $O(n^2|G|\log(|G|))$ where n is the number of primary inputs to the free Binary Decision Diagram G , $|G|$ is the number of nodes in G ,

and $k \geq 0$ is a constant. We have shown that reduced, ordered Binary Decision Diagram construction methods that exploit the strongly canonical form can be modified to apply to free Binary Decision Diagrams.

A *concat* algorithm that computes a free Binary Decision Diagram corresponding to the Boolean AND of two free Binary Decision Diagrams has been developed and is currently being implemented. This *concat* algorithm along with the *k*-reduce algorithm provides the basis for a Boolean manipulation package that can be used to solve many verification and testing problems.

Asynchronous Circuit Verification

We have addressed the problem of verifying that the gate-level implementation of an asynchronous circuit, with given or extracted bounds on wire and gate delays, is equivalent to a specification of the asynchronous circuit behavior described as a classical flow table.

We have developed a procedure to extract the complete set of possible flow tables from a gate-level description of an asynchronous circuit under fixed or bounded wire delay models. Given an extracted flow table and an initial flow table specification, we have implemented procedures to construct a product flow table to check for machine equivalence, under various modes of operation.

We have considered fundamental and non-fundamental modes of operation. We have taken into account single output change and multiple output change flow tables as well as single input change and multiple input change flow tables. Flow table extraction and equivalence checking procedures have been tailored for each mode of operation and each type of asynchronous flow table.

Under the discretized bounded delay model, where each gate can take on integer delay values within a range, we have developed implicit enumeration methods for verification. These Binary Decision Diagram-based methods do not require explicit representation of each possible flow table corresponding to the circuit with bounded gate delays or explicit enumeration of states in the circuit. These methods are more efficient than the corresponding ones for a continuous delay model.

1.10.4 Publications

Ashar, P., A. Ghosh, and S. Devadas. "Boolean Satisfiability and Equivalence Checking Using General Binary Decision Diagrams." *Integration: VLSI J.* 13(1): 1-16 (1992).

Ashar, P., S. Devadas, and K. Keutzer. "Gate-Delay-Fault Testability Properties of Multiplexor-Based Networks." *Formal Meth. VLSI Des.: Int. J.* Forthcoming.

Bryan, M.J., S. Devadas, and K. Keutzer. "Analysis and Design of Regular Structures for Robust Dynamic Fault Testability." *VLSI Des.: Int. Custom-Chip Des. Simul. Test.* Forthcoming.

Bryan, M.J., S. Devadas, and K. Keutzer. "Necessary and Sufficient Conditions for Robust Stuck-Open Fault Testability in Multilevel Networks." *IEEE Trans. Comput.-Aided Des.* 11(16): 800-803 (1992).

Cheng, K-T., S. Devadas, and K. Keutzer, "Robust Delay-Fault Test Generation and Synthesis for Testability Under a Standard Scan Design Methodology." *IEEE Trans. Comput.-Aided Des.* Forthcoming.

Devadas, S. "Comparing Two-Level and Ordered Binary Decision Diagram Representations of Logic Functions." *IEEE Trans. Comput.-Aided Des.* Forthcoming.

Devadas, S., and K. Keutzer. "Validatable Nonrobust Delay-Fault Testable Circuits Via Logic Synthesis." *IEEE Trans. Comput.-Aided Des.* 11(12): 1559-1573 (1992).

Devadas, S., K. Keutzer, S. Malik, and A. Wong. "Computation of Floating Mode Delay in Combinational Logic Circuits: Practice and Implementation." *IEEE Trans. Comput.-Aided Des.* Forthcoming.

Devadas, S., K. Keutzer, and S. Malik. "Computation of Floating Mode Delay in Combinational Logic Circuits: Theory and Algorithms." *IEEE Trans. Comput.-Aided Des.* Forthcoming.

Devadas, S., K. Keutzer, and S. Malik. "A Synthesis-Based Test Generation and Compaction Algorithm for Multifaults." *J. Electron. Testing: Theory Appl.* Forthcoming.

Devadas, S., K. Keutzer, S. Malik, and A. Wang. "Verification of Asynchronous Interface Circuits with Bounded Wire Delays." *J. VLSI Sig. Process.* Forthcoming.

Ghosh, A., S. Devadas, and A.R. Newton. "Heuristic Minimization of Boolean Relations Using Testing Techniques." *IEEE Trans. Comput.-Aided Des.* 11(9): 1166-1172 (1992).

Ghosh, A., S. Devadas, and A.R. Newton. "Sequential Test Generation and Synthesis for Testability at the Register-Transfer and Logic Levels." *IEEE Trans. Comput.-Aided Des.* Forthcoming.

Meeting Papers

Camposano, R., S. Devadas, K. Keutzer, S. Malik, and A. Wang. "Implicit Enumeration Techniques Applied to Asynchronous Circuit Verification." Paper presented at the 26th Hawaii International Conference on System Sciences, Wailea, Hawaii, January 1993.

Devadas, S., H-F. Jyu, K. Keutzer, and S. Malik. "Statistical Timing Analysis of Combinational Logic Circuits." Paper presented at the International Conference on Computer Design: VLSI in Computers and Processors, Cambridge, Massachusetts, October 1992.

Devadas, S., K. Keutzer, S. Malik, and A. Wang. "Certified Timing Verification and the Transition

Delay of a Circuit." Paper presented at the 29th Design Automation Conference, Anaheim, California, June 1992.

Devadas, S., K. Keutzer, S. Malik, and A. Wang. "Verification of Asynchronous Circuits with Bounded Wire Delays." Paper presented at the International Conference on Computer-Aided Design, Santa Clara, California, November 1992.

Ghosh, A., S. Devadas, K. Keutzer, and J. White. "Estimation of Average Power Dissipation in Combinational and Sequential Circuits." Paper presented at the 29th Design Automation Conference, Anaheim, California, June 1992.

Ghosh, A., A. Shen, S. Devadas, and K. Keutzer. "On Average Power Dissipation and Random Pattern Testability of Combinational Logic Circuits." Paper presented at the International Conference on Computer-Aided Design, Santa Clara, California, November 1992.

Van Aelten, F., S. Liao, J. Allen, and S. Devadas. "Automatic Generation and Verification of Sufficient Correctness Properties of Synchronous Processors." Paper presented at the International Conference on Computer-Aided Design, Santa Clara, California, November 1992.



Professor Donald E. Troxel

Chapter 2. Computer-Integrated Design and Manufacture of Integrated Circuits

Academic and Research Staff

Professor Donald E. Troxel, Gregory T. Fischer, Thomas J. Lohman, Michael B. McIlrath

Graduate Students

Michael L. Heytens, Kyle K. Iwai, Nicole S. Love, Albert R. Woo

Technical and Support Staff

Francis M. Dougherty

2.1 Introduction

Sponsors

Defense Advanced Research Projects Agency

Contract MDA 972 88-K-0008

U.S. Navy

Contract N00174-93-C-0035

Computer-Aided Fabrication Environment (CAFE) is a software system being developed at MIT for use in the fabrication of integrated circuits (IC) and microstructures. The distinguishing feature of CAFE is that it can be used in all phases of process design, development, planning, and manufacturing of integrated circuit wafers. CAFE presently provides day-to-day support to research and production facilities at MIT with both flexible and standard product capabilities. This manufacturing software system is unique because a process flow representation (PFR) has been developed and integrated into actual fabrication operations. CAFE provides a platform for work in several active research areas including "technology" (process and device) computer-aided design (TCAD), process modeling, manufacturing quality control, and scheduling.

2.1.1 Architecture

The CAFE architecture is a computer integrated manufacturing (CIM) framework for the deployment and integration of integrated circuit and process design and manufacturing software. CAFE uses an object-oriented database model which is implemented in a layered manner on top of a relational database. Our database schema is based on

GESTALT, an object-oriented, extensible data model. GESTALT is a layer of abstraction which maps user defined objects onto existing database systems (e.g., a relational database management system) while shielding application programs from the details of the underlying database. The integration architecture includes conceptual schema and models used to represent the integrated circuits manufacturing domain in CAFE and user and programmatic interfaces to the various applications. Two important CAFE applications relate process simulation and actual wafer fabrication to the same PFR.

2.1.2 CAFE Applications

The fabrication of wafers with a process represented as a PFR involves several steps. A suitable PFR for the specific process must be created and installed. Then wafer lots must be created and associated with this specific PFR. These lots must then be "started" to create a task data structure which is isomorphic to the hierarchical structure of the PFR.

At this point, actual machine operations can be scheduled and reservations made for both machines and operators. Finally, machine operations can be performed, instructions given to the operator and machines, and data collected from the operator or machine and entered into the database.

Current work involves implementing hierarchical scheduling and using PFR for real time process control and integration of a mechanical TCAD system.

2.2 Principal Objectives

The primary objectives for 1992 were (1) evaluation of the results of the initial experiments with fabrication via PFR, (2) development of applications and improvements responsive to the initial users' comments and suggestions, (3) integration of these improvements into CAFE, and (4) continued use of PFR fabrication for lots using the CMOS baseline process. A fifth objective was to develop an application to serve as the initial integration of the Run-by-Run (RbR) control project into the CAFE software system.

2.3 Principal Accomplishments

2.3.1 Implementation of PFR-based Fabrication

The fabrication of wafers with a process represented as a PFR involves several steps. A suitable PFR must be created and installed to create persistent flow objects. The tree structure of these flow objects reflects the hierarchical decomposition of PFR encoding. Wafer lots must then be created and associated with this PFR. These lots are then "started" to create a task data structure which is isomorphic to the flow data structure. The tasks point to flow objects, and these tasks are used to record lot specific information because multiple lots are usually fabricated from a single flow. At this point, actual machine operations can be scheduled and reservations made for both machines and operators. Finally, the actual machine operations can be performed, instructions given to operator and machines, and data collected from operator or machine and entered into the database.

2.3.2 Processing of All CMOS Baseline Defect Array Lots via PFR

Several lots have been processed via PFR for the MIT CMOS baseline process. All future fabrication runs of the MIT CMOS baseline process used to process test lots known as defect array (DA) lots will be processed with the aid of our PFR-based fabrication. All operations are driven by the CAFE system using a PFR-based representation of the process. Settings and operator instructions are displayed (some are downloaded automatically), and specified readings and data are collected via operator entry or, in some cases, automatically. Both types of information are stored in the GESTALT database. The report generators access the database to retrieve the data and present it in a form suitable for the user.

2.3.3 Development of PFR-based Split Lot Processing Capabilities

We have augmented the MIT PFR to include a mechanism for user specified split lot processing. Users can now specify which wafers in a lot are to be processed by a subflow. With this mechanism, users can specify different parameters or, indeed, completely different processing for individual wafers or groups of wafers.

2.3.4 Traveler and "Op-set" Report Generators In Use

We have completed projects to produce report generators to replace the traveler and "Op-set" reports now in use in our Integrated Circuits Laboratory (ICL) and Technology Research Laboratory (TRL). The traveler reports provide a succinct summary of the current state of processing for a lot augmented with details concerning past and planned special activities. These include (1) when the lot was put on hold, (2) reasons for putting the lot on hold, and (3) what was done to remove the hold status. The Op-set reports are more expansive, including details of processing, recipes used, operator instructions gleaned from PFR, and measurements and other data that were collected in accordance with the PFR used for processing the lot.

2.3.5 Initial Integration of Run-by-Run Control into CAFE

Applications implementing a first integration of RbR process control into the MIT Computer Integrated Manufacturing (CIM) system (CAFE) have been developed. Object oriented data structures have been designed and implemented to support the setup of the RbR control project and ongoing control calculations. The actual processing of wafers is conducted via PFR-based fabrication applications.

This initial control experiment uses a simple process consisting of a pre-process measurement, an oxide etching step, and a post-process measurement. A Nanospec is used for both measurements, and data sent via the RS 232 interface for the Nanospec are automatically collected and stored in the database in accordance with information specified in a PFR. A LAM Model 590 plasma etcher is interfaced to a PC via a SECS II RS 232 link. Etch recipes are uploaded and downloaded to a disk on the computer running CAFE via PCNFS. The soft-

ware which dynamically modifies the etch recipes runs under the CAFE CIM system.

The CAFE system was intended to be used in all phases of process design, development, planning, and manufacturing of integrated circuits. CAFE was to provide a platform for work in TCAD, process modeling, and manufacturing quality control. A requirement for the CAFE architectural framework was to support a wide variety of software modules, including both development tools and on-line applications. The key components of the CAFE architecture are the data model and database schema, user interface, process flow and wafer representations, and application programming and database interfaces.

Particular emphasis was placed on the use of a single PFR to drive both simulation and fabrication and the actual use of PFR-based fabrication in our ICL.

2.3.6 CAFE Installed and Operational at Case Western Reserve University

The CAFE software system has been successfully installed at Case Western Reserve University in Cleveland, Ohio. The hardware configuration consists of a Sun Sparc 2 Workstation with 48 megabytes of memory and a 1 gigabyte disk. This installation required purchase of an INGRES license. Installation was accomplished via network. Several days of familiarization and system manager training were provided at MIT for Case personnel.

2.3.7 PFR-driven Simulation Manager

We have developed a rather remarkable system for the simulation of IC processing from our PFR. Users can enter and/or edit their process flow representation and then run SUPREM III simulations without knowing it specifically. A key feature of this software is the "validator" which checks the validity of previous simulation computations and retains any valid computations after the PFR has been modified. Thus computation time is minimized while maintaining correctness of the final simulations. This software also allows the user to conveniently generate reports, such as plots of impurity concentrations and calculations of sheet resistance, etc.

2.3.8 Dynamic Modification of PFR-based Fabrication Provided

Initial experience with PFR-based fabrication resulted in user requests for applications to enable dynamic modification of fabrication plans. Users wanted to be able to skip planned operations, as well as to insert new operations (or sequences of operations) at arbitrary points in the processing plan. In addition, users wanted to revise their processing plan (and its associated PFR) and fabricate according to this new plan as if it had been in effect from the start. A restart lot mechanism has been provided which permits a user to initiate processing with the best estimate of all future processing. If, in the course of fabrication processing, the user realizes that some modifications are required for future processing of this lot, then the user can edit the PFR and initiate the restart lot operation. The restart lot function will verify that the new PFR calls for precisely the same fabrication operations as the former PFR for all processing that has already been accomplished. This check ensures that actual, completed processing history is not changed. If it is, then this restart lot operation fails; and the program informs the user. If the new PFR passes this test, then the former task structure is deleted and replaced by a new task structure corresponding to the new PFR.

2.3.9 X-based PFR Flow and Task Browser Enables Global View of Hierarchical Structure

An X-based application enables users to browse through the tree structures of either installed PFR flows or the tasks associated with a lot being processed with a PFR-based flow. In addition to providing the user with a more global perspective than provided by individual machine operations, this browser enables detailed examination of task or flow attributes at any point in the hierarchy. It also enables users to easily specify tasks to be skipped and places in the task hierarchy for insertion of additional flows.

2.3.10 User Friendly Hold Application Developed

A fabform-based application has been developed to facilitate the creation of a PFR appropriate to the specification of a hold status for a lot. This application queries the user and collects the reason for placing the lot on hold as well as the necessary conditions for removing the lot from the hold status. A new PFR is then automatically generated, installed, and the corresponding task tree is gener-

ated and installed in the task structure associated with the lot. In a subsequent operation, an operator will be presented with this information and, when the hold status is removed, the operator will enter the appropriate information as specified in this new PFR subflow.

2.3.11 GESTALT Extended to Support Inheritance and CLOS

The current version of GESTALT now supports inheritance and provides transparent access to persistent objects, which are described and manipulated solely via CLOS constructs. This transparency simplifies applications programming, as it frees the programmer from the task of translating between programming language structures and database structures, which is required in many systems. Applications programmers may utilize the rich object modeling, generic functions, interactive debuggers, interpreters, etc., present in the CLOS environment to further simplify programming.

2.4 Process Flow Representation

Project Staff

Michael B. McIlrath, Professor Donald E. Troxel

The objective of this project is the development of a Process Flow Representation (PFR) for the integration of technology (process and device) CAD (TCAD) into integrated circuits semiconductor computer-integrated manufacturing (CIM). The effort has proceeded on three major fronts: fundamental modeling, application to process design and fabrication at MIT, and cooperative work with industry to define and test a process representation standard.

For high performance computing systems and other advanced technology, concurrence in the design of the product, manufacturing process, and factory is crucial. The goal is to achieve fully integrated design and manufacture in which the boundary between design and manufacturing domains is eliminated. In particular, information from the manufacturing floor is continuously available from the earliest stages of process and device design onward, while the manufacturing process, developed concurrently with the product, continues to undergo design improvement and modification while in production. Computer-integrated design and manufacture (CIDM), therefore, requires a coherent manufacturing process representation capable of storing information from a variety of different knowledge domains and disciplines, and supporting access to this information in a consistent manner.

We believe that our general semiconductor process modeling framework organizes the complexity of this interrelated information and puts our PFR on a sound footing by giving it clear semantics.

A high-level conceptual model for describing and understanding semiconductor manufacturing processing is a crucial element of both the CIDM research program and software frameworks for TCAD and CIM, including the MIT Computer Aided Fabrication Environment (CAFE). Initially a "two-stage" generic process step model was used. This described processing steps in terms of two independent components: (1) an equipment-dependent, wafer-independent stage, which maps equipment settings to physical processing environments, and (2) an equipment-independent, wafer-dependent stage, which relates physical environments to changes in the input wafers. Driven by the needs of process control and optimization research, including sophisticated modeling, design, and experimental model verification, our fundamental conceptual process model has evolved from the two-stage generic process model into one which is part of a more general process modeling framework, in which the earlier two-stage model is a special case. Our approach to process representation for both TCAD and CIM is based on this general modeling framework for semiconductor processing. In this framework, state information (e.g., wafer, environment, and equipment state), and models, or transformations, that describe relationships between state descriptions, are formally identified and described. The purpose of this comprehensive framework is to enable an effective representation that can be used throughout the IC semiconductor process life-cycle, from early conception and design phases through fabrication and maintenance.

In the MIT CAFE system, the PFR is expressed in a textual (ASCII) format and then converted into GESTALT objects and loaded into the CAFE database. The textual language of the PFR is extensible, so that it can flexibly accommodate changes and extensions to both the underlying modeling methodology and the needs of specific applications. The object-oriented nature of the GESTALT database interface enables the convenient evolutionary development of CAFE software applications built around the PFR. The PFR allows process step descriptions to be "underdetermined," for example, by expressing only the wafer-state change, making it possible to develop a process incrementally with increasing degrees of detail. In addition to expressing the fundamental concepts of wafer transformation within individual process steps, the PFR supports both hierarchical and parameter abstraction and embedded computation, thereby

providing support for modular process design and development. Processes expressed in the PFR can be simulated using a variety of technology CAD tools; PFR extensibility allows the incorporation of both simulator-dependent and simulator-independent information. A simulation manager application uses the appropriate information in the PFR along with knowledge of specific simulators to invoke simulation tools and maintain simulation state.

Extensions to the textual PFR and corresponding database schema support specification of individual wafers or wafer sets (sublots or splits) within a lot for processing, and specification of engineering holds at a particular step in the process sequence. An engineering hold might be planned, for example, as part of the fabrication specification for a process which is currently under experimental development. In conjunction with developments in CAFE that support dynamic modification of processes in the fabrication line, the "hold" capability in the PFR can also be used in response to unexpected events that occur during fabrication. With these manufacturing extensions, the PFR is used in the CAFE system at the MIT ICL for the fabrication processes supported by the ICL technical staff, with all processing operations driven by CAFE from the PFR stored in the database.

Work has also proceeded on the definition of a standard semiconductor process representation (SPR) for use in both industry and research fabrications, in association with the industry CAD Framework Initiative (CFI) Technical Subcommittee on Technology CAD in defining broadly applicable TCAD framework standards. Mr. McIlrath is currently the chair of the working group on SPR. Based largely on the conceptual process model described above, a high-level information model of semiconductor processes is being developed in conjunction with Motorola, IBM, Texas Instruments, and other industry and university representatives. A prototype SPR implementation and a programming interface have been developed and employed in an experimental TCAD framework, which included an implementation of the semiconductor wafer representation (SWR), and tools developed by industry and other university researchers. An industry survey of specific itemized requirements for SPR has been completed and published as part of a formal CFI Request for Technology, which identifies mandatory requirements and evaluation criteria for complete SPR proposals now under consideration by the working group.

2.5 Technology CAD Framework

Project Staff

Michael B. McIlrath

Contemporary large-scale software system engineering emphasizes frameworks, wherein common structure and interface specifications enable both current and future software components to be integrated in a flexible and modular way. Software may be roughly divided into tools, such as a simulator, which perform some part of an application task, and services, such as a database, which provide some necessary support capability used by various tools. With framework standards, reusable, interchangeable software components from various suppliers may be deployed in systems which comply with the standard. In the broad sense, a framework standard specifies:

- data representations for the objects of discourse in the application domain and their semantics, and programmatic interfaces to those representations, and
- architecture; that is, interactions among software components (tools and services), and how tools fit together to perform tasks for the user.

Frameworks have been particularly successful in development of electronic circuit CAD systems. Standards for CAD frameworks are currently being established by the CFI, a broad organization of vendor and user companies which has now expanded its scope to include technology (process and device) CAD. A TCAD framework standard includes programming representations for the fundamental objects of process and device CAD: physical structures on the wafer, manufacturing process, and structure and behavior of the resulting devices. A TCAD framework standard also specifies how application software is structured to use these representations and the underlying software services in process and device design and simulation activities.

At present, development of TCAD framework architectural standards is limited to (1) specifications of implementation and interfaces for the wafer and process representations, (2) use of domain-independent framework standards, such as intertool communication (ITC), user interface (UI), and (3) extension language specifications. We are beginning to look at higher level architectural issues, such as the interrelationships between the framework data representations and the connection of compliant tools to achieve end-user design objectives. We are also investigating the larger

questions of the relationship between frameworks for different related domains (e.g., circuit CAD and TCAD), and the integration of design frameworks into frameworks for CIM.

We are currently active as members of the TCAD Technical Subcommittee (TSC) of the CFI, contributing to fundamental modeling, implementation (language and database technology), programmatic interfaces, prototyping development, and relation to overall CIM and TCAD architectural frameworks.

2.6 Publications

Journal Articles

Boning, D.S., M.B. McIlrath, P. Penfield, and E.M. Sachs. "A General Semiconductor Process Modeling Framework." *IEEE Trans. Semicond. Manuf.* 5(4): 266-280 (1992).

McIlrath, M.B., D.E. Troxel, M.L. Heytens, P. Penfield, Jr., D.S. Boning, and R. Jayavant. "CAFE—The MIT Computer-Aided Fabrication Environment." *IEEE Trans. Compon., Hybrids, Manuf. Tech.* 15(2): 353-360 (1992).

Internal Publications

Boning, D.S., and M.B. McIlrath. "Guide to the Process Flow Representation." CIDM Memo 92-1. MIT, 1992.

Fischer, G. *Beginner's Guide to CAFE*. CIDM Memo 92-2. MIT, 1992.

Fischer, G. *Beginner's Guide to Fabrication Using CAFE*. CIDM Memo 92-3. MIT, 1992.

Fischer, G. *Creating Manual Pages for CAFE*. CIDM Memo 92-8. MIT, 1992.

Fischer, G. *Sample PFR Encodings*. CIDM Memo 92-4. MIT, 1992.

Troxel, D.E. *Extract of Schema*. CIDM Memo 92-5. MIT, 1992.

Troxel, D.E. *Iterators and Predicates—Optimizing Data Base Accesses by Filtering at Low Levels*. CIDM Memo 92-6. MIT, 1992.

Troxel, D.E. *Microsystems Factory Representation (MFR)*. CIDM Memo 92-7. MIT, 1992.

Meeting Papers and Presentations

Boning, D.S., D.E. Troxel, M.B. McIlrath, M.L. Heytens, D.A. Antoniadis, and P. Penfield, Jr. "CAFE: A System for VLSI Technology Complexity Management." Presentation at the Seventh Annual SRC/DARPA CIM-IC Workshop, Stanford University, Stanford, California, August 5-6, 1992.

Ha, S., E. Sachs, and D.E. Troxel. "On-Line Control of Uniformity in Single Wafer Plasma Etch Process." (Abstract) Presentation at the Seventh Annual SRC/DARPA CIM-IC Workshop, Stanford University, Stanford, California, August 5-6, 1992.

McIlrath, M.B., and G. Chin. "Semiconductor Process Representation and Device Design." Paper presented at the Proceedings of the IEEE International Electronics Technical Conference (ELECTRO/92), Boston, Massachusetts, May 12-14, 1992.

McIlrath, M.B. "Semiconductor Process Representation and Device Design." Presentation at the IEEE International Electronics Technical Conference (ELECTRO/92), Boston, Massachusetts, May 13, 1992.

McIlrath, M.B. "Process Representation for TCAD Frameworks." Presentation at the Conference on CAD for Integrated Circuits, Stanford University, Stanford, California, August 4, 1992.

Troxel, D.E., D.P. McNabb, and M.B. McIlrath. "Dynamically Modified PFR Based Fabrication in a Realistic IC Laboratory." Presentation at the Seventh Annual SRC/DARPA CIM-IC Workshop, Stanford University, Stanford, California, August 5-6, 1992.

Troxel, D.E. "Digital Design Tools." Presentation at the Frontiers in Education 1992 Conference, Nashville, Tennessee, November 11-15, 1992.

Thesis

Heytens, M.L. *The Design and Implementation of a Parallel Persistent Object System*. Ph.D. diss. Dept. of Electr. Eng. and Comput. Sci., MIT, 1992.

Section 2 Digital Signal Processing

Chapter 1 Digital Signal Processing Research Program

Chapter 2 Advanced Television and Signal Processing Program

Chapter 3 Combined Source and Channel Coding for
High-Definition Television

Chapter 1. Digital Signal Processing Research Program

Academic and Research Staff

Professor Alan V. Oppenheim, Professor Arthur B. Baggeroer, Professor Gregory W. Wornell, Giovanni Aliberti

Visiting Scientists and Research Affiliates

Dr. Bernard Gold, Dr. Bruce R. Musicus,¹ Dr. James C. Preisig, Makoto Sakamoto, Dr. Ehud Weinstein²

Graduate Students

Paul E. Beckmann, Saurav Dev Bhatta, John R. Buck, Kevin M. Cuomo, Steven H. Isabelle, Jacek Jachner, Warren M. Lam, James M. Njeru, Haralabos C. Papadopoulos, Brian M. Perreault, James C. Preisig, Michael D. Richard, Stephen F. Scherock, Andrew C. Singer, Shawn M. Verbout, Kathleen E. Wage, Taylen J. Wong, Kambiz C. Zangi

Technical and Support Staff

Sally C. Santiago, Deborah A. Gage

1.1 Introduction

The field of digital signal processing developed because the use of digital computers afforded more flexibility in implementing signal processing algorithms and systems. This field now encompasses a variety of both digital and analog technologies, spanning a wide range of applications, bandwidths, and realizations. The Digital Signal Processing Group at RLE carries out research on algorithms and their applications in signal processing. Currently, we are interested in applying these algorithms to signal enhancement, processing of underwater acoustic signals, advanced beamforming for radar and sonar systems, and signal coding and transmission.

In some of our recent work, we have developed new methods for signal enhancement and noise cancellation with single or multisensor measurements. We have also been developing new methods for representing and analyzing fractal signals. This class of signals, which occurs in a wide variety of physical environments, has potential application in problems involving signal design. We are also exploring potential applications of nonlinear dynamics and chaos theory for signal design and analysis.

In other research, we are investigating applications of signal and array processing to ocean and structural acoustics and geophysics. These problems require the combination of digital signal processing tools with knowledge of wave propagation to develop systems for short-time spectral analysis, wavenumber spectrum estimation, source localization, and matched field processing. We emphasize the use of real-world data from laboratory and field experiments such as the Heard Island Experiment for Acoustic Monitoring of Global Warming and several Arctic acoustic experiments conducted on the polar ice cap.

The DSP group is also involved in research on broadband and secure communication systems. These activities include the development of spread spectrum and multiple-access communication systems exploiting sophisticated signal processing algorithms, used in, for example, personal wireless systems.

Much of our work involves close collaboration with the Woods Hole Oceanographic Institution, MIT Lincoln Laboratory, and a number of high technology companies in the Boston area.

¹ Bolt, Beranek, and Newman, Inc., Cambridge, Massachusetts.

² Department of Electrical Engineering, Systems Division, Faculty of Engineering, Tel-Aviv University, Israel; adjunct scientist, Department of Applied Ocean Physics and Engineering, Woods Hole Oceanographic Institution, Woods Hole, Massachusetts.

1.2 Oceanographic Signal Processing

Sponsor

U.S. Navy - Office of Naval Research
Grant N00014-91-J-1628

Project Staff

Professor Arthur B. Baggeroer

Our research programs in this area involve the application of signal and array processing to problems in ocean acoustics and geophysics. These problems require an understanding of both signal processing and wave propagation; moreover, most rely on data from laboratory or field experiments, so an appreciation of real world issues such as noise, sensor calibrations and modeling errors is needed. Several of the topics provide the opportunity to participate in oceanographic cruises.

1.2.1 Acoustic Thermometry of Ocean Climate

The Heard Island Feasibility Test demonstrated that coded acoustic signals can be transmitted over 10,000 km ranges. This test led to the Acoustic Thermometry of Ocean Climate (ATOC) program, which is funded by the Defense Advanced Projects Agency (DARPA). A network of acoustic sources and receivers will be deployed in the Pacific, Atlantic, and Indian Oceans to monitor them by measuring changes in acoustic travel times. These changes will be used to infer temperature changes.

1.2.2 Signal Processing for Large Aperture Arrays

There is extensive literature on the subject of adaptive processing for arrays with small numbers of sensors. However, when an array has a large number of sensors, some problems can result. The main problem is that the statistical characterization of the ambient field requires an amount of data which exceeds the short-term stationarity of the field. Introducing adaption by adding sensors can lead to lower quality performance because additional degrees of freedom are not well characterized. Our research develops adaptive array processing algorithms which incorporate the statistical characterization of the ambient field with a large number of sensors.

1.2.3 Matched Field Processing

Project Staff

Kathleen E. Wage, Professor Arthur B. Baggeroer

Matched field processing is used in underwater acoustics for processing data from large arrays when the inhomogeneity of the signal field is important. It is particularly applicable to vertical arrays used for low frequency, long-range propagation. Two major applications of matched field methods are to determine: (1) the location (range, depth and bearing) of an acoustic source; and (2) the sound speed of the acoustic channel when the location of the source and receiver (tomography) are known. Matched field processing can improve the resolution performance of an array by a factor of 100 by exploiting coherence among the multipath, or modes, in acoustic propagation. Some of our important research topics include (1) developing robust methods which are tolerant of environmental uncertainties and (2) determining "optimum array geometries" and adaptive processing which incorporates the mesoscale dynamics of the ocean.

1.3 Segmentation of Polarimetric Synthetic Aperture Radar Images Using Markov Random Field Techniques

Sponsors

Defense Advanced Research Projects Agency/
U.S. Navy - Office of Naval Research
Grant N00014-89-J-1489
MIT - Woods Hole Oceanographic Institution
Joint Program

Project Staff

Saurav Dev Bhatta, Dr. Jacques Verly, Professor
Alan V. Oppenheim

Synthetic Aperture Radar (SAR) images constitute one major class of speckled images. Speckle obscures boundaries, so the goal of segmentation is to recover obscured regions from the speckled images. Derin and Kelly³ and their colleagues at the University of Massachusetts at Amherst have developed and tested a technique, which uses Markov Random Field models to segment speckled images. We are developing a method for segmenting Polarimetric SAR (POL-SAR) images, which is based on

³ H. Derin, P.A. Kelly, G. Vezina, and S.G. Labitt, "Modelling and Segmentation of Speckled Images Using Complex Data," *IEEE Trans. Geosci. Remote Sens.* (28 (1): 76-87 (1990).

the technique developed at University of Massachusetts.

The image model used here consists of a two-level hierarchical process that makes use of the fact that speckle exhibits spatial correlation. The first level, called the Region Process, is characterized by a Markov Random Field (MRF) that groups the pixels of the image into regions. The second level, the Speckle Process, is characterized by another random field (not necessarily MRF) peculiar to the region under consideration. The two types of processes are independent of each other and between themselves. Only the Speckle Process is observable. The precise details of the Speckle Process depend upon the kind of imagery under consideration: amplitude (complex) versus intensity (real) and single-look versus multilook.

The algorithm is based on a Maximum a Posteriori (MAP) formulation to estimate segmentation (which is the underlying Region Process), given the observation data (which is directly related to the Speckle Process). In particular, the Simulated Annealing (SA) procedure is used to obtain the MAP estimate of the regions of the image. This algorithm proceeds in a series of iterations, each consisting of an estimation of the necessary region and speckle parameters followed by segmentation based on these estimated parameters. The algorithm is adaptive, estimating necessary parameters automatically, when given the number of regions in the image.

1.4 Signal Synthesis from Marine Mammal Communications

Sponsors

Defense Advanced Research Projects Agency/
U.S. Navy - Office of Naval Research
Grant N00014-89-J-1489
MIT - Woods Hole Oceanographic Institution
Joint Program

Project Staff

John R. Buck, Professor Alan V. Oppenheim, Dr. Josko Catipovic

Marine mammals such as whales and dolphins utilize a wide variety of sounds for underwater acoustic communication while engaging in a variety of complex social behaviors. It is appealing to speculate that millenia of evolution have brought these animals to the point where their signals are in

some sense optimum for the underwater environment. By studying their signals, we hope to discover which features make the signals well-suited for the underwater acoustic environment and under which criteria, if any, the signals are optimal. The knowledge we gain by analyzing the biological signals should indicate an approach for synthesizing new optimal signals for underwater communications.

1.5 Analysis, Synthesis, and Applications of Synchronized Chaotic Systems

Sponsors

Defense Advanced Research Projects Agency/
U.S. Navy - Office of Naval Research
Grant N00014-89-J-1489
Lockheed Sanders, Inc./U.S. Navy
Office of Naval Research
Contract N00014-91-C-0125
U.S. Air Force - Office of Scientific Research
Grant AFOSR-91-0034

Project Staff

Kevin M. Cuomo, Professor Alan V. Oppenheim

Chaotic systems provide a rich mechanism for signal design and generation for communications and a variety of signal processing applications. Because chaotic signals are typically broadband, noiselike, and difficult to predict, they can be utilized in various contexts for masking information-bearing waveforms and as modulating waveforms in spread spectrum systems. It is often desirable to utilize high-dimensional chaotic systems with specified characteristics. However, there is a practical difficulty because the analysis and synthesis of chaotic systems is not well understood due to their highly nonlinear nature. A significant challenge and opportunity exists for exploring and developing new methods for chaotic signal generation and detection.

One objective of this research is to develop theoretical and numerical techniques for synthesizing a class of high-dimensional chaotic systems. Another objective is to develop methods for embedding an information-bearing waveform in a chaotic carrier signal and then recovering the information at the receiver. We show that synchronized chaotic systems (SCSs) are well-suited to this problem because SCSs possess a self-synchronization prop-

erty.⁴ We also show that chaotic signal masking allows analog signals to be privately transmitted and recovered at the intended receivers.⁵ In Cuomo and Oppenheim,⁶ we show that digital bit streams can be privately communicated by modulating a transmitter coefficient with the information waveform and detecting the modulation with an SCS at the receiver.

1.6 High-Resolution Direction Finding for Multidimensional Scenarios

Sponsor

U.S. Navy - Office of Naval Research
Grant N00014-91-J-1628

Project Staff

Jacek Jachner, Professor Alan V. Oppenheim, Dr. Harry B. Lee

Recently, there has been considerable interest in applying high-resolution techniques for direction finding (DF) and time series analysis. Results from the research of Lee and Wengrovitz,⁷ have improved our understanding of high-resolution direction finding techniques in the following areas:

- Beamformer design for beamspace approaches;
- Analytical expressions for the threshold SNR at which algorithms can resolve closely-spaced sources;
- Cramer-Rao lower bounds on the variances of unbiased estimators of direction;
- Covariance matrix eigenstructure for closely-spaced sources.

The results are applicable to far-field planar scenarios in which the location of each source is specified by a single angular parameter.

Many practical applications of DF techniques are multidimensional in nature, requiring estimation of a vector of parameters. For example, two angular parameters are necessary in 3-D far-field problems (azimuth, elevation). Three parameters may be required in some 3-D emitter localization problems (range, azimuth, elevation). Extension of 1-D approaches to multi-D is not always direct, as several high-resolution techniques, including MinNorm and minimum dimension Beamspace algorithms, fail to uniquely locate sources for multi-dimensional scenarios. This research explores the multidimensional direction finding problem and extends recent 1-D results to multi-D scenarios.

1.7 Signal Processing Applications of Chaotic Dynamical Systems

Sponsors

AT&T Laboratories Doctoral Support Program
Defense Advanced Research Projects Agency/
U.S. Navy - Office of Naval Research
Grant N00014-89-J-1489
Lockheed Sanders, Inc./U.S. Navy
Office of Naval Research
Contract N00014-91-C-0125
U.S. Air Force - Office of Scientific Research
Grant AFOSR-91-0034

Project Staff

Steven H. Isabelle, Professor Alan V. Oppenheim

Researchers in areas ranging from animal behavior and medicine to economics and geophysics have found evidence of chaotic behavior in an enormous number of empirically gathered time series. Indeed, the sheer volume of apparently random phenomena which appear to have a deterministic explanation underscores the need for signal processing techniques specifically tailored to the unique characteristics of chaotic signals. In particular, because chaotic signals can generally be observed

⁴ L.M. Pecora and T.L. Carroll, "Synchronization in Chaotic Systems," *Phys. Rev. Lett.* 64(8): 821-824 (1990); T.L. Carroll and L.M. Pecora, "Synchronizing Chaotic Circuits," *IEEE Trans. Circuits Syst.* 38(4): 453-456 (1991).

⁵ K.M. Cuomo, A.V. Oppenheim, and S.H. Isabelle, *Spread Spectrum Modulation and Signal Masking Using Synchronized Chaotic Systems*, RLE TR No. 570 (Cambridge: MIT Research Laboratory of Electronics, 1992); A.V. Oppenheim, G.W. Wornell, S.H. Isabelle, and K.M. Cuomo, "Signal Processing in the Context of Chaotic Signals," *Proc. IEEE ICASSP-92*, March 1992.

⁶ K.M. Cuomo and A.V. Oppenheim, *Synchronized Chaotic Circuits and Systems for Communications*, RLE TR No. 575. (Cambridge: MIT Research Laboratory of Electronics, 1992).

⁷ H.B. Lee and M.S. Wengrovitz, "Resolution Threshold of Beamspace MUSIC for Two Closely Spaced Emitters," *IEEE Trans. ASSP*, 38(9): 1545-1559 (1990); H.B. Lee and M.S. Wengrovitz, "Beamformer Preprocessing for Enhanced Resolution by the MUSIC Algorithm," *IEEE Trans. ASSP*, forthcoming; H.B. Lee, "The Cramer-Rao Bound on Frequency Estimates of Signals Closely Spaced in Frequency," *IEEE Trans. ASSP*, forthcoming.

only indirectly, e.g., through some propagation channel or nonideal laboratory instrumentation, a signal's chaotic structure may be partially obscured by additive noise and convolutional distortion. Consequently, algorithms for reducing this distortion are an important component of signal processing systems for chaotic signals. This research explores the effect of convolutional distortion on chaotic signals along with techniques for reducing such distortions.

In general, the limiting trajectory of a chaotic system will be a highly structured set in the state space, while the scalar output will appear erratic and unstructured. It is this "hidden" structure that makes the signal interesting and allows for a simple description. One measure of structure which has been used to characterize a chaotic signal is the fractal dimension of its strange attractor. We are examining the effect of convolution on fractal dimension and using these results to develop deconvolution algorithms. The major challenge here is developing optimal computationally efficient techniques which are uniformly applicable to a broad class of chaotic signals.

1.8 Wavelet-Based Representation and Algorithms for Generalized Fractal Signals

Sponsors

AT&T Laboratories Doctoral Support Program
 Defense Advanced Research Projects Agency/
 U.S. Navy - Office of Naval Research
 Grant N00014-89-J-1489
 Lockheed Sanders, Inc./U.S. Navy
 Office of Naval Research
 Contract N00014-91-C-0125
 U.S. Air Force - Office of Scientific Research
 Grant AFOSR-91-0034

Project Staff

Warren M. Lam, Professor Gregory W. Wornell

While the $1/f$ family of fractal processes have become increasingly appealing for modeling statistically scale-invariant phenomena, we study a generalization of this signal model to account for more general scaling behavior found in a wide variety of

natural phenomena. Many phenomena exhibit scaling behavior, but a great number of them do this only over a finite range of scales. For example, while seafloor morphology is observed to be self-similar at fine scales, such scaling behavior is absent in long-length scales due to the lack of correlation among points far apart.⁸ On the other hand, many phenomena exhibit scaling behavior which varies over scales. For instance, such varying scaling behavior is encountered in the study of diluted gels and colloidal aggregates in the field of materials science.⁹

In this work, we focus on the development of a class of generalized fractal processes for capturing such nonuniform scaling behavior. Exploiting the role of the wavelet transformation as a whitening filter for these kinds of processes, we formulate algorithms for addressing a number of practical estimation problems involving these signals. Adopting a maximum-likelihood criterion and invoking an estimate-maximize algorithm, we derive consistent, computationally efficient spectral parameter estimators which are useful for the classification of generalized fractals. We also formulate a Bayesian minimum mean-squares error signal estimation scheme which is directly applicable in a variety of signal separation and signal recovery scenarios.

1.9 Acoustic Tomography through Matched Field Processing

Sponsors

Defense Advanced Research Projects Agency/
 U.S. Navy - Office of Naval Research
 Grant N00014-89-J-1489
 MIT - Woods Hole Oceanographic Institution
 Joint Program

Project Staff

James M. Njeru, Dr. James C. Preisig, Dr. James F. Lynch

Ocean Acoustic Tomography is a technique in which sound is transmitted through the sea and, based on the received signal, inferences about properties of the ocean are made. Traditional ocean acoustic tomography has relied on travel time measurements of the signal to infer properties such as sound speed profiles and currents.

⁸ J.A. Goff and T.H. Jordan, "Stochastic Modeling of Seafloor Morphology: Inversion of Sea Beam Data for Second-Order Statistics," *J. Geophys. Res.* 93 (B11): 13589-13608 (1988).

⁹ M. Fleischmann, D.J. Tildesley, R.C. Ball, eds., *Fractals in the Natural Sciences* (Princeton, New Jersey: Princeton University Press, 1989), pp. 35-53.

In this work, we explore the viability of exploiting more than travel time information embedded in the received signal to make tomographic inferences. Using efficient signal processing algorithms, we will initially focus on frontal location (a front is a region where an ocean sound speed profile suddenly changes). Data acquired during the Barents Sea Experiment of 1992 will be used in this investigation.

1.10 Binary Data Transmission and Detection with Chaotic Signals

Sponsors

Defense Advanced Research Projects Agency/
U.S. Navy - Office of Naval Research
Grant N00014-89-J-1489
U.S. Air Force - Office of Scientific Research
Grant AFOSR-91-0034

Project Staff

Haraibos C. Papadopoulos, Professor Gregory W. Wornell

Chaotic waveforms provide a rich family of signals whose behavior and properties are currently being explored in various signal possessing contexts. Classical signal processing corresponds to processing signals that are either deterministic and predictable or stochastic. Chaotic signals provide a qualitatively different workspace. Signals generated from chaotic systems are not predictable even though they are completely deterministic. These signals are very sensitive to infinitesimal changes in initial conditions, so that long-term predictability is impossible. Chaotic waveforms provide excellent candidates for use in a variety of contexts in signal processing due to their resemblance to random signals and their ease of implementation.

In this project, we are considering a very common problem in classical signal processing: the transmission of a binary data stream via waveform representation. Chaotic signals are introduced in coding the binary stream. Chaotic waveforms may prove very powerful in this context due to their ease of implementation, noiselike appearance, and broadband spectra. The signals used in such communication schemes have distinct dynamical behavior and characteristics. Given a sequence of noisy observations, we may readily set up a binary hypothesis test in order to detect the original binary stream.

A previously implemented preliminary heuristic detection algorithm shows that signal detection with sufficiently high SNR may be accomplished if sufficiently long-sequence representations are used. More sophisticated algorithms are explored which take into account properties of the distinct dynamical behavior of the chaotic signals that are used to code the binary stream.

1.11 Real-Time Active Noise Cancellation

Sponsor

National Science Foundation Fellowship

Project Staff

Brian M. Perreault, Professor Alan V. Oppenheim

In many industrial and consumer settings, undesirable acoustic noise often exists. In many cases, the noise is obtrusive enough to warrant an effort to reduce its effect. In situations where the noise cannot be reduced using physical passive methods, active noise cancellation (ANC) techniques are a suitable alternative. Many types of noise have certain predictable characteristics; active noise cancellation exploits these characteristics and uses destructive interference from a secondary acoustic source to eradicate the noise.

Many predictive methods used in active noise cancellation are computationally intensive; to employ them in a practical manner, real-time hybrid techniques must be developed. Intelligent tradeoffs must be made between an algorithm's computational efficiency and its predictational effectiveness.

ANC techniques would be highly effective in a plane or helicopter cockpit. Such a setting has very high noise levels, and the noise is, to a certain degree, predictable. A set of headphones, utilizing a microphone and speaker in each ear cup, is being developed to cancel the cockpit noise. This is desirable because passive attenuation provided by headphones without ANC does not compensate for the noise.

Digital predictive techniques are being used in conjunction with analog to digital (A/D) and digital to analog (D/A) converters to implement active noise cancellation techniques. A digital signal processor, which has high computational ability, was employed to execute the algorithms. A flexible set of hardware has been developed to evaluate different ANC algorithms in real time.

1.12 State and Parameter Estimation with Chaotic Systems

Sponsors

Defense Advanced Research Projects Agency/
U.S. Navy - Office of Naval Research
Grant N00014-89-J-1489
U.S. Air Force - Office of Scientific Research
Grant AFOSR-91-0034

Project Staff

Michael D. Richard, Professor Alan V. Oppenheim

Chaotic systems are nonlinear dynamical systems characterized by extreme sensitivity to initial conditions. A signal generated by a chaotic system may appear random, despite its having been generated by a low-order, deterministic dynamical system. Both random and chaotic signals lack long-term predictability; but, in contrast to truly random signals, chaotic signals exhibit short-term predictability. Evidence of chaotic behavior has been reported in many diverse disciplines including physics, biology, engineering, and economics.

We are exploring techniques for state and parameter estimation with chaotic systems. We have implemented the extended Kalman filter,¹⁰ a recursive state estimator for nonlinear systems, and several related algorithms,¹¹ and have evaluated their effectiveness as state estimators for chaotic systems. Preliminary results have shown these algorithms to perform reasonably well. But these results have also shown that these algorithms suffer potentially unacceptable deficiencies when applied to chaotic systems.

More recently, we have developed and begun testing several related, novel, state-estimation techniques loosely motivated by maximum likelihood state estimation.¹² The techniques exploit a distinguishing property of all chaotic systems—the simultaneous existence of stable and unstable manifolds.¹³ The combination of these techniques

with an Estimate-Maximize (EM) algorithm is also being considered. Finally, we plan to ascertain the value of various state-estimation techniques in improving the short-term predictability of chaotic signals.

1.13 Nonlinear Models for Signal Processing

Sponsors

Defense Advanced Research Projects Agency/
U.S. Navy - Office of Naval Research
Grant N00014-89-J-1489
Lockheed Sanders, Inc./ U.S. Navy - Office of
Naval Research
Contract N00014-91-C-0125

Project Staff

Andrew C. Singer, Professor Alan V. Oppenheim

This research involves the use of nonlinear system models in signal processing. Linear models and algorithms have been predominantly employed in this field due to the tractability of their analysis and richness of the class of signals for which these models are well-suited. However, by trading complexity for tractability, we can further broaden the boundaries of signal processing. For example, recently we have shown that nonlinear signal modeling techniques are both useful and practical for modeling a variety of signals for which linear techniques have proven inadequate. Furthermore, we have begun to find practical applications for nonlinear dynamic systems in chaos. Until recently, these applications were considered to be more paradoxical than practical. Another interesting phenomenon, whose curious behavior has crossed many disciplines of science, is the theory of solitons. It is our goal to exploit the behavior of these solitary waves and other nonlinear phenomena in search of new paradigms and new directions in signal processing.

¹⁰ A. Jazwinski, *Stochastic Processes and Filtering Theory* (New York: Academic Press, 1970); M.D. Richard, *State Estimation with Discrete-Time Chaotic Systems using the Extended Kalman Filter*, unpublished technical report, September 1991.

¹¹ A. Willsky, "Course Notes for 6.433 Recursive Estimation," unpublished, 1989.

¹² M.D. Richard, *State Estimation with Discrete-Time Chaotic Systems using the Extended Kalman Filter*, unpublished technical report, September 1991.

¹³ J. Eckmann and D. Ruelle, "Ergodic Theory of Chaos and Strange Attractors," *Rev. Mod. Phys.* 57(3) Part 1: 617-656 (1985).

1.14 Model-Based Analysis of Music

Sponsors

Defense Advanced Research Projects Agency/
U.S. Navy - Office of Naval Research
Grant N00014-89-J-1489
National Science Foundation Graduate Fellowship

Project Staff

Stephen F. Scherrock, Dr. Bernard Gold

Many digital audio signals can be broadly classified as speech or music. Speech signals have been studied extensively since the 1950s for automatic speech recognition, production, and data compression. Work has advanced toward each of these goals in part because of the development of models for speech production and recognition. While physically based models exist for music production, applying these models for synthetic music production or data compression has not been fully exploited. My research involves model-based compression of music from a single instrument, the trumpet.

1.15 Active Noise Cancellation

Sponsors

Defense Advanced Research Projects Agency/
U.S. Navy - Office of Naval Research
Grant N00014-89-J-1489
U.S. Air Force - Office of Scientific Research
Grant AFOSR-91-0034

Project Staff

Kambiz C. Zangi, Professor Alan V. Oppenheim

Unwanted acoustic noise is a by-product of many industrial processes and systems. With active noise cancellation (ANC), one introduces secondary noise sources to generate an acoustic field that interferes destructively with the unwanted noise, thereby eliminating it. Examples of such unwanted noise include machinery noise, aircraft cabin noise, and fan noise.

Traditional active noise cancellation systems assume a priori knowledge of the transfer function from the cancelling speaker to the point where noise cancellation is desired. Furthermore, almost all existing systems use two microphones, and, as a result, suffer from acoustic feedback between the cancelling speaker and input microphone.¹⁴

We have developed an adaptive active noise cancellation system which uses one microphone only and therefore has no feedback problem. This system uses the estimate maximize (EM) algorithm to simultaneously estimate the noise statistic and transfer function between the cancelling speaker and the microphone. An optimal cancelling signal is then generated based on these estimates.¹⁵

We have also developed a two-microphone version of the system mentioned above which does not suffer from a feedback problem and is more intelligent than the existing algorithms in using the outputs of the two microphones.¹⁶

We are currently studying the problem of noise cancellation in a volume. A topic of fundamental interest is to find analytically simple ways to describe the sound field over a volume from measurements made at a finite set of points in that volume. Similarly, we would like to find ways to alter the sound field in a desirable manner using only a finite number of sources.

¹⁴ L.J. Eriksson, M.C. Allie, and C.D. Bremigan, "Active Noise Control Using Adaptive Digital Signal Processing," *Proc. ICASSP*, New York, 1988, pp. 2594-2597.

¹⁵ E. Weinstein, A. Oppenheim, and M. Feder, *Signal Enhancement Using Single and Multi-Sensor Measurements*, RLE TR No. 560 (Cambridge: MIT Research Laboratory of Electronics, 1990); A. Oppenheim, E. Weinstein, K. Zangi, M. Feder, and D. Gauger, "Single Sensor Active Noise Cancellation Based on the EM Algorithm," submitted to *IEEE Trans. Signal Proc.*

¹⁶ K. Zangi, "A New Two Sensor Active Noise Cancellation Algorithm," *Proc. ICASSP*, Minneapolis, Minnesota, 1993.

Chapter 2. Advanced Television and Signal Processing Program

Academic and Research Staff

Professor Jae S. Lim, Dr. David Forney

Graduate Students

John G. Apostolopoulos, Shiufun Cheung, Ibrahim A. Hajjahmad, John C. Hardwick, Kyle K. Iwai, Eddie F. Lee, Peter A. Monta, Aradhana Narula, Julien J. Nicolas, Lon E. Sunshine, Chang Dong Yoo

Technical and Support Staff

Debra L. Harring, Cindy LeBlanc, Giampiero Sciutto

2.1 Introduction

The present television system was designed nearly 40 years ago. Since then, there have been significant developments in technology which are highly relevant to television industries. For example, advances in very large scale integration (VLSI) technology and signal processing theories make it economically feasible to incorporate frame-store memory and sophisticated signal processing capabilities in a television receiver. To exploit new technology in developing future television systems, Japan and Europe have established large research laboratories which are funded by the government or industry-wide consortia. Because the lack of a research laboratory in the United States was considered detrimental to the broadcasting and equipment manufacturing industries, a consortium of American companies established the Advanced Television Research Program (ATRP) at MIT in 1983.

Currently, the consortium members include ABC, Ampex, General Instrument, Kodak, Motorola, PBS, and Tektronix. The major objectives of the ATRP are:

1. To develop the theoretical and empirical basis for improving existing television systems, as well as for designing future television systems;
2. To educate MIT students through television-related research and development while motivating them toward careers in television-related industries;
3. To facilitate continuing education of scientists and engineers already working in the industry;
4. To establish a resource center where problems and proposals can be discussed and studied in detail;

5. To transfer technology developed from this program to the industries.

The research areas of the program include (1) design of a channel-compatible advanced television (ATV) system, (2) design of a receiver-compatible ATV system and digital ATV system, and (3) development of transcoding methods. Significant advances have already been made in some of these research areas. The digital ATV system we designed was tested in 1992 by the Federal Communications Commission (FCC) for its possible adoption as the U.S. HDTV standard for terrestrial broadcasting. No decision has been made yet on the HDTV standard.

In addition to research on advanced television systems, our program also includes research on speech processing. Current research topics include development of a new speech model and algorithms to enhance speech degraded by background noise.

2.2 Advanced Television Research Program

2.2.1 ATRP Facilities

The ATRP facilities are currently based on a network of eight Sun-4 and three DecStation 5000 workstations. There is approximately 14.0 GB of disk space, distributed among the various machines. Attached to one of the Sun-4s is a VTE display system with 256 MB of RAM. This display system is capable of driving the Sun-4 monitors or a 29-inch Conrac monitor at rates up to 60 frames/second. In addition to displaying high-resolution real-time sequences, the ATRP facilities include a Metheus frame buffer which drives a Sony

2K × 2K monitor. For hard copy output, the lab uses a Kodak XL7700 thermal imaging printer which can produce 2K × 2K color or black and white images on 11 inch × 11 inch photographic paper.

Other peripherals include an Exabyte 8 mm tape drive, 16-bit digital audio interface with two channels and sampling rates up to 48 kHz per channel, and "audio workstation" with power amplifier, speakers, CD player, tape deck, and other relevant equipment. Additionally, the lab has a 650 MB optical disk drive, a CD-ROM drive, and two laser printers. For preparing presentations, the ATRP facilities also include a Macintosh SE30 microcomputer, Mac IIx, and Apple LaserWriter.

We are considering installation of a fast network (FDDI) to augment the current 10 Mbps Ethernet. The new network would enable much faster data transfer to display devices, and it would more easily support large NFS transfers.

2.2.2 Video Representations for Low-bit-rate Applications

Sponsor

Advanced Television Research Program

Project Staff

John G. Apostolopoulos

Video is becoming an important aspect in many of today's applications and is expected to gain even greater importance in the near future. The large raw data rate of a video signal, together with the limited available transmission capacity in many applications, necessitates compression of the video. A number of image and video compression algorithms have been developed for high-definition television, video-conferencing, and video-phone applications. These algorithms create an efficient representation of the video, such as a motion field and error image, which is subsequently quantized and coded for transmission. Each of these algorithms has been specifically tailored for its particular application and operating parameters.

Personal communication devices (PCDs) and other future applications may have different sets of constraints. With possible power and bandwidth limitations, they could be required to encode the video at much lower bit rates. The bit rate could be variable for different applications or could depend on the particular transmission scenario (conditions) existing at the time. For example, PCDs or other portable devices may be able to adjust their transmission to optimally utilize the available channel capacity. The

ability to efficiently operate at very low bit rates as well as at higher bit rates is therefore very important.

A representation of the video which provides a natural coupling among different video acquisition/display resolutions (temporal and spatial) could be very beneficial. For example, in point-to-point communications, knowledge of the characteristics of the acquisition and display devices and channel capacity could be exploited.

The attribute which is most likely of greatest importance for any video compression algorithm is a high-quality, intelligible reconstruction of the important information existing within the video. The ability to adapt the representation to exploit the instantaneous content of the video signal could improve the rendering of important information in each scene.

These issues are much more crucial for applications at low-bit-rates than those at higher bit rates. This research focuses on creating a scalable and adaptive/dynamic representation of the video signal, thereby enabling its very efficient and flexible compression.

2.2.3 Design and Implementation of a Digital Audio Compression System

Project Staff

Shiufun Cheung, Kyle K. Iwai, Peter A. Monta

Currently popular digital sound systems on the commercial market, such as the compact disc (CD) system and the digital audio tape (DAT) system, typically deliver uncompressed audio which is linearly quantized to 16 bits and sampled at a rate of either 44.1 kHz for CDs or, more universally, 48 kHz. These systems result in a raw data rate of over 1.4 Mbits per second per stereo pair. This is too high to be practical for applications such as high-definition television (HDTV) transmission and digital audio broadcast (DAB), both of which have channel bandwidth constraints. Recent developments in audio coding technology show that reduced data rate a sound quality comparable to CD digital audio could be achieved. In this project, we have designed and implemented an audio compression system which delivers perceptually transparent audio at approximately 125 kbits per second per monophonic channel. This represents a reduction factor of close to 6:1 from the uncompressed systems.

This compression scheme performs adaptive transform coding by passing the audio signal sampled at

48 kHz through a critically-sampled single-sideband filterbank, a technique also known in the literature as time domain aliasing cancellation. The dynamic bit allocation is performed on each transformed frame of samples. This allows the coder to adapt to varying characteristics in different sounds. To maintain perceptual transparency, many aspects of the algorithm rely on knowledge of the human auditory system. Key features include critical band analysis and exploitation of the perceptual interband masking model for quantization noise shaping.

The channel compatible digicipher system, a real-time implementation of four full channels of the audio coder, was completed in July 1992. As the audio subsystem of one of the system proposals, we entered this system into the competition for the United States HDTV standard. The real-time system, which employs Motorola 96002 digital signal processors, features color displays for monitoring purposes, direct digital interface to standard AES/EBU audio input and output, and optional Analog-to-Digital and Digital-to-Analog conversion. In October, the system successfully completed all the required subjective and objective tests established by the Advanced Television Testing Center.

Our efforts to improve the audio compression scheme are continuing. Under investigation are the possibility of using adaptive frame lengths for transform coding and the merits of using different signal representations such as the wavelet transform.

2.2.4 Design of an High-Definition Television Display System

Sponsor

Advanced Television Research Program

Project Staff

Eddie F. Lee

Several years ago, a video filter and display unit was built by graduate students to aid in the development of an HDTV system. This unit could read large amounts of digital video data from memory, filter the data, and display it at a high rate on a large, high-resolution monitor. Unfortunately, this display system is very complex and highly unreliable, and there is very little documentation to help diagnose any problems with the system.

This project, which was completed in May 1992, involved the design of a simpler and more reliable display system. Since little documentation was available, work was done to analyze the older system to determine its input specifications.

2.2.5 Transform Coding for High-Definition Television

Sponsor

Advanced Television Research Program

Project Staff

Ibrahim A. Hajjahmad

The field of image coding has many applications. One area is the reduction of channel bandwidth needed for image transmission systems, such as HDTV, video conferencing, and facsimile. Another area is reduction of storage requirements. One class of image coders is known as a transform image coder.¹ In transform image coding, an image is transformed to another domain more suitable for coding than the spatial domain. The transform coefficients obtained are quantized and then coded. At the receiver, the coded coefficients are decoded and then inverse transformed to obtain the reconstructed image.

The discrete cosine transform (DCT), a real transform with two important properties that make it very useful in image coding, has shown promising results.² In the energy compaction property a large amount of energy is concentrated in a small fraction of the transform coefficients (typically low frequency components). This property allows us to code a small fraction of the transform coefficients while sacrificing little in the way of quality and intelligibility of the coded images. In the correlation reduction property, spatial domain is a high correlation among image pixel intensities. The DCT reduces this correlation so that redundant information does not require coding.

Current research is investigating use of the DCT for bandwidth compression. New adaptive techniques are also being studied for quantization and bit allocation that can further reduce the bit rate without reducing image quality and intelligibility.

¹ J.S. Lim, *Two-Dimensional Signal and Image Processing*. Englewood Cliffs, New Jersey: Prentice Hall, 1990; R.J. Clarke, *Transform Coding of Images*, London: Academic Press, 1985.

² N. Ahmed, T. Natarajan, and K.R. Rao, "Discrete Cosine Transform," *IEEE Trans. Comput.* C-23: 90-93 (1974).

2.2.6 Video Source Coding for High-Definition Television

Sponsor

Advanced Television Research Program

Project Staff

Peter A. Monta

Efficient source coding is the enabling technology for high-definition television over the relatively narrow channels envisioned for the new service (e.g., terrestrial broadcast and cable). Coding rates are on the order of 0.3 bits/sample, and high quality is a requirement. This work focuses on developing new source coding techniques for video relating to representation of motion-compensated prediction errors, quantization and entropy coding, and other system issues.

Conventional coders represent video by using block transforms with small support (typically 8x8 pixels). Such independent blocks result in a simple scheme for switching a predictor from a motion-compensated block to a purely spatial block; this is necessary to prevent the coder from wasting capacity in some situations.

Subband coders of the multiresolution or wavelet type, with their more desirable localization properties, lack "blocking" artifacts and match better to motion-compensated prediction errors. Since the blocks overlap, this complicates this process of switching predictors. A novel predictive coding scheme is proposed in which subband coders can combine the benefits of good representation and flexible adaptive prediction.

Source-adaptive coding is a way for HDTV systems to support a more general imaging model than conventional television. With a source coder that can adapt to different spatial resolutions, frame rates, and coding rates, the system can then make tradeoffs among the various imagery types (for example, 60 frames/s video, 24 frames/s film, highly detailed still images, etc.). In general, this effort makes HDTV more of an image transport system rather than a least-common-denominator format to which all sources must either adhere or be hacked to fit. These techniques are also applicable to NTSC to some extent; one result is an algorithm for improved chrominance separation for the case of "3-2" NTSC, that is, NTSC upsampled from film.

Other work includes design and implementation of a high-fidelity audio source coder operating at 125

kb/s per monophonic channel. The coder uses results from psychoacoustics to minimize perceived quantization-noise loudness. This system forms part of the hardware submitted by MIT and General Instrument for the United States HDTV standards process.

2.2.7 Error Concealment for an All-Digital High-Definition Television System

Sponsor

Advanced Television Research Program

Project Staff

Aradhana Narula

Broadcasting high-definition television (HDTV) requires transmission of an enormous amount of information within a highly restricted bandwidth channel. Adhering to channel constraints necessitates use of an efficient coding scheme to compress data. However, compressing data dramatically increases the effect of channel errors. In the uncompressed video representation, a single channel error affects only one pixel in the received image. In the compressed format, a channel error affects a block of pixels in the reconstructed image, perhaps even an entire frame.

One way to combat the effect of channel errors is to add well-structured redundancy to the data through channel coding. Error correction schemes generally, however, require transmitting a significant number of additional bits. For a visual product like HDTV, it may not be necessary to correct all errors. Instead, removing the subjective effects of channel errors using error concealment techniques may be sufficient, and these techniques require fewer additional bits for implementation. Error concealment may also be used in conjunction with error correction coding. For example, it may be used to conceal errors which the error correction codes can detect but not correct.

Error concealment techniques take advantage of the inherent spatial and temporal redundancy within transmitted data to remove the subjective effects of these errors once their location has been determined. In this research, error concealment techniques were developed and analyzed to help protect the system from errors occurring in several parameters transmitted for HDTV images. Specifically, error concealment in the motion vectors and the discrete cosine transform (DCT) coefficients was investigated.

2.2.8 Transmission of High-Definition Television Signals in a Terrestrial Broadcast Environment

Sponsor

Advanced Television Research Program

Project Staff

Julien J. Nicolas

High-definition television systems currently being developed for broadcast applications require 15-20 Mbps to yield good quality images for approximately twice the horizontal and vertical resolutions of the current NTSC standard. Efficient transmission techniques must be found to deliver this signal to a maximum number of receivers while respecting limitations stipulated by the FCC for over-the-air transmission. This research focuses on the principles that should guide the design of such transmission systems.

The major constraints related to the transmission of broadcast HDTV include (1) bandwidth limitation (6 MHz, identical to NTSC); (2) requirement for simultaneous transmission of both NTSC and HDTV signals on two different channels (Simulcast approach); and (3) tight control of the interference effects between NTSC and HDTV, particularly when the signals are sharing the same frequency bands. Other considerations include complexity and cost issues of the receivers, degradation of the signal as a function of range, etc.

A number of ideas are currently being studied. Most systems proposed to date use some form of forward error-correction to combat channel noise and interference from other signals. Overhead data reserved for the error-correction schemes represents up to 30 percent of the total data, and it is therefore worthwhile trying to optimize these schemes. Our current work is focusing on the use of combined modulation/coding schemes capable of exploiting the specific features of the broadcast channel and the interference signals. Other areas of interest include use of combined source/channel coding schemes for HDTV applications and multi-resolution coded modulation schemes.

2.2.9 Fractal Image Compression

Sponsor

Advanced Television Research Program

Project Staff

Lon E. Sunshine

Image compression using transform coding has been a wide area of research over the last few years. The wavelet transform, in particular, decomposes a signal in terms of basis functions which are scaled versions of one another. This allows us to exploit the scale invariance or self-similarity within an image to achieve effective compression.

The self-similarity and pattern within images is a quality which may allow for high compression ratios with little quality degradation. Iterated function systems (IFS) have been shown to synthesize many self-similar (fractal) images with very few parameters. We are investigating the feasibility of using IFSs and their variants to exploit the self-similarity in arbitrary images in order to represent these images reliably with few parameters.

2.3 Speech Signal Processing

2.3.1 A Dual Excitation Speech Model

Sponsor

U.S. Navy - Office of Naval Research
Contract N00014-89-J-1489

Project Staff

John C. Hardwick

One class of speech analysis/synthesis systems (vocoders) which have been extensively studied and used in practice are based on an underlying model of speech. Even though traditional vocoders have been quite successful in synthesizing intelligible speech, they have not successfully synthesized high quality speech. The multi-band excitation (MBE) speech model, introduced by Griffin, improves the quality of vocoder speech through the use of a series of frequency dependent voiced/unvoiced decisions. The MBE speech model, however, still results in a loss of quality as compared to the original speech. This degradation is caused in part by the voiced/unvoiced decision process.

A large number of frequency regions contain a substantial amount of both voiced and unvoiced energy. If a region of this type is declared voiced, then a tonal or hollow quality is added to the synthesized speech. Similarly, if the region is declared unvoiced, then additional noise occurs in the synthesized speech. As the signal-to-noise ratio decreases, classification of speech as either voiced or unvoiced becomes more difficult, and, consequently, degradation is increased.

The dual excitation (DE) speech model, due to its dual excitation and filter structure, has been proposed in response to these problems. The DE speech model is a generalization of most previous speech models, and, with proper selection of model parameters, it reduces to either the MBE speech model or to a variety of more traditional speech models.

Current research is examining the use of this model for speech enhancement, time scale modification, and bandwidth compression. Additional areas of study include further refinements to the model and improvements in the estimation algorithms.

2.3.2 Speech Enhancement Using the Dual Excitation Model

Sponsor

U.S. Navy - Office of Naval Research
Contract N00014-89-J-1489

Project Staff

Chang Dong Yoo

Degradation caused by additive wideband acoustic noise is common in many communication systems where the disturbance varies from low-level office noise in a normal phone conversation to high-volume engine noise in a helicopter or an airplane. In general, addition of noise reduces intelligibility and introduces listener fatigue. Consequently, it is desirable to develop an automated speech enhancement procedure for removing this type of noise from the speech signal.

Many different types of speech enhancement systems have been proposed and tested. The performance of these systems depends upon the type of noise they are designed to remove and the information which they require about the noise. The focus of our work has been on the removal of wideband noise when only a single signal consisting of the sum of the speech and noise is available for processing.

Due to the complexity of the speech signal and the limitations inherent in many previous speech

models, model-based speech analysis/synthesis systems are rarely used for speech enhancement. Typically, model-based speech enhancement systems introduce artifacts into the speech and the quality degrades as the signal-to-noise ratio decreases. As a consequence, most speech enhancement systems to date have attempted to process the speech waveform directly without relying on an underlying speech model.

One common speech enhancement method is spectral subtraction. The basic principle behind this method is to attenuate frequency components which are likely to have a low speech-to-noise ratio while leaving frequency components which are likely to have a high speech-to-noise ratio relatively unchanged. Spectral subtraction is generally considered to be effective at reducing the apparent noise power in degraded speech. However, noise reduction is achieved at the price of speech intelligibility. Moderate amounts of noise reduction can be achieved without significant loss of intelligibility, but a large amount of noise reduction can seriously degrade intelligibility. The attenuation characteristics of spectral subtraction typically lead to a de-emphasis of unvoiced speech and high frequency formants. This property is probably one of the principal reasons for loss of intelligibility. Other distortions introduced by spectral subtraction include tonal noise.

In this work, we introduce a new speech enhancement system based on the DE speech model which overcomes some of these problems. The DE system is used to separate speech into voiced and unvoiced components. Since the acoustic background noise has characteristics which are similar to unvoiced speech, the unvoiced component will be principally composed of the unvoiced speech plus the background noise. The voiced component will be principally composed of the harmonic components of the speech signal. As a consequence, speech enhancement can be achieved through subsequent processing of the unvoiced component to reduce the apparent noise level. New processing methods have been derived which take advantage of the unique properties of the individual components to reduce distortion introduced into the processed speech.

Chapter 3. Combined Source and Channel Coding for High-Definition Television

Academic and Research Staff

Professor William F. Schreiber

Graduate Students

Michael O. Polley, Susie J. Wee

Technical and Support Staff

Deborah S. Manning

3.1 Project Description

The purpose of this project is to develop a high-definition television system (HDTV) for terrestrial broadcasting that has high-spectrum efficiency, effective suppression of analog channel impairments (ghosts, noise, interference, and frequency distortion), a feasible transition scenario, reasonable cost, good interoperability with other media and applications, and permits nondisruptive improvement over time. To this end, a two-stage spread-spectrum system has been simulated in accordance with the plans discussed in *RLE Progress Report Number 134*.

In spread-spectrum television, the video signal is divided into a large number of narrow-band components so that the symbol length is larger than the temporal spread of the echoes. All echoes arrive within one symbol time, eliminating intersymbol interference. Each narrow-band component is spread to the full spectrum width (6 MHz) by multiplying it with a different pseudorandom sequence. All the products are added and transmitted. At the receiver, the components are separated by multiplication by the same sequences, whose orthogonality ensures elimination of crosstalk.

Unfortunately, echoes reduce the orthogonality of the random sequences. While scrambling is helpful because it causes interference to become random noise, the noise level is still excessive. It is not theoretically possible to design sequences that have adequate cross-correlation performance when time-shifted.

We have found a possible solution to this problem by using orthogonal frequency-division multiplex (OFDM). This channel-coding method, invented at Bell Laboratories in the 1960s, also divides the signal into narrow-band components. Each signal is modulated on a separate carrier. The signals in

adjacent channels are orthogonal, permitting their complete separation at the receiver. A guard interval is inserted between symbols to ensure that all ghosts arrive entirely within one integration period. A very simple implementation is provided by the use of the Fourier transform. This generates a baseband version of the transmitted signal in a single operation.

OFDM, which has been used in Europe for digital audio broadcasting, is being investigated now for digital video broadcasting by a number of laboratories. At a meeting held at MIT in October 1992, all European and Canadian OFDM projects were represented. A particularly attractive version of OFDM, called single-frequency networks (SFN), was discussed at some length. In this method, the receiving area of a television station is filled with a cellular network of low-power transmitters, operating on the same frequency. The multiple signals seen at each receiver, particularly if omnidirectional receiving antennas are used, constitute "active echoes," which are suppressed by OFDM. This arrangement results in a much more uniform signal level at the receivers, obviating the need for a soft threshold. It also permits much higher spectrum efficiency, since stations serving contiguous areas can use the same frequency. The "no-man's land" between stations, in which directional antennas would have to be used, are about the same width as the cells. Thus, to provide about 20 independent services in each locality, not much more than 20 (instead of the 68 which are needed at present) channels must be allocated for television service.

We are now actively pursuing the goal of configuring our system to support the SFN concept. There is some uncertainty about the precise manner in which the echoes combine at the receiver and we are considering a field test to elucidate the phenomenon.

Part IV Bioelectronics

Section 1 Genetic Analysis

Section 1 Genetic Analysis

Chapter 1 Genosensor Technology Development

Chapter 1. Genosensor Technology Development

Academic and Research Staff

Dr. Daniel J. Ehrlich, Dr. Mark A. Hollis, Dr. John Melngailis, Dr. Dennis D. Rathman

1.1 Introduction

The primary objective of this cooperative work with the Houston Advanced Research Center is to develop a novel method for automated, low-cost, high-throughput DNA sequence analysis. The overall goal is to demonstrate laboratory prototypes that provide a substantial increase in speed over the conventional DNA sequencing methods now used in the biomedical, pharmaceutical, and agricultural industries.

The basic approach being taken is depicted in figure 1. In a hypothetical DNA sequencing test, a solution of single-stranded "target" DNA strands of identical but unknown sequence is washed onto a specialized microelectronic chip called a genosensor. The genosensor surface contains a large array of test sites, each site containing short pieces of single-stranded DNA known as "probes." These probes are chemically attached to the site. All probes in a given site are of like sequence, and the sequence for each site is unique on the chip. The target DNA strands will bond, or hybridize, strongly to those sites containing probes having an exact complementary sequence match but will hybridize much less strongly to other sites. The sites containing hybridized DNA are identified via electronic sensing on the chip, and this information is used by off-chip instrumentation to reconstruct the sequence of the target strands. MIT's role in this effort is primarily the design and fabrication of the genosensor chips.

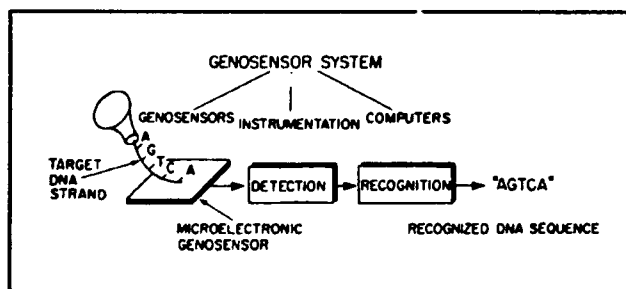


Figure 1. Conceptual genosensor system.

1.2 Development of Genosensor Arrays for DNA Decoding

Sponsor

Houston Advanced Research Center
Contract HRC-HG00665-01

Project Staff

Dr. Daniel J. Ehrlich, Dr. Dennis D. Rathman, Dr. Mark A. Hollis, Dr. John Melngailis

The simplest electrical measurement that can be made at a test site to detect hybridization is probably a measurement of the change in local permittivity due to the addition of long target strands to the site. The complex permittivity $\epsilon^* = \epsilon' - j\epsilon''$ of an aqueous solution containing DNA exhibits a dispersion around a relaxation frequency which is a function of the size (diameter in solution) of the DNA molecule. A measurement of the capacitance and/or conductance between two electrodes in the solution over a range of frequency can therefore differentiate between a site that contains only short probe strands and one that contains long target strands hybridized to the probe strands.

Figure 2 shows a simple conceptual view of a permittivity genosensor wafer that consists of rows and columns of overlapping metal lines having a test site (well) at each crossover. The two metal interconnect lines at each well have one or more electrodes that protrude into the well. A measurement is made by applying a signal to the two lines for a desired well and measuring, for example, the dissipation factor ϵ''/ϵ' of the well capacitance using an RLC meter. In this manner, all the wells of the array can be rapidly interrogated in sequence.

The ideal electronic structure in a test well consists of two parallel plates spaced so that the entire volume between them is filled by the hybridized DNA globules in aqueous solution. For the sizes of target DNA envisioned, this spacing ranges from approximately 200 to a few thousand angstroms. A practical, easily fabricated structure that approximates this ideal is an interdigitated design shown in figure 3. Fabricated by a combination of wet and dry etching with metal liftoff, this design can achieve the required spacings between the upper and lower electrodes at their edges. Results of

electrical tests are shown in figure 4 for a crude version of the device of figure 3, demonstrating that sufficient discrimination between hybridized and nonhybridized DNA can be achieved. More refined versions of these devices are now being fabricated in the Microsystems Technology Laboratory.

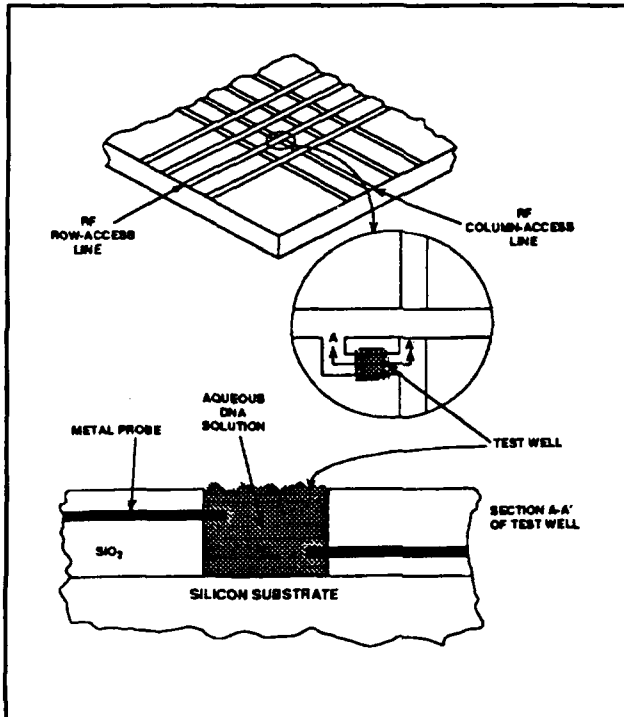


Figure 2. Conceptual view of a microelectronic genosensor.

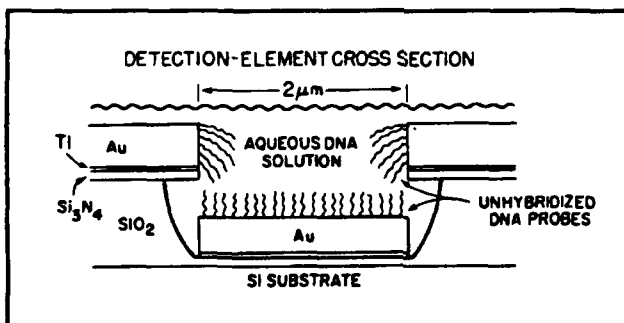


Figure 3. Electrode design for a permittivity genosensor. The basic unit cell shown is repeated many times across a test well to form an interdigitated test structure with the top Au electrodes connected to one access line and the bottom Au electrodes to the other.

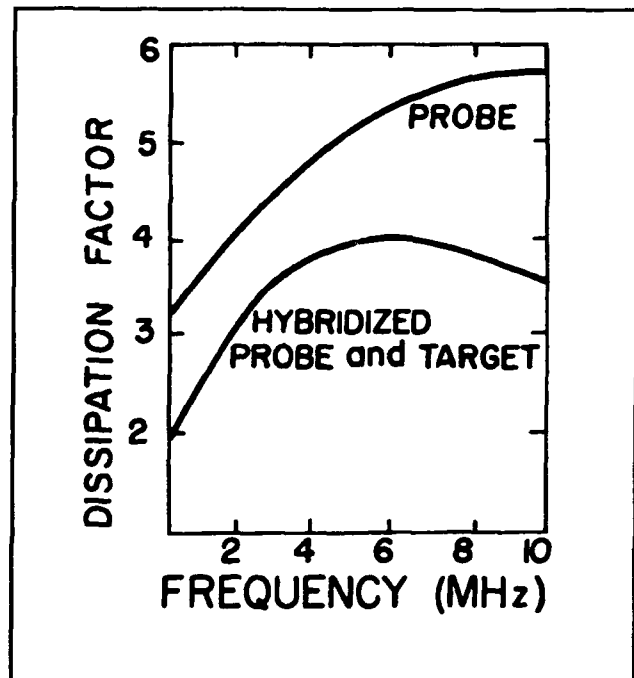


Figure 4. Measured data from a test site containing hybridized probe and target DNA plotted for comparison with data from a site containing only probe DNA.

1.3 Microdetection Technology for Automated DNA Sequencing

Sponsor

Houston Advanced Research Center
Contract HRC-HG00776-01

Project Staff

Dr. Daniel J. Ehrlich, Dr. Dennis D. Rathman, Dr. Mark A. Hollis, Dr. John Melngailis

The primary emphasis of this effort is to complement the program described above. We are performing extensive computer modeling combined with detailed electrical measurements of parasitics to develop a high-sensitivity electrode geometry for a permittivity genosensor. The computer modeling has begun, and a new set of photomasks has been designed and fabricated in which the dimensions of the electrodes are varied to enable experimental determination of the optimum electrode geometry. These photomasks are now being used to fabricate genosensor arrays for the electrical measurements.

Part V Language, Speech and Hearing

Section 1 Speech Communication

Section 2 Sensory Communication

Section 3 Auditory Physiology

Section 4 Linguistics

Section 1 Speech Communication

Chapter 1 Speech Communication

Chapter 1. Speech Communication

Academic and Research Staff

Professor Kenneth N. Stevens, Professor Jonathan Allen, Professor Morris Halle, Professor Samuel J. Keyser, Dr. Melanie Matthies, Dr. Joseph S. Perkell, Dr. Stefanie Shattuck-Hufnagel, Dr. Mario A. Svirsky, Peter C. Guiod, Seth M. Hall

Visiting Scientists and Research Affiliates

Dr. Tirupattur V. Ananthapadmanabha,¹ Dr. Vladimir M. Barsukov, Dr. Corine A. Bickley, Dr. Suzanne E. Boyce,² Dr. Carol Y. Espy-Wilson,³ Dr. Richard S. Goldhor,² Dr. Robert E. Hillman,⁴ Dr. Caroline Huang,⁵ Dr. Harlan Lane,⁶ Dr. John Locke,⁷ Dr. John I. Makhoul,⁸ Dr. Sharon Y. Manuel,⁹ Dr. Carol Ringo,¹⁰ Dr. David Williams,¹¹ Eva B. Holmberg,¹² Giulia Arman Nassi, Torstein Pedersen,¹³ Roeland P. Schaeffer,¹⁴ Jane Wozniak⁴

Graduate Students

Hwa-Ping Chang, Marilyn Y. Chen, Helen M. Hanson, David M. Horowitz, Mark A. Johnson, Sharlene A. Liu, Noel S. Massey, Kelly L. Poort, Lorin F. Wilde

Undergraduate Students

Tracy E. Adams, Kerry L. Beach, Amy S. Chang, Venkatesh R. Chari, Sue O. Kim, Jean Q. Lee, Peggy Li, Henry Y. Lu, Bernadette Upshaw, Janet Wang

Technical and Support Staff

D. Keith North, Arlene E. Wint

¹ Voice and Speech Systems, Bangalore, India.

² Audiofile, Inc., Lexington, Massachusetts.

³ Boston University, Boston, Massachusetts.

⁴ Massachusetts Eye and Ear Infirmary, Boston, Massachusetts.

⁵ Dragon Systems, Inc., Newton, Massachusetts.

⁶ Department of Psychology, Northeastern University, Boston, Massachusetts.

⁷ Massachusetts General Hospital, Boston, Massachusetts.

⁸ Bolt, Beranek and Newman, Cambridge, Massachusetts.

⁹ Wayne State University, Detroit, Michigan.

¹⁰ University of New Hampshire, Durham, New Hampshire.

¹¹ Sensimetrics, Inc., Cambridge, Massachusetts.

¹² MIT and Massachusetts Eye and Ear Infirmary, Boston, Massachusetts.

¹³ University of Karlsruhe, Germany.

¹⁴ University of Utrecht, The Netherlands.

1.1 Introduction

The overall objective of our research in speech communication is to gain an understanding of the processes whereby (1) a speaker transforms a discrete linguistic representation of an utterance into an acoustic signal, and (2) a listener decodes the acoustic signal to retrieve the linguistic representation. The research includes development of models for speech production, speech perception, and lexical access, as well as studies of impaired speech communication.

Sponsors

C.J. Lebel Fellowship
Dennis Klatt Memorial Fund
Digital Equipment Corporation
National Institutes of Health

Grant R01-DC00075

Grant R03-DC01721

Grant R01-DC01291

Grant R01-DC00266¹⁵

Grant P01-DC00361-06A1¹⁵

Contract R01-DC00776¹⁶

National Science Foundation

Grant IRI 89-05249¹⁷

Grant IRI 89-10561

Grant INT 90-24713¹⁸

1.2 Speech Production Planning

1.2.1 Segmental Planning

Speech errors like "lightly britt" (for "brightly lit") suggest that sublexical elements undergo serial ordering in preparation for production, and contextual modifications that accommodate such errors (like "an ignificant amount" (for "a significant amount")) suggest that further phonological processing follows this serial ordering. Our proposed model for sublexical serial ordering postulates a set of abstract phonemic elements provided by the candidate lexical items for the utterance, a prosodically-structured phrasal frame of slots or locations to which the individual segment specifications must be associated, and a mechanism for integrating the segments with their slots. This model includes a

word-based search process through the set of candidate elements; other models suggest a syllable-based search. Distinguishing between these two approaches is difficult on the basis of existing corpora of sublexical errors. The majority of frequently-used words of English are monosyllables so that position similarity constraints on interacting pairs of segments (initial with initial, final with final, etc.) are compatible with both word and syllable structure. In a series of error elicitation experiments, however, we have shown that errors are more likely between pairs of word-initial consonants than between pairs that are not both word-initial, even when both members of the pair are syllable initial. Thus, word structure must play a role in the serial ordering process for sublexical elements; syllable-based structure alone cannot account for the distribution of segmental errors.

Additional experiments in progress explore the possibility that word-final segments, which seldom participate in sublexical errors, are protected against such errors by the phrasal representations of syntactically and prosodically well-formed utterances but not by the planning representations prepared for word lists. We are also developing methods to test the hypothesis that more sublexical errors occur when phrasal prosody is irregular and less rhythmic, and fewer errors when phrasal prosody is highly regular and rhythmic. Such a finding, suggested by our preliminary results, would indicate that the two mechanisms of segmental serial ordering and computation of phrasal prosody invoke some of the same processing capacity, as our model postulates.

1.2.2 Prosodic Planning

Although the major perceptual prominence of a word of American English falls on its main stress syllable when the word is produced by itself (as in "indeSCRibably"), in running speech such polysyllabic words with late stress often have a stronger prominence on an earlier syllable (as in "That was INdescribably TASty"). This phenomenon, formerly described as Stress Shift, has been described as the shift of stress leftward from the main-stress syllable to relieve a Stress Clash, created by the juxtaposition of the main-stress sylla-

¹⁵ Under subcontract to Massachusetts Eye and Ear Infirmary.

¹⁶ Under subcontract to Massachusetts General Hospital.

¹⁷ Under subcontract to Boston University.

¹⁸ U.S.-Sweden Cooperative Science Program.

bles of adjacent words within the same phrase. In acoustic and perceptual analyses of pairs of sentences read aloud in the laboratory, as well as of more than 750 utterances in a corpus of FM radio news style speech recorded at broadcast, we have shown that many instances of apparent stress shift are better described in terms of the placement of phrase-level tonal prominences called pitch accents. That is, apparent stress shift reflects the unmasking of an early pitch accent in the target word, an unmasking which is brought about by the disappearance of the pitch accent from the main stress syllable. We have also found evidence to support the claim that the placement of a pitch accent on the early syllable of the word is affected by two separate prosodic factors: a tendency to place a pitch accent as early as possible in a new prosodic phrase (onset marking) and a tendency to avoid placing pitch accents too close together (pitch accent clash). The possibility that the more traditional form of rhythmic stress shift also occurs in non-pitch-accented stretches of speech is under investigation. This work has been carried out in conjunction with Dr. Mari Ostendorf at Boston University and Dr. Patti Price at SRI International. Published in the proceedings of several meetings and workshops, this work has been submitted for journal publication.

We are also exploring, in conjunction with a number of other laboratories, the feasibility of a new transcription system for prosodic structure—the TOBI system (for TOnes and Break Indices). This system represents the effort of a number of investigators to develop a method of transcribing the core prosodic facts about an utterance including the constituent boundaries, boundary tones, and prominences. We developed this system for use by a large number of laboratories involved in prosody research to more quickly assemble a large database of prosodically labeled speech. We are currently involved in testing whether inexperienced learners can learn to use TOBI in a reasonable amount of time. This collaborative work is attempting to develop teaching materials and a manual and assess the reliability of the transcriptions across different listeners and speech materials.

1.3 Studies of Speech Production

1.3.1 Trading Relations between Tongue-body Raising and Lip Rounding in Production of the Vowel /u/: A Pilot Motor Equivalence Study

Articulatory and acoustic data were used to explore the following hypothesis for the vowel /u/: the goal of articulatory movements is a relatively invariant acoustic target which may be achieved with varying and reciprocal contributions of different articulators. Previous articulatory studies of similar hypotheses, expressed entirely in articulatory terms, have been confounded by interdependencies of the variables being studied (e.g., lip and mandible displacements). One case in which this problem may be minimized is that of lip rounding and tongue-body raising (formation of a velo-palatal constriction) for the vowel /u/. Lip rounding and tongue-body raising should have similar acoustic effects for /u/, mainly to lower F_2 . In multiple repetitions, reciprocal contributions of lip rounding and tongue-body raising could help constrain F_2 variability for /u/; thus, this experiment looked for complementary covariation (negative correlations) in measures of these two parameters. An Electro-Magnetic Midsagittal Articulometer (EMMA) was used to track movements of midsagittal points on the tongue body, upper and lower lips, and mandible for large numbers of repetitions of utterances containing /u/. Three of four subjects showed weak negative correlations, tentatively supporting the hypothesis; a fourth showed the opposite pattern—positive correlations (coordination) of lip rounding and tongue raising. The results are discussed in a recent publication including ideas about motor equivalence, the nature of speech motor programming, and potential improvements to the paradigm.

1.3.2 Tongue Surface Deformation during Obstruent Stop Consonants

When an obstruent stop consonant is produced, there is an increase in intraoral pressure, and this increased pressure can result in outward movement of the vocal-tract walls. Following release of the consonant, the intraoral pressure decreases, and the walls are expected to move inward with a time constant that depends on the physical properties of the surfaces. We used an electromagnetic midsagittal articulometer (EMMA) to measure the vertical position of the tongue dorsum during a number of repetitions of five utterances: /ama/, /apa/, /aba/, /ampa/ and /amba/. Results seem to confirm the physical description given above: the

average lowering in tongue dorsum position from implosion to release of the consonant was 0.4 mm for /m/, 2.7 mm for /b/ and 1.3 mm for /p/. The smaller movement for /p/ than for /b/ may be due to active stiffening of the tongue during /p/, partly counteracting the effect due to intraoral pressure. These displacements and their rates of movement are consistent with published data on average subglottal pressure and compliance and resistance of vocal tract surfaces. These data have been used to refine current estimates of physical parameters of articulator surfaces during speech production.

1.3.3 Advances in Techniques for Studying Temporal Aspects of Inter-articulator Coordination

We are expanding previous analyses of anticipatory labial coarticulation (Perkell and Matthies, 1992) to study the more general issue of inter-articulatory coordination. For this purpose, we have acquired preliminary data on movements of the lips, tongue and mandible from two subjects. In order to analyze these and future data, we have made the following improvements to signal processing and data extraction procedures: (1) Filter selection and signal processing to produce velocity and acceleration signals that are sufficiently smooth for reliable algorithmic event detection but retain analyzable peaks. This signal processing calculates velocity and acceleration magnitudes as well as one-dimensional measures. (2) Program development of a module to facilitate the labeling of the acoustic signals and marking of acoustic events prior to the analysis of the physiological signals. This module allows for the review of assigned labels and the elimination of mispronounced tokens. It has been tested and used extensively. (3) Development of program modules to accomplish algorithmic detection of events in one and two-dimensional displacement, velocity and acceleration signals from multiple articulators. (4) Development of a program which allows for ensemble averaging of multiple articulator movement versus time trajectories. Standard deviation calculations are included as well as displays of multiple y versus x trajectories.

1.3.4 Sequence in Simultaneity: Phonetic "Enhancements" in Ewe Doubly-articulated Stops

This project is being done in collaboration with Ian Maddieson, Department of Linguistics, University of California at Los Angeles.

The timing of labial and velar articulations in the doubly-articulated stops /kp/ and /gb/ in Ewe was investigated with EMMA (articulatory) data from two speakers. The results confirmed the expected temporal asymmetry of the two gestures, as well as the general similarity of these to the gestures in simple velar and labial stops. Backward movement of the tongue in /kp/ and /gb/ was observed, but the timing and spatial orientation of this movement as well as certain acoustic details suggest that, for these speakers, this is due to rarefaction in the pharyngeal cavity rather than to an active attempt to expand the front cavity. The maneuvers involved in production of /kp/ and /gb/ result in asymmetrical acoustic transitions to and from the consonant, additional duration, less aspiration for /kp/, and greater voicing for /gb/ in comparison with singly articulated stops. All of these can be considered "enhancements" of what would otherwise be a non-salient contrast.

1.4 Speech Research Related to Special Populations

1.4.1 Degradation of Speech and Hearing with Bilateral Acoustic Neuromas

In this project we are studying the relation between speech and hearing in people who become deaf from bilateral acoustic neuromas (auditory nerve tumors) associated with the genetic disorder, neurofibromatosis type II (NF2). The primary goal of this study is to increase our understanding of the role of hearing in the control of adult speech production. The rationale and approach for this work are similar to those of our ongoing work on the speech production of cochlear implant patients. Speech acoustic and physiological parameters will be recorded and speech perception will be tested in a group of (still hearing) NF2 patients. Then the same parameters will be recorded at intervals for the subset of patients who suffer further hearing loss.

Thus far, we have developed complete protocols for recording speech acoustic and physiological parameters, as well as procedures for testing non-speech oral-motor capabilities (as control measures). We have obtained baseline recordings from 25 patients. Two to three baseline recordings have been obtained from those facing imminent hearing loss. Two of these patients have recently undergone acoustic neuroma surgery. One patient has more hearing loss as a result of the surgery. The other suffered complete hearing loss but now has an auditory brainstem implant which will

provide some degree of (degraded) hearing. Both of these patients will return soon for further testing.

1.4.2 Speech Production of Cochlear Implant Patients

This project is funded under a subcontract with the Massachusetts Eye and Ear Infirmary, with the collaboration of Professor Harlan Lane of Northeastern University.

This research aims to characterize the speech production of postlingually deafened adults before and after they receive cochlear implants, in order to help evaluate and improve prostheses and to constrain models of the role of hearing in speech production.

We have been making longitudinal measures of speech acoustics. For vowels the measures include: vowel formants, fundamental frequency, sound pressure level, duration, and an acoustically-based measure of inferred glottal aperture. For consonants, the measures are acoustic correlates of place and manner cues in plosives and fricatives. We also measure suprasegmental contours of pitch and amplitude and several parameters of speech breathing: mean air flow, volume of air per syllable, and speech initiation and termination levels.

Consistent with informal reports and limited experimental evidence from other investigators, we have found large changes in the suprasegmental properties of speech following processor activation. In particular, activation of the processor is invariably followed by reductions in sound pressure level and increases in rate, commonly followed by changes in mean airflow in the direction of normal, and sometimes followed by reductions in pitch in the direction of normal. In addition, the pitch and amplitude contours for one subject, which were peculiarly variable, became more smoothly modulated following processor activation. At the segmental level, we have found changes in vowel formants, durations and amplitudes, commonly in the direction of normal. In addition, we have found increasing differentiation of voicing in the plosives and of a place cue in the voiceless fricatives following processor activation in some speakers. An analysis of covariance among parameter changes within and across sessions has led to a model of interactions among supraglottal and glottal articulations and their regulation by auditory feedback from the implant. We have developed software for analyzing fricative sounds to examine the / s / - / ʃ / dis-

tingtion pre- and post-implant. Analyses of data from four subjects is in progress.

1.4.3 Objective Assessment of Vocal Hyperfunction

This project is funded under a subcontract to the Massachusetts Eye and Ear Infirmary in collaboration with Dr. Robert E. Hillman.

In the past year, this project moved from the Department of Communication Disorders, Boston University, to a new Voice and Speech Laboratory at the Massachusetts Eye and Ear Infirmary. Dr. Hillman has been appointed director of the new laboratory, where new facilities have been installed for continuation of this work. Data collection procedures have been expanded to include plethysmographic assessment of respiratory function. These data will be analyzed with software developed for use in the Cochlear Implant and Acoustic Neuroma projects. Software has been developed for automatically running and scoring listener tests of voice quality judgments. The results of these tests will be compared with aerodynamic and acoustic measures.

1.4.4 A Multidimensional Mathematical Model of Vowel Perception for Users of Pulsatile Cochlear Implants

We have continued to work on a mathematical model to account for vowel perception by users of pulsatile cochlear implants. We have extended the model to three dimensions in order to deal with cochlear implants that encode one to three formant frequencies. These cochlear implants estimate the frequency of up to three formants and stimulate one to three channels every fundamental period (one channel per formant). Thus, formant frequencies are encoded by the position of the electrodes that are stimulated at any given moment in time.

The model was assessed using vowel confusion matrices obtained from four subjects who were all tested with stimulation schemes that employed one, two, and three formants.¹⁹ Vowel confusion matrices obtained with the one-formant scheme were used to estimate sensitivity (the ability of each subject to identify which channel has been stimulated) and were also used to estimate each subject's average response bias. The amount of bias was variable, but in all cases it was consistent with the fact that

¹⁹ P.J. Blamey and G.M. Clarke, *J. Acoust. Soc. Am.* 88(2): 667-673 (1988).

for patients with cochlear implants, a given formant frequency causes stimulation of cochlear areas that are more basal than the areas stimulated by the same formant when the subject had normal hearing. These estimates of sensitivity and bias were then used to predict the vowel identification performance of each subject under each stimulation scheme. The model predicted successfully that the two-formant scheme would be better than the one-formant scheme and roughly equal to the three-formant scheme. For three of the subjects, it also made good predictions of the number of correct responses. A fourth subject performed better than expected on the two-formant strategy, perhaps because he employed inter-formant distance as an additional dimension in order to identify vowels.

We also used the model to assess the extent to which different subjects adapted to the more-basal-than-normal stimulation provided by their cochlear implants. Our results show that all subjects adapted to a large extent. One subject seemed to adapt almost completely, while the three others showed different amounts of response bias.

1.4.5 Vowel Nasalization in Hearing-impaired and Normal-hearing Children

In our studies of the nasalization of vowels in speech of hearing-impaired and normal-hearing children, the bandwidth of the first formant and the prominence of the extra peak due to the pole-zero pair have been found to be significant acoustic cues. This result is in accord with the theory of the nasal cavity coupling. In the speech of both hearing-impaired and normal-hearing children, a wider first formant bandwidth and greater peak prominence were observed for those vowels that were judged to be more nasal. In acoustic analysis of nasalized vowels spoken by normal-hearing adults, a prominent peak was apparent around 950 Hz. For hearing-impaired children, the average value was 940 Hz, which is lower than that of the adult, contrary to expectations. This may be due to the sensitivity of measuring the frequency of the peak by using the value of its closest harmonic, which is dependent on the fundamental frequency. The difference between the amplitude of the first formant A_1 , which is inversely related to the bandwidth, and the amplitude of the extra peak P_1 , which is directly related to the amount of separation between the nasal pole and zero, was used as a measure of the degree of vowel nasalization. The magnitude of the correlation coefficient between A_1-P_1 and the average nasality judgment for the speech of hearing-impaired and normal-hearing children was found to be 0.80, indicating that the

difference measure is a very promising parameter for quantifying nasalization.

A perceptual experiment using resynthesized versions of utterances (of the form bVt) from a normal-hearing speaker was carried out to further quantify the relation between A_1-P_1 and judgments of nasality. For most of ten vowels, A_1 predominated over P_1 in determining nasality perception, but the parameter A_1-P_1 was found to be more highly correlated with the judgments than was A_1 alone. Since the locations of the formants, especially the first two formants, affect P_1 , the parameter was normalized using the first formant frequency F_1 and the second formant frequency F_2 . The normalization did not require the use of formant bandwidths to give good approximations. The magnitude of the correlation coefficient of nasal judgments and normalized A_1-P_1 of synthesized words is 0.77, which corresponds to the value from the study of the speech by normal-hearing and hearing-impaired children. The difference between the amplitude of the first formant and the amplitude of the extra peak, A_1-P_1 , is promising in indicating the degree of nasalization. This allows objective assessment of the velopharyngeal opening and thus of the amount of nasalization.

1.4.6 Aiding Dysarthric Speakers

The intelligibility of the speech of some dysarthric individuals is often reduced relative to that of normal speakers, making it difficult for listeners to understand them. We have been examining the possibility of using speech recognition devices to augment the communication abilities of these individuals. In particular, we are attempting to determine whether, with proper design of an inventory of utterances, a speech recognition device can be trained to recognize these utterances even though the utterances may not be intelligible to listeners. In the process of working toward this practical goal, we hope to contribute to the development of procedures for evaluating the nature of the various deficiencies that characterize the articulatory and acoustic patterns of dysarthric speakers.

Our initial research has concentrated on the speech patterns of one individual, with some preliminary evaluation of the speech of two other speakers. The data we have collected are of three kinds: (1) evaluation of the intelligibility of the speaker using testing procedures that are used by other investigators; (2) obtaining measures of the performance of a speech recognition device (Dragon Writer - 1000) when trained and tested on words produced by the dysarthric speaker (the same words that were used in the intelligibility test); (3) detailed

acoustic analysis of the speaker's utterances, and use of these acoustic data to aid in the interpretation of the results in (1) and (2).

These data were analyzed to determine possible patterns of deviant articulatory control for the speaker. Probably the most consistent pattern emerging from this analysis was the inability to form consonants that required raising of the tongue blade, particularly the coronal fricative consonants. As a consequence of these initial experiments, we plan to make a selection of words for this speaker that have the potential of being identified with high accuracy by the speech recognizer.

1.5 Models for Lexical Representation and Lexical Access

In the model for lexical access that we are developing, lexical items are represented in terms of sequences of segments, each of which is described by a list of distinctive features. Acoustic measurements are made to determine selected landmarks in the signal, corresponding roughly to segments. Based on the type of landmark, a further set of acoustic properties is measured in the vicinity of each landmark in order to determine the features for the segment.

During the past year, the lexicon has been expanded to 250 words. Particular attention has been directed toward developing rules for labelling features or feature groups for segments that are susceptible to modification by certain contexts: One aspect of the lexicon is that function words (such as **and**, **the**, **of**) are represented twice—once in a well-articulated, nonreduced form, and once in a form that attempts to capture (in terms of modifiable features) the various reductions that the word can undergo.

Progress has been made in the first step of the procedure for estimating the segments and features from the speech signal, i.e., the automatic detection of landmarks. Initial attention has been given to abrupt consonantal landmarks, at the implosion or release of [+consonantal, -sonorant] segments. A first hypothesis concerning these landmarks is obtained by examining the changes in energy in a low-frequency band (0-1 kHz) smoothed with a 20-ms averaging time. The measure of change is a first difference over a 50-ms time interval. This procedure detects almost all the desired landmarks, but also registers landmarks in the vicinity of some glides. Modifications of the algorithm are being made to improve the performance. These modifications examine changes in energy in higher fre-

quency bands as well as changes in formant frequencies.

Some initial progress has been made toward the development of procedures for estimating articulator-bound features, based on measurements of the acoustic pattern in the vicinity of the landmarks. For each of the features and for each type of landmark, we have prepared a preliminary list of the acoustic properties that contribute to identification of the feature. This list of properties is derived from analysis of speech-production models that predict the acoustic output of the vocal tract when the articulatory movements are given, as well as from analysis of natural speech. For example, the properties that are used to determine which articulator produced a stop consonant release include the burst spectrum, starting frequencies of certain formant transitions, frequencies of the formants in the adjacent vowel, and time course of the formant movements.

We are proceeding with the implementation of some of these procedures for estimating the features from acoustic measurements in the vicinity of the landmarks.

1.6 Studies of the Acoustics, Perception, and Modeling of Speech Sounds

Studies of the acoustics and modeling of speech sounds have continued in four different areas: (1) examining the changing acoustic pattern in the vicinity of the release of fricative consonants; (2) measuring and accounting for rapid changes in spectrum and in amplitude at the times of formation and release of the tongue-blade constriction for lateral consonants; (3) describing the detailed acoustic events at the release of stop consonants that follow the sound /s/ in initial consonant clusters, coupled with the collection of data on jaw movements during production of the consonants; (4) developing quantitative acoustic analysis techniques to estimate the amount and time course of nasalization in a vowel. To aid in our modeling of speech sound production, we have completed a computer-based facility for estimating the transfer function for a multitube model of the vocal tract with two or more parallel paths. In all of these studies, we are attempting to refine our models of production of the different classes of sounds. These models make certain predictions concerning the time-varying acoustic characteristics of the radiated sound, given the articulatory shapes and movements that are used to generate the sounds. Comparisons of the measured acoustic properties with those predicted from the models are then used to

revise the estimates of the articulatory movements so that agreement between measurements and model outputs is achieved.

1.7 Development of Computer and Data Processing Facilities

A program has been written to display high-quality spectrograms on our engineering workstations. The spectrogram display includes a cursor which can be time-aligned with cursors in MITSYN-based programs for interactive data extraction or in the Klatt software used for acoustic analyses. This display will facilitate the identification of abrupt spectral transitions in acoustic signals.

The KLSYN88 speech synthesis facility has been augmented to include a transient source, consisting of a single sample, which can be filtered in the same way as the frication source. This new source is used to simulate the transients that occur at the release of stop or affricate consonants.

1.8 Publications

- Alwan, A. A-H. *Modelling Speech Perception in Noise: The Stop Consonants as a Case Study*. RLE TR-569. Research Laboratory of Electronics, MIT, 1992.
- Burton, M.W., S.E. Blumstein, and K.N. Stevens. "A Phonetic Analysis of Prenasalized Stops in Moru." *J. Phonetics* 20: 127-142 (1992).
- Huang, C.B. "Modelling Human Vowel Identification Using Aspects of Formant Trajectory and Context." In *Speech Perception, Production and Linguistic Structure*. Eds. T. Tohkura, E. Vatikiotis-Bateson, and Y. Sagisaka. Tokyo: Ohmsha, 1992, pages 43-61.
- Kuhl, P.K., K. Williams, F. Lacerda, K.N. Stevens, and B. Lindblom. "Linguistic Experience Alters Phonetic Perception in Infants by Six Months of Age." *Sci.* 255: 606-608 (1992).
- Manuel, S.Y., S. Shattuck-Hufnagel, M. Huffman, K.N. Stevens, R. Carlson, and S. Hunnicutt. "Studies of Vowel and Consonant Reduction." *Proceedings of the International Conference on Spoken Language Processing* 2: 943-946 (1992).
- Perkell, J.S., and M.L. Matthies. "Temporal Measures of Anticipatory Labial Coarticulation for the Vowel /u/: Within- and Cross-subject Variability." *J. Acoust. Soc. Am.* 91: 2911-2925 (1992).
- Perkell, J., M. Cohen, M. Svirsky, M. Matthies, I. Garabieta, and M. Jackson. "Electro-magnetic Midsagittal Articulometer (EMMA) Systems for Transducing Speech Articulatory Movements." *J. Acoust. Soc. Am.* 92: 3078-3096 (1992).
- Perkell, J., H. Lane, M. Svirsky, and J. Webster. "Speech of Cochlear Implant Patients: A Longitudinal Study of Vowel Production." *J. Acoust. Soc. Am.* 91: 2961-2978 (1992).
- Shattuck-Hufnagel, S. "The Role of Word Structure in Segmental Serial Ordering." *Cognition* 42: 213-259 (1992).
- Shattuck-Hufnagel, S., M. Ostendorf, and K. Ross. "Pitch Accent Placement within Words." *Proceedings of the IRCS Workshop on Prosody in Natural Language*, University of Pennsylvania, Philadelphia, Pennsylvania, August, 1992, pp. 181-192.
- Stevens, K.N., S.E. Blumstein, L. Glicksman, M. Burton, and K. Kurowski. "Acoustic and Perceptual Characteristics of Voicing in Fricatives and Fricative Clusters." *J. Acoust. Soc. Am.* 91: 2979-3000 (1992).
- Stevens, K.N. "Speech Synthesis Methods: Homage to Dennis Klatt." In *Talking Machines: Theories, Models and Designs*. Eds. G. Bailly, C. Benoit, and T.R. Sawallis. Amsterdam: Elsevier Science Publishers, 1992, pp. 3-6.
- Stevens, K.N. "Theoretical Aspects of Speech Production." *Volta Rev.* 94(5): 5-32 (1992).
- Stevens, K.N. "Models for Production and Acoustics of Stop Consonants." *Proceedings of the Fourth Australian International Conference on Speech Science and Technology*, Brisbane, Australia, November 30-December 2, 1992, pp. 40-45.
- Stevens, K.N., S.Y. Manuel, S. Shattuck-Hufnagel, and S. Liu. "Implementation of a Model for Lexical Access Based on Features." *Proceedings of the International Conference on Spoken Language Processing* 1: 499-502, 1992.
- Svirsky, M., H. Lane, J. Perkell, and J. Webster. "Effects of Short-term Auditory Deprivation on Speech Production in Adult Cochlear Implant Users." *J. Acoust. Soc. Am.* 92: 1284-1300 (1992).
- Wightman, C., S. Shattuck-Hufnagel, M. Ostendorf, and P.J. Price. "Segmental Durations in the

Vicinity of Prosodic Phrase Boundaries." *J. Acoust. Soc. Am.* 91: 1707-1717 (1992).

Papers Accepted for Publication

Holmberg, E., R. Hillman, J. Perkell, and C. Gress. "Relationships between SPL and Aerodynamic and Acoustic Measures of Voice Production: Inter- and Intra-speaker Variation." *J. Speech Hear. Res.*

Perkell, J.S., Matthies, M.L., Svirsky, M.A. and Jordan, M.I. "Trading Relations between Tongue-body Raising and Lip Rounding in Production of the Vowel /u/: A Pilot Motor Equivalence Study." *J. Acoust. Soc. Am.*

Shattuck-Hufnagel, S. "Slips of the Tongue." In *Encyclopedia of Language and Linguistics*. Eds. R.E. Asher and J.M.Y. Simpson. Oxford: Pergamon Press.

Shattuck-Hufnagel, S. "A Comment on Beckman and Edwards." In *Phonological Structure and Phonetic Form*. Ed. P. Keating. Cambridge: Cambridge University Press.

Stevens, K.N. "Phonetic Evidence for Hierarchies of Features." In *Phonological Structure and Phonetic Form*. Ed. P. Keating. Cambridge: Cambridge University Press.

Stevens, K.N. "Lexical Access from Features." Workshop on Speech Technology for Man-Machine Interaction, Tata Institute of Fundamental Research, Bombay, India.

Stevens, K.N. "Models of Speech Production." In *Handbook of Acoustics*. Ed. M. Crocker. New York: Wiley.

Stevens, K.N. "Models for Production and Acoustics of Stop Consonants." *Speech Commun.*

Stevens, K.N. "Why Is It That Male Voices Are Easier Than Female Voices to Understand Over the Telephone?" *Am. J. Audiol.*

Section 2 Sensory Communication

Chapter 1 Sensory Communication

Chapter 1. Sensory Communication

Academic and Research Staff

Professor Louis D. Braid, Professor Richard M. Held, Lorraine A. Delhorne, Nathaniel I. Durlach, Dr. Donald K. Eddington, Dr. Susan L. Goldman, Seth M. Hall, Dr. William M. Rabinowitz, Dr. Christine M. Rankovic, Dr. Charlotte M. Reed, Dr. Mandayam A. Srinivasan, Dr. Annie H. Takeuchi, Dr. Victor W. Zue, Dr. Rosalie M. Uchanski, Dr. Patrick M. Zurek

Visiting Scientists and Research Affiliates

Dr. Richard L. Freyman, Dr. Kenneth W. Grant, Dr. Janet D. Koehnke, Dr. Jack Kotik, Dr. Neil A. Macmillan, Dr. Karen L. Payton, Dr. Patrick M. Peterson, Yun Shao, Min Wei

Graduate Students

Santosh Ananthraman, Jyh-Shing Chen, Belinda Cheng, Kiran B. Dandekar, Joseph G. Desloge, Paul Duchnowski, Joseph A. Frisbie, Eric M. Fuchs, Julie E. Greenberg, Rajesh K. Gupta, Louise Jandura, Gregory R. Martin, Joseph A. Maxwell, Matthew H. Power, Barbara G. Shinn-Cunningham, Robert W. Stadler, Hong Z. Tan

Undergraduate Students

Daniel A. Alvarez, Susan E. Bach, Maroula S. Bratakos, Bridget L. Coffman, John A. Crouch, Swaroop Gantela, Rajashi Ghosh, Andrew C. Goldish, Andrew H. Grant, Rogeeve J. Gulati, Darby A. Hailes, Albert G. Hong, Mary A. Hou, Michael T. Keagy, Michael H. Lim, David S. Lum, Sandra Y. Ma, Jason Mueller, Philip P. Nadeau, Mark T. Nadelski, Charlie C. Pan, Prashun R. Patel, Diane E. Ronan, Brian A. Rubin, Sumeet Sandhu, James F. Selph, Andrew Ugarov, Jennifer Wozniak, Ross A. Yu

Technical and Support Staff

Ann K. Dix, Eleanora M. Luongo, Timothy J. Stellmach, Michael T. Tuyao

1.1 Introduction

The Sensory Communication Group is conducting research on (1) the auditory and tactual senses, (2) auditory, visual, and tactual aids for individuals who are hearing-impaired or deaf, and (3) human-machine interfaces for teleoperator and virtual-environment systems (involving the visual as well as the auditory and tactual senses). Within the domain of hearing aids, research is being conducted on systems that bypass the outer and middle ear and directly stimulate the auditory nerve electrically (cochlear prostheses), as well as on systems that stimulate the ears acoustically. The research on taction is focused not only on speech reception for the totally deaf, but also on the ability of the human hand to sense and manipulate the environment. Within the domain of human-machine interfaces, topics of special interest concern (1) development of principles for mapping the human sensorimotor system into non-anthropomorphic slave mechanisms (or the equivalent in virtual space) and (2) ability of the human sensorimotor system to adapt to alterations of normal sensorimotor loops caused by the presence of the interface.

1.2 Hearing Aid Research

Sponsor

National Institutes of Health
Grant 5 R01 DC00117

Project Staff

Professor Louis D. Braid, Lorraine A. Delhorne, Paul Duchnowski, Nathaniel I. Durlach, Joseph A. Frisbie, Dr. Susan L. Goldman, Gregory R. Martin, Matthew H. Power, Dr. Christine M. Rankovic, Dr. Charlotte M. Reed, Dr. Rosalie M. Uchanski, Dr. Victor W. Zue, Dr. Patrick M. Zurek, Daniel A. Alvarez, Bridget L. Coffman, Andrew C. Goldish, Michael T. Keagy, David S. Lum, Jason Mueller, Philip P. Nadeau, Mark T. Nadelski, Jennifer Wozniak

During the past year, our research has focused on (1) linear amplification, (2) the effects of token variability, (3) a computational model of speech intelligibility, and (4) aids to speechreading.

1.2.1 Linear Amplification

Adaptive Control of Gain

In our earlier work, we examined the potential of adaptive filtering for improving speech reception in noise. We found a good association between upward spread-of-masking caused by high-intensity octave bands of noise and speech intelligibility scores when test conditions were characterized by the articulation index (AI).¹ These studies support the use of the AI for estimating the effects of noise interference on speech reception both for normal-hearing and hearing-impaired groups of listeners. Given these positive results, the AI model appears to provide a means for defining a frequency-gain characteristic that will maximize intelligibility for any given case of interfering background noise.

During the past year, we have taken a closer look at two potential limitations to applying the AI model to the clinical problem of selecting hearing aid frequency-gain characteristics for listening in noise. These limitations are excess masking demonstrated by hearing-impaired subjects and individual subject differences. With this in mind, we are now conducting a detailed examination of the extensive sets of narrowband noise masking patterns that resulted from our earlier studies.

Our masking pattern corpus includes data obtained from five normal-hearing subjects and seven hearing-impaired subjects. Masking patterns consisted of pure-tone thresholds measured every one-third-octave in the presence of octave bands of noise centered on 0.5, 1.0, or 2.0 kHz and were obtained as a function of masker intensity (70 to 95 dB SPL in 5-dB steps). We have compared the hearing-impaired subjects' masking patterns with the averaged patterns of the normal-hearing subjects. We found: (1) a low-frequency spread-of-masking for both normal-hearing and hearing-impaired subjects that was roughly constant

for the masker levels used here; (2) shallower slopes on the high-frequency side of masking patterns for impaired listeners; and (3) for some impaired listeners, substantially greater masking within the masker band. In addition, our results show that decreasing the masker's intensity did not decrease upward spread of masking as rapidly for the hearing-impaired subjects as it did for normal-hearing subjects. These results provide an explanation for the smaller improvements in speech reception in noise demonstrated by some hearing-impaired subjects following attenuation of the frequency region containing a band of masking noise.²

We have begun to compare individual subject masking patterns to those predicted from algorithms such as that described by Ludvigsen,³ which estimates masked thresholds based on the noise spectrum and audiogram. So far, we have found some cases in which Ludvigsen's model underestimates masking substantially, and we are exploring whether these deviations will cause substantial error in prediction of benefit to speech reception. This type of verification is possible only because we have both the masking patterns and the speech intelligibility for each listening condition. As part of this project, we plan to conduct a similar comparison with the recent masking model proposed by Humes et al.⁴

Another area of research has been the utilization of the AI to evaluate the effectiveness of hearing aid gain-assignment schemes which we have extended to include background noise. We calculated AIs for speech in speech-shaped noise and for speech in a high-intensity, low-frequency octave band noise, following the application of frequency-gain characteristics assigned by several popular gain-assignment prescriptions for more than 30 different audiograms. Results support the contention that varying the frequency-gain characteristic as a function of background noise is required in order to maximize speech spectrum audibility.

¹ C.M. Rankovic, P.M. Zurek, and R.L. Freyman, "Potential Benefits of Varying the Frequency-Gain Characteristic for Speech Reception in Noise for Hearing-impaired Individuals," *J. Acoust. Soc. Am.* 90(Pt.2): 2319 (1991); C.M. Rankovic, R.L. Freyman, and P.M. Zurek, "Potential Benefits of Varying the Frequency-Gain Characteristic for Speech Reception in Noise," *J. Acoust. Soc. Am.* 91: 354-362 (1992).

² C.M. Rankovic, P.M. Zurek, and R.L. Freyman, "Potential Benefits of Varying the Frequency-Gain Characteristic for Speech Reception in Noise for Hearing-impaired Individuals," *J. Acoust. Soc. Am.* 90(Pt.2): 2319 (1991); J.N. van Dijkhuizen, J.M. Festen, and R. Plomp, "The Effect of Frequency-Selective Attenuation on the Speech-Reception Threshold of Sentences in Conditions of Low-frequency Noise," *J. Acoust. Soc. Am.* 90: 885-894 (1991).

³ C. Ludvigsen, "Relations Among Some Psychoacoustic Parameters in Normal and Cochlearly Impaired Listeners," *J. Acoust. Soc. Am.* 78: 1271-1280 (1985).

⁴ L.E. Humes, B. Espinoza-Varas, and C.S. Watson, "Modeling Sensorineural Hearing Loss. I. Model and Restrospective Evaluation," *J. Acoust. Soc. Am.* 83: 188-202 (1988).

Real-time Multiband Adaptive Gain Control

The development of multiband adaptive gain-control algorithms is being pursued for two reasons. First, there is the clear desire for an automatic volume control in hearing aids that would obviate the need for the user to constantly adjust the aid manually for different acoustic environments. Multiband control is being studied because the desired compensation is often frequency dependent (in the case, for example, of head shadow). Second, our work⁵ and that of others (e.g., van Dijkhuizen et al.⁶) has demonstrated the benefit of increased speech intelligibility gained, under some restricted conditions, from adjusting the frequency-gain characteristic to attenuate spectrally-localized interference. A well-designed algorithm should be capable of both controlling loudness and, when possible, improving speech reception by reducing the upward spread of masking.

This study⁷ is an evaluation of two gain-control algorithms, relative to a fixed linear system, for improving intelligibility and reducing noisiness. The fact that the systems under study are time-varying has important implications for how they are implemented and evaluated. One implication is that a real-time system is preferable for the flexibility it offers in introducing transient and time-varying sources of interference. However, because we also seek to evaluate the systems with time-varying interference, this makes traditional intelligibility testing impractical. Such intelligibility tests would also not assess noisiness, the other dimension for which the systems should be evaluated.

In light of these considerations, we implemented a real-time filter bank (fourteen filters with roughly third-octave widths) with adaptive gain controlled independently in each band. A variety of interference sources, both transient, time-varying, and steady, were added to a continuous reading (of a book-on-tape) and presented as the input to each of the systems. Additionally, the input level of speech in quiet was varied. Seven subjects with moderate hearing impairment participated. In an initial session, listeners adjusted the overall level of

speech that had been spectrally shaped to match their threshold curves. These adjustments served to determine the gain in the fixed linear system, as well as the target output band levels in the adaptive systems. In the evaluations, subjects rated the outputs of the systems according to both intelligibility of the speech and overall noisiness on scales from 0 to 100.

The first of the two adaptive-gain systems is called Multiband Automatic Volume Control (MAVC) because it is designed to maintain the output of each band at a fixed level, with a limit on maximum gain. Thus, the static input-output characteristic has a fixed gain to a kneepoint and is horizontal above that point. The second system, the Noise Control system, is similar to the MAVC System, except instead of using fixed band output target levels, its band targets depend on the signal-to-noise ratios, where band SNRs were estimated using an algorithm described by Festen et al.⁸ The idea here is to amplify less when the band is dominated by noise than when it is a clear speech signal. In both systems, the level estimation needed for controlling gain is done with a simple RC envelope detector with a one-second time constant.

Generally, results showed the expected effects of gain control, most of which are beneficial. The average intelligibility ratings for the gain-control systems were significantly higher than for the fixed system when speech (in quiet) is presented below the average level. Also, when the input was only noise at a relatively low level, the gain-control systems were rated to be noisier than the fixed system. When the input noise level was greater than the expected speech level, the fixed system amplified the noise above the target level, while the gain-control systems, in the steady state, presented the noise at or below the target level.

Most of the noisiness ratings for the two gain-control systems were lower than those for the fixed system when the environmental noises lasted long enough for the gain-control systems to react. The Noise Control System was rated the least noisy system in most of the high noise level conditions,

⁵ C.M. Rankovic, R.L. Freyman, and P.M. Zurek, "Potential Benefits of Varying the Frequency-Gain Characteristic for Speech Reception in Noise," *J. Acoust. Soc. Am.* 91: 354-362 (1992).

⁶ J.N. van Dijkhuizen, J.M. Festen, and R. Plomp, "The Effect of Frequency-Selective Attenuation on the Speech-Reception Threshold of Sentences in Conditions of Low-frequency Noise," *J. Acoust. Soc. Am.* 90: 885-894 (1991).

⁷ G.R. Martin, *Studies of Real-Time Multiband Adaptive Gain Hearing Aids*, S.M. thesis, Dept. of Electr. Eng. and Comput. Sci., MIT, 1992.

⁸ J.M. Festen, J.M. van Dijkhuizen, and R. Plomp, "Considerations on Adaptive Gain and Frequency Response in Hearing Aids," *Acta Otolaryn. Suppl.* 469: 196-201 (1990).

showing the effectiveness of SNR-dependent gain control.

Intelligibility enhancements with gain control are expected for noise sources whose average spectrum is different from the speech spectrum. The gain-control systems react to such noise sources by decreasing the gain more in the bands where the noise is strong, thereby reducing spread of masking. The results indicated that this expectation was realized. There was no significant intelligibility enhancement or degradation when speech plus speech-shaped noise was tested. With other noises that are not shaped like speech, intelligibility ratings were better with gain control in most instances. Those noises whose spectra were the least shaped like speech resulted in the largest increases. Generally, intelligibility ratings of the MBAVC and the Noise Control systems were similar under most conditions.

These results show that there is promise for both the Noise Control and MBAVC Systems to outperform the fixed system with respect to the intelligibility of speech and perceived noisiness of slowly varying background noises that are not spectrally shaped like speech. The results also show that there is promise for the Noise Control System to outperform the MBAVC system with respect to the perceived noisiness of slowly varying background noises that are not shaped like speech, while at the same time, not decreasing the intelligibility of the speech.

One drawback of gain-control systems is the time needed to react to changing sound levels (a time constant of one second was used). For instance, during periods of quiet, the gain for these systems would be large, and, if a noise source suddenly occurs, it will be quite loud for a second or so. To address this problem, we are planning to implement a scheme like Moore's "dual-front end" for quickly suppressing strong onsets (and releasing control quickly if the sound is a transient).⁹

Feedback Cancellation

Several signal processing techniques for reducing feedback have been proposed recently. Thus far, however, evaluations of these methods have been limited to measurements of the increase in stable gain that can be achieved. Furthermore, the conditions under which these measurements have been made are very different from one study to another. In this work, our initial goal was to implement the most promising of the existing techniques and compare them not only for stable gain but also for their effects on sound quality and annoyance. In the process of studying these systems, a novel procedure was developed, and this is also included for comparison.

The five feedback-reduction algorithms being examined are an adaptive notch filter and four variants of adaptive cancellation. The adaptive notch method had been previously proposed for use in public-address systems. This system has not been evaluated in applications to hearing aids, though it has been used in an algorithm for detecting oscillation.¹⁰

The adaptive cancellation methods have a common goal of estimating feedback path in order to cancel it with another out-of-phase feedback path. The primary difference among methods is in the way that the estimation is performed. In the algorithm described by Bustamante et al.,¹¹ a delayed version of the output signal of the hearing aid is correlated against the microphone signal. The system of Engebretson et al.¹² is the same but with the intentional addition of noise to the output as a probe signal. In both of these systems, adaptation takes place continuously. Kates' approach differs in that the system waits for oscillation to occur, then interrupts the main signal path and inserts a probe noise for feedback-path estimation. In the novel system developed as part of this work, the estimation is performed by inserting a probe noise during selected time intervals when the input signal is estimated to be low. This approach has three advantages over Kates:¹⁰ (1) it provides a quasi-continuous update of the estimation, not simply waiting for oscillation to occur; (2) it achieves the update without losing large segments of the signal;

⁹ B.C.J. Moore, "How Much Do We Gain by Gain Control in Hearing Aids," *Acta Otolaryn. Suppl.* 469: 250-256 (1990).

¹⁰ K.M. Kates, "Feedback Cancellation in Hearing Aids: Results from a Computer Simulation," *IEEE Trans. Sig. Proc.* 39: 553-562. (1991).

¹¹ D.K. Bustamante, T.L. Worrall, and M.J. Williamson, "Measurement of Adaptive Suppression of Acoustic Feedback in Hearing Aids," *ICASSP-89 2017-2020* (1989).

¹² A.M. Engebretson, M.P. O'Connell, and F. Gong, "An Adaptive Feedback Equalization Algorithm for the CID Digital Hearing Aid," *Proceedings of the 12th Annual International Conference, IEEE Engineering in Medicine and Biology Society*, 1990, pp. 2286-2287.

and (3) because the input signal interferes with the estimation of the feedback path, it provides a better estimate by adapting only during intervals when the input signal is small.

All five methods have been implemented with a Motorola DSP96002 chip and are currently being evaluated for increased stable gain, speech quality, and user annoyance. Real-time implementation is necessary for assessing the performance of the algorithm under dynamic conditions. Increased stable gain is measured physically, while sound quality and annoyance are being determined by subjective listening tests. For system evaluation, the acoustic feedback path is simulated with an electrical feedback path. The electrical feedback path provides more control over the experimental variables, a necessity when comparing performance of the feedback suppression algorithms. This path contains a flexible multfilter for shaping the desired transfer function. Dynamic simulation is accomplished by controlled changes in the feedback path.

We are just beginning the evaluation process. It has already become evident, however, that the continuous-adaptation schemes¹³ are prone to diverge, even in the absence of feedback. Inspection of these systems shows that they are adaptive recursive filters, for which special precautions must be taken to assure convergence. Both of the other adaptive schemes allow adaptation only during times when the feedback loop is opened, and thereby avoid this problem.

1.2.2 Speech Token Variability

This research consists of three components: (1) characterizing the variability in the acoustic properties of speech sounds, (2) measuring the perceptual effects of token variability on intelligibility in normal and hearing impaired listeners, and (3) developing a model that relates acoustical and perceptual effects. Progress in previous years generally was made in the first component, i.e., measurement of the physical variability in vowels and fricatives. Recently, we have made progress on the second and third components.

The stimuli used in all the perceptual experiments are repetitions of vowels in an /h/-V-/d/ context by

the same speaker. The /h/-V-/d/ syllables were digitally distorted in a manner described by Schroeder (1968). Three new experiments have been performed.¹⁴ The first experiment examined the ability of trained listeners to identify different tokens of the same vowel sound as the number of utterances or tokens was varied. For tokens of the vowel /i/, identification scores declined from 85 percent for four tokens, to 64 percent for eight tokens, and 50 percent for 16 tokens. This suggests that the perceptual differences between tokens are not sufficiently salient to permit reliable identification. The second experiment investigated the extent to which variability in the multiplicative distortion of the stimuli affected discriminability. The results show that for the vowel pair /i/-/u/, effects of the distortion are minimal compared to the effects of token variability. For the vowel pair eh-uh, on the other hand, effects of both token and distortion variation are comparable.

In the third experiment, vowel discrimination was measured for the vowel pair ae-ah as a function of the token composition of the stimulus set. In this experiment, eight tokens were used to represent each vowel sound. In general, the relative discriminability of each vowel sound was not strongly affected by the composition of the stimulus set. This permits the relative discriminability to be correlated with the physical characteristics of the stimuli that were made earlier. Linear combinations of the physical parameters computed by Multiple Regression Analysis were generally able to predict more than 60 percent of the variance in the perceptual variables.

1.2.3 Prediction of Speech Intelligibility

This project involves development and evaluation of computational methods for determining the intelligibility of speech subjected to a waveform degradation or signal-processing transformation. The methods employ a model of the human auditory system which reduces a speech waveform to a sequence of discrete symbols, each representing a prototypical vector of parameter values measured in a single frame (e.g., 10 ms) of speech. The perceptual effect of the transformation is estimated by measuring the consistency between the symbol

¹³ D.K. Bustamante, T.L. Worrall, and M.J. Williamson, "Measurement of Adaptive Suppression of Acoustic Feedback in Hearing Aids," *ICASSP-89 2017-2020* (1989); A.M. Engebretson, M.P. O'Connell, and F. Gong, "An Adaptive Feedback Equalization Algorithm for the CID Digital Hearing Aid," *Proceedings of the 12th Annual International Conference, IEEE Engineering in Medicine and Biology Society*, 1990, pp. 2286-2287.

¹⁴ D. Ronan, *Further Studies in the Perceptual Effects of Multiple Speech Tokens on Vowel Resolution*, S.B. thesis, Dept. of Electr. Eng. and Comput. Sci., MIT, 1992.

sequence derived from an untransformed (input) speech signal and the symbol sequence derived from a transformed (output) signal. This estimate is implemented via calculation of percent transmitted information (%TI).

Previous research used the energy in each of 20 critical bands as the source of the parameter vector. During the past year, we have focused instead on a different set of 20 parameters, derived from the Ensemble Interval Histogram (EIH) model developed by Ghitza¹⁵ at AT&T Bell Laboratories. The central idea of this model is that speech information is represented in the lengths of intervals between crossings of certain waveform-amplitude values. Implementations of this model (e.g., Ghitza, 1992; Jankowski, 1992)¹⁶ are largely comprised of two major stages: (1) filtering speech into a number of bands, and (2) computing crossing intervals for the individual band waveforms. In the current study, a primary goal was to keep the implementation as similar as possible to that used for computing the band-energy parameter set. In particular, the new computation maintained the frequency region spanned by the bandpass filters, number of bandpass filters, frame rate of the short-time speech analysis, and total number of parameters extracted.

The %TI values obtained via this model can be compared to those obtained via the band-energy computation for each of three types of degradation: additive noise, highpass filtering, and lowpass filtering. Results for the two parameter sets were quite similar in the case of noise. At low SNRs, %TI values for EIH were higher than those for band-energy by about 2 percentage points. At high SNRs, %TI values for EIH were lower than those for band-energy by about 4 percentage points. The crossover point at which the two parameter sets gave equal results was approximately +10 dB SNR. Since the EIH model seemed slightly more resistant to noise than the band-energy model, results were also calculated for negative SNRs, which had not been previously considered. These were much lower than those for the positive SNRs, with %TI values ranging from 17.2 at -5 dB SNR to 3.6 at -20 dB SNR.

For the highpass-filtering degradation, %TI values for EIH were much lower than for band-energy. The

average difference was about 17 percentage points; this was fairly uniform across cutoff frequencies. For lowpass filtering, the %TI values were again lower for EIH, but with a smaller discrepancy averaging about 9 percentage points. Differences were greater at higher cutoff frequencies than at lower ones. In fact, at the 500-Hz cutoff frequency, the %TI value for EIH was the higher one (but by less than one percentage point). Because of these differences in the highpass and lowpass conditions, the crossover frequency calculated from the EIH results was much lower than that calculated from the band-energy results: 1000 Hz vs 1750 Hz.

Across all conditions tested, %TI results for the EIH model were usually lower than those for the band-energy model. This suggests that degradations generally affected the consistency of level-crossing information more than they affected the consistency of band-energy information. The absolute numerical values of %TI are of greatest interest in the low-SNR noise conditions. In particular, it would be useful if these values provided an adequate characterization of intelligibility across all noise levels for which humans retain some reasonable speech-reception ability. However, the -20 dB SNR result, 3.6 %TI, is comparable to the 2.0 %TI obtained from randomly generated symbol sequences of the length used in these calculations. Thus, considerably more speech data would need to be processed for reliable %TI results in intense noise degradations.

However, absolute %TI values are not the only data of interest; instead, the relationship between %TI values for noise and filtering is also important. In particular, one characteristic of the result pattern for the band-energy model is that noise degradations of little perceptual significance reduced %TI as much as did filtering degradations that have a somewhat larger perceptual effect. In going from the band-energy model to the EIH model, the %TI values for filtering dropped more than did the %TI values for noise, therefore leading to a result pattern that is more perceptually realistic.

One final observation of the EIH results is the presence of particularly low %TI values for highpass filtering. One possible explanation for this can be found in the selection of the amplitude levels for which crossings are located. These levels span the

¹⁵ O. Ghitza, "Temporal Non-Place Information in the Auditory-Nerve Firing Patterns as a Front-End for Speech Recognition in a Noisy Environment," *J. Phonetics* 16: 109-123 (1988).

¹⁶ O. Ghitza, "Auditory Nerve Representation as a Basis for Speech Processing," In *Advances in Speech Signal Processing*, S. Furui and M.M. Sondhi, eds. (New York: Marcel Dekker, 1992), pp. 453-485; C.R. Jankowski, Jr., *A Comparison of Auditory Models for Automatic Speech Recognition*, S.M. thesis, Dept. of Electr. Eng. and Comput. Sci., MIT, 1992.

amplitude range found in wideband speech. Highpass-filtered speech is considerably attenuated and rarely crosses the higher levels. This leads to the EIH parameters providing a poorer representation of the speech information. Also, independent of these characteristics of the results, another disadvantage to use of the EIH model is that its computation time is approximately ten times that of the band-energy model.

In addition to work on the EIH model, some supplementary computations were executed during the past year to address the issue of why very slight degradations result in %TI values that are considerably less than 100. Of these, one that seemed insightful had a complete absence of degradation at the waveform level, and instead perturbed the calculation of the symbol sequence by use of a different initial guess in the vector-quantization stage. These experiments helped to confirm the hypothesis that a substantial drop in %TI is caused solely by reassignment of prototype vectors. In some cases of particularly mild degradation, it can be beneficial to omit this reassignment and simply use the prototype vectors from undegraded speech.

Finally, there were some calculations performed to validate portions of the experimental methods. Issues of interest included whether the %TI results were strongly dependent on the particular VQ initialization method, whether accounting for waveform delays due to filtering (either for degradation purposes or within a filter bank) would affect the results, and whether the %TI measure had a reasonable relationship to percentage of exact symbol matches (i.e., a percent-correct measure). None of these uncovered any significant methodological difficulty.

1.2.4 Aids to Speechreading

During the past grant year, our research on aids to speechreading has continued to focus on (1) evaluating the effectiveness of Cornett's (1967) Manual Cued Speech system and (2) developing low bandwidth acoustic signals that enhance speechreading.¹⁷

Cued Speech

The system of Manual Cued Speech was developed by Cornett (1967) as a supplement for speechreading that could be taught to very young deaf children and used in day-to-day communication. In Cued Speech, eight visually distinct hand shapes are used to distinguish between consonants that are not well resolved via speechreading and four hand positions near the mouth provide distinctions within groups of vowels often confused in speechreading. During the past year, we completed our initial study of the effectiveness of Cued Speech and developed an analysis that can be used to estimate the effectiveness of automatic cueing systems based on automatic speech recognizers.¹⁸

As previously reported, we have documented the sentence reception ability of four highly-trained receivers of Manual Cued Speech. The availability of cues permitted near perfect reception of high-context everyday sentences spoken at near normal speaking rates, and very high scores (roughly 85 percent of the words were correct) were obtained for low-context sentences.¹⁹ In control tests on cued and uncued sentences, selected speechreaders who had no previous experience with Cued Speech achieved word scores in the range of 24-36 percent on everyday sentences and 15-22 percent on the low-context sentences. Although the levels of speech reception achieved by the trained receivers is impressive, further analysis indicates that a significant fraction (10-20 percent) of speech segments were not correctly perceived. In a related study, we measured how well spectrogram readers and an ASR system could assign segments to cue groups for various cue systems. Well-trained spectrogram readers were able to assign six consonant cues with an accuracy of 85 percent and eleven vowel cues with an accuracy of 62 percent; an expert reader was able to achieve scores of 94 percent and 83 percent on these tasks. An automatic speech recognizer recently developed at MIT achieved accuracies of 77 percent and 65 percent on comparable tasks. In the third study, we applied the Post-Labeling Model of audiovisual integration²⁰ to these recognizer measurements and data on

¹⁷ R.O. Cornett, "Cued Speech," *Am. Ann. Deaf* 112: 3-13 (1967).

¹⁸ R.M. Uchanski, K.M. Millier, C.M. Reed, and L.D. Braida, "Effects of Token Variability on Vowel Identification," in *The Processing of Speech: From the Auditory Periphery to Word Recognition*. (Berlin: Mouton de Gruyter, 1992).

¹⁹ Institute of Electrical and Electronics Engineers, *IEEE Recommended Practice for Speech Quality Measurements*, No. 297 (New York: IEEE, 1969).

²⁰ L.D. Braida, "Crossmodal Integration in the Identification of Consonant Segments," *Q.J. Expt. Psych.* 43A(3): 647-677 (1991).

human recognition of consonant and vowel segments via speechreading to estimate the benefit to speechreading provided by such cues. The analysis suggests that with cues derived from current recognizers, consonant and vowel segments would be received with accuracies in excess of 80 percent. This level of accuracy is roughly sufficient to account for the scores our subjects achieved on Manual Cued Speech reception. Use of the Post-labeling Model provides analytic means for (1) determining optimum cue groups for a given recognizer and speechreader and (2) estimating the cueing performance that might be achieved if the accuracy of current recognizers were improved in various ways, e.g., by reducing the frequency of voicing errors.

Based on these results, it seems appropriate to begin development of an automatic cueing system based on an automatic speech recognizer and a synthetic visual display of cues. Major uncertainties in the design of such a system concern the effects of recognizer errors, appropriate choice of cue groups, and specification of visual display of cue symbols. We are planning a series of experiments to evaluate the effects of recognizer errors on speech reception using an automatic cueing system. If the ASR does not identify a phoneme correctly, the displayed cue will not correspond to the spoken phoneme and therefore will be incorrect. Our strategy is to simulate the performance of automatic cueing systems that use recognizers with various error rates and patterns of error structures. These systems will use the traditional cue groups of manual cued speech so that highly trained cue receivers can evaluate speech reception.

In a preliminary experiment, we tested the percent of phonemes that could be inaccurate and still allow normal listeners to identify speech. We used only auditory stimuli, not the cues from cued speech to give a baseline for further experiments with cued speech. The stimuli were the Clarke sentences,²¹ with portions corresponding to selected phonemes replaced by white noise. A given phoneme was replaced by noise in the same proportion that it was misidentified by a known speech recognition system (BBN system). If two percent of the misidentifications that the speech recognition system made were /ah/'s then two percent of the phonemes replaced would be /ah/'s. There were four condi-

tions: 10, 20, 30, and 40 percent of the phonemes in the group of sentences were replaced with noise. Subjects heard the sentences and were instructed to guess what a word was even if they were not sure.

We calculated two measures from a preliminary test. First, we counted the percent of phonemes accurately identified. In general, a higher percent of phonemes were correctly identified in sentences with a lower percent of phonemes replaced by noise. Second, we categorized the guesses subjects made by the number of phonemes from which they differed from the original phoneme. A one phoneme change indicated that a guess was either a change of one phoneme to another phoneme /p/ to /b/, for example, or the addition or deletion of phoneme. We grouped the guesses into one, two, three, or greater than three phoneme changes. The results showed that in general the category of the substitution varied with the percent of phonemes replaced by noise. In sentences with lower percents of phonemes replaced by noise, lower phoneme substitutions were more prevalent than higher phoneme substitutions. Listeners were more likely to guess a word which was acoustically closer to the target word. Similarly, in sentences with higher percents of phonemes replaced by noise, phoneme changes were more likely to be greater than three phonemes from the target than in sentences with lower percents of phonemes replaced by noise. Listeners were less likely to guess a word which was acoustically closer to the target word, and more likely to guess a word which was semantically and syntactically appropriate.

Frequency Lowering of Amplitude Envelopes

Acoustic signals that retain much of the intelligibility of the unprocessed speech signal can be synthesized by extracting the amplitude envelopes of filtered bands of speech and using these envelopes to modulate the amplitudes of tones with frequencies at the centers of the bands. These signals successfully supplement speechreading by normal-hearing listeners.²² However, when the center frequency of the carrier bands is lowered to match the residual hearing of listeners with severe high-frequency loss, the signals no longer successfully

²¹ M.E. Magner, *A Speech Intelligibility Test for Deaf Children* (Northampton, Massachusetts: Clarke School for the Deaf, 1972).

²² M. Breeuwer and R. Plomp, "Speechreading Supplemented with Frequency-Selective Sound-Pressure Information," *J. Acoust. Soc. Am.* 76: 686-691 (1984); K.W. Grant, L.D. Braida, and R.J. Renn, "Auditory Supplements to Speechreading: Combining Amplitude Envelope Cues From Different Spectral Regions of Speech," *J. Acoust. Soc. Am.* 92: 2345 (1992); K.W. Grant and L.D. Braida, "Evaluating the Articulation Index for Audiovisual Input," *J. Acoust. Soc. Am.* 89: 2952-2960 (1991).

supplement speechreading.²³ In response to a report by Sheft and Yost²⁴ that the failure of frequency-lowered amplitude envelopes to supplement speechreading may arise because listeners are unable to compare the amplitude envelopes of signals across changes in the center frequency of the signal, Annie Takeuchi has been examining the effect of systematic training on the ability of normal-hearing listeners to match amplitude envelopes of signals at different center frequencies.

The amplitude envelopes were carried by narrow-band noise signals 50-Hz wide, centered at 500, 1600, and 3160 Hz. These baseline frequencies were selected because they are the center frequencies of the filtered bands of speech from which amplitude envelopes have been extracted to supplement speechreading. Subjects were trained on a roving XAB matching-to-sample task, in which the center frequencies of the A and B signals were systematically increased or decreased in increments of 10 percent up to 100 percent and down to -90 percent from the baseline frequency, while the center frequency of the X signal was fixed at the baseline frequency.

For all three baseline frequencies, performance as measured by d' was best when there was no frequency difference between the X, A, and B signals, and d' generally decreased when any frequency difference was present. However, for all frequency differences except decreases of more than 60 percent (-5.7 Barks) from the 1600-Hz baseline frequency, d' remained well above 1.76, which corresponds to 70.7 percent correct unbiased responding on the roving XAB task, the threshold value most commonly measured in psychophysical experiments. For the 500- and 3160-Hz baseline conditions, increases and decreases in frequency produced similar results. For the 1600-Hz condition, increases in frequency produced much smaller decrements in performance relative to no frequency difference than did decreases in frequency. This study demonstrates that with systematic training, listeners are generally able to compare amplitude modulation patterns across large frequency differences.

1.2.5 Human Subjects

There have been no changes in our protocols during the past year, and we do not plan any for the coming year. These protocols were evaluated during the competitive review and have been renewed for the coming grant year.

1.2.6 Publications and Talks

Braida, L.D., P.M. Zurek, K.W. Grant, J.E. Greenberg, and C.M. Rankovic. "Research on Hearing Aids at MIT: Recent Results and Future Directions." In *Proceedings of the International Symposium on Hearing Aids and Speech Training for the Hearing Impaired*, Osaka, Japan, July 16-17, 1991. Eds. H. Levitt and T. Nitta. Forthcoming.

Grant, K.W., L.D. Braida, L.D., and R.J. Renn. "Auditory Supplements to Speechreading: Combining Amplitude Envelope Cues from Different Spectral Regions of Speech." Submitted to *J. Acoust. Soc. Am.*

Payton, K.L., R.M. Uchanski, and L.D. Braida. "Intelligibility of Conversational and Clear Speech in Noise and Reverberation for Listeners with Normal and Impaired Hearing." Submitted to *J. Acoust. Soc. Am.*

Posen, M.P., C.M. Reed, and L.D. Braida. "The Intelligibility of Frequency-Lowered Speech Produced by a Channel Vocoder." *J. Rehab. Res. Dev.* Forthcoming.

Rankovic, C.M., P.M. Zurek, and R.L. Freyman. "Research on Adaptive Frequency Shaping." Invited lecture presented at the House Ear Institute-sponsored conference *Issues in Advanced Hearing Aid Research*, Lake Arrowhead, California, May 25-29, 1992.

Rankovic, C.M., Freyman, R.L., and P.M. Zurek. "Potential Benefits of Varying the Frequency-gain Characteristic for Speech Reception in Noise." *J. Acoust. Soc. Am.* 91: 354-362 (1992).

²³ K.W. Grant, L.D. Braida, and R.J. Renn, "Auditory Supplements to Speechreading: Combining Amplitude Envelope Cues From Different Spectral Regions of Speech," *J. Acoust. Soc. Am.* 92: 2345 (1992); K.W. Grant and L.D. Braida, "Evaluating the Articulation Index for Audiovisual Input," *J. Acoust. Soc. Am.* 89: 2952-2960 (1991).

²⁴ S. Sheft and W.A. Yost, "Spectral Transposition of Envelope Modulation," *J. Acoust. Soc. Am.* 91: S2333 (1992).

Uchanski, R.M., K.M. Millier, C.M. Reed, and L.D. Braida. "Effects of Token Variability on Vowel Identification." In *The Processing of Speech: From the Auditory Periphery to Word Recognition*. Mouton de Gruyter, Berlin, 1992.

Uchanski, R.M., L.A. Delhorne, A.K. Dix, L.D. Braida, C.M. Reed, and N.I. Durlach. "Automatic Speech Recognition to Aid the Hearing Impaired. Prospects for the Automatic Generation of Cued Speech." *J. Rehab. Res. Dev.* Forthcoming.

Uchanski, R.M., S. Choi, L.D. Braida, C.M. Reed, and N.I. Durlach. "Speaking Clearly for the Hard of Hearing IV: Further Studies of the Role of Speaking Rate." Submitted to *J. Speech Hear. Res.*

Theses

Martin, G.R. *Studies of Real-time Multiband Adaptive Gain Hearing Aids*. S.M. thesis, Dept. of Electr. Eng. and Comput. Sci., MIT, 1992.

Maxwell, J.A. *Acoustic Feedback in Hearing Aids*. S.M. thesis, Dept. of Electr. Eng. and Comput. Sci., MIT. Forthcoming.

Ronan, D.E. *Effects of Token Variability on Speech Intelligibility for Vowel Sounds*. S.B. Thesis, Dept. of Electr. Eng. and Comput. Sci., MIT, 1992.

1.3 Multimicrophone Hearing Aids

Sponsor

National Institutes of Health
Grant 5 R01 DC00270

Project Staff

Joseph G. Desloge, Nathaniel I. Durlach, Julie E. Greenberg, Dr. William M. Rabinowitz, Robert W. Stadler, Dr. Patrick M. Zurek

The long-term goal of this research is the development of sensory aids that improve, through the use of microphone arrays, the ability of hearing-impaired listeners to function in complex acoustic environments. Since the reception of speech is the most important problem for the hearing impaired, the target signal of primary interest is speech.

To enhance monaural speech reception, we envision a microphone array that resolves the incoming signals into simultaneous directional channels, followed by a coding operation that transforms these resolved signals in such a way that resolution is preserved at the perceptual level after the signals are summed for presentation to a single ear.²⁵ Such a system would permit the monaural listener (like the normal binaural listener) to monitor all directions simultaneously, detect and localize in the same operation, and focus on a single direction. Our current work on microphone arrays is directed toward the creation of a single directional channel containing the target signal (assumed to arise from a target source straight ahead of the listener) and reduction of interference from sources directionally distinct from the target source. Parallel processing of array outputs to achieve simultaneous multiple directional channels will be considered only after further progress on the coding problem has been achieved.

While development of adaptive arrays has continued,²⁶ considerable effort in the past year has gone into the design of fixed arrays.

1.3.1 Fixed Arrays for Hearing Aids

Microphone arrays with fixed (time-invariant) weights are directed at enhancing a desired signal from one direction (straight ahead) while attenuating spatially distributed interference and reverberation. Using the theory of sensitivity-constrained optimal beamforming,²⁷ free-field arrays of head-sized extents were studied.²⁸ The key parameters affecting array design and performance are the set of transfer functions from the target direction to each array microphone $H_i(f)$ and the intermicrophone cross-spectral densities for isotropic noise $S_{zz}(f)$. Design variables included ori-

²⁵ N.I. Durlach, R.C. Corbett, M.V. McConnell, W.M. Rabinowitz, P.M. Peterson, and P.M. Zurek, "Multimicrophone Monaural Hearing Aids," RESNA 10th Annual Conference, San Jose, California, 1987.

²⁶ J.E. Greenberg and P.M. Zurek, "Evaluation of an Adaptive Beamforming Method for Hearing Aids," *J. Acoust. Soc. Am.* 91: 1662-1676 (1992).

²⁷ H. Cox, R.M. Zeskind, and T. Kooij, "Practical Supergain," *IEEE Trans. Acoust. Speech Sig. Proc.* ASSP-34: 393-398 (1986).

²⁸ R.W. Stadler and W.M. Rabinowitz, "On the Potential of Fixed Arrays for Hearing Aids," submitted to *J. Acoust. Soc. Am.*

entation of the array, number and directionality of the microphones within the array,²⁹ complexity, and robustness of the required processing. For broadside orientation, a variety of arrays based on cardioid and hypercardioid microphones gave very similar performance. They can provide broadband intelligibility-weighted directivities (direct-target gain against isotropic noise) of 7-8 dB with easily implemented weights (simple scalars). For endfire orientation, similar directivities result with weights based on analog gains and pure time delays. However, with weightings that are chosen independently for each frequency, directivities up to ~11 dB may be practical. Because of sound diffraction, placement of arrays onto the head potentially impacts both their design and performance. *In-situ* measurements of $H(f)$ and $S_{zz}(f)$, as well as simplified theoretical models, are suggested to explore the optimization of head-mounted arrays.

1.3.2 Intelligibility-weighted Measures of Speech-to-Interference Ratio

Many of our multimicrophone subprojects require assessment of the improvement in intelligibility provided by processing systems that are essentially linear. For this purpose, we have developed measures of speech-to-interference ratio and system gain that incorporate factors affecting speech intelligibility.³⁰ Such measures result from simple modifications of the Articulation and Speech Transmission Indices³¹ and are applicable to the same kinds of signal degradations to which the indices apply. Under restricted conditions, such measures are linear transformations of either the Articulation Index or the Speech Transmission Index and are as accurate as these indices in predicting speech intelligibility. This is a point that we have illustrated through a validation study. Depending on the type of signal degradation, measures of reduced complexity can be employed. Such measures may prove convenient in characterizing listening conditions and performance of speech-transmission systems.

1.4 Cochlear Prostheses

Sponsor

National Institutes of Health
Contract 2 P01 DC00361³²

Project Staff

Professor Louis D. Braida, Lorraine A. Delhorne, Dr. Donald K. Eddington, Dr. William M. Rabinowitz

The overall goals of this research are to determine and understand the potential and limitations of cochlear prostheses and develop improved prostheses. Postlingually deafened adults are implanted with the Ineraid multichannel cochlear prosthesis and participate in intensive multifactorial studies. This research capitalizes on the direct accessibility of the implanted electrode array via a percutaneous connector.

During the past year, work has focused on (1) analysis of cue integration in audiovisual speech reception and (2) alternative speech processing for improved implant performance. Progress in (1) is described below. The work in (2) is performed with Joseph Tierney, and Marc Zissmann; progress is described in Part V, Section 3, Chapter 1, section 1.7.2.

The work on audiovisual integration assesses the ability of an implantee to combine cues that are available from separately using vision and audition. Because most implantees require audiovisual input for reliable communication, analysis of integration is particularly significant.

A series of experiments on closed-set identification of consonants and vowels were begun. The stimuli are presented via computer-controlled videodisc. Results are being obtained using vision alone, audio alone, and audiovisually. At present, most subjects are nearing completion of the testing; asymptotic levels of performance have been reached and sufficient data have been obtained to provide reliable estimates of confusion patterns for each of the three test modes. Analyses to deter-

²⁹ W. Soede, *Improvement of Speech Intelligibility in Noise: Development and Evaluation of a New Hearing Instrument Based on Array Technology*, Ph.D. diss., Delft University of Technology, The Netherlands, 1990.

³⁰ J.E. Greenberg, P.M. Peterson, and P.M. Zurek, "Intelligibility-Weighted Measures of Speech-to-Interference Ratio and Speech System Gain," submitted to *J. Acoust. Soc. Am.*

³¹ American National Standard Institute, "American National Standard Methods for the Calculation of the Articulation Index," (New York, : ANSI, 1969); H.J.M. Steeneken and T. Houtgast, "A Physical Method for Measuring Speech-transmission Quality," *J. Acoust. Soc. Am.* 67: 318-326 (1980).

³² Subcontract from Massachusetts Eye and Ear Infirmary. Dr. Joseph B. Nadol, M.D., Principal Investigator.

mine the quantitative efficiency of audiovisual integration are underway. These analyses exploit an analytical framework (Braida, 1990) that quantifies how performance in a combined mode (e.g., audiovisual stimulation) is influenced by integration or interference of cues available in the isolated component modes (e.g., audio and visual stimulation alone).

1.5 Binaural Hearing

Sponsor

National Institutes of Health
Grant 5 R01 DC00100³³

Project Staff

Nathaniel I. Durlach, Dr. Patrick M. Zurek

The long-term goal of this program is (1) to develop an integrated, quantitative theory of binaural interaction that is consistent with psychophysical and physiological data on normal and impaired auditory systems and (2) to apply our results to the diagnosis and treatment of hearing impairments.

Experimental research in this area has focused on identifying the stimulus variables responsible for in-head lateralization of auditory images. It is well established that the interaural relations that exist early after the onset of a sound have a strong influence on where the subsequent sound image is heard.³⁴ It is believed that this effect allows very good sound source localization in highly reverberant environments. Our recent work has confirmed that such effects measured using an acoustic pointer correspond well with measurements of interaural parameter resolution.³⁵ Further work has shown that the influence of the onset cue can extend over a relatively long (hundreds of milliseconds) subsequent stimulus, depending on both the ambiguity of

the interaural cues in the subsequent stimulus and on whether it appears to constitute a separate "auditory object".³⁶

1.6 Clinical Applications of Binaural Hearing

Sponsor

National Institutes of Health
Contract 7 R29 DC00428³⁷

Project Staff

Dr. Patrick M. Zurek

In this project, we seek to apply our understanding of binaural advantages in speech reception³⁸ to the prescription of hearing aids, both monaural and binaural, and to test this understanding further. In particular, the experimental work is focused on the performance of both normal hearing and hearing-impaired listeners on tests of binaural detection, localization, and contralateral masking with various amplification patterns applied at both ears.

1.7 Tactile Communication of Speech

Sponsor

National Institutes of Health
Grant 2 R01 DC00126

Project Staff

Lorraine A. Delhorne, Nathaniel I. Durlach, Hong Z. Tan, Dr. William M. Rabinowitz, Dr. Charlotte M. Reed, Dr. Mandayam A. Srinivasan

The ultimate goal of this research is to develop tactual aids for the deaf and deaf-blind that can serve as substitutes for hearing in speech commu-

³³ Subcontract from Boston University. Professor H. Steven Colburn, Principal Investigator.

³⁴ P.M. Zurek, "The Precedence Effect," in *Directional Hearing*, eds. W.A. Yost and G. Gourevitch (New York: Springer-Verlag, 1987); P.M. Zurek, "A Note on Onset Effects in Binaural Hearing," *J. Acoust. Soc. Am.* 93: 1200-1201 (1993).

³⁵ B.G. Shinn-Cunningham, P.M. Zurek, and N.I. Durlach, "Adjustment and Discrimination Measurements of the Precedence Effect" *J. Acoust. Soc. Am.*, forthcoming.

³⁶ R.L. Freyman, P.M. Zurek, U. Balakrishnan, and C. Yuan-Chuan, "Onset Dominance in Lateralization," submitted to *J. Acoust. Soc. Am.*

³⁷ Subcontract from University of Connecticut. Dr. Janet D. Koehnke, Principal Investigator.

³⁸ P.M. Zurek, "Binaural Advantages and Directional Effects in Speech Intelligibility," in *Acoustical Factors Affecting Hearing-aid Performance*, eds. G.A. Studebaker and I. Hochberg (Boston: Allyn and Bacon, 1993.)

nication.³⁹ The objectives and specific aims of our research are as follows:

1. Basic study of encoding and display schemes to develop methods of displaying acoustic signals to the tactual sense for optimal information transfer.
2. Research on tactual systems designed specifically to aid speechreading, including systems based on both acoustic and articulatory-based signal processing.
3. Evaluations of experienced deaf users of portable, wearable tactual aids to (a) determine improvements to speech reception provided by these aids and (b) compare this performance to that of users of other types of auditory prostheses.

1.7.1 Basic Study of Encoding and Display Schemes

A study of joint-angle discrimination (JND) and identification of the proximal interpalangeal (PIP) joint of the index finger has been completed. During the current year, additional data have been collected on the discriminability of the PIP joint angle as a function of metacarpal phalangeal (MCP) joint position. The data indicate that JNDs for PIP joint position are independent of the MCP joint position and average 2.6 degrees. Additional data on PIP joint-angle discrimination as a function of the PIP joint reference position indicate subject-dependent results: JNDs for two subjects are roughly independent of the reference position (averaging 2.4-2.5 degrees), while JNDs for a third subject increased with greater flexion of the PIP joint.

Preliminary work has begun on a study concerned with defining the range of amplitudes and frequencies that can be used to stimulate the tactual system, as well as specifying independent perceptual channels and resolution within these channels.

This work includes development of a device for stimulus presentation consisting of a plastic bar attached to a rotary motor with 2000 discrete, specifiable steps. Pilot studies indicate that this device is capable of presenting signals in the range of 1 to 100 Hz over a fairly broad dynamic range. Existing software has been modified to collect data on amplitude and frequency resolution in a one-interval two-alternative forced-choice procedure.

Work has also begun on a study of the manual discrimination of the property of thickness. A series of plates varying in thickness has been prepared for use as the stimuli in this study, and a device has been built for presenting these plates to subjects in experiments concerned with the ability to discriminate thickness as a function of the reference value. Finally, a manuscript summarizing research on the manual discrimination of length, force, and compliance has been prepared.⁴⁰

1.7.2 Tactual Supplements to Speechreading

In the area of acoustic supplements to speechreading, work during the current year has been concerned with developing a more complete understanding of the differential results obtained for auditory and tactile presentation of acoustic-based low-bandwidth supplements to speechreading.⁴¹ This work has included signal processing and software development for a set of psychophysical measurements of modulation resolution. In the area of articulatory supplements to speechreading, work has been concerned with designing an encoding scheme for presenting various types of articulatory information through a seven-channel vibratory array. The vibrators can be controlled through sine-wave inputs and various vibratory patterns can be used to encode articulatory features of consonants and vowels. Preliminary psychophysical studies are being conducted to determine a set of vibratory patterns that provide sufficient information for this problem.

³⁹ C.M. Reed, N.I. Durlach, and L.A. Delhorne, "Historical Overview of Tactile Aid Research," *Proceedings of the Second International Conference on Tactile Aids, Hearing Aids, and Cochlear Implants*, eds. A. Risberg and K.-E. Spens (Stockholm, Sweden: Royal Institute of Technology, forthcoming).

⁴⁰ H.Z. Tan, X.D. Pang, and N.I. Durlach, "Manual Resolution of Length, Force, and Compliance," *Winter Annual Meeting of the American Society of Mechanical Engineers*, Anaheim, California, November 8-13, 1992.

⁴¹ M.J. Besing, C.M. Reed, and K.W. Grant, "Tactual Presentation of Low-Bandwidth Envelope Signals: Benefits to Speechreading," *ASHA* 33: 212, 1991.

1.7.3 Evaluation of Practical Aids

Three new subjects have joined our field study of tactile-aid users, bringing the total number of subjects to eight. During the current year, six of the eight subjects visited our laboratory for evaluations of their speechreading performance with the Tactaid VII. Data are now available from three separate testing sessions with one subject (JL), two testing sessions with two subjects (RM, RS), and one session with each of the remaining subjects. The evaluations have been concerned primarily with assessing speechreading ability with and without tactile devices, as well as with measuring discriminability of simple speech segments through the use of tactile devices by themselves. Thus far, tactile devices employed in the study include Tactaid VII (which all subjects in the field evaluation have received), Tactaid II (tested only on three of the subjects who had used the Tactaid II prior to Tactaid VII), and a high-performance single-channel vibrator (Alpha-M AV-6 Minishaker) employed only in laboratory testing.

Results of segmental discrimination tests conducted with Tactaid VII indicate that, averaged across subjects and across consonant and vowel pairs, performance is roughly 70 percent correct.⁴² Additional data collected on one subject with Tactaid II showed that performance for both devices was approximately similar. Results of tests conducted for speechreading alone and speechreading in combination with a tactile device (using sentence and continuous-discourse materials) showed a range of performance across subjects. For example, for the reception of words in CUNY sentences, scores from all subjects ranged from 32 to 86 percent correct (averaging 53 percent) for speechreading alone and 29 to 93 percent (averaging 58 percent) for speechreading plus Tactaid VII. Of the six subjects for whom data are currently available on this task, improvements to speechreading with the use of Tactaid VII were observed for four subjects (ranging

from 5 to 17 percentage points improvement), while two subjects have shown no improvements to speechreading of CUNY sentences with Tactaid VII thus far. Data from three subjects tested with Tactaid II (as well as with Tactaid VII) on this task indicate greater improvements to speechreading (by approximately 8 percentage points) when using Tactaid II compared with Tactaid VII. Some preliminary data obtained on three subjects for speechreading of CUNY sentences with the Minishaker indicate that the benefits provided by this device are comparable to those observed with Tactaid II. The results of a questionnaire assessing subjects' use of tactile devices indicate that most prefer Tactaid VII to Tactaid II. This is primarily because of the greater utility of Tactaid VII in detecting and recognizing environmental sounds in addition to the benefits it provides for speechreading.⁴³

1.7.4 Continuation and Completion of Previous Work on Natural Methods of Tactual Communication

During the past year, we have published summaries of our work on the communication abilities of deaf-blind subjects who use various natural methods of tactual communication, including the Tadoma method of speech reception and tactual reception of fingerspelling and sign language.⁴⁴ A manuscript describing a series of experiments conducted to demonstrate improvements to speech reception through Tadoma using supplementary tactual information has also been published.⁴⁵

1.8 Super-Auditory Localization for Improved Human-Machine Interfaces

Sponsor

U.S. Air Force - Office of Scientific Research
Grant AFOSR 90-0200

⁴² C.M. Reed, L.A. Delhorne, and N.I. Durlach, "Results Obtained with Tactaid II and Tactaid VII," *Proceedings of the Second International Conference on Tactile Aids, Hearing Aids, and Cochlear Implants*, eds. A. Risberg and K.-E. Spens (Stockholm, Sweden: Royal Institute of Technology, forthcoming).

⁴³ C.M. Reed and L.A. Delhorne, "Field Study of Deaf Adult Users of Tactaid II and Tactaid VII," Presentation made at the Annual Convention of the Association for Late Deafened Adults, Boston, Massachusetts, September 10-13, 1992.

⁴⁴ C.M. Reed, N.I. Durlach, and L.A. Delhorne, "Natural Methods of Tactual Communication," chapter in *Tactile Aids for the Hearing Impaired*, ed. Ian P. Summers, (Whurr Publishers Limited, 1992), pages 218-230; C.M. Reed, N.I. Durlach, and L.A. Delhorne, "The Tactual Reception of Speech, Fingerspelling, and Sign Language by the Deaf-Blind," *SID Digest* 102-105 (1992).

⁴⁵ C.M. Reed, W.M. Rabinowitz, N.I. Durlach, L.A. Delhorne, L.D. Braida, J.C. Pemberton, B.D. Mulcahey, and D.L. Washington, "Analytic Study of the Tadoma Method: Improving Performance through the Use of Supplementary Tactual Displays," *J. Speech Hear. Res.* 35: 450-465 (1992).

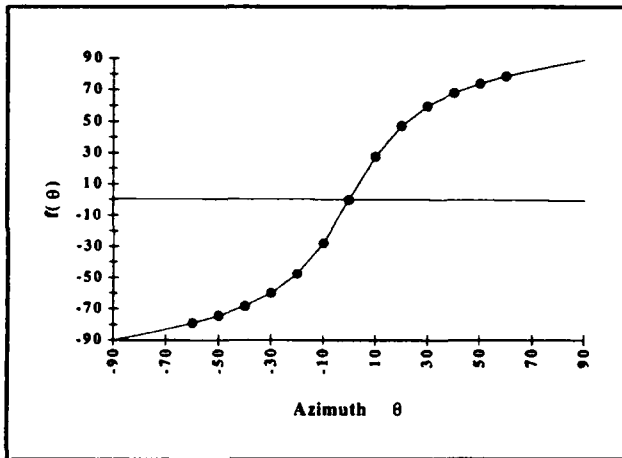


Figure 1.

Project Staff

Nathaniel I. Durlach, Eric M. Fuchs, Dr. Richard M. Held, Dr. William M. Rabinowitz, Yun Shao, Barbara G. Shinn-Cunningham, Min Wei

General background on this project was presented in pages 312-313 of the annual *RLE Progress Report Number 134*. During the past year, work has advanced along the following fronts.

1. Further localization identification experiments have been conducted using a transformation of the function relating head-related transfer function to azimuth such that azimuthal space is magnified in front and minified off to the side (see figure 1). As expected, results show increased resolution in the center and decreased resolution to the side. In addition, in contrast to our initial impression that no sensorimotor adaptation took place, i.e., that response bias failed to decay with an increase in exposure time, our results now clearly show consistent and substantial adaptation (in terms of both the direct effect and the negative after effect). However, results also indicate that the decrease in response bias over time is accompanied by a decrease in resolution over time. We are now studying these data as well as performing further experiments to determine the underlying causes of this phenomenon. Illustrative data showing the changes in both resolution and bias are presented in figure 2.
2. Further work on facilities development has included four projects. First, we have acquired, integrated, and tested a new analog hardware processor to cross-check the results already obtained with the convolvotron. Second, we have constructed a pseudophone (a head-worn microphone/earphone/amplification system with

controllable geometry and acoustic characteristics) to provide us with a system in which localization cues are transformed acoustically rather than by signal processing and in which no head-tracking is required. Third, we have begun to develop a new head tracker based on inertial sensors for use with acoustical simulation systems. Fourth, and finally, we have developed an additional experimental set-up which allows us to simulate a sound source held in the hand so that we can make direct comparisons with classical studies on adaption in the visual sense using optical prisms and a manual pointing response.

3. Further work on the dissemination of our results has included talks at the Society for Information Displays, the First International Conference on Auditory Displays, and the Acoustical Society of America, as well as the publication of an article in *Presence* (Durlach et al., 1992).

1.9 Research on Reduced-Capability Human Hands

Sponsor

U.S. Navy - Office of Naval Research
Grant N00014-90-J-1935

Project Staff

Lorraine A. Delhorne, Nathaniel I. Durlach, Dr. Mandayam A. Srinivasan

General background on this project was presented in *RLE Progress Report Number 134* (pages 313-314). During the past year, attention has been focused on further data collection and data analysis for constrained-hand performance in a subset of the tasks previously used by the Navy in the TOPS teleoperator study (Smith and Shimamoto, 1991).

Although direct comparisons between the results of our tests and those contained in the TOPS project are difficult to interpret because of the many differences in the two testing situations (e.g., direct vision versus vision through a helmet mounted display, working in air versus working under water, etc.), our results suggest a number of important conclusions.

First, the results indicate that all tasks considered were essentially two-finger tasks. We say this because (1) the results obtained with two fingers were nearly as good as those obtained with more fingers (both for the real hands and for the teleoperator hands) and (2) we know from casual observa-

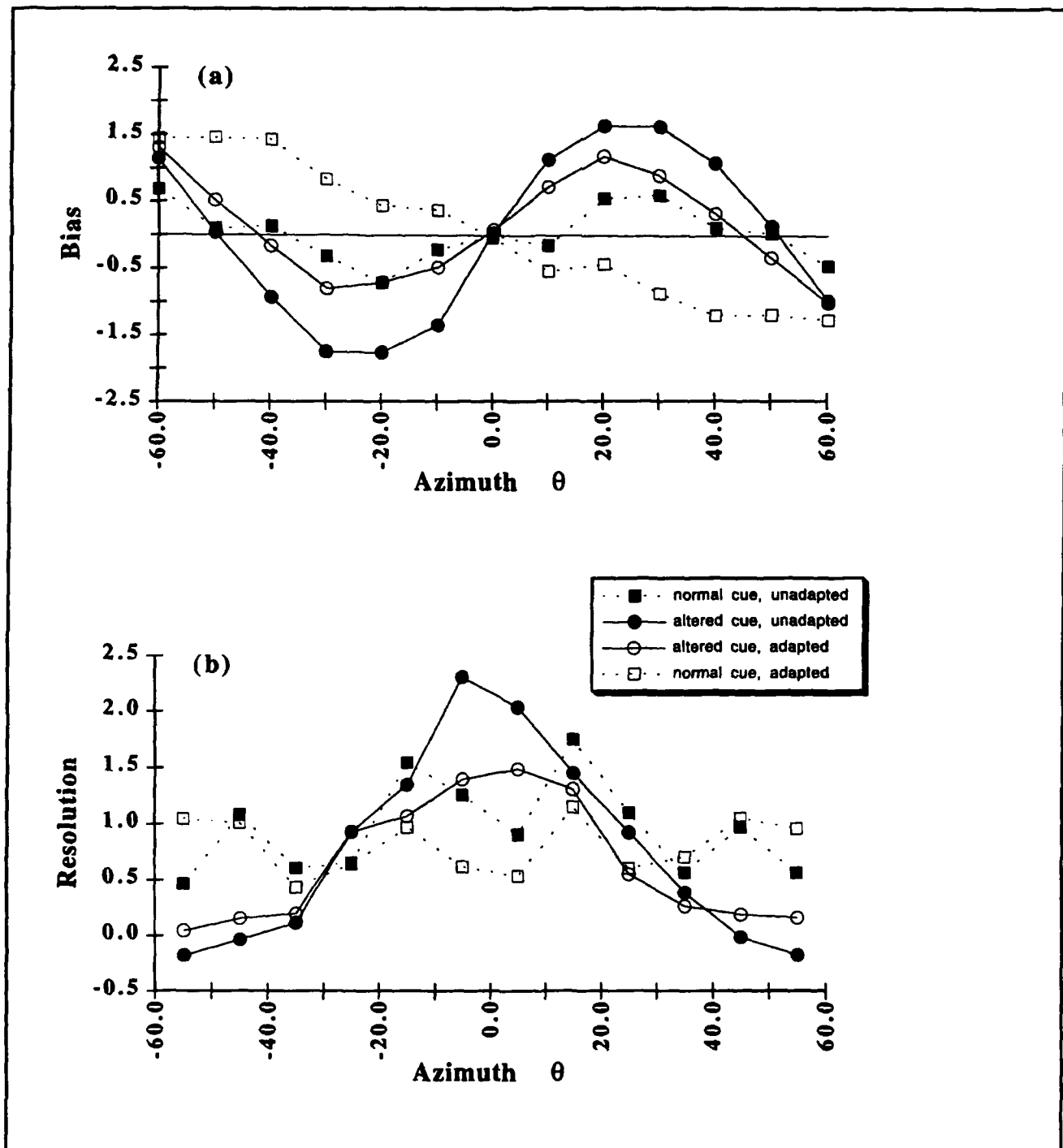


Figure 2.

tion that there exist many tasks for which two fingers are grossly inadequate.

Second, the results indicate, quite surprisingly, that performing the task with a normal human hand using a pair of pliers is (1) much superior to performing the task with either of the teleoperator systems and (2) nearly as good as performing the task with the system consisting of the thumb and

index finger of the normal human hand. Result (1) suggests that the two teleoperator systems had a great deal of mechanical "slop," i.e., that information on position and force (in one or both directions) exhibited only a low level of fidelity. Item (2) suggests that for the given tasks both the compliant nature of the human finger pads and the tactile sensing in the human finger pads were relatively

unimportant. (This result has been confirmed by recent experiments with anesthetized fingers.) In our opinion, this feature of the results would have been radically different if the operator were deprived of visual information. Overall, we believe our results are consistent with the idea that visual information is more redundant with tactile information than with force information. Stated differently, for non-compliant objects, vision can tell you a lot about shape and texture, but not about applied force.

As discussed in our previous report (*RLE Progress Report Number 134*), we believe that the problem of defining an adequate set of basis tasks is the most crucial research problem now facing the study of hand function and its applications to the design and evaluation of artificial hands.

Current work on this project is being devoted to preparation of a final report for this grant. It is anticipated that further research in this area will be carried out under our other grants concerned with manual sensing and manipulation.

1.10 Mechanistic Modeling of Primate Fingertip

Sponsor

National Institutes of Health
Grant 5 R29 DC00625

Project Staff

Kiran B. Dandekar, Dr. Mandayam A. Srinivasan, Ravee J. Gulati

Whenever we touch an object, the source of all tactile information is the spatio-temporal distribution of mechanical loads on the skin at the contact interface. The relationship between these loads and the resulting stresses and strains at the nerve terminals within the skin plays a fundamental role in the neural coding of tactile information. Although empirical determination of the stress or strain state of a mechanoreceptor is not possible at present, mechanistic models of the skin and subcutaneous tissues enable us to generate testable hypotheses on skin deformations and associated peripheral neural responses. Then verification of the hypotheses can be accomplished by comparing the calcu-

lated results from the models with biomechanical data on the deformation of skin and subcutaneous tissues, and neurophysiological data from recordings of the responses of single neural fibers. The research under this grant is directed towards applying analytical and computational mechanics to analyze the biomechanical aspects of touch—the mechanics of contact, transmission of mechanical signals through skin, and their transduction into neural impulses by the mechanoreceptors.

1.10.1 Determination of Geometric and Material Properties of the Primate Fingertip (distal phalanx)

The first step in performing mechanistic analyses of the primate fingertip is to determine its geometric and material properties. The three-dimensional (3D) external geometry of the primate fingertips was determined from accurate epoxy replicas of human and monkey fingertips. Using a videomicroscopy setup, we obtained images of orthographic projections of the epoxy replicas at various known orientations. The images were then digitized and processed to determine the boundary of the finger at each orientation. By combining the boundary data for all the different orientations, we were able to reconstruct the 3D external geometry of the fingertip.⁴⁶ We have reconstructed several human and monkey fingertips by this method.

For mechanical modeling of the human fingerpad, the Poisson's ratio, which is a measure of its compressibility, is required as an input to mathematical models. The Poisson's ratio for the human fingerpad *in vivo* is unknown at present. Available *in vitro* data for skin cannot be used as the mechanical properties are known to be different for *in vivo* and *in vitro* conditions. Also, the fingerpad as a heterogeneous structure behaves differently from the skin by itself. We have established an experimental setup where non-invasive measurements of the *in vivo* compressibility of the fingertip can be done on human subjects.⁴⁷ We have indented the fingerpads of four subjects with three different indentors and measured the change in volume of the fingerpad. Our results show that the compressibility of the fingertip increases with increases in both depth of indentation and contact area with the indenter. The highest change in

⁴⁶ T.R.R. Perez and M.A. Srinivasan, "Videomicroscopic Reconstruction of the Human Finger," Project report to the MIT Minority Summer Science Research Program, 1992.

⁴⁷ M.A. Srinivasan, R.J. Gulati, and K. Dandekar, "In Vivo Compressibility of the Human Fingertip," *Proceedings of the Bioengineering Division, American Society of Mechanical Engineers Winter Annual Meeting*, Anaheim, California, November 8-13, 1992.

fingertip volume was about 5 percent, indicating that the Poisson's ratio of the fingerpad is close to, but not equal to 0.5.⁴⁸

1.10.2 Fingertip Models and Finite Element Analyses

In past experiments, we have indented the fingerpads of humans and monkeys *in vivo* using a line load delivered by a sharp wedge and then photographed the resulting skin surface deflections. We have shown that the homogeneous elastic model of the fingertip only roughly approximates the experimental data, while a simple alternative model, which views the fingertip as an elastic membrane filled with an incompressible fluid (like a "waterbed") predicted the observed profiles very well.⁴⁹

More recently, we have performed linear and non-linear finite element analyses of a series of mechanistic models of the fingerpad under a variety of mechanical stimuli.⁵⁰ The models range from a semi-infinite medium to a three-dimensional model based on the actual finger geometry, composed of either a homogeneous elastic material or a thick elastic shell containing a fluid. Simulations of the mechanistic aspects of neurophysiological experiments involving mapping of receptive fields with single point loads, determination of spatial resolution of two-point stimuli, and indentations by single bars as well as periodic and aperiodic gratings have been carried out for 2D homogeneous models. We have also solved the nonlinear contact problem of indentations by cylindrical objects. The large number of numerical calculations needed even for the linear two-dimensional models necessitated the use of the MIT supercomputer. The results show, for example, that the strain energy density at the

receptor site is probably the relevant stimulus that causes the responses recorded from slowly adapting afferent fibers.

After analyzing the 2D models, we found that a 3D model based on the actual geometry of the fingerpad was necessary to generate testable hypotheses about the transduction of mechanical stimuli in primate tactile sense. Using the fingertip geometry data obtained by employing the videomicroscopy system, we constructed a realistic computer model of the primate fingerpad. We then generated a finite element mesh in the model using the solid modeler software PATRAN. After having completed some preliminary checks, we are currently simulating neurophysiological experiments using the 3D model.

1.10.3 Tactile Sensing of Microtexture, Shape, and Softness

We have been collaborating with Professor R.H. LaMotte of Yale University School of Medicine in conducting psychophysical and neurophysiological studies on how humans sense by touch alone the microtextures, shapes and softness of objects.⁵¹ By using methods of photolithography, we etched sub-micron-high bar gratings on glass plates. We have shown that humans can detect extremely fine textures composed of parallel bars only 50 nanometers high.⁵² Our earlier neurophysiological recordings with bigger texture elements indicate that when such fine textures are stroked, skin vibrates and causes Pacinian Corpuscles to respond, thus enabling detection of the microtexture.⁵³

Based on a theoretical analysis of the mechanics of contact, we have demonstrated that the receptors

⁴⁸ M.A. Srinivasan, R.J. Gulati, and K. Dandekar, "Effect of Indenter Shape on the *in vivo* Compressibility of the Human Fingertip," submitted to *J. Biomech.* (1992).

⁴⁹ M.A. Srinivasan, "Surface Deflection of Primate Fingertip Under Line Load," *J. Biomech.* 22(4): 343-349 (1989).

⁵⁰ M.A. Srinivasan and K. Dandekar, "Role of Mechanics in Cutaneous Mechanoreceptor Response," *Soc. Neurosci. Abstr.* (1991); M.A. Srinivasan and K. Dandekar, "Role of Fingertip Geometry in the Transmission of Tactile Mechanical Signals," *Proceedings of the Bioengineering Division, American Society of Mechanical Engineers Winter Annual Meeting*, Anaheim, California, November 8-13, 1992.

⁵¹ M.A. Srinivasan, "Tactual Interfaces: The Human Perceiver," in *Human-Machine Interfaces for Teleoperators and Virtual Environments*, eds. N.I. Durlach, T.B. Sheridan, and S.R. Ellis, NASA Conference Publication 10071, 1991; M.A. Srinivasan and R.H. LaMotte, "Tactile Discrimination and Representation of Texture, Shape, and Softness," *Human-Machine Interfaces for Teleoperators and Virtual Environments*, eds. N.I. Durlach, T.B. Sheridan, and S.R. Ellis, NASA Conference Publication 10071, 1991.

⁵² R.H. LaMotte and M.A. Srinivasan, "Surface Microgeometry: Neural Encoding and Perception," in *Information Processing in the Somatosensory System*, eds. O. Franzen and J. Westman, Wenner-Gren International Symposium Series (London: Macmillan Press, 1991).

⁵³ M.A. Srinivasan, J.M. Whitehouse, and R.H. LaMotte, "Tactile Detection of Slip: Surface Microgeometry and Peripheral Neural Codes," *J. Neurophys.* 63(6): 1323-1332 (1990).

respond to the low-pass filtered versions of surface pressures.⁵⁴ Thus, curvature of the skin surface under an object, which we know from differential geometry is approximated by the second spatial derivative of surface deflection, is coded by exploiting its relation to surface pressure rather than differentiating (which is a noise enhancing process). For the next set of experiments, we have designed and fabricated a high performance tactile stimulator controlled by a PC through transputers. Our ongoing experiments on shape sensing involve use of precisely manufactured cylindrical, ellipsoidal, and spherical surfaces as stimuli.⁵⁵

We have also shown that the human discriminability of compliance of objects depends on whether the object has a deformable or rigid surface. When the surface is deformable, the spatial pressure distribution within the contact region is dependent on object compliance, and hence information from cutaneous mechanoreceptors is sufficient for discrimination of subtle differences in compliance. When the surface is rigid, kinesthetic information is necessary for discrimination, and the discriminability is much poorer than that for objects with deformable surfaces.

1.10.4 Development of a Computational Theory of Touch

Although the "hardware" of the tactile apparatus in humans and robots is different, they have the common feature of mechanosensors embedded in a deformable medium. Thus, the computational problem of coding (predicting sensor response for a given mechanical stimulus at the surface) and decoding (inferring the mechanical stimulus at the surface by suitably processing the sensor response) need similar mechanistic analyses for their solution. We have developed a computational theory for an idealized medium subjected to arbitrary pressure or displacement loading conditions and have provided

explicit formulae for the coding and decoding problems.⁵⁶

In collaboration with Dr. Annaswamy of the Department of Mechanical Engineering at MIT, we have investigated some of the identification and control problems that occur in the context of manipulation when compliance is present in the end-effectors as well as in the object.⁵⁷ In order to understand the fundamental aspects of these tasks, we have analyzed the problem of identification of compliant objects with a single finger contact, as well as under a two-finger grasp. Assuming that the finger and the compliant object are constrained to deform along a single spatial dimension, we have carried out parameter identification using either force or displacement inputs to the rigid backing of the end-effector. Based on this analysis, control strategies are developed to achieve a desired manipulation of the object in the workspace. Animated graphical renderings have been developed to visually illustrate the presence or absence of slipping and crushing during an active manipulation task. The theoretical results can be used to generate testable hypotheses for human or robot experiments on tactual sense.

1.11 Biomechanics of Skin-Object Contact

Sponsor

U.S. Navy - Office of Naval Research
Grant N00014-91-J-1454

Project Staff

Dr. Mandayam A. Srinivasan, Jyh-Shing Chen,
Rogeve J. Gulati, Louise Jandura

Although physical contact is ubiquitous in our interactions with objects in the environment, we do not yet understand the phenomena occurring at the

⁵⁴ M.A. Srinivasan and R.H. LaMotte, "Encoding of Shape in the Responses of Cutaneous Mechanoreceptors," in *Information Processing in the Somatosensory System*, eds. O. Franzen and J. Westman, Wenner-Gren International Symposium Series, (London: Macmillan Press, 1991).

⁵⁵ R.H. LaMotte, M.A. Srinivasan, and A. Klusch-Petersen, "Tactile Discrimination and Identification of the Shapes and Orientations of Ellipsoidal Objects," *Soc. Neurosci. Abstr.* (1992).

⁵⁶ M.A. Srinivasan, *Tactile Sensing in Humans and Robots: Computational Theory and Algorithms*, Newman Laboratory Technical Report, Dept. of Mech. Eng., MIT, 1988; M.A. Srinivasan, "Computations in Tactile Sensing," *Proceedings of Computation and Neural Systems (CNS '92) Meeting*, San Francisco, California, 1992.

⁵⁷ A.M. Annaswamy and M.A. Srinivasan, "Adaptive Control for Grasping and Manipulation of Compliant Objects with Compliant Fingerpads," *Proceedings of the American Control Conference*, Boston, Massachusetts, 1991; A.M. Annaswamy, M.A. Srinivasan, and S. Weibel, "Identification for Grasping and Manipulation of Compliant Objects with Compliant Fingerpads," submitted to *IEEE Trans. Automatic Control*.

skin-object interface. As mentioned before, the spatio-temporal distribution of mechanical loads on skin at the contact interface is the source of all tactile information. These loads, specified as pressure, displacements, etc., depend on the geometrical and material properties of both the contacting entities as well as the overall forces of interaction. The goal of this project is to determine the growth and motion of contact regions and associated force variations over time between the human fingerpad and carefully chosen transparent test objects whose microtexture, shape or softness is varied in a controlled manner. These results are being used to gain a deeper understanding of the data we have already obtained for the same test objects, such as electrophysiologically recorded responses of cutaneous mechanoreceptive afferent fibers, and psychophysically determined human discriminabilities.

Our initial goal was to record the forces and video-images of contact under active touch when subjects press or stroke various transparent specimens mounted on a force transducer. Accordingly, we designed a videomicroscopy system and a force sensing system, both interfaced to a computer. The videomicroscopy system consists of a set of video zoom lenses attached to a high-resolution CCD camera whose output can either be digitized directly at about 5 frames/s or stored on a laserdisk at real-time frame rates (30 frames/s) for off-line digitization. The zoom lenses enable continuous variation of magnification with the field of view covering the entire fingerpad or only a few fingerprint ridges. High contrast images are achieved with coaxial lighting. In collaboration with our colleagues at the Artificial Intelligence Laboratory at MIT, we designed and built two 6-axis force sensors that are customized to our application. These sensors have much higher resolutions (10 bit) than commercial sensors operating in comparable range of forces (5 Newtons). The transparent test objects can be attached to these sensors for both biomechanical and psychophysical experiments.

Using the test facility described above, we have performed a set of experiments with human subjects to investigate the relationship between the contact force, contact area, and compliance of the object. The experiments involved active indentation of transparent compliant rubber specimens and a glass plate with the subjects' fingerpads. Static video images of the contact regions were captured at various force levels and magnifications. In order to minimize the effects of non-uniform illumination, we implemented homomorphic image processing algorithms. This essentially consisted of high-pass filtering to remove the low frequency (spatial) illumination intensity variations so that only the higher

frequency variations due to the fingerprint patterns remained in the image. For high magnification images, since the spatial frequency of non-uniform lighting was of the same order as the finger ridge frequency, image decimation techniques had to be employed in addition to homomorphic processing. The processed images showed that contact regions consisted of discontinuous "islands" along each finger ridge with clear distinction between contact and non-contact regions over the entire field of view.

As expected, the results show that the nominal overall contact area increases as the contact force increases for all the specimens. More interestingly, the percentage of actual contact area relative to the nominal (overall) contact area also increases and is a function of the object compliance. For the plane glass plate, the percentage contact area is only around 18 percent for 0.1 N force and about 22 percent for 1.5 N force. In contrast, the percentage contact area for a compliant rubber specimen is much higher than that for the plane glass plate, about 43 percent for 0.1 N force and more than 80 percent for 1.5 N force. The implication to tactual discrimination of softness is that for objects whose compliances can be discriminated even when the overall contact areas under a given contact force are the same, the actual contact areas can differ by a factor of two or more. The actual pressure distribution, which acts only within the discontinuous contact islands on the skin, will therefore be radically different for the different objects. Consequently, a spatio-temporal neural code for object compliance emerges with far higher resolution than an intensive code such as the average pressure over the overall contact area. These results are in agreement with our hypothesis that the neural coding of objects with deformable surfaces (such as rubber) is based on the spatio-temporal pressure distribution on the skin. This was one of the conclusions from our psychophysical, biomechanical, and neurophysiological experiments in a companion project conducted in collaboration with Professor R.H. LaMotte of the Yale University School of Medicine.

In addition to helping us develop an understanding of the processes involved in the peripheral neural encoding of object compliance information, the results of these experiments provide testable hypotheses for investigating cortical representation of this information and the processing algorithms used by the central nervous system for decoding the peripheral neural signals. These results are also useful in the design of tactile displays that convey object compliance information to human operators in teleoperation and virtual environment

systems.⁵⁸ The results of the experiments also help in the design of tactile sensors for robots and development of algorithms to decode the sensor information on object compliance.

1.12 Human and Robot Hands: Mechanics, Sensorimotor Functions and Cognition

Sponsor

U.S. Navy - Office of Naval Research
Grant N00014-92-J-1814

Project Staff

Dr. Mandayam A. Srinivasan, Dr. J. Kenneth Salisbury, Nathaniel I. Durlach, Louise Jandura, Kiran B. Dandekar

This is a new project funded by the University Research Initiative Program of the Office of Naval Research (ONR) which involves several investigators from MIT, Harvard University, and Yale University. The premise is that humans and robots can be viewed as two implementations of systems that perform tactual sensorimotor tasks under a common set of constraints. By devising a research plan for the study of human and robot hands that focuses on the commonalities rather than the differences, we propose to achieve mutually beneficial advances in both fields. Specifically, we propose to carry out a program of research with the following related thrusts. We will:

1. Construct a high precision "glass smooth" robot which will serve as the core of both human and robotic experiments. This robot will have an integrated design of tactile sensing and mechanical subsystems. Initially, the sensors will include force and motion sensors; subsequently, we will incorporate a newly developed tactile array using micromechanics techniques.
2. Carry out a suite of experiments aimed at (1) determining the abilities and limitations of the sensorimotor functions of human and robot hands and (2) understanding the mechanisms and information representations they employ. We propose to design and fabricate several experimental stations based on robotic technology for conducting a wide range of

biomechanical, neurophysiological, and psychophysical experiments on human and animal tactual systems as well as measurements on robotic prototypes.

3. Develop methods applicable to both humans and robots for integrating tactual data from multiple types of sensors, multiple spatially separated sensors, and sequences of multiple contacts to achieve a consistent perception of the external environment. We will explore methods for using this integrated information for carrying out exploratory and manipulation tasks as well as inferring object structure and function.
4. Articulate design criteria for robot systems to be employed in tactual tasks. We will test these criteria in a number of robotic testbeds.

During the past few months, a two degree of freedom robot capable of motion in a plane has been fabricated and assembled and is currently being tested for use as a tactile stimulator. The original version of the robot was designed by Professor R. Howe of Harvard University and minor modifications were made to enhance its use as a tactile stimulator. The stimulator can be operated under both position and force control. It will be used to conduct a variety of biomechanical and psychophysical experiments to investigate human tactile sense.

In collaboration with Dr. J.K. Salisbury of MIT and his students, the first generation design of an Instrumented Screwdriver (ISD) has been completed, and its fabrication is underway. This device will simulate the task of using a screwdriver in order to test the force control capability of humans. The "target screw" is simulated by a computer-controlled magnetic particle brake. For example, during the performance of force tracking tasks by a subject, the force vector under each of two or three fingerpads can be measured by custom-designed six-axis force sensors. The subject will perform the tasks using active touch with his or her fingerpads under both normal and locally anesthetized conditions to isolate the sources of tactual information. We have completed a set of similar force tracking experiments using a stationary six-axis force sensor and the data is being analyzed. Preliminary results show that local anesthesia, which blocks tactile information from cutaneous mechanoreceptors,

⁵⁸ M.A. Srinivasan, sections on haptic perception and haptic interfaces, in *Research Directions in Virtual Environments: Report of an NSF Invitational Workshop, Computer Graphics*, ed. G. Bishop et al. 26(3): 153-177 (1992); M.A. Srinivasan and J.K. Salisbury, sections on haptics, in *Virtual Environment Technology for Training*, BBN Report No. 7661, Prepared by the Virtual Environment and Teleoperator Research Consortium (VETREC) affiliated with MIT, 1992.

does not seriously impair the performance of the subjects. This implies that among the tactile and kinesthetic sources of force information, humans may be relying on the kinesthetic channel for force control, even though the tactile channel has better sensory resolution.

1.13 Publications

- Durlach, N.I., A. Rigopoulos, X.D. Pang, W.S. Woods, A. Kulkarni, H.S. Colburn, and E.M. Wenzel. "On the Externalization of Auditory Images." *Presence* 1: 251-257 (1992).
- Durlach, N.I. "Virtual Environments: Introductory Remarks." *J. Acoust. Soc. Am.* 4: 2331-2332 (1992).
- Durlach, N.I., R.M. Held, and B.G. Shinn-Cunningham. "Super Auditory Localization Displays." *Society for Information Display International Symposium, Digest of Technical Papers* 23: 98-101 (1992).
- Greenberg, J.E., and P.M. Zurek. "Evaluation of an Adaptive Beamforming Method for Hearing Aids." *J. Acoust. Soc. Am.* 91: 1662-1676 (1992).
- LaMotte, R.H., Srinivasan M.A., and A. Klusch-Petersen. "Tactile Discrimination and Identification of the Shapes and Orientations of Ellipsoidal Objects." *Soc. Neurosci. Abstr.* (1992).
- Rabinowitz, W.M., D.K. Eddington, L.A. Delhorne, and P.A. Cuneo. "Relations Among Different Measures of Speech Reception in Subjects Using a Cochlear Implant." *J. Acoust. Soc. Am.* 92: 1869-1881 (1992).
- Rankovic, C.M., R.L. Freyman, and P.M. Zurek. "Potential Benefits of Adaptive Frequency-Gain Characteristics for Speech Reception in Noise." *J. Acoust. Soc. Am.* 91: 354-362 (1992).
- Reed, C.M., N.I. Durlach, and L.A. Delhorne. "Historical Overview of Tactile Aid Research." In *Proceedings of the Second International Conference on Tactile Aids, Hearing Aids, and Cochlear Implants*. Eds. A. Risberg and K.-E. Spens. Stockholm, Sweden: Royal Institute of Technology, 1992. Forthcoming.
- Reed, C.M., L.A. Delhorne, and N.I. Durlach. "Results Obtained with Tactaid II and Tactaid VII." *Proceedings of the Second International Conference on Tactile Aids, Hearing Aids, and Cochlear Implants*. Eds. A. Risberg and K.-E. Spens. Stockholm, Sweden: Royal Institute of Technology, 1992. Forthcoming.
- Reed, C.M., and L.A. Delhorne. "Field Study of Deaf Adult Users of Tactaid II and Tactaid VII." Presentation made at the Annual Convention of the Association for Late Deafened Adults, Boston, Massachusetts, September 10-13, 1992.
- Reed, C.M., N.I. Durlach, and L.A. Delhorne. "Natural Methods of Tactual Communication." In *Tactile Aids for the Hearing Impaired*. Ed. Ian R. Summers. Whurr Publishers Limited, 1992, pages 218-230.
- Reed, C.M., N.I. Durlach, and L.A. Delhorne. "The Tactual Reception of Speech, Fingerspelling, and Sign Language by the Deaf-Blind." *SID 92 Digest* pp. 102-105 (1992).
- Reed, C.M., W.M. Rabinowitz, N.I. Durlach, L.A. Delhorne, L.D. Braida, J.C. Pemberton, B.D. Mulcahey, and D.L. Washington. "Analytic Study of the Tadoma Method: Improving Performance through the Use of Supplementary Tactual Displays." *J. Speech Hear. Res.* 35: 450-465 (1992).
- Shinn-Cunningham, B.G., N.I. Durlach, and R.M. Held. "Adaptation to Transformed Auditory Localization Cues in a Hybrid Real/Virtual Environment." *J. Acoust. Soc. Am.* 4: 2334 (1992).
- Shinn-Cunningham, B.G., P.M. Zurek, and N.I. Durlach. "Adjustment and Discrimination Measurements of the Precedence Effect." *J. Acoust. Soc. Am.* Forthcoming.
- Srinivasan, M.A. "Computations in Tactile Sensing." *Proceedings of Computation and Neural Systems (CNS '92) Meeting*, San Francisco, California, 1992.
- Srinivasan, M.A. Sections on haptic perception and haptic interfaces. In *Research Directions in Virtual Environments: Report of an NSF Invitational Workshop*. Ed. G. Bishop et al. *Comput. Graphics* 26 (3): 153-177 (1992).
- Srinivasan, M.A., and K. Dandekar. "Role of Fingertip Geometry in the Transmission of Tactile Mechanical Signals." *Proceedings of the Bioengineering Division, American Society of Mechanical Engineers Winter Annual Meeting*, Anaheim, California, November 8-13, 1992.
- Srinivasan, M.A., R.J. Gulati, and K. Dandekar. "In vivo Compressibility of the Human Fingertip."

Proceedings of the Bioengineering Division, American Society of Mechanical Engineers Winter Annual Meeting, Anaheim, California, November 8-13, 1992.

Srinivasan, M.A., and J.K. Salisbury. Sections on haptics, In *Virtual Environment Technology for Training*, BBN Report No. 7661, The Virtual Environment and Teleoperator Research Consortium (VETREC) affiliated with MIT, 1992.

Tan, H.Z., X.D. Pang, and N.I. Durlach. "Manual Resolution of Length, Force, and Compliance." *Proceedings of the American Society of Mechanical Engineers, Winter Annual Meeting, Anaheim, California, November 8-13, 1992.*

Uchanski, R.M., K.M. Millier, C.M. Reed, and L.D. Braida. "Effects of Token Variability on Vowel Identification." In *The Processing of Speech: From the Auditory Periphery to Word Recognition*. Berlin: Mouton de Gruyter. Forthcoming.

Zurek, P.M. "Binaural Advantages and Directional Effects in Speech Intelligibility." In *Acoustical Factors Affecting Hearing Aid Performance II*, Eds. G.A. Studebaker and I. Hochberg. Boston: Allyn and Bacon, 1992.

Zurek, P.M. "Detectability of Transient and Sinusoidal Otoacoustic Emissions." *Ear Hear.* 13: 307-310 (1992).

Theses

Gulati, R. *In Vitro Compressibility of the Human Fingerpad*. B.S. thesis., Dept. of Mech. Eng., MIT, 1992.

Martin, G.R. *Studies of Real-Time Multiband Adaptive Gain Hearing Aids*. S.M. thesis, Dept. Electr. Eng. and Comput. Sci., MIT, 1992.

Stadler, R.W. *Optimally Directive Microphones for Hearing Aids*. S.M. thesis, Dept. Electr. Eng. and Comput. Sci., MIT, 1992.

Section 3 Auditory Physiology

Chapter 1 Signal Transmission in the Auditory System

Chapter 1. Signal Transmission in the Auditory System

Academic and Research Staff

Professor Lawrence S. Frishkopf, Professor Nelson Y.S. Kiang, Professor William T. Peake, Professor William M. Siebert, Professor Thomas F. Weiss, Dr. Alice M. Berglund, Dr. Peter A. Cariani, Dr. Bertrand Delgutte, Dr. Donald K. Eddington, Dr. Dennis M. Freeman, Dr. John J. Guinan, Jr., Dr. William M. Rabinowitz, Dr. John J. Rosowski, Seth M. Hall, Joseph Tierney, Marc A. Zissman

Visiting Scientists and Research Affiliates

Dr. Sunil Puria, Dr. Jay T. Rubinstein, Mark R. Nilsen, Frank J. Stefanov-Wagner, Meng Y. Zhu

Graduate Students

Charles C. Abnet, Charles Q. Davis, Scott B.C. Dynes, Michael P. McCue, Jennifer R. Melcher, Lisa F. Shatz

Undergraduate Students

Henry E. Chung

Technical and Support Staff

Janice L. Balzer, David A. Steffens

1.1 Introduction

Research on the auditory system is carried out in cooperation with two laboratories at the Massachusetts Eye and Ear Infirmary (MEEI). Investigations of signal transmission in the auditory system involve the Eaton-Peabody Laboratory for Auditory Physiology, whose long-term objective is to determine the anatomical structures and physiological mechanisms that underlie vertebrate hearing and to apply this knowledge to clinical problems. Studies of cochlear implants in humans are carried out at the MEEI Cochlear Implant Research Laboratory. The ultimate goal for these devices is to provide speech communication for the deaf. Cochlear implants electrically stimulate intracochlear electrodes to elicit patterns of auditory nerve fiber activity that the brain can learn to interpret.

1.2 Signal Transmission in the External and Middle Ear

The goal of this work is to understand the relationship between the structure and function of the external and middle ear.

1.2.1 Structure-Function Relations in Middle Ears

Sponsors

National Institutes of Health
Grant R01-DC-00194

Project Staff

Dr. John J. Rosowski, Professor William T. Peake, David A. Steffens

In this project, we have determined how structural variations in the middle- and external ears of various vertebrate species contribute to differences in auditory function. Our work in this area has taken two interrelated paths. One path has been to make acoustic measurements of middle- and external-ear function in the gerbil, a small mammal with a highly specialized middle-ear air space and life style.¹ Measurements of middle-ear input impedance were made before and after manipulations of the middle-ear air space (figure 1). The impedance measured with the air spaces sealed, vented, partially opened and widely opened are all consistent with a model in which the impedance of

¹ M.E. Ravicz, J.J. Rosowski and H.F. Voigt, "Sound-power Collection by the Auditory Periphery of the Mongolian Gerbil *Meriones unguiculatus*. I: Middle-ear Input Impedance," *J. Acoust. Soc. Am.* 92: 157-177 (1992).

the middle-ear air spaces is in series with the rest of the middle-ear (figure 2). Furthermore, the data and model analysis indicate that the air-space impedance is primarily reactive except at the lowest frequencies. When extrapolated to human ears, these results can be used to predict the effects of certain middle-ear pathologies.

The second method we use to investigate middle-ear structure and function is comparison of the dimensions of various middle-ear structures in mammals with known auditory capabilities. The results of this analysis illustrate that mammals with good hearing sensitivity at frequencies less than 1 kHz tend to have larger middle-ear dimensions while those species with sensitive hearing restricted to the high and ultrasonic frequencies ($f > 10$ kHz) have smaller middle-ear dimensions. The results of this analysis have been used to predict the auditory capabilities of very early fossil mammals.² These predictions suggest that the small shrew-like mammals that existed at the reptile-mammal transition 200 million years ago were not sensitive to low-frequency sounds as modern reptiles are but, like modern shrews and rats, were most sensitive to high-frequency sounds.

1.2.2 Basic and Clinical Studies of Middle-Ear Function

Sponsor

National Institutes of Health
Contract P01-DC-00119
Fellowship F32-DC00073

Project Staff

Dr. John J. Rosowski, Professor William T. Peake,
Dr. Sunil Puria

Our goal is to understand the relationship between the structure and function of auditory periphery including definition of the effect of middle- and external-ear pathologies on auditory function. To help achieve this goal, we are measuring function in human ears using temporal-bones donated at the time of death, and we have applied models from our animal work to questions concerning middle-ear pathologies and treatments.

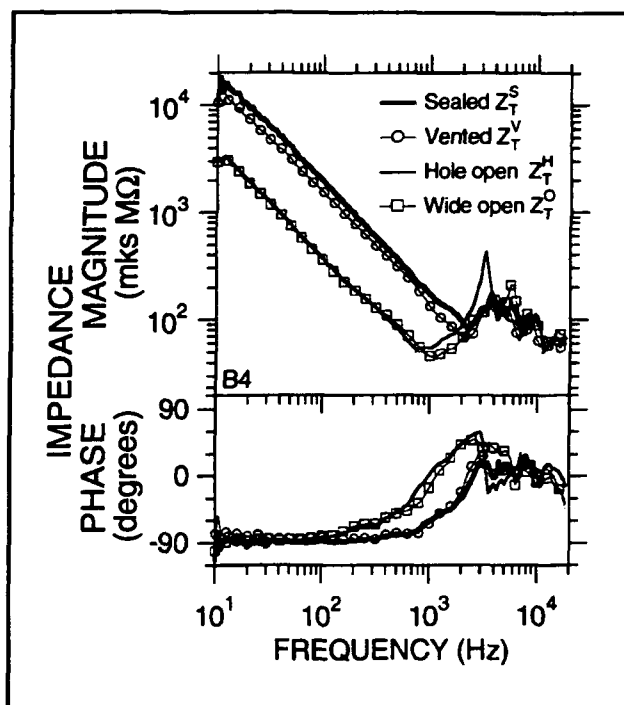


Figure 1. Measurements of middle-ear input impedance in a gerbil ear before and after various manipulations of the middle-ear air spaces: sealed, the air spaces are closed; vented, a long-narrow tube is placed through the bony walls of the air space, the tube vents any excess pressure in the air space to the atmosphere; hole open, a small 2 mm diameter, hole is made in the air space walls; wide open, the bony walls of the air space are widely opened.

In conjunction with Dr. Saumil Merchant, a physician member of the Otolaryngology Department at the Massachusetts Eye and Ear Infirmary, measurements were made of the cochlear input impedance (the acoustic load on the middle ear) in seven fresh and thawed temporal-bone specimens. Preliminary results of these measurements³ suggest that the cochlear impedance is loosely approximated by a series combination of a cochlear resistance and the stiffness of the oval window membrane (annular ligament) at the entrance to the inner ear, which has been observed in animal ears. However, these measurements also indicate a resistive component to the annular-ligament impedance which has not been seen in animal work. This work is being expanded to include measurements of the

² J.J. Rosowski, "Hearing in Transitional Mammals: Predictions from the Middle-ear Anatomy and Hearing Capabilities of Extant Mammals," in *The Evolutionary Biology of Hearing*, eds. D.B. Webster, R.R. Fay and A.N. Popper (New York: Springer-Verlag, 1992) pp. 615-631.

³ S.N. Merchant, M.E. Ravicz and J.J. Rosowski, "The Acoustic Impedance of the Stapes and Cochlea in Human Temporal Bones," Abstracts of the 15th Mid-Winter Research Meeting of the Association for Research in Otolaryngology, pg. 98 (1992).

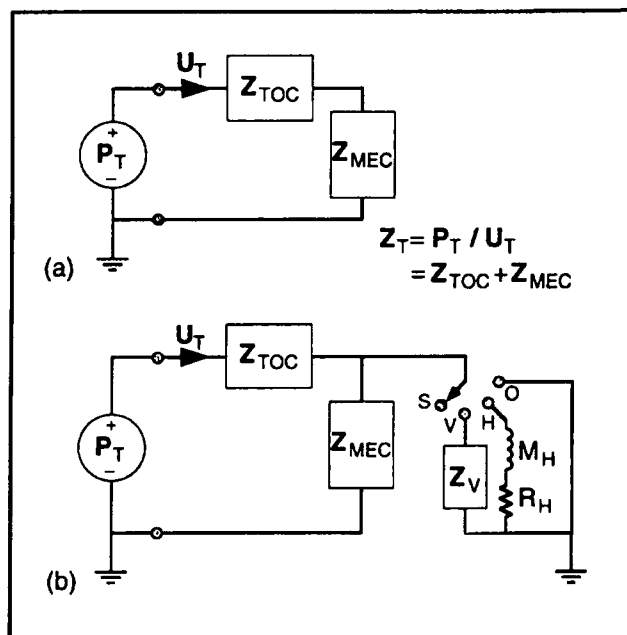


Figure 2. (a) The series model of the middle ear, relating the middle-ear input impedance Z_T to the impedance of the air spaces Z_{MEC} , and the rest of the middle ear Z_{TOC} . (b) Model interpretations of the effect of sealing the air spaces. Moving the switch on the right to each of the four possible positions models: a sealed middle-ear air space S , venting V , opening a small hole H , and widely opening O . Z_V is the impedance of the vent tube and the series combination of M_H and R_H is the acoustic impedance of the small hole.

middle-ear transfer function in isolated temporal bones.

Measurements and models from our animal work were used to produce a model (figure 3) of the effect of direct acoustic stimulation of the cochlear windows, which bypass the tympanic membrane and ossicles in normal and pathological human ears.⁴ Analysis of the model demonstrates that the alternate "acoustic" pathway for sound entry to the inner ear is not important in normal auditory function but may be a major component of that function in pathological ears in which the normal conduction mechanism is interrupted. Comparisons of the model's predictions of hearing function in pathological cases with patient audiograms support the hypothesized role of direct-acoustic stimulation in pathological ears (figure 4).

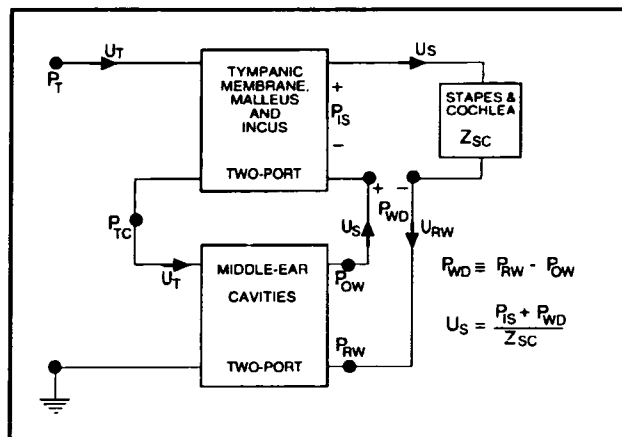


Figure 3. A model of the combination of "ossicular" and "acoustic" middle-ear sound transmission. The ossicular path models motions of the tympanic membrane and ossicles that produce a pressure on the stapes and cochlea P_{IS} . The effective stimulus from the "acoustic" path is the sound pressure difference acting on the inner ear windows P_{WD} .

1.3 Cochlear Mechanisms

Sponsor

National Institutes of Health
Contract P01-DC00119
Grant R01-DC00238
Grant R01-DC00473

Project Staff

Professor Thomas F. Weiss, Dr. Dennis M. Freeman, Lisa F. Shatz, Charles Q. Davis, Charles C. Abnet, Henry E. Chung

Our goal is to study the mechanisms by which motions of macroscopic structures in the inner ear produce motions of the mechanically sensitive hair bundles of sensory receptor (hair) cells. Because of its strategic location, the tectorial membrane must play an important role in the mechanical stimulation of hair bundles. However, there have been few direct observations of the tectorial membrane, and its critical properties remain obscure. During the past year, we have continued our efforts to measure the physicochemical properties of the tectorial membrane.

Changes in the ionic composition of the bath induce changes in the volume of the isolated tectorial

⁴ W.T. Peake, J.J. Rosowski, and T.J. Lynch, III, "Middle-ear Transmission: Acoustic Versus Ossicular Coupling in Cat and Human," *Hear. Res.* 57: 245-268 (1992).

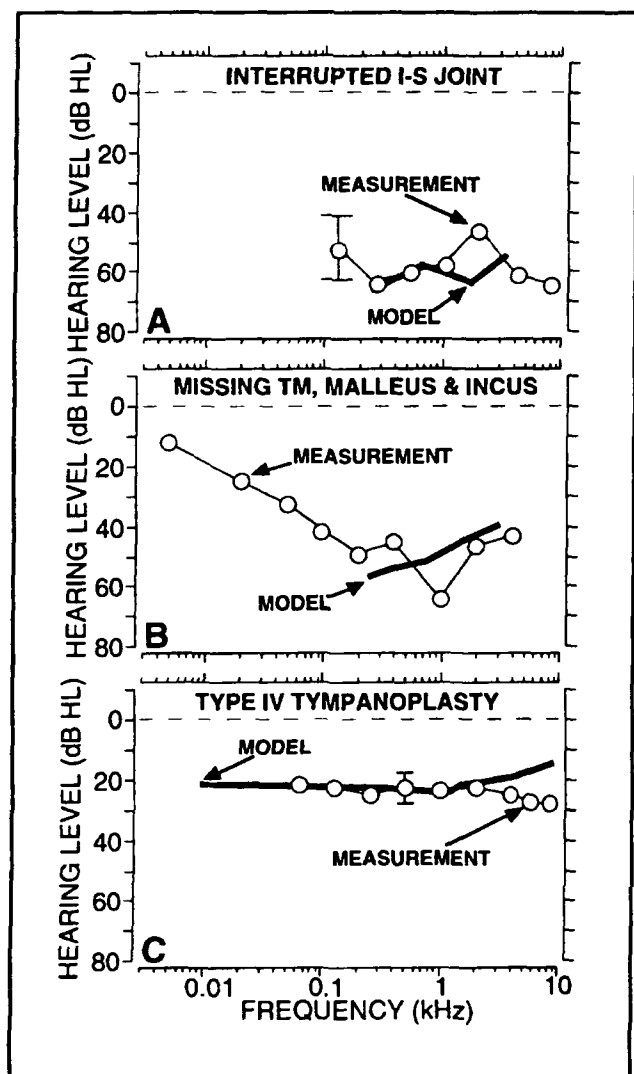


Figure 4. Comparisons of the predictions from the model of figure 3 and measured audiograms for cases of: (a) interrupted incudo-stapedial joint, (b) missing tympanic membrane, malleus and incus, and (c) direct acoustic stimulation of the oval window only, a condition that mimics a Type IV tympanoplastic procedure to reconstruct the middle ear after severe middle-ear disease. The dashed lines illustrate normal hearing levels. Hearing losses are illustrated by increased hearing levels.

membrane of the chick.⁵ The volume changes can be large, often increasing the thickness of the tectorial membrane by more than a factor of two, and have a slow time course, often continuing for hours. Although many of the changes are reversed

when the original bath composition is restored, permanent changes in the structure of the tectorial membrane can result from long exposures to high-sodium, low-calcium solutions.

During the past year, we have studied the effects of brief (15 minute) exposures to test solutions. We have found (1) that responses to brief exposures are consistent with those for long exposures and (2) that the effects of brief exposures are more nearly reversible. Therefore, we have been able to measure responses to brief exposures of as many as 20 different ionic solutions in a single preparation. Results show that even very low levels of calcium ($< 10 \mu\text{mol/L}$) significantly change the structure of the tectorial membrane.

Because of the considerable diversity in tectorial membrane structure across species, it is important to compare results obtained for chick tectorial membrane with results from other species. During the past year, we have initiated studies of physicochemical properties of the tectorial membrane of the alligator lizard—a species in which the importance of mechanical processes at the level of individual hair bundles has been directly demonstrated. Initial results suggest that the tectorial membrane of the lizard (1) swells when high-potassium, low-calcium solutions are replaced by high-sodium, low-calcium solutions and (2) shrinks when calcium is increased from $\mu\text{mol/L}$ to mmol/L concentrations. These results are qualitatively similar to results with chick tectorial membrane.

Publications

Freeman, D.M., D.H. Hendrix, D. Shah, L.F. Fan, and T.F. Weiss. "Effect of Lymph Composition on an *in vitro* Preparation of the Alligator Lizard Cochlea." *Hear. Res.* 65: 83-98 (1993).

1.3.1 Stimulus Coding in the Auditory Nerve and Cochlear Nucleus

Sponsor

National Institutes of Health
Contract P01-DC00119
Grant T32-DC00006
Grant T32-DC00038⁶

⁵ D.M. Freeman, D.A. Cotanche, F. Ehsani, and T.F. Weiss, "Effect of Na^+ , K^+ , and Ca^{++} Concentration on the Isolated Tectorial Membrane of the Chick." In preparation.

⁶ NIH Training Grant for the HST Speech and Hearing Science Program. This grant's Principal Investigator is Nelson Y.S. Kiang.

Project Staff

Dr. Bertrand Delgutte, Dr. Peter A. Cariani

We have been investigating the correspondence between human auditory psychophysics and neural activity patterns at the level of the auditory nerve and the cochlear nucleus. We want to gain insight into what kinds of information the auditory system uses to represent complex acoustic stimuli. We have recorded from representative samples of auditory nerve fibers in anesthetized cats and computed autocorrelation histograms to estimate the aggregate interspike interval distribution over the entire auditory nerve. Our results for a wide range of complex stimuli suggest that the pitch heard by human listeners corresponds to the most frequent interspike interval in the auditory nerve.

In the past year, we ran a physiological analog of a classical psychophysical experiment in which all three components of a harmonic complex are shifted in frequency by the same amount, resulting in a shift in perceived pitch. Our results showed that the pitch shifts estimated from the interspike interval distributions closely followed those observed in psychophysical studies. We also carried out a physiological analog of a pitch dominance experiment in which two harmonic complexes (harmonics 3-5 versus harmonics 6-12) with slightly different fundamental frequencies (F_0) were presented together. At F_0 s above 150 Hz, the most frequent interspike interval in the auditory nerve always corresponded to the pitch associated with harmonics 3-5 rather than the pitch of harmonics 6-12, consistent with human psychophysical data. These results show that models of pitch perception based on aggregate interspike interval distributions can account for classical experimental results for pitch shift and pitch dominance.

Psychophysical experiments show that listeners can identify better both constituents of a pair of simultaneously-presented vowels if the pitches of the two vowels are slightly different. In a physiological experiment motivated by this result, we have found that (1) each single vowel evokes a characteristic aggregate interspike interval distribution, (2) one single vowel constituent of a double vowel pair can always be identified from correlations between the double vowel pattern and the various single vowel patterns, (3) the second single vowel constituent can often be identified if the first correctly identified vowel is "subtracted" from the double vowel pattern (via partial correlation), and (4) vowel identification through this method improves when the voice pitches are made slightly different. These results suggest that vowels can be discriminated using aggregate temporal information alone and

that explicit pitch identification may not be necessary to account for improved identification of constituent vowels with increasing voice pitch differences.

When two sounds with different pitches are played simultaneously, certain pitch ratios appear to be pleasant or consonant, while others appear harsh or dissonant. In order to investigate neural correlates of these phenomena, we have recorded the responses of auditory-nerve to stimuli associated with different degrees of consonance and dissonance. Response patterns to pairs of pure tones forming dissonant intervals showed beating for all responding fibers. No beating patterns were found for pure-tone consonant intervals. Beating patterns were also found for dissonant pairs of complex tones, but were restricted to fibers whose characteristic frequencies were close to two partials of the complex tones. These beating patterns in the frequency range 20-200 Hz are thought to be physiological correlates of roughness. A quantitative model that sums the physiologic roughness across the array of auditory-nerve fibers can predict the relative dissonances of the different musical intervals. These results suggest that certain aspects of harmony perception are encoded in the temporal patterns of discharge of auditory-nerve fibers.

Publications

- Cariani, P., B. Delgutte, and N.Y.S. Kiang. "The Pitch of Complex Sounds is Simply Coded in Interspike Interval Distributions of Auditory Nerve Fibers." *Soc. Neurosci. Abstr.* 18(1): 383 (1992).
- Cariani, P., and B. Delgutte. "Interspike Interval Distributions of Auditory Nerve Fibers in Response to Concurrent Vowels with Same and Different Fundamental Frequencies." *Abstr. Assoc. Res. Otolaryngol.* 16 (1993).
- Delgutte, B., and P. Cariani. "Coding of the Pitch of Harmonic and Inharmonic Complex Tones in the Interspike Intervals of Auditory-nerve Fibers." In *Audition, Speech, and Language*. Ed. M.E.H. Schouten. Berlin: Mouton-De Gruyter, 1992, pp. 37-45.
- Tramo, M.J., P.A. Cariani, and B. Delgutte. "Representation of Tonal Consonance and Dissonance in the Temporal Firing Patterns of Auditory Nerve Fibers: Responses to Musical Intervals Composed of Pure Tones vs. Harmonic Complexes." *Soc Neurosci Abstr.* 18(1): 382 (1992).

1.4 Electrical Stimulation of the Auditory Nerve

Sponsor

National Institutes of Health
Contract P01-DC00361

Project Staff

Dr. Bertrand Delgutte, Scott B.C. Dynes

The goal of these studies is to understand the mechanisms of electrical stimulation of the auditory nerve to design better cochlear implants. For this purpose, we record from auditory-nerve fibers in anesthetized cats in response to electric stimuli applied through electrodes similar to those used in humans. In the past year, we have measured the responses to pairs of brief monophasic pulses separated by short intervals. This stimulus is the simplest configuration that can show some of the interpulse interactions that are likely to occur in interleaved sampling speech processors. For suprathreshold first pulses, the threshold for the second pulse was found to decrease with increasing interpulse delay, as expected from the refractory properties of nerve fibers. Interpulse delays at thresholds were consistently shorter for a cathodal first pulse than for an anodal first pulse with the same amplitude. (The second pulse was always anodal.) This latency difference can be interpreted as the spike conduction time from a peripherally-located cathodal site of excitation to the more central anodal site of excitation. Consistent with this interpretation, the difference in latencies between cathodal and anodal single pulses was approximately equal to the conduction time estimated from the two-pulse experiment. We plan to pursue these experiments to identify the different sites of nerve excitation for various stimulus conditions.

Another series of experiments examined whether responses to two-pulse stimuli can be used to predict responses for more complex stimulus conditions. Three pulses of equal amplitude were presented in rapid succession. The pulse amplitude was chosen so that each pulse would, by itself, be well above threshold. The delay between Pulses 1 and 2 was adjusted so that Pulse 2 would just produce a spike with high probability, and the delay between Pulses 2 and 3 was adjusted so that Pulse 3 would meet the same criterion. The delay between Pulses 2 and 3 was found to be consistently longer than the delay between Pulses 1 and

2. This result shows that the refractory period cannot be seen as a fixed characteristic of a neuron because it depends on past history of stimulation. Model simulations show that the magnitude of the changes in refractory period are severely underestimated by classical Hodgkin-Huxley dynamics. This result has implications for the design of interleaved sampling speech processors in which one attempts to minimize interactions between successive pulses.

1.5 Interactions of Middle-Ear Muscles and Olivocochlear Efferents

Sponsor

National Institutes of Health
Contract P01-DC00119

Project Staff

John J. Guinan, Jr.

1.5.1 Basic and Clinical Studies of the Auditory System

Our aim is to determine the actions and interactions of the acoustically elicited middle-ear muscle reflexes and the olivocochlear efferent reflexes.⁷

As a first step in our project to measure the sound-level dependence of the middle-ear acoustic reflexes with and without activation of medial olivocochlear (MOC) efferents, we have begun studying MOC effects on brain stem evoked potentials (BAEPs). In anesthetized cats, we measured BAEPs at the vertex in response to clicks at a variety of sound levels, with and without activation of MOC efferents and before and after the efferents were cut near the vestibulo-cochlear anastomosis. This cut severs the axons to the cochlea but leaves the collaterals to the cochlear nucleus intact.

Before the cuts, stimulation of MOC efferents with an electrode at the midline of the floor of the fourth ventricle shifted the BAEP responses to higher sound levels by approximately the same amount as auditory-nerve responses (N1) were shifted to higher sound levels. After the cuts, no changes in BAEPs were produced by MOC stimulation. Thus, from experiments to date, the effects of efferent stimulation on BAEPs appear to be due solely to MOC inhibition of cochlear responses with no effect attributable to the MOC collaterals to the cochlear

⁷ This project is the direct successor of the 1991 project: Middle-Ear Muscle Reflex.

nucleus. The lack of effect of MOC collaterals to the cochlear nucleus on BAEPs is consistent with these collaterals not innervating bushy cells in the cochlear nucleus⁸ and the hypothesis that bushy cells are the dominant cochlear-nucleus cell type involved in producing BAEPs.⁹ Additionally, the absence of changes in BAEPs due to severing efferents near the vestibulo-cochlear anastomosis means that measurements of BAEPs can serve as a good control for the integrity of the auditory brainstem in experiments on middle-ear muscle reflexes involving such efferent cuts.

During the past year, final manuscript revision was done for publication of our results on the sound-frequency selectivity of single stapedius motoneurons in cats which has now appeared in the *Journal of Neurophysiology*.¹⁰

Publications

Kobler, J.B., J.J. Guinan, Jr., S.R. Vacher, and B.E. Norris. "Acoustic-Reflex Frequency Selectivity in Single Stapedius Motoneurons of the Cat." *J. Neurophysiol.* 68: 807-817 (1992).

1.6 Cochlear Efferent System

Sponsor

National Institutes of Health
Grant R01-DC00235

Project Staff

John J. Guinan, Jr., Michael P. McCue

1.6.1 Olivocochlear Efferent Systems

Our aim is to understand the physiological effects produced by medial olivocochlear efferents which terminate on outer hair cells in the mammalian cochlea.

During the past year, we made a serendipitous discovery that some vestibular afferent fibers respond to sound at high sound levels. An earlier study on the responses of mammalian vestibular fibers to sound stimuli¹¹ concluded that sound does not increase the firing rate of vestibular fibers until sound levels of 120 dB SPL or more which is outside of the normal range of hearing. That work led to the widespread assumption that the auditory responses of vestibular fibers play no role in hearing. The fibers we have found respond to 90 dB SPL tones. This is a high sound level, but is not outside the range of every-day hearing. (It is approximately the level of a loud shout or the level at which middle-ear muscles begin to contract.) Our result, coupled with the finding of Kevetter et al.¹² that showed that some vestibular fibers in gerbils innervate both vestibular brain-stem nuclei and parts of the cochlear nucleus, suggests that the vestibular-auditory fibers which we have discovered might play a role in hearing at high sound levels. We recorded from single units in the inferior vestibular nerve of barbiturate-anesthetized cats. The vestibular-auditory fibers (1) respond to sound with a latency of 2-4 ms., (2) have broad tuning curves with CFs around 1 kHz, (3) have low spontaneous firing rates (0-5/sec), (4) have increased firing in response to efferent shocks (like other vestibular fibers but opposite to the effect of efferents on cochlear-nerve fibers), and (5) have bipolar ganglion cells in the inferior division of Scarpa's ganglion with peripheral processes extending into the saccular nerve and central processes entering the brain stem in the vestibular nerve root (from single-fiber labeling of four neurons). In many lower vertebrates the saccule is both a hearing organ and a vestibular organ, and it may serve as both in mammals. A preliminary

⁸ M.C. Brown, S. Pierce, and A.M. Berglund, "Cochlear-nucleus Branches of Thick (Medial) Olivocochlear Fibers in the Mouse: A Cochleotopic Projection," *J. Comp. Neurol.* 303: 300-315 (1991).

⁹ J.M. Melcher, B.C. Fullerton, J.J. Guinan, Jr., N.Y.S. Kiang, and I.M. Knudson, "Cellular Generators of the Brainstem Auditory Evoked Potential in the Cat," *Soc. Neurosci. Abstr.* 20: 723 (1990).

¹⁰ J.B. Kobler, J.J. Guinan, Jr., S.R. Vacher, and B.E. Norris, "Acoustic-Reflex Frequency Selectivity in Single Stapedius Motoneurons of the Cat," *J. Neurophysiol.* 68: 807-817 (1992).

¹¹ E.D. Young, C. Fernandez, and J.M. Goldberg, "Responses of Squirrel Monkey Vestibular Neurons to Audio-frequency Sound and Head Vibration," *Acta Otolaryn.* 84: 352-360 (1977).

¹² G.A. Kevetter, and A.A. Perachio, "Projections from the Sacculus to the Cochlear Nuclei in the Mongolian Gerbil," *Brain Behav. Evol.* 34: 193-200 (1989).

version of this work will be presented early in 1993.¹³

Publications

McCue, M.P., and J.J. Guinan, Jr. "Acoustic Responses from Primary Afferent Neurons of the Mammalian Sacculus." *Assoc. for Res. in Otolaryngol.* Abstr. 16. Forthcoming.

1.7 Cochlear Implants

Sponsor

National Institutes of Health
Contract P01-DC00361
Contract N01-DC22402

Project Staff

Donald K. Eddington, William M. Rabinowitz, Jay T. Rubinstein, Joseph Tierney, Marc A. Zissman

1.7.1 Project A: Models of Current Spread and Nerve Excitation During Intracochlear Stimulation

Project Staff

Dr. Donald K. Eddington, Dr. Jay T. Rubinstein

The basic function of a cochlear prosthesis is to elicit patterns of activity on the array of surviving auditory nerve fibers by stimulating electrodes that are placed in and/or around the cochlea. By modulating these patterns of neural activity, these devices attempt to present information that the implanted subject can learn to interpret. The spike activity patterns elicited by electrical stimulation depend on several factors: the complex, electrically heterogeneous structure of the cochlea, the geometry and placement of the stimulating electrodes, the stimulus waveform, and the distribution of excitable auditory nerve fibers. An understanding of how these factors interact to determine the activity patterns is fundamental to designing better devices and to interpreting the results of experiments involving intracochlear stimulation of animal and human subjects. As a first step towards this understanding, the goal of this project is to construct a software model of the cochlea that predicts the distribution of potential produced by the stimu-

lation of arbitrarily placed, intracochlear electrodes and use these potential distributions as inputs that drive models of auditory nerve fibers.

This year we continued the development of the three-dimensional, finite difference model of the human cochlea that predicts the potential distribution produced in this structure by electrical stimulation using model electrodes of arbitrary position and geometry. In order to make the use of this model more practical by reducing the time to compute a solution, the model was implemented on a SUN SPARCstation-2 where solutions are computed in twenty minutes rather than the eight hours required by the original VAX-750 system.

A series of solutions were computed to test the model's sensitivity to variations in the resistivity of the major cochlear components (e.g., perilymph, endolymph, bone, nerve and basilar membrane). These solutions documented the stability of the model and confirmed our intuition that the asymmetric potential distributions predicted by the model and reported in previous years reflect the basic, three-dimensional anatomy of this structure.

We are in the final stages of the morphological work on one rat ear that will represent the anatomical component of the electro-anatomical model for this animal. From registered serial sections of the cochlea, we are currently generating the database through which the tissues and their electrical resistances are represented in the three-dimensional model. Using the rat, we will be able to make alterations in the anatomy of the cochlea and make measurements that would be impossible in our human subjects. This will provide an important tool in the future testing and refinement of this electroanatomical model.

Continued development of a single-fiber computer model of myelinated excitation by electrical stimulation has led us to model formulations that more accurately predict the following measurements in the cat: (1) strength-duration time constants for cathodal stimulation of 260 μ s instead of the 80 μ s predicted by the classical model, (2) anodal/cathodal threshold ratios between 1 and 4 instead of the 4.9 predicted by the classical model, (3) conduction velocity 4-6 m/sec/micron that are greater than found in the classical model, and (4) refractory periods that are three times shorter than predicted by the classical model. The anodal/cathodal threshold predictions have also been confirmed qualitatively by measurements made in the rat.

¹³ M.P. McCue and J.J. Guinan, Jr., "Acoustic Responses from Primary Afferent Neurons of the Mammalian Sacculus," *Assoc. for Res. in Otolaryngol.*, Abstr. 16, forthcoming.

1.7.2 Project B: New Sound Processors for Auditory Prostheses

Project Staff

Dr. Donald K. Eddington, Dr. William M. Rabinowitz, Joseph Tierney, Marc A. Zissman

Our collaboration with colleagues at Duke University and the Research Triangle Institute in the development of new processing algorithms to improve the speech reception of cochlear implant users has resulted in laboratory-based systems that increase the average single-syllable word recognition scores by 20 percentage points for the seven subjects tested.¹⁴ In addition to increasing the number of stimulating channels from four to six and implementing a different compression technique, the new algorithms were designed to reduce interference assumed to be caused by simultaneously activating intracochlear electrodes.

As a first step in our investigation to determine which of the differences between the new and old sound processing systems contributed to increased performance, we compared a subject's speech reception ability using three sound processing schemes. These schemes were: (1) the current commercial processor that uses four bandpass filters to segment the frequency spectrum from approximately 100 Hz to 4,000 Hz and presents the analogue outputs of these filters as simultaneous current waveforms to four of the implanted electrodes, (2) a 4-channel processor in which the envelopes of the four bandpass filter outputs are used to modulate biphasic pulse trains that are presented as interleaved stimuli to four of the implanted electrodes, and (3) a 6-channel version of processor (2). The 4-channel and 6-channel interleaved systems shared an amplitude compression scheme in which the top 60 dB of the envelope output range was logarithmically mapped into the subject's dynamic range. The commercial, 4-channel analogue system uses an automatic gain control that acts on the signal before processing by the bandpass filters.

One subject's ability to identify closed sets of consonants (24 consonants presented in a /aCa/

context) and vowels (8 vowels presented in a /bV/ context) has been measured for these three processing schemes. Scores for consonant recognition using the analogue and interleaved, 4-channel processors were 87 percent and 89 percent respectively. While the difference in consonant recognition is not significant for the 4-channel processors, these scores are significantly different from the 96 percent scored with the 6-channel, interleaved processor. This implies that for consonant identification, differences in performance were due to increasing the number of channels but differences in compression and interleaving were probably not significant. The vowel scores were 79 percent and 87 percent for the 4-channel systems (analogue and interleaved respectively) and 98 percent for the 6-channel, interleaved system. Differences in the two 4-channel system scores suggest that differences in compression and/or interleaving may contribute to better vowel recognition. As with the consonant scores, increasing the number of channels also contributes to better vowel scores.

Two different psychophysical tests conducted with implanted subjects this year are leading to the design of new speech processors that will be tested next year. Loudness scaling experiments using electrical stimulation of the subjects' intracochlear electrodes show that the shape of the loudness growth function varies across electrodes. These results suggest customizing the function used to map channel energy to stimulus amplitude for each electrode rather than using the same function as is currently done. Psychophysical measures of interaction during electrical stimulation of nonsimultaneous stimuli at the same or different electrodes have revealed complex patterns of masking and unmasking that depend on the amplitude of the masker and the separation of the masker and test stimuli in both time and space. These measures of nonsimultaneous interactions have suggested new stimulus waveforms that may reduce these interactions. These waveforms are being tested in our single-unit models and, in the next year, will be tested as part of a 6-channel, interleaved sound processor.

¹⁴ Wilson, B.S., C.C. Finley, D.T. Lawson, R.D. Wolford, D.K. Eddington and W.M. Rabinowitz, "Better Speech Recognition with Cochlear Implants," *Nature* 352: 236-238 (1991).

Section 4 Linguistics

Chapter 1 Linguistics

Chapter 1. Linguistics

Academic and Research Staff

Professor Morris Halle, Professor Noam A. Chomsky

1.1 Introduction

The work of the Linguistics group is directed towards a better understanding of the mental capacities of human beings through the study of the nature, acquisition and use of language. Language is a uniquely human faculty: only humans appear to be capable of learning and using a language, and every normal human acquires knowledge of one or more languages.

We are trying to understand how this linguistic knowledge is represented in the speaker's mind. The central issues of linguistics research are:

1. What is the nature of linguistic knowledge? What do speakers of a particular language such as Latvian, Spanish or Walpiri know, and how does knowledge of one language resemble or differ from that of another language?
2. How do speakers acquire this knowledge?
3. How do speakers put this knowledge to use in producing and understanding utterances?
4. What are the physiological mechanisms that provide the material basis for storage, acquisition and utilization of linguistic knowledge?

Our ability to answer these questions differs considerably, and our research reflects these differences. At present, we have progressed further with regard to answering the questions posed by item one and have made less progress with item four. Currently, our research is heavily concentrated on issues concerned with the nature of the knowledge that characterizes fluent speakers of various languages. However, we are making a significant effort to solve the other questions also.

We are studying these topics along a number of parallel lines. Linguists have investigated the principles by which words are concatenated to form meaningful sentences. These principles have been the primary domain of inquiry into the disciplines of syntax and semantics. Phonology studies the

sound structure of words while morphology examines the manner in which different languages combine different meaning-bearing units (specifically, stems, prefixes, suffixes and infixes) to form words. The latter topic has attracted increasing interest in recent years and will probably become more prominent in our research efforts in the future.

1.2 Abstracts of Doctoral Dissertations

The following are abstracts of dissertations submitted in 1992 to the Department of Linguistics and Philosophy in partial fulfillment of the requirements for the degree of Doctor of Philosophy in Linguistics.

1.2.1 Subjects and Complementizers

Philip Branigan

Abstract

This thesis is concerned with the position that subject and objects occupy at LF. It is demonstrated that objects must occupy a Case position outside of VP at LF in order to account for the effects of objects in participle agreement configurations and in configurations in which they interact with 'dependent' elements in VP adjuncts. It is shown that subjects occupy a non-Case position located between CP and IP, a position which can also be occupied by inverted locative phrases in English. The A-bar status of this position leads to 'that-trace' effects and a greater sensitivity to A-bar extraction of the subject from inside an island.

1.2.2 Adjunct Extraction and Chain Configurations

Michael V. Hegarty

Abstract

This study is concerned with the semantic content of complementizers, and with the modes of interpretation of adverbial *wh* elements and with their possibilities for *wh* movement. It examines the event structure of complement clauses, revealing a difference of semantic function between the complementizers in tensed factive complement clauses and propositional complement clauses. This yields a difference in their effects on adverbial *wh* extraction. The effect of complementizers on *wh* extraction points to the Minimality Condition, taking effect for nongoverning heads such as complementizers. An attempt is made to define antecedent government in such a way as to capture the Minimality effects of complementizers.

Chapter 1 reviews some pertinent aspects of the underlying syntactic and semantic frameworks, and contains a brief outline of the thesis.

Chapter 2 examines the event structure of complement clauses. It argues that the event position of factive complements is discharged by the factive complementizer, yielding an interpretation of factive complements as involving discourse binding of the event position of the complement clause. It then examines the event position of various infinitival complement clauses and of gerunds, as well as some other contexts which involve discourse binding of an event variable, and which exhibit the resulting presupposition that the event occurred. In all cases, event positions which are not bound are found to exhibit the possibility of unselective binding by an adverb of quantification.

Chapter 3 examines the pattern of adverbial *wh* extraction from factive and propositional complement clauses and shows that this pattern depends on the event structures of the complement clauses detailed in Chapter 2. Adverbial *wh* extraction out of infinitivals and gerunds is then examined, along with extraction from some other contexts which involve discourse binding of the event variable.

Chapter 4 examines some simplifications in extraction theory that follow from a typology of chains at LF proposed by Chomsky. On the basis of these simplifications, a radically reduced system of γ -marking is proposed for extraction theory. A definition of antecedent government is then formulated so as to capture the Minimality effects on antecedent government of intervening complementizers.

Chapter 5 summarizes the results of the thesis and discusses them in the light of some recent literature.

1.2.3 The Computation of Prosody

William J. Idsardi

Abstract

This thesis presents a new theory of metrical representations and computations. This theory emphasizes that the metrical grid is a separate module for the phonology, devoted to the calculation of partitioning of phonological elements. The metrical grid consists of parallel tiers composed of three kinds of elements: grid marks and left and right boundaries. A single boundary serves to define a metrical constituent: a left boundary creates a grouping of the elements to its right, a right boundary creates a grouping of the elements to its left.

The calculation of the metrical grid is accomplished through the use of both rules and constraints. This division of labor accounts for observed properties of stress systems in a succinct manner. Metrical rules apply successively in a derivation, thus modelling the functional character of metrical structure assignment. The constraints prevent the application of metrical rules that would generate universal or language-particular disfavored configurations.

The interface to the metrical grid module is controlled by two parameters of projection, which provide the initial grid marks and boundaries. Further parameterized rules of Edge marking, Iterative constituent construction and Headedness complete the construction of the grid.

This theory allows the derivation of Extrametrical effects through the interaction between Edge marking and Iterative constituent construction. Constraints against particular configurations yield both clash effects and a ternary parsing ability.

Further, the Edge marking parameter provides the requisite formal power to deal with stress introduced by specific morphemes in such languages as Turkish, Macedonian, Polish, Russian, Cayuvava, Shuswap (Salish) and Moses-Columbian (Salish).

1.2.4 Japanese Syntactic Structures and Their Constructional Meanings

Miori Kubo

Abstract

This dissertation explores the sentential structures of Japanese, of both matrix and embedded clauses, with special attention given to the configurational relation between a predicate head X^0 and its arguments. It is argued that two quite distinct sentential forms, IP and CP, are possible in Japanese. A leading idea pursued here is that crucial factors determining the configurational relations are (i) whether a head goes through syntactic head movement (Travis 1984, Baker 1988) and (ii) whether a head is syntactically filled or empty (Emonds 1985). Among the sentence types researched are included not only sentences with single verbs, but also predicate attribute sentences, complex verb sentences containing causative, desiderative and potential suffixes, and a representative range of embedded sentences.

In relation to head movement, I argue for a strict structural case marking analysis in the spirit of Takezawa (1987) and Morikawa (1989) and show that the configurational relations between case-assigning heads and NPs are directly mirrored by morphological case. Both SPEC-HEAD agreement and government are motivated as case assigning mechanisms, the former being reserved, however, for only subject-predicate relations. A central discovery here is that the functional categories in Japanese, C, I, and D, each uniformly assign one and only one so-called nominative case *ga*; this in turn supports the existence of functional categories as a class.

Another effect of head movement, via case marking, related to possible positions for subjects and their associated configurational meanings. That is, the two well-known interpretations of NP-*ga*, neutral and exhaustive, are argued to result from them occupying different positions in SPEC(I) and SPEC(C). The distributional distinctions between SPEC(C) and SPEC(I) are in turn determined by positions of the corresponding heads, which are governed by various syntactic constraints. In the course of investigation, quite interesting parallels, until now obscured, are brought out between noun phrases and sentences.

This research can be taken as a concrete effort to investigate various structural configurations and their configurational meanings, on the basis of the idea that meaning is in essential parts simply form. Among the contrasts investigated are activity versus stative verbs, exhaustive versus neutral interpretations of NP-*ga*, and the differing syntactic and interpretive behaviors of the two clausal types CP and IP. In a final chapter, I motivate a correlation

between these two clausal structures and Kant's two types of judgements, analytic and synthetic.

1.2.5 Coordination and Comparatives

Friederike Moltmann

Abstract

This thesis deals with three topics, coordination (chapter 1-3), comparatives (chapter 4) and exception phrases (chapter 5).

In the first three chapters, I will present a new three-dimensional theory of coordination and a particular way of compositionally interpreting three-dimensional syntactic structures. The theory is applied to ATB constructions in chapter 1 and to constructions with split antecedents in different conjuncts of coordinate in chapter 2. I propose that both ATB extraction and the constructions with split antecedents involve a new construction type of implicit coordination. In chapter 3, I will discuss the possibility of implicit coordination in constructions other than 'and'-coordination and ATB extraction.

Chapter 4 presents a general syntactic and semantic analysis of comparative constructions. In particular, it presents answers to the following three questions. First, how do quantifier scope interactions come about in comparative clauses and other *wh* constructions. Second, how is the empty element in comparative deletion contexts identified. Third, what is the syntactic basis for evaluating comparative clauses the way they are most plausibly evaluated, namely as universal quantifiers over degree. In the fourth chapter, I will also address the issue of whether comparatives involve coordination. I will argue that comparative sentences may have two syntactic structures simultaneously, a coordinate structure and a subordinate structure. This also holds for phrasal comparatives.

Chapter 5 deals with various kinds of exception phrases and a number of other constructions which are either semantically or syntactically related to exception constructions, namely 'extent clauses', 'almost'-phrases and amount relatives. I propose a general semantic condition to account for the quantifier constraint imposed by exception phrases and semantically related constructions. Furthermore, I will argue that exception constructions may involve polyadic quantification. Regarding the syntax of exception phrases, I will discuss the issue of whether exception constructions syntactically involve coordination, but argue against this possibility.

1.2.6 Crossing and Nested Paths: NP Movement in Accusative and Ergative Languages

Kumiko Murasugi

Abstract

This thesis develops a theory of syntactic ergativity based on the Case feature requirements which motivate NP movement. In Chapter 1, I present an Ergative Parameter derived from the Case features of twofunctional heads, T(ense) and Tr(ansitivity). In an ergative language, the Case features of the higher T(ense) are strong, requiring movement to its SPEC at s-structure. In an accusative language, the Case features of the lower Tr(ansitivity) are strong, forcing s-structure movement to its SPEC. Economy Principles determine that it is always the subject, generated in SPEC VP, which raises to the SPEC of T or Tr (depending on the language) at s-structure. At LF, the object raises to the remaining SPEC position. This results in two types of movement: "Crossing Paths" in accusative languages, and "Nested Paths" in ergative languages. The two paths reflect the different Case and agreement patterns found in the two language types, as each functional head is associated with a particular Case: nominative/absolutive with T, and accusative/ergative with Tr. In an intransitive clause, the subject raises to SPEC TP in both types of languages.

Chapter 2 investigates consequences of the proposed theory for NP movement and verb raising in accusative languages. The topics relating to NP movement include expletives in SPEC TP, the EPP in infinitival clauses, and raising constructions in English. I also discuss verb fronting in V2 and VSO languages, proposing that this movement is required by a [finite] feature in C.

In chapter 3, I provide evidence for my claim that ergativity involves the raising of the object (O) and intransitive subject (S) to SPEC TP, the position of transitive (A) and intransitive (S) subjects in accusative languages. I discuss properties shared by O/S in an ergative language, and A/S in an accusative language, such as the availability for relativization.

In Chapter 4, I investigate syntactic and semantic properties which group together S and A in both language types, claiming that they involve the notion of highest s-structure argument, and thematic roles. Chapter 5 discusses various issues pertaining to ergativity.

1.2.7 Features, Positions and Affixes in Autonomous Morphological Structure

Robert R. Noyer

Abstract

This thesis develops a theory of the mapping from the output of syntactic rules to the input to phonology within a component of Morphology. Three types of information are shown to be independently manipulable in the algorithm deriving fully inflected words: morphosyntactic features, phonological material (affixes), and positions-of-exponence.

To capture categorial neutralizations at the morphological level, a filter-based approach to the impoverishment of morphosyntactic representations is proposed. Filters are argued to be automatically assumed unless positive evidence suppresses them in the learner. Neutralizations are also shown to occur at three other levels: (1) underspecification of realization rules/affixes, (2) disjunction of affixes competing for a position-of-exponence, and (3) transparency of redundant morphosyntactic values. A hierarchy of features is proposed, which, in the unmarked instance, governs the direction of categorial neutralization and the ordering of affixes and morphological rules, where not determined by syntax or by the principle of descending complexity due to Panini.

The mapping to phonological form is proposed to take place in two phases. In the first phase, morphosyntactic well-formedness is established through the impoverishment of morphosyntactic features and the Linearization, Rebracketing, Merger (Marantz 1988) and Fusion of syntactic heads, giving a level of constituents termed M^0 s. In the second phase, the string M^0 is mapped to the well-formed morphological word through rules and affixes. Morphological words are shown to display idiosyncratic non-phonological conditions of well-formedness (obligatory or limited positions-of-exponence) which comprise *autonomous morphological structure*. Particular attention is paid to cases of M^0 splitting, where features from a single morphosyntactic source are realized at multiple positions.

Features in input morphosyntactic representations are argued to be *discharged* through the instantiation of affixes, sometimes at obligatory positions-of-exponence, which are also then discharged. This discharge constitutes spell-out or realization of phonological material. Because both features and positions may be discharged independently, it becomes possible to express disjunction

across position classes, termed here *discontinuous bleeding*. Further, the Rule-Affix Hypothesis states that rules change phonological material and do not discharge morphosyntactic features; affixes add phonological material and do discharge such features.

The Introduction situates the current proposal within prevailing theories of inflection, Lieber (1980, 1992), Anderson (1981, 1992), and Halle (1989a, 1992). Chapter 1 exemplifies the theory through a detailed analysis of the Afroasiatic prefix-conjugation. Chapter 2 gives an explicit theory of person-number features and their interpretation, in particular the inherent number system of Kiowa-Tanoan. Chapter 3 treats complex multiple argument agreement systems with particular attention to the transitive clitic sequences of Nunggubuyu and Ket.

1.2.8 Syllables and Templates: Evidence from Southern Sierra Miwok

Kelly D. Sloan

Abstract

This thesis examines aspects of the syllable structure and templatic phonology of Southern Sierra Miwok (henceforth SSM). SSM provides strong evidence for a model of phonological organization incorporating an x-slot tier (a 'segmental model'). I advance three arguments in favor of a segmental model. First, I argue that SSM exhibits floating x-slots and floating phonemes. SSM has a complex array of length and alternation phenomena. I demonstrate that by utilizing singly-linked phonemes, doubly-linked phonemes, floating x-slots, floating phonemes and combinations of these, all of the surface forms can be derived by syllabification without recourse to any special lengthening, shortening or deletion rules. I propose a hierarchy of elements in which x-slots with phonemic content have precedence over floating x-slots which in turn have precedence over floating phonemes.

Second, I show that the behavior of morpheme-final geminates in SSM is inconsistent with the moraic analysis of gemination proposed in Hayes (1989). Only a model which represents geminates as holding two positions or 'slots' will properly account for the gemination facts. The third type of evidence comes from the templatic system of SSM. I demonstrate that SSM exhibits the three distinct templates CVCVC, CVCVX and CVCVV. I propose that these can be represented by taking advantage of the distinctions between branching and non-branching Nucleus and between floating and non-

floating x-slots. These distinctions readily follow from the x-slot model I advance herein but are unavailable in a moraic model of phonological organization.

The properties of syllabification in SSM appear paradoxical. On the one hand, it can be demonstrated that syllabification must apply at the word-level in order to account for the surface variation in vowel length. On the other hand, in order to explain the distribution of epenthesis, syllabification must arguably take place prior to the word-level. I propose a solution to this dilemma by arguing that syllabification in SSM takes place at two discrete stages. CV(X) syllables are constructed at the lexical level. Subsequent word-level syllabification builds syllables from right-to-left, respecting previously built structure and Maximality. I demonstrate that Prosodic Syllabification, as proposed in Ito (1986, 1989) cannot correctly derive the SSM facts. This results from two (potentially) problematic aspects of SSM syllabification: (i) although syllabification must not apply cyclically, there are certain cyclic effects observed and (ii) epenthesis can only occur at morpheme boundaries even though these boundaries are not visible at the point in the phonology where syllabification must occur. These effects fall out of the analysis that I propose herein.

1.2.9 Deletion, Deaccenting, and Presupposition

Christopher D. Tancredi

Abstract

In this dissertation, I examine the effects of deaccenting—the removal of phonological accent from a constituent—on interpretation. In general, deaccenting of an element is possible only if that element is salient in the discourse context. Salience alone, however, is not a sufficient condition for deaccenting. The discourse context in (1) makes salient both the verb *hit* and the NP *John*, and it is consequently possible for these elements to be deaccented in (1a,b). However, in (1c), it is not possible to deaccent both of these elements simultaneously. (Focus is indicated by CAPITALIZATION, deaccenting by *small italics*.)

- (1) Mary hit John. Then,
 a. BILL *hit* SUE.
 b. BILL KICKED Mary.
 c. #BILL *hit* Mary.

Deaccenting of both the verb *hit* and its direct object *Mary* in (1c) requires that the discourse

context make salient a hitting of Mary, but this condition is not met in (1).

To account for the facts illustrated above, I propose that deaccenting plays a role in identifying the focus-related topic of a sentence, where it is a necessary condition for a sentence to be felicitous in a given context that the focus-related topic of that sentence be instantiated in the context. The focus-related topic of a sentence is generated (roughly) by replacing all focused constituents by variables and combining the resulting structure so as to end up with the smallest structure within which all properties of the remaining lexical elements are satisfied. The resulting structure will be instantiated in a context if there is another element in the context with which it is non-distinct, where variables count as non-distinct from other elements of the same semantic type. By this process, the sentences in (1) will have the focus-related topics in (2).

- (2) a. x hit y
- b. Mary
- c. x hit Mary

The representations in (2a,b) are instantiated in the context consisting of the sentence *Mary hit John* in (1) above, and hence (1a,b) are felicitous. (2c), however, is not instantiated in this context, and hence is infelicitous.

The analysis sketched above provides an explanation for the felicity or infelicity of a sentence in a larger context based upon the focus structure of the sentence and the composition of the context. While the analysis is of some interest by itself, even more important is the use to which the analysis can be put in accounting for certain phenomena typically associated with VP deletion. Since Sag (1976) and Williams (1977), it has standardly been assumed that restrictions on pronominal interpretations in VP deletion contexts are to be explained in terms of the mechanism that assigns an interpretation to an empty VP. However, we find that identical restrictions appear in contexts in which a VP has been deaccented but not deleted. Thus, parallel to the sentence in (3a) which has only a strict and a sloppy reading available for the (deleted) pronoun, we find an identical restriction for the deaccented pronoun in (3b).

- (3) a. John_i said he_i is a genius because Bill did.
- b. John_i said he_i is a genius because Bill *said* *he's intelligent*.

No analysis of VP deletion in the current literature is capable of accounting for this parallelism. If we assume that a phonologically deleted VP is represented in the LF representation of a sentence as a deaccented VP, however, it becomes possible to account for this parallelism in a principled fashion by assimilating the deletion cases to the deaccenting ones.

Appendices

Appendix A RLE Publications and Papers Presented

Appendix B Current RLE Personnel

Appendix C Milestones

Appendix D RLE Research Support Index

Appendix A. RLE Publications and Papers Presented

The first section of this bibliography includes papers and talks presented by RLE faculty, staff and students during 1992 and is in alphabetical order by conference name. Reprints of these papers may be obtained by contacting the authors directly.

Section 2 includes an alphabetical listing by author of journal articles that were published and accepted or submitted for publication. Book chapters by RLE authors are listed in section 3. Section 4 of this bibliography lists RLE general publications and technical reports, and section 5 is a list of RLE theses submitted during 1992. Section 6 contains miscellaneous publications.

A.1 Meeting Papers

A.1.1 Papers Presented

- ALAA Space Programs and Technologies Conference*, Huntsville, Alabama, March 24-27, 1992.
- Canizares, C.R., D. Dewey, E.B. Galton, T.H. Markert, H.I. Smith, M.L. Schattenburg, B.E. Woodgate, and S. Jordan. "The MIT High Resolution X-ray Spectroscopy Instruments on AXAF."
- Acoustical Society of America Meeting*, 123rd, Salt Lake City, Utah, May 11-15, 1992.
- Baggeroer, A.B., and W.A. Kuperman. "Stochastic Matched Field Processing."
- Chen, M.Y. "Acoustic Parameters of Nasal Utterances in the Hearing-impaired and Normal-hearing Speakers."
- Johnson, M. "Using Beam Elements to Model the Vocal Fold Length in Breathily Voicing."
- Manuel, S.Y. "Vowel Reduction and Perceptual Recovery in Casual Speech."
- Acoustical Society of America Meeting*, 124th, New Orleans, Louisiana, October 31-November 4, 1992.
- Svirsky, M.A., and S.H. Svirsky. "A Multidimensional Mathematical Model of Vowel Perception by Users of Pulsatile Cochlear Implants."
- Svirsky, M.A., K.N. Stevens, M.L. Matthies, and J.S. Perkell. "Tongue Surface Deformation During Obstruent Stop Consonants."
- Wozniak, J.F., M.L. Matthies, J.S. Perkell, and H.L. Lane. "Timing and Magnitudes of Oral and Nasal Flow in Cochlear Implant Patients and Normals."
- Advanced Heterostructure Transistors Conference*, Keauhou-Kona, Hawaii, November 29 - December 4, 1992.
- del Alamo, J.A., S.R. Bahl, and D.R. Greenberg. "In-P-Based High Breakdown Voltage HFETs."
- Hu, Q., C. Eugster, and J.A. del Alamo. "Photon-assisted Quantum Transport in Quantum Point Contacts."
- American Astronomical Society Meeting*, Atlanta, Georgia, January 12-16, 1992.
- Griffith, M., B.F. Burke, and A. Fletcher. "The Parkes-MIT-NRAO (PMN) Southern Sky Survey at 4850 MHz."
- American Chemical Society Meeting*, Washington, DC, August 24-28, 1992.
- Pullman, D.P., Y.L. Li, J.J. Yang, and S.T. Ceyer. "Reaction Dynamics of F₂ on Si(100)."
- American Physical Society and the American Association of Physics Teachers Joint Meeting*, Washington, DC, April 20-24, 1992.
- Conde, M.E., G. Bekefi, and J.S. Wurtele. "Tests of a 33 GHz High Gradient Accelerating Structure."
- American Physical Society Meeting*, Indianapolis, Indiana, March 16-20, 1992.
- Aalberts, D.P., and A.N. Berker. "Hard-Spin Mean-Field Theory: Variational Free Energy and First-Order Phase Transitions."
- Arias, T.A., and J.D. Joannopoulos. "Impurity Segregation at Grain Boundaries."
- Bailey, D.W., C.J. Stanton, M. Ulman, L.H. Acioli, and J.G. Fujimoto. "Tunable Pump-probe Nonlinear Absorption Spectroscopy in AlGaAs."
- Berker, A.N., and R.R. Netz. "Smectic C Order, In-Plane Domains, and Nematic Reentrance in

- a Frustrated Microscopic Model of Liquid Crystals."
- Dal Pino, A., Jr., A.M. Rappe, and J.D. Joannopoulos. "Isovalent Impurities and Related Defects in Silicon."
- Hu, Q., R.A. Wyss, C.C. Eugster, and J. del Alamo. "Photon-Assisted Transport through Quantum Point Contacts."
- Joannopoulos, J.D. "The Enchanting Properties of Oxygen Atoms in Silicon" (invited talk).
- Kumar, A. "Electron States and Potentials in Quantum Dot Structures."
- Meade, R.D., K.D. Brommer, J.D. Joannopoulos, and A.M. Rappe. "Localization, Defects and Surfaces of Photonic Crystals."
- Netz, R.R. "Symmetry-Breaking Fields in Frustrated Ising Systems on Square and Cubic Lattices."
- Sanders, G.D., C.J. Stanton, and Y.C. Chang. "Theory of Optical Gain in Silicon Quantum Wire Lasers."
- Stanton, C.J., and D.W. Bailey. "Rate Equations for the Study of Intervalley Scattering in Compound Semiconductors."
- Zhao, Y., D.C. Tsui, K. Hirakawa, M. Santos, M. Shayegan, R. Ghanbari, D.A. Antoniadis, and H.I. Smith. "Far Infrared Magneto-Absorption by the 2 DEG in GaAs/AlGaAs Heterostructures with Grid Gates."
- American Physical Society*, Division of Plasma Physics, Annual Meeting, Seattle, Washington, November 16-20, 1992
- Bers, A., A.K. Ram, and G. Bekefi. "Linear Analysis of the Double Stream Cyclotron Maser."
- Chen, C. "Theory of Cyclotron Resonance Laser Accelerator."
- Migliuolo, S. "Impurity Modes in Sheared Magnetic Fields."
- Migliuolo, S., P.T. Bonoli, and M. Porkolab. "Fast Wave Heating in JET and SSAT; A Comparison."
- Nassi, M., B. Coppi, and L.E. Sugiyama. "Approach to Ignition by Compact Experiments."
- Ram, A.K., A. Bers, V. Fuchs, R.W. Harvey, and M.G. McCoy. "Current Drive by Lower Hybrid Waves in Presence of Fast Alfvén Waves."
- Sugiyama, L.E., and B. Coppi. "Heating Schemes for High Beta Tokamak Fusion Experiments."
- American Physical Society Meeting*, Seattle, Washington, March 22-26, 1993.
- Berker, A.N., and K. Hui. "Closed-Form Expression for the Global Phase Diagram of the Ising Model on the Square Lattice with Crossed Diagonal Bonds."
- Netz, R.R., and A.N. Berker. "Renormalization-Group Theory of an Internal Critical Endpoint Structure: The Blume-Emery-Griffiths Model with Biquadratic Repulsion."
- American Society of Mechanical Engineers*, Annual Winter Meeting, Anaheim, California, November 8-13, 1992.
- Srinivasan, M.A., and K. Dandekar. "Role of Fingertip Geometry in the Transmission of Tactile Mechanical Signals."
- Srinivasan, M.A., R.J. Gulati, and K. Dandekar. "In Vivo Compressibility of the Human Fingertip."
- Tan, H.Z., X.D. Pang, and N.I. Durlach. "Manual Resolution of Length, Force, and Compliance."
- American Vacuum Society Meeting*, Chicago, Illinois, November 9-13, 1992.
- Pullman, D.P., Y.L. Li, J.J. Yang, and S.T. Ceyer. "Reaction Dynamics of F₂ on Si(100)."
- Smith, H.I., and M.L. Schattenburg. "Proximity X-ray Nanolithography: Current Performance and Theoretical Limits."
- Applied Superconductivity Conference*, Chicago, Illinois, August 23-28, 1992.
- Lam, C-W., S.M. Ali, and D.E. Oates. "Modeling of the Nonlinear Resistance of Superconducting Striplines."
- Lee, L.H., S.M. Ali, W.G. Lyons, D.E. Oates, and J.D. Goettee. "Analysis of Superconducting Transmission-Line Structures for Passive Microwave Device Applications."
- Asilomar Conference on Signals, Systems, and Computers*, 20th Annual, Pacific Grove, California, October 26-28, 1992.
- Lim, J.S. "Design of HDTV System."
- Association for Research in Otolaryngology Meeting*, 15th, St. Petersburg, Florida, February 2-6, 1992.

Merchant, S.N., M.E. Ravicz, and J.J. Rosowski.
"The Acoustic Input Impedance of the Stapes
and Cochlea in Human Temporal Bones"
(poster presentation).

*Association for Research in Vision and
Ophthalmology*, Sarasota, Florida, May 3-8, 1992.

Hee, M.R., E.A. Swanson, D. Huang, J.A. Izatt,
C.P. Lin, J.S. Schuman, C.A. Puliafito, and
J.G. Fujimoto. "Optical Coherence Tomog-
raphy."

Izatt, J.A., E.A. Swanson, M.R. Hee, D. Huang,
J. Schuman, C.P. Lin, C.A. Puliafito, and J.G.
Fujimoto. "Quantitative Assessment of
Cataract Development with Optical Coherence
Domain Reflectometry and Optical Coherence
Tomography."

*CLEO/QELS-Conference on Lasers and Electro-Op-
tics/Quantum Electronics and Laser Science*,
Anaheim, California, May 10-15, 1992.

Brener, I., M. Zahler, G. Lenz, J. Salzman, E.
Cohen, and L. Pfeiffer. "Experimental Evi-
dence of Bragg Confinement of Carriers in a
Quantum Barrier."

Doerr, C.R., K. Bergman, M. Shirasaki, and H.A.
Haus. "Stabilization of Squeezing with a Non-
linear Fiber Interferometer."

Hall, K.L., G. Lenz, and E.P. Ippen. "Novel,
Heterodyne Pump-Probe Measurement of
Femtosecond Nonlinearities in Waveguides."

Hon, S., K. Bergman, A. Mecozzi, and H.A.
Haus. "Noise Spectra of Mode-Locked Laser
Pulses."

Hultgren, C.T., D.J. Dougherty, and E.P. Ippen.
"Femtosecond Gain and Refractive Index
Nonlinearities in AlGaAs Diode Laser Ampli-
fiers."

Jacobson, J.M., A.G. Jacobson, K. Naganuma,
H.A. Haus, and J.G. Fujimoto. "Generation of
28 fs Pulses from a $\text{Ti:Al}_2\text{O}_3$ Laser Using
Second and Third Order Intracavity Dispersion
Compensation."

Pang, L.Y., J.G. Fujimoto, and E.S. Kintzer.
"High-Power Mode-Locked Diode Array Using
Intracavity Nonlinearity."

Pritchard, D.E. "Atom Interferometry."

Swanson, E., M. Hee, D. Huang, J.A. Izatt, J.G.
Fujimoto, C.P. Lin, J.S. Schuman, and C.A.
Puliafito. "Optical Coherence Tomography."

Ulman, M., L.H. Acioli, C.J. Stanton, E.P. Ippen,
and J.G. Fujimoto. "Studies of Intervalley

Scattering Using Tunable Femtosecond
Pulses."

Ulman, M., L.H. Acioli, F. Vallee, E.P. Ippen, D.
Bailey, C.J. Stanton, and J.G. Fujimoto.
"Femtosecond Carrier Dynamics in AlGaAs."

*Conference on the Role of Wavelets in Signal Pro-
cessing Applications*, Wright-Patterson Air Force
Base, Ohio, March 11-13, 1992.

Wornell, G.W., and A.V. Oppenheim.
"Wavelets, Self-Similar Signals, and Fractal
Modulation."

Conference on Imaging in Ophthalmology, San
Antonio, Texas, June 26-27, 1992.

Huang, D., E.A. Swanson, J.A. Izatt, M.R. Hee,
C.P. Lin, J. Schuman, T. Flotte, C.A. Puliafito,
and J.G. Fujimoto. "Optical Coherence
Tomography."

*Convention of the Association for Late Deafened
Adults*, Annual, Boston, Massachusetts, Sep-
tember 10-13, 1992.

Reed, C.M., and L.A. Delhorne. "Field Study of
Deaf Adult Users of Tactaid II and Tactaid
VII."

Czechoslovak Society of Arts and Sciences (SVU),
Prague and Bratislava, Czechoslovakia, June 26
- July 2, 1992.

Bekefi, G. "The Free Electron Laser—A New
Source of Coherent Photons."

DARPA Automatic Sensor Interpretation Workshop,
Fairfax, Virginia, October 1-2, 1992.

Wornell, G.W. "Detection of Fractal Signals
Using Wavelets."

*DARPA Symposium on Photonics Systems for
Antenna Applications*, Third Annual, Monterey,
California, January 20-22, 1993.

Haus, H.A., and E.P. Ippen. "Optically Con-
trolled Phased Array Radar."

DARPA Meeting, Semi-Annual, Daytona Beach,
Florida, September 21-25, 1992.

Devadas, S. "Synthesis for Testability and Low
Power."

DARPA Meeting, Washington, DC, January 14-16,
1992.

Lim, J.S. "Design of an HDTV System."

- DARPA Semi-Annual Contractors Meeting*, Salt Lake City, Utah, January 6-7, 1992.
- Wyatt, J.L. "Analog VLSI for Robot Vision."
- DARPA Ultra Electronics Program Review*, Santa Fe, New Mexico, October 19-21, 1992.
- Melngailis, J. "Nanofabrication by Focused Ion Beams."
- DARPA Workshop on Computational Sensors*, Philadelphia, Pennsylvania, May 11-12, 1992.
- Wyatt, J.L. "Analog VLSI for Robot Vision."
- Department of Defense Fiber Optic Conference*, McLean, Virginia, March 23, 1992.
- Haus, H.A., and K. Bergman. "Beating the Shot-Noise Limit with Squeezed Light."
- Design Automation Conference*, 29th, Anaheim, California, June 1992.
- Devadas, S., K. Keutzer, S. Malik, and A. Wang. "Certified Timing Verification and the Transition Delay of a Circuit."
- Ghosh, A., S. Devadas, K. Keutzer, and J. White. "Estimation of Average Power Dissipation in Combinational and Sequential Circuits."
- Digital Signal Processing Workshop*, Fifth, Starved Rock State Park, Illinois, September 13-16, 1992.
- Isabelle, S.H. "Properties of a Class of Chaotic Signals."
- Richard, M.D. "State Estimation with Chaotic Maps."
- Wornell, G.W., and W.W. Lam. "Spectral Analysis on a Log-Frequency Scale and the Modeling of Scaling Behavior in Fractal Signals."
- Division of Atomic, Molecular, and Optical Physics*, Annual Meeting, Chicago, Illinois, May 20-22, 1992.
- Paine, S., P. Chang, R. Lutwak, J. Holley, and D. Kleppner. "Millimeter-Wave Measurement of the Rydberg Frequency."
- Drexel Symposium on Quantum Nonintegrability*, Philadelphia, Pennsylvania, May 20-22, 1992.
- Kleppner, D.E. "Quantum Chaos."
- European Solid-State Circuits Conference*, Copenhagen, Denmark, September 1992.
- Hakkarainen, J.M., and H-S. Lee. "A 40x40 CCD/CMOS AVD Processor for Use in a Stereo Vision System."
- Yu, P.C., and H-S. Lee. "A CMOS Resistive-fuse Processor for 2-D Image Acquisition, Smoothing and Segmentation."
- European Space Agency Symposium on Targets for Space-Based Interferometry*, Beaulieu, France, October 1992.
- Burke, B.F. "Searching for Exoplanets."
- Europhysics Topical Conference on RF Heating and Current Drive of Fusion Plasmas*, Brussels, Belgium, July 7-10, 1992.
- Harvey, R.W., M.G. McCoy, A.K. Ram, A. Bers, and V. Fuchs. "Scaling of Lower Hybrid Current Drive with Temperature."
- Ram, A.K., A. Bers, V. Fuchs, R.W. Harvey, and M.G. McCoy. "Effects of Fast Alfvén Waves in Lower Hybrid Current Drive."
- Frontiers in Education Conference*, Nashville, Tennessee, November 12-15, 1992.
- Troxel, D.E. "Digital Design Tools."
- Future Vision 2002*, Princeton, New Jersey, October 4-6, 1992.
- Wyatt, J.L. "Analog VLSI for Robot Vision and Visual Prosthesis."
- General Conference of the Condensed Matter Division of the European Physical Society*, 13th, Regensburg, Germany, March 29-April 2, 1993.
- Netz, R.R., and A.N. Berker. "Renormalization-Group Theory of the Blume-Emery-Griffiths Model with Repulsive Biquadratic Coupling."
- Gordon Conference on Lasers in Medicine and Biology*, New London, New Hampshire, July 6-10, 1992.
- Fujimoto, J.G. "Optical Coherence Tomography."
- Ground Target Modeling and Validation Conference*, Third, Houghton, Michigan, August 18-20, 1992.
- Hsu, C.C., Y.E. Yang, R.T. Shin, J.A. Kong, C. Kohler, T. Nguyen, H. Nguyen, and J. Ho. "Applications of EMSARS Background Model to MMW Vegetation Scattering Simulation."

Hawaii International Conference on System Sciences, 26th, Wailea, Hawaii, January 1993.

Camposano, R., S. Devadas, K. Keutzer, S. Malik, and A. Wang. "Implicit Enumeration Techniques Applied to Asynchronous Circuit Verification."

I.A.E.A. International Conference on Plasma Physics and Controlled Nuclear Fusion Research, 14th, Wurzburg, Germany, September 30-Oct. 7, 1992.

Coppi, B., P. Detragiache, S. Migliuolo, M. Nassi, B. Rogers, L. Sugiyama, and L. Zakharov. "Reconnection and Transport in High Temperature Regimes."

IBM International Digital Video/HDTV/Multimedia Conference, Somers, New York, December 8-10, 1992

Lim, J.S. "HDTV/Digital TV Alliances and Consortia."

IEEE International Conference on Acoustics, Speech, and Signal Processing, San Francisco, California, March 23-26, 1992.

Ayazifar, B. and J.S. Lim. "Pel-Adaptive Model-Based Interpolation of Spatially Subsampled Images."

Beckmann, P.E., and B.R. Musicus. "A Group-Theoretic Framework for Fault-Tolerant Computation."

Isabelle, S.H., A.V. Oppenheim, and G.W. Wornell. "Effects of Convolution on Chaotic Signals."

Jachner, J., and H. Lee. "Cramer Rao Bounds on Direction Estimates for Closely Spaced Emitters in Multi-Dimensional Applications."

Myers, C., A.C. Singer, F. Shin, and E. Church. "Modelling Chaotic Systems with Hidden Markov Models."

Oppenheim, A.V., E. Weinstein, K.C. Zangi, M. Feder, and D. Gauger. "Single Sensor Active Noise Cancellation Based on the EM Algorithm."

Oppenheim, A.V., G.W. Wornell, S.H. Isabelle, and K.M. Cuomo. "Signal Processing in the Context of Chaotic Signals."

Preisig, J.C. "Optimal Minmax Estimation and the Development of Minmax Estimation Error Bounds."

Singer, A.C., G.W. Wornell, and A.V. Oppenheim. "Codebook Prediction: A Non-linear Signal Modeling Paradigm."

IEEE International Conference on Consumer Electronics, Chicago, Illinois, June 2-4, 1992.

Lim, J.S., P.A. Monta, J. Nicolas, J. Apostolopoulos, S. Cheung, W. Paik, E. Krause, and V. Liu. "Channel-Compatible Digicipher HDTV System."

IEEE International Electronics Technical Conference (ELECTRO/92), Boston, Massachusetts, May 13, 1992.

McIlrath, M.B. "Semiconductor Process Representation and Device Design."

IEEE International Plasma Science Conference, 19th, Tampa, Florida, June 1-3, 1992.

Bekefi, G. "Double Stream Cyclotron Maser."

Conde, M.E., and G. Bekefi. "A High-Efficiency 33 GHz Free-Electron Laser with a Reversed Axial Magnetic Field."

Ram, A.K., C. Chen, A. Bers, W. Hu, and G. Bekefi. "Linear and Nonlinear Analysis of the Double Stream Cyclotron Maser" (poster session).

Taylor, C.J., M.E. Conde, G. Bekefi, G. Shvets, and J.S. Wurtele. "Observations of Frequency Upshifts in a Raman, Free-Electron Laser Amplifier" (poster session).

IEEE Joint Symposia American Physical Society/Union of Radio Science/NEM Meeting, Chicago, Illinois, July 18-25, 1992.

Wornell, G.W. "Wavelet Representations for Self-Similar Signals and Systems."

Xia, J., A.K. Jordan, and J.A. Kong. "Electromagnetic Profile Reconstruction Using the Riccati Equation Approach."

IEEE MTT-S International Microwave Symposium, Albuquerque, New Mexico, June 1-5, 1992.

Lam, C.W., D.M. Sheen, S.M. Ali, and D.E. Oates. "Nonlinear Model of Superconducting Strip Transmission Lines."

IEEE Systems Readiness and Automatic Testing Conference, Dayton, Ohio, September 21-24, 1992.

Chu, A., H.M. Cronson, J.F. Devine, S. Soares, M.N. Solomon, H.J. Lezec, and C.R. Musil. "RF Built-In Test and Enabling Technologies for Integrated Diagnostics."

IEEE Workshop on Visual Signal Processing and Communications, Raleigh, North Carolina, September 2-3, 1992.

Apostolopoulos, J.G., and J.S. Lim. "Coding of the Motion-Compensated Residual for an All-Digital System."

Intelligent Vehicles Symposium, Detroit, Michigan, June 29-July 1, 1992.

Wyatt, J.L., Jr., C. Keast, M. Seidel, D. Standley, B. Horn, T. Knight, C. Sodini, and H-S. Lee. "Small, Fast Analog VLSI Systems for Early Vision Processing."

International Center for Condensed Matter Physics Conference on Nonlinear and Quantum Optics, Brasilia, Brazil, October 19-23, 1992.

Fujimoto, J.G. "Femtosecond Pulse Generation in Solid State and Diode Lasers."

International Colloquium on X-ray Lasers, Third, Schliersee, Germany, May 18-22, 1992.

Basu S., J. Goodberlet, M. Muendel, S. Kaushik, and P.L. Hagelstein. "Spectral Measurements of Ni-like Mo Plasma."

International Conference on the Fundamental Aspects of Quantum Theory, Columbia, South Carolina, December 9-12, 1992.

Pritchard, D.E. "Experiments Using Atom Interferometers."

International Conference on the Physics of Semiconductors, 21st, Beijing, China, August 10-14, 1992.

Zhao, Y., D.C. Tsui, K. Hirakawa, M. Santos, M. Shayegan, R. Ghanbari, D.A. Antoniadis, and H.I. Smith. "Far Infrared Magneto-Absorption by the 2 DEG in GaAs/AlGaAs Heterostructures with Grid Gates."

International Conference on Atomic Masses and Fundamental Constants, Ninth, Bernkastel-Kues, Germany, July 19-24, 1992.

Natarajan, V., K.R. Boyce, F. DiFilippo, and D.E. Pritchard. "Improved Precision Mass Comparison in a Penning Trap—Techniques and Results."

International Conference on Atomic Physics, 13th, Munich, Germany, August 3-7, 1992.

Joffe, M.A., W. Ketterle, A. Martin, and D.E. Pritchard. "Transverse Cooling and Deflection

of an Intense Atomic Beam Inside a Zeeman Slower."

International Conference on Computer Design: VLSI in Computers and Processors, Cambridge, Massachusetts, October 1992.

Devadas, S., H-F. Jyu, K. Keutzer, and S. Malik. "Statistical Timing Analysis of Combinational Logic Circuits."

International Conference on Computer-Aided Design, Santa Clara, California, November 7-12, 1992.

Allen, J. "Curriculum Change Plan: First Professional Degree in Five Years."

Armstrong, R.C., and J. Allen. "FICOM: A Framework for Incremental Consistency Maintenance in Multi-Representation. Structural VLSI Databases."

Devadas, S., K. Keutzer, S. Malik, and A. Wang. "Verification of Asynchronous Interface Circuits with Bounded Wire Delays."

Ghosh, A., A. Shen, S. Devadas, and K. Keutzer. "On Average Power Dissipation and Random Pattern Testability of Combinational Logic Circuits."

Kamon, M., M.J. Tsuk, C. Smithhisler, and J. White. "Efficient Techniques for Inductance Extraction of Complex 3-D Geometries."

Pillage, L., Z. Cendes, J. White. "Interconnect and Packaging Tutorial."

Shen, A., A. Ghosh, S. Devadas, and K. Keutzer. "On Average Power Dissipation and Random Pattern Testability of CMOS Combinational Logic Networks."

Van Aelten, F., S.Y. Liao, J. Allen, and S. Devadas. "Automatic Generation and Verification of Sufficient Correctness Properties for Synchronous Processors."

International Conference on Industrial Electronics, Control, and Instrumentation, San Diego, California, November 1992.

Masaki, I. "Function-oriented Vision Chips for Factory Automation."

International Conference on InP and Related Materials, Fourth, Newport, Rhode Island, May 21-24, 1992.

Bahl, S.R., B.R. Bennett, and J.A. del Alamo. "A High-Voltage, Doubly-Strained $\text{In}_{0.41}\text{Al}_{0.59}\text{As}/\text{n}^+-\text{In}_{0.65}\text{Ga}_{0.35}\text{As}$ HFET."

International Conference on Ion Beam Modification of Materials, Eighth, Heidelberg, Germany, September 7-11, 1992.

Melngailis, J. "Focused Ion Beam Lithography."

International Conference on Solid State Devices and Materials, Tsukuba, Japan, August 26-28, 1992.

Smith, H.I., and D.A. Antoniadis. "Mesoscopic Devices: Will They Supersede Transistors in ULSI?"

International Conference on Spoken Language Processing, Banff, Canada, October 12-16, 1992.

Bickley, C.A., and S. Hunnicutt. "Acoustic Analysis of Laughter."

Manuel, S.Y., S. Shattuck-Hufnagel, M. Huffman, K.N. Stevens, R. Carlson, and S. Hunnicutt. "Studies of Vowel and Consonant Reduction."

Ross, K., M. Ostendorf, and S. Shattuck-Hufnagel. "Factors Affecting Pitch Accent Placement."

Shattuck-Hufnagel, S. "Stress Shift as Pitch Accent Placement: Within-Word Early Accent Placement in American English."

Stevens, K.N., S.Y. Manuel, S. Shattuck-Hufnagel, and S. Liu. "Implementation of a Model for Lexical Access Based on Features."

Williams, D.R., C.A. Bickley, and K.N. Stevens. "Inventory of Phonetic Contrasts Generated by High-Level Control of a Formant Synthesizer."

International Conference on Tactile Aids, Hearing Aids, and Cochlear Implants, Second, Stockholm, Sweden, June 9-12, 1992.

Reed, C.M., L.A. Delhorne, and N.I. Durlach. "Results Obtained with Tactaid II and Tactaid VII."

Reed, C.M., N.I. Durlach, and L.A. Delhorne. "Historical Overview of Tactile Aid Research."

International Conference on Thermodynamics and Statistical Mechanics, Berlin, Germany, August 2-8, 1992.

Berker, A.N. "Critical Behavior Induced by Quenched Disorder."

Netz, R.R., and A.N. Berker. "Smectic C/A₂ Order, Domains, Reentrance in a Microscopic Model of Liquid Crystals."

International Conference on Ultrafast Phenomena, Eighth, Antibes, Juan-Les-Pins, France, June 8-12, 1992.

Pang, L.Y., J.G. Fujimoto, and E.S. Kintzer. "Ultrashort Pulse Generation from High Power Diode Arrays Using Intracavity Nonlinearities."

International Electromagnetic Compatibility Symposium, Singapore, December 7-9, 1992.

Kong, J.A. "Progress in Electromagnetics and Future Developments."

International Free Electron Laser Conference, Kobe, Japan, August 1992.

Jerby, E., G. Bekefi, and T. Hara. "Self and Active Mode-locking in a Free-electron Laser Oscillator - Experiments and Theory."

International Geoscience and Remote Sensing Symposium, Houston, Texas, May 26-29, 1992.

Beaudoin, A., T. Le Toan, C.C. Hsu, H.C. Han, J.A. Kong, R.T. Shin. "Simulation of Forest Backscatter as a Function of Forest and Ground Parameters."

Han, H.C., J.A. Kong, R.T. Shin, S.V. Nghiem, and R. Kwok. "Application of Theoretical Models to Active and Passive Remote Sensing of Saline Ice."

Hsu, C.C., H.C. Han, R.T. Shin, J.A. Kong, A. Beaudoin, and T. LeToan. "Radiative Transfer Theory for Polarimetric Remote Sensing of Pine Forest."

Nghiem, S.V., R. Kwok, J.A. Kong, R.T. Shin, A.J. Gow, and S.A. Arcone. "Effective Permittivity of Saline Ice Under Thermal Variation."

International Organization for Standardization Coding of Moving Pictures and Associated Audio (ISO-MPEG), London, England, November 2-6, 1992.

Apostolopoulos, J., and J.S. Lim. "Position-Dependent Runlength Encoding."

International Quantum Electronics Conference, Vienna, Austria, June 14-19, 1992.

Huang, D., E.A. Swanson, M. Hee, J.A. Izatt, C.P. Lin, J.S. Schuman, C.A. Puliafito, and J.G. Fujimoto. "Optical Coherence Domain Reflectometry and Optical Coherence Tomography."

Kärtner, F.X., and H.A. Haus. "Classical and Quantum Dynamics of a Pulse Propagating through a Nonlinear Fiber."

- Wong, N.C., D. Lee, and L.R. Brothers. "Tunable Optical Frequency Division."
- International Radio Science Union Specialists Meeting on Microwave Radiometry and Remote Sensing*, Boulder, Colorado, January 24-26, 1992.
- Kong, J.A. "Theoretical Modeling for Passive Microwave Remote Sensing of Earth Terrain."
- Rosenkranz, P.W. "Emission and Absorption of Microwaves by Atmospheric Oxygen and Water Vapor."
- Staelin, D.H. "Passive Microwave Observations of Atmospheric Parameters from Space."
- International Sherwood Fusion Theory Conference*, Santa Fe, New Mexico, April 6-8, 1992.
- Coppi, B., and S. Migliuolo. "The Isotopic Effect and Impurity Drift Modes."
- Coppi, B., M. Nassi, and L. Sugiyama. "Physics Principles of Ignition Experiments."
- Detragiache, P., and B. Coppi. "Magnetic Topology Transitions in Collisionless Plasmas."
- Migliuolo, S. "Impurity Effects on Toroidal ITG Modes."
- Pegoraro, F., and B. Coppi. "Energy and Current Transport: Symmetry Breaking and Degradation."
- Ram, A.K., A. Bers, V. Fuchs, R.W. Harvey, and M.G. McCoy. "Current Drive by Lower Hybrid Waves in Combination with Fast Alfvén Waves."
- Sugiyama, L.E., and W. Park. "A Three Dimensional, Toroidal Two Fluid Model with Hot Particles."
- International Solid-State Circuit Conference*, San Francisco, California, February 1993.
- Yu, P.C., and H-S. Lee. "A High-Swing 2-V CMOS Operational Amplifier with Grain Enhancement Using a Replica Amplifier."
- International Symposium on Circuits and Systems*, San Diego, California, May 10-13, 1992.
- Wyatt, J.L., Jr., C. Keast, M. Seidel, D. Standley, B. Horn, T. Knight, C. Sodini, H-S. Lee, and T. Poggio. "Analog VLSI Systems for Early Vision Processing."
- International Symposium on Electron, Ion, and Photon Beams*, 36th, Orlando, Florida, May 26-31, 1992.
- Carter, J.M., D.B. Olster, M.L. Schattenburg, A. Yen, and H.I. Smith. "Spatially-coherent, Large-area, Free-standing Gratings for Atom Interferometry Produced Using Holographic Lithography."
- Chu, W., C.C. Eugster, A. Moel, E.E. Moon, J.A. del Alamo, and H.I. Smith. "Conductance Quantization in a GaAs Electron Waveguide Device Fabricated by X-ray Lithography."
- Ghanbari, R.A., M. Burkhardt, D.A. Antoniadis, H.I. Smith, M.R. Melloch, K.W. Rhee, and M.C. Peckerar. "Comparative Mobility Degradation in Modulation-doped GaAs Devices after E-beam and X-ray Irradiation."
- Ghanbari, R.A., W. Chu, E.E. Moon, M. Burkhardt, K. Yee, D.A. Antoniadis, H.I. Smith, M.L. Schattenburg, K.W. Rhee, R. Bass, M.C. Peckerar, and M.R. Melloch. "Fabrication of Parallel Quasi-one-dimensional Wires Using a Novel Conformable X-ray Mask Technology."
- Hector, S.D., M.L. Schattenburg, E.H. Anderson, W. Chu, U. Wong, and H.I. Smith. "Modeling and Experimental Verification of Illumination and Diffraction Effects on Image Quality in X-ray Lithography."
- Ku, Y.C., M.H. Lim, J.M. Carter, M.K. Mondol, A. Moel, and H.I. Smith. "Correlation of In-Plane and Out-of-Plane Distortion in X-ray Lithography Masks."
- Xu, X., A.D. Della Ratta, J. Sosonkina, and J. Melngailis. "Focused Ion Beam Induced Deposition and Ion Milling as a Function of Angle of Ion Incidence."
- Ion Cyclotron Radio Frequency Modeling and Theory Workshop*, Princeton, New Jersey, August 17-18, 1992.
- Ram, A.K., A. Bers, V. Fuchs, R.W. Harvey, and M.G. McCoy. "Effects of ICRF Waves on Lower Hybrid Current Drive."
- Issues in Advanced Hearing Aid Research*, Lake Arrowhead, California, May 25-29, 1992.
- Zurek, P.M., and J.E. Greenberg. "Current Research on Adaptive Beamforming for Hearing Aids."
- Journées Microelectronique et Optoelectronique III-V*, Fourth, Al Grande Motte, France, October 21-23, 1992.

- Dumas, J.M., P. Audren, M.P. Favennec, S. Praquin, S.R. Bahl, and J.A. del Alamo. "Une Etude des Niveaux Profonds dans le Transistor a Effet de Champ de Puissance a Heterostructure InAlAs/n⁺ - InGaAs"
- MIT/Brown Conference on Advanced Research in VLSI and Parallel Systems*, Providence, Rhode Island, March 25-27, 1992.
- Devadas, S., K. Keutzer, S. Malik, and A. Wang. "Event Suppression: Improving the Efficiency of Timing Simulation for Synchronous Digital Circuits."
- Van Aelten, F., J. Allen, and S. Devadas. "Compositional Verification of Systems with Synchronous Globally Timed Control."
- Materials Research Society Symposium*, San Francisco, California, April 27-May 1, 1992.
- Coronado, C.A., E. Ho, L.A. Kolodziejski, and C.A. Huber. "Laser-Assisted Growth of ZnSe by Metalorganic Molecular Beam Epitaxy."
- Materials Science Seminar*, Hanover, New Hampshire, January 14-15, 1993.
- Kolodziejski, L.A. "Photo-Assisted Metalorganic Molecular Beam Epitaxy of ZnSe."
- National Association of Broadcasters Meeting*, Las Vegas, Nevada, April 11-16, 1992.
- Lim, J.S. "HDTV Research at MIT-ATRP."
- National Center for Integrated Photonic Technology*, Annual Review of Photonics, Newport Beach, California, July 9-10, 1992.
- Haus, H.A. "Optically Controlled Phased Array Antennas and Components."
- Ippen, E.P. "Ultrafast Photonics (plenary talk)."
- National Center for Integrated Photonic Technology*, Fall Meeting, Columbia University, New York, New York, December 4-6, 1992.
- Haus, H.A. "Integrated Resonant Optical Filter and Some of Its Applications."
- Hultgren, C.T., D. Dougherty, K.L. Hall, G. Lenz, and E.P. Ippen. "Dynamic Nonlinearities in Active Waveguides."
- National Radio Science Meeting*, Boulder, Colorado, January 7-10, 1992.
- Xia, J., T.M. Habashy, R.T. Shin, and J.A. Kong. "The Renormalized STIE Approach Applied to Inversion of Soil Moisture Profiles."
- National Science Foundation Workshop on Spoken Language Understanding*, Arlington, Virginia, February 10-11, 1992.
- Stevens, K.N. "Review of Speech Recognition Research in Speech Group of RLE."
- National Science Foundation-Quantum Electronics, Waves, and Beams Workshop*, Third, New York, New York, June 4-5, 1992.
- Bers, A. "Waves and Chaos in the Electrodynamics of Plasmas."
- New England Molecular Beam Epitaxy Workshop*, Seventh, Cambridge, Massachusetts, May 13, 1992.
- Bahl, S.R., B.R. Bennett, and J.A. del Alamo. "High Quality Heterostructures for Doubly-Strained InAlAs/InGaAs HFETs."
- Opticon '92*, Boston, Massachusetts, November 15-20, 1992.
- Smith, H.I. "History of X-ray Lithography."
- Optical Fiber Communication Conference*, San Jose, California, February 2-7, 1992.
- Damask, J.N., and H.A. Haus. "Wavelength-Division (DE) Multiplexing Using Cascaded DFB Filters."
- Mecozzi, A., J.D. Moores, H.A. Haus, and Y. Lai. "Modulation and Filtering Control of Soliton Transmission."
- Optical Society of America Meeting*, Annual, Albuquerque, New Mexico, September 20-25, 1992.
- Bergman, K., C. Doerr, H.A. Haus, and M. Shirasaki. "Subquantum Limit Measurements with Optical Pulses."
- Fujimoto, J.G. "Femtosecond Lasers and Ultrafast Measurement Techniques."
- Haus, H.A. "Control Filters for Repeaterless Soliton Transmission (invited talk)."
- Pritchard, D.E. "Atom Optics and Atom Interferometers."
- Shapiro, J.H., and K-X. Sun. "Direct Detection of Gaussian State Light."
- Shapiro, J.H., and N.C. Wong. "Optical Amplifiers, Phase-Shift Keying, and Signal-to-Noise Ratio."
- Sun, K-X., N.C. Wong, and J.H. Shapiro. "Squeezed Amplification with Cavity Detunings: Mean-Field Behavior."

- Sun, K-X., and J.H. Shapiro. "Squeezed Amplification with Cavity Detunings: Noise Behavior."
- Wong, N.C., and D. Lee. "Optical Frequency Division Using a Parametric Oscillator."
- Optical Society of America Topical Meeting on Non-linear Optics*, Maui, Hawaii, August 17-21, 1992.
- Haus, H.A., E.P. Ippen, and K. Tamura. "Additive Pulse Modelocking in Fiber Lasers."
- Optical Society of America Topical Meeting*, New Orleans, Louisiana, April 13-15, 1992.
- Ippen, E.P. "Ultrafast Waveguide Optics" (plenary talk)
- Xia, J.J., and J.A. Kong. "Electromagnetic Inverse Scattering in Remote Sensing."
- Optical Society of America Topical Meeting on Ultrafast Electronics and Opto-electronics*, San Francisco, California, January 25-27, 1993.
- Ippen, E.P. "Ultrafast Dynamics in Active Semiconductor Waveguides."
- Physical Electronics Conference*, Irvine, California, June 20-25, 1992.
- Li, Y.L., J.J. Yang, D.P. Pullman, and S.T. Ceyer. "Reaction Dynamics of F_2 on $Xi(100)$."
- Quantum Electronics and Laser Science Conference*, Baltimore, Maryland, May 2-7, 1993.
- Joneckis, L.G., and J.H. Shapiro. "Quantum Propagation in Single-Mode Fiber."
- SPIE Conference on Frequency Stabilized Lasers and Their Applications*, Boston, Massachusetts, November 15-20, 1992.
- Lee, D., and N.C. Wong. "A High-Performance Tunable Optical Parametric Oscillator."
- SPIE International Society for Optical Engineering*, Los Angeles, California, January 14-21, 1993.
- Bekefi, G., P. Catravas, C. Chen, and I. Mastovsky. "Experimental and Theoretical Studies of the Proposed MIT Relativistic Klystron Amplifier."
- Catravas, P., C. Chen, and G. Bekefi. "Dispersion Characteristics of a Two-Stream Relativistic Klystron Amplifier."
- Chen, C., W. Hu, and G. Bekefi. "Two-Dimensional Nonlinear Theory of Double-Stream Cyclotron Masers."
- SPIE International Society for Optical Engineering*, Los Angeles, California, January 19-24, 1992.
- Bekefi, G., A. Bers, and A. Ram. "Double Stream Cyclotron Maser."
- Chen, C., P. Catravas, and G. Bekefi. "Design Studies of a 3.3-GHz Relativistic Klystron Amplifier."
- Conde, M.E., and G. Bekefi. "Experimental Study of a 33.3 GHz Free-Electron Laser Amplifier with a Reversed Axial Guide Magnetic Field."
- SPIE International Symposium on Optical Applied Science and Engineering*, San Diego, California, July 19-24, 1992
- Elfadel, I.M., and A.L. Yuille. "Mean-Field Phase Transitions for Gibbs Random Fields."
- SPIE International Symposium on Optical Engineering and Photonics*, San Jose, California, March 7-9, 1992.
- Smith, H.I., and M.L. Schattenburg. "Why Bother with X-ray Lithography?"
- Sea Ice Workshop*, Hanover, New Hampshire, October 13-15, 1992.
- Kong, J.A. "Sea Ice Remote Sensing Modeling."
- Semiconductor Research Corporation/DARPA Computer-Integrated Manufacturing of Integrated Circuits Workshop*, Seventh Annual, Stanford, California, August 5-6, 1992.
- Boning, D.S., D.E. Troxel, M.B. McIlrath, M.L. Heytens, D.A. Antoniadis, and P. Penfield. "CAFE: A System for VLSI Technology Complexity Management."
- Ha, S., E. Sachs, and D.E. Troxel. "On-Line Control of Uniformity in Single Wafer Plasma Etch Process."
- McIlrath, M.B. "Process Representation for TCAD Frameworks."
- Troxel, D.E., D.P. McNabb, and M.B. McIlrath. "Dynamically Modified PFR Based Fabrication in a Realistic IC Laboratory."
- Semiconductor Research Corporation X-ray Lithography Review*, Stoughton, Wisconsin, October 20-22, 1992.
- Melngailis, J. "X-ray Lithography Masks Made by Focused Ion Beams."

- Sub-Arcsecond Radio Astronomy Meeting*, Manchester, England, July 20-24, 1992.
- Burke, B.F. "Einstein Rings and Einstein Quads."
- Conner, S., A. Fletcher, L. Herold, and B.F. Burke. "The MIT-Green Bank-VLA Gravitational Lens Search: Prospects for Detecting a Population of Small Angular Size Lens Systems" (poster session).
- Symposium on Frequency Control*, 46th Annual, Hershey, Pennsylvania, May 27-29, 1992.
- Wong, N.C., and D. Lee. "Optical Parametric Division."
- Symposium on VLSI Circuits*, Seattle, Washington, June 1992.
- Keast, C.L., and C.G. Sodini. "A CCD/CMOS Based Imager with Integrated Focal Plane Signal Processing."
- Topical Meeting on Electrical Performance of Electronic Packaging*, Tucson, Arizona, April 1992.
- Lee, L.H., G. Arjavalingham, S.M. Ali, and T.R. Dinger. "Hybrid-mode Analysis of Coplanar Strips and Coplanar Waveguides."
- U.S.-Japan Workshop on Ion Temperature Gradient Turbulence*, University of Texas, Austin, Texas, January 11-14, 1993.
- Migliuolo, S. "Ion Temperature Gradient Driven Impurity Modes."
- U.S.-Japan Workshop on Non-Inductive Current Drive and Profile Control*, Princeton, New Jersey, December 14-16, 1992.
- Ram, A.K., A. Bers, V. Fuchs, R.W. Harvey, and M.G. McCoy. "Effect of ICRF Waves on Lower Hybrid Current Drive."
- University of Maryland Department of Electrical Engineering Seminar*, College Park, Maryland, December 11, 1992.
- Melngailis, J. "Focused Ion Beam Microfabrication."
- Workshop on Advanced Accelerator Concepts*, Third, Port Jefferson, New York, June 14-20, 1992.
- Conde, M.E., and G. Bekefi. "A High Efficiency 33 GHz Free Electron Laser with a Reversed Axial Magnetic Field."
- Conde, M.E., G. Bekefi, J.S. Wurtele, P. Volfbeyn, and K. Ricci. "Tests of a 33 GHz High Gradient Accelerating Structure."
- Workshop on Atom Optics and Atom Interferometry*, Konstanz, Germany, June 9-12, 1992.
- Ekstrom, C.R. "Squared Beam Experiments with a Three Grating Atom Interferometer."
- Workshop on Compound Semiconductor Microwave Materials and Analog Devices*, San Antonio, Texas, February 17-19, 1992.
- Bahl, S.R., B.R. Bennett, and J.A. del Alamo. "Doubly-Strained InAlAs/n⁺-InGaAs HFETs."
- Fonstad, C.G. "Quantum-Wave Tunnel Barrier n-n-n Transistors."
- Workshop on High Power Ion Cyclotron Resonance Frequency Antenna Design and Physics*, Sixth, Boulder, Colorado, January 20-22, 1993.
- Sugiyama, L., M. Nassi, and B. Coppi. "Predicted Ignition Scenarios in Ignitor and the Role of ICRH."
- Workshop on Nanostructure Fabrication for Opto/Electronics*, Los Angeles, California, August 14-15, 1992.
- Smith, H.I. "X-ray Nanolithography for Optoelectronic Integrated Circuits."
- Workshop on Numerical Modeling of Processes and Devices for Integrated Circuits*, Seattle, Washington, May 31-June 1, 1992.
- Nabors, K., and J. White. "An Improved Approach to Including Conformal Dielectrics in Multipole-Accelerated Three-dimensional Capacitance."
- Reicheit, M.W., J. White, and J. Allen. "Waveform Frequency-Dependent Overrelaxation for Transient Two-Dimensional Simulation of MOS Devices."

A.1.2 Papers to be Presented

- IEEE MTT-S International Microwave Symposium*, Atlanta, Georgia, June 1993.
- Lee, L.H., S.M. Ali, W.G. Lyons, R.S. Withers, and T.P. Orlando. "Full-wave Analysis of Superconducting Microstrip Lines on Sapphire Substrates."

Summer School on Recent Developments in Statistical Physics, Istanbul, Turkey, July 26-August 6, 1993.

Berker, A.N. "Phase Transitions in Disordered Systems."

A.1.3 Published Meeting Papers

Bers, A., and A.K. Ram. "Lower Hybrid and Fast Wave Current Drive-Status of Theory." *Proceedings of the I.A.E.A. Technical Meeting on Fast Wave Current in Reactor Scale Tokamaks (Synergy and Complementarity with LHCD and ECRH)*, Arles, France, September 23-25, 1991.

Chow, C.C., A. Bers, and A.K. Ram. "Spatiotemporal Chaos in the Langmuir Decay and its Implications on the Saturation of SRS." *Proceedings of the 22nd Anomalous Absorption Conference*, Lake Placid, New York, July 12-17, 1992.

Conde, M.E., and G. Bekefi. "Experimental Study of a 33.3 GHz Free-Electron Laser Amplifier with a Reversed Axial Guide Magnetic Field." *Proceedings of SPIE*, Los Angeles, California, January 20-24, 1992. Vol. 1629 Intense Microwave and Particle Beams III 1629: 153-158 (1992).

Coppi, B., and F. Pegoraro. "Near-Term Experiments on Advanced Fusion." *Proceedings of the Enrico Fermi International School of Physics*, Course CXVII, Milan, Italy, July 1992.

Dron, L. "System-Level Design of Specialized VLSI Hardware for Computation Relative Orientation." *Proceedings of the IEEE Workshop on Applications of Computer Vision*, Palm Springs, California, November 30-December 2, 1992.

Lee, P.A. "Few Electron Nanostructures: A New Laboratory for Studying Strongly Correlated Systems." *Proceedings of the NATO Workshop*, Nordwig, the Netherlands, May 1992.

Lumsdaine, A., and J.K. White. "Accelerating Dynamic Iteration Methods with Application to Semiconductor Device Simulation." *Proceedings of the Copper Mountain Conference on Iterative Methods*, Copper Mountain, Colorado, April 1992.

Pritchard, D.E. "Atom Interferometers." *Proceedings of the International Conference on*

Atomic Physics, 13th, Munich, Germany, August 3-7, 1992.

Pritchard, D.E., and W. Ketterle. "Atom Traps and Atom Optics." *Proceedings of the Enrico Fermi International School of Physics*, Milan, Italy, July 1992.

Shattuck-Hufnagel, S., M. Ostendorf, and K. Ross. "Pitch Accent Placement Within Words." *Proceedings of the Institute for Research and Computer Science Workshop on Prosody in Natural Language*, Philadelphia, Pennsylvania, August 1992.

Srinivasan, M.A. "Computations in Tactile Sensing." *Proceedings of the Computation and Neural Systems (CNS '92) Meeting*, San Francisco, California, July 25-28, 1992.

Stevens, K.N. "Models for Production and Acoustics of Stop Consonants." *Proceedings of the Fourth Australian International Conference on Speech Science and Technology*, Brisbane, Australia, November 30-December 2, 1992.

Tan, H.Z., X.D. Pang, and N.I. Durlach. "Manual Resolution of Length, Force, and Compliance." *Proceedings of the American Society of Mechanical Engineers Annual Winter Meeting*, Anaheim, California, November 8-13, 1992. DSC-42: 13-18. Ed. H. Kazerooni. Book No. G00751.

Zangi, K. "A New Two Sensor Active Noise Cancellation Algorithm." *Proceedings of the IEEE International Conference on Acoustics, Speech, and Signal Processing*, San Francisco, California, March 23-26, 1992.

A.2 Journal Articles

A.2.1 Published Journal Articles

Tramo, M.J., P.A. Cariani, and B. Delgutte. "Representation of Tonal Consonance and Dissonance in the Temporal Firing Patterns of Auditory Nerve Fibers: Responses to Musical Intervals Composed of Pure Tones vs. Harmonic Complexes." *Soc. Neurosci. Abstr.* 18(1): 382 (1992).

Abernathy, D.L., S.G.J. Mochrie, D.M. Zehner, G. Grubel, and D. Gibbs. "Thermal Roughness of a Close-Packed Metal Surface: Pt(001)." *Phys. Rev. Lett.* 69: 941 (1992).

- Altshuler, B.L., and L.B. Ioffe. "Motion of Fast Particles in Strongly Fluctuating Magnetic Fields." *Phys. Rev. Lett.* 69: 2979 (1992).
- Arias, T.A., and J.D. Joannopoulos. "Ab Initio Prediction of Dopant Segregation at Elemental Semiconductor Grain Boundaries without Coordination Defects." *Phys. Rev. Lett.* 69(23): 3330-3333 (1992).
- Arias, T.A., M.C. Payne, and J.D. Joannopoulos. "Ab initio Molecular-Dynamics Techniques Extended to Large-Length-Scale Systems." *Phys. Rev. B* 45(4): 1538-1549 (1992).
- Asher, P., A. Ghosh, and S. Devadas. "Boolean Satisfiability and Equivalence Checking Using General Binary Decision Diagrams." *Integration: VLSI J.* 13(1): 1-16 (1992).
- Bagwell, P.F., S.L. Park, A. Yen, D.A. Antoniadis, H.I. Smith, T.P. Orlando, and M.A. Kastner. "Magnetotransport in Multiple Narrow Silicon Inversion Channels Opened Electrostatically into a Two-dimensional Electron Gas." *Phys. Rev. B* 45(16): 9214-9221 (1992).
- Bahl, S.R., and J.A. del Alamo. "Elimination of Mesa-Sidewall Gate Leakage in InAlAs/InGaAs Heterostructures by Selective Sidewall Recessing." *IEEE Electron Device Lett.* 13(4): 195-197 (1992).
- Bahl, S.R., M.H. Leary, and J.A. del Alamo. "Mesa-Sidewall Gate Leakage in InAlAs/InGaAs Heterostructure Field-Effect Transistors." *IEEE Trans. Electron Devices* 39(9): 2037-2043 (1992).
- Bailey, D.W., and C.J. Stanton. "Carrier Diffusion Effects in Time-Resolved Photoluminescence." *Appl. Phys. Lett.* 60: 880 (1992).
- Baylon, D.M., and J.S. Lim. "Video Compression and Noise Reduction Using Transform/Subband Coding and Adaptive Amplitude Modulation." *SMPTTE J.* 101(6): 404-406 (1992).
- Bekefi, G. "Double Stream Cyclotron Maser." *SPIE Proc.* 1629: 130-143 (1992).
- Bergman, K., H.A. Haus, and M. Shirasaki. "Analysis and Measurement of GAWBS Spectrum in a Nonlinear Fiber Ring." *Appl. Phys. B* 55: 242-249 (1992).
- Berkovitz, R., and B.L. Altshuler. "Electric Field Outside a Neutral Mesoscopic Grain." *Europhys. Lett.* 19: 115 (1992).
- Bers, A., A.K. Ram, and G. Bekefi. "Linear Analysis of the Double Stream Cyclotron Maser." *Bull. Am. Phys. Soc.* 37(6): 1536 (1992).
- Boning, D.S., M.B. McIlrath, P. Penfield, and E.M. Sachs. "A General Semiconductor Process Modeling Framework." *IEEE Trans. Semicond. Manuf.* 5(4): 266-280 (1992).
- Brommer, K.D., M. Needels, B.E. Larson, and J.D. Joannopoulos. "Ab-Initio Theory of the Si(111)-(7x7) Surface Reconstruction - A Challenge for Massively Parallel Computation." *Phys. Rev. Lett.* 68(9): 1355-1358 (1992).
- Bryan, M.J., S. Devadas, and K. Keutzer. "Necessary and Sufficient Conditions for Robust Stuck-Open Fault Testability in Multilevel Networks." *IEEE Trans. Comput.-Aided Des.* 11(6): 800-803 (1992).
- Burke, B.F., J. Lehar, J.N. Hewitt, and D.H. Roberts. "The Radio Time Delay in the Double Quasar 0957+561." *Astrophys. J.* 384: 453-466 (1992).
- Burke, B.F., S.R. Conner, and J. Lehar. "Reconciling the Image Brightness Ratios in the Gravitational Lens System 0957+561." *Astrophys. J. Lett.* 387 LC: 61-64 (1992).
- Burton, M.W., S.E. Blumstein, and K.N. Stevens. "A Phonetic Analysis of Prenasalized Stops in Moru." *J. Phon.* 20: 127-142 (1992).
- Cariani, P., B. Delgutte, and N.Y.S. Kiang. "The Pitch of Complex Sounds is Simply Coded in Interspike Interval Distributions of Auditory Nerve Fibers." *Soc. Neurosci. Abstr.* 18(1): 383 (1992).
- Carter, J.M., D.B. Olster, M.L. Schattenburg, A. Yen, and H.I. Smith. "Large-area, Free-Standing Gratings for Atom Interferometry Produced Using Holographic Lithography." *J. Vac. Sci. Technol. B* 10(6): 2909-2911 (1992).
- Chamon, C. deC., C.K. Sun, H.A. Haus, and J.G. Fujimoto. "Femtosecond Time Division Interferometry Technique for Measuring the Tensor Components of X(3)." *Appl. Phys. Lett.* 60(5): 533-535 (1992).
- Cheung, S., and J.S. Lim. "Combined Multiresolution (Wide-Band/Narrow-Band) Spectrogram." *IEEE Trans. Signal Process.* 40(4): 975-977 (1992).

- Cho, K., and J.D. Joannopoulos. "Ergodicity and Dynamical Properties of Constant Temperature Molecular Dynamics." *Phys. Rev. A* 45(10): 7089-7097 (1992).
- Chow, C.C., A. Bers, and A.K. Ram. "Spatiotemporal Chaos in the Nonlinear Three-Wave Interaction." *Phys. Rev. Lett.* 68(23): 3379-3382 (1992).
- Chu, N.C., J.A. Kong, H.A. Yueh, and S.V. Nghiem. "Variance of Phase Fluctuations of Waves Propagation Through a Random Medium." *J. Electromag. Wave Appl.* 6(2): 169-197 (1992).
- Chu, W., C.C. Eugster, A. Moel, E.E. Moon, J.A. del Alamo, H.I. Smith, M.L. Schattenburg, K.W. Rhee, M.C. Peckerar, and M.R. Melloch.. "Conductance Quantization in a GaAs Electron Waveguide Device Fabricated by X-ray Lithography." *J. Vac. Sci. Technol. B* 10(6): 2966-2969 (1992).
- Chu, W., H.I. Smith, S.A. Rishton, D.P. Kern, and M.L. Schattenburg. "Fabrication of 50 nm Line-and-Space X-ray Masks in Thick Au Using a 50 keV Electron Beam System." *J. Vacuum Sci. Tech. B* 10(1): 118-121 (1992).
- Cobra, D.T., A.V. Oppenheim, and J.S. Jaffe. "Geometric Distortions in Side-Scan Sonar Images: A Procedure for Their Estimation and Correction." *IEEE J. Oceanic Eng.* 17(3): 252-268 (1992).
- Conner, S.R., J. Lehar, and B.F. Burke. "Reconciling the Image Brightness Ratios in the Gravitational Lens System 0957+561." *Astrophys. J.* 387: L61-L64 (1992).
- Coppi, A.C., and B. Coppi. "Stability of Global Modes in Advanced Plasma Confinement Configurations." *Nucl. Fusion* 32(2): 205-216 (1992).
- Coppi, B., M. Nassi, and L.E. Sugiyama. "Physics Basis for Compact Ignition Experiments." *Phys. Scr.* 45: 112-132 (1992).
- Corcoran, C.J., and R.H. Rediker. "The Dependence of the Output of an External-Cavity Laser on the Relative Phases of Inputs from Five Gain Elements." *IEEE Photonics Technol. Lett.* 4(11): 1197-1200 (1992).
- Cornell, E.A., K.R. Boyce, D.L.K. Fygenson, and D.E. Pritchard. "Two Ions in a Penning Trap: Implications for Precision Mass Spectroscopy." *Phys. Rev. A* 45(5): 3049-3059 (1992).
- Coronado, C.A., E. Ho, L.A. Kolodziejski, and C.A. Huber. "Photoassisted Metalorganic Molecular Beam Epitaxy of ZnSe." *Appl. Phys. Lett.* 61(5): 534-536 (1992).
- Dal Pino, A., Jr., M. Needels, and J.D. Joannopoulos. "Oxygen Induced Broken-Bond Defect in Silicon." *Phys. Rev. B* 45(7): 3304-3308 (1992).
- Devadas, S., and K. Keutzer. "Validatable Nonrobust Delay-Fault Testable Circuits Via Logic Synthesis." *IEEE Trans. Comput.-Aided Des.* 11(12): 1559-1573 (1992).
- Ding, K.H., C.E. Mandt, L. Tsang, and J.A. Kong. "Monte Carlo Simulations of Pair Distribution Functions of Dense Discrete Random Media with Multiple Sizes of Particles." *J. Electromag. Wave Appl.* 6(8): 1015-1030 (1992).
- DiFilippo, F., V. Natarajan, K.R. Boyce, and D.E. Pritchard. "Classical Amplitude Squeezing for Precision Measurements." *Phys. Rev. Lett.* 68(19): 2859-2862 (1992).
- Doerr, C.R., M. Shirasaki, and H.A. Haus. "Dispersion of Pulsed Squeezing for Reduction of Sensor Nonlinearity." *Opt. Lett.* 17(22): 1617-1619 (1992).
- Delin, K.A., T.P. Orlando, E.J. McNiff, Jr., S. Foner, R.B. van Dover, L.F. Schneemeyer, and J.V. Waszczak. "High-Field Magnetization Scaling Relations for Pure and Ni-Substituted Single-Crystal YBa₂Cu₃O₇." *Phys. Rev. B* 46: 11092 (1992).
- Durlach, N.I. "Virtual Environments: Introductory Remarks." *J. Acoust. Soc. Am.* 4: 2331-2332 (1992).
- Durlach, N.I., A. Rigopoulos, X.D. Pang, W.S. Woods, A. Kulkarni, H.S. Colburn, and E.M. Wenzel. "On the Externalization of Auditory Images." *Presence* 1: 251-257 (1992).
- Durlach, N.I., R.M. Held, and B.G. Shinn-Cunningham. "Super Auditory Localization Displays." *Society for Information Display International Symposium, Digest of Technical Papers* 23: 98-101 (1992).
- Ekstrom, C.R., D.W. Keith, and D.E. Pritchard. "Atom Optics Using Microfabricated Structures." *Appl. Phys. B* 54: 369-374 (1992).

- Friedland, L., and A. Bers. "Hermitian Description of Interacting Inhomogeneous Electron Beams." *Phys. Fluids B, Plasma Phys.* 4: 1457 (1992).
- Ghanbari, R.A., M. Burkhardt, D.A. Antoniadis, H.I. Smith, M.R. Melloch, K.W. Rhee, and M.C. Peckerar. "Comparative Mobility Degradation in Modulation-doped GaAs Devices after E-beam and X-ray Irradiation." *J. Vac. Sci. Technol. B* 10(6): 2890-2892 (1992).
- Ghanbari, R.A., W. Chu, E.E. Moon, M. Burkhardt, K. Yee, D.A. Antoniadis, H.I. Smith, M.L. Schattenburg, K.W. Rhee, R. Bass, M.C. Perkerar, and M.R. Melloch. "Fabrication of Parallel Quasi-one-dimensional Wires Using a Novel Conformable X-ray Mask Technology." *J. Vac. Sci. Technol. B* 10(6): 3196-3199 (1992).
- Ghosh, A., S. Devadas, and A.R. Newton. "Heuristic Minimization of Boolean Relations Using Testing Techniques." *IEEE Trans. Comput.-Aided Des.* 11(9): 1166-1172 (1992).
- Green, T.J., Jr., and J.H. Shapiro. "Maximum-likelihood Laser Radar Range Profiling with the Expectation-maximization Algorithm." *Opt. Eng.* 31(11): 2343-2354 (1992).
- Greenberg, J.E., and P.M. Zurek. "Evaluation of an Adaptive Beamforming Method for Hearing Aids." *J. Acoust. Soc. Am.* 91(3): 1662-1676 (1992).
- Grishchuk, L., H.A. Haus, and K. Bergman. "Generation of Squeezed Radiation from Vacuum in the Cosmos and the Laboratory." *Phys. Rev. D* 46(4): 1440-1449 (1992).
- Hall, K.L., G. Lenz, and E.P. Ippen. "Femtosecond Time Domain Measurements of Group Velocity Dispersion in Diode Lasers at 1.5 μm ." *J. Lightwave Technol.* 10(5): 616-619 (1992).
- Hall, K.L., G. Lenz, E.P. Ippen, and G. Raybon. "Heterodyne Pump-Probe Technique for Time-Domain Studies of Optical Nonlinearities in Waveguides." *Opt. Lett.* 17(12): 874-876 (1992).
- Haus, H.A. "Matching of Distributed-Feedback Structures." *Opt. Lett.* 17(16): 1134-1136 (1992).
- Haus, H.A., and A. Mecozzi. "Long-term Storage of a Bit Stream of Solitons." *Opt. Lett.* 17(21): 1500-1502 (1992).
- Haus, H.A., and F.X. Kartner. "Quantization of the Nonlinear Schrodinger Equation." *Phys. Rev. A* 46(3): R1175-R1176 (1992).
- Haus, H.A., and Y. Lai. "Theory of Cascaded Quarter Wave Shifted Distributed Feedback Resonators." *IEEE J. Quantum Electron.* 28(1): 205-213 (1992).
- Haus, H.A., and Y. Lai. "Narrow-Band Optical Channel-Dropping Filter." *J. Lightwave Technol.* 10(1): 57-62 (1992).
- Haus, H.A., J.G. Fujimoto, and E.P. Ippen. "Analytic Theory of Additive Pulse and Kerr Lens Mode Locking." *IEEE J. Quantum Electron.* 28(10): 2086-2096 (1992).
- Hector, S.D., M.L. Schattenburg, E.H. Anderson, W. Chu, V.V. Wong, and H.I. Smith. "Modeling and Experimental Verification of Illumination and Diffraction Effects on Image Quality in X-ray Lithography." *J. Vac. Sci. Technol. B* 10(6): 3164-3168 (1992).
- Hee, M.R., D. Huang, E.A. Swanson, and J.G. Fujimoto. "Polarization Sensitive Low Coherence Reflectometer for Birefringence Characterization and Ranging." *J. Opt. Soc. Am. B* 9(6): 903-908 (1992).
- Helmerson, K., A. Martin, and D.E. Pritchard. "Laser and rf Spectroscopy of Magnetically Trapped Neutral Atoms." *J. Opt. Soc. Am. B* 9(4): 483-492 (1992).
- Herrmann, F., and C. Sodini. "A Dynamic Associative Processor for Machine Vision Applications." *IEEE Micromag.* 12(3): 31-41 (1992).
- Hradil, Z., and J.H. Shapiro. "Quantum Phase Measurements with Infinite Peak-Likelihood and Zero Phase Information." *Quantum Opt.* 4: 31-37 (1992).
- Huang, D., M. Ulman, L.H. Acioli, H.A. Haus, and J.G. Fujimoto. "Self-Focusing Induced Saturable Loss for Laser Modelocking." *Opt. Lett.* 17(7): 511-513 (1992).
- Hultgren, C.T., D.J. Dougherty, and E.P. Ippen. "Above- and Below-band Femtosecond Nonlinearities in Active AlGaAs Waveguides." *Appl. Phys. Lett.* 61(23): 2767-2769 (1992).
- Hung, T-Y., and P.L. Hagelstein. "Investigations of Whisper Gallery Mirrors for Extreme Ultraviolet (EUV) and Soft X-Rays." *IEEE J. Quantum Electron.* 28(5): 1376-1383 (1992).
- Jacobson, J.M., K. Naganuma, H.A. Haus, J.G. Fujimoto, and A.G. Jacobson. "Femtosecond

- Pulse Generation in a $\text{Ti:Al}_2\text{O}_3$ Laser by Using Second- and Third-Order Intracavity Dispersion." *Opt. Lett.* 17(22): 1608-1610 (1992).
- Juang, J.Y., D.A. Rudman, and T.P. Orlando. "On the Fermi Liquid Effects in the Upper Critical Field of NbN Thin Films." *Appl. Phys. Lett.* A172: 91 (1992).
- Kartner, F.X., L. Joneckis, and H.A. Haus. "Classical and Quantum Dynamics of a Pulse in a Dispersionless Non-linear Fibre." *Quantum Opt.* 4: 379-396 (1992).
- Kastner, M.A. "The Single-electron Transistor." *Rev. Mod. Phys.* 64(3): 849-858 (1992).
- Kaxiras, E., O. Alerhand, J. Wang, and J.D. Joannopoulos. "Theoretical Modeling of Hetero-epitaxial Growth Initiation." *Mat. Sci. Eng. B* 14: 245 (1992).
- Ketterle, W., and D.E. Pritchard. "Trapping and Focusing Ground State Atoms with Static Fields." *Appl. Phys. B* 54: 403-406 (1992).
- Ketterle, W., A. Martin, M.A. Joffe, and D.E. Pritchard. "Slowing and Cooling Atoms in Isotropic Laser Light." *Phys. Rev. Lett.* 69(17): 2483-2486 (1992).
- Kobler, J.B., J.J. Guinan, Jr., S.R. Vacher, and B.E. Norris. "Acoustic-Reflex Frequency Selectivity in Single Stapedius Motoneurons of the Cat." *J. Neurophysiol.* 68: 807-817 (1992).
- Ku, Y.C., M.H. Lim, J.M. Carter, M.K. Mondol, A. Moel, and H.I. Smith. "Correlation of In-plane and Out-of-plane Distortion in X-ray Lithography Masks." *J. Vac. Sci. Technol. B* 10(6): 3169-3172 (1992).
- Kucera, J.T., T.P. Orlando, G. Virship, and J.N. Eckstein. "Magnetic-field and Temperature Dependence of the Thermally Activated Dissipation in Thin Films of $\text{Bi}_2\text{Sr}_2\text{CaCu}_2\text{O}_{8-x}$." *Phys. Rev. B* 45: 11004 (1992).
- Kuhl, P.K., K. Williams, F. Lacerda, K.N. Stevens, and B. Lindblom. "Linguistic Experience Alters Phonetic Perception in Infants by Six Months of Age." *Sci.* 255: 606-608 (1992).
- Kunz, R., D.J. Ehrlich, J. Melngailis, and M.W. Horn. "Selective Area Growth of Metal Oxide Films Induced by Patterned Excimer Laser Surface Photolysis." *Proc. Mat. Res. Soc. Symp.* 236: 105 (1992).
- Lam, C-W., D.M. Sheen, S.M. Ali, and D.E. Oates. "Modeling the Nonlinearity of Superconducting Strip Transmission Lines." *IEEE Trans. Appl. Superconduct.* 2(2): 58-66 (1992).
- Lashmore-Davies, C.N., A. Bers, and A.K. Ram. "Enhanced Electron Power Absorption of the Fast Wave in the Vicinity of the Two Ion Hybrid Resonance." *Bull. Am. Phys. Soc.* 37(6): 1583 (1992).
- Lattes, A.L., S.C. Munroe, M.M. Seaver, J.E. Murguia, and J. Melngailis. "Improved Drift in Two-Phase, Long-Channel, Shallow-Buried-Channel CCDs with Longitudinally Nonuniform Storage-Gate Implants." *IEEE Trans. Electron Devices* 39: 1772 (1992).
- Lee, C.F., R.T. Shin, and J.A. Kong. "Time Domain Modeling of Impedance Boundary Condition." *IEEE Trans. Microwave Theory Tech.* 40(9): 1847-1850 (1992).
- Lee, D., and N.C. Wong. "Tunable Optical Frequency Division Using a Phase Locked Optical Parametric Oscillator." *Opt. Lett.* 17(1): 13-15 (1992).
- Lee, L.H., S.M. Ali, and W.G. Lyons. "Full-Wave Characterization of High-Tc Superconducting Transmission Lines." *IEEE Trans. Appl. Superconduct.* 2(2): 49-57 (1992).
- Lehar, J., J.N. Hewitt, D.H. Roberts, and B.F. Burke. "The Radio Time Delay in the Double Quasar 0957+561." *Astrophys. J.* 384: 453-466 (1992).
- Li, K., M.A. Tassoudji, R.T. Shin, and J.A. Kong. "Simulation of Electromagnetic Radiation and Scattering Using a Finite Difference-Time Domain Technique." *Comput. Appl. Eng. Ed.* 1(1): 45-63 (1992).
- Liebe, H.J., P.W. Rosenkranz, and G.A. Hufford. "Atmospheric 60-GHz Oxygen Spectrum: New Laboratory Measurements and Line Parameters." *J. Quant. Spectrosc. Radiat. Transfer* 48(5/6): 629-643 (1992).
- Liu, S.C., and J.G. Harris. "Dynamic Wires: An Analog VLSI Model for Object Processing." *Int. J. Comput. Vision* 8(3): 231-239 (1992).
- Luo, J., T.P. Orlando, J.M. Graybeal, X.D. Wu, and R. Muenchausen. "Comparison of the Longitudinal and Hall Resistivities from Vortex Motion in YBCO." *Phys. Rev. Lett.* 68: 690 (1992).

- McEuen, P.L., E.B. Foxman, J. Kinaret, U. Meirav, M.A. Kastner, N.S. Wingreen, and S.J. Wind. "Self-consistent Addition Spectrum of a Coulomb Island in the Quantum Hall Regime." *Phys. Rev. B* 45(19): 11419-11422 (1992).
- McIlrath, M.B., D.E. Troxel, M.L. Heytens, P. Penfield, D.S. Boning, and R. Jayavant. "CAFE-The MIT Computer-Aided Fabrication Environment." *IEEE Trans. Compon., Hybrids, Manuf. Tech.* 15(2): 353-360 (1992).
- Meade, R.D., K.D. Brommer, A.M. Rappe, J.D. Joannopoulos. "Existence of a Photonic Bandgap in Two Dimensions." *Appl. Phys. Lett.* 61(4): 495-497 (1992).
- Mecozzi, A., and H.A. Haus. "Effect of Filters on Soliton Interactions in WDM Systems." *Opt. Lett.* 17(14): 988-990 (1992).
- Mecozzi, A., J.D. Moores, H.A. Haus, and Y. Lai. "Modulation and Filtering Control of Soliton Transmission." *J. Opt. Soc. Am. B* 9(8): 1350-1357 (1992).
- Migliuolo, S. "Ion Temperature Gradient Driven Impurity Modes." *Nucl. Fusion* 32(8): 1331-1340 (1992).
- Moores, J.D. "Ultra-Long Distance Wavelength-Division-Multiplexed Soliton Transmission Using Inhomogeneously Broadened Fiber Amplifiers." *J. Lightwave Technol.* 10(4): 482-487 (1992).
- Nabors, K., S. Kim, and J. White. "Fast Capacitance Extraction of General Three-Dimensional Structures." *IEEE Trans. Microwave Theory Tech.* 40(7): 1496-1506 (1992).
- Naganuma, K., G. Lenz, and E.P. Ippen. "Variable Bandwidth Birefringent Filter for Tunable Femtosecond Lasers." *IEEE J. Quantum Electron.* 28(10): 2142-2150 (1992).
- Needels, M., A.M. Rappe, P.D. Bristowe, and J.D. Joannopoulos. "Ab Initio Study of a Grain Boundary in Gold." *Phys. Rev. B* 46(15): 9768-9771 (1992).
- Netz, R.R. "New Phases and Multiple Reentrance of the Blume-Emery-Griffiths Model with Repulsive Biquadratic Coupling: Monte Carlo Renormalization-Group Theory." *Europhys. Lett.* 17(4): 373-377 (1992).
- Netz, R.R., and A.N. Berker. "Smectic-C Order, In-Plane Domains, and Nematic Reentrance in a Microscopic Model of Liquid Crystals." *Phys. Rev. Lett.* 68(3): 333-336 (1992).
- Payne, M.C., M.P. Teter, D.C. Allan, T.A. Arias, and J.D. Joannopoulos. "Iterative Minimization Techniques for Ab Initio Total-energy Calculations: Molecular Dynamics and Conjugate Gradients." *Rev. Mod. Phys.* 64(4): 1045-1098 (1992).
- Peake, W.T., J.J. Rosowski, T.J. Lynch III. "Middle-ear Transmission: Acoustic Versus Ossicular Coupling in Cat and Human." *Hear. Res.* 57: 245-268 (1992).
- Perkell, J., H. Lane, M. Svirsky, and J. Webster. "Speech of Cochlear Implant Patients: A Longitudinal Study of Vowel Production." *J. Acoust. Soc. Am.* 91: 2961-2978 (1992).
- Perkell, J.S., and M.L. Matthies. "Temporal Measures of Anticipatory Labial Coarticulation for the Vowel /u/: Within- and Cross-subject Variability." *J. Acoust. Soc. Am.* 91(5): 2911-2925 (1992).
- Perkell, J.S., M.H. Cohen, M.A. Svirsky, M.L. Matthies, I. Garabieta, and M.T.T. Jackson. "Electromagnetic Midsagittal Articulator Systems for Transducing Speech Articulatory Movements." *J. Acoust. Soc. Am.* 92(6): 3078-3096 (1992).
- Rabinowitz, W.M., D.K. Eddington, L.A. Delhorne, and P.A. Cuneo. "Relations Among Different Measures of Speech Reception in Subjects Using a Cochlear Implant." *J. Acoust. Soc. Am.* 92(4): 1869-1881 (1992).
- Ram, A.K., and A. Bers. "Comments on Absolute and Convective Instabilities." *Geophys. Res. Lett.* 19(2): 143-145 (1992).
- Ram, A.K., A. Bers, V. Fuchs, R.W. Harvey, and M.G. McCoy. "Current Drive by Lower Hybrid Waves in Presence of Fast Alfvén Waves." *Bull. Am. Phys. Soc.* 37(6): 1605 (1992).
- Rankovic, C.M., R.L. Freyman, and P.M. Zurek. "Potential Benefits of Adaptive Frequency-gain Characteristics for Speech Reception in Noise." *J. Acoust. Soc. Am.* 91(1): 354-362 (1992).
- Rappe, A.M., A. Dal Pino, Jr., M. Needels, and J.D. Joannopoulos. "Mixed-Basis Pseudopotential Method Applied to Iterative Diagonalization Techniques." *Phys. Rev. B* 46(12): 7353-7357 (1992).

- Rappe, A.M., J.D. Joannopoulos, and P.A. Bash. "A Test of the Utility of Plane Waves for the Study of Molecules from First Principles." *J. Am. Chem. Soc.* 114(16): 6466-6469 (1992).
- Ravicz, M.E., J.J. Rosowski, and H.F. Voigt. "Sound-Power Collection by the Auditory Periphery of the Mongolian Gerbil *Meriones Unguiculatus*: I. Middle-Ear Input Impedance." *J. Acoust. Soc. Am.* 92(1): 157-177 (1992).
- Reed, C.M., N.I. Durlach, and L.A. Delhorne. "The Tactual Reception of Speech, Fingerspelling, and Sign Language by the Deaf-Blind." *SID Dig.* 92: 102-105 (1992).
- Reed, C.M., W.M. Rabinowitz, N.I. Durlach, L.A. Delhorne, L.D. Braida, J.C. Pemberton, B.D. Mulcahey, and D.L. Washington. "Analytic Study of the Tadoma Method: Improving Performance Through the Use of Supplementary Tactual Displays." *J. Speech Hear. Res.* 35: 450-465 (1992).
- Rhee, K.W., D.I. Ma, M.E. Peckerar, R.A. Ghanbari, and H.I. Smith. "Proximity Effect Reduction in X-ray Mask Making Using Thin Silicon Dioxide Layers." *J. Vac. Sci. Technol. B* 10: 3062-3066 (1992).
- Rittenhouse, G.E., K. Early, B.S. Meyerson, H.I. Smith, and J.M. Graybeal. "Novel Vertical Silicon-Membrane Structure and Its Application to Josephson Devices." *J. Vac. Sci. Technol. B* 10: 2860-2863 (1992).
- Robertson, W.M., G. Arjavalingam, R.D. Meade, A. Rappe, K. Brommer, and J.D. Joannopoulos. "Measurement of Photonic Bandstructure in a Two-Dimensional Periodic Dielectric Array." *Phys. Rev. Lett.* 68: 2023 (1992).
- Rosenkranz, P.W. "Rough-Sea Microwave Emissivities Measured with the SSM/I." *IEEE Trans. Geosci. Remote Sensing* 30(5): 1081-1085 (1992).
- Rubin, L.M., T.P. Orlando, J.B. VenderSande, G. Gormer, R. Savoy, R. Swope, and R. Beyers. "Phase Stability Limits and Solid-State Decomposition of $\text{Bi}_2\text{Sr}_2\text{CaCu}_2\text{O}_{8.45}$ and $\text{Bi}_2\text{Sr}_2\text{Ca}_2\text{Cu}_3\text{O}_{10.45}$ in Reduced Oxygen Pressures." *Appl. Phys. Lett.* 61(16): 1977 (1992).
- Shapiro, J.H. "On the Performance of Optical Phase-Shift-Keying with Preamplify-Feedforward-Homodyne Reception." *IEEE Photonics Technol. Lett.* 4(6): 647-649 (1992).
- Shattuck-Hufnagel, S. "The Role of Word Structure in Segmental Serial Ordering." *Cognition* 42: 213-259 (1992).
- Shinn-Cunningham, B.G., N.I. Durlach, and R.M. Held. "Adaption to Transformed Auditory Localization Cues in a Hybrid Real/Virtual Environment." *J. Acoust. Soc. Am.* 4: 2334 (1992).
- Shirasaki, M., and H.A. Haus. "Reduction of Guided Acoustic Wave Brillouin Scattering Noise in a Squeezer." *Opt. Lett.* 17(17): 1225-1227 (1992).
- Stanton, C.J., and D.W. Bailey. "Rate Equations for the Study of Femtosecond Inter-valley Scattering in Compound Semiconductors." *Phys. Rev. B* 45(15): 8369-8377 (1992).
- Stevens, K.N. "Lexical Access from Features." *RLE Speech Commun. Group Work. Pap.* 8: 119-144 (1992).
- Stevens, K.N., S.E. Blumstein, L. Glicksman, M. Burton, and K. Kurowski. "Acoustic and Perceptual Characteristics of Voicing in Fricatives and Fricative Clusters." *J. Acoust. Soc. Am.* 91(5): 2979-3000 (1992).
- Sugiyama, L.E. "Lower Hybrid Heating in a High-Field Deuterium-Tritium Ignition Experiment." *Fusion Technol.* 22: 236-242 (1992).
- Sugiyama, L.E., and M. Nassi. "Free Boundary Current Ramp and Current Profile Control in a D-T Ignition Experiment." *Nucl. Fusion* 32(3): 387-404 (1992).
- Svirsky, M., H. Lane, J. Perkell, and J. Webster. "Effects of Short-term Auditory Deprivation on Speech Production in Adult Cochlear Implant Users." *J. Acoust. Soc. Am.* 92: 1284-1300 (1992).
- Tsang, L., C.H. Chan, J.A. Kong, and J. Joseph. "Polarimetric Signatures of a Canopy of Dielectric Cylinders Based on First and Second Order Vector Radiative Transfer Theory." *J. Electromag. Wave Appl.* 6(1): 19-51 (1992).
- Turchette, Q.A., D.E. Pritchard, and D.W. Keith. "Numerical Model of a Multiple Grating Interferometer." *J. Opt. Soc. Am. A* 9(9): 1601-1606 (1992).
- Vignaud, D., S. Etchin, K.S. Liao, C.R. Musil, D.A. Antoniadis, and J. Melngailis. "Lateral Straggle of Focused-Ion-Beam Implanted Be in GaAs." *Appl. Phys. Lett.* 60: 2267 (1992).

- Wightman, C., S. Shattuck-Hufnagel, M. Ostendorf, and P.J. Price. "Segmental Durations in the Vicinity of Prosodic Phrase Boundaries." *J. Acoust. Soc. Am.* 91: 1707-1717 (1992).
- Wolfe, R.H., M. Needels, T. Arias, and J.D. Joannopoulos. "New Revelations in the Electronic Structure of Silicon as Derived from Volume Visualization of Ab-Initio Calculations." *IEEE Comput. Graphics Appl.* 12(4) (1992).
- Wong, N.C. "Gravity-Wave Detection Via an Optical Parametric Oscillator." *Phys. Rev. A.* 45(5): 3176-3183 (1992).
- Wornell, G.W., and A.V. Oppenheim. "Estimation of Fractal Signals from Noisy Measurements Using Wavelets." *IEEE Trans. Signal Process.* 40(3): 611-623 (1992).
- Wyatt, J.L., Jr., C. Keast, M. Deidel, D. Standley, B. Horn, T. Knight, C. Sodini, H-S. Lee, and T. Poggio. "Analog VLSI Systems for Image Acquisition and Fast Early Vision Processing." *Int. J. Comput. Vision* 8(3): 217-230 (1992).
- Xia, J., A.K. Jordan, and J.A. Kong. "Inverse Scattering View of Modal Structures in Inhomogeneous Optical Waveguides." *J. Opt. Soc. Am. A* 9(5): 740-748 (1992).
- Xu, X., A.D. Della Ratta, J. Sosonkina, and J. Melngailis. "Focused Ion Beam Induced Deposition and Ion Milling as a Function of Angle of Ion Incidence." *J. Vac. Sci. Technol. B* 10(6): 2675-2680 (1992).
- Yablonovitch, E., T. Gmitter, K. Leung, R. Meade, A. Rappe, K. Brommer, and J.D. Joannopoulos. "Electromagnetic Microresonators in 3D Photonic Band Structures." *Opt. Quantum Electron.* 24: 273 (1992).
- Yen, A., H.I. Smith, M.L. Schattenburg, and G.N. Taylor. "An Anti-Reflection Coating for Use with PMMA at 193 nm." *J. Electrochem. Soc.* 139(2): 616-619 (1992).
- Yen, A., M.L. Schattenburg, and H.I. Smith. "Proposed Method for Fabricating 50 nm-period Gratings by Achromatic Holographic Lithography." *Appl. Opt.* 31(16): 2972-2973 (1992).
- Yen, A., E.H. Anderson, R.A. Ghanbari, M.L. Schattenburg, and H.I. Smith. "Achromatic Holographic Configuration for 100-nm-period Lithography." *Appl. Opt.* 31(22): 4540-4545 (1992).
- Yu, P.C., S.J. Decker, H-S Lee, C.G. Sodini, and J.L. Wyatt, Jr. "CMOS Resistive Fuses for Image Smoothing and Segmentation." *IEEE J. Solid-State Circuits* 27(4): 545-553 (1992).
- Yueh, S.H., J.A. Kong, and R.T. Shin. "External Calibration of Polarimetric Radars using Point and Distributed Targets." *J. Electromag. Wave Appl.* 6(7): 921-941 (1992).
- Yueh, S.H., J.A. Kong, J.K. Jao, R.T. Shin, and T. Letoan. "Branching Model for Vegetation." *IEEE Trans. Geosci. Remote Sens.* 30(2): 390-402 (1992).
- Zhao, Y., D.C. Tsui, M. Santos, M. Shayegan, R.A. Ghanbari, D.A. Antoniadis, and H.I. Smith. "Magneto-optical Absorption in a Two Dimensional Electron Grid." *Appl. Phys. Lett.* 12: 1510-1512 (1992).
- Zurek, P.M. "Detectability of Transient and Sinusoidal Otoacoustic Emissions." *Ear Hear.* 13: 307-310 (1992).

A.2.2 Journal Articles Accepted for Publication

- Ashar, P., S. Devadas, and K. Keutzer. "Gate-Delay-Fault Testability Properties of Multiplexor-Based Networks." *Formal Meth. VLSI Des.: Int. J.*
- Bekefi, G. "Double Stream Cyclotron Maser." *J. Appl. Phys.*
- Berker, A.N. "Critical Behavior Induced by Quenched Disorder." *Physica A.*
- Berker, A.N., and K. Hui. "Phase Diagram of the Ising Model on the Square Lattice with Crossed Diagonal Bonds." *Phys. Rev. B.*
- Bryan, M.J., S. Devadas, and K. Keutzer. "Analysis and Design of Regular Structures for Robust Dynamic Fault Testability." *VLSI Des.: Int. J. Custom-Chip Des. Simul. Test.*
- Buck, J.R., and P.L. Tyack. "A Quantitative Measure of Similarity for Tursiops truncatus Signature Whistles." *J. Acoust. Soc. Am.*
- Cariani, P., and B. Delgutte. "Interspike Interval Distributions of Auditory Nerve Fibers in Response to Concurrent Vowels with Same and Different Fundamental Frequencies." *Abstr. Assoc. Res. Otolaryngol.*

- Chan, H.W., C. Chen, and R.C. Davidson. "Numerical Study of Relativistic Magnetrons." *J. Appl. Phys.*
- Chen, C., P. Catravas, and G. Bekefi. "Growth and Saturation of Stimulated Beam Modulation in a Two-Stream Relativistic Klystron Amplifier." *Appl. Phys. Lett.*
- Cheng, K-T., S. Devadas, and K. Keutzer. "Robust Delay-Fault Test Generation and Synthesis for Testability Under a Standard Scan Design Methodology." *IEEE Trans. Comput.-Aided Des.*
- Cheng, T.K., J. Vidal, H.J. Zeiger, E.P. Ippen, G. Dresselhaus, and M.S. Dresselhaus. "Displacive Excitation of Coherent Phonons." *Ultrafast Phenomena VIII.*
- Coronado, C.A., E. Ho, and L.A. Kolodziejski. "Laser-Assisted Growth of ZnSe by Metalorganic Molecular Beam Epitaxy." *Pro. Mat. Res. Soc.*
- Devadas, S. "Comparing Two-Level and Ordered Binary Decision Diagram Representations of Logic Functions." *IEEE Trans. Comput.-Aided Des.*
- Devadas, S., K. Keutzer, and S. Malik. "A Synthesis-Based Test Generation and Compaction Algorithm for Multifaults." *J. Electron. Testing: Theory Appl.*
- Devadas, S., K. Keutzer, S. Malik, and A. Wang. "Verification of Asynchronous Interface Circuits with Bounded Wire Delays." *J. VLSI Sig. Process.*
- Dron, L. "The Multi-Scale Veto Model: A Two-Stage Analog Network for Edge Detection and Image Reconstruction." *Int. J. Comput. Vision.*
- Elfadel, I.M., and A.L. Yuille. "Mean-Field Phase Transitions and Correlation Function for Gibbs Random Fields." *J. Math. Imag. Vision.*
- Elfadel, I.M., and R.W. Picard. "Gibbs Random Fields, Co-Occurrences, and Texture Modeling." *IEEE Trans. Pattern Anal. Mach. Intell.*
- Feder, M., E. Weinstein, and A.V. Oppenheim. "Multi-channel Signal Separation by Decorrelation." *IEEE Trans. Signal Process.*
- Foxnian, E.B., P.L. McEuen, U. Meirav, N.S. Wingreen, Y. Meir, P.A. Belk, N.R. Belk, and M.A. Kastner. "The Effects of Quantum Levels on Transport Through a Coulomb Island." *Phys. Rev. Lett.*
- Freeman, D.M., D.H. Hendrix, D. Shah, L.F. Fan, and T.F. Weiss. "Effect of Lymph Composition on an in vitro Preparation of the Alligator Lizard Cochlea." *Hear. Res.*
- Ghosh, A., S. Devadas, and A.R. Newton. "Sequential Test Generation and Synthesis for Testability at the Register-Transfer and Logic Levels." *IEEE Trans. Comput.-Aided Des.*
- Hall, K.L., G. Lenz, E.P. Ippen, U. Koren, and G. Raybon. "Carrier Heating and Spectral Hole Burning in Strained-Layer Quantum Well Laser Amplifiers at 1.5 μm ." *Appl. Phys. Lett.*
- Haus, H.A. "Additive Pulse Modelocking and Kerr Lens Modelocking." *Ultrafast Phenomena VIII.*
- Ho, E., C.A. Coronado, and L.A. Kolodziejski. "Elimination of Surface Site Blockage due to Ethyl Species in MOMBE of ZnSe." *J. Electron. Mat.*
- Holmberg, E., R. Hillman, J. Perkell, and C. Gress. "Relationships Between SPL and Aerodynamic and Acoustic Measures of Voice Production: Inter- and Intra-speaker Variation." *J. Speech Hear. Res.*
- Hultgren, C.T., D.J. Dougherty, and E.P. Ippen. "Above- and Below-band Femtosecond Nonlinearities in Active AlGaAs Waveguides." *Appl. Phys. Lett.*
- Ippen, E.P. "Modelocking, Stabilizing, and Starting Ultrashort Pulse Lasers." *Ultrafast Phenomena VIII.*
- Joffe, M.A., W. Ketterle, A. Martin, and D.E. Pritchard. "Transverse Cooling and Deflection of an Atomic Beam Inside a Zeeman Slower." *J. Opt. Soc. Am. B.*
- Joneckis, L.G., and J.H. Shapiro. "Quantum Propagation in a Kerr Medium: Lossless, Dispersionless Fiber." *J. Opt. Soc. Am. B.*
- Ketterle, W., K.B. Davis, M.A. Joffe, A. Martin, and D.E. Pritchard. "High Densities of Cold Atoms in a Dark Spontaneous-force Optical Trap." *Phys. Rev. Lett.*
- Lam, C-W., D.M. Sheen, S.M. Ali, and D.E. Oates. "Modeling the Nonlinearity of Superconducting Strip Transmission Lines." *IEEE Trans. Appl. Superconduct.*

- Lau, S.D., J.P. Donnelly, C.A. Wang, and R.H. Rediker. "Integrated AlGaAs Waveguide Components for Optical Phase Difference Measurements and Correction." *IEEE J. Quantum Electron.*
- LaMotte, R.H., M.A. Srinivasan, and A. Klusch-Petersen. "Tactile Discrimination and Identification of the Shapes and Orientations of Ellipsoidal Objects." *Soc. Neurosci. Abstr.*
- Lee, D., and N.C. Wong. "High-Performance Tunable Optical Parametric Oscillator." *SPIE Proc.*
- Li, Y.L., D.P. Pullman, J.J. Yang, A.A. Tsekouras, D.B. Gosalvez, K.B. Laughlin, M.T. Schulberg, D.J. Gladstone, M. McGonigal, and S.T. Ceyer. "Observation of a New Mechanism for Dissociative Chemisorption: F Atom Abstraction on Si(100)." *Phys. Rev. Lett.*
- McCue, M.P., and J.J. Guinan, Jr. "Acoustic Responses from Primary Afferent Neurons of the Mammalian Sacculus." *Abstr. Assoc. Res. Otolaryngol.*
- Meir, Y., N. Wingreen, and P.A. Lee. "Low Temperature Transport through a Quantum Dot: The Anderson Model out of Equilibrium." *Phys. Rev. Lett.*
- Migliuolo, S. "Ion Temperature Gradient Modes and Impurities in Toroidal Shaped Plasmas." *Nucl. Fusion.*
- Nabors, K., S. Kim, and J. White. "Fast Capacitance Extraction of General Three-Dimensional Structures." *IEEE Trans. Microwave Theory Tech.*
- Netz, R.R., and A.N. Berker. "Renormalization-Group Theory of an Internal Critical Endpoint Structure: The Blume-Emery-Griffiths Model with Biquadratic Repulsion." *Phys. Rev. B.*
- Perkell, J.S., M.L. Matthies, M.A. Svirsky, and M.I. Jordan. "Trading Relations Between Tongue-body Raising and Lip Rounding in Production of the Vowel /u/: A Pilot Motor Equivalence Study." *J. Acoust. Soc. Am.*
- Picard, P.W., and I.M. Elfadel. "On the Structure of Aura and Co-Occurrence Matrices for the Gibbs Texture Model." *J. Math. Imag. Vision.*
- Posen, M.P., C.M. Reed, and L.D. Braida. "The Intelligibility of Frequency-Lowered Speech Produced by a Channel Vocoder." *J. Rehabil. Res. Dev.*
- Preisig, J.C. "Adaptive Matched Field Processing in an Uncertain Propagation Environment Part I: Background and Processor Formulation." *IEEE Trans. Signal Process.*
- Sarpeshkar, R., J.L. Wyatt, N.C. Lu, P.D. Gerber. "Analysis of Mismatch Sensitivity in a Simultaneously Latched CMOS Sense Amplifier." *IEEE Trans. Circuits Syst.*
- Shapiro, J.H. "On the Performance of Optical Phase Shift Keying with Preamplify-Feedforward-Homodyne Reception." *IEEE Photon. Technol. Lett.*
- Shinn-Cunningham, B.G., P.M. Zurek, and N.I. Durlach. "Adjustment and Discrimination Measurements of the Precedence Effect." *J. Acoust. Soc. Am.*
- Silveira, L.M., J.K. White, H. Neto, and L. Vidigal. "On Exponential Fitting for Circuit Simulation." *IEEE Trans. Comput.-Aided Des.*
- Smith, H.I., and M.L. Schattenburg. "X-ray Lithography, from 500 to 30 nm: X-ray Nanolithography." *IBM J. Res. Dev.*
- Stanton, C.J., and D.W. Bailey. "Coulomb Enhancement of the Above-band Edge Pump-continuum Probe Nonlinear Absorption." *Phys. Rev. B.*
- Stevens, K.N. "Models for Production and Acoustics of Stop Consonants." *Speech Commun.*
- Sun, C.K., H.K. Choi, C.A. Wang, and J.G. Fujimoto. "Studies of Carrier Heating in InGaAs/AlGaAs Strained-Layer Quantum-Well Diode Lasers Using a Multiple Wavelength Pump Probe Technique." *Appl. Phys. Lett.*
- Szafer, A., and B.L. Altshuler. "Universal Correlation in the Spectra of Chaotic Systems with an Aharonon-Bohm Flux." *Phys. Rev. Lett.*
- Tamura, K., H.A. Haus, and E.P. Ippen. "Self-starting Additive Pulse Modelocked Erbium Fiber Ring Laser." *Electron. Lett.*
- Umminger, C.B., and C.G. Sodini. "Switched Capacitor Networks for Focal Plane Image Processing Systems." *IEEE Trans. Circuits Syst. Video Technol.*

van der Zant, H.S.J., E.H. Visscher, D.R. Curd, T.P. Orlando, and K.A. Delin. "Vortex Dynamics in One-dimensional Parallel Arrays of Underdamped Josephson Junctions." *IEEE Trans. Appl. Superconduct.*

Vignaud, D., C.R. Musil, S. Etchin, D.A. Antoniadis, and J. Melngailis. "Lateral Straggle of Si and Be Focused-Ion-Beam Implanted in GaAs." *J. Vac. Sci. Technol.*

Wornell, G.W. "Wavelet-Based Representations for the $1/f$ Family of Fractal Processes." *Proceedings of the IEEE Special Section on Applied Fractals in Electrical Engineering*.

A.3 Books/Chapters in Books

Bagwell, P.F., A. Kumar, and R. Lake. "Scattering and Quantum Localization of Electrons in a Waveguide by Static and Time-Varying Potentials." In *Quantum Effect Physics, Electronics and Applications*, 2: 45. Eds. I.T. Ikoma and H.I. Smith. Philadelphia: Institute of Physics Publishing, 1992.

Berker, A.N., R.G. Caflisch, and M. Kardar. "Statistical Mechanics of Phase Transitions with a Hierarchy of Structures." In *Hierarchically Structured Materials*. Ed. I.A. Aksay. Pittsburgh, Pennsylvania: Materials Research Society, 1992.

Borgeaud, M., J.A. Kong, R.T. Shin, and S.V. Nghiem. "Theoretical Models for Polarimetric Microwave Remote Sensing of Earth Terrain." In *Direct and Inverse Methods in Radar Polarimetry*, Part 2: 1139-1190. Ed. W-M. Boerner. Dordrecht, the Netherlands: Kluwer Academic Publishers, 1992.

Chow, C.C., A. Bers, and A.K. Ram. "The Three Wave Interaction and Spatiotemporal Chaos." In *Physics of Space Plasmas (1991), SPI Conference Proceedings and Reprint Series*, No. 11: 179-195. Eds. T. Chang, G.B. Crew, and J.R. Jasperse. Cambridge, Massachusetts: Scientific Publishers, 1992.

Chow, C.C., A.K. Ram, and A. Bers. "Spatiotemporal Chaos in the Nonlinear Three Wave Interaction." In *Research Trends in Physics: Chaotic Dynamics and Transport in Fluids and Plasmas*. Eds. I. Prigogine et al. New York: American Institute of Physics. Forthcoming.

Covell, M.M., C.S. Myers, and A.V. Oppenheim. "Computer-Aided Algorithm Design and Rearrangement." In *Symbolic and Knowledge-Based Signal Processing*. Eds. A.V. Oppenheim and S.H. Nawab. Englewood Cliffs, New Jersey: Prentice-Hall, 1992.

Delgutte, B., and P. Cariani. "Coding of the Pitch of Harmonic and Inharmonic Complex Tones in the Interspike Intervals of Auditory-nerve Fibers." In *Audition, Speech, and Language*, pp. 37-45. Ed. M.E.H. Schouten. Berlin: Mouton-de-Gruyter, 1992.

Delin, K.A., and T.P. Orlando. "Superconductivity." In *The Electrical Engineering Handbook*. Ed. R.C. Dorf. Boca Raton, Florida: CRC Press. Forthcoming.

Ehrlich, D.J., R.R. Kunz, M.A. Hartney, M.W. Horn, and J. Melngailis. "New Photoresist Processes at UV Wavelengths Less Than 200 nm." In *Irradiation of Polymeric Materials*, p. 527. Eds. Reichmann, O'Donnel, and Frank. ACS Symposium Series, Vol. 527. Forthcoming.

Fujimoto, J.G. "Femtosecond Techniques for the Characterization of Nonlinear and Linear Properties of Waveguide Devices and Studies of All Optical Switching." In *Waveguide Optoelectronics*, pp. 327-360. Eds. J.H. March and R.M. DeLaRue. Dordrecht, the Netherlands: Kluwer Academic Publishers, 1992.

Haus, H.A. "Nonlinear Optics." In *Waveguide Optoelectronics*. Ed. J.H. Marsh and R.M. DeLaRue. Dordrecht, the Netherlands: Kluwer Academic Publishers, 1992.

Huang, C.B. "Modeling Human Vowel Identification Using Aspects of Formant Trajectory and Context." In *Speech Perception, Production and Linguistic Structure*, pp. 43-61. Eds. T. Tohkura, E. Vatikiotis-Bateson, and Y. Sagisaka. Tokyo: Ohmsha, 1992.

Ismail, K., T. Ikoma, and H.I. Smith, eds. *Quantum Effect Physics, Electronics and Applications*. Institute of Physics Conference Series No. 127. Philadelphia: Institute of Physics Publishing, 1992.

Kastner, M.A., E.B. Foxman, P.L. McEuen, U. Meirav, A. Kumar, and S.J. Wind. "Transport Spectroscopy of a Coulomb Island." In *Nanostructures and Mesoscopic Systems*. Eds. W.P. Kirk and M.A. Reed. San Diego, California: Academic Press, 1992.

- Netz, R.R. "Microscopic Theory of the Ripple Phase." In *The Structure and Conformation of Amphiphilic Membranes*. Eds. R. Lipowsky, D. Richter, and K. Kremer. Berlin: Springer-Verlag, 1992.
- Netz, R.R., and A.N. Berker. "Microscopic Liquid Crystal Theory of Nematic Reentrance, Smectic C Ordering, and In-Plane Domain Formation." In *Phase Transitions in Liquid Crystals*. Eds. S. Martellucci and A.N. Chester. New York: Plenum Press, 1992.
- Rabe, K.M., and J.D. Joannopoulos. "Ab Initio Statistical Mechanics of Structural Phase Transitions." In *Electronic Phase Transitions*, 3: 135-175. Eds. W. Hanke and Y.V. Kopayev. Amsterdam, the Netherlands: Elsevier Science Publishers, 1992.
- Reed, C.M., L.A. Delhorne, and N.I. Durlach. "Results Obtained with Tactaid II and Tactaid VII." In *Proceedings of the Second International Conference on Tactile Aids, Hearing Aids, and Cochlear Implants*. Eds. A. Risberg and K-E. Spens. Stockholm, Sweden: Royal Institute of Technology. Forthcoming.
- Reed, C.M., N.I. Durlach, and L.A. Delhorne. "Historical Overview of Tactile Aid Research." In *Proceedings of the Second International Conference on Tactile Aids, Hearing Aids, and Cochlear Implants*. Eds. A. Risberg and K-E. Spens. Stockholm, Sweden: Royal Institute of Technology. Forthcoming.
- Shattuck-Hufnagel, S. "Slips of the Tongue." In *Encyclopedia of Language and Linguistics*. Eds. R.E. Asher and J.M.Y. Simpson. Oxford: Pergamon Press. Forthcoming.
- Smith, H.I., and M.L. Schattenburg. "Lithography for Manufacturing at 0.25 Micrometer and Below." In *Crucial Issues in Semiconductor Materials and Processing Technologies* 222: 153. Eds. S. Coffa, F. Priolo, E. Rimini, and J.M. Poate. NATO ASI Series E, 1992.
- Srinivasan, M.A. "Sections on Haptic Perception and Haptic Interfaces." In *Research Directions in Virtual Environments: Report of an NSF Invitational Workshop* 26(3): 153-177. Ed. G. Bishop et al. Computer Graphics, 1992.
- Srinivasan, M.A., and J.K. Salisbury. "Sections on Haptics." In *Virtual Environment Technology for Training*. BBN Report No. 7661, The Virtual Environment and Teleoperator Research Consortium (VETREC) affiliated with MIT, 1992.
- Stevens, K.N. "Models of Speech Production." In *Handbook of Acoustics*. Ed. M. Crocker. New York: Wiley. Forthcoming.
- Uchanski, R.M., K.M. Millier, C.M. Reed, and L.D. Braida. "Effects of Token Variability on Vowel Identification." In *The Processing of Speech: From the Auditory Periphery to Word Recognition*. Eds. V.J. vanHeuven and L.C.W. Pols. Berlin: Mouton de Gruyter. Forthcoming.
- Zurek, P.M. "Binaural Advantages and Directional Effects in Speech Intelligibility." In *Acoustical Factors Affecting Hearing Aid Performance II*. Eds. G.A. Studebaker and I. Hochberg. Boston: Allyn and Bacon, 1992.

A.4 RLE Publications

RLE publications may be obtained by writing the Communications Office, Building 36-412, Research Laboratory of Electronics, Massachusetts Institute of Technology, Cambridge, Massachusetts 02139-4307, at the listed cost.

Prepayment is required. Please include a check in U.S. dollars payable to MIT RLE and allow six to eight weeks for surface mail. For foreign airmail, include an additional \$4.00 for each report ordered.

RLE PTP Reports are available from the office of Professor Bruno Coppi, Building 26-215.

RLE 45th Anniversary Brochure. MIT, 1991. 72 pp. \$6.50.

RLE currents 5(2): (1992). Topic: Chipping Away at VLSI Computer-Aided Design. 24 pp. No charge.

RLE currents 6(1): (1992). Topic: Discovering the Universal Importance of Plasmas at RLE. 24 pp. No charge.

RLE Progress Report No. 134: January - December 1991. MIT, 1992. 368 pp. No charge.

RLE Speech Communication Group Working Papers. Vol. 8. MIT, 1992. 154 pp. No charge.

Alkhairy, A. *Optimal Product and Manufacturing Process Selection - Issues of Formulation and Methods for Parameter Design*. RLE TR-572. MIT, 1992. \$15.00.

- Alwan, A.A.H. *Modeling Speech Perception in Noise: The Stop Consonants as a Case Study*. RLE TR-569. MIT, 1992. \$16.00.
- Basu, B., and B. Coppi. *Change of Confinement Properties and Transition from Absolute to Non-Normal Mode Microinstabilities*. RLE PTP Report 92/01. MIT, 1992.
- Coppi, B. *Origin of Radiation Emission Induced by Fusion Reaction Products*. RLE PTP Report 92/10. MIT, 1992.
- Coppi, B. *Perceptions of Science*. RLE PTP Report 92/13. MIT, 1992.
- Coppi, B. *Valori Dell'Universita*. RLE PTP Report 92/14. MIT, 1992.
- Coppi, B., and F. Pegoraro. *Energy and Current Transport: Symmetry Breaking and Degradation*. RLE PTP Report 92/03. MIT, 1992.
- Coppi, B., and P. Detragiache. *Mesoscopic Plasma Modes Producing Magnetic Reconnection*. RLE PTP Report 92/9. MIT, 1992.
- Coppi, B., M. Nassi, and the Ignitor Construction Group. *Characteristics of the Ignitor ULT Experiment*. RLE PTP Report 92/8. MIT, 1992.
- Cuomo, K.M., and A.V. Oppenheim. *Synchronized Chaotic Circuits and Systems for Communications*. RLE TR-575. MIT, 1992. \$11.00.
- Cuomo, K.M., A.V. Oppenheim, and S.H. Isabelle. *Spread Spectrum Modulation and Signal Masking Using Synchronized Chaotic Systems*. RLE TR-570. MIT, 1992. \$10.00.
- Lumsdaine, A. *Theoretical and Practical Aspects of Parallel Numerical Algorithms for Initial Value Problems, with Applications*. RLE TR-574. MIT, 1992. \$17.00.
- Migliuolo, S. *Theory of Resistive and Ideal Internal Kinks*. RLE TR-568. MIT, 1992. \$15.00.
- Preisig, J.C. *Adaptive Matched Field Processing in an Uncertain Propagation Environment*. RLE TR-567. MIT, 1992. \$17.00.
- Richard, M.D. *Probabilistic State Estimation with Discrete-Time Chaotic Systems*. RLE TR-571. MIT, 1992. \$12.00.
- Weinstein, E., M. Feder, and A.V. Oppenheim. *Multi-Channel Signal Separation Based on Decorrelation*. RLE TR-573. MIT, 1992. \$9.00.
- Zakharov, L., and B. Rogers. *Fast Nonlinear Exponential $m=1$ Reconnection in Tokamaks*. RLE PTP Report 92/04. MIT, 1992.
- Zakharov, L., B. Rogers, and B. Coppi. *Two-Fluid MHD Description of the Internal Kink Mode in Tokamaks*. RLE PTP Report 92/02. MIT, 1992.

A.5 RLE Theses

Theses are available from the Microreproduction Laboratory, Building 14-0551, Massachusetts Institute of Technology, Cambridge, Massachusetts 02139-4307. Write for individual prices.

Alwan, A.A.H. *Modeling Speech Perception in Noise: The Stop Consonants as a Case Study*. Ph.D. diss., Dept. of Electr. Eng. and Comput. Sci., MIT, 1992.

Armstrong, R.C. *A Formal Approach to Incremental Consistency Maintenance in Multirepresentation VLSI Databases*. Ph.D. diss., Dept. of Electr. Eng. and Comput. Sci., MIT, 1992.

Berberian, J.E. *Measuring the Isotropic Polarizability of the Sodium Ground State*. S.B. thesis, Dept. of Physics, MIT, 1992.

Boyce, K.R. *Improved Single Ion Cyclotron Resonance Mass Spectroscopy*. Ph.D. diss., Dept. of Physics, MIT, 1992.

Braud, J.P. *Whispering-Gallery Mirrors and Laser Cavities for Soft X-rays and the Extreme Ultraviolet*. Ph.D. diss., Dept. of Electr. Eng. and Comput. Sci., MIT, 1992.

Broekaert, T.P.E. *Characterization of InGaAlAs Resonant Tunneling Transistors*. Ph.D. diss., Dept. of Electr. Eng. and Comput. Sci., MIT, 1992.

Chang, P.P. *Measurement of the Rydberg Frequency Using Circular Rydberg States of Atomic Hydrogen*. Ph.D. diss., Dept. of Physics, MIT, 1992.

Colborn, J.A. *Current-Drive and Plasma-Formation Experiments on the Versator-II Tokamak Using Lower-Hybrid and Electron-Cyclotron Waves*. Ph.D. diss., Dept. of Electr. Eng. and Comput. Sci., MIT, 1992.

Conde, M.E. *A 33 GHz Free Electron Laser Amplifier with Reversed Axial Guide Magnetic Field*. Ph.D. diss., Dept. of Physics, MIT, 1992.

- Corcoran, C.J. *Operation of Five Individual Laser Diodes as a Coherent Ensemble by Fiber Coupling into an External Cavity*. Ph.D. diss., Dept. of Physics, MIT, 1992.
- Dana, K.J. *Three Dimensional Reconstruction of the Tectorial Membrane: An Image Processing Method using Nomarski Differential Interference Contrast Microscopy*. S.M. thesis, Dept. of Electr. Eng. and Comput. Sci., MIT, 1992.
- Eshghi, K. *A System Demonstration of VLSI Early Vision Processors*. S.M. thesis, Dept. of Electr. Eng. and Comput. Sci., MIT, 1992.
- Eswein, G.W. *Broadband Impedance Matching Networks for Bandwidth Enhancement of Microstrip Radiators*. S.M. thesis, Dept. of Electr. Eng. and Comput. Sci., MIT, 1992.
- Garcia, E.A. *Fabrication of All-Nb SIS Tunnel Junctions for Submillimeter-wave Detectors*. S.M. thesis., Dept. of Electr. Eng. and Comput. Sci., MIT, 1992.
- Green, Jr., T.J. *Three-Dimensional Object Recognition Using Laser Radar*. Ph.D. diss., Dept. of Electr. Eng. and Comput. Sci., MIT, 1992.
- Hakkarainen, J.M. *A Real-Time Stereo Vision System in CCD/CMOS Technology*. Ph.D. diss., Dept. of Electr. Eng. and Comput. Sci., MIT, 1992.
- Han, Hsi Chi *Electromagnetic Wave Phenomena in Inhomogeneous and Anisotropic Media*. Ph.D. diss., Dept. of Electr. Eng. and Comput. Sci., MIT, 1992.
- Heytens, M.L. *The Design and Implementation of a Parallel Persistent Object System*. Ph.D. diss., Dept. of Electr. Eng. and Comput. Sci., MIT, 1992.
- Hon, S. *Noise Measurements of Modelocked Laser Pulses*. S.B. thesis, Dept. of Electr. Eng. and Comput. Sci., MIT, 1992.
- Huxley, J.M. *Ultrashort Pulse Generation and Applications in Optical Fibers*. Ph.D. diss., Dept. of Electr. Eng. and Comput. Sci., MIT, 1992.
- Keast, C.L. *An Integrated Image Acquisition, Smoothing and Segmentation Focal Plane Processor*. Ph.D. diss., Dept. of Electr. Eng. and Comput. Sci., MIT, 1992.
- Khatri, F.I. *Numerical Studies of Additive Pulse Mode-locked Laser with Empty Cavity*. S.M. thesis, Dept. of Electr. Eng. and Comput. Sci., MIT, 1992.
- Kucera, J.T. *Thermally Activated Dissipation in Superconducting Thin Films of Bi-Sr-Ca-Cu-Oxide*. Ph.D. diss., Dept. of Electr. Eng. and Comput. Sci., MIT, 1992.
- Lau, S.D. *Optical Phase Difference Measurement and Correction Using AlGaAs Guided-Wave Components*. Ph.D. diss., Dept. of Electr. Eng. and Comput. Sci., MIT, 1992.
- Lezec, H.J. *Tunable-Frequency Gunn Diodes Fabricated by Focused Ion-Beam Implantation*. Ph.D. diss., Dept. of Electr. Eng. and Comput. Sci., MIT, 1992.
- Liao, S. Y-H. *Automatic Generation and Verification of Sufficient Correctness Properties of Synchronous Array Processors*. S.M. thesis, Dept. of Electr. Eng. and Comput. Sci., MIT, 1992.
- Lumsdaine, A. *Theoretical and Practical Aspects of Parallel Numerical Algorithms for Initial Value Problems, with Applications*. Ph.D. diss., Dept. of Electr. Eng. and Comput. Sci., MIT, 1992.
- Martin, G.R. *Studies of Real-Time Multiband Adaptive Gain Hearing Aids*. S.M. thesis, Dept. of Electr. Eng. and Comput. Sci., MIT, 1992.
- Modiano, A.M. *An Aligner for X-ray Nanolithography*. Ph.D. diss., Dept. of Electr. Eng. and Comput. Sci., MIT, 1992.
- Narula, A. *Error Concealment Techniques for an All-Digital HDTV System*. S.M. thesis, Dept. of Electr. Eng. and Comput. Sci., MIT, 1992.
- Olster, D.B. *Refining the Process of Achromatic Holographic Lithography*. S.B. thesis, Dept. of Electr. Eng. and Comput. Sci., MIT, 1992.
- Osgood, Gene. *Evenly Sampling a Rotation Space*. S.B. thesis, Dept. of Electr. Eng. and Comput. Sci., MIT, 1992.
- Paine, S.N. *High Precision Millimeter-Wave Spectroscopy of Atomic Hydrogen*. Ph.D. diss., Dept. of Physics, MIT, 1992.
- Pheiffer, B.K. *Integrated AlGaAs Reduced-Confinement Tapered Waveguide Antennas*. S.M. thesis, Dept. of Electr. Eng. and Comput. Sci., MIT, 1992.

Pickelsimer, L.A. *A Structured Design Methodology for Speed-Optimized True Single-Phase-Clock Dynamic CMOS*. S.M. thesis, Dept. of Electr. Eng. and Comput. Sci., MIT, 1992.

Preisig, J.C. *Adaptive Matched Field Processing in an Uncertain Propagation Environment*. Ph.D. diss., Dept. of Electr. Eng. and Comput. Sci., MIT, 1992.

Ronan, D.E. *Effects of Token Variability on Speech Intelligibility for Vowel Sounds*. S.B. thesis, Dept. of Electr. Eng. and Comput. Sci., MIT, 1992.

Shepard, S.R. *Phase of the Quantum Harmonic Oscillator*. Ph.D. diss., Dept. of Electr. Eng. and Comput. Sci., MIT, 1992.

Stadler, R.W. *Optimally Directive Microphones for Hearing*. S.M. thesis, Dept. of Electr. Eng. and Comput. Sci., MIT, 1992.

Van Aelten, F. *Automatic Procedures for the Behavioral Verification of Digital Designs*. Ph.D. diss., Dept. of Electr. Eng. and Comput. Sci., MIT, 1992.

Xia, J.J. *Electromagnetic Inverse Methods and Applications for Inhomogeneous Media Probing and Synthesis*. Ph.D. diss., Dept. of Electr. Eng. and Comput. Sci., MIT, 1992.

A.6 Miscellaneous

Bers, A., and A.K. Ram. *Lower Hybrid and Fast Wave Current Drive-Status of Theory*. Plasma Fusion Center Report PFC/JA-92-3. MIT, 1992.

Boning, D.S., and M.B. McIlrath. *Guide to the Process Flow Representation*. CIDM Memo 92-1. MIT, 1992.

Burke, B.F. "The Search for Other Planetary Systems." Talk presented at the Royal Astronomical Society, London, England, December 1992.

Burke, B.F. "Gravitational Lenses." Talk presented at Arecibo Radio Observatory, Puerto Rico, March 1992.

Burke, B.F. "Gravitational Lenses in the Ultraviolet." Talk presented at University College, London, England, June 1992.

Burke, B.F. "The TOPS Program." Talk presented at the California Institute of Technology Summer School, Pasadena, California, August 1992.

Burke, B.F. "Searching for Exoplanets." Talk presented at the University of Massachusetts, Amherst, Massachusetts, April 1992, and the University of Manchester, Manchester, England, November 1992.

Chow, C.C., and A. Bers. *Chaotic Stimulated Brillouin Scattering in a Finite Length Medium*. Plasma Fusion Center Report PFC/JA-92-36. MIT, 1992.

Chow, C.C., A. Bers, and A.K. Ram. *The Three Wave Interaction and Spatiotemporal Chaos*. Plasma Fusion Center Report PFC/JA-92-1. MIT, 1992.

Chow, C.C., A. Bers, and A.K. Ram. *Spatiotemporal Chaos in the Nonlinear Three Wave Interaction*. Plasma Fusion Center Report PFC/JA-92-2. MIT, 1992.

Chow, C.C., A. Bers, and A.K. Ram. *Spatiotemporal Chaos in Three Wave Interaction*. Plasma Fusion Center Report PFC/JA-92-27. MIT, 1992.

Fischer, G. *Beginner's Guide to CAFE*. CIDM Memo 92-2. MIT, 1992.

Fischer, G. *Beginner's Guide to Fabrication Using CAFE*. CIDM Memo 92-3. MIT, 1992.

Fischer, G. *Sample PFR Encodings*. CIDM Memo 92-4. MIT, 1992.

Fischer, G. *Creating Manual Pages for CAFE*. CIDM Memo 92-8. MIT, 1992.

Friedland, L., and A. Bers. *Hermitian Description of Interacting Inhomogeneous Electron Beams*. Plasma Fusion Center Report PFC/JA-92-15. MIT, 1992.

Ram, A.K., A. Bers, V. Fuchs, R.W. Harvey, and M.G. McCoy. *Effects of Fast Alfvén Waves in Lower-Hybrid Current Drive*. Plasma Fusion Center Report PFC/JA-92-33. MIT, 1992.

Troxel, D.E. *Extract of Schema*. CIDM Memo 92-5. MIT, 1992.

Troxel, D.E. *Iterators and Predicates-Optimizing Data Base Accesses by Filtering at Low Levels*. CIDM Memo 92-6. MIT, 1992.

Troxel, D.E. *Microsystems Factory Representation (MFR)*. CIDM Memo 92-7. MIT, 1992.

Appendix B. Current RLE Personnel

Director: Jonathan Allen

Associate Director: Daniel Kleppner

Professors

Jonathan Allen
Boris Altshuler
Dimitri A. Antoniadis
Arthur B. Baggeroer
George Bekefi
A. Nihat Berker
Abraham Bers
Robert J. Birgeneau
Amar G. Bose
Louis D. Braid
Bernard E. Burke
Sylvia T. Ceyer
Bruno Coppi
Shaoul Ezekiel
Clifton G. Fonstad, Jr.

Lawrence S. Frishkopf
Hermann A. Haus
Albert Hill¹
Erich P. Ippen
John D. Joannopoulos
Marc A. Kastner
Nelson Y.-S. Kiang
John G. King
Daniel Kleppner
Jin A. Kong
Patrick A. Lee
Jerome Y. Lettvin¹
Jae S. Lim
Alan V. Oppenheim
William T. Peake

Miklos Porkolab
David E. Pritchard
William F. Schreiber¹
Campbell L. Searle
Jeffrey H. Shapiro
William M. Siebert
Henry I. Smith
David H. Staelin
Kenneth N. Stevens
Julius A. Stratton¹
Donald E. Troxel
Thomas F. Weiss
Jerome B. Wiesner¹
John L. Wyatt, Jr.
Henry J. Zimmermann¹

Associate Professors

Jesús A. del Alamo
Srinivas Devadas
James G. Fujimoto

Peter L. Hagelstein
Leslie A. Kolodziejski
Simon G.J. Mochrie

Jacob K. White
Jonathan S. Wurtele

Assistant Professors

Raymond C. Ashoori
Jacqueline N. Hewitt

Qing Hu

Gregory W. Wornell

Senior Research Scientists

Nathaniel I. Durlach
John Melngailis

Joseph S. Perkell

Robert H. Rediker

Principal Research Scientists

Donald K. Eddington
John J. Guinan, Jr.
William M. Rabinowitz

Charlotte M. Reed
Philip W. Rosenkranz
Kenneth Salisbury

Mandayam A. Srinivasan
David Zeltzer
Patrick M. Zurek

¹ Professor Emeritus.

Research Scientists and Research Specialists

Giovanni Aliberti
John W. Barrett
James M. Carter
Bertrand Delgutte
Lorraine A. Delhorne
Andy B. Dobrzeniecki
Sergey Etchin
Gregory T. Fischer
David W. Foss

Dennis M. Freeman
Seth M. Hall
Thomas J. Lohman
Joyce Manzella
Ivan Mastovsky
Melanie L. Matthies
Michael B. McIlrath
Stefano Migliuolo
Euclid E. Moon

Abhay K. Ram
Dennis D. Rathman
John J. Rosowski
Stefanie Shattuck-Hufnagel
Linda E. Sugiyama
Mario A. Svirsky
Hong Z. Tan
Ngai Chuen Wong
Y. Eric Yang

Administrative Staff

Joseph F. Connolly
Donald F. Duffy
Virginia R. Lauricella

Barbara J. Passero
John S. Peck
Gerrard F. Power

William H. Smith
Vicky-Lynn Taylor

Support and Technical Staff

Mary C. Aldridge
Janice L. Balzer
Felicia G. Brady
Manuel Cabral, Jr.
Susan E. Chafe
Donald A. Clements
John F. Cook
Carol A. Costa
Ann K. Dix
Francis M. Doughty
Laura B. Doughty
Dorothy A. Fleischer
Kerry L. Gafney

Donna L. Gale
Mary S. Greene
Peter C. Guid
Maureen C. Howard
Wendy E. Hunter
Barbara A. King
Cynthia Y. Kopf
Kit-Wah F. Lai
Cindy LeBlanc
Catherine Lorusso
Eleanora M. Luongo
Deborah S. Manning
Rita C. McKinnon

Gina L.B. Milton
Mark K. Mondol
Donald K. North
Robert H. Priest
Bruce A. Russell
Maxine P. Samuels
Sally C. Santiago
Robert D. Sisson
Clare F. Smith
Mabayoje Tuyo
Arlene E. Wint
Sharon J. Worley
Mary J. Ziegler

Postdoctoral Fellows and Associates

Tomas A. Arias
Robert C. Armstrong
Alice M. Berglund
Peter A. Cariani
Ibrahim M. Elfadel
Susan L. Goldman
Joseph A. Izatt

Wolfgang Ketterle
Pauline M. McMahon
Robert D. Meade
Gale S. Petrich
David P. Pullman
Sunil Puria
Christine M. Rankovic

Barrett Rogers
M. Selim Shahriar
Annie H. Takeuchi
Xin Xu
Xinglong Yan
Yi Yuan

Research Assistants

Charles C. Abnet
Daniel P. Aalberts
Mazher M. Alidina
Christopher B. Anderson
John G. Apostolopoulos
Mark A. Armstrong
Neer R. Asherie

David B. Askey
William W. Au
Walter A. Aviles
Ian M. Avruch
Sandeep Bahl
Donald G. Baltus
Deborah J. Becker

Paul A. Belk
Keren Bergman
Vishal L. Bhagwati
Igor P. Bilinsky
Luc Boivin
Michael P. Bradley
Louis R. Brothers

Martin Burkhardt
 Carlos R. Cabrera
 Xuejun Cai
 Claudio L. Cesar
 Michael S. Chapman
 Grace H. Chen
 Jerry C. Chen
 Jyh-Shing Chen
 Tak K. Cheng
 Tony Chiang
 Dmitri Chklovskii
 Kyeongjae Cho
 Woo-Young Choi
 Mike T. Chou
 Jeffrey A. Colborn
 Samuel R. Conner
 Christopher A. Coronado
 Michael W. Courtney
 Pierre Coutu
 Jay H. Damask
 Kiran B. Dandekar
 Charles Q. Davis
 Kendall Davis
 Anthony D. Della Ratta
 Frank DiFilippo
 Christopher R. Doerr
 David J. Dougherty
 Paul Duchnowski
 Scott B. Dynes
 Christopher R. Ekstrom
 John D. Ellithorpe
 Darin R. Ernst
 Hong T. Ewe
 Alexis Falicov
 Paul W. Fieguth
 Siegfried B. Fleischer
 Andre B. Fletcher
 Ethan B. Foxman
 Joseph A. Frisbie
 Eric M. Fuchs
 Alex W. Fung
 Svetlana Gaffron
 Edouard A. Garcia
 Boris Golubovic
 James G. Goodberlet
 Mark R. Griffith
 Andrew E. Grumet
 Nitin Gupta

Rakesh Gupta
 Troy D. Hammond
 Scott D. Hector
 Michael R. Hee
 Lori K. Herold
 Eason Ho
 Jeffrey R. Holley
 William C. Hoston
 Chih-Chien Hsu
 Wen Hu
 David Huang
 Charles T. Hultgren
 Brian R. Jacobson
 Louise Jandura
 Hong Jiao
 Michael A. Joffe
 Joel T. Johnson
 Mark A. Johnson
 Mattan Kamon
 Charles A. Katz
 Sumanth Kaushik
 Farzana I. Khatri
 Songmin Kim
 Hong-Kwang J. Kuo
 Bobby Y. Lai
 Cheung-Wei Lam
 Warren M. Lam
 Dicky Lee
 Laurence H. Lee
 Zachary K. Lee
 Gadi Lenz
 Stan Y. Liao
 Sharlene A. Liu
 Kan Lu
 Robert I. Lutwak
 Ilya Lyubomirsky
 Kamal M. Malek
 Paul S. Martin
 Noel S. Massey
 Alexander Matusis
 Joseph A. Maxwell
 Marc O. Mewes
 Peter A. Monta
 Christopher B. Moore
 John D. Moores
 Martin Muendel
 Christian R. Musil
 Keith S. Nabors

Malini V. Narayanan
 Vasant Natarajan
 Julien J. Nicolas
 James M. Njeru
 Lily Y. Pang
 Hanalabos Papadopoulos
 Thomas J. Paul
 Gregory E. Penn
 Michael O. Polley
 Kelly L. Poort
 Matthew H. Power
 Khalid Rahmat
 Malini Ramaswamy
 Monte J. Ramstad
 Mark W. Reichelt
 Michael D. Richard
 Caterina Riconda
 Michael J. Schwartz
 Mark N. Seidel
 Lisa Shatz
 Amelia H. Shen
 Gennady Shvets
 Luis M. Silveira
 Andrew C. Singer
 Jurgen H. Smet
 Stephen P. Smith
 Gideon P. Stein
 Richard E. Stoner
 Ke-Xun Sun
 Lon E. Sunshine
 Kohichi R. Tamura
 Guillermo J. Tearney
 Farzam Toudeh-Fallah
 Morrison Ulman
 Jesus Noel Villaseñor
 Pavel S. Volfbeyn
 Susie J. Wee
 Lorin F. Wilde
 Timothy A. Wilson
 John W. Wissinger
 Vincent V. Wong
 Albert R. Woo
 Rolf A. Wyss
 Julius J. Yang
 Nathan Yang
 Kenneth W. Yee
 Chang D. Yoo
 Kambiz C. Zangi

Teaching Assistants

John R. Buck
 Shiufun Cheung
 Kevin G. Christian

Kyle K. Iwai
 Stephen F. Scherock
 Mohammad A. Tassoudji

Murat E. Veysoglu
 Kathleen E. Wage
 Li-Fang Wang

Graduate Students

Laura E. Adams
 Aaron J. Berg
 Karl K. Berggren
 Philippe Berisset
 Jeffrey K. Bounds
 Stanley W. Brown
 Palmyra E. Catravas
 Hwa-Ping Chang
 Irfan U. Chaudhary
 Marilyn Y. Chen
 Yiu Y. Chu
 Kevin M. Cuomo
 Ali Darwish
 William S. Daughton
 David M. DeCaprio
 Joseph G. Desloge
 Daniel J. DiLorenzo
 Shepard S. Doeleman
 Philip A. Fisher
 Jun Funatsu
 Eric J. Gaidos
 Renato Gatto

David S. Gloss
 Julie E. Greenberg
 Ibrahim A. Hajjahmad
 Katherine L. Hall
 Jody House
 Steven H. Isabelle
 Erik B. Iverson
 Yasuo Kamatani
 Chwen-yuen Ku
 Volkan C. Kubali
 Daniel D. Lee
 Kevin Li
 Peggy Li
 Nicole Love
 Kent H. Lundberg
 Artem Maloratsky
 Michael M. McCue
 Ignacio S. McQuirk
 Mark D. Messier
 Michael C. Moldoveanu
 Ann W. Morgenthaler
 Alex X. Mou

Aradhana Narula
 Lynn E. Nelson
 Janet L. Pan
 Pamela M. Paufler
 Denis J. Peregrym
 Aleksandar Pfajfer
 Joel R. Phillips
 Adam D. Polcyn
 David V. Pynadath
 Todd H. Rider
 Frank L. Ross
 Ante Salcedo
 Jon C. Sandberg
 Steven D. Schultz
 Hugh E. Secker-Walker
 Barbara G. Shinn
 Chin H. Tan
 Ricardo Telichevesky
 Christopher B. Umminger
 Luigi Vacca
 Shawn M. Verbout

Undergraduate Students

Tracy E. Adams
 Daniel A. Alvarez
 Michele M. Bierbaum
 Amy S. Chang
 Beth L. Chen
 Erika Chuang
 Henry E. Chung
 Leanne C. Clarke
 John A. Crouch
 Gail Denesvich
 Laura C. Dilley
 Jonathan C. Doan
 Ilya Entin
 Mauricio A. Escobar
 Darlene J. Ford
 Helena H. Geng
 Rajashi Ghosh
 Andrew C. Goldish
 Daniel I. Goldman
 Matthew K. Gray
 Marnie Harker
 Akikazu Hashimoto
 Todd A. Hay
 David H. Hijirida
 Jason Hintersteiner
 Surendranauth Hiranman

Elliot E. Hui
 Mohammad J. Khan
 Sungtae Kim
 Teresa W. Lau
 Jean Q. Lee
 William K. Lee
 Julie C. Lew
 Huiying Li
 Kuo-Yi Lim
 Michael H. Lim
 Adam P. London
 Henry Y. Lu
 David S. Lum
 Kristine W. Ma
 Robert J. Macke
 Mahbubul A. Majumdar
 Alexander R. Mallin
 Michael L. McComas
 Chad H. Mikkelson
 Rachel E. Molenaar
 Jason T. Mueller
 Philip M. Nadeau
 Lee P. Ng
 Hana Ohkawa
 Dennis O. Ouma
 Charlie C. Pan

Amrit R. Pant
 Sang H. Park
 Jonathan D. Pelly
 Michael T. Pierce
 Vlad Portnoy
 Farhan Rana
 Kenneth N. Ricci
 Brian A. Rubin
 Gaeta H. Sankappanavar
 Anthony R. Scherer
 Jiri Schindler
 Satyen Shah
 Christopher M. Smithhisler
 Abraham D. Stroock
 Jie Sun
 Prasanna B. Tambe
 Bridget E. Tannian
 Stanley H. Thompson
 Ann L. Torres
 Andrew Ugarov
 Monika K. Walczak
 Janet Wang
 Joshua N. Winn
 John J. Wu
 Ross A. Yu

Visiting Scientists

Vladimir Barsukov
Corine A. Bickley
Franco Carpignano
Guang-Sup Cho
Steve Cohn
Paolo Detragiache
Theodore W. Ducas
Anna Esposito
Kaigham J. Gabriel
Artur D. Gouveia-Neto
Rogeve Gulati
Christian V. Hafner
Yie He

James J. Hugunin
Arthur K. Jordan
Hae M. Jung
Stephan Jungling
Franz X. Kärtner
Nobuyoshi Koshida
Jack Kotik
Takahide Matsuoka
Jose C. Monteiro
Phylis Morrison
Thomas B. Mueller
Guilia A. Nassi

Marco Nassi
Hamid Nawab
Kevin O'Neill
Jerome M. Paye
Karen L. Payton
Geoffrey L. Plant
Stanley J. Rosenthal
Makoto Sakamoto
Masataka Shirasaki
Chi-Kuang Sun
George M. Svolos
Yunxian Tong

Research Affiliates

Mitchell R. Balonon-Rosen
John S. Barlow
Herbert J. Bernstein
Giuseppe Bertin
Suzanne Boyce
Frank S. Cardarelli
H. Steven Colburn
Daniel Ehrlich
Carol Y. Espy-Wilson
Ignacio Garcia-Otero
Gad Geiger
Bernard Gold
Richard S. Goldhor
Kenneth W. Grant
Robert D. Hall
Philip R. Hemmer
Robert E. Hillman
Mark A. Hollis

Eva B. Holmberg
Caroline B. Huang
Yoshiko Ito
Joseph A. Jarrell
John D. Kierstead
Lance G. Joneckis
Harlan Lane
Charles P. Lin
Neil A. Macmillan
John I. Makhoul
Sharon Y. Manuel
Bruce R. Musicus
Mark R. Nilsen
Leonard L. Picard
Soon Y. Poh
James C. Preisig
Mara G. Prentiss
Stephen A. Raymond

Joseph F. Rizzo
Jay T. Rubinstein
Steven R. Rueman
Madhav K. Setty
Robert T. Shin
Richard J. Solomon
Elizabeth E. Sperry
Frank J. Stefanov-Wagner
David A. Steffens
Joseph Tierney
Michael J. Tsuk
Kenneth P. Wacks
Ehud Weinstein
David R. Williams
Jane W. Wozniak
Jiqing Xia
Marc Zissman



Professor Srinivas Devadas (Photo by John F. Cook)



Professor Leslie A. Kolodziejski (Photo by Paul J. McGrath)



Mr. Qizheng Gu (Photo by John F. Cook)

Promotions

RLE is pleased to acknowledge that the faculty and staff shown on this page received promotions during 1992.



Dr. John J. Guinan, Jr. (Photo by John F. Cook)



Dr. Melanie L. Matthies (Photo by John F. Cook)

Appendix C. Milestones

C.1 New Faculty and Staff

Dr. Raymond C. Ashoori joined RLE's Quantum-Effect Devices Group as Assistant Professor of Physics in January 1993.

Mr. Joseph F. Connolly was appointed RLE Administrative Officer in October 1992.

Dr. David L. Zeltzer joined RLE's Sensory Communication Group in January 1993.

C.2 Promotions

Dr. Srinivas Devadas was promoted to Associate Professor of Electrical Engineering and Computer Science in July 1992. Dr. Devadas is a member of RLE's Circuits and Systems Group.

Mr. Qizheng Gu was appointed Research Scientist in RLE's Center for Electromagnetic Theory and Applications in February 1992.

Dr. John J. Guinan, Jr., Principal Research Scientist in RLE's Auditory Physiology Group, was appointed Associate Director at the Massachusetts Eye and Ear Infirmary in January 1992.

Dr. Leslie A. Kolodziejski, Karl Van Tassel Career Development Assistant Professor, was promoted to Associate Professor of Electrical Engineering and Computer Science in July 1992.

Dr. Melanie L. Matthies was promoted to Research Scientist in RLE's Speech Communication Group in May 1992.

C.3 Chair Appointments

Dr. Thomas F. Weiss, Professor of Electrical and Bioengineering and faculty member in RLE's Auditory Physiology Group, was appointed Thomas and Gerd Perkins Professor of Electrical Engineering and Computer Science in May 1992.

C.4 Awards and Honors

Dr. Sylvia T. Ceyer, Professor of Chemistry and faculty member in RLE's Surfaces and Interfaces Group, was elected fellow of the American Academy of Arts and Sciences in April 1992.

Dr. Srinivas Devadas, Associate Professor of Electrical Engineering and Computer Science and a member of RLE's Circuits and Systems Group, received a 1992 Young Investigator Award from the National Science Foundation.

Dr. Daniel Kleppner, Associate Director of RLE and Lester Wolfe Professor of Physics, was elected fellow of the Optical Society of America in May 1992. Professor Kleppner is also a faculty member in RLE's Atomic, Molecular, and Optical Physics Group.

Dr. Joseph S. Perkell, Senior Research Scientist in the Speech Communication Group, was elected fellow of the Acoustical Society of America in May 1992.

Dr. William F. Schreiber, Professor Emeritus of Electrical Engineering and Computer Science, was awarded the 1992 Journal Award of the Society of Motion Picture and Television Engineers (SMPTE). This was the fourth time Professor Schreiber received the Journal Award.

Dr. Jerome B. Wiesner, President Emeritus of MIT and Director Emeritus of RLE, received the National Science Board's Vannevar Bush Award in April 1992.

Appendix D. RLE Research Support Index

- 3M Company 26-29
Ampex 263-267
Advanced Television Research Program 263-267
American Broadcasting Corporation 263-267
Analog Devices, Inc. 227-229
AT&T Bell Laboratories 17, 258-259
Bose Corporation 90-94
Consortium for Superconducting Electronics 63-64, 209-210
Defense Advanced Research Projects Agency (DARPA) 7-8, 10-13, 17, 26-33, 47-50, 53-54, 63-66, 112-113, 209-210, 242-245, 247-252, 256-262
Dennis Klatt Memorial Fund 282-289
Digital Equipment Corporation 205-206, 241-242, 282-289
Draper (Charles S.) Laboratory 10-11, 19-23, 26, 72-74, 105-106, 151-153
Federal Bureau of Investigation 240-241
Friedman (F.L.) Chair 171-172
Fujitsu Laboratories 19-23, 73-74
Future Energy Applied Technology, Inc. 100-102
General Instrument 263-267
GTE Laboratories 12
Hertz Foundation 11-14
Houston Advanced Research Center 275-276
IBM Corporation 54-56, 227-229, 238-245
Joint Services Electronics Program (JSEP) 7-10, 19-23, 26-30, 39-48, 50-56, 61-62, 65, 71-72, 75-85, 119-127, 131-140, 155-157, 161-169, 205-206
Kodak Corporation 263-267
Lawrence Livermore National Laboratories 90-94, 181-184
LeBel (C.J.) Foundation 282-288
Lockheed Sanders, Inc. 257-259, 261
Maryland Procurement Office 103-105
Micron 34
MIT Leaders for Manufacturing Program 219-221
MIT Lincoln Laboratory 72, 94-98, 109-110, 218-219
MIT-Woods Hole Oceanographic Institution Joint Program 256-257, 259-260
MOSIS 12-13
Motorola Corporation 263-267
NCIPT 7-8, 10-13, 17
National Aeronautics and Space Administration 65-66, 109-110, 181, 184-186, 189-191, 203-205, 216-219
National Center for Integrated Photonics 74-77
National Institute of Standards and Technology 105-106
National Institutes of Health 85-90, 282-289, 293-306, 309-311, 319-327
National Science Foundation 8-9, 12-17, 26-29, 33-34, 41-44, 47-53, 61, 72-77, 79-85, 110-112, 128-129, 155-163, 175-186, 189, 209, 215-219, 229-242, 260, 262, 282-289
Northeastern University 16
Packard (David and Lucille) Foundation 217-218
Public Broadcasting System 263-267
Rockwell International Corporation 97-98
Semiconductor Research Corporation 33-34
SM Systems and Research, Inc. 218-219
Space Exploration Associates 100-102
Tektronix Corporation 263-267
Texas Instruments, Inc. 14, 19-23
Toshiba Corporation, Ltd. 8-9
TRW Systems 16-17
U.S. Air Force - Electronic Systems Division 145-151
U.S. Air Force - Office of Scientific Research 57-62, 71-72, 75-85, 107, 175-181, 257-262, 306-307
U.S. Army - Corps of Engineers 203-205
U.S. Army - Harry Diamond Laboratories 175-181
U.S. Army Research Office 14-16, 31-34, 50-52, 62-63, 105-106, 114-116, 163-166
U.S. Department of Energy 90-94, 129-130, 175-181, 184-189, 192-199
U.S. Department of Transportation 207
U.S. Navy - Office of Naval Research 34, 73-74, 79-90, 106-107, 148-149, 158-161, 163-169, 175-181, 203-206, 238-245, 247-252, 256-262, 267-268, 307-309, 311-315
Vitesse Semiconductor 11-12

Project Staff and Subject Index

Project Staff and Subject Index

A

Aalberts, Daniel P. 119, 120
 Abernathy, Douglas L. 137
 Abnet, Charles C. 319, 321
 Acioli, Lucio H. 71, 79, 81
 Acoustic Thermometry of Ocean Climate (ATOC) Program 256
 Adams, Laura E. 71
 Adams, Tracy E. 281
 Advanced Microwave Sounding Unit 218, 219
 Advanced Television Research Program 263—267
 Advanced X-ray Astrophysics Facility 65
 Aggarwal, Rajni J. 7, 14
 Air traffic control systems 207
 Alcator C-MOD 192
 Aldridge, Mary C. 71
 Ali, Sami M. 203, 209—212, 227
 Aliberti, Giovanni 255
 Alidina, Mazhar M. 227, 242
 Alkhairy, Ashraf S. 215, 220
 Allen, Jonathan 227—245, 281
 Altshuler, Boris L. 39—40
 Alvarez, Daniel A. 293
 Analog processing
 Wavefront correction 107
 Ananthapadmanabha, Tirupattur V. 281
 Ananthraman, Santosh 293
 Annaswamy, Anuradha 311
 Antoniadis, Dimitri A. 31, 32, 33, 54, 57, 58, 59, 61, 227, 239
 Apostolopoulos, John G. 263, 264
 Arias, Tomas A. 131
 Ariei, Imadiel 39, 45, 131
 Armstrong, Mark A. 31, 33
 Armstrong, Robert C. 227, 229
 Arnold, David V. 203, 206
 Array processing 256
 Articulation index 294
 Asherie, Neer R. 175, 192
 Ashoori, Raymond C. 371
 AT&T Bell Laboratories 269
 Atkins, Robert G. 203, 206
 Atom-beam interferometry 47
 Atomic physics 155—169
 Atoms
 Diffraction of 163
 Structure in magnetic fields 155, 158
 Trapping and cooling 166
 Au, William W. 203
 Aucoin, Richard J. 47, 66

Auditory system 319—327
 Avruch, Ian M. 215, 216

B

Bach, Susan E. 293
 Baggeroer, Arthur B. 255, 256
 Bahl, Sandeep R. 19
 Bai, Kelly S. 227, 242
 Baltus, Donald G. 227, 228
 Balzer, Janice L. 319
 Barrett, John W. 215, 219
 Barsukov, Vladimir M. 281
 Basu, Santanu 71, 90, 93
 Beach, Kerry L. 281
 Becker, Deborah J. 215, 216
 Beckmann, Paul E. 255
 Bekefi, George 175—181
 Belk, Paul A. 41
 Benford, Gregory A. 175
 Berberian, John E. 155, 163
 Berglund, Alice M. 319
 Bergman, Keren 71, 73
 Berisset Philippe 203
 Berker, A. Nihat 119—122
 Berkovits, Richard 39
 Berman, David 203
 Bers, Abraham 175, 181—191
 Bhagwati, Vishal L. 227, 242
 Bhatta, Saurav Dev 255, 256
 Bickley, Corine A. 281
 Bioelectronics 275
 Biomechanics
 Skin 309, 311
 Birgeneau, Robert J. 123—125
 Blum, Kenneth I. 123
 Bock, Robert D. 203, 209
 Boivin, Luc 71, 73
 Boston University 282
 Bounds, Jeffrey K. 71, 73
 Bowring, Kristine M. 39
 Boyce, Kevin R. 155, 161
 Boyce, Suzanne E. 281
 Bradley, Michael P. 155, 161
 Brady, Felicia G. 175
 Braida, Louis D. 293, 303
 Branigan, Philip 331
 Bratakos, Maroula S. 293
 Brothers, L. Reginald 103, 105
 Brothers, Margery E. 203

Buck, John R. 255, 257
 Burke, Bernard F. 215—217
 Burkhardt, Martin 47, 58, 59, 61

C

Cabrera, Carlos R. 215, 219
 Cai, Xuejun 227, 240
 Canizares, Claude R. 65
 Cariani, Peter A. 319, 323
 Carter, James M. 47, 48, 51, 53, 62, 65
 Case Western Reserve University 249
 Catipovic, Josko 257
 Catravas, Palmyra E. 175
 Ceyer, Sylvia T. 7, 127—130, 371
 Chafe, Susan E. 227
 Chakrabati, Upanishad K. 203
 Chalcopyrite 119
 Chang, Amy S. 281
 Chang, Hwa-Ping 281
 Chang, Pin P. 155
 Chaotic systems 257, 258, 260, 261
 Chapman, Michael S. 155, 163
 Chari, Venkatesh R. 281
 Chaudhary, Irfan U. 71, 98
 Chemical beam epitaxy 25
 Chen, Chipping 175
 Chen, Grace H. 215, 217
 Chen, Jyh-Shing 293, 311
 Chen, Marilyn R. 281
 Chen, Shien-Chi 175
 Chenausky, Karen 7, 25, 203
 Cheng, Belinda 293
 Cheng, Tak K. 71, 77
 Cheung, Shiufun 263, 264
 Chiang, Tony P. 31, 33
 Chklovskii, Dimitri 45
 Cho, Guang-Sup 31
 Cho, Kyeongjae 131
 Choi, Woo-Young 7, 8, 9, 62
 Chomsky, Noam A. 331—336
 Chou, Mike T. 47, 59
 Chow, Carson C. 175, 181
 Christian, Kevin G. 215, 221
 Chu, Alex 32
 Chu, Arthur 145
 Chu, Jack 63
 Chu, William 47, 48, 57, 58, 59, 61
 Chung, Henry E. 319, 321
 Chung, James E. 54
 Cobb, M.H. 33
 Coffman, Bridget L. 293

Colburn, H. Steven 304
 Cold fusion 98
 Columbia University 192
 Communications
 See Optical communication
 See Sensory communication
 See Speech communication
 See Telecommunications
 Computer vision 229
 Computer-aided design 240, 247
 Computer-Aided Fabrication Environment (CAFE) 247
 Conde, Manoel E. 175
 Conner, Samuel R. 215, 216
 Connolly, Joseph F. 371
 Coppi, Bruno 175, 192—198
 Corcoran, Christopher J. 103, 106
 Cornell University 164
 National Nanofabrication Facility 164
 Coronado, Christopher A. 25
 Costa, Carol A. 155
 Coulomb blockade 41, 45
 Courtney, Michael W. 155, 158
 Coutu, Pierre 203, 206
 Crouch, John A. 293
 Cudjoe-Flanders, Charmaine A. 7, 19, 25, 203
 Cued speech 299
 Cuomo, Kevin M. 255, 257
 Curd, Derek R. 203
 Custom integrated circuits 227—245
 Computer vision 229
 Computer-aided design 227
 Device simulation 238
 Fault tolerance 242
 Reliability 242
 Vision chip designs 229
 VLSI 229
 Cyclotron resonance 161

D

Dal Pino, Arnaldo 131
 Daley, Sean P. 127, 128, 129
 Dally, William J. 227, 240
 Damask, Jay N. 25, 47, 63, 71, 74
 Dandekar, Kiran B. 293, 309, 313
 Darwish, Ali M. 71, 75
 Davis, Charles Q. 319, 321
 Davis, Kendall B. 155, 166
 Decker, Steven J. 227, 233
 del Alamo, Jesús A. 19—24, 58, 61, 110
 Delgutte, Bertrand 319, 323, 324

Delhorne, Lorraine A. 293, 303, 304, 307
 Delin, K.A. 203
 Della Ratta, Anthony D. 31, 34
 Desloge, Joseph G. 293, 302
 Detragiache, Paolo 175
 Devadas, Srinivas 227, 242—245, 371
 DiFilippo, Frank 155, 161
 Digital signal processing 255—262
 Fractals 259
 Digital video broadcasting 269
 Dix, Ann K. 293
 DNA decoding 275
 DNA sequencing 275
 Doan, Jonathan C. 175
 Doeleman, Sheperd S. 215
 Doerr, Christopher R. 71, 72, 73
 Dolphins
 Communication 221
 Donoghue, John J. 145
 Donovan, Kelley S. 25
 Dougherty, David J. 71, 76
 Doughty, Francis M. 247
 Doughty, Laura B. 175
 Dresselhaus, Mildred S. 77
 Drew, Tracie M. 155, 161
 Dron, Lisa G. 227, 232
 Ducas, Theodore W. 155
 Duchnowski, Paul 293
 Durlach, Nathaniel I. 293, 302, 304, 307, 313
 Dwarf stars 218
 Dynes, Scott B.C. 319, 324

E

Ear 319—327
 See also Hearing
 Cochlear efferents 324, 325
 Cochlear implants 303, 326
 Cochlear mechanisms 321
 External 319
 Middle-ear 319, 324
 Stapedius 324
 Vestibular system 325
 Ecklund, P. 78
 Eddington, Donald K. 293, 303, 319, 326, 327
 Ehrenrich, Victor 15, 16
 Ehrlich, Daniel J. 275, 276
 Ekstrom, Christopher R. 155, 163
 Electric charge conservation 171
 Electric charge quantization 171
 Electromagnetics
 Superconducting transmission lines 209

Electronic conduction models 119
 Electronic devices
 Quantum dots 39, 45
 Semiconductors 47
 Single electron transistors 41
 Superconductors 109
 Electronic materials
 Field-effect transistors 19
 Focused ion beam lithography 31
 Heterostructures 19
 InGaAs 19
 InP 19
 Quantum heterostructures 7
 Semiconductors 25, 47, 77
 Submicron structures 47
 Ultrafast phenomena 81
 Elfadel, Ibrahim M. 227, 235
 Ellithorpe, John D. 215, 217, 218
 Elman, B. 12
 Energia Nucleare e Energie Alternative (Italy) 192
 Englade, Ronald C. 192
 Eshghi, Kamyar 227, 234
 Espy-Wilson, Carol Y. 281
 Etchin, Sergey 31, 32, 33
 Eugster, Cristopher C. 47, 57, 61, 110
 Ewe, Hong-Tat 203, 206, 207
 Ezekiel, Shaoul 145—153

F

Faas, Michael 39
 Falicov, Alexis 119
 Fang, Hao 54
 Farber, D. 100
 Feenstra, R.M. 124
 Ferrera, Juan 47, 48, 51, 62
 Fiber optic gyroscopes 151
 Fiber optics 72
 Fieguth, Paul W. 215, 219, 220
 Fischer, Gregory T. 247
 Fisher, Philip A. 25
 Fitzgerald, Edward W. 175, 198
 Fleischer, Dorothy A. 227
 Fleischer, Siegfried B. 71, 78
 Fleming, Robert C., Jr. 47, 48, 65
 Fletcher, André B. 215, 216
 Focused ion beams
 Implantation 31
 Lithography 31
 Fonstad, Clifton G., Jr. 7—18, 62, 74, 114
 Ford, Darlene J. 71
 Forney, David 263

Foxman, Ethan B. 41
 Frankel, Robert 51
 Free electron lasers 175
 Freeman, Dennis M. 319, 321
 Freyman, Richard L. 293
 Frisbie, Joseph A. 293
 Frishkopf, Lawrence S. 319
 Fuchs, Eric M. 293, 307
 Fuchs, Vladimir 175, 181
 Fujimoto, James G. 7, 71, 79—90
 Fullerenes 78
 Fusion 192

G

Gafney, Kerry L. 175
 Gage, Deborah A. 255
 Gaidos, Eric J. 215
 Gale, Donna L. 71
 Gantela, Swaroop 293
 Garcia, Edouard A. 109
 Genosensor technology 275
 Geophysics 256
 GESTALT 247
 Ghanbari, Reza A. 47, 48, 51, 58, 61
 Ghosh, Rajashi 293
 Gloss, David S. 175, 192
 Gold, Bernard 255, 262
 Goldhor, Richard S. 281
 Goldish, Andrew C. 293
 Goldman, Daniel I. 171
 Goldman, Susan L. 293
 Golubovic, Boris 103, 107
 Goodberlet, James G. 71, 90, 92
 Gosalvez, David B. 127
 Grant, Andrew H. 293
 Grant, Kenneth W. 293
 Gravitational lenses 217
 Einstein rings 215
 Gray, Matthew K. 215, 217
 Graybeal, John M. 63
 Green, Thomas J., Jr. 103
 Greenberg, Julie E. 293, 302
 Griffith, Mark R. 215, 216
 Grot, A. 13
 Gu, Qizheng 203, 207, 371
 Guinan, John J., Jr. 319, 324, 325, 371
 Guiod, Peter C. 281
 Gulati, Rogeeve J. 293, 309, 311
 Gupta, Nitin 47, 53, 66
 Gupta, Rajesh K. 109, 112, 293
 Gyroscopes
 Fiber optic 151

Gyroscopes (*continued*)
 Laser 145

H

Hagelstein, Peter L. 71, 90—102
 Hailes, Darby A. 293
 Hajjahmad, Ibrahim A. 263, 265
 Hakkarainen, J. Mikko 227, 230
 Hall, Katherine L. 71, 75
 Hall, Seth M. 281, 293, 319
 Halle, Morris 281, 331—336
 Hammond, Troy D. 155, 163
 Han, Hsiu C. 203, 206
 Handicapped individuals 307
 Hands 307
 Fingers 309
 Sensorimotor functions 313
 Touch 309
 Hanson, Helen M. 281
 Hardwick, John C. 263, 267
 Harring, Debra L. 263
 Harris, John G. 227
 Harvard University 15, 16, 313
 Hashimoto, Akikazu 71, 98, 100
 Haus, Hermann A. 7, 10, 30, 63, 71—75
 Hay, Todd A. 175
 Haynes, Tony E. 32
 Heard Island Feasibility Test 256
 Hearing 293—315, 319—327
 See also Ear
 Binaural 304
 Hearing aids 293—304
 Cochlear prostheses 303
 Hearing-impaired individuals 282, 284, 293—315, 326
 See also Ear
 Tactile aids 293, 304
 Hector, Scott D. 47, 53
 Hedgcock, John M. 293
 Hee, Michael R. 71, 85
 Heflin, Michael B. 215, 216
 Hegarty, Michael V. 331
 Held, G.A. 124
 Held, Richard M. 293, 307
 Hemmer, Philip R. 145
 Hermann, Frederick P. 227
 Herold, Lori K. 215, 216
 Herrmann, Frederick P. 233
 Hewitt, Jacqueline N. 215, 217—218
 Heytens, Michael L. 247
 High-Definition Television 263—267, 269

Hillman, Robert E. 281, 285
 Hirayama, Yuzo 7, 8, 9, 71, 77
 Ho, Easen 25
 Holley, Jeffrey R. 155
 Hollis, Mark A. 275, 276
 Holmberg, Eva B. 281
 Holographic lithography 47
 Hong, Albert G. 293
 Hopps, J.H. 10
 Horn, Berthold K.P. 227, 229, 231, 232, 233, 234, 235, 237
 Horowitz, David M. 281
 Hoshino, Isako 7, 17
 Hoston, William C., Jr. 119, 120
 Hou, Mary A. 293
 House, Jody L. 25
 Howe, R. 313
 Hsu, Chih-Chien 203, 206, 207
 Hu, Hang 47, 54
 Hu, Qing 8, 14, 109—116
 Hu, Wen 175
 Huang, Caroline 281
 Huang, David 71, 79, 85
 Huang, Gregory T. 203, 206
 Hugunin, James J. 47
 Hui, Elliot E. 109
 Hultgren, Charles T. 71, 76
 Human-machine Interfaces 306
 Hunter, Wendy E. 215

I

IBM Corporation 50, 123
 Thomas J. Watson Research Center 47
 Idsardi, William J. 332
 Ignitor-Ult experiment 192
 Image processing 229, 255—262, 263—267
 Induced stochasticity and chaos 181
 Integrated circuits 31, 47, 227—245
 Computer-aided design 227, 247
 Computer-aided fabrication 247
 Custom 227—245
 Fault tolerance 242
 Process flow representation 247
 Reliability 242
 Vision chip designs 229
 VLSI 7, 11
 Interferometry
 Atom wave 163
 Ions 161
 Ippen, Erich P. 7, 8, 30, 71, 72, 75—79, 81
 Isabelle, Steven H. 255, 258

Ismail, Khalid 47, 66
 Iwai, Kyle K. 247, 263, 264
 Izatt, Joseph A. 71, 79, 85

J

Jachner, Jacek 255, 258
 Jacobson, Brian R. 109
 Jacobson, Joseph M. 71, 79
 Jandura, Louise 293, 311, 313
 Jarrell, Joseph A. 171
 Jerby, Eli 175
 Jha, Pallavi 175
 Jiao, Hong 155, 158
 Joannopoulos, John D. 131
 Joffe, Michael A. 155, 166
 Johnson, Joel T. 203, 206
 Johnson, Mark A. 281
 Joint European Tokamak 192
 Joneckis, Lance G. 103
 Jones, R. Victor 15, 16
 Jordan, Arthur 203

K

Kahn, Jalil 71
 Kamon, Mattan 227, 240, 241
 Kang, Joseph H. 203
 Karam, Nasser 66
 Kärtner, Franz X. 71, 73
 Kastner, Marc A. 41
 Katz, Charles A. 215, 217
 Katz, Daniel 145
 Kaushik, Sumanth 71, 90, 96, 98
 Kazior, T.E. 33
 Keagy, Michael T. 293
 Keast, Craig L. 227
 Ketterle, Wolfgang 155, 166
 Keyser, Samuel J. 281
 Khatri, Farzana I. 71, 73
 Khohayting, Jerome S. 203, 207
 Kiang, Nelson Y.S. 319
 Kierstead, John D. 145
 Kim, Che Y. 203
 Kim, Jason S. 109
 Kim, M. 16
 Kim, Songmin 227, 241
 Kim, Sue O. 281
 Kinaret, Jari M. 45
 King, Barbara A. 103, 109
 King, John G. 171—172

Kleppner, Daniel 155—161, 371
 Knecht, Wolfgang G. 293
 Knight, Thomas F., Jr. 233
 Koehnke, Janet D. 293, 304
 Kolodziejski, Leslie A. 25—30, 63, 74, 371
 Kondo effect 45
 Kong, Jin Au 203—209
 Kopf, Cynthia Y. 71
 Koshida, Nubuyoshi 47
 Kotik, Jack 293
 Ku, Yao-Ching 47
 Kubo, Miori 332
 Kumar, Arvind 47, 57, 203

L

Lai, Kit-Wah F. 203
 Lai, Yinchieh 73
 Lam, Cheung-Wei 203, 206, 210
 Lam, Warren M. 255, 259
 LaMotte, R.H. 310, 312
 Lane, Harlan 281, 285
 Lasers 7, 10, 12, 71, 75
 Diode 83, 106
 Femtosecond 77, 79, 81
 Fiber optic 72, 145, 151
 Free electron 175
 Medical 85
 Quantum dot diode 97
 Semiconductor 74
 Solid-state 79
 Solid-state far infrared 114
 Ultrafast 76, 81
 Ultrashort 79, 85
 Wave-guides 75
 X-ray 90
 Lau, Suzanne D. 103, 107
 Lauritzen, Lisbeth N. 71
 Lawrence Livermore National Laboratory 192
 Leary, Michael H. 19
 LeBlanc, Cindy 263
 Lee, David S. 25
 Lee, Dicky 103, 105
 Lee, Eddie F. 263, 265
 Lee, Hae-Seung 227, 229, 231, 235
 Lee, Harry B. 258
 Lee, Hongsing 203, 206
 Lee, Jae-Jin 7
 Lee, Jean Q. 281
 Lee, Laurence H. 203, 210
 Lee, Patrick A. 45—46
 Lee, William K. 203

Lee, Zachary K. 109, 114
 Leeb, Steven B. 227, 239
 Lenz, Gadi 71, 75, 77
 Lew, Julie C. 47, 65
 Lezec, Henri J. 31, 32
 Li, Huiying 47
 Li, Kevin 203, 206
 Li, Peggy 281
 Li, Yulin 127
 Liao, Stan Y. 227, 242
 Lim, Harold H. 203
 Lim, Jae S. 263—268
 Lim, Kuo-yi 25
 Lim, Michael H.Y. 47, 48, 293
 Lin, Charles P. 71, 85
 Linden, Derek S. 203
 Linguistics 331—336
 Liu, Sharlene A. 281
 Liu, Yong 203, 207
 Locke, John 281
 Lohman, Thomas J. 247
 London, Adam P. 171
 Lorusso, Catherine 175
 Love, Nicole S. 247
 Lu, Henry Y. 281
 Lu, Kan 25
 Lum, David S. 293
 Lumsdaine, Andrew 227, 234, 238
 Luongo, Eleanora M. 293
 Lutwak, Robert P. 155
 Lynch, James F. 259
 Lyons, W. Gregory 210
 Lyubomirsky, Ilya 71, 73

M

Ma, Kristine W. 47
 Ma, Sandra Y. 293
 Macmillan, Neil A. 293
 Maddieson, Ian 284
 Mahoney, Leonard J. 32
 Makhoul, John I. 281
 Manning, Deborah S. 269
 Manuel, Sharon Y. 281
 Manufacturing processes 219, 220
 Marine mammal communication 257
 Marjanovic, Matthew J. 155, 161
 Martin, Alexander 155, 166
 Martin, David R. 227, 235
 Martin, Gregory R. 293
 Martin, Paul S. 7, 10, 74
 Martinez, Donna R. 31, 47

Masaki, Ichiro 227, 229, 235
 Massachusetts Eye and Ear Infirmary
 Voice and Speech Laboratory 285
 Massey, Noel S. 281
 Mastovsky, Ivan 175
 Matthies, Melanie L. 281, 371
 Matusis, Alexander 175
 Maxwell, Joseph A. 293
 McCaffery, Elizabeth M. 123
 McCue, Michael P. 319, 325
 McIlrath, Michael B. 247, 250, 251
 McMahon, Pauline 215, 217
 McQuirk, Ignacio S. 227, 231, 234
 Meade, Robert D. 131
 Mecozzi, Antonio 71, 73
 Meirelles-Filho, Cesar 175, 192
 Melcher, Jennifer R. 319
 Melngailis, John 31—35, 275, 276
 Merchant, Saumil 320
 Mermelstein, Michael S. 171
 Mervis, Juliet 145
 Meskoob, B. 16
 Messier, Mark D. 215, 217
 Metal surface studies
 Chemical reactions 127
 Frustration 119
 Phase transitions 119, 123
 Semiconductors 119, 123, 131
 Structural analysis 123
 Mewes, Marc O. 155, 166
 Meyerson, Bernard S. 63
 Microfabrication 275
 Microwaves
 Atmospheric studies 218, 219
 Middle-ear
 See Ear
 Migliuolo, Stefano 175, 192
 Mikkelsen, Chad H. 47
 Mikkleson, J. 11, 12
 Minami, Tadatsugu 7
 MIT Artificial Intelligence Laboratory 311
 MIT Center for Electromagnetic Theory and Appli-
 cations 203
 MIT Center for Materials Science and
 Engineering 77
 MIT Center for Space Research 65
 MIT Department of Mechanical Engineering 311
 MIT Integrated Circuits Laboratory 31, 47, 48, 74,
 247
 MIT Lincoln Laboratory 84, 109, 110, 205, 255,
 275
 MIT Microsystems Technology Laboratories 31,
 114, 275
 MIT Microwave Temperature Sounder 219

MIT Photonic Semiconductors Laboratory 74
 MIT Submicron Structures Laboratory 8, 47—68
 MIT Technology Research Laboratory 248
 MIT-Green Bank survey 215
 MIT-Woods Hole Oceanographic Institution Joint
 Program 255
 Mochrie, Simon G.J. 123, 137—140
 Moel, Alberto M. 47, 51
 Moldoveanu, Michael C. 175, 181, 203, 206
 Moltmann, Friederike 333
 Mondol, Mark K. 47, 48
 Monta, Peter A. 263, 264, 266
 Monteiro, Jose C. 227, 242
 Moolji, Akbar A. 19
 Moon, Euclid E. 47
 Moore, Christopher B. 215, 217, 218
 Moores, John D. 71
 Morgenthaler, Ann W. 71, 94
 Mou, Alex 203
 Mueller, Jason 293
 Muendel, Martin 71, 90, 93, 100
 Murasugi, Kumiko 334
 Music
 Mathematical models 262
 Musicus, Bruce R. 255
 Musil, Christian R. 31, 32

N

Nabors, Keith S. 227, 241
 Nadeau, Philip P. 293
 Nadelski, Mark T. 293
 Nadol, Joseph B. 303
 Narula, Aradhana 263, 266
 Nassi, Giulia Arman 281
 Nassi, Marco 175, 192
 Natarajan, Vasant 155, 161
 National Nanofabrication Facility 164
 National Radio Astronomy Observatory 216
 National Synchrotron Light Source 123, 137
 Nee, Phillip T. 103, 105
 Nelson, Lynn E. 71, 72
 Netz, Roland R. 119, 121
 Neutrality of matter
 Electrical limits 171
 Nicolas, Julien J. 263, 267
 Nilsen, Mark R. 319
 Njeru, James M. 255, 259
 Noh, Do-Young 123
 Noise cancellation 260
 Nonlinear waves in plasmas 181
 North, D. Keith 281

Northeastern University 285
 Noyer, Robert R. 334
 Nuttall, William J. 123
 Nuytkens, P. 12, 14

O

O'Neill, Kevin 203
 Oates, Daniel E. 210
 Oates, John H. 203, 206
 Oceanography 256
 Odoardi, Angela R. 7, 19, 25, 203
 Ogno, Alexa 293
 Ohkawa, Hana 175, 192
 Olster, Daniel B. 47
 Oppenheim, Alan V. 255—262
 Optical coherence tomography 87
 Optical communication 103—106, 107
 Devices 7—18
 Squeezed states 103
 Optical frequency 105
 Division 105
 Synthesis 105
 Optics 71—102
 Amplifiers 75
 Fiber 72, 73
 Integrated guided-wave 107
 Order-disorder phenomena 137
 Orlando, Terry P. 57, 58, 61, 203, 209—212, 227, 241
 Osgood, Gene T. 227, 237
 Ostendorf, Mari 282

P

Paine, Scott N. 155
 Pan, Charlie C. 293
 Pan, Janet L. 71, 94, 97
 Pang, Lily Y. 71
 Papadopoulos, Haralabos C. 255, 260
 Park, Sang H. 25
 Patel, Prashun R. 293
 Paye, Jérôme M. 71, 77
 Payton, Karen L. 293
 Peake, William T. 319, 320
 Pedersen, Torstein 281
 Pelly, J. David 155, 166
 Peng, Lung-Han 7, 15, 16
 Penn, Gregory E. 175, 192
 Perilli, Richard R. 7
 Perkell, Joseph S. 281, 371

Perreault, Brian M. 255, 260
 Peterson, Patrick M. 293
 Petrich, Gale S. 25, 74
 Pheiffer, Brian K. 103, 107
 Phillips, Joel R. 203, 209, 227, 241
 Phillips Laboratory 192
 Pickelsimer, Lisa A. 227
 Plasma Physics 175—199
 RF heating and current drive 181
 Thermonuclear plasmas 192
 Poh, Soon Y. 203, 206
 Polley, Michael O. 269
 Poort, Kelly L. 281
 Porkolab, Miklos 175, 198
 Porter, Jean P. 47
 Portnoy, Vladislav 175, 192
 Power, Matthew H. 293
 Prasad, Sheila 7, 16
 Preisig, James C. 255, 259
 Prentiss, Mara G. 145
 Price, Patti 282
 Princeton University 61, 192
 Pritchard, David E. 65, 155, 161—169
 Psaltis, D. 13
 Pullman, David P. 127
 Puria, Sunil 319, 320

Q

Quantum dots 39, 45, 61, 97
 Quantum studies
 Optics 103
 Quantum wires 61
 Quataert, Eliot J. 155, 163

R

Rabinowitz, William M. 293, 302, 303, 304, 307, 319, 326, 327
 Radar 256
 Radio astronomy 215—221
 Very large array (VLA) 215
 Very long baseline interferometry 218
 Rahmat, Khalid 227, 238, 239
 Ram, Abhay K. 175, 181
 Ramaswamy, Malini 71, 79, 81
 Ramstad, Monte J. 123
 Rankovic, Christine M. 293
 Rappe, Andrew M. 131
 Rathman, Dennis D. 275, 276
 Rediker, Robert H. 103, 106, 107

Reed, Charlotte M. 293, 304
 Reichelt, Mark W. 227, 234, 238
 Reisman, Charles A. 293
 Remote sensing
 Renormalization-group theory 119
 Ricci, Kenneth N. 175
 Richard, Michael D. 255, 261
 Riconda, Caterina 175, 192
 Rider, Todd H. 175, 192
 Rigopoulos, Alexander P. 293
 Ringo, Carol 281
 Rittenhouse, George E. 47, 63
 Robot systems
 Mechanics 313
 Rogalla, Horst 113
 Rogers, Barrett 175
 Roman, Barbara A. 203, 207
 Ronan, Diane E. 293
 Rooks, Michael 57
 Rosenhagen, Kerry D. 103
 Rosenkranz, Philip W. 215, 218, 219
 Rosenthal, Stanley J. 171
 Rosowski, John J. 319, 320
 Royter, Yakov 7, 10
 Rubin, Brian A. 293
 Rubin, Leonard M. 203
 Rubinstein, Jay T. 319, 326

S

Sakamoto, Makoto 255
 Salisbury, J. Kenneth 313
 Sandhu, Sumeet 293
 Sang-hun, Song 61
 Santiago, Sally C. 255
 Schaeffer, Roeland P. 281
 Schattenburg, Mark L. 47, 48, 51, 65, 66
 Scherrock, Stephen F. 255, 262
 Schmidt, Martin A. 227, 240
 Schmiedmayer, H. Joerg 155, 163
 Schreiber, William F. 269
 Schultz, Steven D. 175, 181
 Schwartz, Michael J. 215, 219
 Sciutto, Giampiero 263
 Seidel, Mark N. 227, 233, 236
 Selph, James F. 293
 Semiconductor surface studies 119, 123, 131
 Semiconductors 25
 Compound 19
 Sensory aids 326
 Sensory communication 293—315
 Senturia, Stephen D. 227, 240

Shah, Satyen N. 47, 53
 Shahriar, M. Selim 145
 Shao, Michael 215, 216
 Shao, Yun 293, 307
 Shapiro, Jeffrey H. 103—106
 Shattuck-Hufnagel, Stephanie R. 281
 Shatz, Lisa F. 319, 321
 Shayegan, M. 61
 Shen, Amelia H. 227, 242
 Shenoy, Krishna V. 7, 11, 12, 13
 Shepard, Scott R. 103
 Shin, Robert T. 203, 206, 207
 Shinn-Cunningham, Barbara G. 293, 307
 Shirasaki, Masataka 71, 73
 Siebert, William M. 319
 Signal processing 7, 221, 255—262, 263—268,
 282, 326
 Chaotic systems 257, 258, 260, 261
 Mathematical models 261
 Noise 260, 262
 Noise cancellation 262
 Speech 262
 Videos 264
 Silicon surfaces 137
 Silitch, Alexis P. 155, 166
 Silveira, Luis M. 227, 239, 240
 Singer, Andrew C. 255, 261
 Single electron transistors 41
 Sisson, Robert D. 47
 Sloan, Kelly D. 335
 Smet, Jurgen H. 7, 8, 14, 109, 114
 Smith, Clare F. 215
 Smith, Henry I. 7, 8, 30, 47—68, 74
 Smith, Stephen P. 145
 Smullin, Louis D. 100
 Sodini, Charles G. 227, 229, 233, 234, 235
 Solid-state far-infrared lasers 114
 Sosonkina, Jane 31, 34
 Speech communication 281—289, 304
 Tactile 304
 Speech intelligibility 293
 Speech physiology 282—289
 Speech processing 267—268
 Enhancement models 268
 Vocoders 267
 Speech reception 293—315
 Speechreading 293, 299, 304
 Squire, Jared P. 175, 198
 SRI International 282
 Srinivasan, Mandayam A. 293, 304, 307, 309,
 311, 313
 Stadler, Robert W. 293, 302
 Staelin, David H. 215, 218—221
 Standard model 171

Stannite 119
 Stefanov-Wagner, Frank J. 319
 Steffens, David A. 319
 Stein, Gideon P. 227, 234
 Stellmach, Timothy J. 293
 Stevens, Kenneth N. 281—289
 Stollerman, Anne 127
 Stoner, Richard E. 175
 Stroock, Abraham D. 155, 161
 Su, Lisa T-F. 47
 Sugiyama, Linda E. 175, 192
 Sun, Chi-Kuang 71, 81, 84
 Sun, Jie 215, 217
 Sun, Ke-Xun 103
 Sunshine, Lon E. 263, 267
 Superconducting Josephson Devices 112
 Superconducting transmission lines 209
 Superconductors 109
 Surface structure 137
 Svirsky, Mario A. 281
 Synthetic aperture radar 256
 Szafer, Aaron 39

T

Tactile communication 304, 313
 Takeuchi, Annie H. 293, 300
 Tamura, Kohichi R. 71, 72
 Tan, Chin Hwee 227
 Tan, Hong Z. 293, 304
 Tancredi, Christopher D. 335
 Tannian, Bridget E. 155, 163
 Tassoudji, M. Ali 203, 206, 207
 Technology computer-aided design 247
 Telecommunications 19
 Teleoperators 313
 Television research
 High-Definition 263, 267, 269
 Telichevsky, Ricard 227, 240
 Thin films 123
 Thompson, Carl V. 31, 34
 Tierney, Joseph 319, 326, 327
 Ting, Leon L. 293
 Tokamaks 192
 Versator II 198—199
 Touch 311
 Toudeh-Fallah, Farzam 47
 Trautman, Theodore R. 127, 128, 129
 Troxel, Donald E. 247
 Tsekouras, Athanassios A. 127
 Tso, Katherine 203, 207
 Tsui, Daniel 61

Tsuk, Michael 203
 Tuyu, Michael T. 293
 Twente University (The Netherlands) 112
 Two-dimensional phase transformations 137

U

U.S. Navy
 Naval Research Laboratory 50, 72
 Office of Naval Research 313
 Uchanski, Rosalie M. 293
 Ugarov, Andrew 293
 Ulman, Morrison 71, 79
 Umminger, Christopher B. 227, 233
 Underwater acoustics 256, 257, 259
 University of California at Los Angeles
 Department of Linguistics 284
 University of Kentucky 78
 University of Massachusetts at Amherst 256
 University of Southampton 72
 University of Texas 192
 University of Wisconsin
 Center for X-ray Lithography 33
 Upshaw, Bernadette 281
 Utz, Arthur L. 127, 128, 129

V

Vacca, Luigi 175, 181
 Vallee, Fabrice 71, 81
 Van Aelten, Filip J. 227, 242
 van der Zant, Herre S.J. 203, 209, 227, 241
 Verbout, Shawn M. 255
 Verly, Jacques 256
 Veysoğlu, Murat E. 203, 206
 Videos 264
 Vignaud, Dominique 31, 32
 Villaseñor, Jesus Noel 175, 198
 Virtual-environment systems 313
 VLSI 229
 Volfbeyn, Pavel S. 175

W

Wage, Kathleen E. 255, 256
 Wang, Janet 281
 Wang, Jing 131
 Wang, Li-Fang 203, 206, 207
 Wave propagation 256
 Weather satellites 218, 219

Wee, Susie J. 269
 Wei, Min 293, 307
 Weinstein, Ehud 255
 Weisner, Jerome B. 371
 Weiss, Thomas F. 319—327, 371
 White, Jacob K. 209, 227, 229, 234, 238—242
 Wilde, Lorin F. 281
 Williams, David 281
 Wind, Shalom 41
 Wint, Arlene E. 281
 Wong, Ngai C. 103, 105
 Wong, Taylen J. 255
 Wong, Vincent V. 47, 48, 51, 62, 63, 74
 Woo, Albert R. 247
 Woods Hole Oceanographic Institution 255, 256, 257
 Wornell, Gregory W. 255, 259, 260
 Wozniak, Jane 281
 Wozniak, Jennifer 293
 Wright, Alan 215, 216
 Wurtele, Jonathan S. 175
 Wu, John J. 155, 166
 Wyatt, John L., Jr. 227, 229—238
 Wyss, Rolf A. 109, 110

X

X-ray lithography 47
 Xia, Jiqing 203, 206
 Xu, Rongqing 203
 Xu, Xin 31, 34

Y

Yale University
 School of Medicine 310, 312, 313
 Yamaguchi, Masanori 203
 Yang, Julius J. 127
 Yang, Y. Eric 203, 206, 207
 Yao, Shih-Jih 203
 Yee, Kenneth 47, 61, 66
 Yen, Anthony 47
 Yesley, Peter 155
 Yiu, Elaine C. 203, 207
 Yoo, Chang Dong 263, 268
 Yu, Paul C. 227, 231
 Yu, Peter T. 103
 Yu, Ross A. 293
 Yuan, Yi 203
 Yuille, Alan 235
 Yuksel, Ayca 25

Z

Zakharov, Leonid E. 175, 192
 Zangi, Kambiz C. 255, 262
 Zarinetchi, Farhad 145
 Zhao, Yang 47, 61
 Zheng, Q. 100
 Zhu, Meng Y. 319
 Zinblende 119
 Zissman, Marc A. 319, 326, 327
 Zue, Victor W. 293
 Zurek, Patrick M. 293, 302, 304